Aerodynamics of Asymmetrical Land Speed Record Vehicles

By

Kevin Clemens

A thesis presented for the Degree of

Doctor of Philosophy

at

The University of Canterbury

Department of Mechanical Engineering

Christchurch, New Zealand

September 2017

Abstract

Although current market penetration of battery electric cars is low (0.1% worldwide), it is rapidly growing as the advantages of electric vehicles (EV) in reduced pollution, CO_2 emissions and lower operating costs overcome their higher initial purchase price. As battery systems carry far less energy than traditional liquid fuels, EVs face challenges to maximize efficiency to achieve acceptable performance and range. One way to enhance EV efficiency is to reduce aerodynamic drag.

In racing, the goal is to achieve maximum performance for a given available energy, which provides a laboratory to study vehicle system optimization. This is especially true for land speed racing where the singular aim is to safely achieve the highest possible speed on a long, closed course, for example the Bonneville Salt Flats in Utah. The goal in this form of racing is to minimize aerodynamic drag while maintaining dynamic stability.

In this work, aerodynamic, rolling resistance, and tractive forces and moments were examined for an asymmetrical land speed record vehicle through computational fluid dynamics (CFD) studies and the analysis of the equations of motion. Validation of CFD technique was performed by comparison of numerical results to published drag and lift, velocity profile, and flow topology of a 25° and 35° Ahmed body using Reynolds Averaged Navier-Stokes (RANS) turbulence models (25° and 35° Ahmed body) and Large Eddy Simulation (LES) (25° Ahmed body). RANS simulations were found to predict C_d (-1.4% of published values) and C_l (+2.3% of published values), while LES was less successful for C_d (+8.4%), and C_l (-11.6%). Both methods predicted velocity profiles and wake structures well.

Studies were undertaken to characterize the dynamic and aerodynamic stability of a bluff-body four “wheel” (Ahmed Body) vehicle and a two-wheel streamlined electric land speed record motorcycle. The Ahmed body was found (from CFD) to have positive lift between 0° and 45° yaw angles, and then transition to negative lift (downforce) between 45° and 55° of yaw angle at a speed of 150 mph (67 m/s). The two-wheel streamlined motorcycle was found (from CFD) to create lift greater than the vehicle weight at yaw angles greater than 50° at 150 mph (67 m/s) and at yaw angles greater than 20° at speeds of 250 mph (112 m/s), the design speed of the vehicle. The addition of a longitudinal, dorsal “shark fin” was found to reduce this lift to below the vehicle weight even at a yaw angle of 90° at a speed of 150 mph (67 m/s).

Three-dimensional computational fluid dynamics (CFD) simulations were also used to characterize and enhance the aerodynamic performance of an electrically-powered racing sidecar. From the starting point of a Solidworks model from the laser-scan of an existing road-racing sidecar motorcycle, an extensive optimization program using ANSYS Fluent 17.0 (CFD), with 6-10 million-element, unstructured, tetrahedral meshes and a RANS turbulence model, was undertaken. Compared to the original starting point, the optimised sidecar CFD results indicated

a 24.4% reduction in C_d, a change in C_l from +0.0026 (lift) to -0.255 (downforce). Lateral force coefficient (C_Y) was reduced 11% compared to the original sidecar. From visualisations of the flow topology, large streamwise vortical structures originating from the shoulder regions of the rider were found to be the most significant sources of aerodynamic drag. Other parts of the sidecar body also produced streamwise vortices that contributed to pressure drag. Negative lift (downforce) was found to result primarily from the formation of a primary vortex along the leading edge of the underside of the splitter at the front of the vehicle.

Based upon these results, a new body for the sidecar was fabricated from composite materials. The modified sidecar was successful, setting four FIM world land speed records and one U.S. national land speed record in electric sidecar motorcycle classes at the Bonneville Salt Flats in Utah, U.S.A. in August 2016. Further validation of the new sidecar bodywork was undertaken with testing in a full-scale wind tunnel facility.

The asymmetrical aerodynamic forces generated by the sidecar, predicted from CFD, were found by the rider to not create significant dynamic instabilities at high speeds. Dynamic stability analyses predicted cross winds would require minor steering corrections by the rider and were found to have different effects depending upon their direction due to the aerodynamic asymmetry of the vehicle. Pitch and roll moments were found to show asymmetries but were judged by the rider to be negligible in their effect on vehicle stability. The stability predicted from CFD and dynamic modelling was thus confirmed by the rider's experiences during successful land speed record attempts.

Acknowledgment

Dr. Mark Jermy is a unique polymath whose knowledge, experience and enthusiasm for an unusual research project and his willingness to mentor an atypical doctoral student has provided me with the opportunity of a lifetime. Simple thanks seem inadequate for his friendship, support and encouragement during my time at the University of Canterbury.

I would also like to recognize and thank Dr. Patrick Geoghegan for the many interesting discussions we have shared and for his assistance in revieweing this manuscript. I also appreciate the help of Bruce Robertson of the UC Mechanical Engineering department and his expertise in SolidWorks and Dr. John Sullivan of Purdue University whose land speed record efforts on electric motorcycles have continued to inspire me to always go faster.

I am ever grateful to my wife, Loree Kalliainen, who has not only supported my academic adventures halfway around the word but who is always an enthusiastic partner in my life. I would also like to recognize my parents, Helga and Conny Clemens, who instilled within me a thirst for knowledge and passion for education, my children, Jessica and Jeremy, and my grandson Daniel—I dedicate this work to all of you.

Contents

List of Figures

List of Tables

CHAPTER 1 INTRODUCTION

1.1 MOTIVATION FOR THIS RESEARCH

This thesis uses an electrically-powered sidecar motorcycle as an example for developing analysis tools for the study of the aerodynamics and dynamic stability of asymmetrical vehicles. Sidecar motorcycles, with their sidecar wheel offset from the inline front and rear wheels are highly asymmetrical. Because asymmetrical vehicles are uncommon, little published research is available on their dynamic characteristics and aerodynamic high-speed stability.

Of all forms of motor racing, land speed racing gives the widest scope for creative design. Through hundreds of classes covering two, three and four-wheel vehicles with a variety of engines and propulsion systems, "Land speed racing represents the ultimate in freedom, ingenuity and creativity for engineers and constructors," (Metz, 2004). The primary challenge in land speed racing is to maximise the propulsion forces created by the drive system and minimise the forces that resist motion, with a vehicle which is controllable and stable.

Electric land speed record vehicles also present a particularly interesting challenge as, compared to liquid-fuelled vehicles—they are able to carry only limited amounts of on-board energy in their battery systems. Increasing power requires an increase in mass greater than that for an equivalent combustion-driven vehicle. Thus, aerodynamic drag becomes an even greater factor for such electric vehicles. Optimizing aerodynamics for these vehicles also has implications for improved stability and fuel economy for street motorcycles and small urban vehicles for use in future transportation systems.

Aerodynamic drag consumes ever-increasing amounts of energy as a vehicle speed increases, becoming the dominant retarding force at speeds above 64 kph (40 mph) (Tamai, 1999). Reducing drag by optimizing the shape of the vehicle can be difficult. This is especially true for land speed record vehicles where the objective is to reach the highest possible speeds within a framework of national and international rules. Characterizing aerodynamic drag for a given vehicle configuration can be accomplished with on-road testing, by using scale models tested in a wind tunnel and with detailed computer models through Computational Fluid Dynamics (CFD) (Katz, 1995). To date, high-speed aerodynamic land vehicle research has only considered symmetrical vehicles.

While oval-track racing cars can be designed with asymmetrical suspension and aerodynamic setups to turn only one direction on specific tracks (the Indianapolis 500, for example), ordinary land vehicles have traditionally been developed with bilaterally symmetrical configurations. Although this has largely resulted from styling considerations, a requirement for symmetry was also derived from the need to package the driver, occupants, cargo and a traditional mechanical drivetrain.

With the advent of the electrification of transportation, replacing a single combustion engine with multiple smaller electric motors, the need for the drivetrain to be symmetrically located within the vehicle chassis is no longer paramount. Further, as designers explore the potential for comfort and human factors in driverless autonomous vehicles, the requirement for traditional symmetrical placement of vehicle seating may no longer exist.

The practical result of the research reported in this thesis was the development of modelling techniques to characterize the performance and stability of extremely low drag land vehicles (particularly electric), including those that may be highly asymmetrical in their configuration. The models developed here have a wider application for the development of modern electric vehicles, which is of increasing importance to the motor industry now and into the future.

1.2 AIMS AND OBJECTIVES

In 2014, the author competed at the Bonneville Salt Flats in Utah, U.S.A. with a Baker Formula One road-racing sidecar, modified with electric drive, to set an American Motorcyclist Association (AMA) U.S. national land speed record. The aim of this thesis in part is to examine the performance results of that 2014 sidecar design through physical vehicle testing and CFD studies and to produce an improved version to attempt to set an FIM world land speed record at Bonneville for unlimited (over 300 kg) electric sidecar motorcycles. In a broader sense, the main goal of this thesis is to establish a method for performance and vehicle stability predictions based upon modelling results and to characterize air flow over asymmetrical vehicle designs using the sidecar as a base analysis tool.

The objectives that will help achieve the aim of this thesis include:

- Predict electric sidecar land speed record performance by establishing a physical model of the land speed record sidecar tractive and resistive forces
- Examine dynamic and aerodynamic stability of a symmetrical bluff-body four-wheel vehicle and a two-wheel single-track aerodynamic streamliner
- Use dynamic and aerodynamic stability methods to examine three-wheel symmetrical trike and three-wheel asymmetrical sidecar motorcycle vehicles

- Validation of CFD techniques to provide a tool to study the aerodynamics of an asymmetrical sidecar.
- Undertake an aerodynamic optimization study to undertake modifications to the sidecar body to develop a lower drag configuration
- Fabricate new chassis and body panels in composite materials based upon the optimization study
- Test the full-scale modified vehicle on a chassis dynamometer, in a wind tunnel, and at a test track and compare results to predictions
- Set FIM world land speed records for unlimited electric sidecar motorcycles

1.3 THESIS STRUCTURE

This thesis is divided into eight chapters. Following this introduction, Chapter 2 is a historical and literature review of land speed record racing, three-wheel vehicle configurations, and computational fluid dynamics (CFD) to provide a background for the current investigations. Also included in Chapter 2 are a series of questions that the current work will seek to answer.

Chapter 3 describes the theory and some of the techniques used in CFD to model external air flow around a vehicle. Published results for aerodynamic forces, wake velocity profiles, surface shear stress lines, and wake topology for two Ahmed body configurations are compared to CFD simulations developed with ANSYS Fluent to validate the CFD approach.

Chapter 4 is an optimization study, using CFD to develop modifications to the existing sidecar to improve (reduce) aerodynamic drag and lift. The fabrication of new composite bodywork components is described in an appendix.

In Chapter 5, the results from testing at an airport runway, the results from the land speed record efforts at Bonneville, the data from chassis dynamometer testing and the results from a full-scale wind tunnel session with the actual sidecar are compared with predictions from physical modelling.

Chapter 6 examines dynamic stability of symmetrical vehicles by reducing the equations of motion to characteristic polynomials to establish criteria for stability. A four-wheel generic vehicle and a two-wheel single-track streamliner vehicle are used as computational examples. Aerodynamic stability in yaw is also examined for a symmetrical low-drag vehicle.

In Chapter 7, the results and techniques to establish stability from Chapter 6 are applied to the asymmetrical three-wheel sidecar land speed record motorcycle; dynamic stability and aerodynamic yaw, roll, and pitch stability and aerodynamic flow topology of the Baker sidecar are investigated.

Finally, Chapter 8 summarizes the work and draws conclusions about the effects of asymmetry on aerodynamic flow and the characterization of stability for land speed record vehicles. Suggestions for future studies and investigations in these areas are provided.

Author's note: Although SI units are used throughout this thesis, the traditional units for distance and speed reported in land speed racing are miles and miles per hour (mph), and thus will be used when appropriate.

CHAPTER 2 HISTORICAL AND LITERATURE REVIEW

2.1 A BRIEF HISTORY OF LAND SPEED RACING

The first official Land Speed World Record was set in 1898 by Gaston de Chasseloup-Laubat driving a Jeantaud electric car. His top speed of 39.24 mph (63.15 kph) in a standard production machine was improved upon in 1899 when he built a streamlined body for the car—this was probably the first ever attempt at improving the aerodynamics of an automobile. Later, while competing against Camille Jenatzy's electrically-powered *Le Jamais Contente,* (Figure 2.1), Chasseloup-Laubat's streamlined Jeantaud reached a speed of 57.65 mph (92.78 kph).

Figure 2.1- Camille Jenatzy with *Le Jamais Contente*

It would be Jenatzy's torpedo-shaped aerodynamic machine that was the first to break 100 kph, reaching a speed of 65.79 mph (105.88 kph) in 1899. As successful as these early electric automobiles were, the limitation with electric vehicles, then and now, was the amount of energy that could be carried in the battery. *Le Jamais Contente* would be the last electric vehicle to hold the "ultimate" land speed record—defined as the fastest vehicle regardless of power source.

For the next sixty years, the world record became the exclusive realm of petrol-engine cars, speeds gradually increasing with Malcolm Campbell the first to exceed 150 mph (242 kph) on a Sunbeam-powered machine in 1925. The next five years would see 200 mph reached (Henry Segrave in 1927), but also the deaths of Parry-Thomas, Bible, and Lockhart in cars that were all traveling at speeds nearing or exceeding 200 mph (322.6 kph) (Rose & Abrams, 2016).

2.2 AERODYNAMICS IN THE DESIGN

Problems associated with aerodynamic instability were recognized by both Henry Segrave and Malcolm Campbell. In 1928, each began building cars using wind tunnel scale model testing to better understand the aerodynamics of land speed record vehicles (Dacy, 1930). Segrave's *"Golden Arrow"* took the ultimate record in 1929 at 231 mph (372 kph). *Golden Arrow* featured a large tail fin and a low aerodynamic nose. Campbell's "*Bluebird"* set a record in 1931 at 246 mph (397 kph) and he continued to set records and refine his car with a larger tail fins (Figure 2.2) and smoother bodywork. He eventually raised the ultimate record to 301.13 mph (481 kph) in 1935 at the Bonneville Salt Flats in Utah (Campbell & Meech, 1988). Seagrave and Campbell both found that a tail fin helped move the centre of aerodynamic pressure significantly behind the centre of mass to promote stability in case of yaw.

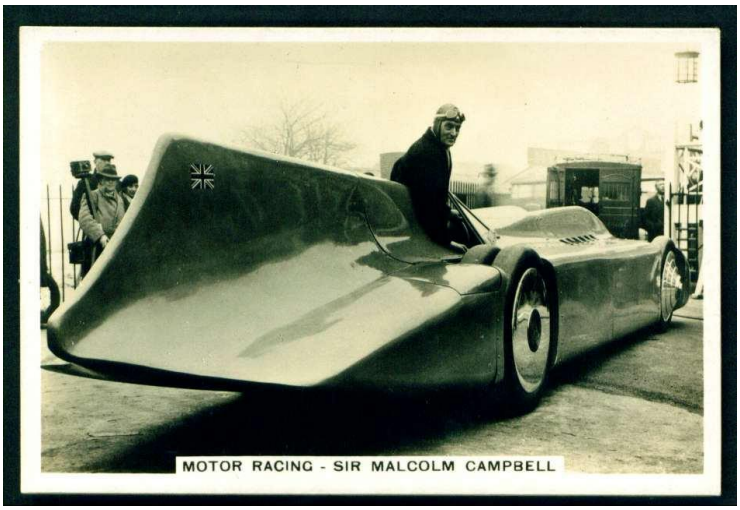

Figure 2.2- Sir Malcolm Campbell and *Bluebird*

2.3 THE BONNEVILLE SALT FLATS

More automobile speed records have been set on the Bonneville Salt Flats than any other place on Earth (White, 2006). Around 17,000 years ago Lake Bonneville covered 20,000 square miles of north western Utah and parts of Idaho and Nevada. Over time the lake level fell and collected sediments that made it extremely salty. The water levels dropped to the point that the surface water evaporates for several months every summer, leaving an immense expanse of smooth hard salt (Figure 2.3). As early as 1914, the salt flats were used to test how fast an automobile could go (Thawley, 1980). The first recognized world land speed record was set there by Campbell in his 301-mph run in 1935 (White, 2006).

Figure 2.3- Bonneville Salt Flats *(author)*

Several organizing bodies promote racing on the salt flats in the summer and early fall when the salt dries out and becomes hard enough to drive upon. The Bonneville Motorcycle Speed Trials (BMST) occurs at the end of August—an event exclusively for motorcycles where it is possible to set US national records ratified by the American Motorcyclist Association (AMA) and world records ratified by the *Fédération Internationale de Motocyclisme* (FIM).

In general, two courses are created at the BMST for land speed record attempts at the motorcycle-only event. In general teams compete for records in the "flying" mile, where several miles are available to come to top speed. The "standing" mile is for the average speed with the vehicle at a dead stop at the beginning of the measured mile. The Mountain Course is five miles long with flying mile timing taking place between miles 3 and 4. The International Course length depends upon salt conditions but is typically 8 miles in length, with timing taking place between miles 3.5 and 4.5. To set a record requires two passes, in opposite directions on the same course, with the speeds through the one mile measured sections in each direction averaged. For AMA national records, the two passes must be within the same calendar day, for FIM world records the two passes must take place within two hours and an official FIM observer must certify any work done on the vehicle between runs.

2.4 TWO AND THREE WHEELS

The 1930s saw a great deal of activity in motorcycle speed records, including efforts by BMW with both solo and sidecar machines. In 1929, Ernst Henne rode his supercharged 750cc BMW (Figure 2.4) to 134 mph (216 kph), establishing BMW as the world's fastest motorcycle (Bacon, 1982). His effort was quickly overshadowed by Joe Wright, who rode a bespoke British machine to 150.4 mph (242.59 kph), becoming the first to break 150 mph on two wheels. Henne's BMW was also fitted with a sidecar which allowed him to take the sidecar record in 1931 at a speed of 119.3 mph (190.83 kph). Aerodynamic streamlining played a significant role in BMW machines, with wheel discs, torpedo-shaped fully-faired bodies, tail fins and aerodynamically shaped helmets (Bacon R. , 1982).

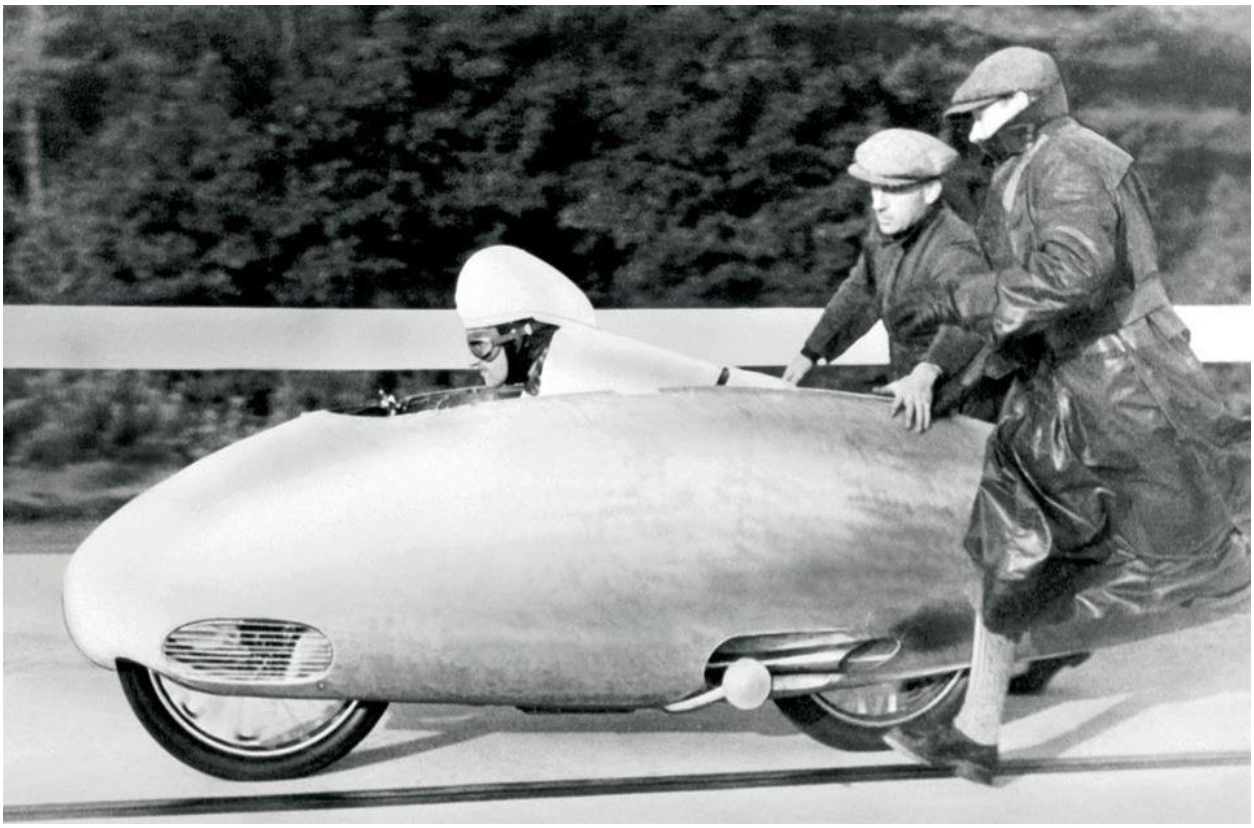

Figure 2.4- Ernest Henne with a supercharged BMW motorcycle *(BMW Motorad)*

In 1954, New Zealand motorcyclist Bob Burns set a record for sidecar motorcycles on a Vincent-powered streamlined machine that went 155.2 mph (250.3 kph) (Swanson & Spinks, 2007). The same machine, without sidecar, was used by fellow New Zealander Russell Wright to set a solo motorcycle record of 185.18 mph (298.7 kph). Both records were set on public roads in New Zealand's South Island.

NSU brought a variety of low aerodynamic drag motorcycles to the Bonneville Salt Flats in 1956 (Figure 2.5) with Willhelm Herz setting a 211 mph (340.3 kph) two-wheel top speed record

(Fisher, 2012). The aerodynamic NSU machines moved away from traditional motorcycles by introducing long low-drag projectile-like vehicles that would come to be called streamliners.

Figure 2.5- NSU streamlined motorcycle at Bonneville

The current two-wheel motorcycle streamliner land speed record stands at 360.913 mph (582.1 kph), set in 2008 at Bonneville by Rocky Robinson on *"Ack Attack"* (Figure 2.6) (Fisher, 2012).

Figure 2.6- *Ack Attack (Ack Attack)*

2.5 Electric Vehicles

Despite their initial dominance, electric vehicles had almost no visibility in the history of land speed racing for over 100 years. In 1968, the *"Lead Wedge"* driven by Jerry Kugel ran a speed of 138 mph (222 kph) to set a record for electric vehicles at Bonneville (Figure 2.7).

Figure 2.7- *Lead Wedge* electric vehicle (*Autolite*)

Through the 1970s and 1980s, several efforts moved the electric vehicle records higher with Ed Rannberg setting a record in 1997 at 201.703 mph (325 kph) in "*Lightning Rod"*, becoming the first to exceed 200 mph on electric battery power. Table 2.1 details significant land speed records set by electric vehicles.

Table 2.1: Significant Records by Electric Vehicles

Year	Vehicle	Driver	Speed (mph)	Notes/Class
1899	Jeantaud (FR)	Chasseloup-Laubat	57.6	First Land Speed Record
1899	Jamais Contente (FR)	Jenatzy	68.8	Official
1901	Riker Torpedo (USA)	Riker	57	Unofficial
1902	Baker Torpedo (USA)	Baker	100	Unofficial
1968	Lead Wedge (USA)	Kugel	138	Bonneville
1971	Silver Eagle (USA)	Reed	146.437	14 national 7 world records
1974	Battery Box (USA)	Headlund	174.918	
1997	Lightning Rod	Rannberg	201.703	
1999	White Lightning	Rammerfield	245.523	
2004	Buckeye Bullet 1		314.958	AMA National Record

2005	Honda	DeSimone	20.256	AMA Modified 300 kg Motorcycle
2007	Electrobike	Ingber	68.848	150 kg motorcycle
2010	Kawasaki	Carey	60.583	Sidecar 150 kg
2011	Kawasaki	Carey	50.407	Sidecar 300 kg
2011	Honda	Clemens	61.538	AMA Modified 150 kg
2011	Swigz	Yates	173.574	Altered 300 kg motorcycle
2011	Swigz	Yates	187.142	Partially streamlined 300kg motorcycle
2011	Swigz	Yates	181.439	Over 300 kg motorcycle
2011	Swigz	Yates	196.42	Partial streamlined over 300kg motorcycle
2011	KillaJoule	Hakansson	138.586	Streamliner sidecar over 300 kg
2012	Electric Ninja	Clemens	64.094	Unstreamlined 150 kg motorcycle
2012	Electric Ninja	Clemens	78.424	Partially streamlined 150 kg electric motorcycle
2013	Electric Conversion	Sullivan	114.488	Altered 150 kg motorcycle
2013	Electric Conversion	Sullivan	113.079	Altered partially streamlined 150 kg motorcycle
2013	Lightning	Hoogerhyde	203.361	Altered partially streamlined

				300 kg motorcycle
2013	Honda	Clemens	54.651	Sidecar 300 kg
2013	KillaJoule	Hakansson	212.047	Streamliner sidecar over 300 kg
2014	Electric Blue	Burkdoll	204.9	BYU 500 kg Streamliner automobile
2014	Baker Sidecar	Clemens	64.475	AMA: Sidecar over 300kg
2014	KillaJoule	Hakansson	240.726	Streamliner sidecar over 300 kg
2016	Baker Sidecar	Clemens	108.499	FIM: Sidecar over 300kg
2016	Baker Sidecar	Clemens	89.113	FIM: Unstreamlined Sidecar over 300 kg
2016	KillaJoule	Hakansson	248.674	FIM: Streamliner sidecar over 300kg

2.6 CHALLENGES FACED BY ELECTRIC VEHICLES

Land speed racing differs from most other forms of motor racing in that the primary goal is to achieve the highest possible speed while travelling in a straight line, over a course that can be more than 10 miles in length. In contrast, modern motor racing puts a premium on cornering performance and aerodynamic development has focused on dramatically increasing downforce (negative lift) to develop higher levels of cornering traction from the tyres. It is well established (Milliken & Milliken, 1995) that quicker lap times on a road course can result from high downforce, even at the expense of increased aerodynamic drag.

One reason that downforce has dominated aerodynamic considerations in racing is that petrol (and more recently diesel) fuels contain high power density allowing internal combustion engines to produce large amounts of power from the combustion of a relatively small amount of hydrocarbon fuel. Powerful internal combustion engines encourage aerodynamic packages that allow both high top speeds and prodigious cornering forces. Because petrol and diesel fuels have high specific energy and energy density, it is also easy to carry enough liquid fuel to travel significant distances.

The dramatically lower specific energy of storage batteries when compared to traditional liquid fuels (Table 2.2) requires racing designers of electrically powered vehicles to increase efficiency and reduce energy consumption wherever possible. The Formula E series racing cars, which are designed with high downforce aerodynamics, only carry enough on-board energy to cover half the race distance—drivers physically change cars to a fully charged one during the race. Intensive research into new chemistries is underway to increase the performance of batteries for electric vehicles (Gallagher, Ahmed, Nelson, & Dees, 2015).

Table 2.2: Specific Energy of traditional liquid fuels versus batteries

Energy Source	**Specific Energy WH/kg**
Gasoline	12,700
Diesel	11,600
Lead Acid battery	33-42
Ni Cad battery	40-60
Ni Metal Hydride battery	60-120
Ni Zinc battery	100
Lithium ion battery	100-265
Lithium Polymer battery	100-265
LiFePO4 battery	90-110
Lithium Sulphur	500
Lithium Air (theoretical)	11,140

Source: Greentransportation.info

It is reasonable to assume that as electric vehicle racing becomes more prevalent, the need for aerodynamic solutions with lower drag and lower downforce will result, requiring lower cornering speeds, but higher top speeds and a longer range with a given size of on-board energy storage. Solar vehicle racing provides an extreme example of ultra-high efficiency racing given the extremely low amounts of energy available from on-board solar cells. Solar racing cars have among the lowest aerodynamic drag of any road-going vehicle (Figure 2.8) (Tamai, 1999).

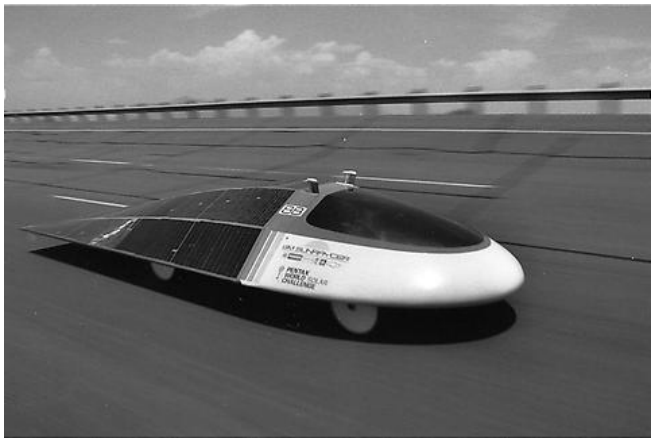

Figure 2.8- GM *Sunraycer (Smithsonian Institution)*

2.7 DYNAMIC AND AERODYNAMIC STABILITY OF A SIDECAR VEHICLE

The stability of two wheel vehicles is complex because they are unstable when standing still and may also be unstable in certain speed ranges. The presence of, and oscillation frequencies in, the unstable speeds ranges can be calculated from the Equations of Motion (Chapters 6 and 7). There are mathematical techniques to help examine the roots and their effects on stability.

The addition of a third wheel to the single-track vehicle raises entirely different stability questions. The additional wheel can be added so that it produces three tracks (a traditional tricycle with one front and two rear wheels, or a reverse tricycle with two wheels at the front and one at the rear). Three-wheel vehicles of this sort are usually symmetrical around a plane connecting the single front or rear wheel and at the midpoint between the other two wheels. Three-wheel trikes have been variously popular from the early 1910s to the present day where they provide a way to reduce rolling resistance for solar-powered racing vehicles. Analyses of symmetrical three-wheel tricycle type vehicles often follows the same approach as would be used in analysing four-wheel vehicles (Starr, 2006).

Instead of adding the third wheel in a plane to form a symmetrical tricycle, the wheel can also be added offset from the line connecting the front and rear wheels, like an outrigger, resulting in an asymmetrical sidecar vehicle. Although sidecar outfits have been in use nearly as long as motorcycles, there is almost no literature that examines the equations of motions or stability of an asymmetrical three-wheel vehicle. Lurie (2012) examined the directional stability of a sidecar negotiating a turn by developing linearized equations of motion. His analyses examined only the lateral forces resulting from the change in slip angle caused by cornering and did not consider the asymmetry of lateral and longitudinal forces created by asymmetrical geometry or aerodynamics. These asymmetries result in forces and non-zero yaw angles that occur even when the sidecar is traveling along a straight path.

A more complete development of dynamic stability equations, taking into account forces and moments resulting from geometric and aerodynamic asymmetries for a generic sidecar is one of the goals of the current research.

2.7.1 Asymmetric vehicle aerodynamics

As with the dynamic stability of an asymmetrical sidecar vehicle, the effects of airflow over geometrically asymmetrical vehicles has received little attention. In most cases, designers of land and air vehicles work with a well-defined plane of longitudinal symmetry with the primary goal of reducing or eliminating the generation of lateral forces and potential instabilities caused by different air flow paths over each side of the vehicle body. Generally speaking, the design with the lowest possible drag will be a symmetric body. Bulky components, where possible, are placed on the axis of symmetry to minimize moment of inertia and aerodynamic yaw forces. Cases do exist however, where asymmetry either cannot be avoided or becomes a feature of the vehicle design.

Immediately prior to World War II, the German aircraft firm Blohm und Voss (BV) designed and flew a single-engine prototype reconnaissance aircraft (called the BV141) that offset its passenger compartment onto the right wing (Figure 2.9). Its designer, Dr.-Ing Richard Vogt,

adjusted the size of the wings and tail structure to balance the forces and moments to produce an aircraft that was reportedly more stable in flight than a traditional symmetrical single-engine machine (Green, 1979).

Figure 2.9- Blohm und Voss BV141 asymmetrical aircraft *(Bundesarchiv)*

More recently, Reisenthel and Childs (Reisenthel & Childs, 2007) used computational fluid dynamics (CFD) to design an optimized payload fairing for a rocket launch vehicle. The payload in this case was a satellite with a large mirror that was twice the diameter of the launch vehicle. The fairing needed to cover this asymmetrical payload and generate low lateral forces over a range of attack angles and at speeds approaching Mach 1.

Other asymmetrical air vehicle studies have included work by Bacon and Gregory (Bacon & Gregory, 2007) who studied the unequal forces generated when an aircraft sustains wing damage, producing different flow on one wing versus the other. CFD has also been used to characterize the asymmetrical aerodynamics of Space Shuttle launch debris (booster rockets and main fuel tank) as it falls back to Earth following an ascent (Murman, Aftosmis, & Rogers, 2005). Almost no air vehicles are asymmetrical in yaw, but almost all fixed wing and rotor vehicles are pitch asymmetric.

Air vehicles must use their aerodynamic surfaces to change the path of airflow, producing forces that are used to control the vehicle. Caughey & Hafez (Caughey & Hafez, 2005) describe the importance of symmetry in flight vehicles in terms of a longitudinal equilibrium state. In this state, “changes in flight speed, angle of attack, or pitch angle cannot induce a side force, a rolling moment, or yawing moment.” Thus, except in special design cases or due to unanticipated accidental wing damage, air vehicles are generally designed to be symmetrical along their longitudinal plane.

Land vehicles use tyres (or steel flanged-wheels and rails for railroads) as their primary means of producing and countering lateral forces. The generation of lateral forces through development of a tyre slip angle creates yaw to change the vehicle path. Lateral aerodynamic forces due to cross winds are also countered by the addition of a small steering angle, generating the counter force via the cornering stiffness of the tyre.

Symmetrical land vehicles generate little or no lateral force when traveling straight ahead without a crosswind. Further, it is a characteristic of symmetrical vehicles that they produce equal but opposite aerodynamic lateral forces when yawed by equal positive or negative angles around the vertical axis of rotation. This symmetry of force generation simplifies control, particularly as vehicle speed rises to levels where significant aerodynamic forces are generated.

The main driver for analyses of asymmetrical aerodynamic forces generated by land vehicles has been in motorsports. The examination of airflow around one vehicle overtaking another using CFD programs to optimize race car design is of interest to race car designers and top racing teams (Fiumara, 2008). The flow over a combination of two or more cars disrupt symmetrical flow to create unequal lateral and lift forces that can induce vehicle instability when racing cars travel in close proximity.

Although most asymmetrical flow is accidental or unintentional, there is one class of racing motorcycle that is highly asymmetrical in its geometric design and its airflow characteristics. Three wheel sidecars were developed shortly after the introduction of the motorcycle as an inexpensive two-passenger vehicle. Racing sidecars quickly became popular and have been developed since the early 1970s with highly aerodynamic shapes that must be designed to accommodate both the machine’s pilot and also a second person or “swinger”. The swinger’s job is to shift their weight from one side of the motorcycle to the other to maintain vehicle road holding on right or left corners. Because the platform for the swinger and the sidecar wheel are both offset from the centreline of the other two wheels, the racing sidecar is by necessity an asymmetrical vehicle. As a consequence, its bodywork generates aerodynamic forces that are also asymmetrical.

Because land speed record vehicles are almost always designed to be completely symmetrical with respect to a longitudinal axis, the generation of aerodynamic lateral forces in the absence of crosswinds or vehicle yaw is rarely a consideration. Sidecars are, by their nature, highly

asymmetrical and the generation of aerodynamic lateral forces caused by this asymmetry will be considered in this work.

2.8 CONSIDERATION OF AERODYNAMIC STABILITY

The primary aerodynamic concern with land speed record attempts has historically been the reduction of aerodynamic drag. In general, concern for aerodynamic stability has been met by ensuring that the centre of aerodynamic pressure is located behind the vehicle centre of mass to help promote directional stability in the event of a crosswind. This is often accomplished through the addition of a rear fin when the rules permit it, and/or by the addition of ballast in the front part of the vehicle to shift the centre of mass forward.

Aerodynamic lift is a concern for land speed record vehicles, as it can cause the vehicle to leave the ground, particularly if the vehicle is caught by a crosswind or suffers any other perturbation that causes the loss of directional stability. The balance of lift with drag becomes one of the primary concern for aerodynamicists working on sub-sonic land speed record designs. Adding aerodynamic downforce (negative lift) generally adds aerodynamic drag and reduces the vehicle's top speed. The additional generation of lateral forces created by an asymmetrical land speed record vehicle and their effect on stability has not been previously studied.

2.8.1 Flow field around a vehicle

As bluff bodies move through the air, they develop regions of separated flow exhibiting (especially in 3D) often complex structures (Ahmed, Ramm, & Faltin, 1984). The presence of such structures in the disturbed region, downstream from the vehicle, are a major contributor to the aerodynamic drag experienced by the vehicle (Ahmed, et al., 1984).

The definition of two terms will be helpful:

- Wake- region downstream of the vehicle where the flow field is affected by the presence of the body
- Separation zone- region of closed streamlines delineated by separation stream surfaces.

Characterization of wake structures can provide a qualitative and quantitative insight into the mechanisms of aerodynamic drag experienced by the body. Vortices are usually present in the wake region, produced by shear and pressure gradients between streams traveling over different parts of the geometric shape of the vehicle body and separating from the body surface at different points.

In the past, the characterization of aerodynamic flow was primarily accomplished through flow visualization schemes (smoke trails, yarn tufts, patterns of fluids on surfaces) and careful physical measurements of generated aerodynamic forces, pressure distributions and three-dimensional flow velocity around the vehicle and in the wake region, most frequently performed in a wind tunnel. Wind tunnel studies have supported land speed record attempts as early as the late 1920s

(Dacy, 1930) and access to scale model and full-size wind tunnels has benefitted well-funded teams in their pursuit of speed.

More recently, as computational capability has dramatically increased, the development of Computational Fluid Dynamics (CFD) as a tool for the study of airflow became a standard practice in the automobile industry (Brzustowicz, Lounsberry, & Esclafer de La Rode, 2002). Computational Fluid Dynamic (CFD) simulations of flow fields, including visualizations of flow characteristics, when properly validated against the physical experimentation, can be used to provide understanding of flow characteristics and as a design tool for development of lower-drag vehicles.

Among the first land speed record vehicles to extensively use CFD to guide the development process was "*Thrust SSC"*, (Figure 2.10) which set the current supersonic land speed record of 763.035 mph in 1997 (Noble, 1998). The team used rocket-powered scale models to validate its CFD calculations, providing some level of confidence that the vehicle would remain stable at the transonic speeds for which it was aiming.

Figure 2.10- *Thrust SSC (Bloodhound SSC photo)*

2.8.2 Validation of CFD

In 1998, the American Institute of Aeronautics and Astronautics (AIAA) published its *Guide for the Verification and Validation of Computational Fluid Dynamics Simulations* (AIAA, 1998). The guidelines defined Verification as, "…the process of determining that a model implementation accurately represents the developer's conceptual description of the model and the solution to be modelled." Validation is defined by the AIAA as "…the process of determining the degree to

which a model is an accurate representation of the real world from the perspective of the intended use of the model."

The National Aeronautics and Space Administration (NASA) created the National Program for Applications-Oriented Research in CFD (NPARC) (NASA, 2012) which, in 2008, developed a web-based tutorial on Verification and Validation. Verification, according to NPARC, "…determines if the programming and computational implementation of the conceptual model is correct." Thus, the Verification step "examines for computer programming errors." Because, in the current study, the CFD program is the well-established ANSYS Fluent, no further Verification assessments will be undertaken for this research. Because this software has been extensively used and validated in both academic and industrial settings, it is assumed that any errors in programming or mathematics that might exist have already be been discovered or produce variations in results that are not significant for the sidecar simulations in the current research.

Both AIAA and NPARC define validation as a determination of the agreement of the CFD results with physical reality. An objective in the current work is to assess the validity of the CFD approach employed to evaluate a low drag asymmetrical land speed record vehicle. This was accomplished using the well-known Ahmed body to validate CFD flow simulations. The Ahmed body was chosen as it is a bluff body that is close to a ground plane with wake structures of the type found with ground vehicles that have not been fully streamlined.

2.8.3 Validation Using Ahmed Body

Current automotive aerodynamic research favours simplified vehicle shapes over representations of actual vehicles (Keogh, Barber, Diasinos, & Doig, 2016). The Ahmed body is often chosen to establish a baseline for a simulated symmetrical land vehicle and also to validate the CFD procedure used to evaluate airflow over the sidecar vehicle. The Ahmed body is a simplified vehicle geometry designed primarily to study aerodynamic flow, particularly in the wake regions behind the vehicle (Ahmed et al., 1984). Numerous investigations have been performed in both wind tunnels and using CFD and the values of forces and pressure and velocity flow fields are well established under a variety of test conditions and Reynolds Number (Re).

The Ahmed body has a rounded front section, a slanted rear plane at the rear section (often referred to as the "backlight" and that can be specified at 0, 5, 10, 12.5, 15, 20, 25, 30, 35, and 40 degrees to the horizontal), and a rectangular box that connects the front and rear. Four small round legs protrude from the bottom of the box, analogous to wheels. The standard wind tunnel Ahmed body is 0.389 metres wide, 0.288 metres high, 1.044 metres long, and has a "wheelbase" of 0.470 metres and a projected frontal area of 0.112 m^2 at zero degrees of yaw (Figure 2.11).

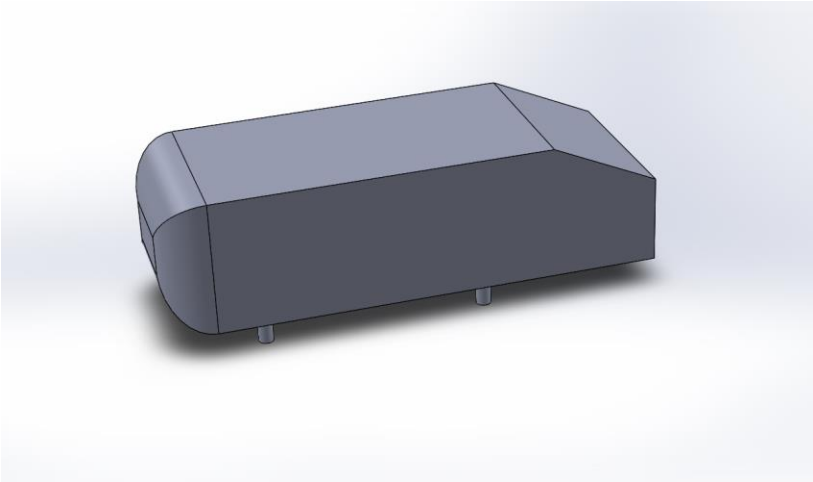

Figure 2.11- Ahmed body with 25-degree rear slant

2.8.4 Flow Characteristics for the Ahmed body

Air flow over the Ahmed body and the structure of the wake region has been investigated in detail (Ahmed, Ramm, & Faltin, 1984; Keogh, Barber, Diasinos, & Doig, 2016; Meile W. , Brenn, Reppenhagen, Lechner, & Fuchs, 2011; Wang, Zhou, Pin, & Chan, 2013; Baysal & Bayraktar, 2001; Lienhart, Stoots, & Becker, 2003). Flow over the 25 ° backlight separates at the leading edge of the downward sloped region and then reattaches before reaching the trailing edge of the backlight (Figure 2.12).

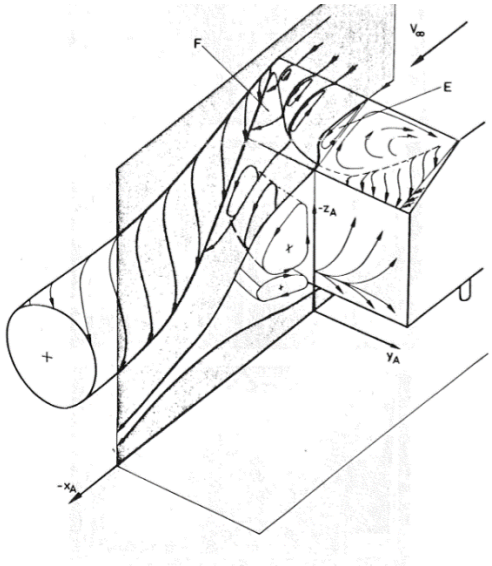

Figure 2.12- Air flow over rear section of 25° Ahmed body [Ahmed, et al., 1984]

Vino et al. (2005) has reported that flow does not fully reattach to the backlight of a 25° Ahmed body but mixes with the large separated region behind the vertical base, sometimes making the reattachment difficult to detect. The low-pressure region over the backlight and the shear between air moving along the side of the body form a pair of longitudinal counter-rotating streamwise vortices originating along the edge of each side of the slanted portion of the backlight are sometimes called C-pillar vortices, as on a conventional automobile, the rearmost roof support is referred to as the C-pillar. The vortices also promote reattachment of the flow to the backlight (Lienhart, Stoots, & Becker, 2003). Between 12.5° and 30° the flow over the roof reattaches, however at a backlight angle above 30° the flow fails to reattach (Keogh, Barber, Diasinos, & Doig, 2016) and intensity of the trailing streamwise vortices reduces, resulting in lower overall drag (Serre E. , et al., 2013).

At the rear of the Ahmed body, behind the vertical section of the tail, when the flow leaves the trailing edge of the backlight a pair of counter-rotating vortices form, one above the other, in the separation region behind the base of the Ahmed body (Vino, Watkins, Mousley, Watmuff, & Prasad, 2005).

In the current work, 25° and 35° Ahmed bodies were used to validate the CFD approach that was subsequently applied to the sidecar design phase that resulted in a new rear bodywork section and other details that reduced both aerodynamic drag and promoted greater stability through a reduction in aerodynamic lift. Both the 25° and 35° Ahmed bodies were chosen because they represent a case where strong streamwise longitudinal vortices form and the flow reattaches to the backlight (25° Ahmed) and a case where the flow over the backlight remains separated and the streamwise vorticity and drag coefficient are both reduced (35° Ahmed). By validating both cases it was intended that the flow topology of the sidecar vehicle could be more reliably characterized.

The validation was primarily through a comparison of CFD lift and drag force coefficients to published data, primarily generated through wind tunnel studies. CFD was also used to analyse the flow topology in the wake region of Ahmed body for validation purposes and also the revised sidecar design to understand the effects of body shape on flow.

This work will also briefly study a highly streamlined two-wheel land speed record vehicle. The purpose of this portion of the investigation is to contrast the stability of a two-wheel single track vehicle with that of the three-wheel two-track asymmetrical sidecar. The streamlined two-wheel vehicle was also designed to operate at a higher top speed (250 mph) and at these speeds the aerodynamic forces are larger resulting in greater risk if control is lost.

2.9 QUESTIONS ADDRESSED IN THE CURRENT WORK

Land speed record racing has inherent dangers which are made greater when the aerodynamic forces generated are not well understood or characterized. In this review of the history and literature relating to land speed record aerodynamics, it is apparent that there have been no

prior published studies of asymmetrical vehicles used for this purpose. The current study seeks to remedy this by addressing the following:

- How can the drag of an asymmetric vehicle (compliant with a specific set of international rules) be reduced without adversely affecting vehicle aerodynamic stability by increasing lateral or lift forces?
- What CFD methodology reliably predicts force coefficients for a land speed record sidecar motorcycle at Reynolds numbers representative of racing speeds?
- How does the wake topology affect the drag, lift, and lateral forces of an asymmetrical land speed record sidecar motorcycle and how does it change with changes to the geometric design of the sidecar bodywork?
- Does the addition of aerodynamic lateral forces developed by an asymmetrical sidecar motorcycle adversely affect the dynamic stability of the vehicle at speeds up to or in excess of 150 mph?
- Does the asymmetry of aerodynamic forces created by vehicle yaw adversely affect the stability of symmetric highly streamlined vehicles at high speed?

To address these questions, a series of CFD investigations of an Ahmed body, several versions of an asymmetrical land speed record electric sidecar motorcycle leading to an optimized racing sidecar, and a highly aerodynamic symmetrical electric streamliner motorcycle were undertaken. Aerodynamic drag, lift, and lateral forces were determined and used in three-body Equations of Motion dynamic stability analyses to predict vehicle stability.

Vehicle stability was more than purely an academic exercise in the optimization portion of this study—the safety of the rider of the asymmetrical electric sidecar at high speed was dependent upon the design choices made based upon the CFD data. As previously discussed, aerodynamic stability of land speed record vehicles has been a subject of concern for almost 90 years. Accidents in straight-line racing usually involve the reaction of the vehicle to yaw angles during or after an initial loss of control. Historically, yaw provides the greatest potential for lifting off and subsequent rolling resulting in the most dangerous type of accident for land speed record vehicles. Partly because of the vast runoff area of a venue like Bonneville, land speed vehicles are far safer if they spin on the ground and remain on their tyres.

Because these land speed record vehicles are designed to operate in a specific speed range (150-250 mph), the range of Re examined was restricted to a range between approximately 1 and 10 million. Speeds below 0.3 Mach allow the incompressibility of air to be assumed. Other independent variables examined in this work included yaw angles of 0°-15 and 45°-90° to streamwise flow, and conditions used in the CFD simulations including the choice of turbulence model, and the size and nature of the meshing. Geometry of the sidecar is also an independent variable, although the geometric complexity of the vehicle poses significant challenges. It was planned that the use of an Ahmed body, not only for CFD validation but as a simplified

symmetrical vehicle analogue (albeit one with complicated flow characteristics), would aid in subsequent study of the dynamics and aerodynamics of the asymmetrical sidecar. The examination of the dynamics and aerodynamics of a streamliner motorcycle in Chapter 6 had the same aim.

Dependent variables include drag, lift, and lateral force coefficients, aerodynamic moments and stability expressed as composite criteria which describe whether instabilities are self-correcting and/or damped.

Although this study deals specifically with a highly specialized competition vehicle that operates in a specific racing environment, the study of the airflow topologies and the effects of aerodynamic forces and moments on vehicle stability have applicability beyond record setting. The electrification of the world's transportation system will necessitate smaller, more aerodynamically efficient (low drag) vehicles whose safety will depend upon the ability of their designers to use many of the same tools and techniques employed in this study to ensure dynamic stability over a range of operating conditions and speed ranges.

CHAPTER 3 CFD METHODOLOGY FOR VEHICLE DESIGN

3.1 OVERVIEW

Computational fluid dynamics (CFD) has been well established as a method for the characterization of external flow over vehicle body (Serre E. , et al., 2013; Lanfrit, 2005; Bayraktar, Landman, & Baysal, 2001). The success of Reynolds-averaged Navier-Stokes (RANS) algorithms to model external flow over air and land craft has allowed CFD to replace wind tunnel testing in many stages of vehicle design (Malik & Bushnell, 2012). Though CFD has proven to be a valuable tool, an inappropriate choice of turbulence models or improper meshing can lead to errors in predicted flow fields and force and moment coefficients. The validation of results from CFD modelling is a worthwhile endeavour to ensure accuracy of predictions and provide confidence in design decisions. Results obtained through CFD can be compared with data from the testing of full-sized actual vehicles either on the road or in wind tunnels that are capable of testing vehicles at full-size, or by testing of scaled models within smaller wind tunnels. The primary results obtained from such wind tunnel studies for comparison to CFD work could include coefficients for drag and lift, velocity at key points near the surface, flow topology and especially wake structure from flow visualisation, characteristics of surface and wake vorticity, and quantitative methods such as hot wire anemometry, Laser Doppler Anemometry (LDA), and Particle Image Velocimetry (PIV).

3.2 COEFFICIENTS OF DRAG, LIFT AND LATERAL FORCE

A vehicle, at its top speed, balances its available power for thrust against retarding forces that include tyre rolling resistance (usually also including losses from the drive system and wheel bearings) and aerodynamic drag. At low speeds (less than 20 mph), rolling resistance provides the majority of retarding force, while as speed increases aerodynamic effects become dominant.

Aerodynamic drag results from several sources (Carroll, 2003):

- **Pressure drag**- Ordinary automobiles have bluff-shaped bodies whose contours (and particularly corners) result in a disturbed region of flow in the wake, downstream of the vehicle. For a bluff body, streamwise trailing and/or spanwise vortices are the dominant structures in this wake region (Hucho & Sovran, 1993). The retarding force is often referred to as pressure or form drag as it is associated with the pressure distribution on the body surface. Pressure drag coefficients are most often calculated using the projected frontal area of the vehicle body.
- **Viscous drag**- When airflow remains attached to a highly streamlined body the friction

between the air and the body surface causes a drag force. Smooth skin surfaces produce less skin surface friction than rough surfaces. This is often the dominant drag force for highly streamlined vehicles (Cd < 0.1) at zero yaw (or without crosswind) and is roughly proportional to the total (or wetted) surface area of the vehicle (Tamai, 1999).

- **Induced Drag**- All vehicle surfaces are capable of generating lift (negative lift is often called downforce), depending upon their angle of attack relative to the airstream. The drag on a body increases as lift (up or down) increases and minimum drag typically occurs when a body is producing zero lift.
- **Interference Drag**- Because vehicles are manufactured objects that must contain joints, seams, vents, wheels openings and other imperfections, some contribution of these features to the overall drag is unavoidable. It can be minimized through careful design and fabrication.

These sources of aerodynamic drag are combined in the measurement of the drag force. Drag force is proportional to the frontal area of the vehicle (A in m^2), the density of the fluid (air) passing over the vehicle (ρ in $\mathrm{kg/m^3}$) and the square of the velocity of the vehicle (V^2 $(m/s)^2$). An equation comparing the x-force (F_x in Newtons) to these factors is written:

$$F_x = ½\ \rho \cdot V^2 \cdot C_d \cdot A \tag{3.1}$$

The drag coefficient, or C_d, used to compare the ease with which a vehicle passes through a fluid is calculated from:

$$C_d = \frac{2 \cdot F_x}{V^2 \cdot A \cdot \rho} \tag{3.2}$$

Similarly, a lift coefficient, C_l, and a lateral force coefficient, C_y, can be calculated using the F_z and F_y forces, respectively.

$$C_l = \frac{2 \cdot F_z}{V^2 \cdot A \cdot \rho} \tag{3.3}$$

$$C_y = \frac{2 \cdot F_y}{V^2 \cdot A \cdot \rho} \tag{3.4}$$

Aeronautical wing designers working with highly aerodynamic bodies experience viscous drag forces that are generally higher than pressure drag forces and thus use planar surface area for drag and lift coefficient calculations. In automobile vehicle studies, pressure drag dominates and the relevant area is the frontal surface area (A) for flow over a body. Highly streamlined land vehicles (such as those used in land speed record attempts and solar-powered racing vehicles) also traditionally use frontal surface area for drag and lift calculations, despite exhibiting a high percentage of viscous drag.

3.3 NAVIER-STOKES EQUATIONS

The Navier-Stokes equations are derived from consideration of conservation of momentum and are solved alongside conservation of mass and energy equations (Versteeg & Malalasekera, 1995). Although the equations can be determined with the inclusion of thermal, phase-change energy and fluid density considerations, these effects can be ignored for sub-sonic (Ma< 0.3) external air flow over a vehicle. The following is a brief description of the origin of the Navier-Stokes equations.

Assumptions:

- Velocity is Ma < 0.3
- Fluid is incompressible so density is constant throughout domain
- No thermal effects will be considered
- Steady flow over the vehicle surface: Although flow varies with time over the surface, steady state solvers have been established to work well for race car design and development as changes in vehicle attitude happen over longer timescales than flow relaxation

Using these assumptions, the only equations that are required are those that ensure mass and momentum are conserved. In the treatment below, source terms are neglected.

Conservation of mass

The conservation of mass may be expressed as a single differential equation:

$$\frac{\partial \rho}{\partial t} + \nabla \cdot (\rho \vec{u}) = \frac{\partial \rho}{\partial t} + \frac{\partial (\rho u)}{\partial x} + \frac{\partial (\rho v)}{\partial y} + \frac{\partial (\rho w)}{\partial z} = 0, \quad (3.5)$$

where ρ is the density of the fluid, and u, v, w are the velocity components in the x, y, and z direction. This is called the "continuity equation."

Because the fluid is incompressible, the mass of a specific fluid volume will remain constant and so the variation in the mass of the fluid volume is zero. The equation above can be therefore re-written as:

$$\frac{\partial u}{\partial x} + \frac{\partial v}{\partial y} + \frac{\partial w}{\partial z} = 0 \quad (3.6)$$

Conservation of momentum

The Conservation of momentum equation for the x-direction is given by:

$$\rho \frac{Du}{Dt} = \frac{\partial (-p + \tau_{xx})}{\partial x} + \frac{\partial \tau_{yx}}{\partial y} + \frac{\partial \tau_{zx}}{\partial z} \quad (3.7)$$

(where τ_{yx} and τ_{zx} are viscous stresses acting parallel to the volume's surfaces).

For the *y* and *z* directions conservation of momentum is given by:

$$\rho \frac{Dv}{Dt} = \frac{\partial(-p+\tau_{yy})}{\partial y} + \frac{\partial \tau_{yx}}{\partial x} + \frac{\partial \tau_{zy}}{\partial z}, \quad (3.8)$$

$$\rho \frac{Dw}{Dt} = \frac{\partial(-p+\tau_{zz})}{\partial z} + \frac{\partial \tau_{yz}}{\partial y} + \frac{\partial \tau_{zx}}{\partial x}. \quad (3.9)$$

The viscous stress is proportional to the rate of strain and the dynamic viscosity, μ, and relates the linear stress to the linear deformation. The relationship of the stress to the volumetric deformation is provided by the bulk viscosity λ.

Because air is an isotropic and incompressible fluid (in this analysis), the viscous stresses can be described by:

$$\tau_{xx} = 2\mu \frac{\partial u}{\partial x} + \lambda \nabla \cdot \vec{u} \quad (3.10)$$

$$\tau_{yy} = 2\mu \frac{\partial v}{\partial y} + \lambda \nabla \cdot \vec{u} \quad (3.11)$$

$$\tau_{zz} = 2\mu \frac{\partial w}{\partial z} + \lambda \nabla \cdot \vec{u} \quad (3.12)$$

$$\tau_{xy} = \tau_{yx} = \mu \left(\frac{\partial u}{\partial y} + \frac{\partial v}{\partial x} \right) \quad (3.13)$$

$$\tau_{xz} = \tau_{zx} = \mu \left(\frac{\partial w}{\partial x} + \frac{\partial u}{\partial z} \right) \quad (3.14)$$

$$\tau_{yz} = \tau_{zy} = \mu \left(\frac{\partial v}{\partial z} + \frac{\partial w}{\partial y} \right) \quad (3.15)$$

These stress equations can be substituted into the previous three momentum equations to give the following momentum equations in the incompressible form:

$$\frac{\partial(\rho u)}{\partial t} + div\,(\rho u \vec{u}) = \frac{\partial p}{\partial x} + div\,(\mu\, grad\, u) \quad (3.16)$$

$$\frac{\partial(\rho v)}{\partial t} + div\,(\rho v \vec{u}) = \frac{\partial p}{\partial y} + div\,(\mu\, grad\, v) \quad (3.17)$$

$$\frac{\partial(\rho w)}{\partial t} + div\,(\rho w \vec{u}) = \frac{\partial p}{\partial z} + div\,(\mu\, grad\, w) \quad (3.18)$$

These three momentum equations, along with the continuity equation described earlier (3.6) are called the Navier-Stokes equations.

The study of turbulent flow at high Re is facilitated by modifications to the governing equations. The velocity terms in the Navier-Stokes equations are replaced with a mean ($\bar{U}$) and a fluctuating (u') component.

$$u = \overline{U} + u' \quad v = \overline{V} + v' \quad w = \overline{W} + w' \quad (3.19)$$

In addition, the pressure term is re-written as:

$$p = \overline{P} + p' \tag{3.20}$$

Replacing these terms into the Navier-Stokes equations and averaging them over time results in the Reynolds Averaged Navier-Stokes (RANS) equations. The averaging process to derive the RANS equations results in a new "Reynolds Stress" term which requires additional turbulence model equations to be solved. A way to provide these additional equations was first proposed by Boussinesq in 1877 by relating the Reynolds Stresses to the mean velocity gradients as indicated in Equation 3.21 (Versteeg & Malalasekera, 1995).

$$R_{ij} = -\rho \overline{u_i' u_j'} = \mu_t \left(\frac{\partial U_i}{\partial x_j} + \frac{\partial U_j}{\partial x_i} \right) \tag{3.21}$$

3.4 Principles of CFD

Computational Fluid Dynamics (CFD) is essentially the prediction of a flow field by numerical solution of the Navier-Stokes and continuity equations (and where required, other equations describing additional phenomena). The three key elements involved in CFD include: 1) grid or mesh generation, 2) algorithm development, and 3) turbulence modelling. Typical sources of error in a CFD simulation (Versteeg & Malalasekera, 1995) include:

- inaccuracies in the identification and set up of the flow problem and the mathematical model of a physical phenomenon
- incorrect assumptions in description or simplification of physical phenomenon
- errors arising from the manner in which the computation domain is defined
- incorrect or inaccurate representation of boundary and initial conditions
- incomplete convergence errors during simulations
- errors due to poor mesh refinement

A mesh (also called a grid) for CFD calculation must meet several requirements. For bluff bodies such as cars, trucks and other similar vehicles, "the accuracy of the drag and lift predictions are largely determined by the accuracy of the predicted static pressure distribution on the body," (Lanfrit, 2005). To accurately determine the pressure distribution on the vehicle model requires a surface mesh that incorporates the relevant geometric details of the vehicle model and accounts for the pressure gradient that forms in the boundary layer above the surface. In the current work, meshing was performed using the functions available within ANSYS Fluent 17.0.

Meshing for vehicle external flow studies typically consists of a cuboid computational domain consisting of a velocity inlet, a pressure outlet, three no-slip smooth boundaries and a smooth stationary or moving floor. The inlet and side boundaries are typically 1-3 body lengths away from the vehicle to reduce any vehicle/wall interactions, while the pressure outlet is typically set 5 or more body lengths downstream to allow formation and decay of the wake region. A "body of influence" mesh refinement box is generally placed around the vehicle and often another in the

vehicle wake region to allow a greater refinement of the mesh in those regions that influence most the flow characteristics. In the creation of a mesh for CFD, a choice must be made between structured and unstructured meshing. A structured 3D mesh consists of primarily hexahedral elements (although pyramids and wedges are possible) which are orthogonal within an i, j, k space. Because the elements are arranged orthogonally in a structured mesh there are coding advantages that allow the mesh to contain fewer elements and be more computationally efficient. A structured mesh however, may not be able to conform adequately to intricacies of vehicle surfaces, requiring an unstructured mesh, primarily made up of tetrahedral elements. Unstructured meshes do not use an i, j, k orthogonal reference and instead use nodes and a connectivity scheme. For this work, because of the complexities of the geometry of the sidecar vehicle, unstructured tetrahedral meshing of the volume within the computational domain was used.

A series of stacked "inflation layers" of (usually) prismatic shaped cells in the region of the mesh just above the vehicle surface are often used to account for the transition from the laminar sublayer (nearest the surface) through the buffer layer to the turbulent log-law layer and beyond.

When modelling the near-surface region the y+ (*yplus*) value is a critical parameter as it is used to determine whether the first cell of the CFD mesh resides within the viscous sub-layer or the log-law region. The y+ parameter is described as "the ratio between the turbulent and laminar influences in a cell," (Salim & Cheah, 2009). The transition from the viscous sublayer to the log-law region takes place at a y+ value of 11.225 (LEAP CFD, 2013). The log-law layer can extend to a y+ level of several thousand with flows with high Reynolds numbers, while an upper y+ limit of 100 may be typical of low Reynolds number turbulent flow conditions. The appropriate y+ value to determine the thickness of the first cell also depends upon what turbulence model and wall functions (see section 3.4.1) are being used in the calculations. Experience with similar flow conditions is often the best way to determine a target for y+ values, and a y+ between 30 and 300 for vehicle aerodynamic flow RANS simulations is recommended (Lanfrit, 2005; Bordei & Popescu, 2011). Others (Ashton, West, Lardeau, & Revell, 2016; Keogh, Barber, Diasinos, & Doig, 2016) have recommended y+ values closer to 1 for RANS simulations.

The thickness of the initial mesh cell, Δy, is usually chosen to capture the laminar layer such that subsequent inflation layers can account for the transition to turbulent flow, particularly in cases where flow separation is expected.

To calculate an initial cell distance Δy using the desired value of non-dimensional y+ it is first necessary to calculate the Reynolds number from:

$$\mathrm{Re} = \frac{\rho V L}{\mu}, \tag{3.22}$$

where V is the freestream velocity (in m/s) and L is the characteristic length (vehicle length is usually used for external flow over land vehicles).

When the fluid properties and the target y+ values are known, the wall shear stress, τ_w is calculated from:

$$\tau_w = \frac{1}{2} C_f \rho V^2 \quad (3.23)$$

where C_f is the skin friction coefficient which can be estimated from an empirical flat plate formulation (LEAP, 2013) as:

$$C_f = 0.058 \, Re^{-0.2} \quad (3.24)$$

Using the value for the shear wall stress, the friction velocity u_τ is calculated from

$$u_\tau = \sqrt{\tau_w / \rho} \quad , \quad (3.25)$$

then Δy, the height of the first cell from the wall is calculated from

$$\Delta y = \frac{(y+)(\mu)}{\rho \, (u_\tau)} \quad . \quad (3.26)$$

Typically, 5 to 11 inflation layers with a 1.2 expansion ratio provide adequate characterization of the surface region for a Re in the 10^6 range (Lanfrit, 2005). Values for y+ were rechecked after the CFD flow was solved from a y+ surface contour plot created in the ANSYS Fluent Solutions using SOLUTIONS→RESULTS→Graphics→Contours→Turbulence→Wall Yplus→Display.

3.4.1 RANS turbulence models

There are a variety of commercial and open source CFD programs available. Most provide several choices for modelling flow in the turbulent regions. ANSYS Fluent 17.0, for example, offers several different RANS turbulence models to solve for the flow field (LEAP CFD, 2013) including:

Spalart-Allmaras

- Single equation
- Originally designed for transonic flow over wings
- Stable and good convergence
- Does not accurately represent shear flow, separated flow, or decaying turbulence

k-epsilon and k-epsilon Realizable

- Solves for two variables: k, the turbulence kinetic energy and epsilon, the rate of dissipation of kinetic energy
- Popular for industrial applications
- Good convergence and relatively low memory requirements
- Often used to solve airflow around bluff bodies
- As with k-epsilon but modified for more greater accuracy for flow involving jets or separation

- Improved formulation for turbulence, viscosity, and dissipation rate
- Improved ability to predict flow in separation
- Requires a semi-empirical Wall Function to model near surface effects
- Can be described by (Versteeg & Malalasekera, 1995):
  (Rate of Change of k or ε) + (Transport of k or ε by convection) = (Transport of k or ε by diffusion) + (Rate of production of k or ε) – (Rate of dissipation of k or ε)

Some of the more common Wall Functions available with ANSYS Fluent include (LEAP CFD, 2013):

Standard Wall Function

- Accurate and stable for a broad range of bounded flow
- Inaccurate with strong adverse pressure gradients

Non-Equilibrium Wall Function

- Sensitized to pressure gradient effects
- Formulated on a two-layer boundary layer concept

Enhanced Wall Function

- Near wall modelling represents surface features
- Two layer zones
- Suitable for coarse and fine meshes

Scalable Wall Function

- Automatically sets y+ to 11.225
- Avoids erroneous modelling of sublayer
- Recommended for its robust modelling ability

Shear Stress Transport (SST) Models

k-ω SST

- Combines k-epsilon model in free stream and k-omega model near the walls and surfaces
- Gradually changes from k-omega in the inner region of the boundary layer to k-epsilon in the far field region away from the surface
- Does not always converge quickly

- Most accurate when solving flow near a wall

4 –Equation Transition SST (NASA Langley Research Center, 2017)

- Adds equations for "γ" and "Re_θ" to the SST "k" and "ω" equations
- Effects of laminar-turbulent transitions are introduced by modifying the TKE source terms
- The two additional transport equations are based upon intermittency (γ) and transition onset (Re_θ) criteria
- Re_θ is a function of free-stream turbulence intensity and pressure gradients

The majority of the CFD studies in the current work used the k-ε Realizable turbulence model with the Scalable Wall Function (chosen initially for Ahmed body validation and the design study work in Chapter 4 due to its robust ability to avoid sublayer modelling errors) or the Transition SST (4 equation) model, chosen for streamliner and sidecar yaw studies in Chapters 6 and 7 due to its ability to better model flow transition location on the vehicle surface.

Large Eddy Simulation (LES)

Although steady-state RANS simulations are effective at predicting many aspects of the flow around a vehicle, they are less successful at predicting the effects of separation and an unsteady wake (Caridi, Cokljat, Schuetze, & Lechner, 2012). Transient simulations, using LES can better predict the pressure and velocity field at the rear of a vehicle, but the rear wall resolution required to represent flow structures in the vehicle surface boundary layer requires an extremely fine mesh with a large number of elements. In the LES approach, fluctuations are decomposed into spatially-filtered resolved scales, which are likely to be anisotropic, and subgrid unresolved scales (which may be isotropic). The subgrid stresses resulting from this filtering are unknown and require modelling. The practical application of LES is provided in section 3.5.4.

3.5 VALIDATION OF CFD

3.5.1 Validation Using Ahmed Body

As discussed in Chapter 2, the Ahmed body is a simplified vehicle geometry designed to study air flow, particularly in the wake regions behind the vehicle (Ahmed, Ramm, & Faltin, 1984).

The objective of an Ahmed body study in the current investigation is two-fold. First, to use the simple Ahmed body shape to find a turbulence model that yields a flow field and drag coefficient which is consistent with published Ahmed body data and, second, to establish a meshing and Fluent simulation process that can be applied to the sidecar CFD model with a high degree of confidence in its ability to predict flow characteristics and force coefficients. The bluff Ahmed body produces the majority of its drag from the rear section of the bodywork (Ahmed et al, 1984) and trailing vortices in the flow topology and it was anticipated the original and modified sidecar

designs would exhibit similar flow characteristics. For the initial study, a 25° Ahmed body was used.

3.5.1.1 Mesh dependency

The first step in validating the CFD simulation was to examine mesh dependency. A basic unstructured mesh was created for the 25° Ahmed body (0.389 metres wide) using the meshing capability of ANSYS Fluent 17.0 in a computational domain enclosure that was constructed with the walls 1 metre, the ceiling 1.4 metres, the inlet 2 metres and the pressure outlet 6 metres from the Ahmed body. The Ahmed body was positioned so that the body was 0.50 metres above the floor, consistent with the original studies by Ahmed, et al (1984). A body of influence refinement box (diagonal dimensions x-=3 m, y= 1 m z= 0.6 m) was placed around the Ahmed body and extended beyond the vehicle and into its wake region. Mesh sizes varying from 160,000 elements to 13.1 million elements were created by adjusting the size of the face sizing, number and thickness of inflation layers, refinement box and computational domain. The velocity was 40 m/s, with a stationary floor (to simulate wind tunnel data), using a k-ω SST turbulence model with an inlet turbulence intensity of 1% and a turbulence viscosity ratio of 10. An inlet turbulence intensity of 5% (ANSYS Fluent's default value) was also investigated, but resulted in the same C_d and C_l values. A coupled scheme was used for pressure and velocity and spatial discretization used a least squares gradient and second order upwind pressure, momentum, turbulence kinetic energy and dissipation rates. Other Fluent setup parameters as described in Appendix A.

The results are plotted of Figure 3.1. Wind tunnel data from Ahmed, et al, 1984 indicates at a test speed of 40 m/s a C_d value of 0.299.

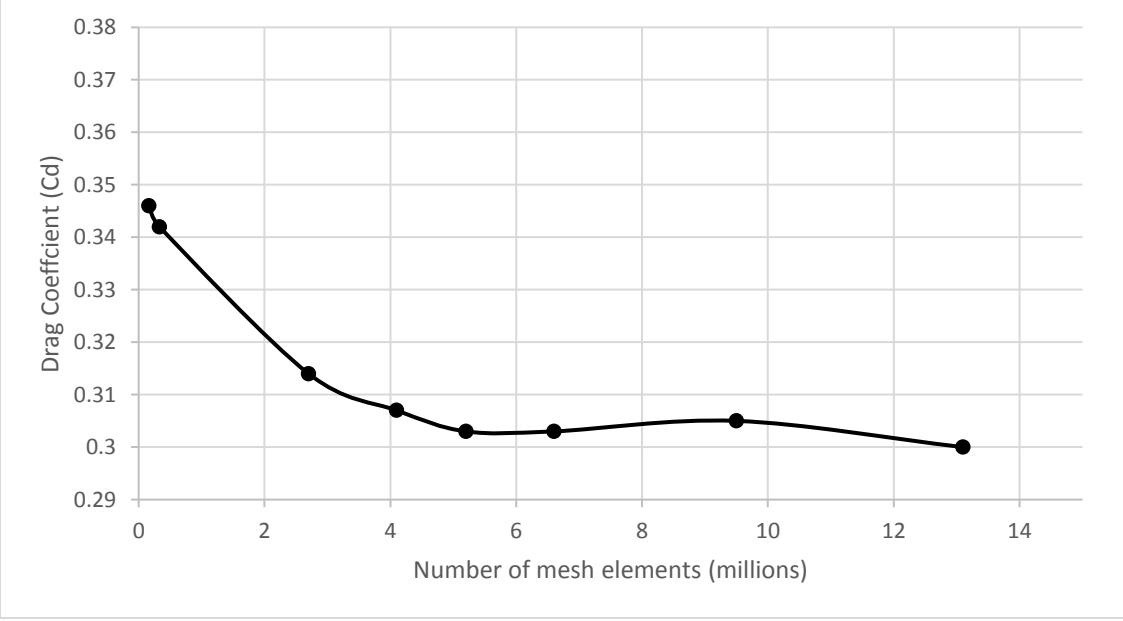

Figure 3.1- 25° Ahmed drag coefficient variation with CFD mesh size at 40 m/s

Figure 3.1 indicates that the mesh size of 6 million elements is well within the region of stable results and as long as the mesh size is greater than 5 million elements, the results for drag coefficient returned from ANSYS Fluent 17.0 for the Ahmed body should differ by 1% or less.

3.5.1.2 RANS turbulence modelling

Four different turbulence models were examined, using a 13.1 million element mesh, as described above and including 11 inflation layers. The results are indicated in Table 3.1.

TABLE 3.1: 25 ° Ahmed body turbulence modelling (40 m/s)

Turbulence Model	**Drag Coefficient**	**Percent Difference from Published**
Spalart- Allmaras (1eqn)	0.312	+4.3%
k-ε Realisable with Scalable Wall Function	0.302	+1.0%
k-ω SST (3 eqn)	0.295	-0.3%
4 eqn Transition SST	0.307	+1.0%
Published Data (Ahmed et al., 1984)	0.299	--------

From Table 3.1, it is evident that the k-ε, k-ω SST, and 4 equation Transition SST turbulence models all provide acceptable results when compared to the Ahmed et al. (1984) wind tunnel data for predicting drag coefficient. For the remainder of the Ahmed validation studies the k-ω SST turbulence model was used as it offered the greatest accuracy at an acceptable convergence rate.

3.5.2 Comparison to wind tunnel data

3.5.2.1 Re sensitivity

The sensitivity of aerodynamic drag of a 25° Ahmed body to Re has been studied experimentally by Ahmed et al. (1984), Bayraktar et al. (2001) and Meile et al., 2011 and provides a good opportunity to validate the CFD methodology over a range of Re from 0.7 to 13.4 million. Bayraktar increased the Re to a value realistic for a road vehicle by increasing the scale of the Ahmed body by a factor of 4.7. Figure 3.2 provides a plot of the published data versus the data obtained from the current work. The lower value at a Re of 2.784 x 10^6 comes from the original size Ahmed body while the two higher values for the current work come from a 4.7-scale Ahmed body (per Bayraktar, et al. 2001). CFD was performed using the k-ω SST turbulence model with conditions and settings as described previously but with a range of mesh sizes.

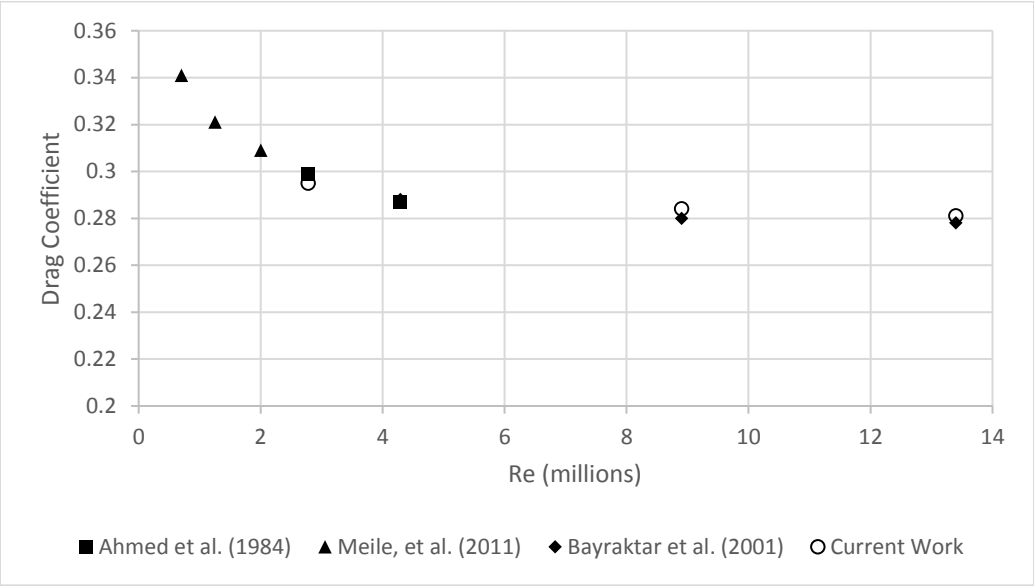

Figure 3.2- 25 ° Ahmed Re sensitivity- Comparison of current work to published data

From Figure 3.2 it is evident that the current work matches the published data for Re sensitivity of the 25° Ahmed body over a range of 2.3-13x10^6.

3.5.2.2 Drag and lift comparison

Experimental wind tunnel data can be used to validate the drag and lift coefficient values produced by CFD studies. Both the 25° and 35° Ahmed bodies were examined. Validating the CFD simulation by drag and lift coefficients against both the 25° (Figure 3.3) and 35° (Figure 3.4) Ahmed bodies provides a greater confidence in the ability of the CFD methodology to simulate a variety of flow fields.

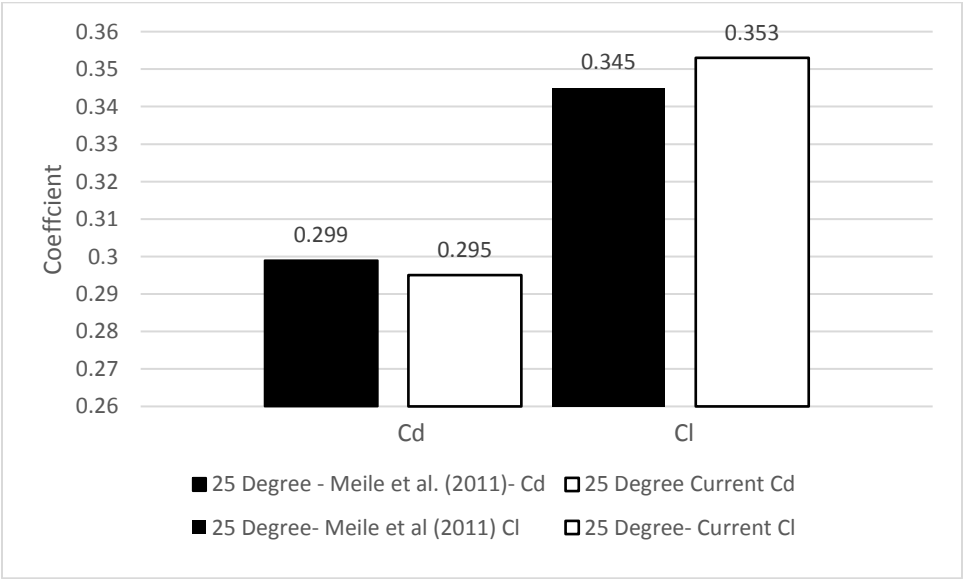

Figure 3.3- 25° Ahmed body drag and lift coefficients versus published wind tunnel data

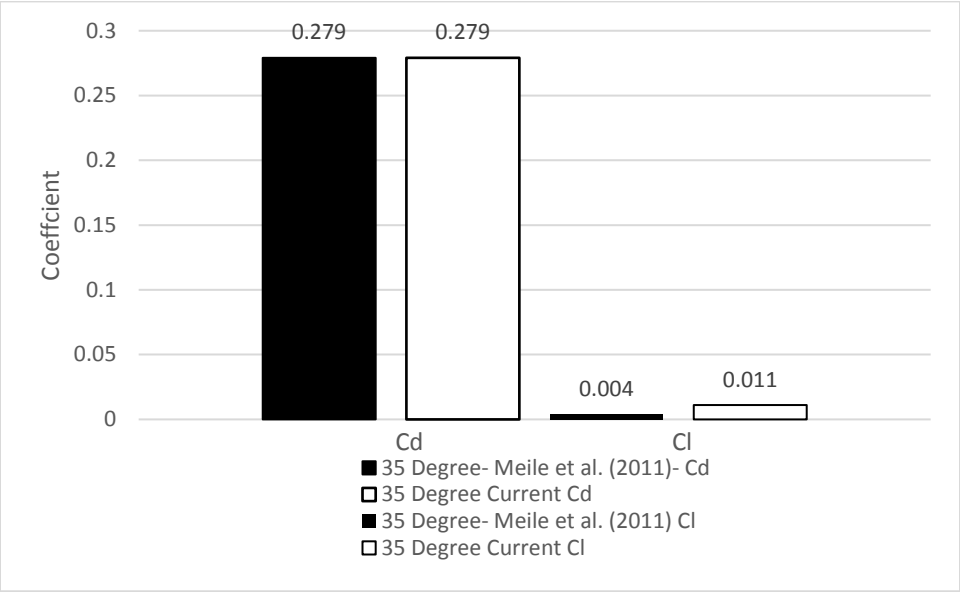

Figure 3.4- 35° Ahmed body drag and lift coefficients versus published wind tunnel data

From Figure 3.3 and 3.4 it is evident that the CFD predicts the drag and lift coefficients accurately for both the 25° and 35° Ahmed bodies and the results are acceptable to use as a design tool as validated in both cases.

3.5.2.3 Velocity field

Figure 3.5 depicts streamwise profiles plotted at various x-axis (longitudinal) positions in the y=0 (symmetry) plane for a 25° Ahmed body with the same CFD conditions used for the drag and lift comparisons above. The profiles are plotted with data from the ERCOFTAC database (Lienhart, Becker, & Stoots, 2017) which were measured in the LSTM wind tunnel at a velocity of 40 m/s (Meile W. , Brenn, Reppenhagen, Lechner, & Fuchs, 2011).

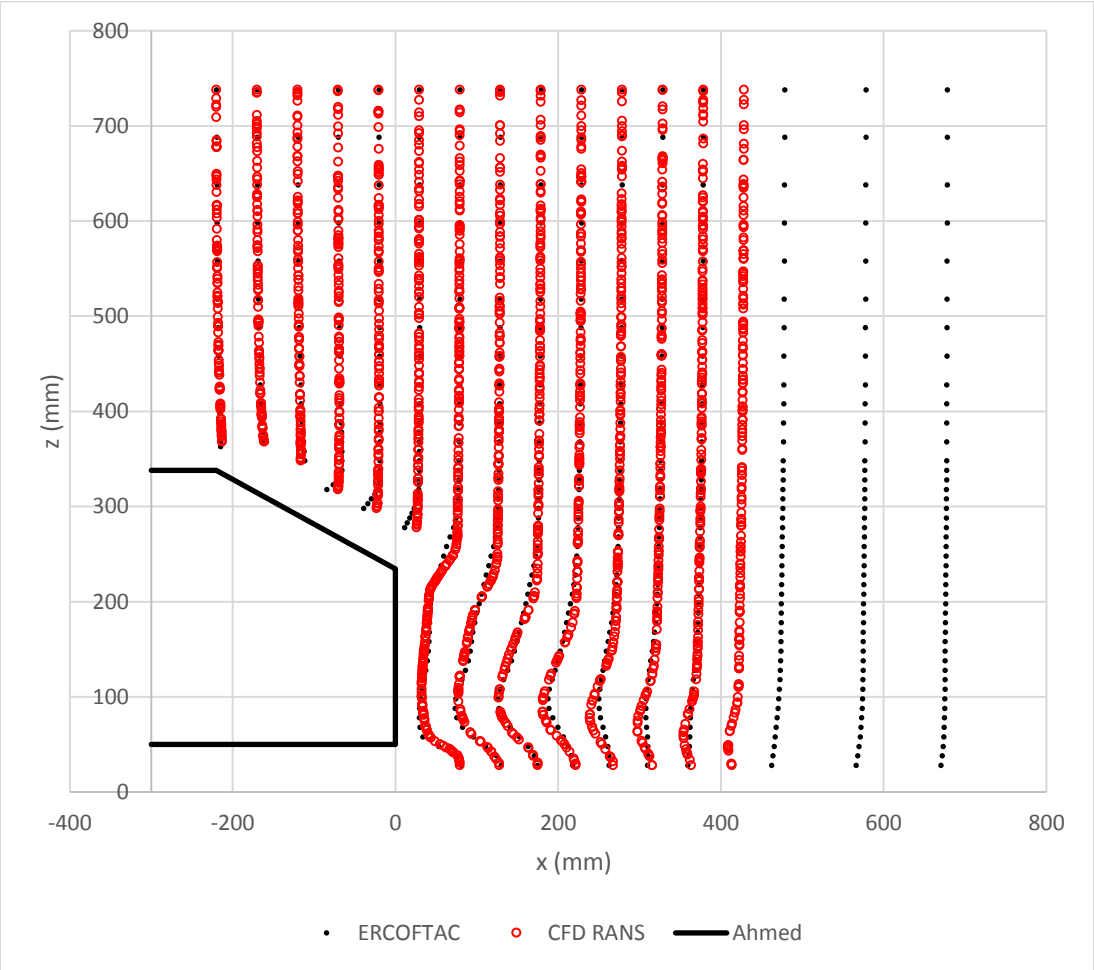

Figure 3.5- Streamwise velocity profiles for a 25° Ahmed body

From Figure 3.5 it is evident that the velocity profiles along the first portion of the rear slanted section (backlight) of the 25° Ahmed body from the experimental wind tunnel data are well simulated by the CFD flow study. From about midpoint of the slant onward, (at or near the point of reattachment per Ahmed et al. (1984)) the CFD does not show the same reduction in velocity that was observed in the wind tunnel data. In the wake region, the CFD data shows only minor deviations from the experimental data (~ 1 m/s), becoming slightly less accurate and slightly under predicting the degree by which the wake is diminished as the flow moves downstream away from the rear of the vehicle.

As previously stated (Chapter 2 and Serre, et al. (2013)), the separation that occurs on the backlight surface of the 25° Ahmed body reattaches before the end of the section, reinforcing the streamwise C-pillar vortices and increasing the drag force. Figure 3.6 shows pressure contours over the 25° Ahmed body from the RANS model.

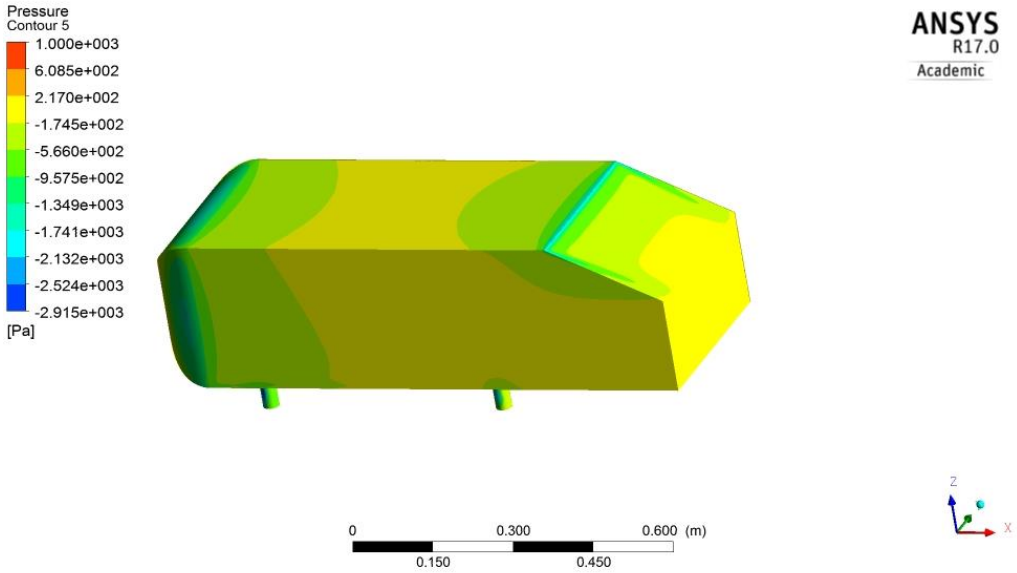

Figure 3.6- Pressure contours over the 25° Ahmed body

From Figure 3.6, a region of lower pressure clearly forms at the edge of the backlight section and exists to approximately halfway down the section. The upper edges of the C-pillars also exhibit lower pressure. The airflow over the backlight region can be examined through a plot of velocity vectors on a symmetrical mid plane at position y=0 (centreline) as provided in Figure 3.7.

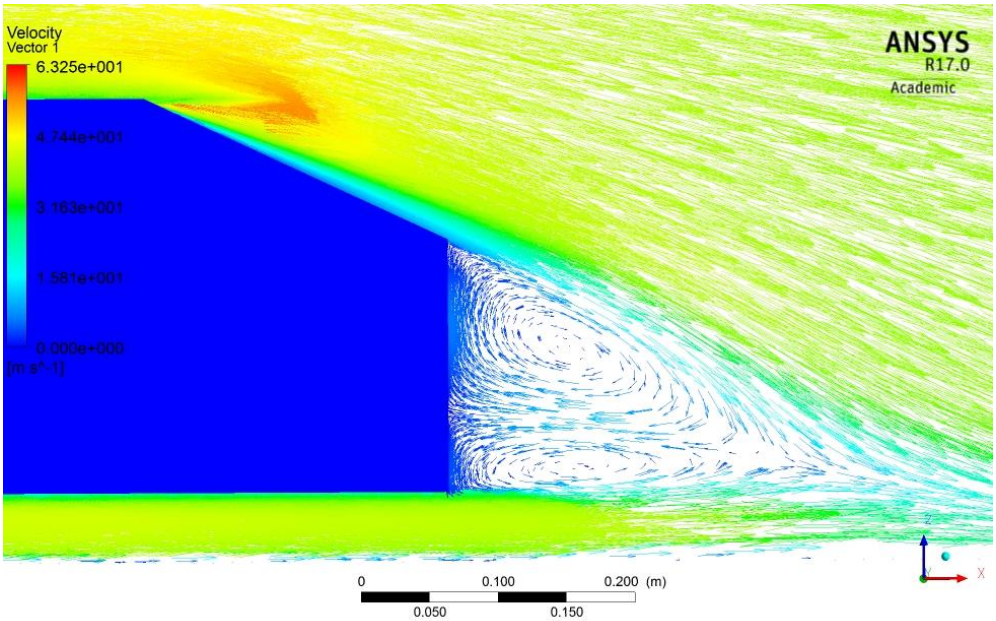

Figure 3.7- Velocity vectors over rear section of 25° Ahmed body

Figure 3.7 demonstrates the existence of two counter-rotating vortices in the separated region directly behind the 25° Ahmed body.

The presence of these vortices was also observed in Ahmed et al. (1984) as in Figure 2.12 and are further evidenced in a plot of velocity streamlines over the 25° Ahmed body in Figure 3.8.

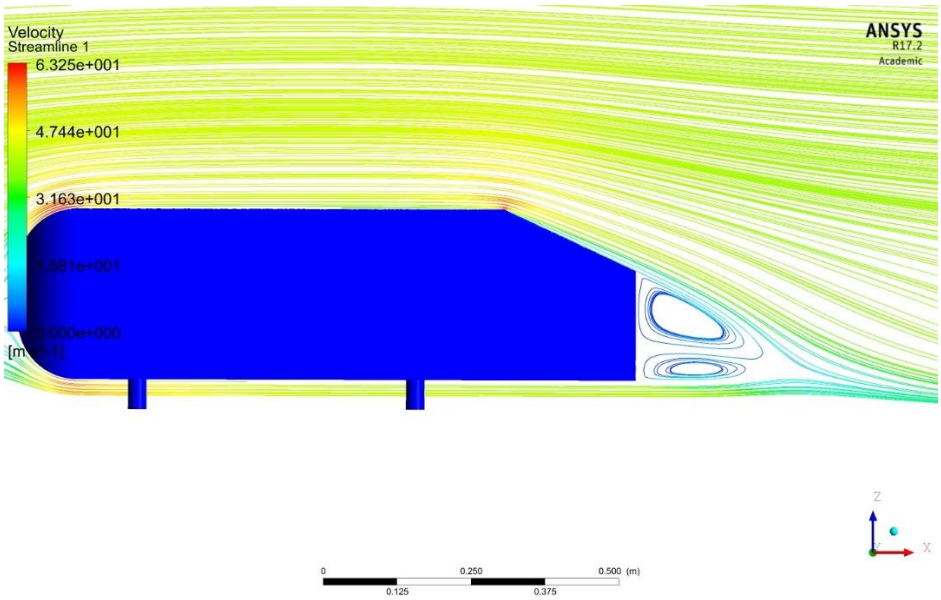

Figure 3.8- Velocity streamlines over 25° Ahmed body

Figure 3.8 shows separation of flow over the 25° Ahmed body backlight but no reattachment and indicates the presence of a pair of lateral vortices in the region directly behind the vehicle.

From Figure 2.12, it was evident from Ahmed et al. (1984) that a pair of streamwise vortices exist beginning on the C-pillars and carrying on into the wake region behind the 25° Ahmed body. Evidence of these can be seen in Figure 3.9, which indicates velocity vectors on a horizontal plane at the level of the trailing edge of the backlight.

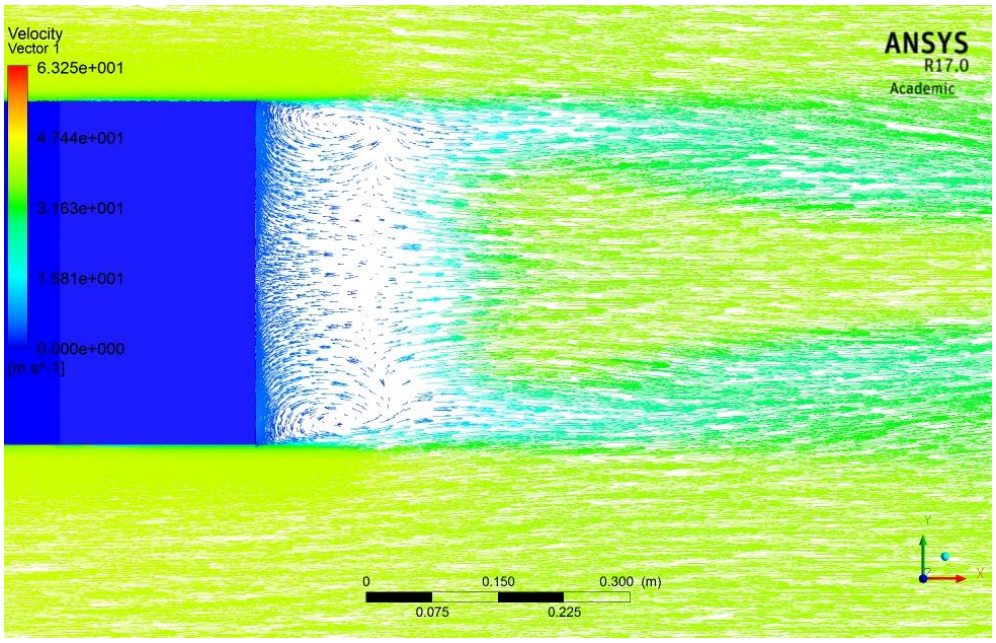

Figure 3.9- Velocity vectors on a plane at the level of the horizontal trailing edge of the backlight- 25° Ahmed body

3.5.2.4 Characteristic flow topologies

Visualisation of the origination and development of vortex flow structures around a vehicle provides important clues about how to reduce pressure drag forces. Air flow over the complex geometric shapes of a vehicle creates a distribution of surface pressures that can vary widely over small distances on the surface. These surface pressure distributions dictate the creation of aerodynamic forces and the formation of small and large-scale flow topology. The regions of the vehicle body that contribute most to the development of large-scale separation regions can be targeted for redesign to reduce large scale flow disturbances and aerodynamic drag forces. Here, the term separation is used to mean that streamlines which are initially both near and parallel to the surface, follow paths that take them away from the surface (Hornung & Perry, 1984).

The visualisation of three-dimensional flow is a difficult task that requires the application of a variety of techniques to understand the flow mechanisms (Délery, Legende, & Werlé, 2001).

Surface friction patterns

Flow topologies arising from complex three-dimensional flow over a vehicle surface can be elucidated by visualizing surface lines using an “oil flow” technique. In physical experimentation (frequently in wind tunnels) a mixture of oil and a dye are spread on the vehicle surface. The flow of air over the surface causes the oil to flow and form lines of constant surface shear stress. These lines are referred to as the skin-friction surface patterns.

Tobak and Peake (1982) (Tobak & Peake, 1982), have identified critical singularity points that use skin surface friction patterns to help identify flow topologies, including flow separation and reattachment, indicated in Figure 3.10.

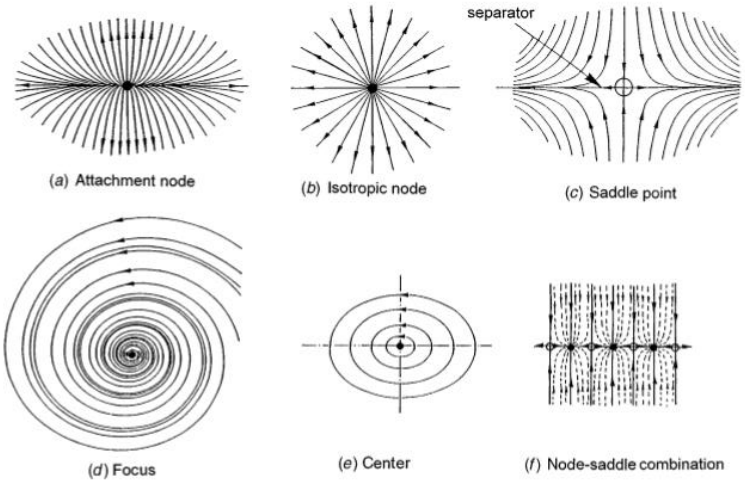

Figure 3.10- Skin surface patterns that identify critical points [Tobak & Peake, 1982]

Tobak et al. (1982) described the flow characteristics associated with the skin friction surface patterns, calling lines passing through a saddle point "separators." A separator can be of a separation or an attachment type (Figure 3.10a)—when the skin friction lines converge toward the separator, separation occurs as flow lifts from the surface. If the lines diverge from the separator, attachment of flow is present. When the skin surface patterns form into a spiral (Figure 3.10d) the flow forms a vortex, centred on the spiral. Hornung & Perry (1984) referred to the separators as bifurcation lines and indicated that the lines may be curved and can occur without any well-defined beginning or end.

ANSYS Fluent provides a surface shear stress line visualisation (analogous to oil flow in a wind tunnel) as a part of CFD-Post. In Fluent this is performed by setting up a surface streamline.

Wake structures

Major separated flow regions can often be identified by large scale streamwise vortices that trail into the wake region. The geometry and profile of the vehicle body and the subsequent air flow and shear of airflow streams has a significant effect on the formation and intensity of such vortices.

Although vorticity can be observed in CFD using iso-surfaces of TKE, ANSYS CFD-Post has several other provisions for visualisation through vortex cores. A vortex core is an iso-surface displaying vortices that are detected as spatial regions by evaluating a set of specific formulae. Eight options are available through CFD-Post (Absolute Helicity, Eigen Helicity, Lambda 2-Criterion, Q-Criterion, Real Eigen Helicity, Swirling Discriminant, Swirling Strength, and Vorticity) to provide

visualisations, although ANSYS makes no recommendation for a vortex core method as the choice is case dependent (SHARCNET: Vortex Core Region, 2017).

In Figure 3.8, although the RANS model averages the exact position of the streamwise vortices, evidence of their presence is observed from the lower edges of each of the C-pillars. The presence of these streamwise vortices are clearly seen in a plot of swirling strength in the vortex core region (Figure 3.11).

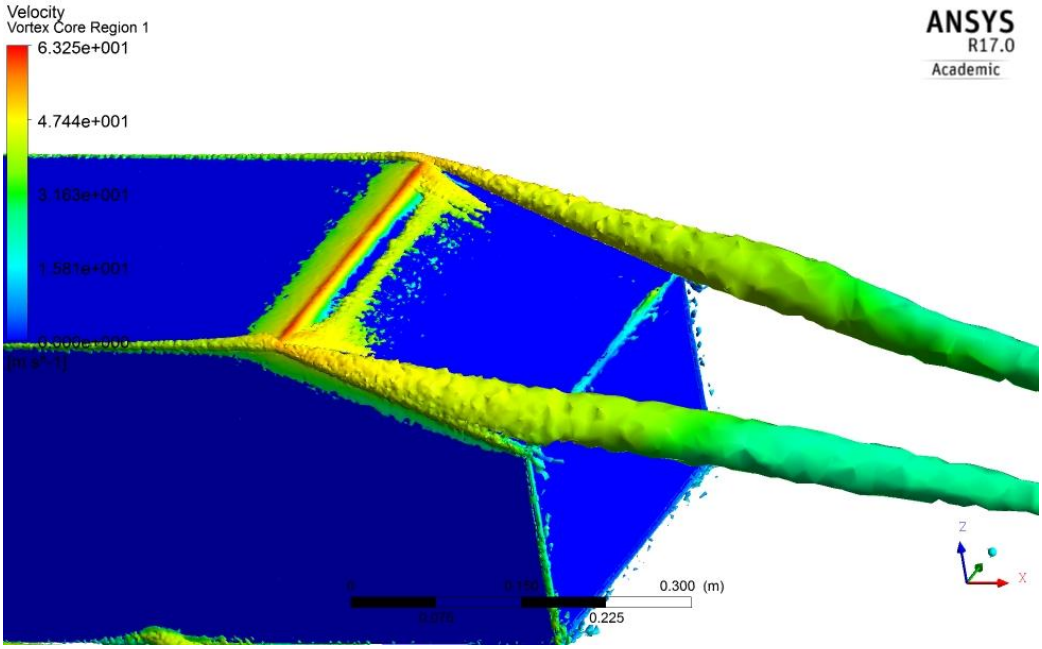

Figure 3.11- Velocity in the vortex core region for 25° Ahmed body

In Figure 3.11, the presence of streamwise vortices, originating on the upper C-pillar edges is clear. Referring back to Figure 2.12, these are identical to the streamwise vortices observed by Ahmed, et al. (1984) and others (Keogh et al. (2016), Meile et al. (2011), Wang et al. (2013), Baysal et al. (2001)).

The development of the streamwise vortices results from the shear that occurs when the flow along the sides of the Ahmed body meets the flow traveling along the 25° backlight at the location of the C-pillars. In Figure 3.12, surface lines indicating shear stress show the separation that occurs along the C-pillars (on either side) and the separation at the rear vertical face of the Ahmed body.

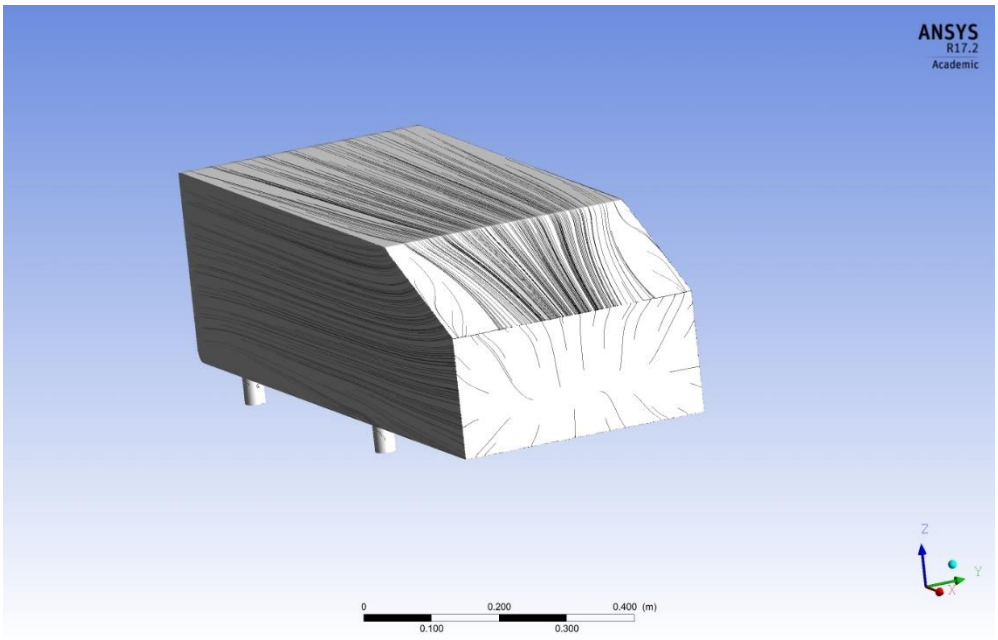

Figure 3.12- Surface lines of shear stress on the 25° Ahmed body

The surface lines of shear stress in Figure 3.12 from CFD compare well to the wind tunnel surface skin friction patterns produced in a wind tunnel study by Vino, et al (2005) as indicated in Figure 3.13.

Figure 3.13- Surface skin friction patterns on rear of 25° Ahmed body [(Vino, Watkins, Mousley, Watmuff, & Prasad, 2005)]

In Figure 3.13, there is evidence of separation of flow over the leading edge of the backlight. This separation is not strong in the CFD shear stress lines in Figure 3.12, indicative of the uncertainties involved in complex flow topology visualisation as mentioned earlier (Délery, et a., 2001). Just inboard of both C-pillars in both Figure 3.12 (CFD) and Figure 3.13 (wind tunnel) there are separation lines that run the entire length of the backlight. These two separation lines are the

result of the streamwise vortices that begin at the upper edge of the C-pillar (Vino, Watkins, Mousley, Watmuff, & Prasad, 2005).

Figure 3.14 is a closer view of the backlight region with a plot of Turbulence Kinetic Energy (TKE) and shows the streamwise vortices but no evidence of separation across the top of the backlight and hence no evidence of reattachment of flow on the backlight.

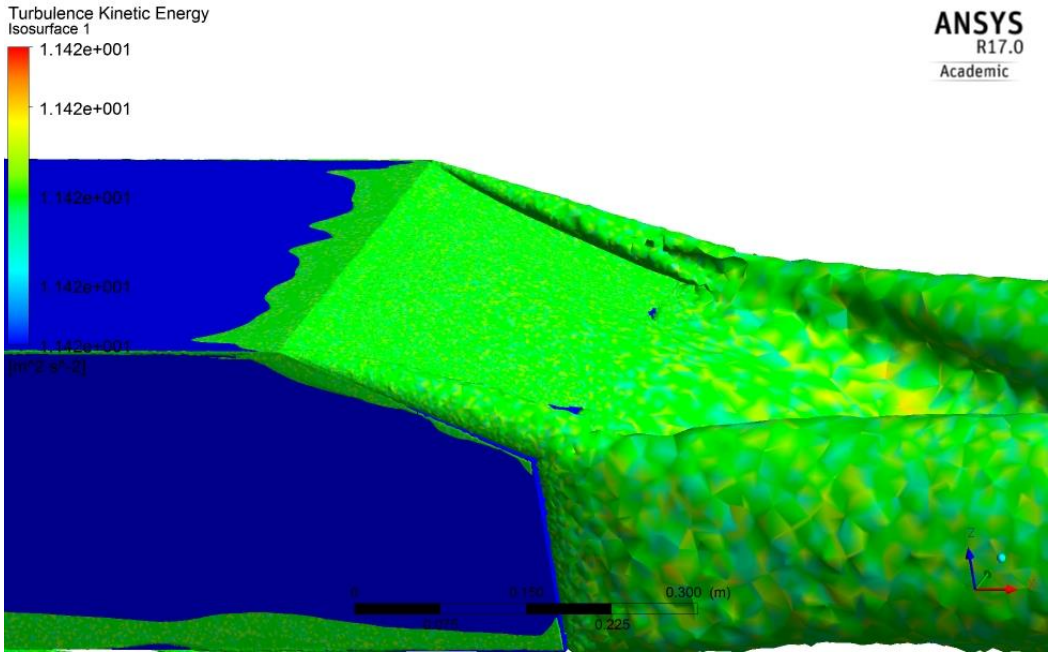

Figure 3.14- Turbulence Kinetic Energy plot over backlight of a 25° Ahmed body

3.5.3 35° Ahmed body

Although the 25° Ahmed body provided a validation of the CFD methodology for this work, it was decided to also examine the 35° Ahmed body as it has been reported (Ahmed et al., 1984) that it provided a different flow field over the backlight and in the wake. CFD meshing and methodology were the same as with the 25° Ahmed body. Figure 3.15 depicts streamwise profiles at various x-axis (longitudinal) positions in the y=0 (symmetry) plane for a 35° Ahmed body. As before, the profiles are plotted with data from the ERCOFTAC database (Lienhart, Becker, & Stoots, 2017) which were created in the LSTM wind tunnel at a velocity of 40 m/s and the profiles are plotted with the same scale as in Figure 3.5 (Meile W. , Brenn, Reppenhagen, Lechner, & Fuchs, 2011).

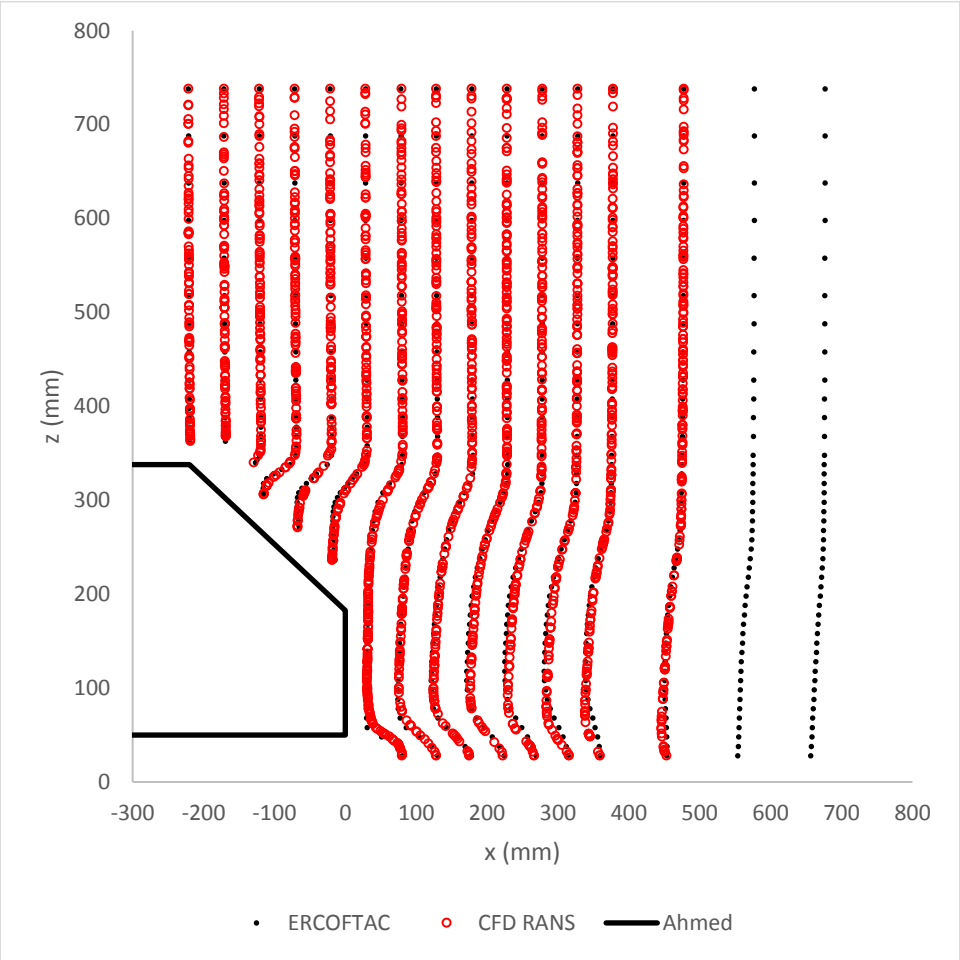

Figure 3.15- Streamwise velocity profiles for a 35° Ahmed body

Figure 3.15 demonstrates a high degree of fidelity between the velocity profiles calculated from CFD and the ERCOFTAC wind tunnel data. The velocity profiles are accurately matched to the wind tunnel data for the 35° Ahmed body as is the match between drag and lift coefficient for the 35° Ahmed body and wind tunnel data (Figure 3.4).

Ahmed et al. (1984), Meile, et al. (2011) and others have shown that, unlike the 25° Ahmed body, the 35° angle of the backlight of the Ahmed body produces separation at the leading edge of the backlight which does not reattach before reaching the trailing edge of the section.

The separation that occurs on the slant region of the 35° Ahmed body does not reattach, the streamwise vortices from the C-pillars are greatly diminished and the drag force is less than that of the 25° Ahmed body. This lack of reattachment is evident from a pressure plot on the surface of the backlight (Figure 3.16).

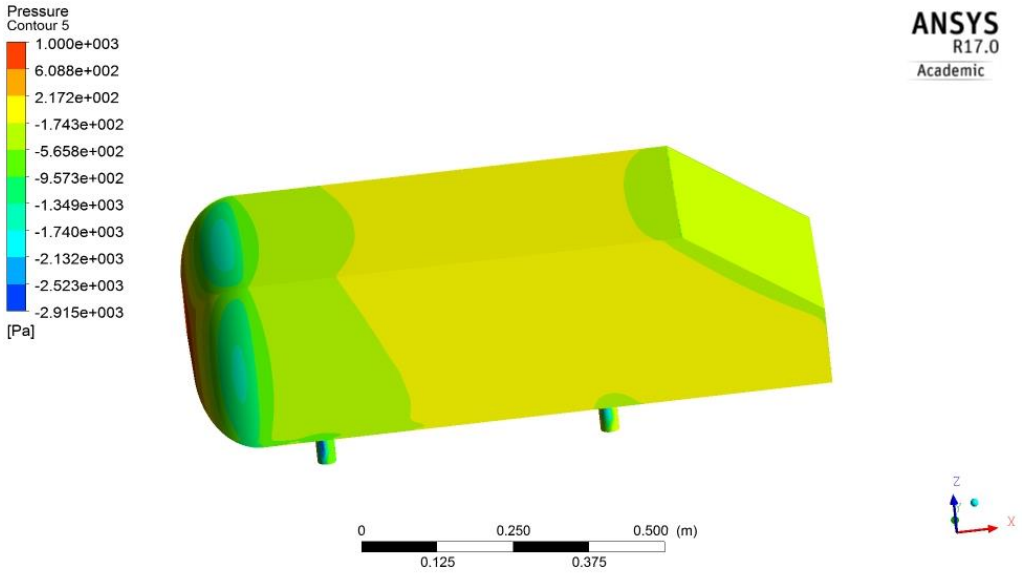

Figure 3.16- Pressure plot on 35° Ahmed body

In Figure 3.16, a lower pressure region exists over the entire backlight. Contrast this to the 25° Ahmed body pressure plot (Figure 3.6) where evidence of reattachment is present. In Figure 3.17, velocity streamlines over the rear section of the 35° Ahmed body further confirm the lack of reattachment over the backlight.

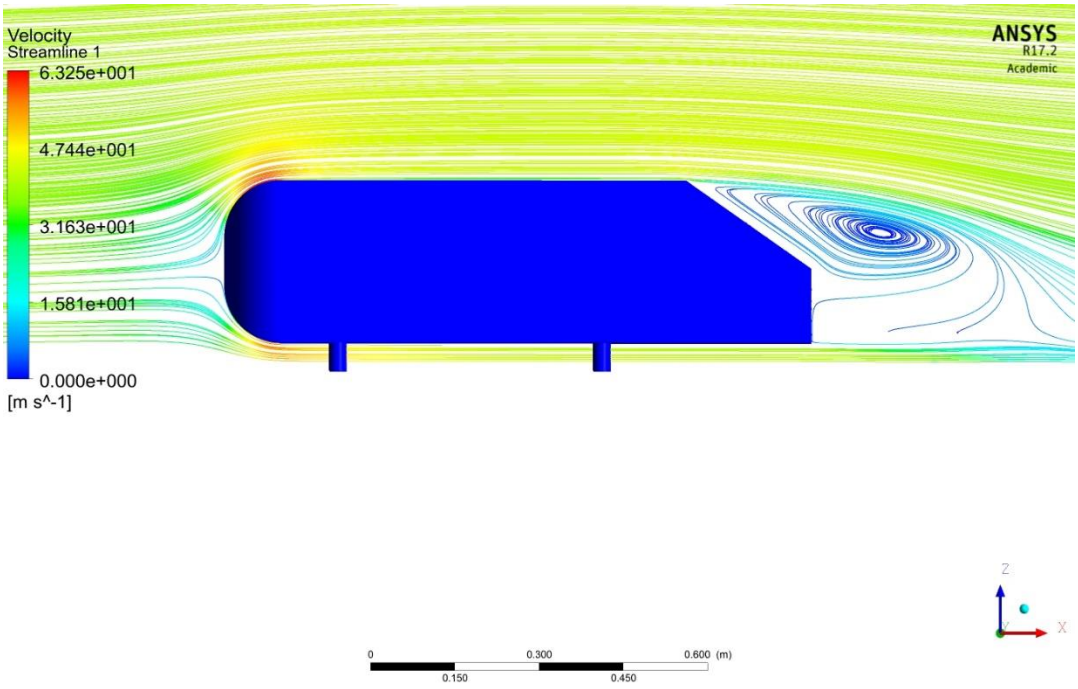

Figure 3.17- Velocity streamlines over the 35° Ahmed body

The lack of reattachment over the backlight is also evident from a velocity vector plot over the same backlight region (Figure 3.18).

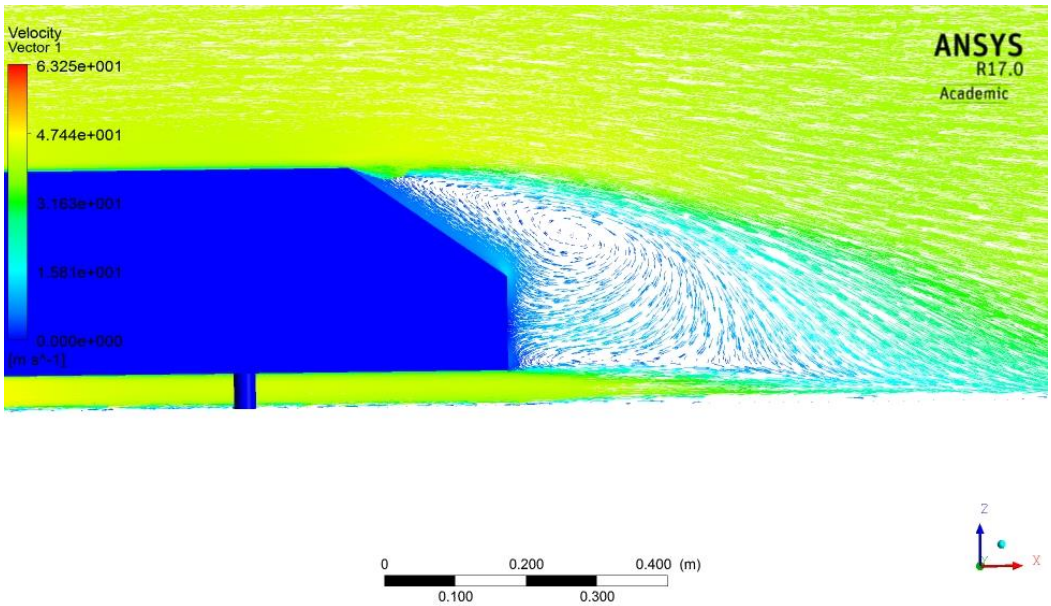

Figure 3.18- Velocity vectors over the backlight of a 35° Ahmed body

A large vortex in the separation region above the backlight and extending into the area directly behind the region is evident in Figure 3.17. From another view (Figure 3.19), it is evident that this is actually two counter-rotating vortices that result in streamwise vortices that extend downstream.

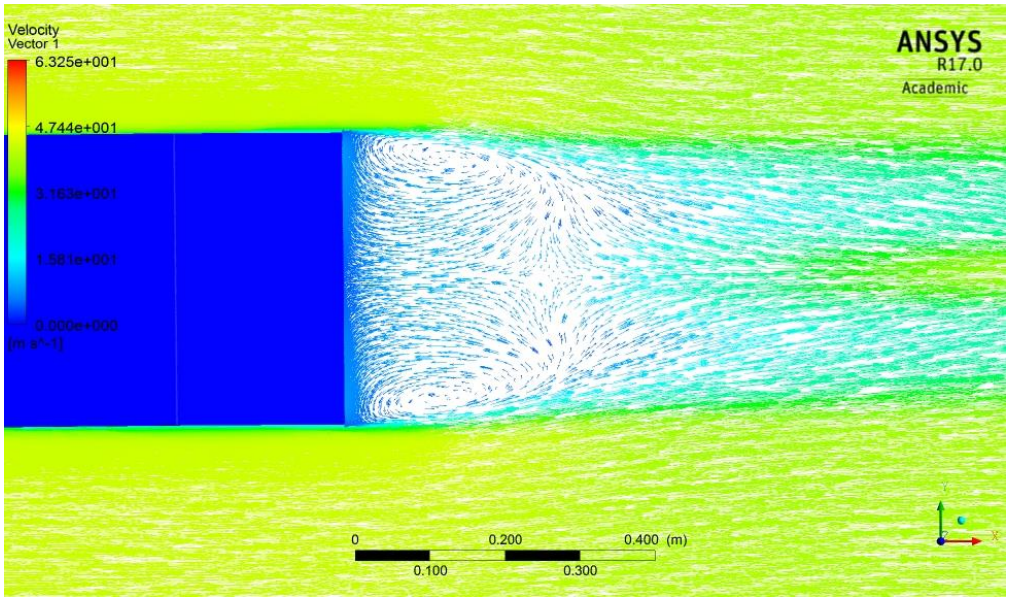

Figure 3.19- Velocity vectors from above for 35° Ahmed body

In Figures 3.11 and 3.14, the presence of streamwise vortices originating at the top edge of each of the C-pillars of a 25° Ahmed body were clearly evident. In Figure 3.20 showing velocity in the vortex core, these streamwise vortices are not present from the C-pillars, reinforcing the observation by Ahmed et al. (1984) that these vortices are minimal with a 35° backlight.

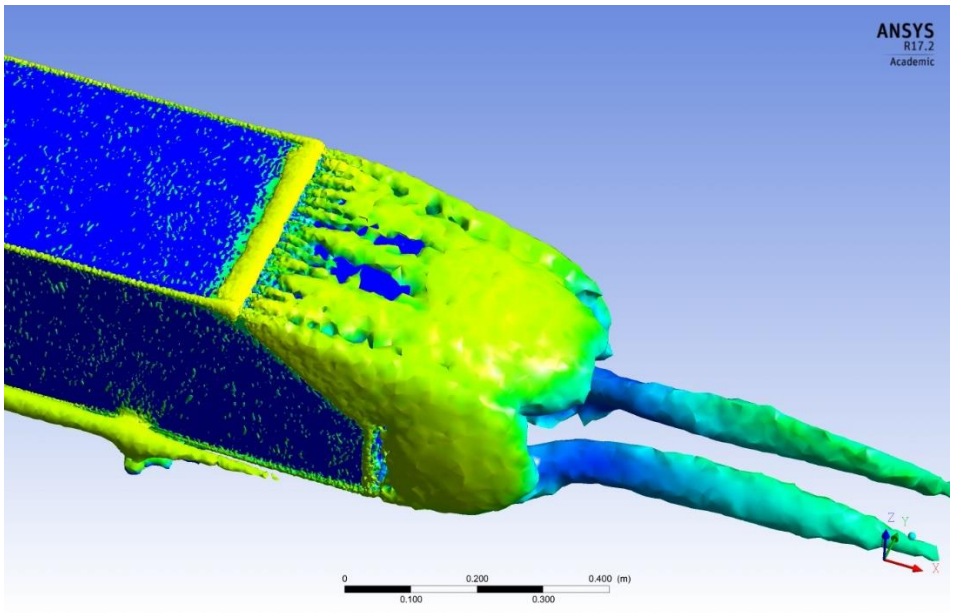

Figure 3.20- Velocity in the vortex core for 35° Ahmed body

From another angle (Figure 3.21) it is evident that the large counter rotating vortices shown in Figure 3.16 result in a pair of streamwise vortices that continue in to the wake. It is noted that these streamwise vortices are below the trailing edge of the backlight, while the streamwise trailing vortices on the 25° Ahmed body are above the trailing edge of the backlight (Figure 3.10).

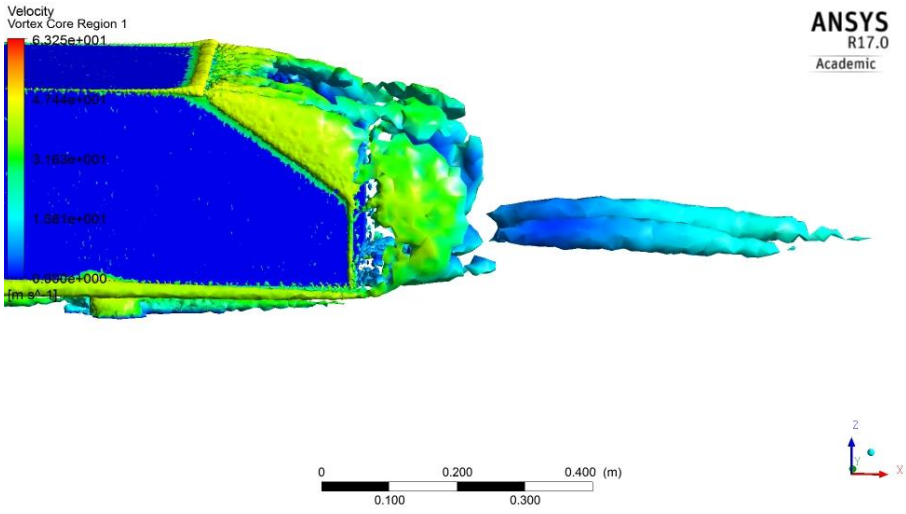

Figure 3.21- Velocity in the vortex core for 35° Ahmed body showing lower streamwise vortices

Figure 3.22 and Figure 3.23 indicate the surface lines of shear stress on the 35° Ahmed body backlight and rear panel.

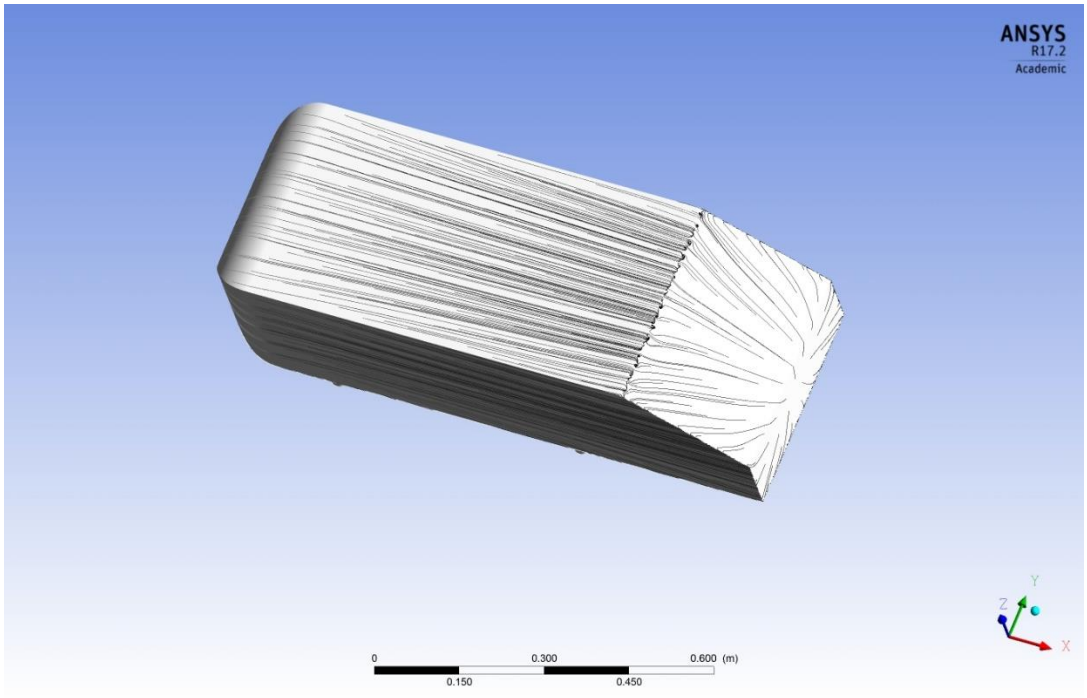

Figure 3.22- Surface lines of shear stress on 35° Ahmed body backlight

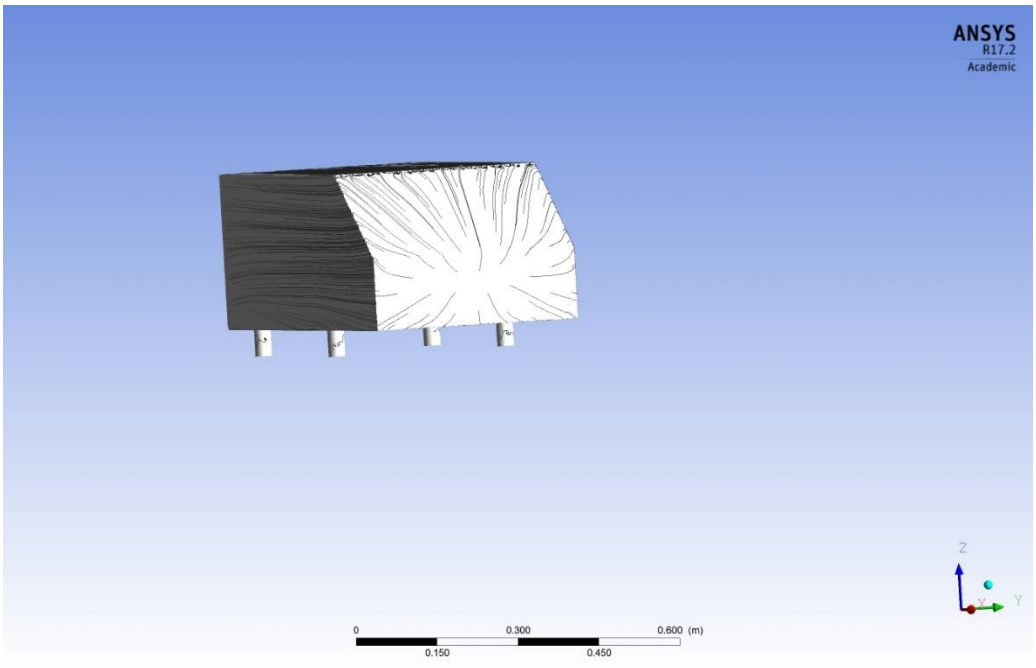

Figure 3.23- Surface lines of shear stress on 35° Ahmed body- rear panel

From both Figure 3.22 and Figure 3.23, it is evident that flow has separated across the entire of the backlight and across the entire rear of the 35° Ahmed body.

3.5.4 Large Eddy Simulations (LES)

Although the RANS simulations have shown good fidelity in modelling flow behaviours, external flow around vehicles produces flow instabilities that produce unsteady turbulence that is not always well represented by a steady state approach, particularly in the wake region (ANSYS, 2009). Large Eddy Simulation (LES) is a transient approach that is particularly effective at modelling the large-scale vorticity in the flow separated region behind a bluff body (ANSYS, 2009). The disadvantage to LES is that it requires an extremely large number of mesh elements that scale as the 1.8^{th} power of the Reynolds Number ($Re^{1.8}$) (Malik & Bushnell, 2012). As a result, even with significantly large computing capacity, LES can take many hours, days or even weeks to simulate high Re flows over complex geometries.

To examine how drag coefficient values using LES modelling matched RANS results and evaluate flow visualizations, a survey study using a 25° Ahmed body at 40 m/s was undertaken. Although a RANS model with an unstructured mesh of more than 5 million elements produced drag coefficients within 1% of published wind tunnel data (Table 3.1), it was hoped that better characterization of the wake region through LES region would produce more accurate drag and lift coefficient results. The 13.1 million element unstructured tetrahedral mesh used for the RANS studies was modified to bring the y+ value (which was in the 10-50 range for the RANS studies) to a value of 1-2 (Keogh, Barber, Diasinos, & Doig, 2016; Bayraktar, Landman, & Baysal, 2001). This was accomplished by changing the initial inflation layer thickness on the Ahmed body from 0.005 m for the RANS study to 0.0005 m for the LES study and increasing the number of inflation layers from 5 to 11. The resulting unstructured mesh had 15.3 million mostly tetrahedral elements. Using practices recommended by ANSYS a time step of 0.01 seconds was chosen with 1100 time steps and 5 iterations per step. Following the Ahmed body LES example of Keogh et al. (2016), the Smagorinsky-Lily stress-tensor model was selected with a fixed Smagorinsky constant (C_s) of 0.1. SIMPLEC pressure-velocity coupling scheme was used along with bounded central differencing for momentum, second order accuracy for pressure, and the transient formulation used was bounded second-order implicit (Gerasimov, 2016). The results are shown in Table 3.2.

Table 3.2: LES Modelling of 25° Ahmed Body at 40 m/s

Configuration	Mesh Size(millions)	Approximate run time (hrs) (10-core processor with 64 Gb RAM memory)	C_d	C_l
Published Wind Tunnel Data	----	----	0.299	0.345

(Meile, et. Al, 2011)				
CFD Using k-ω SST RANS model- steady state	13.1	5.5	0.295 (-1.4%)	0.353 (+2.3%)
CFD Using LES model- transient Smagorinsky-Lily	15.3	58	0.324 (+8.4%)	0.305 (-11.6%)

The drag and lift coefficients from the LES CFD simulations show a greater difference from the wind tunnel experimental data than does the RANS simulation. This is supported by results from others. For example, (Delassaux, Herbert, Mortazavi, & and Ribes, 2016) applied hybrid RANS/LES turbulence modelling to an Ahmed body, with a mesh size of 22 million elements and producing drag values within 2% and lift values within 8% of published wind tunnel data.

Castro, Mejia, and Munoz (2013) (Castro, Lopez, & Munoz, 2013) in a study of a station wagon, with an LES optimized mesh of approximately 50 million cells, found that the drag coefficient was 13.8% higher than the result obtained from a wind tunnel test.

Keogh, et al. (2016), using an LES simulation of a 25° Ahmed body and a mesh of 30 million elements found a drag coefficient that was 7% higher than that provided from wind tunnel data.

Serre, et al. (2013) found a good match between velocity profiles for their LES simulation when compared to ERCOFTAC wind tunnel data, but drag coefficient values were 44% higher than wind tunnel data.

Because LES is a transient analysis, the C_d and C_l with each time step. Averaged for the final 100 times steps (1000-1100) and the value of the C_d= 0.333 with a standard deviation of 0.0079. The standard deviation for the C_d was 0.0079. The average for C_l for final 100 time steps was 0.351, with a standard deviation of 0.0404. Using the average for C_l gave a closer (+1.7%) value to the published wind tunnel data, but the C_d was still different (+11.1%) than the published value. The velocity at any point in the wake also fluctuates with respect to each time step and it is not appropriate to examine the velocity profile at just one (or even the last) time step. The velocity profiles from ten times steps, equally spaced in in the final 100 time steps (time steps 1000-1100) were averaged to create an averaged velocity profile for the transient LES simulation. In Figure 3.24, streamwise profiles from the averaged LES simulation at various x-axis (longitudinal) positions in the y=0 (symmetry) plane for a 25° Ahmed body. As before, the profiles are plotted with data from the ERCOFTAC database (Lienhart, Becker, & Stoots, 2017) which were created in the LSTM wind tunnel at a velocity of 40 m/s (Meile W. , Brenn, Reppenhagen, Lechner, & Fuchs, 2011).

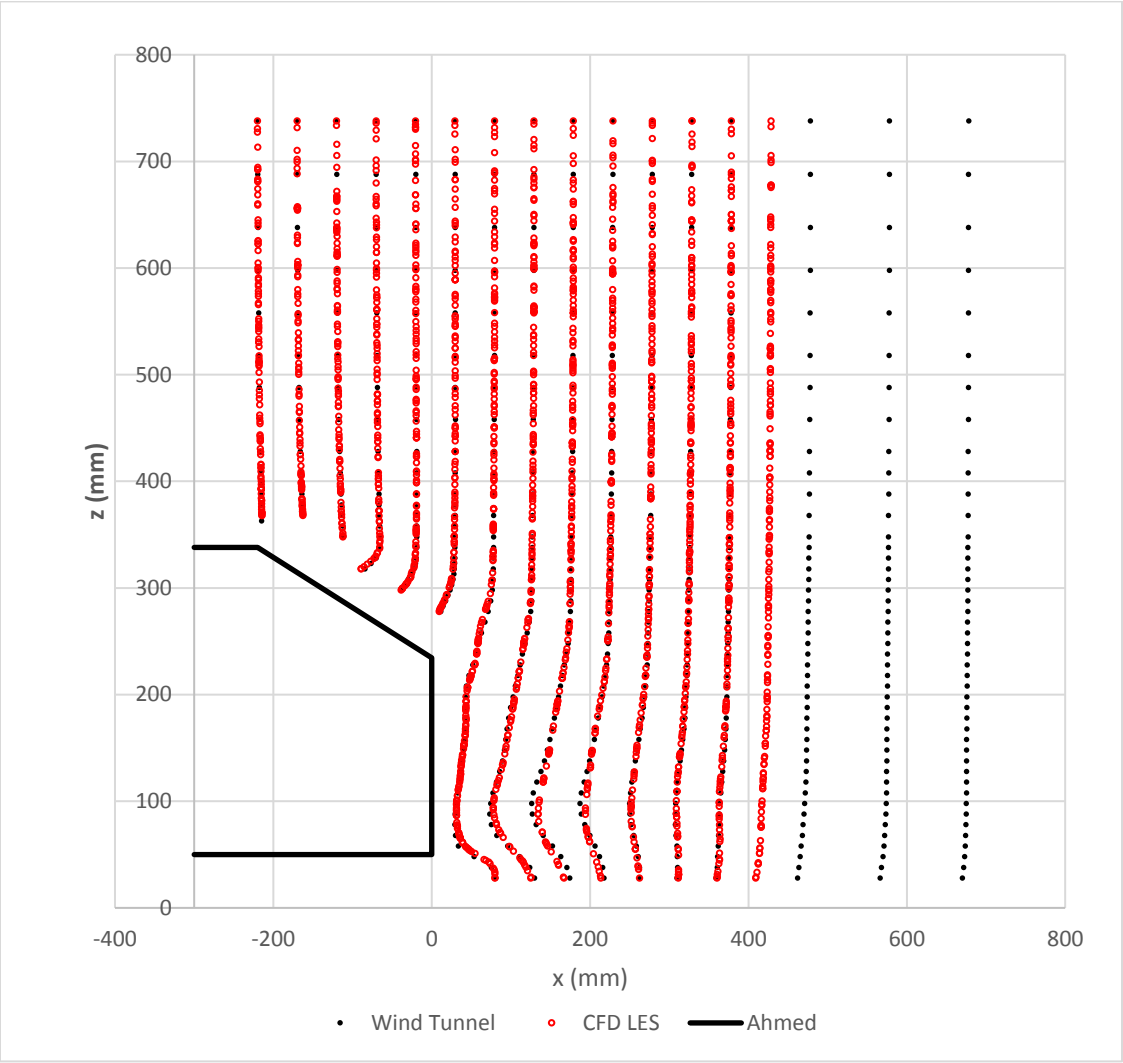

Figure 3.24- Streamwise velocity profiles for a 25° Ahmed body from LES

The streamwise velocity profiles for the LES CFD in Figure 3.24 show a good match to the velocity profiles from the ERCOFTAC wind tunnel results over the backlight and into the wake of the Ahmed body. As previously mentioned, velocity profiles of LES simulations are reported to closely match wind tunnel data (Serre, et al. 2013).

An examination of the pressure distribution from the LES on the 25° Ahmed body in Figure 3.25 indicates, as with the RANS case (Figure 3.6) that a lower pressure region forms at the leading edge of the backlight and along the upper parts of the C-pillars, and exists approximately halfway down the backlight region.

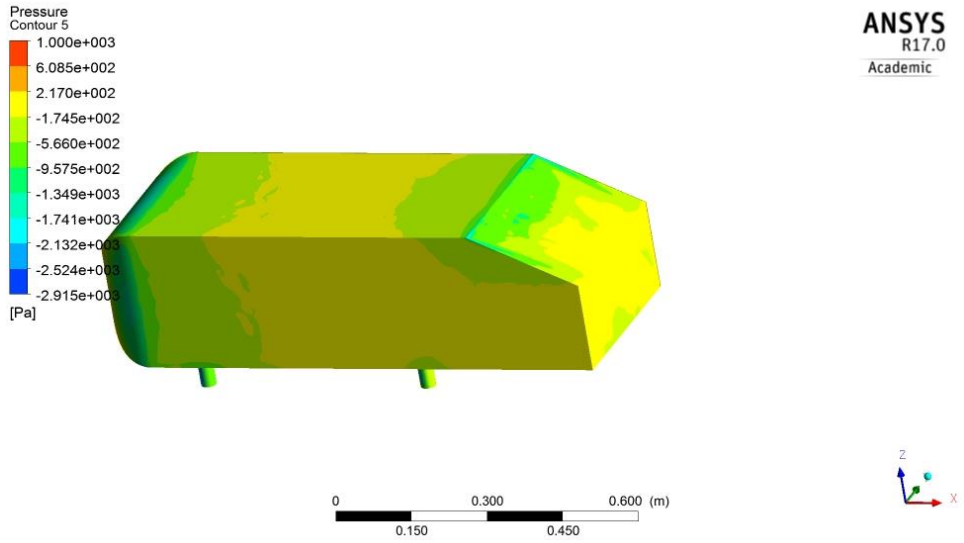

Figure 3.25- Pressure contours on 25° Ahmed body from LES

A plot in Figure 3.26 of velocity streamlines over the Ahmed body indicates a separation and reattachment of the flow over the backlight, forming a bubble. This separation bubble is consistent with the observations of Ahmed et al. (1984) and is illustrated in Figure 2.12. Figure 3.26 also demonstrates the existence of two counter-rotating vortices in the separated region directly behind the 25° Ahmed body. The presence of these vortices is also observed in Figure 2.12 and are further evidenced in a plot of velocity vectors over the 25° Ahmed body in Figure 3.27.

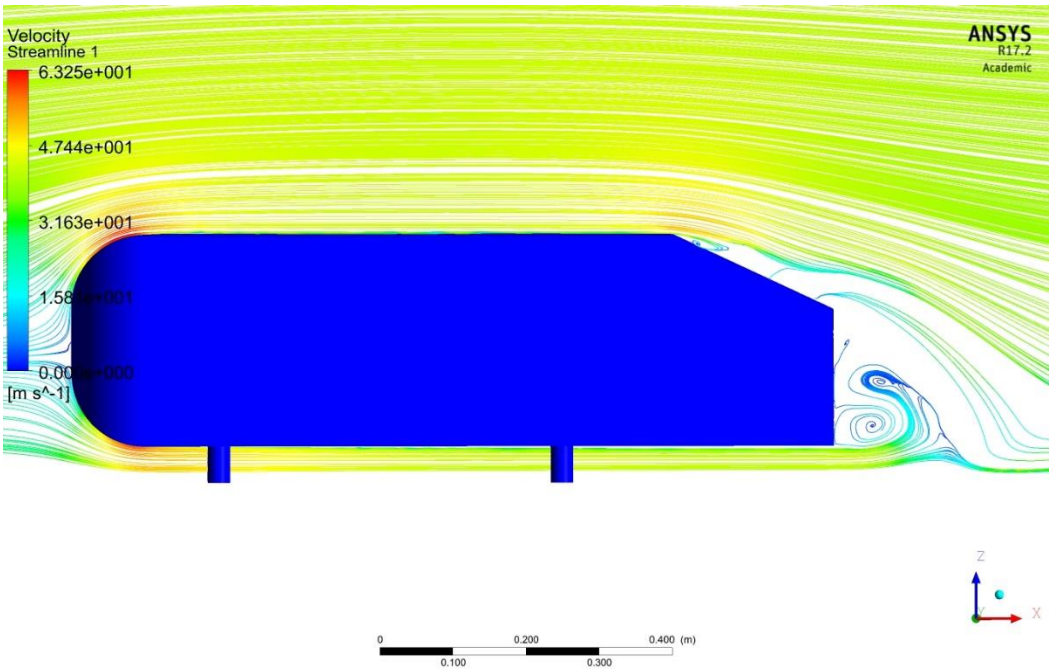

Figure 3.26- Velocity streamlines over the 25° Ahmed body from LES

In Figure 3.26, the streamlines which appear to originate from the backlight in fact travel parallel to the backlight for some distance before separating away from the surface.

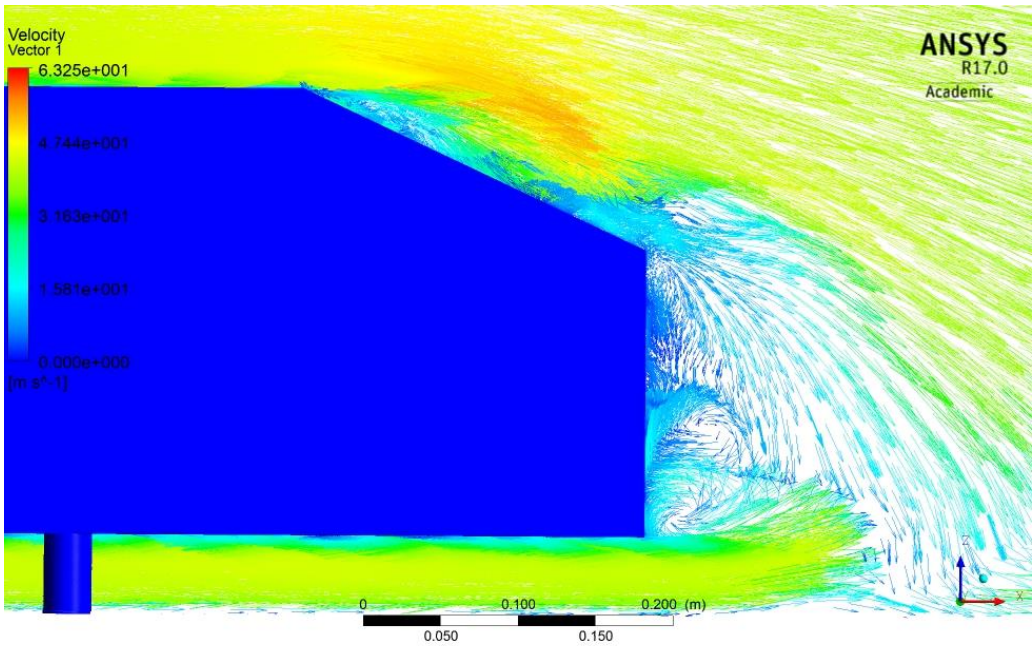

Figure 3.27- Velocity vectors over 25° Ahmed body from LES

From Figure 3.27, the velocity vectors indicate the presence of vorticity structure in the wake, both from the outer edges and directly behind the vertical tail of the vehicle. This is further evidenced in Figure 3.28.

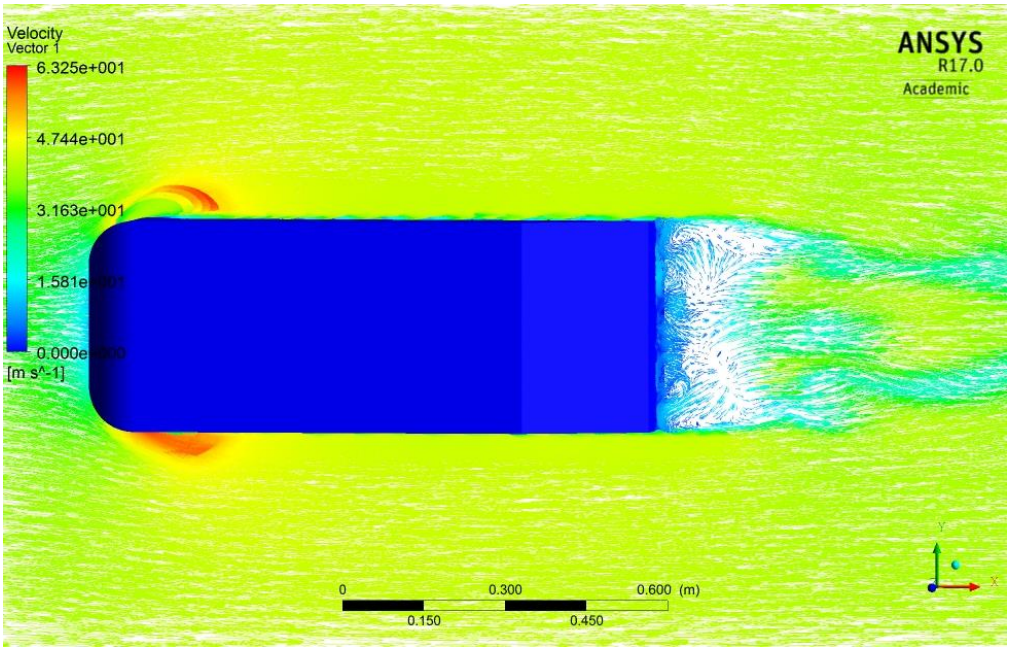

Figure 3.28- Velocity vectors of 25° Ahmed body from above from LES

The vortex structures in the wake region are further examined with an examination of velocity in the vortex core in Figure 3.29.

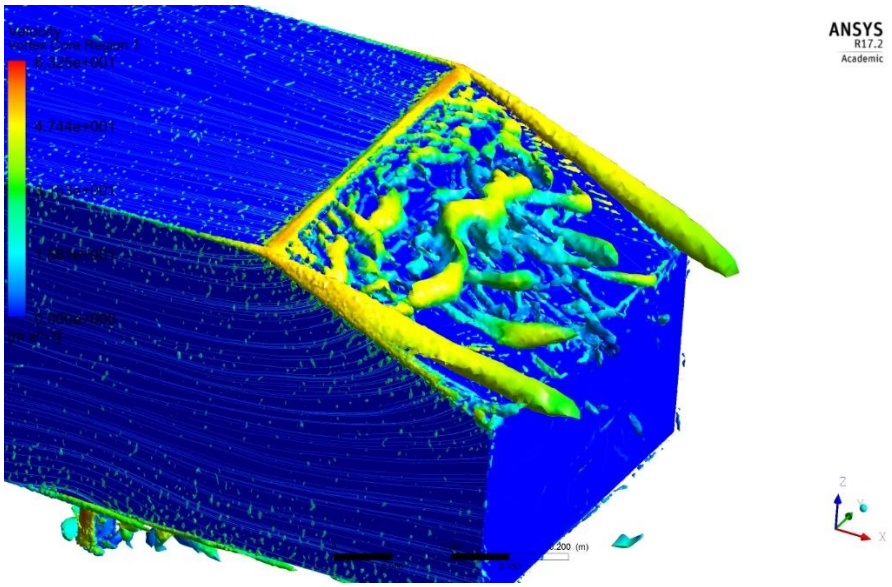

Figure 3.29- Velocity in the vortex core for 25° Ahmed body from LES

In Figure 3.29, the formation of streamwise vortices from the C-pillars is clear (Ahmed et al. 1984) as is an indication of reattachment of the separation approximately halfway down the backlight. This reattachment of flow onto the lower section of the backlight may also appear on the shear stress lines in Figure 3.30, although the separation lines that result from the formation of streamwise vortices from shear at the C-pillars are not evident. Note that LES shows streamwise and spanwise secondary structures on the backlight, which may be periodic in space and time.

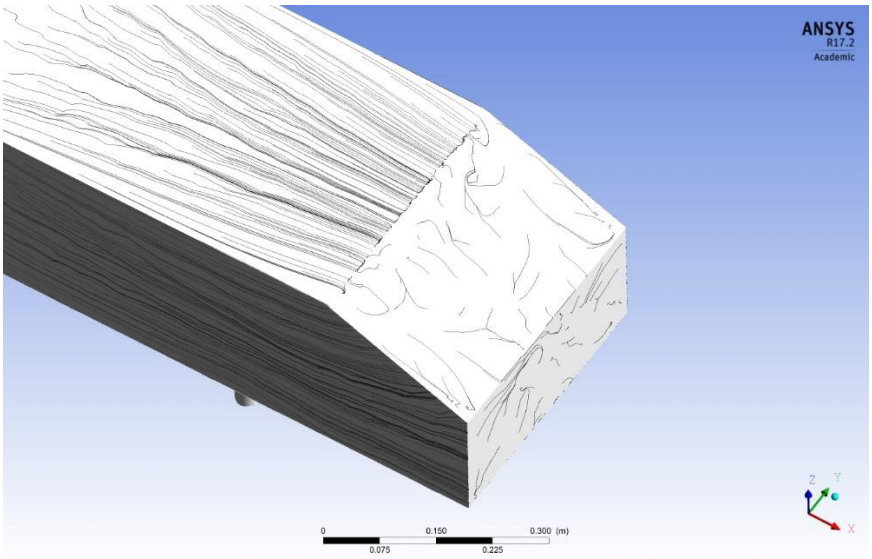

Figure 3.30- Shear stress surface lines of the 25° Ahmed body from LES

3.5.4.1 Summary of LES results

The LES results did not produce the same accuracy for drag and lift coefficients as the RANS simulations when compared to published wind tunnel data for a 25° Ahmed body. LES did demonstrate a greater capability (as evidenced by closely matching streamwise velocity profiles and patterns evident in velocity vectors) to reproduce vortex structures in the vehicle wake that compare favourably to published wind tunnel studies. It should be noted that this LES study was only a preliminary survey and the setup conditions were largely from published data (especially Keogh et al. (2011)). There is significant complexity in the application of any CFD, but particularly in LES due to consideration of time scales and the transient nature of the analyses. Further work with LES simulations might produce more accurate results, although as mentioned previously, published work would indicate that predicting drag and lift coefficients is not a strong point of LES simulations. In the current work, the target was a y+ value of approximately 1, however after the simulation was run the actual y+ value was found to be between 4 and 19. This may have affected the accuracy of the results as the subgrid region was not adequately modelled. A subsequent repeat of the LES with a smaller first inflation layer (and additional inflation layers) and with a y+ of 0.7 to 1.0, produced approximately the same C_d and C_l results. Although C_d and C_l values had reached steady values (within three decimal places) it is possible that the solution had not fully converged after 5500 iterations and possibly the simulation needed to run for a longer period. One factor that made LES CFD a difficult prospect for the sidecar optimization phase (Chapter 4) of the current work was the long time required to provide results. The 58 hours computer time for one CFD simulation would severely limit the number of sidecar optimizations that could be explored.

3.6 SUMMARY OF CHAPTER 3

A technique and procedure for CFD has been developed and validated with published ERCOFTAC wind tunnel data that was generated for an Ahmed body vehicle. The CFD procedure was verified over a range of wind velocities (Re), and with two different vehicle geometries (25° and 35° backlight angles). The drag and lift coefficients calculated from CFD show a good match to those found in published sources. A comparison of the vortex structures formed over the Ahmed body backlight and the topology of the wake showed good fidelity to observations of Ahmed body flow by published sources.

An LES modelling scheme was also examined but was found to produce larger inaccuracies in drag and lift coefficients when validated against published wind tunnel data than the RANS simulations. The vortex and wake structures created by the LES CFD simulation were found to have greater fidelity compared to published sources, but the long computational time required to generate the drag and lift coefficient values needed for the sidecar optimization study in Chapter 4 were felt to be excessive.

In Chapter 3 a variety of methods of characterizing aerodynamic flow over a bluff body were found of value. These include:

- drag, lift, and lateral force coefficients
- contour plots of surface pressure distribution to identify adverse pressure gradients
- plotting of velocity profiles in the wake region to examine the extent of disturbed flow
- plotting of velocity vectors to examine flow in critical areas
- plotting of velocity streamlines to examine flow paths and formation of vortex structures
- plotting of surface skin friction patterns to help predict separation of flow and formation of vortices
- visualisation of TKE contours and the presence of vortices through cut planes in the wake region
- visualisation of vortices through iso-surfaces of TKE
- visualisation of vortices and wake structures through swirling strength in velocity core iso-surfaces

Chapter 4 will involve creation of a CAD model of an asymmetrical land speed record sidecar from laser scans, RANS CFD modelling of the sidecar, and a wide range of geometrical changes in an effort to reduce the aerodynamic drag of the sidecar. Many of the methods for characterization of aerodynamic flow that were validated in Chapter 3 will be used to evaluate the sidecar changes in Chapter 4.

CHAPTER 4 OPTIMISATION PHASE

4.1 VEHICLE STARTING POINT

Following significant previous success with solo electric motorcycle land speed record breaking (including setting four FIM World Records), it was decided to expand record attempts to a faster and more sophisticated electric vehicle. Motorcycle sidecars have their own land-speed racing categories for electric and combustion powered designs and promised to provide an interesting engineering challenge. Rather than starting from scratch, a Baker Formula One road racing sidecar was purchased and the 1000-cc Suzuki GSX-R four-cylinder petrol engine and transmission was removed and replaced with an electric drive. The sidecar chosen had been built in the U.K. and competed in the 1988 and 1989 Isle of Man TT races (Brown, 2016). Subsequently it was shipped to the U.S. where it set seven national road-racing championships.

Figure 4.1- Brown and Nelson racing the Baker sidecar at the Isle of Man in 1989 *(Dennis Brown Collection)*

4.2 CREATION OF CFD MODEL

To create an accurate three-dimensional CAD model for CFD simulations a laser scan of the full-scale sidecar vehicle was commissioned from a professional laser scan company (LaserDesign, Minneapolis, MN). After spraying the shiny sidecar surfaces with a commercially available product to reduce reflections, scanning was performed with the rider in full safety gear (leathers and helmet) in place and positioned to represent the vehicle as it would be in competition (Figure 4.2).

Figure 4.2- Laser scanning of the sidecar and rider *(author)*

The point cloud produced by this scan (accuracy +/- 5μm) was further processed by the scanning company to produce a SolidWorks 16.0 part file that could then be used to create source files for CFD.

The initial SolidWorks model from the scan was simplified compared to the actual racing sidecar. The vehicle floor became a horizontal plane that was completely flat and intersected the tyres without introducing the hollow cavities that surround each wheel. All openings were sealed and the region surrounding the rear wheel and rear bodywork was simplified to allow the sidecar to be represented by a fully enclosed Solidworks body. These deviations in geometry from the actual sidecar would make direct comparisons between the modelling and actual speed results potentially less accurate, however the loss in accuracy was offset by the allowance a simpler body configuration and the “water tight” vehicle body (no open cavities or gaps in the bodywork and between panels) required for ANSYS Fluent CFD simulations (Figure 4.3).

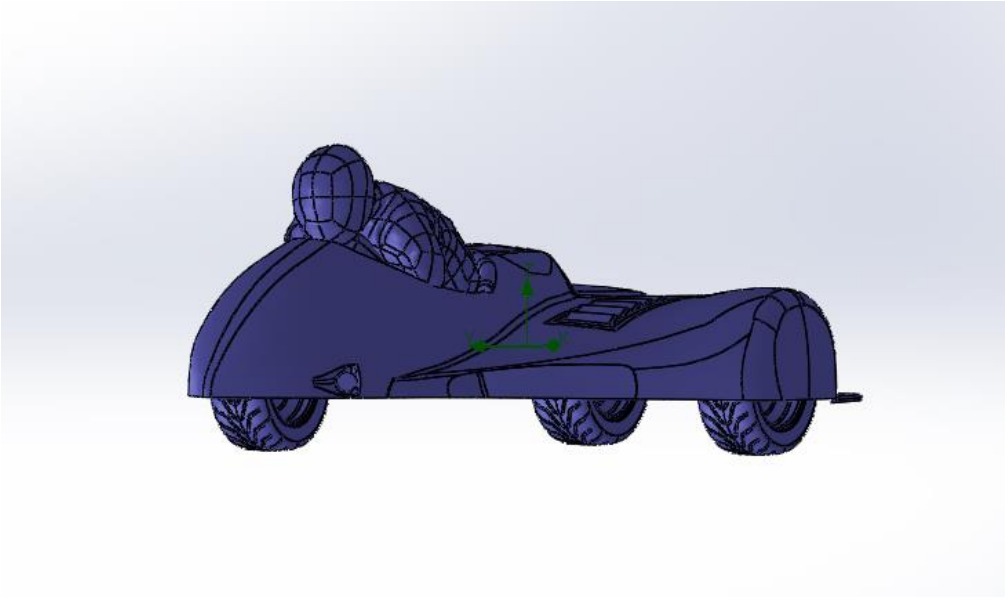

Figure 4.3- SolidWorks model of sidecar from laser scan

4.3 COMPUTATIONAL FLUID DYNAMICS (CFD) METHODOLOGY FOR SIDECAR

To setup the computational conditions for external flow of a vehicle in ANSYS Fluent 17.0, consideration was given to the recommendations for vehicle simulations by ANSYS from Lanfrit (2005) and the CFD validation study described in Chapter 3. The length of the sidecar is 3.28 metres, and the region behind the sidecar was set to have a length of 20 metres. The side spacing between the no-slip walls and the sidecar was chosen as 3 metres to each side. The model was tested on the ground plane or "road" surface with the distance to the zero-slip top plane surface (ceiling) was set to 6 metres. The distance between the bottom of the "wheels" on the sidecar and the no-slip non-moving road was set to 0.005 metres to avoid having the surface mesh in contact with the road surface. Although rotating wheel simulations were considered, and a trial simulation was undertaken, it was found to have no discernible effect on the lift and drag coefficients. This is because the wheels of the sidecar are completely covered by the bodywork. The dimensions of the enclosure were examined using flow visualisation in Fluent to ensure that the slipstreams and flow from the model would not be interfered with by the presence of a wall or inlet or outlet.

Based upon the Ahmed body testing in Chapter 3, an initial mesh Independence study was performed using a k-ε Realizable turbulence model with a Scalable Wall Function. A body of influence refinement box was placed around the sidecar body and also extended beyond the vehicle 6 metres and into its wake region. The velocity was 67 m/s ($Re \approx 1.5 \times 10^7$), with a stationary floor with an inlet turbulence intensity of 5% and a turbulence viscosity ratio of 10. A coupled scheme was used for pressure-velocity coupling, and spatial discretization used a least squares gradient and second order upwind pressure, momentum, turbulence kinetic energy and dissipation rates. Other Fluent setup parameters are as described in Appendix A. Using ANSYS

Fluent 17.0, mesh sizes between 18,000 and 11.3 million unstructured elements were created and used to determine the minimum mesh size for accurate results (Figure 4.4). It is shown that a mesh greater than approximately 3 million elements was sufficient for this study.

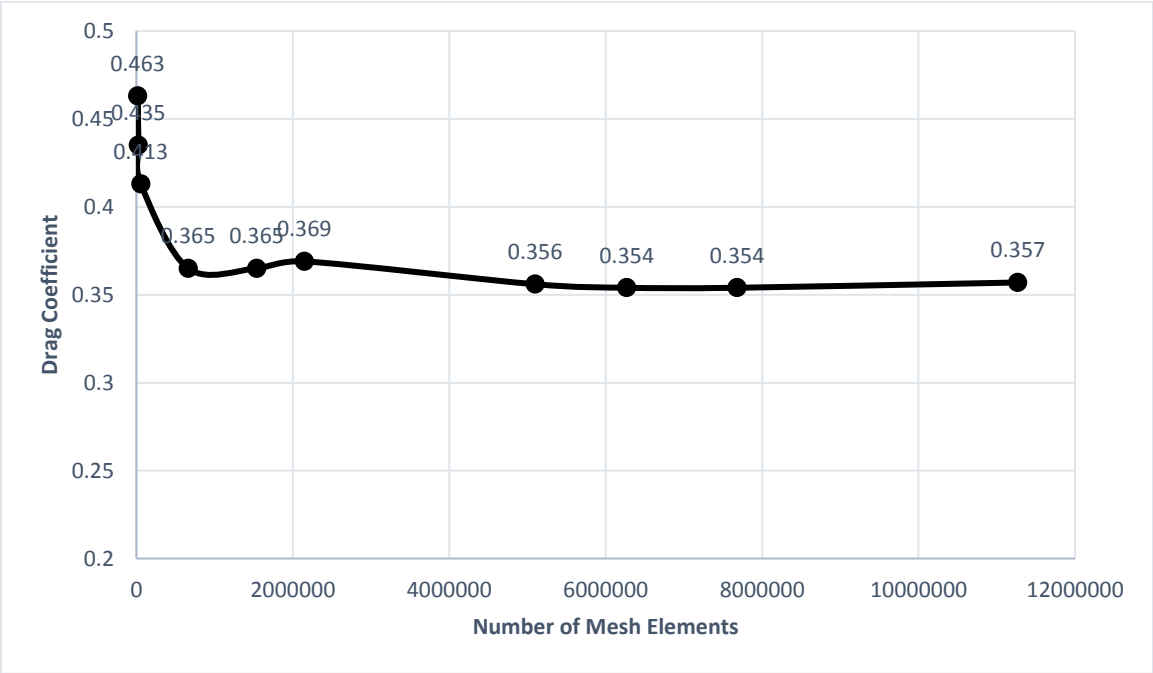

Figure 4.4- Mesh independence of initial sidecar version with stationary road at 67 m/s

4.3.1 Creation of an easier-to-mesh model

Although the initial SolidWorks part proved adequate for initial CFD tests, it was observed that the geometry created from the laser scan, due to sharp edges and multiple radii, was difficult to mesh and occasionally resulted in divergence of the solver during CFD calculations. For subsequent investigations of new sidecar configurations, a new SolidWorks part was created to allow easier changes to the part geometry and to assist in easier meshing. This part was created by intersecting the existing sidecar profile with horizontal and vertical planes and placing spline curves along the intersections to provide a more mathematically robust geometrical model. In Figure 4.5, the outer surfaces of the original sidecar (in blue) and the newly-created easier-to-mesh (in red) sidecar bodies are compared.

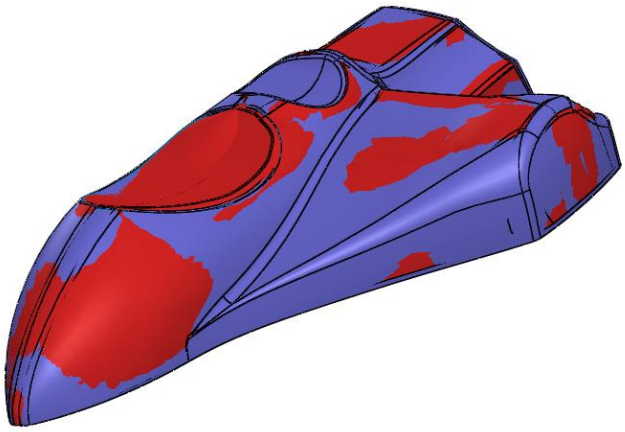

Figure 4.5- Original sidecar body in blue compared to new body surface in red

In addition to the body surface, the wheels were simplified (tread pattern removed) and space was provided around the wheels to better represent the gaps on the actual sidecar. The original version of the sidecar from the laser scan was compared to the simplified version that was constructed from the new body and wheels. The CFD results at 67 m/s with a stationary road as shown in Table 4.1 indicates that the new version of the sidecar model generates 8.3% higher drag and a significant amount of lift compared to the original sidecar model.

Table 4.1: Original Sidecar versus Sidecar from new surface

Sidecar Version	**Road**	**Velocity m/s**	**C_d**	**C_l**		**C_y**
Original	stationary	67	0.361	0.174		0.025
New Surface	stationary	67	0.391 (+8.3%)	0.245 (+40%)		0.030 (+20%)

4.3.2 CFD model modifications

During the course of the development of the sidecar for record attempts in Colorado, Ohio, and the Bonneville Salt Flats in Utah, it was necessary to add a large battery box and small water cooling tank on the rear platform (as described in Chapter 5). A modification of the original SolidWorks model to represent the revised vehicle is shown in Figure 4.6 within its computational domain and was used as the starting point for the design study (see also Figure 4.8).

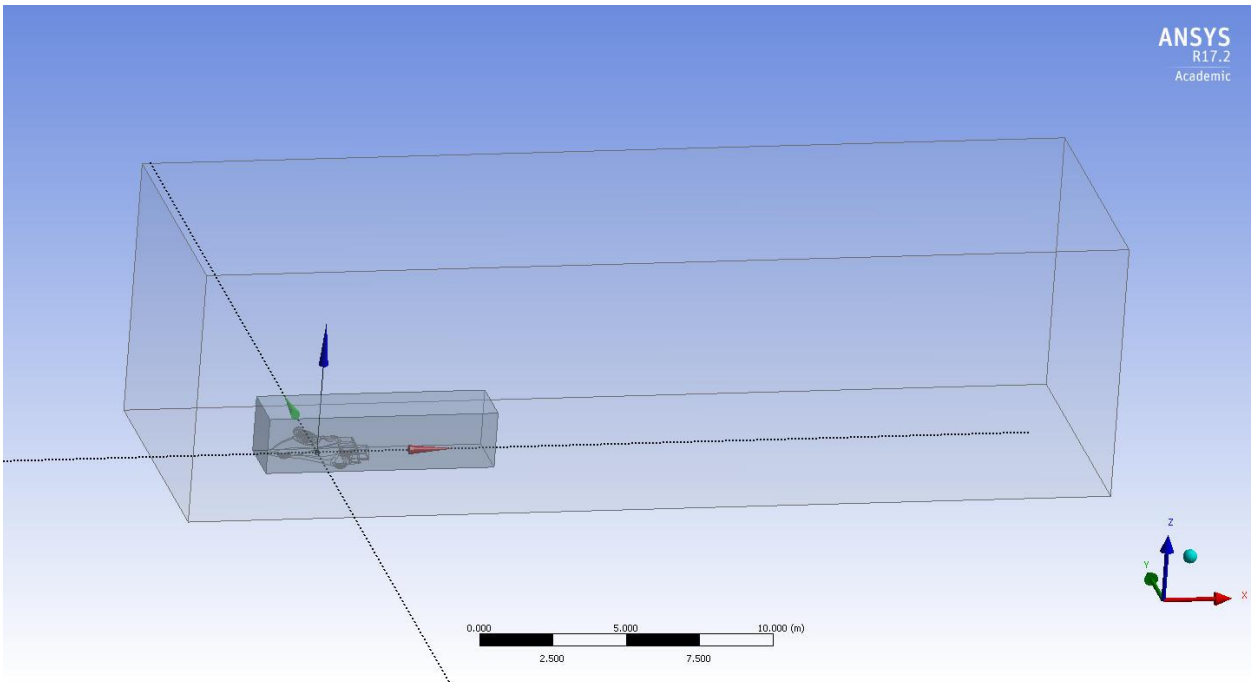

Figure 4.6- Sidecar configuration for CFD with battery box and cooling tank in computational domain

Using ANSYS Fluent 17.0 with an unstructured tetrahedral mesh of 8 million elements and a k-ε Realizable turbulence model with a Scalable Wall Function, the following coefficients were calculated from the drag, lift and lateral forces generated at 67 m/s (150 mph) with a stationary road surface.

$C_d = 0.365$

$C_l = 0.175$

$C_y = 0.025$

The addition of the rear battery pack and water cooling tank resulted in a CFD calculated decrease in drag (-6.7%), reduction of lift (-29%) and reduction in lateral force (-20%) when compared to the drag, lift and lateral forces values determined from CFD of the new surface sidecar with just an open rear platform.

4.3.3 Re Sensitivity

To test the sensitivity of the sidecar CFD studies to the Re, a series of simulations were run with speeds ranging from 2 m/s (Re= 446,000) to 90 m/s (Re = 20.07 million), calculated with a vehicle length of 3.28 metres as the length scale. The results are plotted in Figure 4.7, which shows a similar degree of sensitivity to Re as was observed with the 25° Ahmed body plot in Figure 3.2.

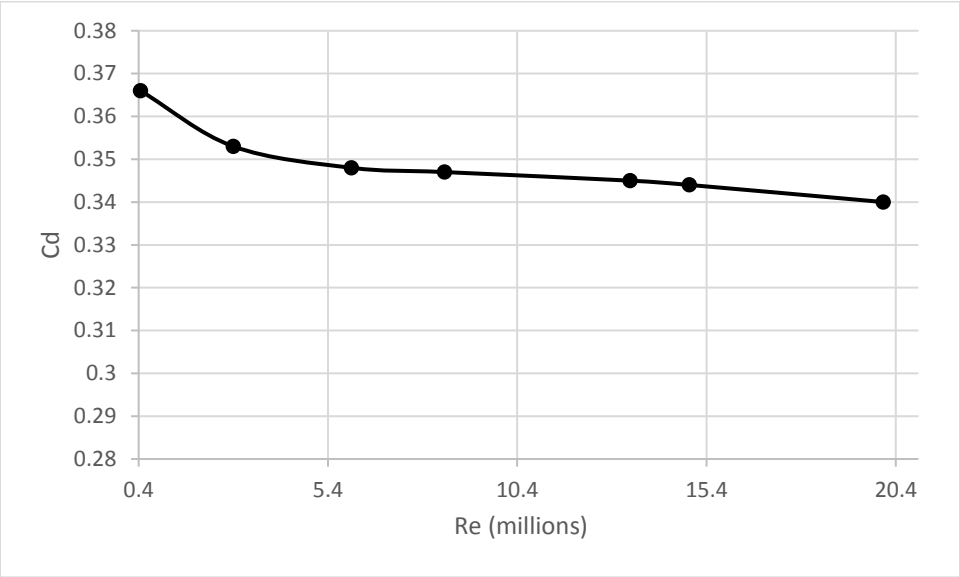

Figure 4.7- Re sensitivity of CFD for original sidecar

4.4 OVERVIEW OF AERODYNAMIC DESIGN

There were two goals in the development of a revised aerodynamic solution for this project. As this is a land speed record vehicle, the reduction of longitudinal aerodynamic drag to improve top speed was the primary goal. The amount of power required to overcome aerodynamic drag increases with velocity cubed. This drag depends upon both the frontal area and the C_d, as well as the air density (Bonneville and Colorado for example, are at significant altitude, giving a useful reduction in air density). The frontal area of the Baker racing sidecar is approximately one square metre and because of reuse of the existing body and packaging of the large components (motors, batteries, controllers, control electronics) it is difficult to reduce the frontal area of this vehicle, especially given the overall length constraint of a land speed racing sidecar from the FIM of 3,300 mm. The reduction of drag therefore falls to development of a body shape that reduces C_d.

The second goal, of nearly equal importance, was the development of a safe and stable vehicle up to maximum speeds in excess of 150 mph (241 km/h). As in most motorsports, modern technology has helped to mitigate the risks to personal injury in this form of racing, however fatalities are not unknown in the sport. Although few (if any) formal studies have been performed, anecdotal evidence would suggest that land speed record fatalities are generally related to a loss of control due to either inherent vehicle instabilities, or the presence of an unexpected outside perturbation force (side wind, blown tyre, mechanical failure). From an aerodynamic perspective, instability is frequently a result of the generation of lift and lateral forces that are unable to be countered by the mass of the vehicle or by the frictional interaction of the tyres with the ground surface. The generation of lift and lateral forces are largely determined by the shape of the bodywork that the air flows over and the point along the longitudinal axis of the vehicle where the lateral forces act. In addition, the effects of side winds

and vehicle yaw can promote significantly larger lift and/or lateral forces that can decrease vehicle stability, sometimes with catastrophic consequences.

Since a sidecar is asymmetrical in its geometry, the lift and lateral forces can be different when the vehicle yaws one direction compared to the other or when the side winds come from the opposite directions. With the sidecar wheel offset from the centreline of the front and rear wheels (offset to the right in the U.S., offset to the left in most other countries, particularly those that drive on the left), the rider feels a higher degree of confidence when making turns away from the sidecar placement—turns that load the sidecar wheel, than when turning toward the sidecar, which can completely unload the sidecar wheel. These differences in control response can result in rider confusion in an emergency.

Due to a sidecar's inherent asymmetry and the expected generation of residual lateral forces, the generation of both lift and lateral forces received significant scrutiny during the design and development of the modifications to the sidecar body.

4.5 Optimisation Phase of the Baker sidecar

A series of iterations were undertaken, using SolidWorks 16.0 CAD modelling, to create three-dimensional representations of the modified sidecar. ANSYS Fluent 17.0 was used to simulate aerodynamic flow over each vehicle design. The validated CFD methodology developed to properly capture the aerodynamic forces of an Ahmed body from Chapter 3 was used to determine and compare the drag, lift, and lateral force coefficients generated by the different body shapes in the design phase.

The computational domain for the simulations was set to be large enough to prevent interaction with flow along the walls and ceiling. The velocity inlet was 4 metres ahead of the vehicle, the ceiling was 6 metres above the vehicle, the walls were 3 metres away from each side of the vehicle and the pressure outlet was 25 metres downstream of the vehicle. The vehicle was placed in close proximity to the floor (0.005 m) which was moving at the same velocity as the airflow (67 m/s unless otherwise indicated). For the initial design series, the k-epsilon Realizable turbulence model was used with Scalable Wall Functions and unstructured, primarily tetrahedral meshes of between 6 and 12 million elements were created for the simulations, with refinement boxes located over the vehicle and from the tail of the vehicle up to a distance of 6 metres behind the vehicle to capture wake topology and up to 10 inflation layers to capture surface effects. A coupled scheme was used for pressure and velocity and spatial discretization used a least squares gradient and second order upwind pressure, momentum, turbulence kinetic energy and dissipation rates. Convergence was determined by examining the third decimal place of the C_d and C_l coefficients—when they began to repeat the solution was judged to be adequately converged for determination of lift and drag values. Residuals (which are often used for convergence) were found to be in the 10^{-4} to 10^{-6} ranges when the C_d and C_l convergence criteria was met—typically after 200 iterations. A larger number of iterations were not found to

appreciably change the drag and lift values. The details of the CFD setup are provided in Appendix A.

The starting point for this optimisation series was the SolidWorks model of the sidecar motorcycle with battery box and cooling tank, as depicted in Figure 4.8.

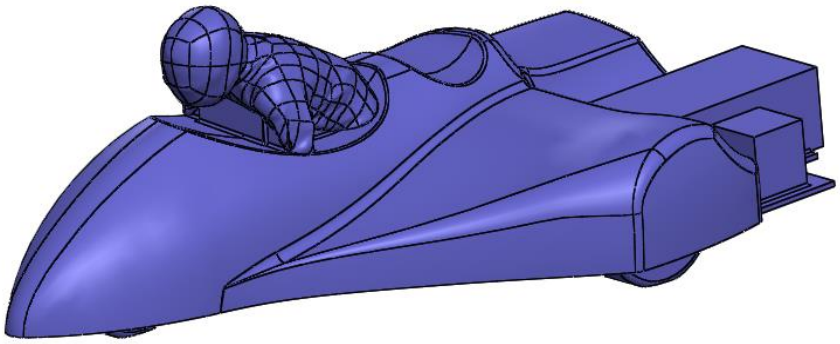

Figure 4.8- Baseline for the sidecar redesign study

The following coefficients were calculated from the drag, lift and lateral forces generated at 67 m/s (150 mph) with a moving road surface for this configuration.

$C_d = 0.344$

$C_l = 0.0026$

$C_y = 0.065$

$C_m = 0.045$

Note that C_m is the yaw moment coefficient around the vertical z-axis. A positive direction means a moment exists that will work to rotate the sidecar in the clockwise direction (away from the sidecar).

Figure 4.9 is a plot of the pressure distribution over the surface of the initial sidecar design at 67 m/s with a moving road surface.

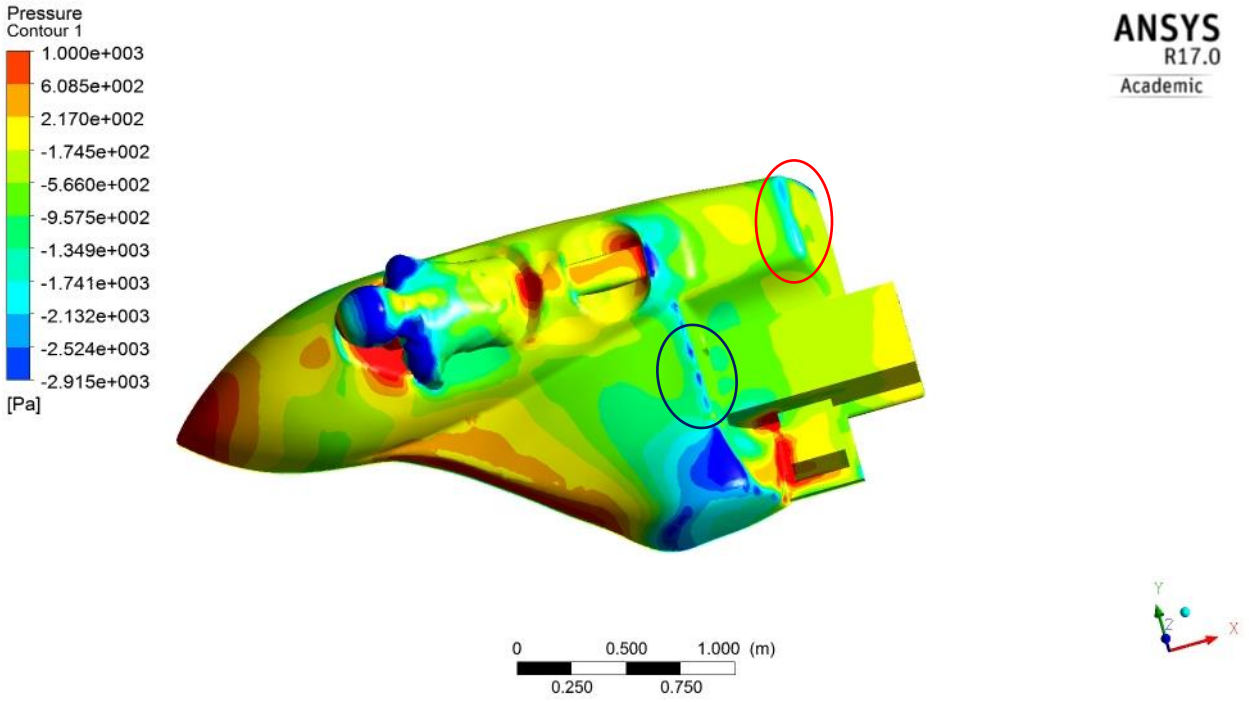

Figure 4.9- Pressure distribution over initial sidecar at 67 m/s with moving road surface

From Figure 4.9 it is evident that the distribution of pressure over the surface is much more complex than the pressure distribution over the Ahmed body (Figure 3.6) used for the CFD validation work in Chapter 3.

There are several areas of interest in Figure 4.9 that can be compared to regions evidenced on the 25° and 35° Ahmed bodies. The trailing edges of the rear of the flat section well behind the rider (highlighted in red) and of the step down portion just ahead of the battery box exhibit low pressure along the edge (highlighted blue) in Figure 4.9 in the same way that the edge at the leading edge of the backlight does in the Ahmed body. Similarly, the flat region on the top surface of the rectangular battery box transitions from low pressure back to high pressure, suggesting that the flow might reattach to the top of the battery body after separating over the edge that is located just ahead of the battery box.

In figure 4.10, velocity vectors on a plane below the edge of the battery box show two separation regions, one behind the vertical surface of the battery box (indicated in red) and one directly behind the rear wheel of the sidecar (indicated in green).

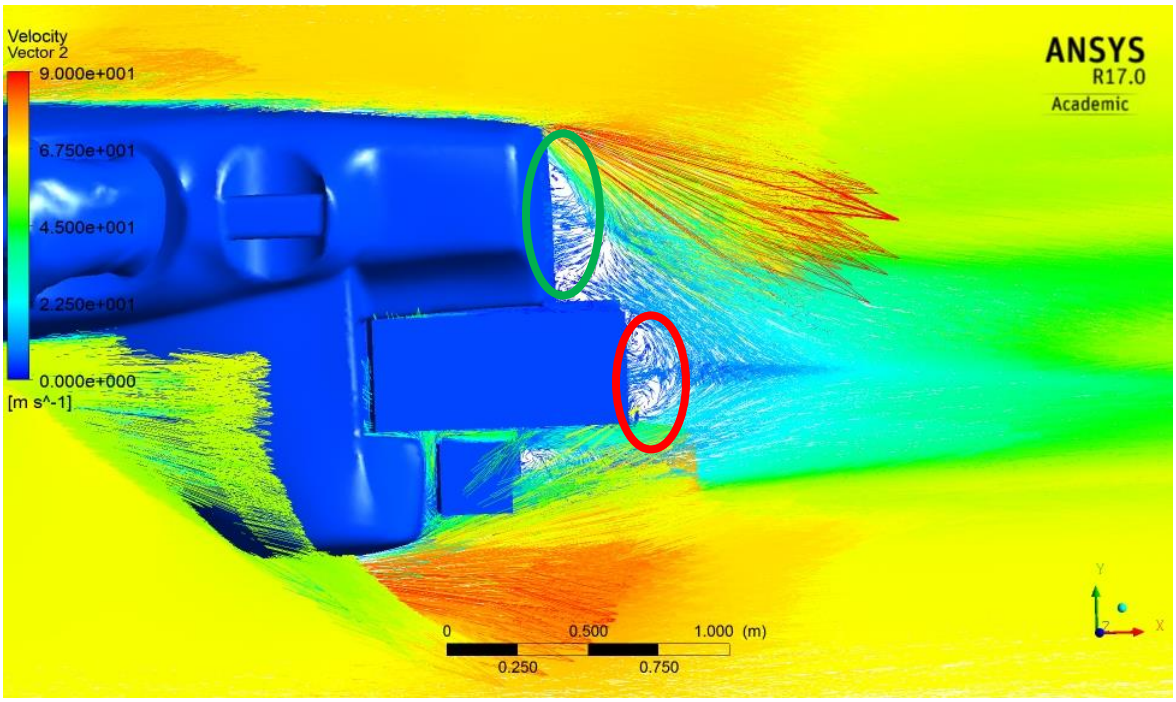

Figure 4.10- Velocity vectors at rear of original sidecar

To further examine the vorticity in the wake region of the sidecar, an iso-surface of Turbulence Kinetic Energy (TKE) with a threshold set to 21.0 m^2s^{-2} was plotted in Figure 4.11.

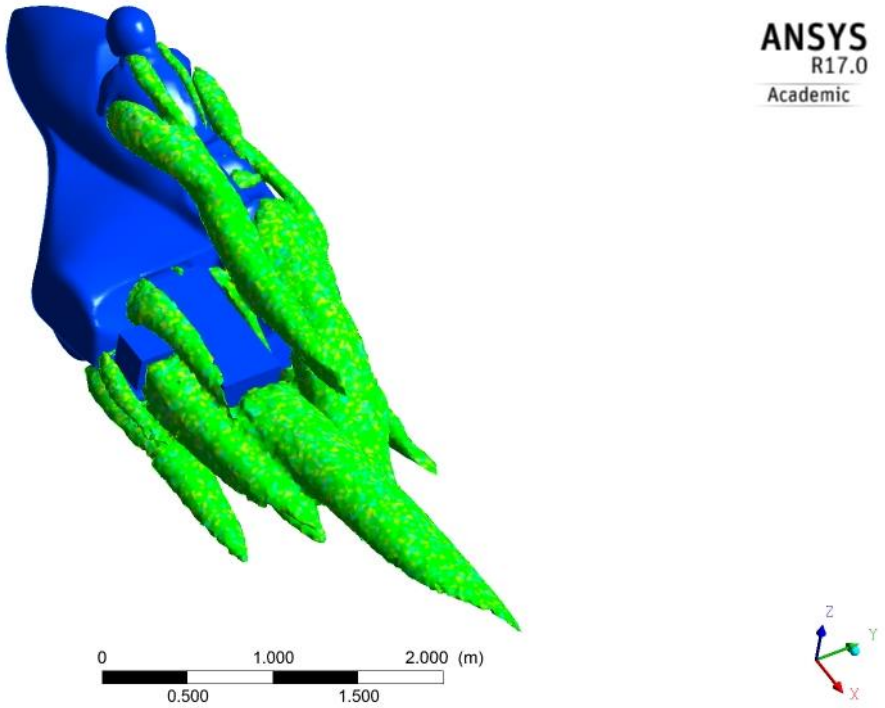

Figure 4.11- Iso-surface plot of TKE on the original sidecar

In Figure 4.11, at least six streamwise vortices are seen to originate at different parts of the sidecar body and rider and continue out into the wake region. The position of these streamwise vortices can be seen in Figures 4.12 through 4.15 where parallel planes are cut through at the rear of the sidecar (Figure 4.12) at x = 1.6 m and through the wake region at selected regions traversing downstream from the side car (Figure 4.13-4.15). The origin for the sidecar is located at approximately the vehicle midpoint.

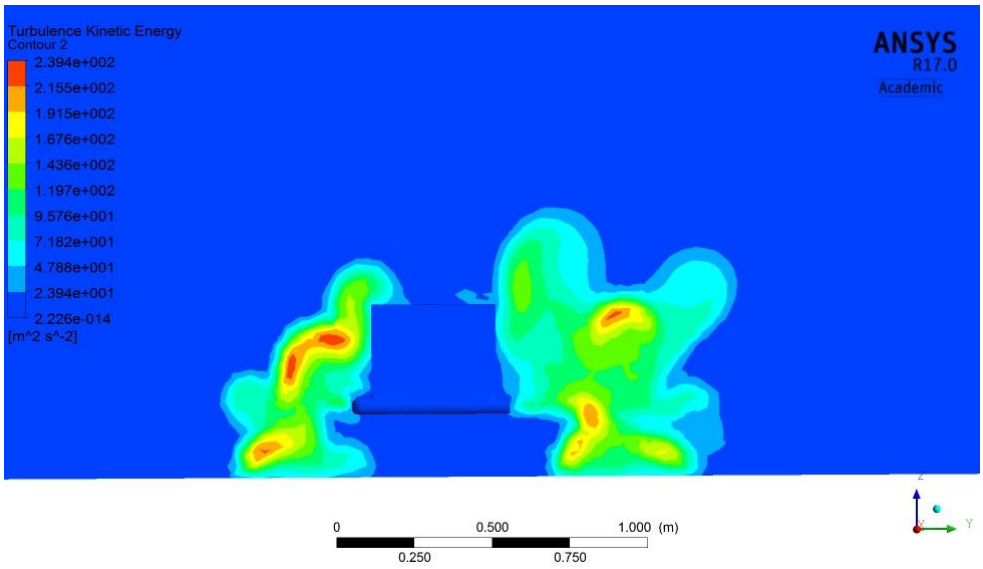

Figure 4.12- TKE of original sidecar- cut plane locate at x= 1.6 m from origin

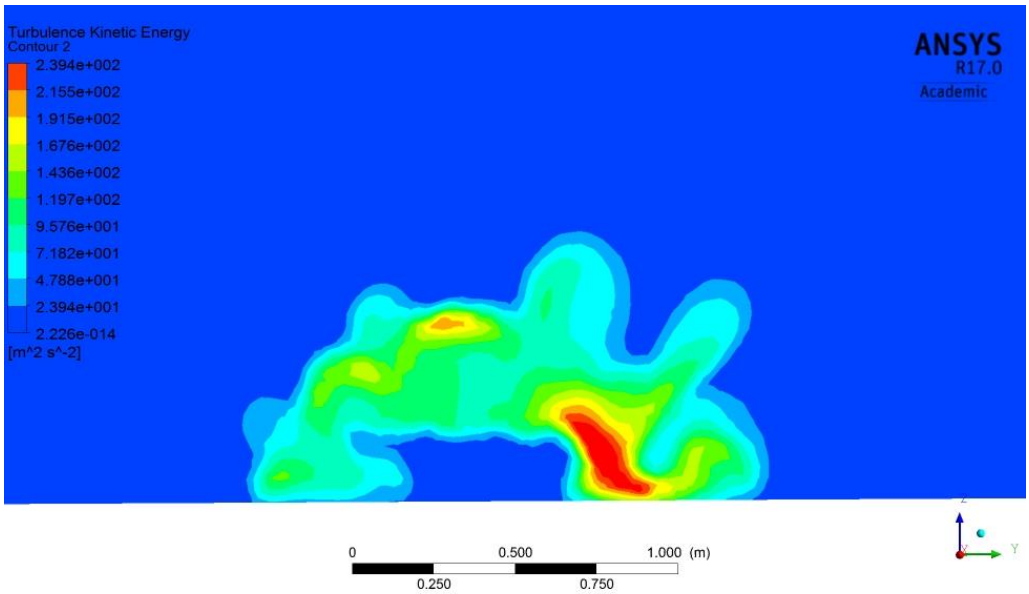

Figure 4.13- TKE of original sidecar- cut plane locate at x= 2.0 m from origin

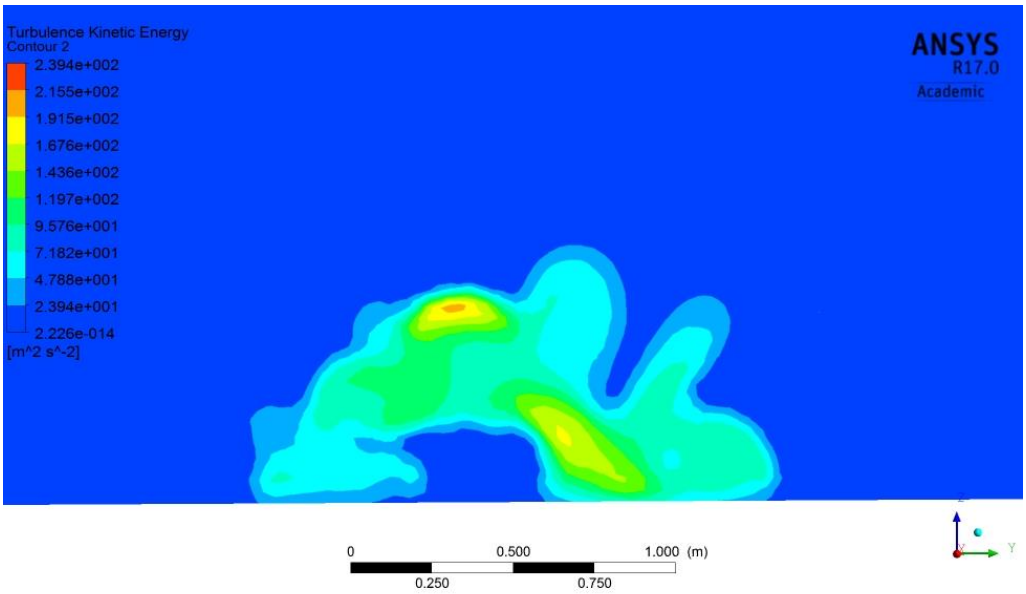

Figure 4.14- TKE of original sidecar- cut plane locate at x= 2.4 m from origin

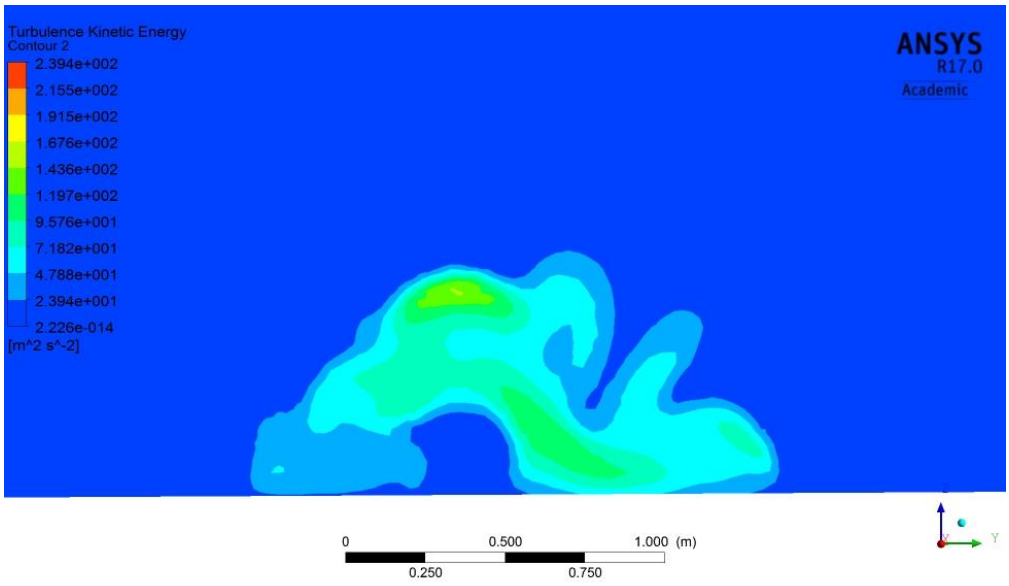

Figure 4.15- TKE of original sidecar- cut plane locate at x= 2.8 m from origin

In Figure 4.12 and Figure 4.13, along with Figure 4.11, the source of the largest and strongest vortex, located behind the rear wheel, appears to be a combination of the streamwise vortex that originates from the riders left shoulder and the lateral (spanwise) vortex that forms behind the rear wheel. A streamwise vortex also forms over the top surface of the battery box and along

the left side of the battery box between it and the water cooling tank. The last major streamwise vortex that forms is along the left side of the bodywork.

Figure 4.16 presents a velocity vector plot that demonstrates the rotational direction of the vortices in the wake region at x = 2.8 m. This plane is 1.2 m behind the tail end of the sidecar.

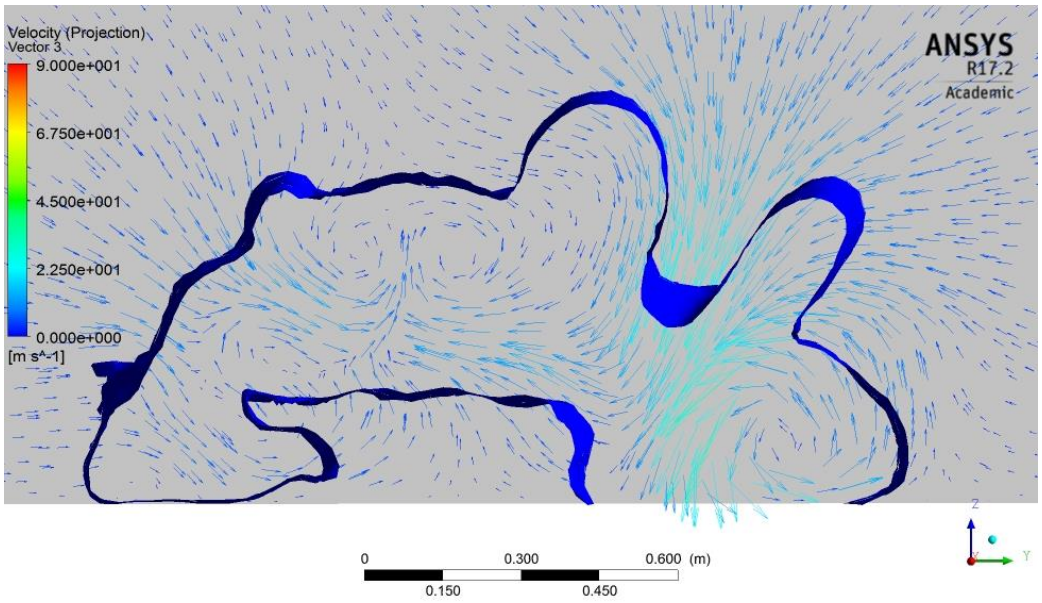

Figure 4.16- Rotation direction of vortices in wake region of original sidecar at x=2.8 m

Figure 4.16 was created by placing a clip plane at a location x=2.9 m and a surface plane at x=2.8 m and onto which velocity vectors tangent to the plane are displayed. An iso-surface of TKE is also plotted on Figure 4.16 and appears as a dark blue ring that surrounds the area of TKE at a constant value of 45.3 m^2s^{-2} This TKE ring helps identify the boundary of the wake as depicted in Figure 4.15.

From Figure 4.16, looking from the rear of the sidecar, it is evident that the streamwise vortex that forms behind the rear wheel rotates in an anti-clockwise direction. The streamwise vortex that forms over the rider's left shoulder rotates in a clockwise direction. The vortex that forms over the top surface of the battery box rotates clockwise and the streamwise vortex between the battery box and cooling tank rotates in an anti-clockwise direction, as does the streamwise vortex produced along the left side of the side car bodywork.

To more closely examine regions of interest, three longitudinal surface planes were placed on the sidecar, based upon the location of the streamwise vortices in Figure 4.11. Figure 4.17 details the position of these planes.

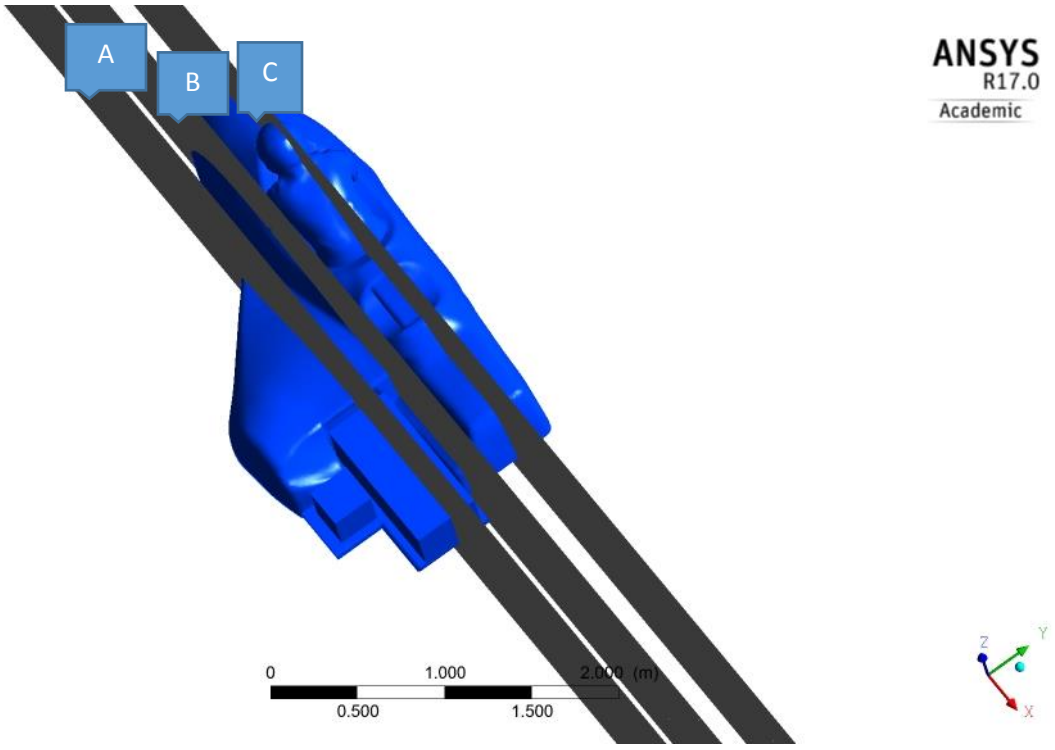

Figure 4.17- Location of surface planes on sidecar: A: y=-0.1, B: y=0.15, C: y=0.48

In Figure 4.18, the velocity vectors over the battery box plane in plane A (y=-0.1) are examined. The area of separation and recirculation directly behind the vertical surface of the battery box is evident. There is also some evidence on the top surface of the battery box that the flow has separated and reattached before reaching the trailing edge of the battery box top surface. This same flow topology was observed on the backlight with a RANS study of the 25° Ahmed body.

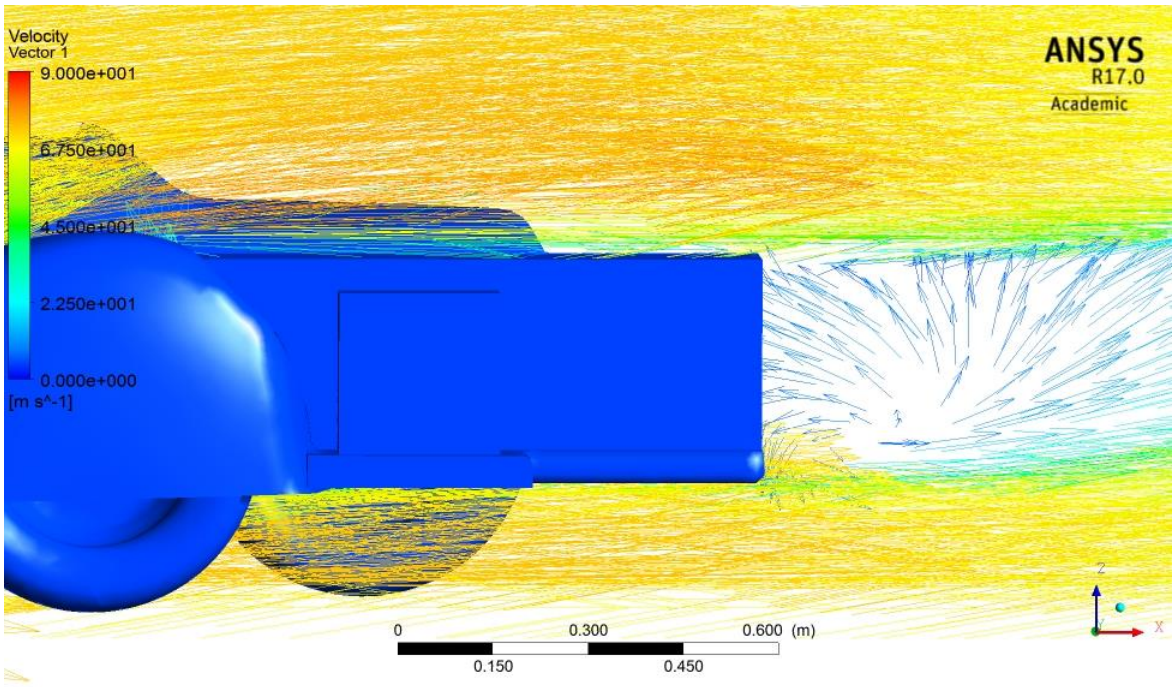

Figure 4.18- Velocity vectors on plane A (y=-0.1) on battery box of sidecar

In Figure 4.19, velocity vectors in the region behind the rear wheel (plane C at y=0.48) were plotted. The recirculation in the separation zone behind the rear wheel is evident but not as strong as behind the battery box.

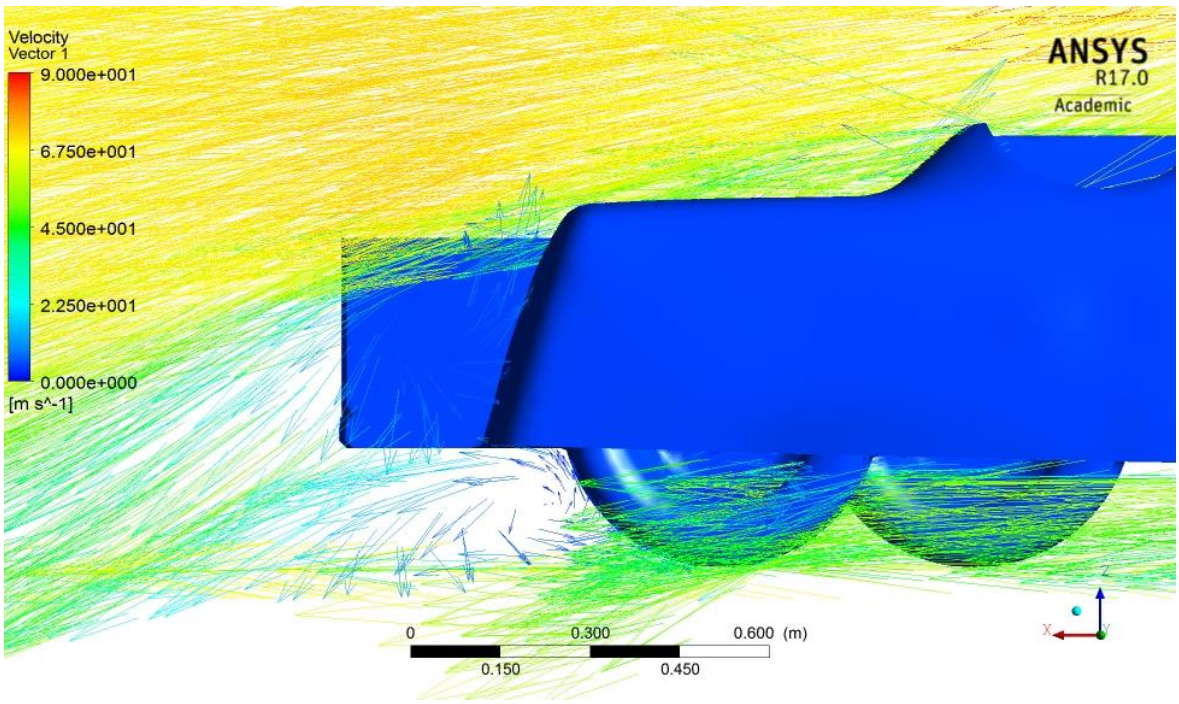

Figure 4.19- Velocity vectors on sidecar surface plane C (y=0.48)

Velocity profile plots along each of the three planes detailed in Figure 4.17 provide an indication of the velocity at various points in the wake region. Figure 4.20 is a plot positioned over the battery box region at plane A (y= -0.1 m).

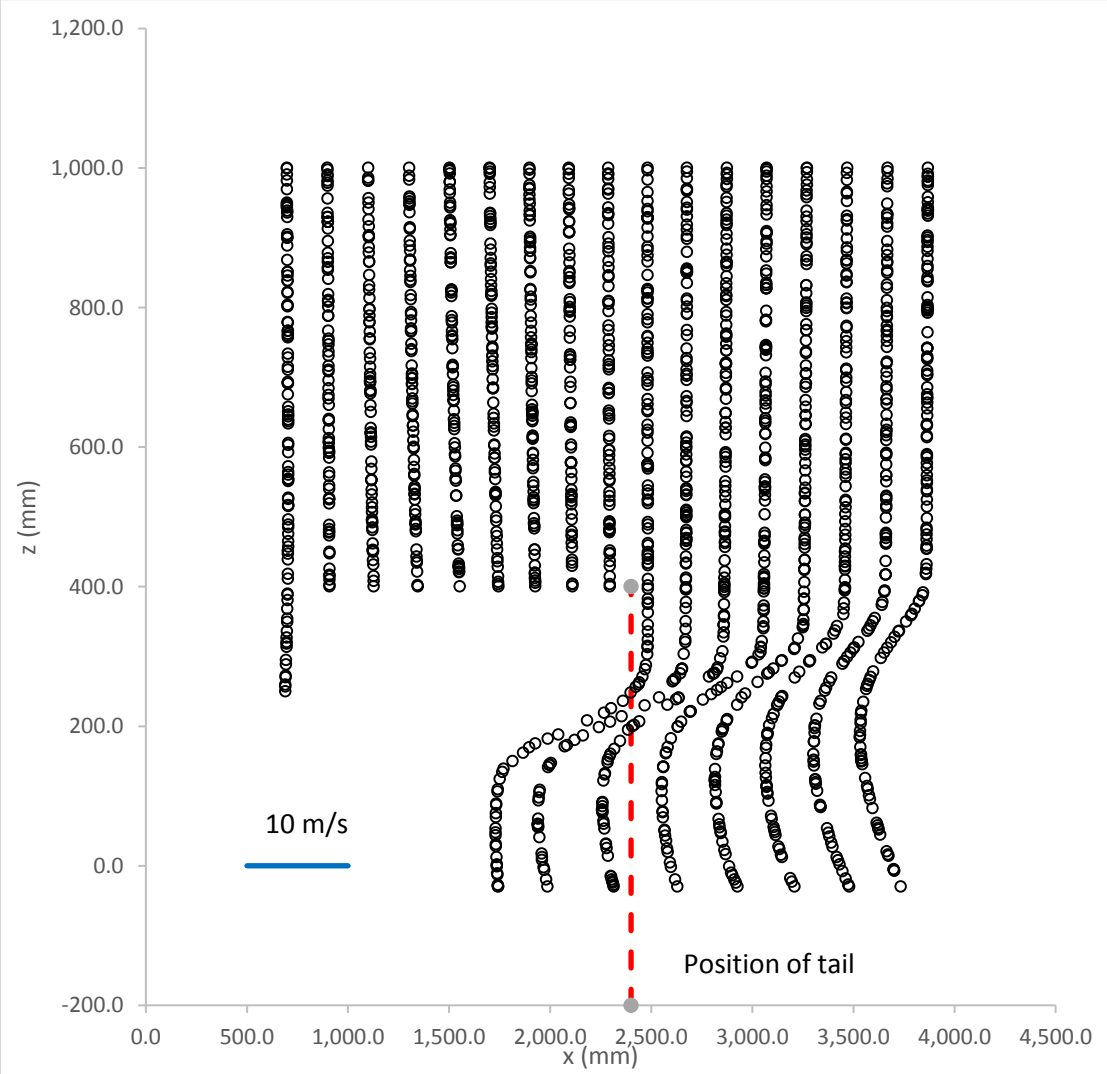

Figure 4.20- Velocity profile of sidecar rear and wake region along plane A (y= -0.1 m)

In Figure 4.20, the reversed flow region directly behind the vertical wall of the battery box (seen in Figure 4.10) is evident by the negative velocity regions, which are also reflected in Figure 4.18. These regions of reversed flow are not as evident in the area between the battery box and the rear wheel (the middle plane B at y= 0.15 m in Figure 4.17) as shown in Figure 4.21.

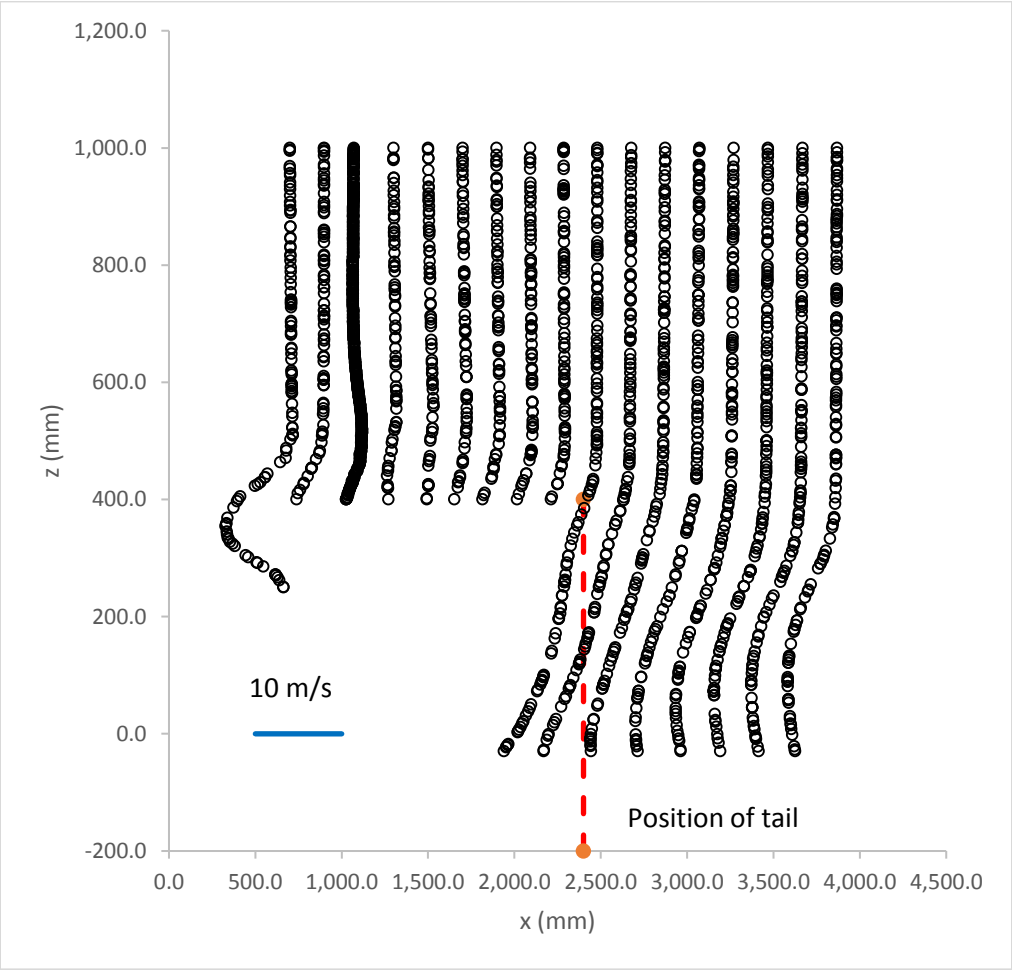

Figure 4.21- Velocity profile of sidecar rear and wake between battery box and rear wheel at plane B (y=0.15)

In Figure 4.22, the velocity profile on the rightmost plane C in Figure 4.17 (y=0.48), the amount of recirculation and negative flow is not as strong as it was behind the vertical surface of the battery box. This is also evidenced from Figure 4.19.

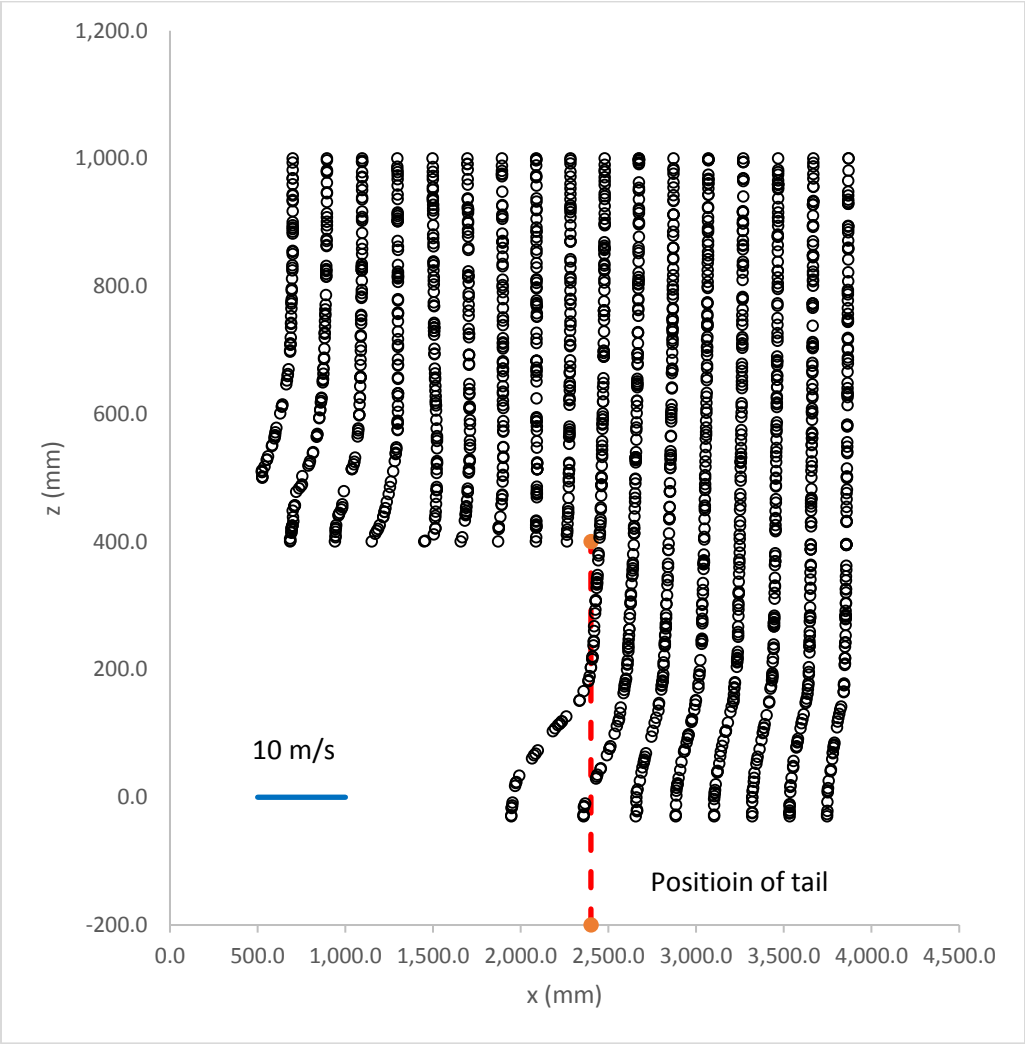

Figure 4.22- Velocity profile of sidecar rear and wake at rear wheel plane C (y=0.48)

The geometry of the sidecar suggests that the forward section of the sidecar produced minimal drag. The area forward of the rider smoothly tapers to a pointed nose while the section covering the sidecar also allowed for clean flow of relatively undisturbed air. The presence of the rider, and particularly the shoulders and helmet of the rider, predictably create trailing vortices and low-pressure regions on the rear surfaces, producing drag. The trailing edge of the sidecar bodywork, ahead of the rectangular battery box, produced vortices that trail behind the sidecar vehicle.

In Figure 4.23, streamwise vortices trailing into the wake region are evident from the velocity core region swirling strength visualisation. As noted in Chapter 3, after a brief comparison of the choices available, the Swirling Strength option was found to provide the clearest visualisation of vortices in the wake region of the sidecar. A swirling strength setting of 0.0083745 was used for these visualisations, unless otherwise indicated.

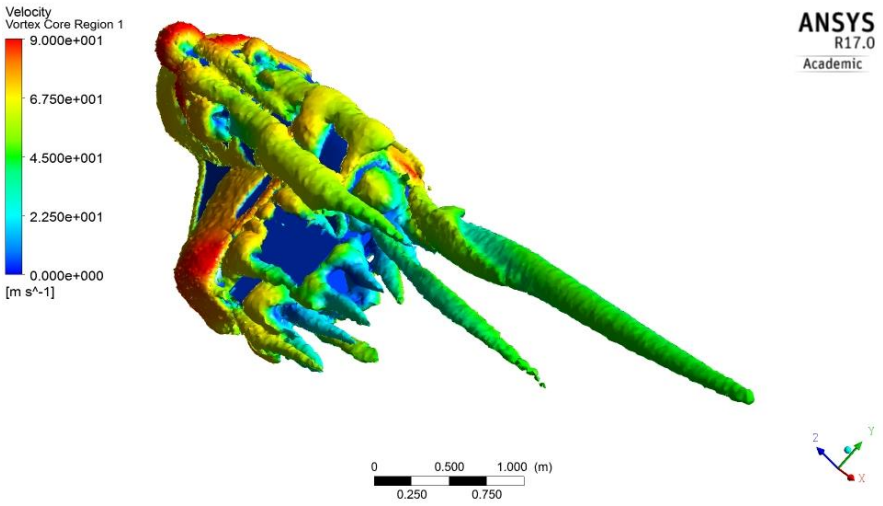

Figure 4.23- The presence of streamwise vortices for into the sidecar wake

In Figure 4.23 it is evident that the streamwise vortices produce asymmetrical drag—the right side of the sidecar has longer and more significant streamwise vortices than does the left (sidecar) side (when viewed from the rear). This evidenced asymmetry, with more drag created on the right side of the vehicle results in a positive yaw moment (clockwise rotation). This will be further discussed in the next section and in Chapters 5 and 6.

In Figure 4.24, streamwise vortices from the wheels and underside of the sidecar are evident. The presence of streamwise vortices from the three wheels of the sidecar contribute to the formation or strengthening of vortices at the rear of the vehicle.

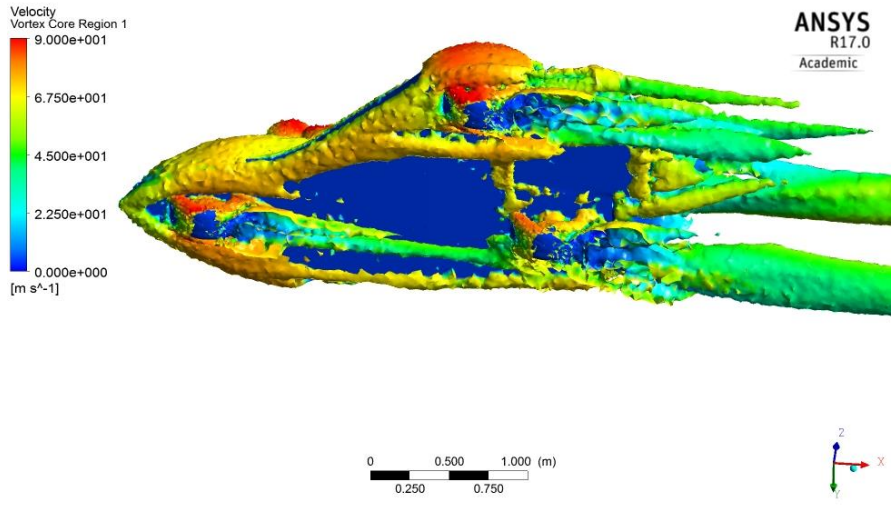

Figure 4.24- The presence of streamwise vortices from the wheels on the underside of the sidecar

As explained in Chapter 3, surface shear stress lines can help predict flow separation and the initiation locations of vortices. In Figure 4.25, surface shear stress lines for the sidecar are shown.

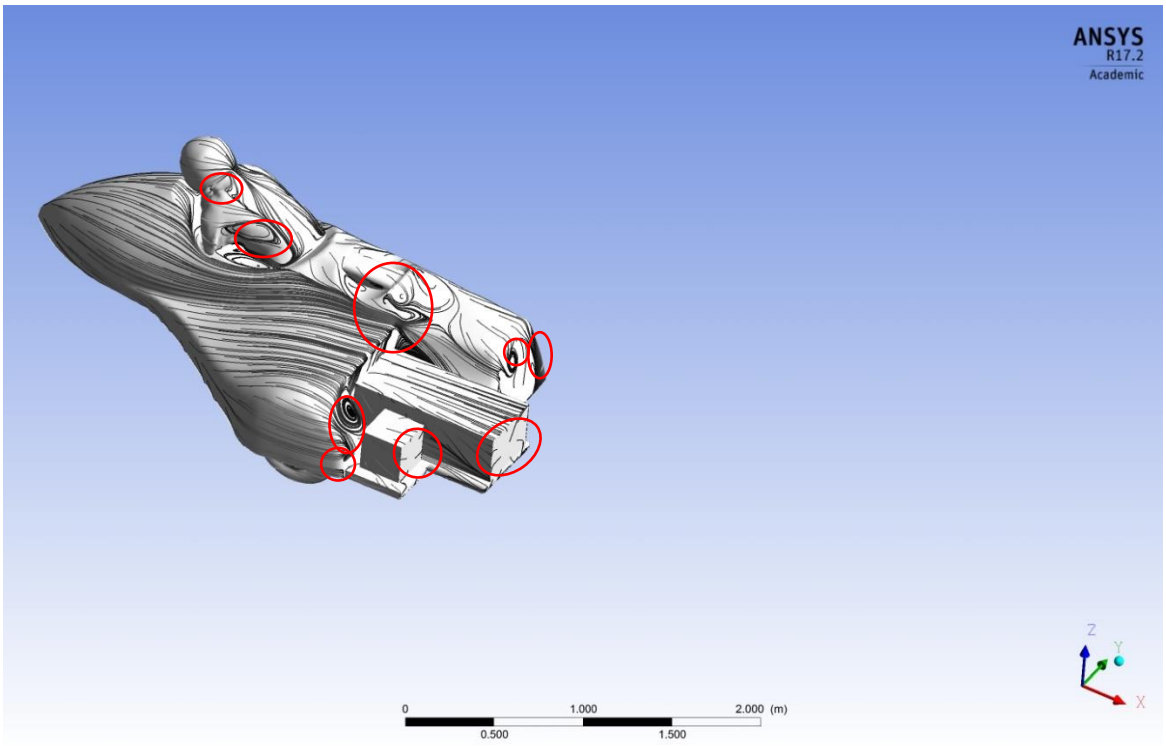

Figure 4.25- Shear stress lines for the original sidecar

In Figure 4.25, critical points, of the type described by Tobak, et al. (1982) are evident on the sidecar and rider and are circled in red. These areas can be directly compared to the evidence of separation and vortices in Figure 4-26.

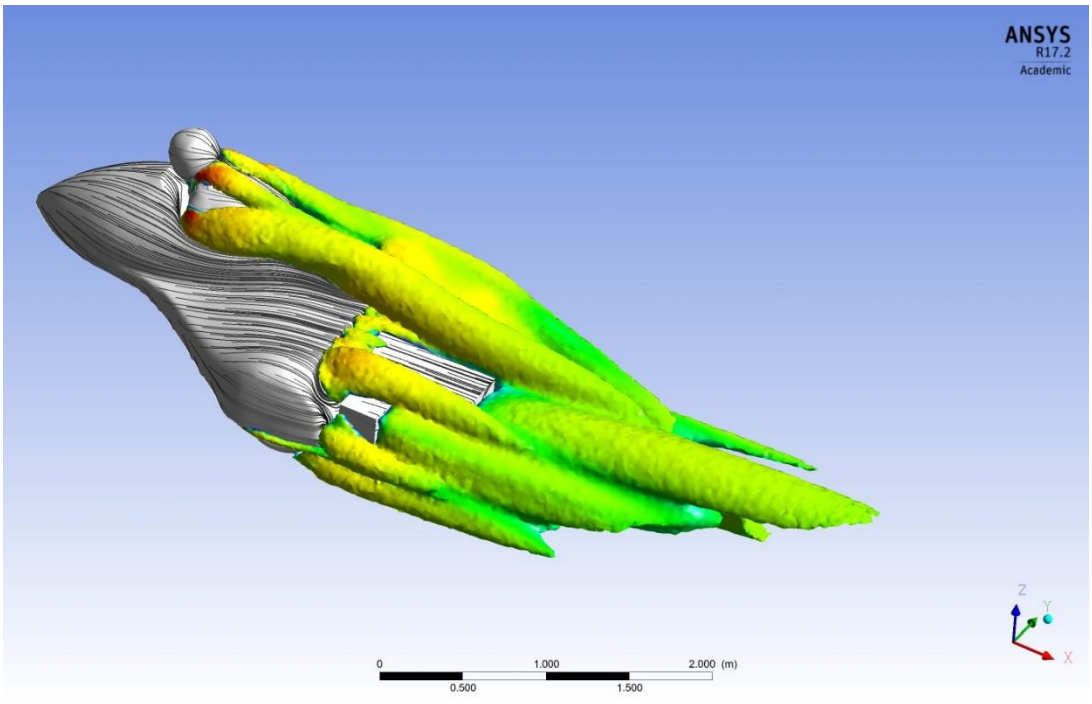

Figure 4.26- Streamwise vortices and separation evident on the sidecar and rider

Figure 4.27 is a closer view of the shear stress lines on the rider.

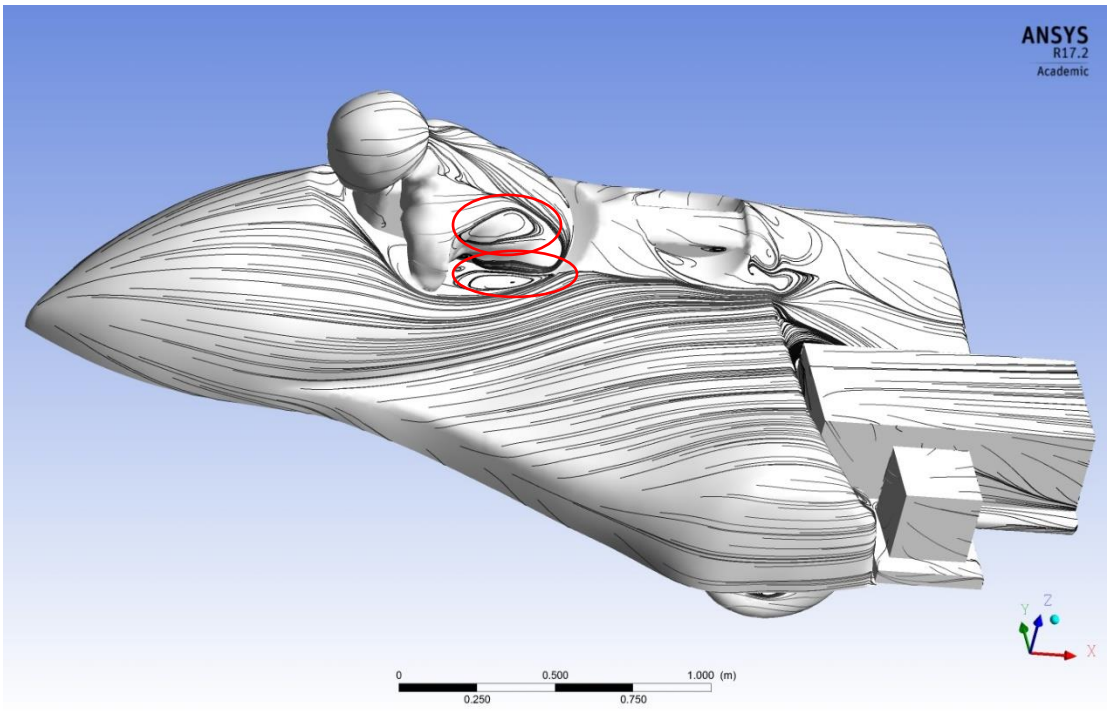

Figure 4.27- Closer view of the shear stress lines on the rider

Examining figure 4.26 and 4.27 it is evident that the “focus” critical point under the shoulder of the rider and on the top of the shoulder of the rider (circled in red) correspond to the locations of streamwise vortices in Figure 4.26. The spiral of focus-type critical points are also visible on several locations at the rear of the sidecar (Figure 4.28).

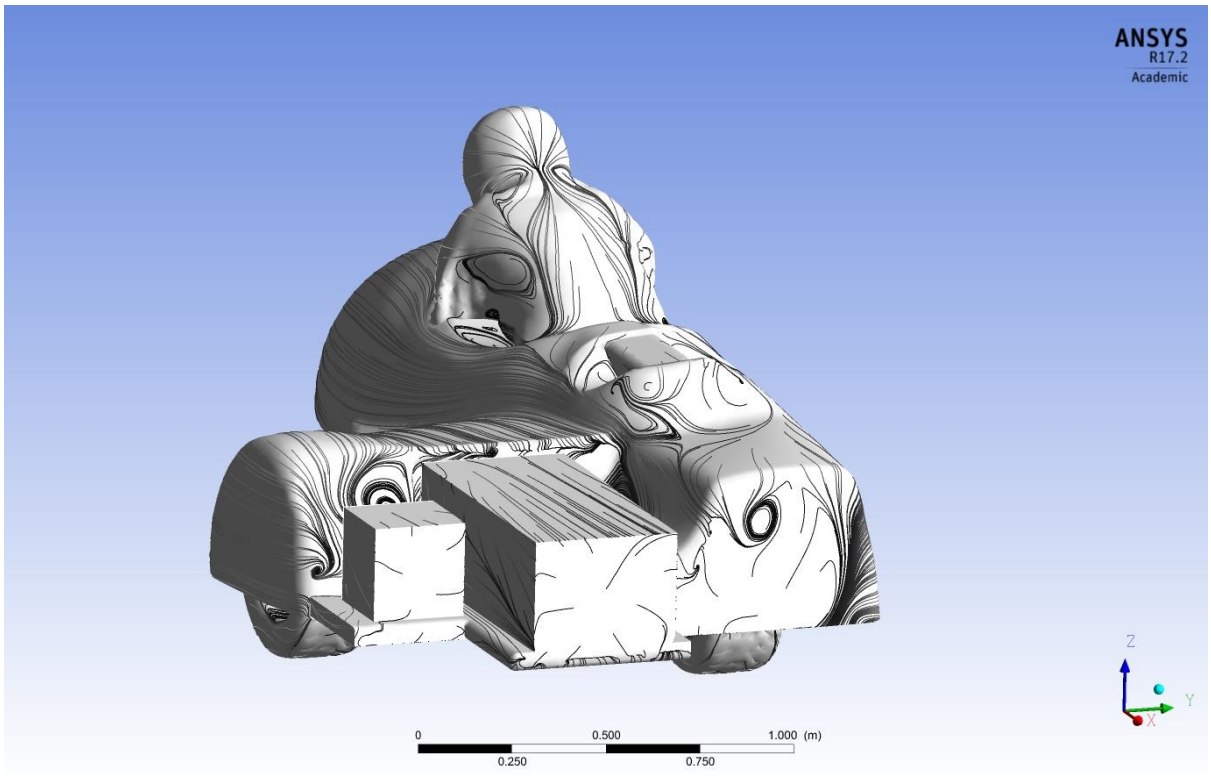

Figure 4.28- Shear stress lines at the rear of the original sidecar

Comparing the location of the foci on the rear of the sidecar with the location of the streamwise vortices evidenced in Figure 4.23 indicates that the shear stress lines provide a good indication from where these topologies originate. For example, in Figure 4.28, tightly wound foci are seen on the sidecar body just ahead of the cooling tank, in the cavity to the right side of the battery box and on the upper portion of the vertical tail section of the bodywork. In Figures 4.23 and 4.26 these are seen as the origins of vortices. In Figure 4.28, the flat vertical surface also suggests separation will occur, which is confirmed by Figures 4.10 and 4.18.

The assortment of streamwise vortices that extend into the wake region create a degree of asymmetry and the wake of the vehicle, as viewed from above in Figure 4.29, reflects this.

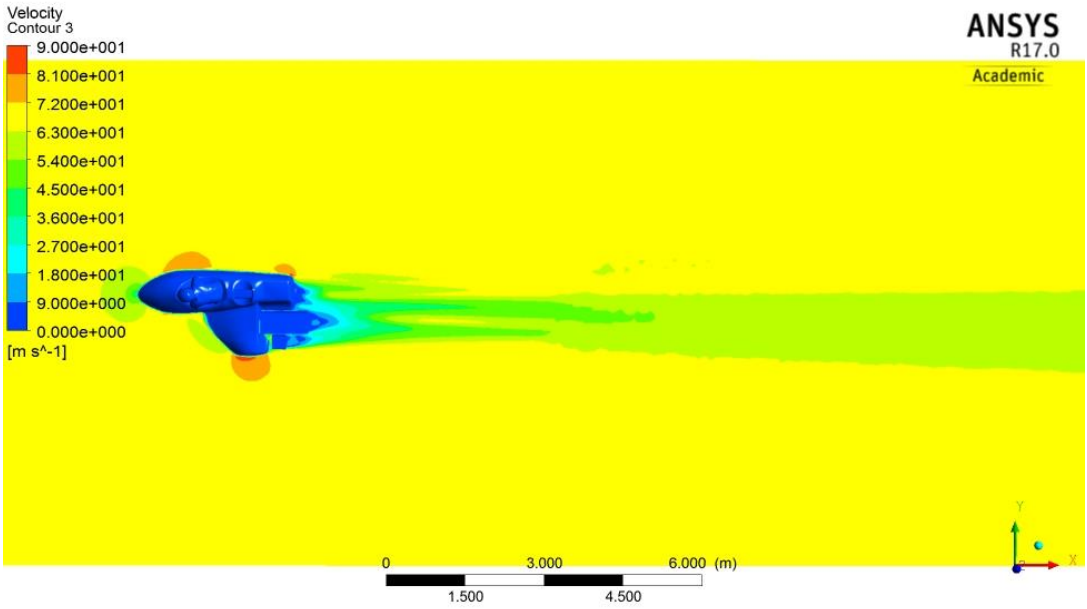

Figure 4.29- Velocity contours showing asymmetry of the vehicle wake

4.5.1 Design of the Rear Body Section

From the initial studies of the sidecar design, and from Hucho, et al. (1994), the rear section of the body of the sidecar was judged to be the area where the greatest reduction in aerodynamic drag would be possible. In Figure 4.23, the presence of several streamwise vortices that travel into the wake region after initiating in the region around the battery box and water cooling tank provide further indication that a revised rear body section would be a good place to start.

Tamai (1999), in his book "The Leading Edge: Aerodynamic Design of Ultra-Streamlined Land Vehicles," suggests that it is desirable to keep "the tangent of any surface patch less than about 17-20° from the freestream flow" (p.62). Here, the objective is to provide an angle of taper at the rear of the vehicle that delays separation of the boundary layer. Separation and the resulting low-pressure regions are the primary cause of drag on a bluff body.

McBeath (McBeath, 2015), notes that separation within the diffuser on the underside of a vehicle occurs when the angle exceeds 5-11 degrees, leading to less downforce generation. Diffusers are designed with wall to wall (included) angles of 11-12 degrees (5.5-6 degrees between wall and axis, i.e. half angle), in concord with the observed sidewall angles of the vehicle.

The rear sections of various high-speed vehicles are observed to have tapered tails with small angles to the direction of travel. Indeed, the existing bodywork of the Baker sidecar used in this study has its sides tapered back from the widest point of the vehicle—6° on the left side and 5° on the right.

Lift

The lift generated by the sidecar body can result in instability, particularly if it is greater in magnitude than the mass of the vehicle. It should be noted that downforce (negative lift) is generally beneficial to vehicle stability. Airflow over the smooth top surface of the land vehicle and the resulting negative pressure on that surface, can result in lift (Katz, 1995). If the lift created by the top surface of the vehicle is greater than that produced by the bottom surface, the net resulting reduction of downward force can reduce the traction available from the tyres, or in the most extreme cases result in vehicle lift off and flight. If the front of the vehicle exhibits excessive lift, the vehicle can also pitch nose upward, creating an unfavourable angle of attack that can then rapidly increase aerodynamic lift. The reduction of lift (or generation of downforce) almost invariably results in increased aerodynamic drag (McBeath, 2015). A design goal is therefore to reduce aerodynamic drag without creating instability caused by excessive aerodynamic lift or side force.

Lateral force

In some ways, the generation of aerodynamic lateral force is analogous to the generation of aerodynamic lift. Air flow over the side surfaces of the vehicle body produce a force normal to the surface. On a symmetrical vehicle, without yaw or cross winds, the forces generated on one side are matched by the forces on the other side of the symmetry plane and no resulting lateral force is created. With an asymmetrical vehicle however, the lateral forces generated in one direction are not necessarily balanced completely by forces generated in the opposite direction, resulting in a residual lateral force. This lateral force pushes the vehicle sideways without a change in heading (slew). If the lateral force generated by the asymmetric aerodynamics is large enough to overcome the ability of the tyres to provide countering lateral force, vehicle stability suffers. An important goal in the current work was to reduce lateral force as much as possible to ensure that, even at significant imposed yaw angles, it would not exceed the amount of lateral traction available from the tyres, particularly on the inconsistent and sometimes low traction salt surface at Bonneville.

Yaw Moment

An additional consideration for lateral force with respect to vehicle stability comes from the position of the COP relative to the vehicle centre of mass (Milliken & Milliken, 1995). It is well known among aircraft, missile and rocket designers that placing the COP longitudinally, significantly ahead of the centre of mass results in a vehicle that can exhibit instability, particularly if the vehicle path is perturbed into yaw by a side wind or surface non-uniformity. The generation of a lateral (yaw) aligning moment, M_y, the product of the distance between the COP and centre of mass and the magnitude of the lateral force, is one way to characterize the potential for vehicle lateral instability from this cause. As mentioned, a yaw moment around the vehicle centre of mass is generated by the asymmetrical lateral forces acting on the COP at a distance from the centre of mass. With an asymmetrical vehicle, a yawing moment can also be

created by the difference in pressure drag developed on one side of the vehicle compared to the other. The geometric asymmetry of a sidecar, with two wheels on one side and one on the other can also create an imbalance of rolling resistance forces that impart a non-aerodynamic yaw moment around the vehicle centre of mass. These sidecar asymmetries that result in yawing moments and their effect on stability will be further discussed in Chapter 7.

Optimisation iterations

Over the course of the optimisation study more than 60 iterations were examined using CFD with the calculation parameters previously described. In the following section, only those iterations that were judged interesting or significant in their contribution to the goal of reduced aerodynamic drag and/or improved aerodynamic stability are detailed. Further, design iterations that represented milestones in reduced drag, lift or lateral forces were further investigated by examination of surface pressure, flow characteristics, and/or wake topology.

The first step was to create a rear body section that enclosed the battery box and cooling tank under bodywork. This was accomplished by extending rearward and upward the tapered sides of the sidecar and connecting them together with surface planes. The bodywork depicted in Figure 4.30 is the result.

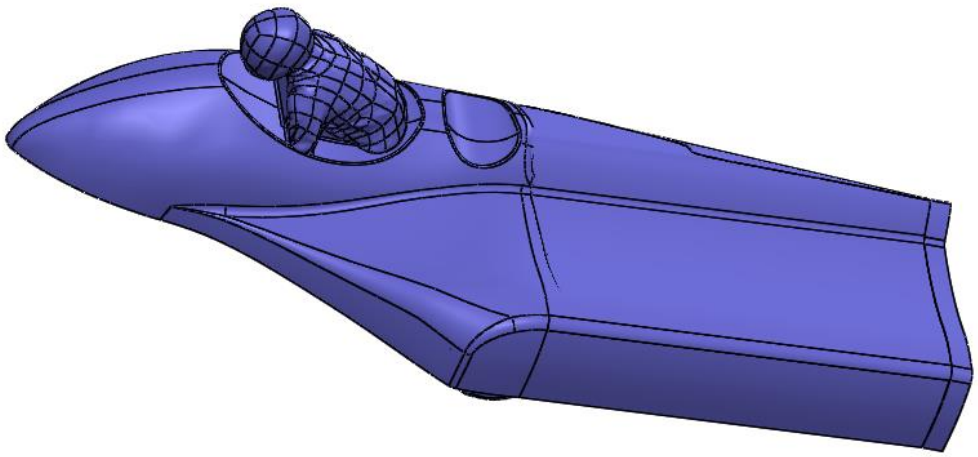

Figure 4.30- Sides extended rearward (version 50-4)

C_d = 0.348

C_l = -0.131

C_y = 0.067

C_m= 0.058

Extending the rear bodywork of the sidecar resulted in a drag increase of 1%, the development of slight downforce and a slight decrease in lateral force when compared to the initial sidecar design. The increase (or little change) in drag with a longer tail was unexpected. Traditionally in racing (particularly at high speed venues like Le Mans), vehicles with long extended tails are known to have reduced levels of aerodynamic drag. Clearly, simply stretching the body rearward would not provide a reduction in drag forces.

For the next study, the upper surface of the tail beyond the end of the original bodywork was tapered downward at an angle of approximately 10 degrees. In Figure 4.31 it is evident that the upper surface effectively meets the lower surface at the termination of the body.

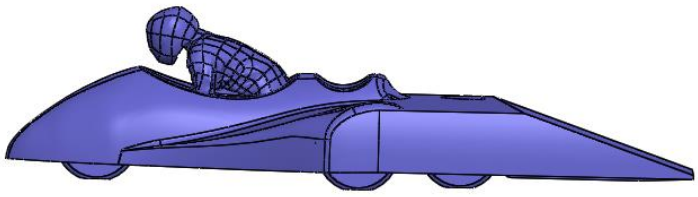

Figure 4.31- Taper of the upper surface of the tail (Version 50-6) – Long tail sidecar

C_d = 0.267

C_l = 0.159

C_y = 0.063

C_m= 0.068

Tapering the upper surface resulted in a dramatic reduction in drag (reduced by 22.4%) and also resulted in a change from almost neutral downforce to overall lift for the vehicle when compared to the original sidecar. Because this was such a significant decrease in C_d, further analyses of the flow and flow topology was undertaken. Figure 4.32 is a plot of the pressure contours on the long tail sidecar from Figure 4.31.

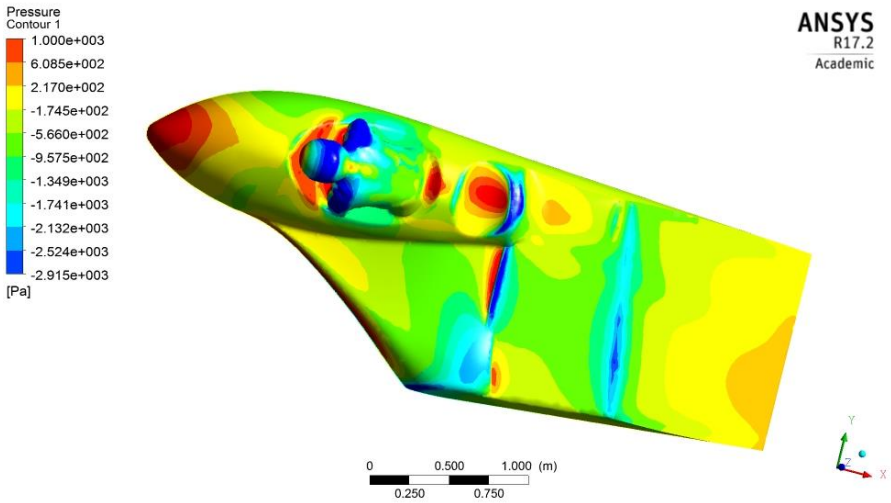

Figure 4.32- Pressure contour plot of long tail sidecar design

In Figure 4.32 there are several mechanisms that may be occurring over the rear surface of the long-tail sidecar. The front part of the vehicle exhibits the same pressure distribution as the short-tailed vehicle (Figure 4.8) up to the point at which the long tail section has been added on. The pressure gradient on the horizontal portion of the new tail section evidenced in Figure 4.32 is decreasing in the flow direction. This gradient should slightly increase the speed of the flow over this section, reducing its internal (pressure) energy and increasing its kinetic energy. At the point at which it encounters the second part of the rear section, the tapered part, a line of low pressure has formed at the point of the break over into the rear taper. This was also observed on the top surface of the Ahmed body at the leading edge of the backlight and could be expected to initiate separation of the flow. Over the rear tapered section, there is an adverse pressure gradient—the pressure increases while travelling down the surface with an expected decrease in speed and kinetic energy.

Figure 4.33 is a plot of velocity vortex core for the long-tail sidecar. Comparing Figure 4.33 to the short-tail Figure 4.23 it is evident that the flow over the rear section is significantly different for the long-tail sidecar. At the point at which the break over occurs, Figure 4.33 shows a lateral vortex that extends from one side of the body to the other at the same position as the line of low-pressure indicated in Figure 4.32. Also, conspicuously absent in Figure 4.33 are the large lateral vortices directly behind the sidecar. The tapering of the upper surface of the tail down to the bottom surface has effectively eliminated the formation of these large lateral vortices.

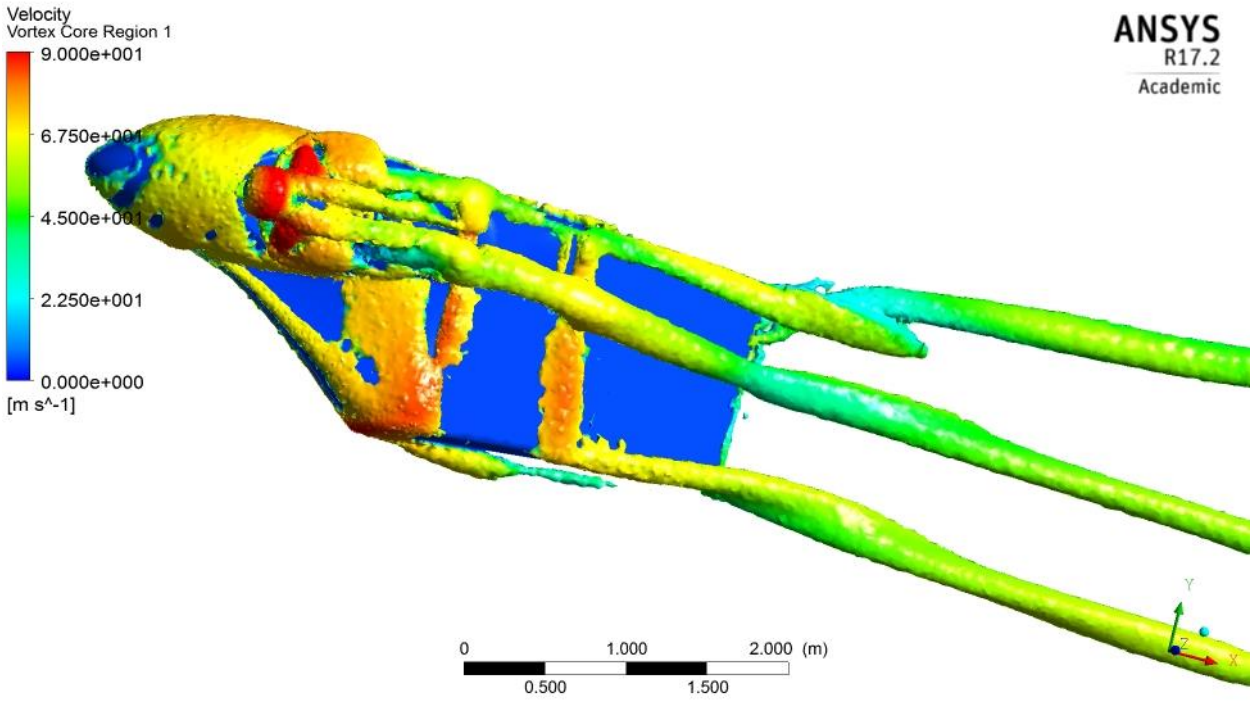

Figure 4.33- Velocity vortex core for the long-tail sidecar

Shear stress lines can be used to examine the origin of each of these three major streamwise vortices. In Figure 4.34, it is evident that a focus exists (as noted before) at the rider's shoulder, and from Figure 4.35, the centre streamwise vortex originates from that region. There is also a focus on the body section behind the rider which may contribute to the same streamwise vortex.

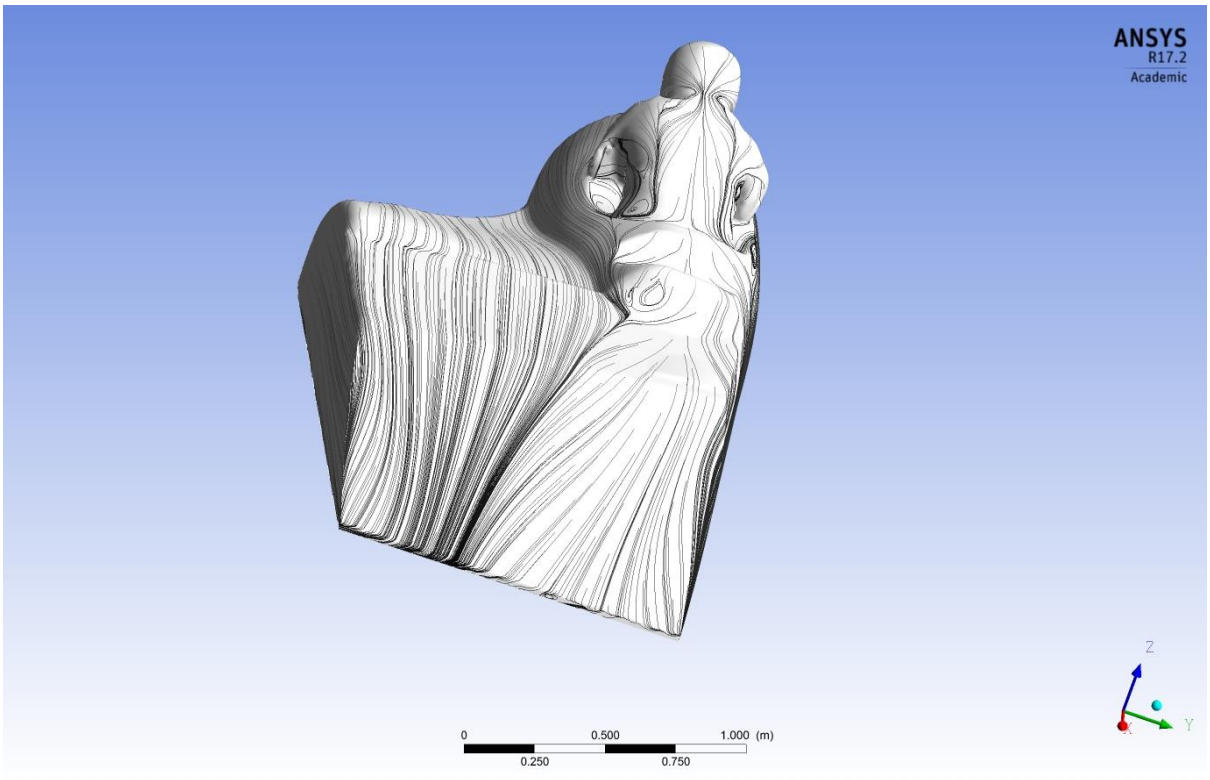

Figure 4.34- Shear stress lines of rear of long-tail sidecar

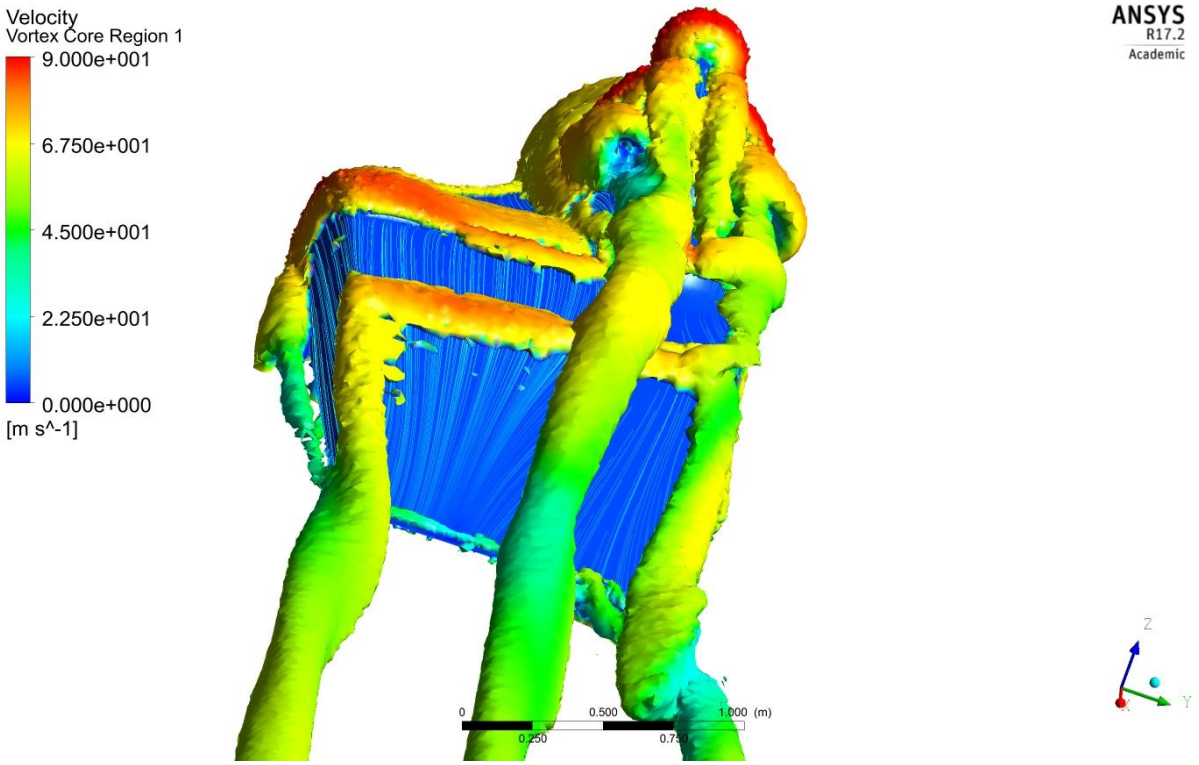

Figure 4.35- Velocity vortex core showing origins of streamwise vortices

From Figure 4.34, it is also evident that a shear flow occurs on both the left and right-side edges of the sloped back section, analogous to the C-pillars on the 25° Ahmed body. The shear in these regions, as evidenced in Figure 4.35, produce streamwise vortices that extend into the wake region.

Velocity profile plots on the same three planes in the same locations from Figure 4.17 are indicated in Figure 4.36 plane A (y= -0.1), Figure 4.37 plane B (y= 0.15), and Figure 4.38 plane C (y= 0.48).

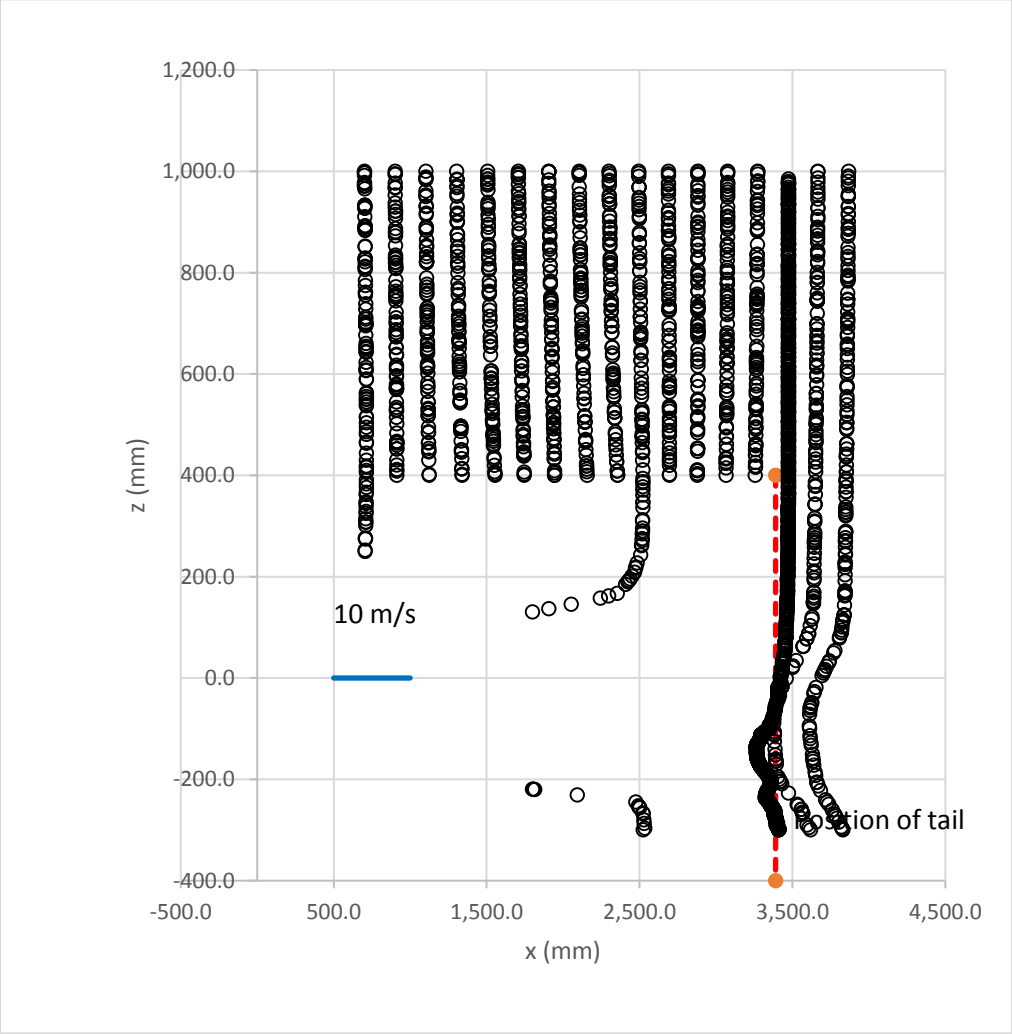

Figure 4.36- Velocity profile plot for long-tail sidecar at plane A (y= -0.1 m)

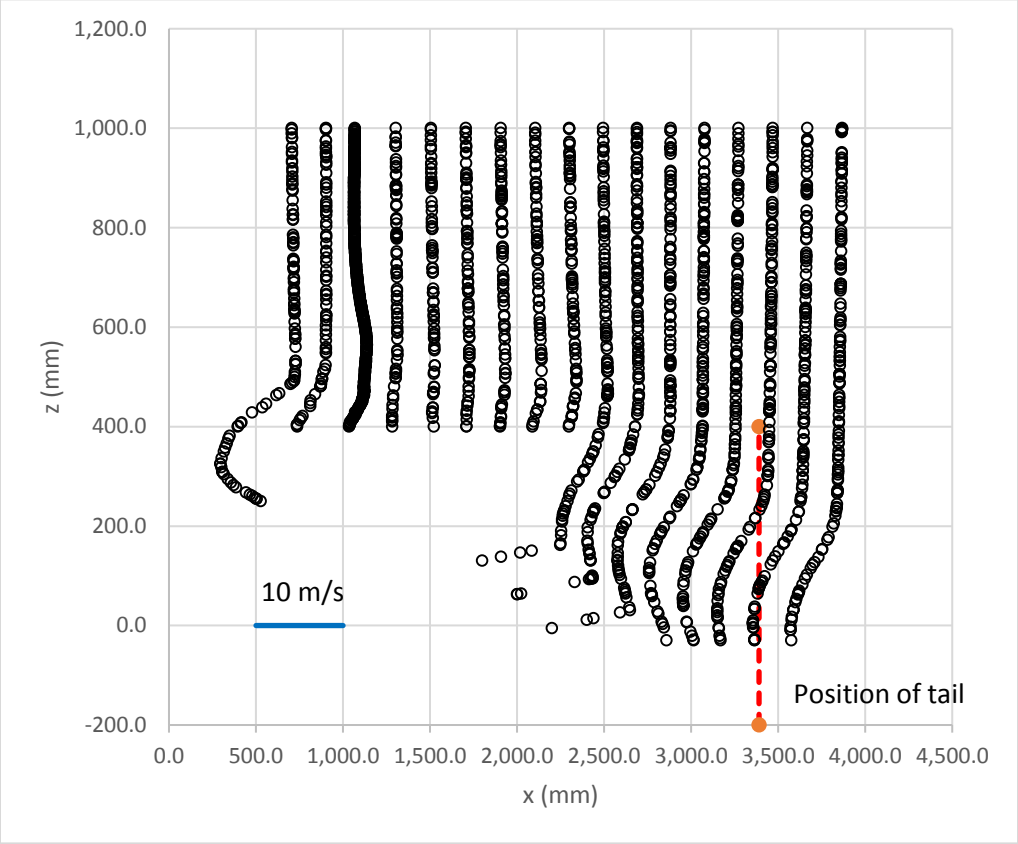

Figure 4.37- Velocity profile plot for long-tail sidecar at plane B (y= 0.15 m)

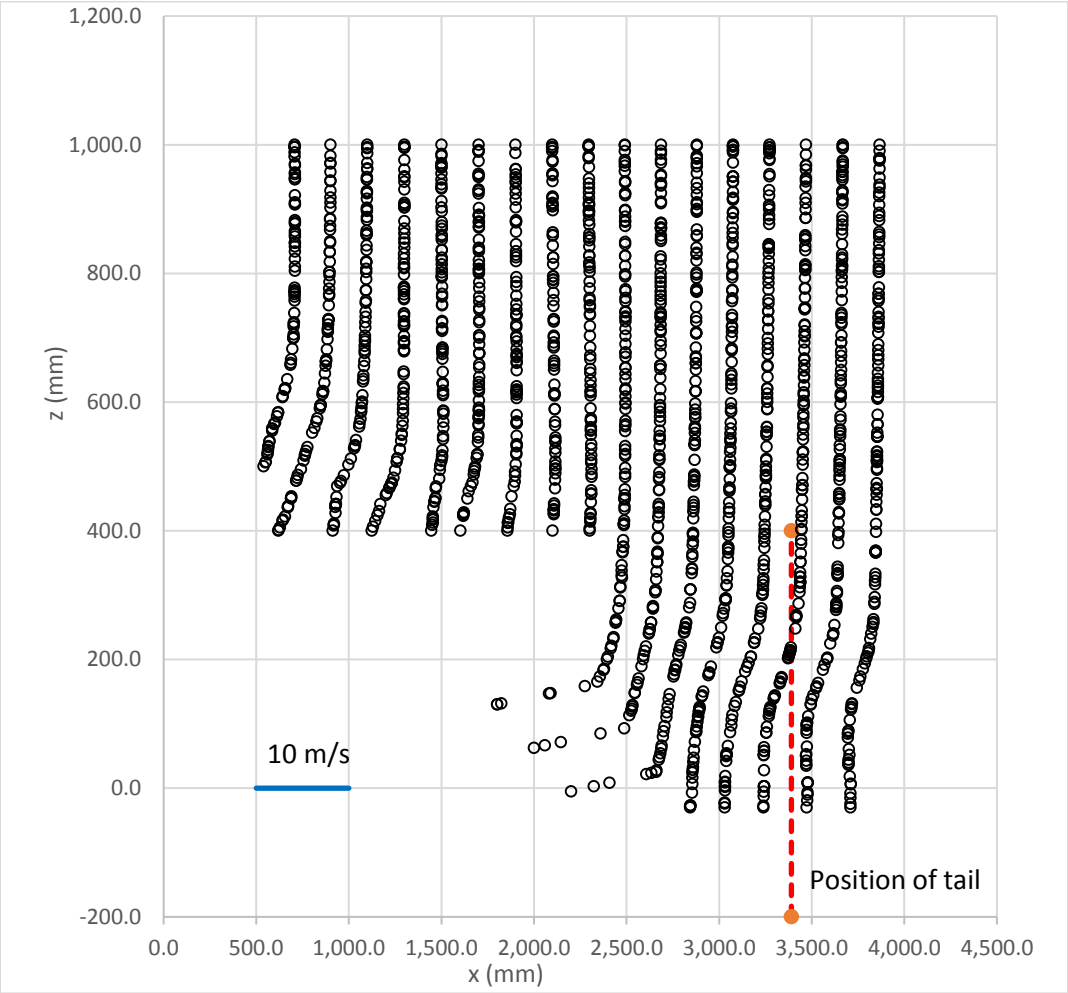

Figure 4.38- Velocity profile plot for long-tail sidecar at plane C (y= 0.48 m)

From the velocity profile plots in Figures 4.36-38, it is evident that the wake region is much less disturbed (the velocity deficit between the wake velocity and freestream is less) than it had been for the short-tail original sidecar from Figures 4.20-22. Figure 4.39 indicates the position of the streamwise vortices behind the vehicle and the lack of the large lateral vortices in the region directly behind the tail.

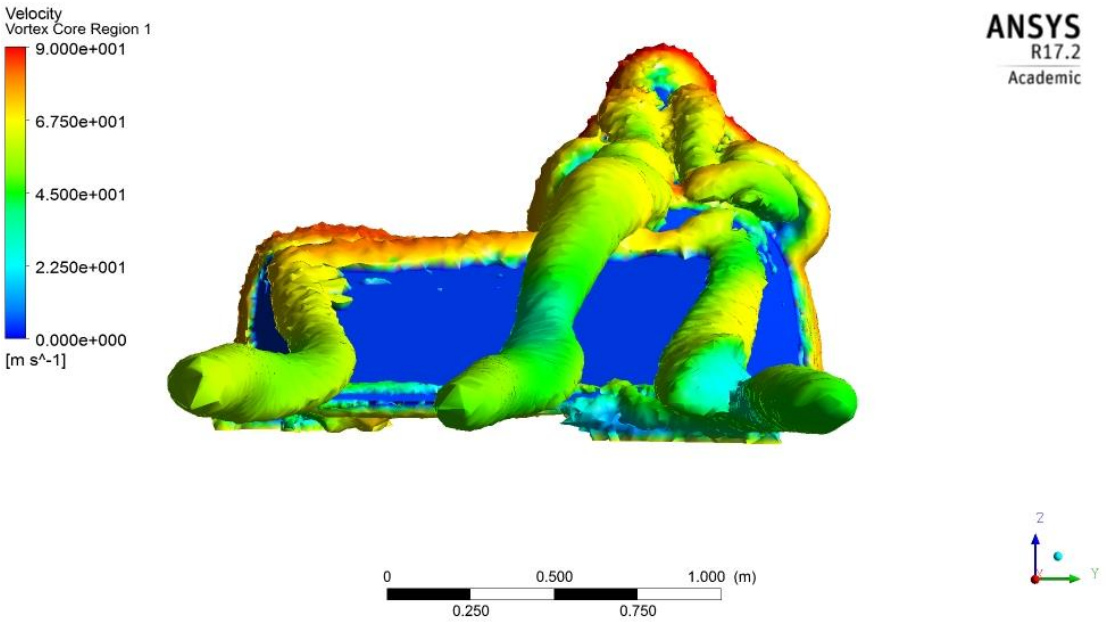

Figure 4.39- Streamwise vortices in the wake of the long-tail sidecar

The lower intensity of the streamwise vortices at the tail and wake region of the long-tail sidecar are evident in plots of TKE in Figure 4.40 (at x=2.4 m) and in the wake in Figure 4.41 (at x=2.8 m).

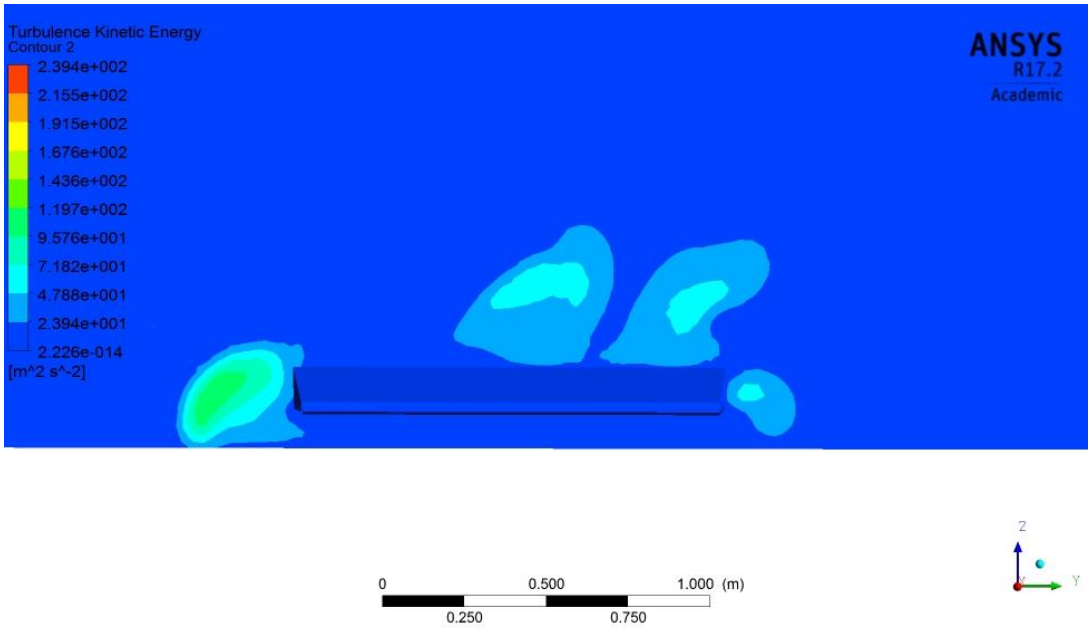

Figure 4.40- TKE contour at the rear of the long-tail sidecar at x=2.4 m

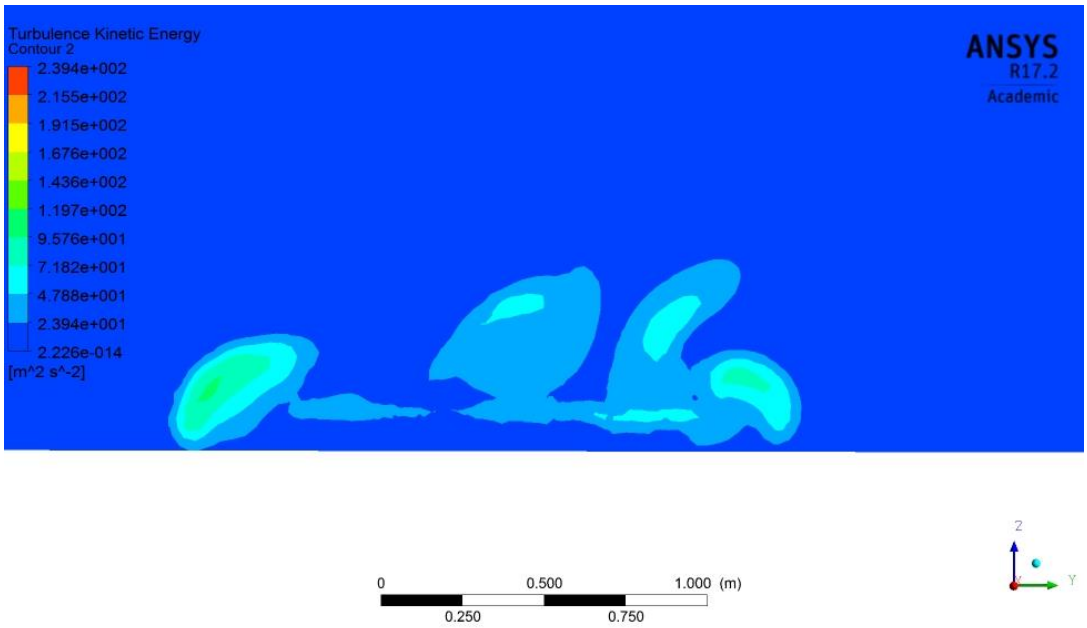

Figure 4.41- TKE contour of rear wake region for long-tail sidecar at x-=2.8 m

The direction of rotation of these vortices can be determined from a velocity vector plot on the x= 2.8 m plane (Figure 4.42).

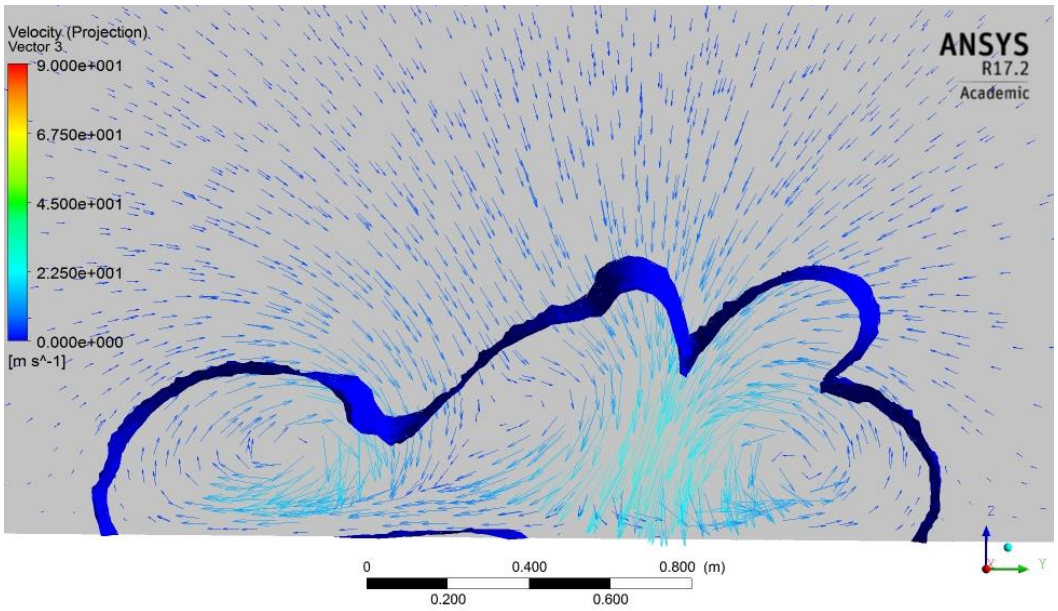

Figure 4.42- Velocity vector plot on plane at x=2.8 m with TKE iso-surface

The streamwise vortices on the outer edges of the rear slanting panel are counter-rotating—the left vortex rotates clockwise and the right vortex anti-clockwise. The streamwise vortex originating with the rider rotates clockwise.

The lack of significant lateral vortices at the trailing edge of the long-tail sidecar is also evident for a plot of velocity vectors on a horizontal plane cutting through the trailing edge (Figure 4.43).

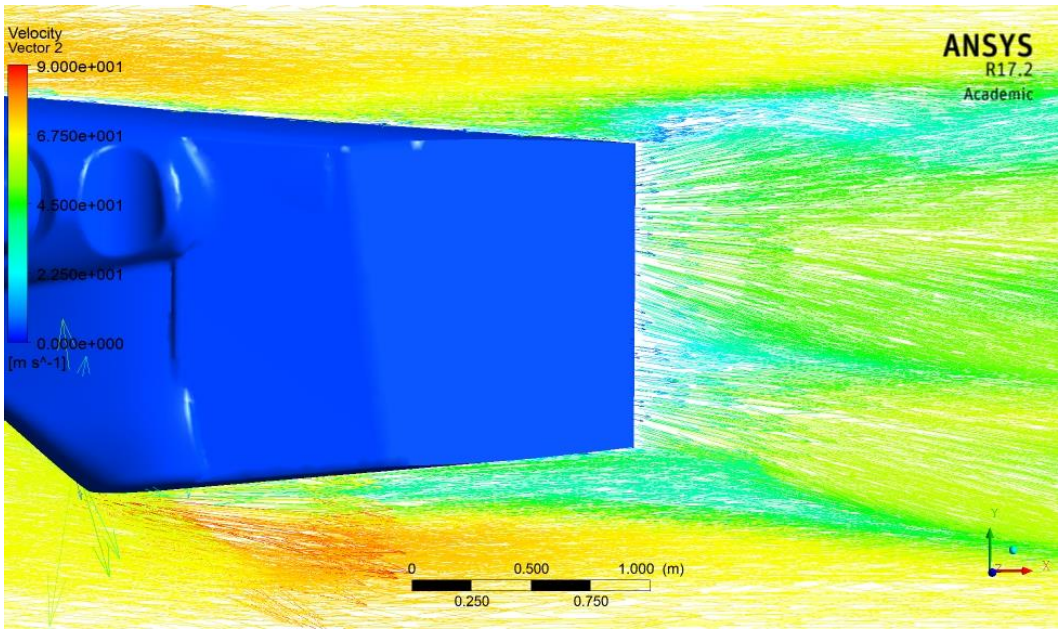

Figure 4.43- Plot of velocity vectors on a plane cut through the trailing edge of the long-tail sidecar

From the side view of velocity vectors over the tail region in Figure 4.44 at y = -0.1 m, it is evident that the flow is slower over the rear taper region, consistent with the pressure contours indicated in Figure 4.32 and as discussed above.

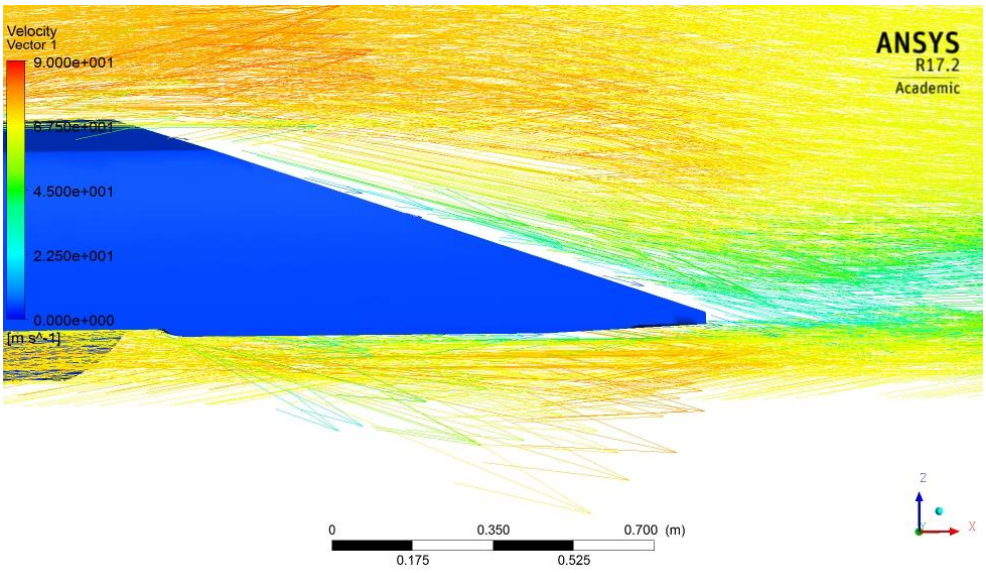

Figure 4.44- Velocity vectors over tapered tail section of long-tail sidecar plane A (y= -0.1 m)

In Figure 4.45, the three prominent streamwise vortices that extend into the wake region are clearly visible.

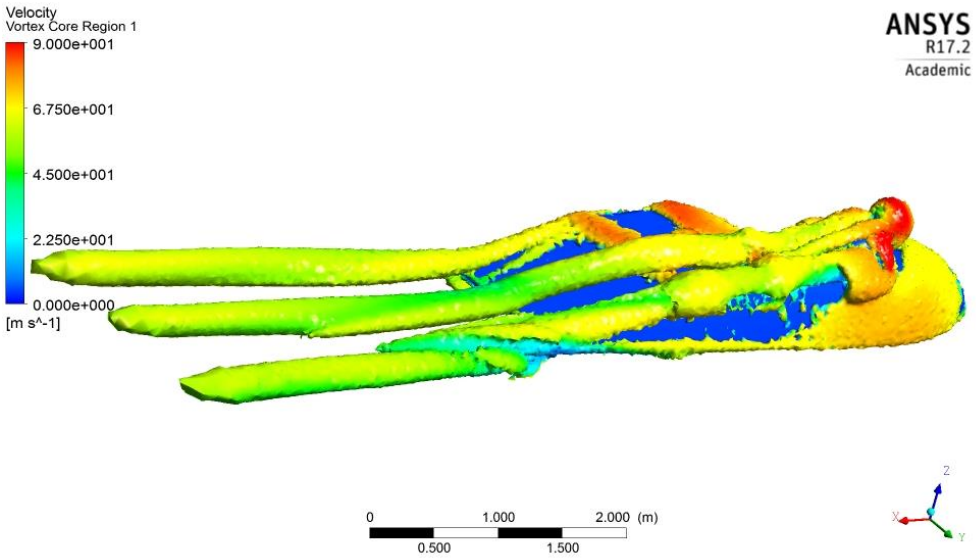

Figure 4.45- Streamwise vortices into wake region of long-tail sidecar

The presence of these streamwise vortices is also clear in a contour plot of velocity from above, as indicated in Figure 4.46. The plot shows that the vortices are more symmetrically arranged as they travel out into the wake region when compared with the original sidecar.

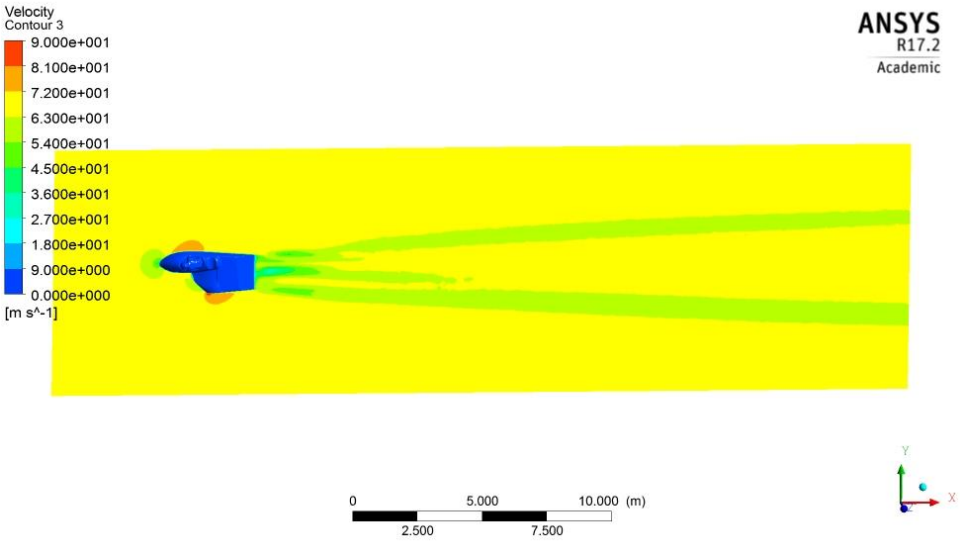

Figure 4.46- Contour plot of velocity for long-tail sidecar

It is clear that much of the drag is a result of the rider, as evidenced by the streamwise vortex extending into the wake from the rider's shoulder. Unfortunately, the rules are written in such a way that the rider's torso must be visible from the sides of the vehicle and from above which precludes removing the rider from the airstream. The use of a windshield will be examined later in this chapter.

The reduction of drag by more than 20% with the use of the long-tail would have been desirable, however the long-tail version of the sidecar had several problems associated with it. The logistics of transporting and racing the long tail version of the sidecar needed to be considered. The long tail would not fit into the existing team trailer and would need to be removed for transport. In addition, the FIM rules for a world land speed record specify a maximum length of 3300 mm and the existing sidecar with battery pack was already at a length of 3280 mm. It was decided to work to develop a shorter tail version of the sidecar, consistent with the FIM rules, to see if it was possible to attain the same low aerodynamic drag that the long tail version had achieved.

The first step in this phase of study was to simply truncate the long tail version with a plane cutting across the rear of the sidecar, as depicted in Figure 4.47.

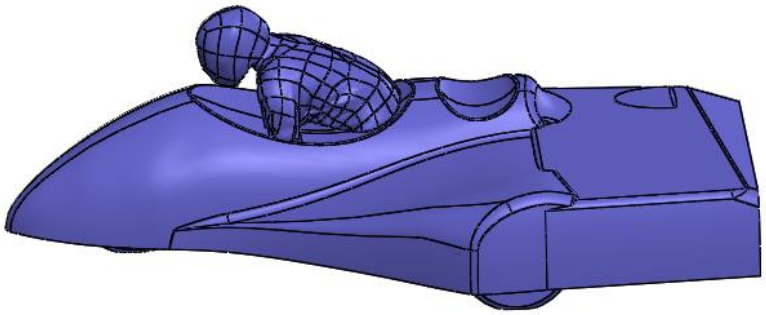

Figure 4.47- Rear section truncated (Version 50-13)

C_d = 0.353

C_l = 0.202

C_y = 0.071

C_m= 0.063

When compared to the long tail version, the results of the truncated tail did not look promising. Drag was 32% higher, lift was 27% higher, and lateral force was approximately equal.

Simply truncating the long tail body was not going to work. An all new rear section was designed (Figure 4.48) with sides tapered to follow the existing sidecar sides, a flat floor, and a radiused upper surface.

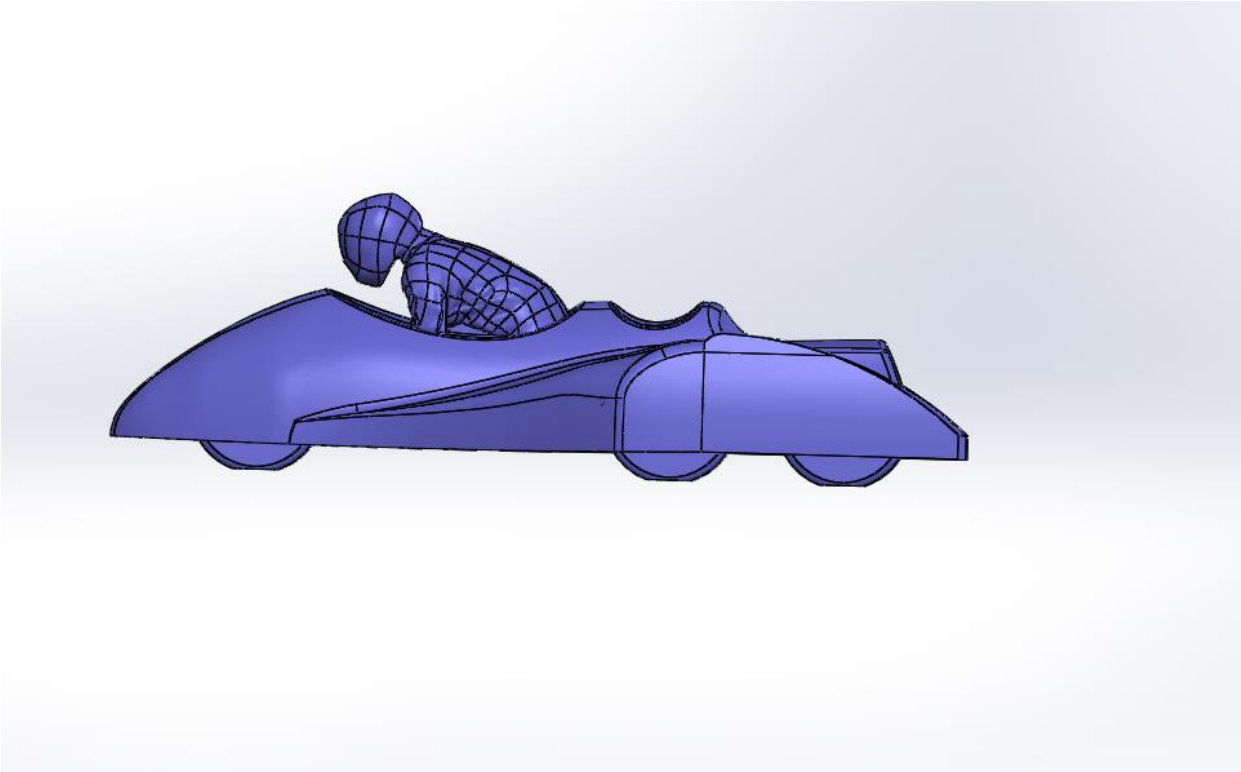

Figure 4.48- New rear section with radiused upper surface and flat floor (Version 60-1)

C_d = 0.349

C_l = 0.291

C_y = 0.039

C_m= 0.067

This design provided slightly less drag than the simply truncated version in Figure 4.39, but did not improve in other areas.

As depicted in 4.49, the next design used the radiused upper surface and tapered the rear floor upward at 7°.

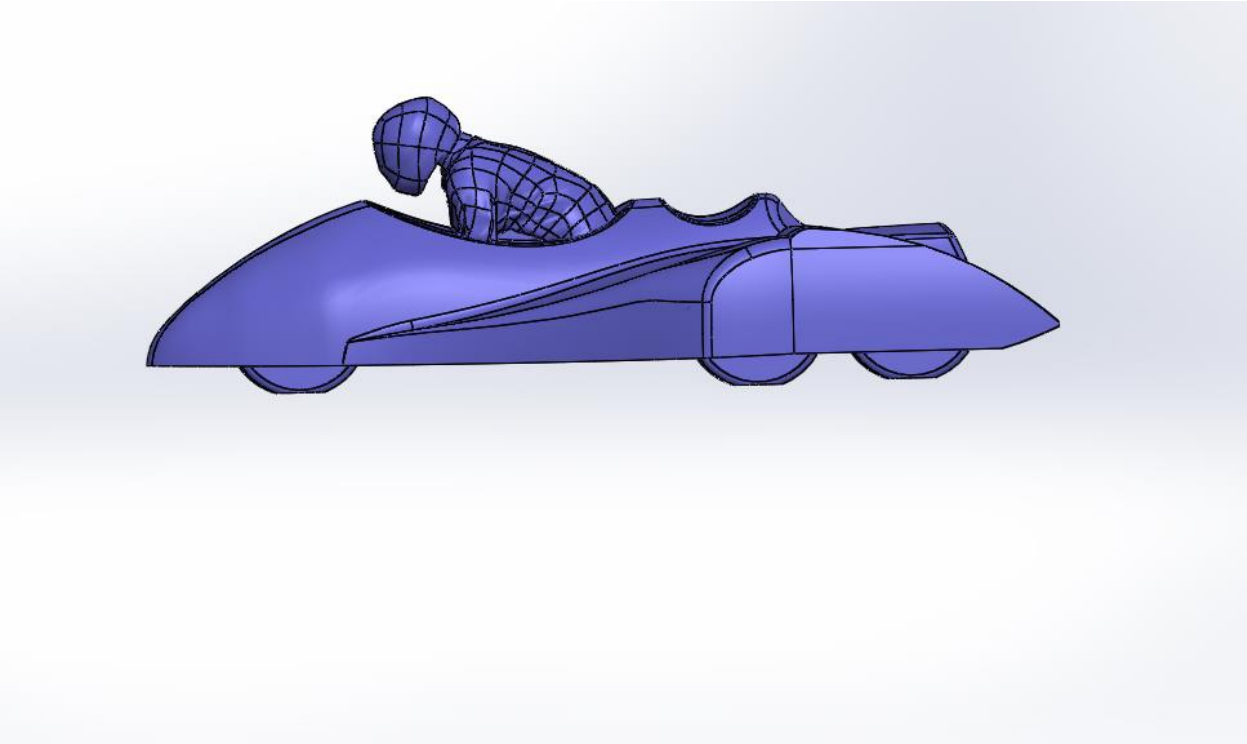

Figure 4.49- Radiused upper with tapered floor (Version 60-2)

C_d = 0.412

C_l = 0.766

C_y = -0.032

C_m= 0.061

The results for the upward slanting floor showed large increases in both drag and lift and a reversal in the direction of lateral force generation. The results were in the wrong direction, so for further studies a flat floor would be used.

It was unclear how the rear flat panel across the rear of the sidecar was changing the drag, lift and lateral forces generated. To investigate this, the geometry depicted in Figure 4.50 cut away the rear panel.

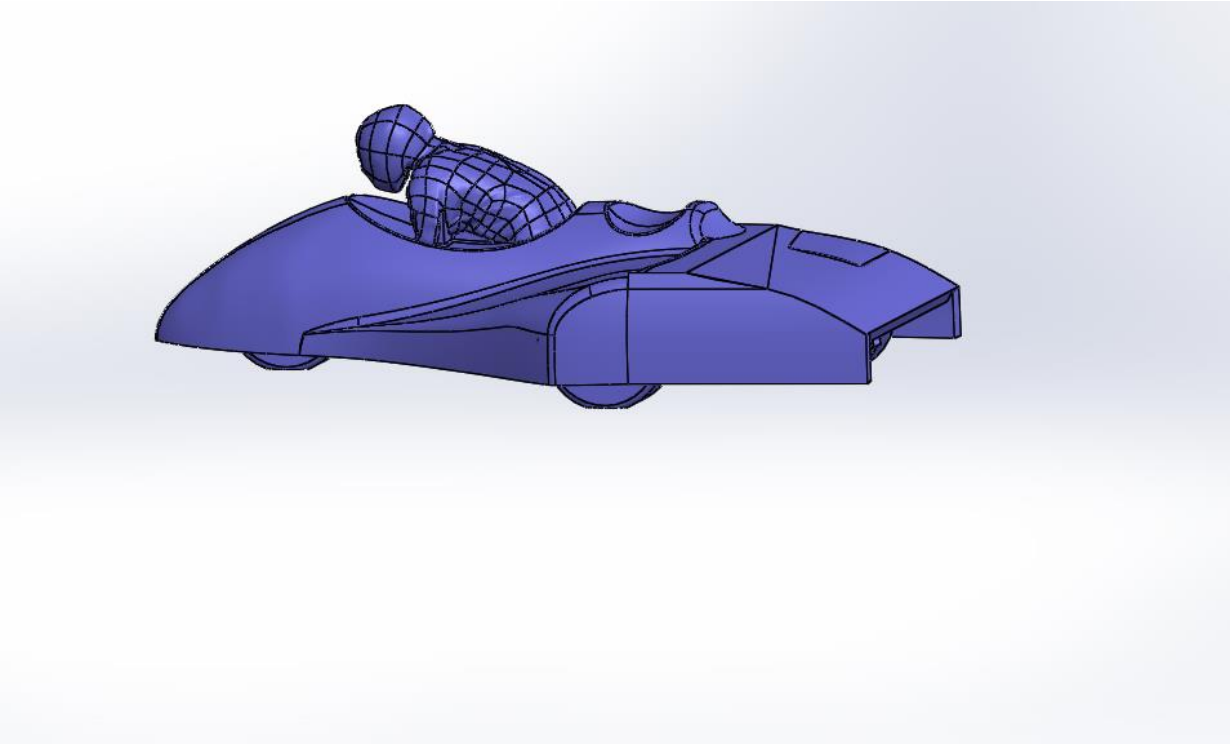

Figure 4.50- Cutaway of rear panel (Version 60-3)

C_d = 0.365

C_l = 0.489

C_y = 0.038

C_m= 0.062

In this geometry, drag and lift both increased significantly and further designs would use a closed off rear panel.

It was at this point in the geometric studies of the sidecar that the work of Professor Wunibald Kamm from the 1930s was revisited. Working in Germany, Kamm and his assistant, Reinhard von Koenig-Faschsenfeld studied automotive aerodynamics, particularly as applied to sports and racing cars of the period (Yankolonis & Simeone, 2015). They discovered that a “teardrop” shape, with a rear taper of 15° or less (wall to axis of flow), produced extremely low levels of aerodynamic drag. Significantly, Kamm and his assistant also discovered that by tapering the shape at a 7°-degree angle and then chopping off the tail at approximately half the cross section of the tallest midsection of the car gives approximately the same aerodynamic effect (reduced drag) as shaping the rear of the car to a point like a teardrop. (p. 5)

The sidecar with the Kamm tail is shown in Figure 4.51. The sides taper the same as the existing sidecar (5 and 6 degrees), while the upper surface tapers to the rear at 5.5°. The area of the

bodywork at the point where it is truncated is 48% of the maximum cross section area, as measured from the front of the vehicle.

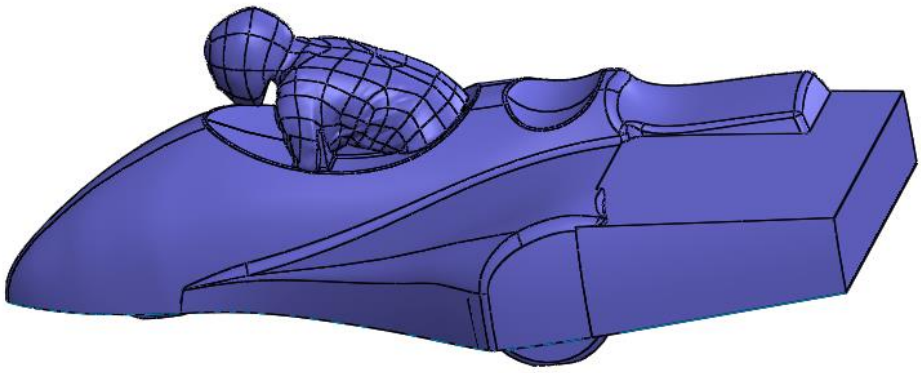

Figure 4.51- Tapered tail and truncated body following the work of Kamm (Version 80-2)

C_d = 0.336

C_l = 0.142

C_y = -0.021

C_m= 0.065

There is a significant reduction in aerodynamic drag (5% compared to the simply truncated rear in Figure 4.47), as well as a reduction in lift and lateral force. This design was further refined, as indicated in Figure 4.52, adding curvature to the sides as they taper to the rear.

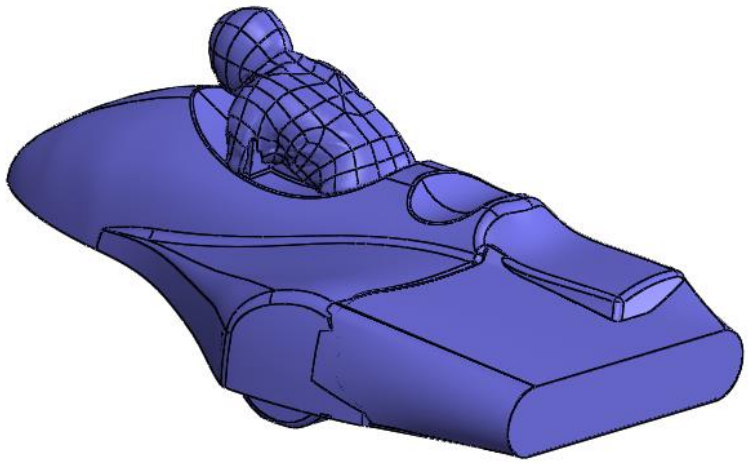

Figure 4.52- Refined version of Kamm-inspired design (Version 90-0)

C_d = 0.281

C_l = -0.069

C_y = 0.044

C_m= 0.062

With the design in Figure 4.52, the drag is much lower (-16%) compared to the sharp-edged version in Figure 4.51. Lift is slightly negative (downforce) and lateral force is low and in the opposite direction. The drag is significantly closer to the long-tail version. It was decided to more closely examine the pressure distribution and flow characteristics for this design. Figure 4.53 is a contour plot of the pressure distribution over the truncated sidecar.

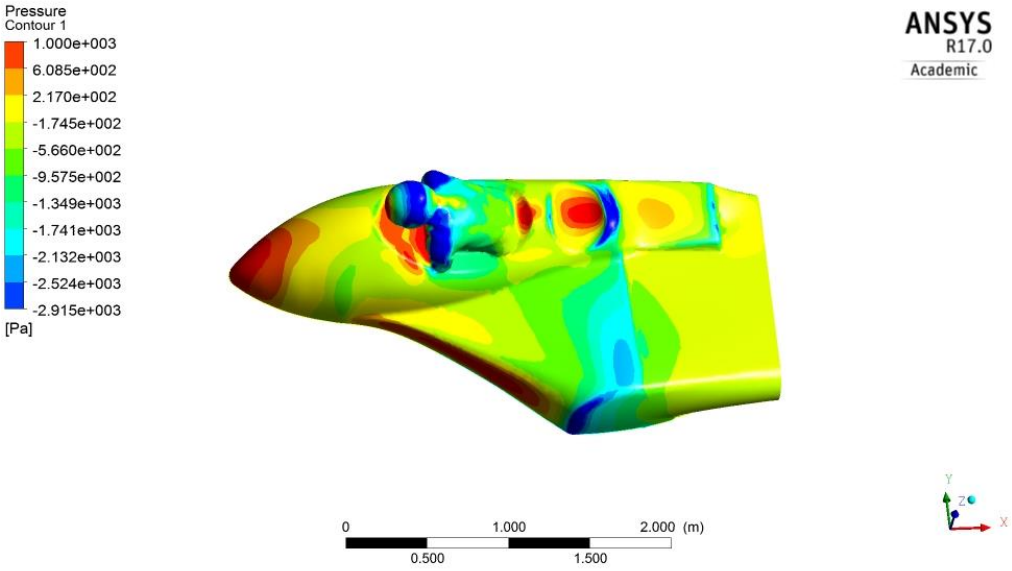

Figure 4.53- Pressure contour plot over Kamm-inspired sidecar design

The pressure gradient over the rear section of the sidecar body in Figure 4.53 is less severe than that exhibited by the original sidecar (Figure 4.8) or the long-tail version (4.31). The pressure gradient on the new tail section evidenced in Figure 4.53 is increasing in the flow direction. This gradient should slightly decrease the speed of the flow over this section, increasing its potential energy and decreasing its kinetic energy. Over the rear tapered section, there is thus an adverse pressure gradient—but one that is slight. A plot of velocity vectors over this region in Figure 4.54 indicates little or no separation until the flow reaches the trailing edge of the body section.

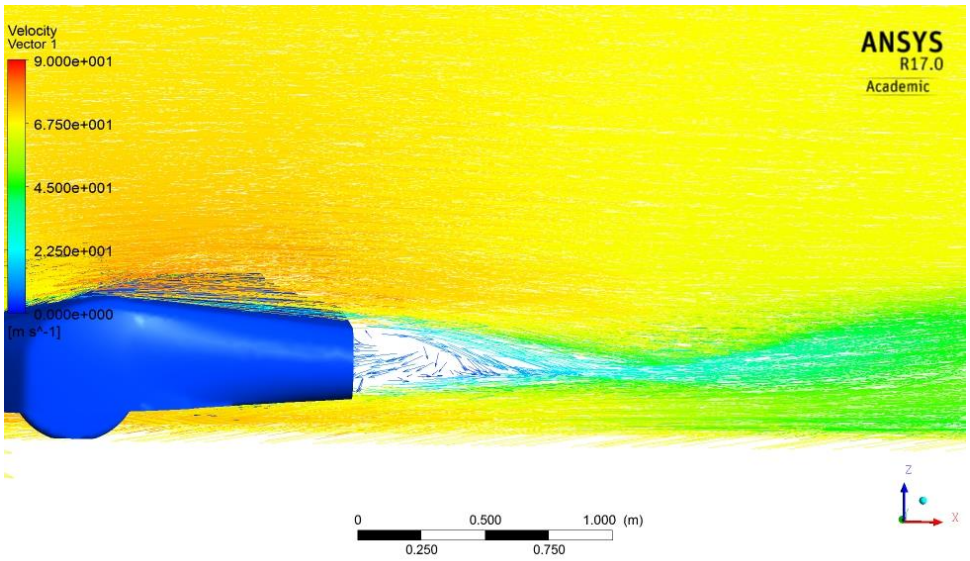

Figure 4.54- Velocity vector plot of flow over the Kamm-inspired rear section at plane A (y= -0.1 m)

The presence of this separated region is also evident from a plot of velocity vectors from above, in Figure 4.55.

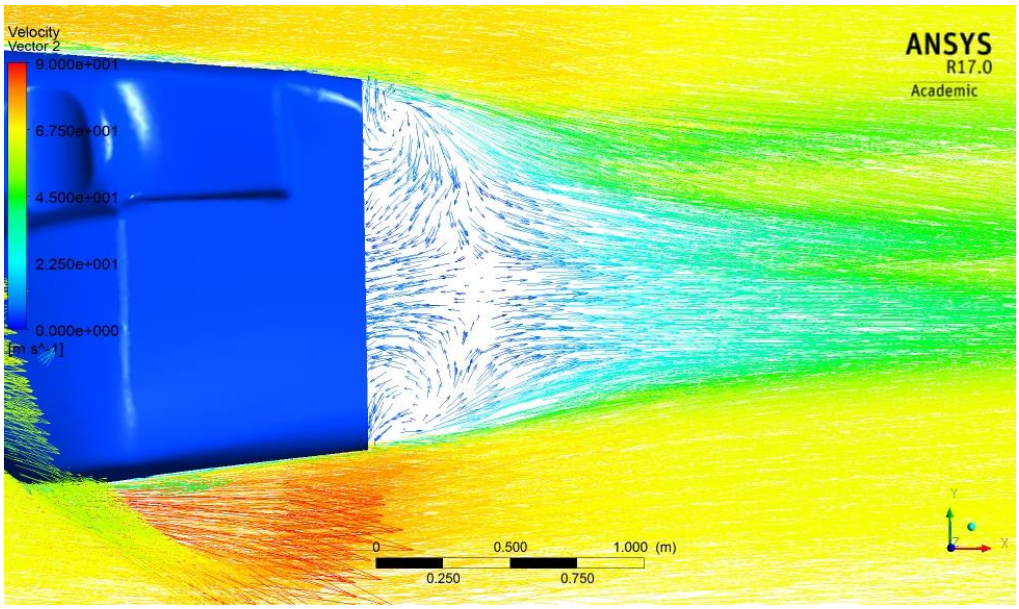

Figure 4.55- Velocity vector plot of flow over the Kamm-inspired rear section from above

Although there is a large region of separation behind the vertical tail of the sidecar, it is shaped differently from the separation behind the original sidecar (figure 4.10). The tapering of the region of separation behind the Kamm-inspired sidecar body appears to allow the flow to move into the wake region with less overall disturbance. This is evidenced in the velocity profile plots (Figures 4.56-4.58), where the disturbance from the separated region does not extend as far into the wake region as the original sidecar.

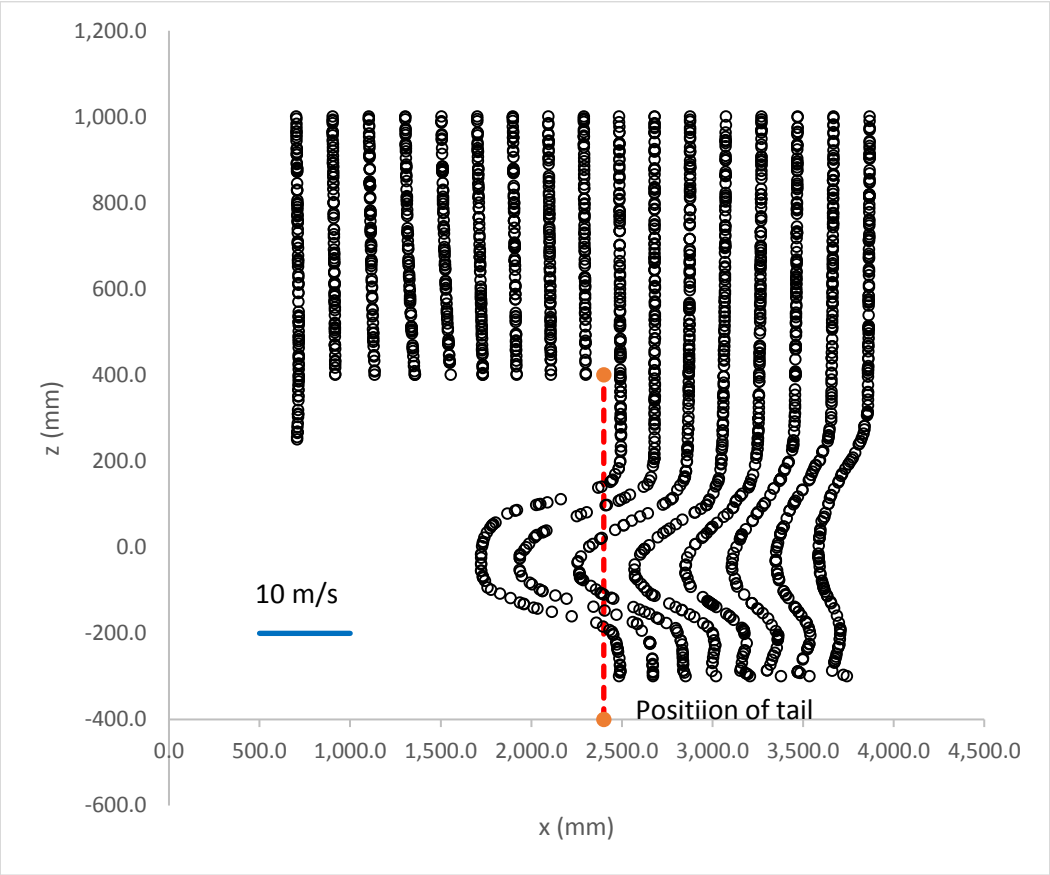

Figure 4.56- Velocity profile plot of Kamm-inspired sidecar plane A (y= -0.1 m)

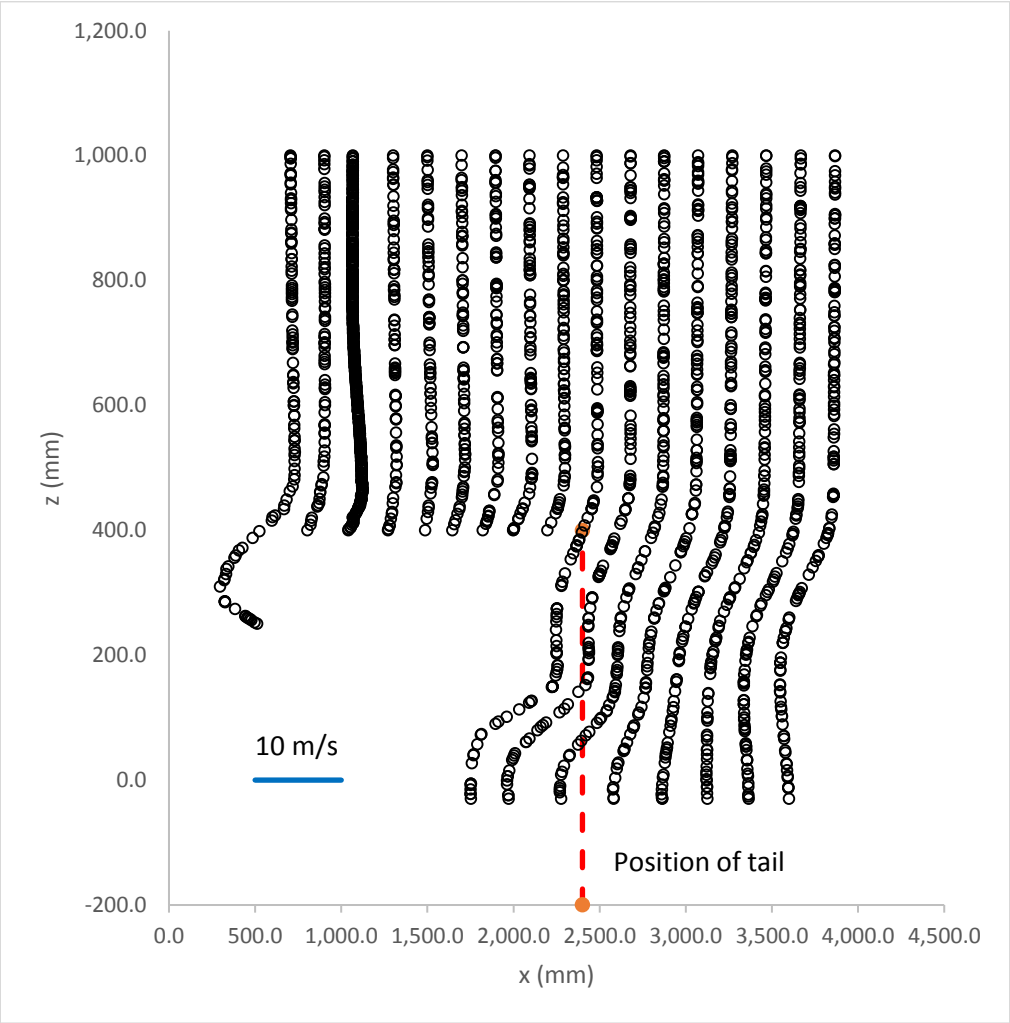

Figure 4.57- Velocity profile plot of Kamm-inspired sidecar plane B (y= 0.15 m)

In Figure 4.57, the maximum velocity deficit (local V < freestream V) is similar to the original sidecar (Figures 4.20-22) but this maximum exists over a smaller area giving a smaller total momentum deficit, and hence lower drag.

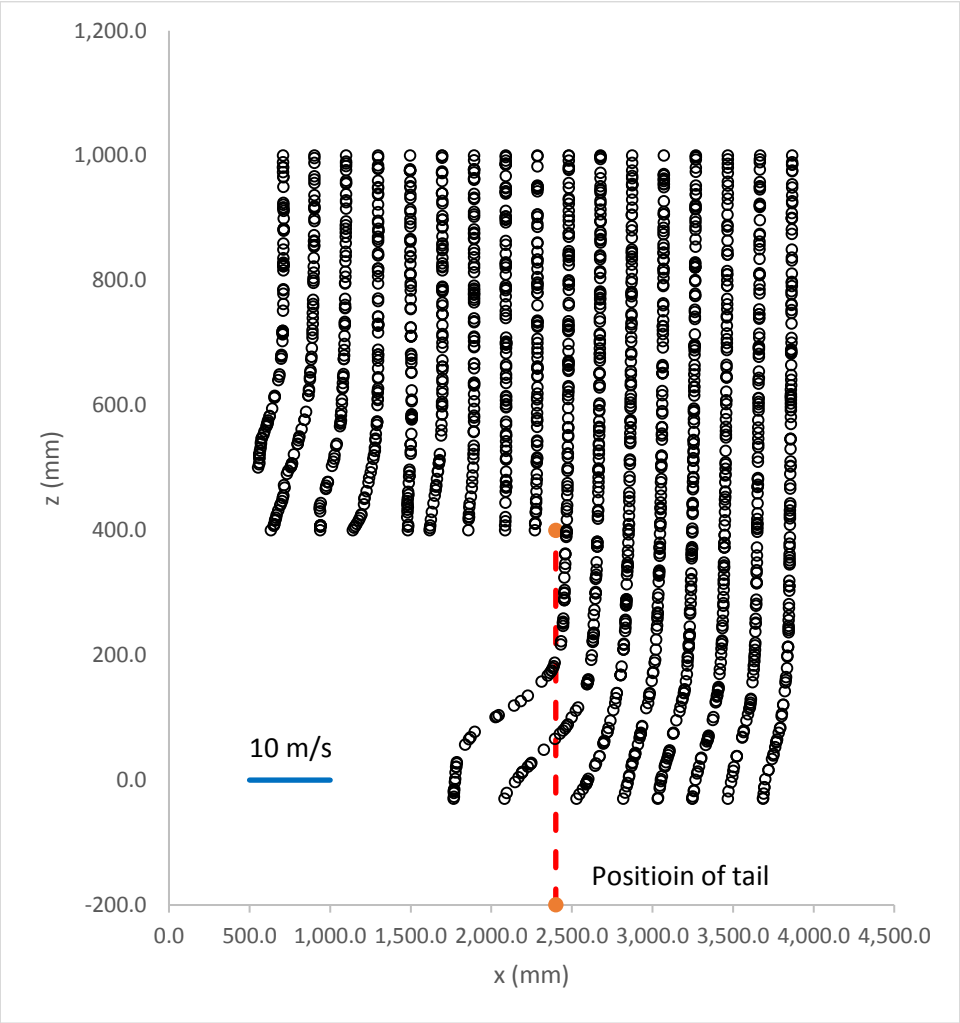

Figure 4.58- Velocity profile plot of Kamm-inspired sidecar plane C (y= 0.48 m)

The lower amount of disturbance in the wake compared to the original sidecar is also evident from plots of TKE at the rear and in parallel planes in the wake region of the Kamm inspired sidecar (Figures 4.59-4.62).

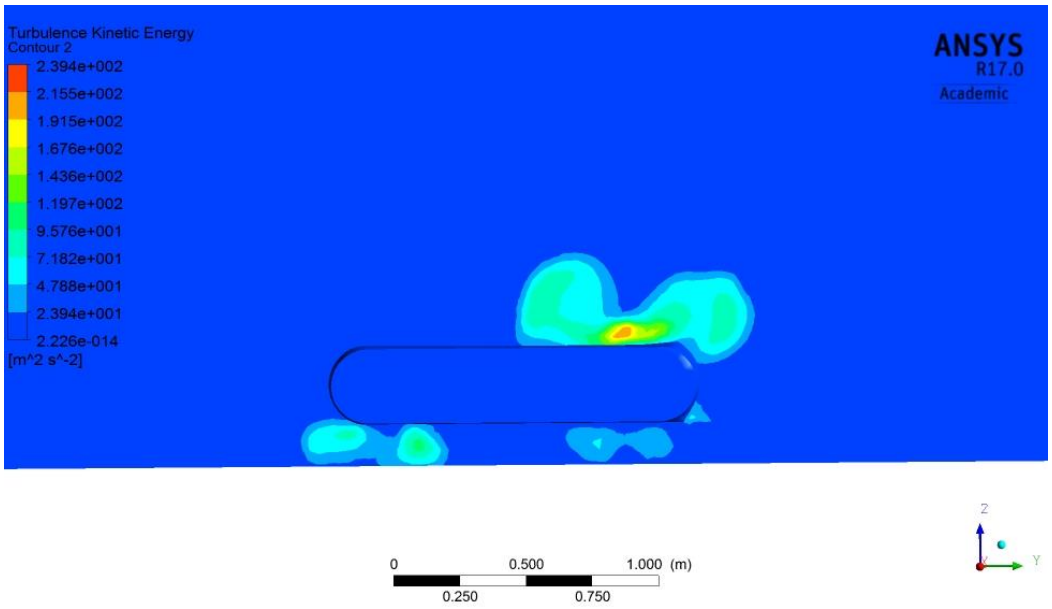

Figure 4.59- TKE contour plot of Kamm-inspired sidecar at x= 1.6 m

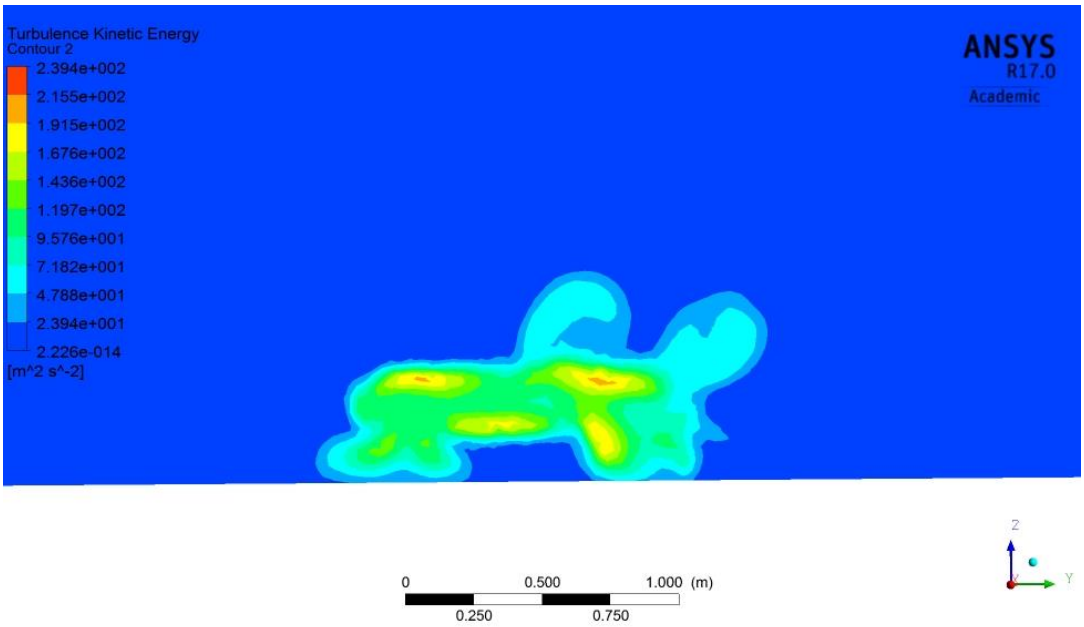

Figure 4.60- TKE contour plot of Kamm-inspired sidecar at x= 2.0 m

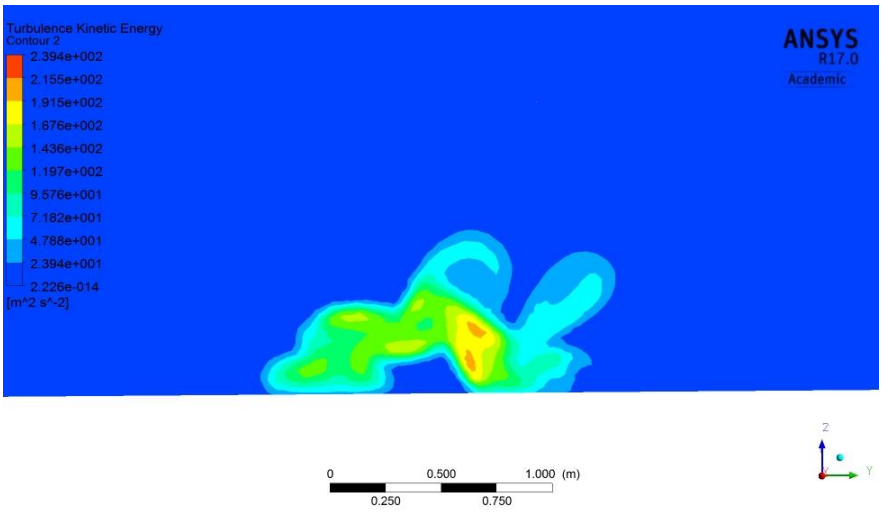

Figure 4.61- TKE contour plot of Kamm-inspired sidecar at x= 2.4 m

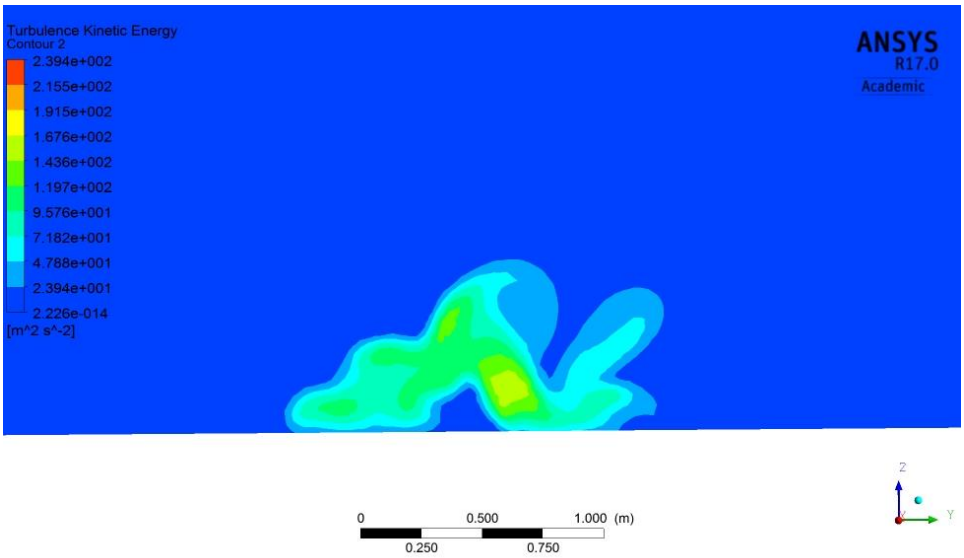

Figure 4.62- TKE contour plot of Kamm-inspired sidecar at x= 2.8 m

It is possible to determine the rotation direction of the main vortices that extend into the wake region. Figure 4.63 is a velocity vector plot on the x=2.8 m plane with an outline of the TKE iso-surface at the same plane region.

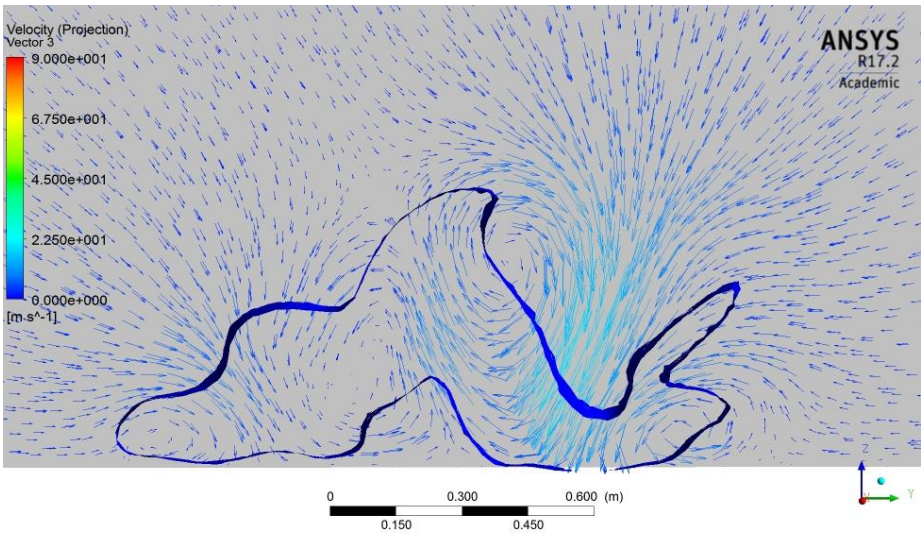

Figure 4.63- Velocity vectors on the x= 2.8 m plane with TKE iso-surface for Kamm tail

In Figure 4.63, four major vortices are identified. The one originating at the rider rotates in a clockwise direction, as does the one resulting from shear along the left side of the rear body section as with the original sidecar. The right side of the body produces an anti-clockwise rotating streamwise vortex as does the shear over the lateral vortex located directly behind the vertical wall section of the rear bodywork, again similar to the original sidecar.

It is particularly interesting to compare Figure 4.62 at x= 2.8 m with Figure 4.15, the TKE plot on the same plane for the original sidecar. The intensity of the TKE for the Kamm-inspired sidecar body is lower.

Figure 4.64 is a plot of the velocity vortex core indicating that the major vortex in the wake region is nearly centred behind the tapering lateral vortex that has formed directly behind the vertical panel at the rear of the Kamm-inspired body.

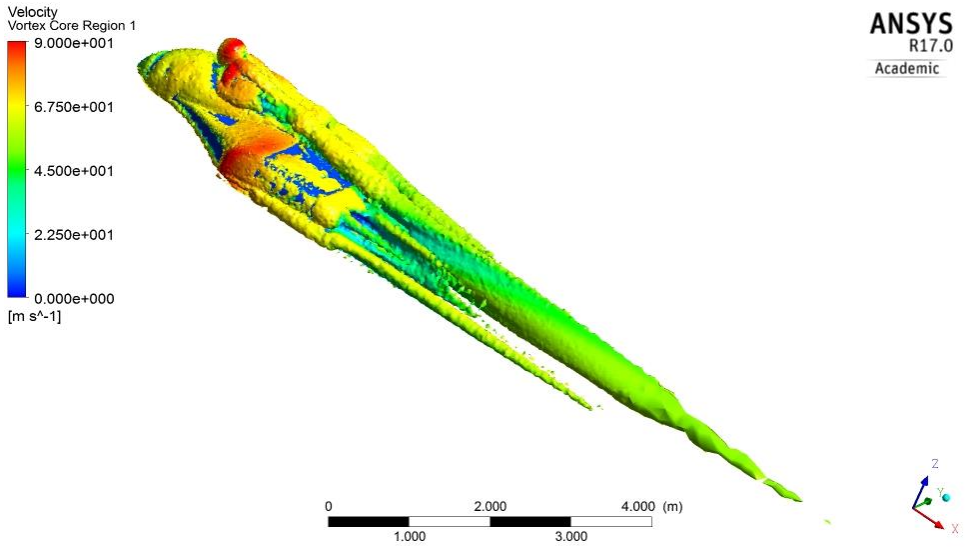

Figure 4.64- Velocity vortex core plot of Kamm-inspired sidecar

The presence of the major vortex into the wake region is also evident from a plot of the velocity contour from above in Figure 4.65.

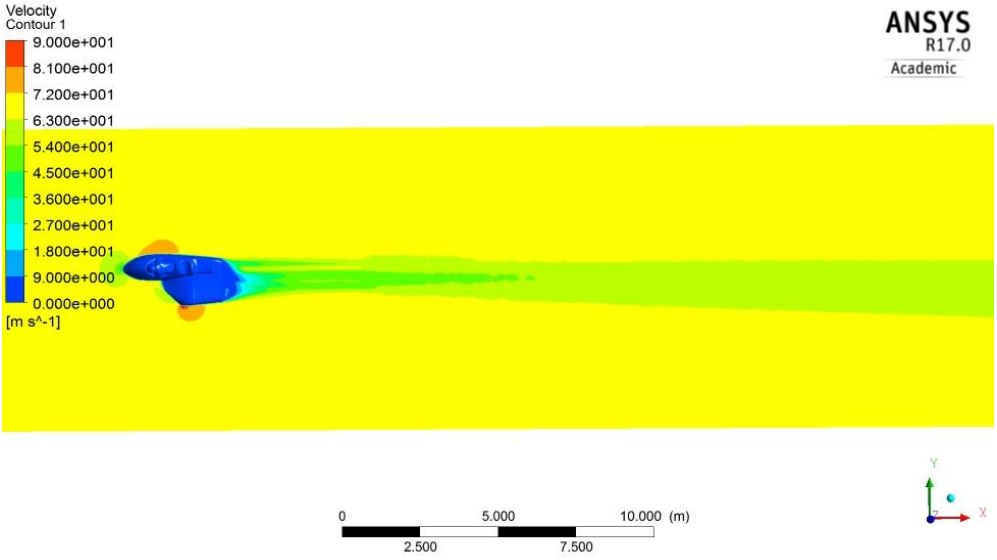

Figure 4.65- Velocity contour of Kamm-inspired sidecar from above

As observed with the long-tail sidecar, the disturbance into the wake with the Kamm-inspired sidecar design is nearly symmetrical and this is also reflected in a low value for the lateral force coefficient, C_Y. From a practical standpoint, the problem with the design depicted in Figure 4.52 is that the upper surface taper results in no room for the large battery box at the rear. The potential for remounting the battery transversely and further forward was briefly investigated,

but was rejected as it would interfere with the sidecar wheel location. Removing the taper from the upper section allowed space for the battery box. This design is shown in Figure 4.66.

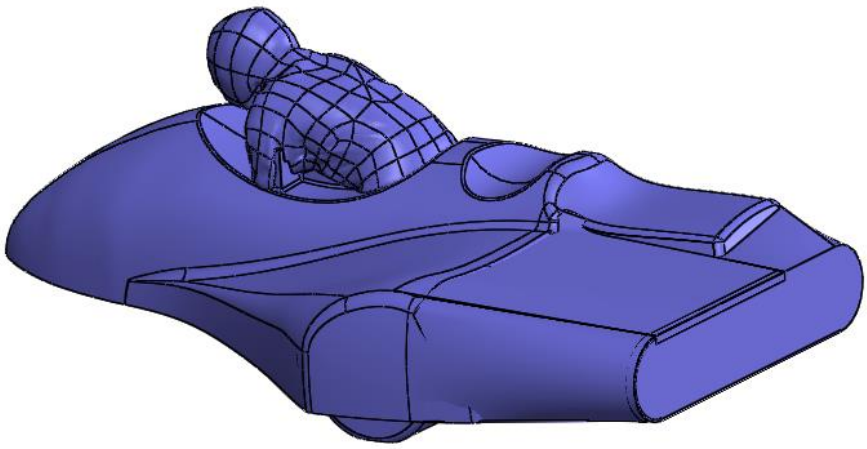

Figure 4.66- Remove taper from upper section to allow room for the battery box (Version 90-9)

C_d = 0.310

C_l = -0.040

C_y = -0.0046

C_m= 0.072

The results from Figure 4.66 were promising. Flattening the surface increased drag by +10%, and slightly decreased the small amount of downforce. Lateral force remained nearly the same.

4.5.2 Section behind rider

During the course of the rear bodywork section development, it was noticed that there was significant vorticity in the region behind the rider, and around the top of the twin motor drive. (Figure 4.67)

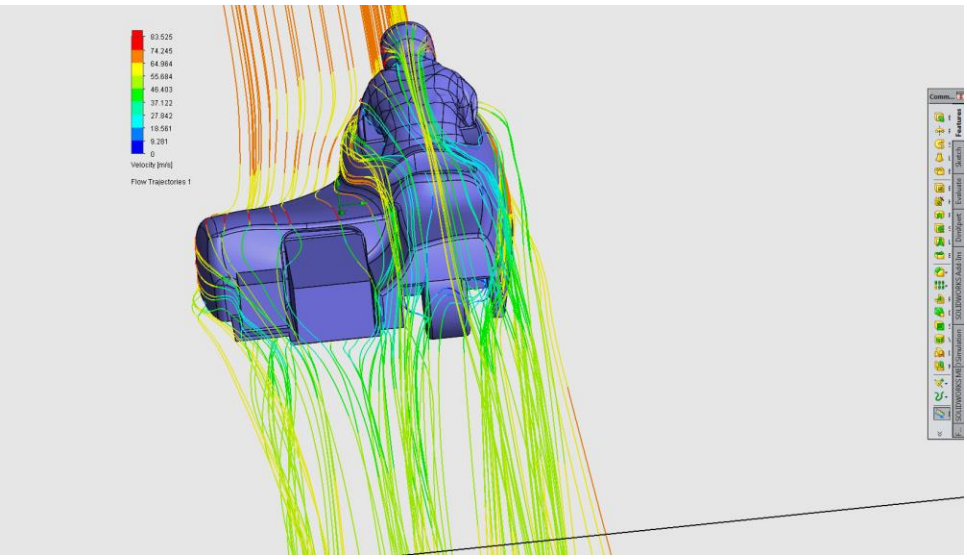

Figure 4.67- Vorticity region forms behind the rider

International (FIM) rules restrict the overall height of the sidecar to 800 mm, limiting the ability to reduce the streamwise vortices that form behind the rider. Nevertheless, it was felt that producing a smoother cover over the motor region beginning as close to the rider's back as possible would provide a benefit in the quest for drag reduction. A variety of designs were created using SolidWorks and tested with ANSYS Fluent CFD simulation to develop a motor covering that would help smooth airflow behind the rider and over this region. Two examples are presented in Figure 4.68 and Figure 4.69.

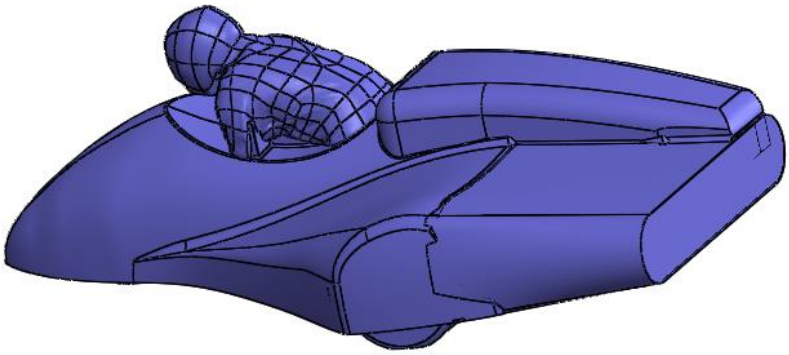

Figure 4.68- Tapered rear body with high line motor cover (Version 90-1)

C_d = 0.328

C_l = 0.214

C_y = -0.031

C_m= 0.067

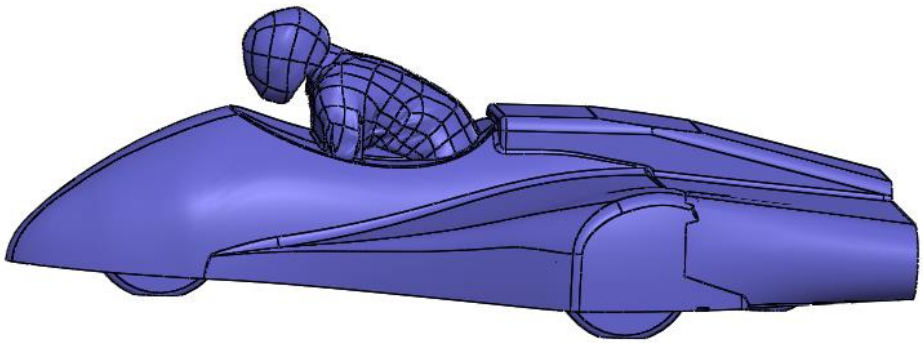

Figure 4.69- Tapered rear body with low line motor cover (Version 90-4)

C_d = 0.273

C_l = -0.048

C_y =0.035

C_m= 0.069

The low-line motor cover depicted in Figure 4.69 provided a reduction of 3% in drag compared to the Kamm-inspired short tail shown in Figure 4.52. Downforce was slightly decreased as was the lateral force coefficient. The effect of the motor cover on the airflow was further investigated. Figure 4.70 is a contour plot of the surface pressure on the sidecar body.

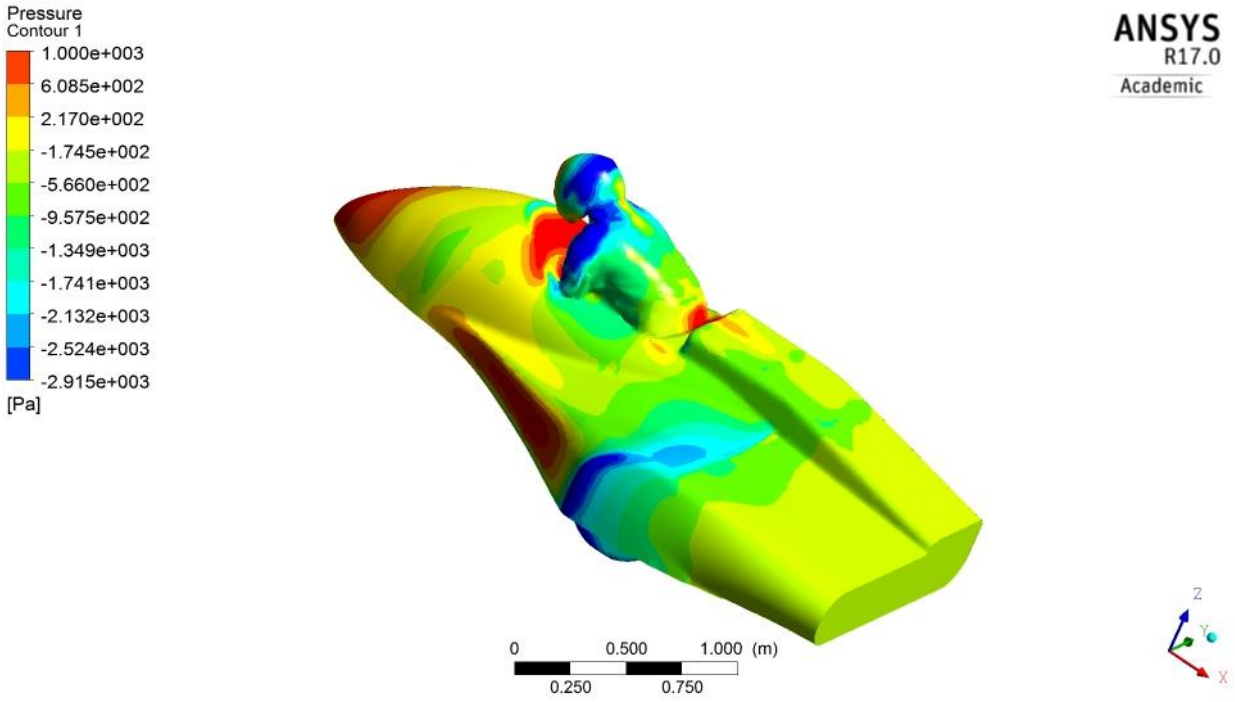

Figure 4.70- Surface pressure on sidecar with low-line motor cover

The pressure over the motor cover in Figure 4.70 shows a much smoother transition of the pressure in that region than does the same area without a cover as indicated in Figure 4.45. The velocity profile plot in Figure 4.71 at plane C (y = 0.48) (the plane positioned at the centreline of the new motor cover) shows much less disturbance in the vehicle wake than does the version of the sidecar without a motor cover (Figure 4.58).

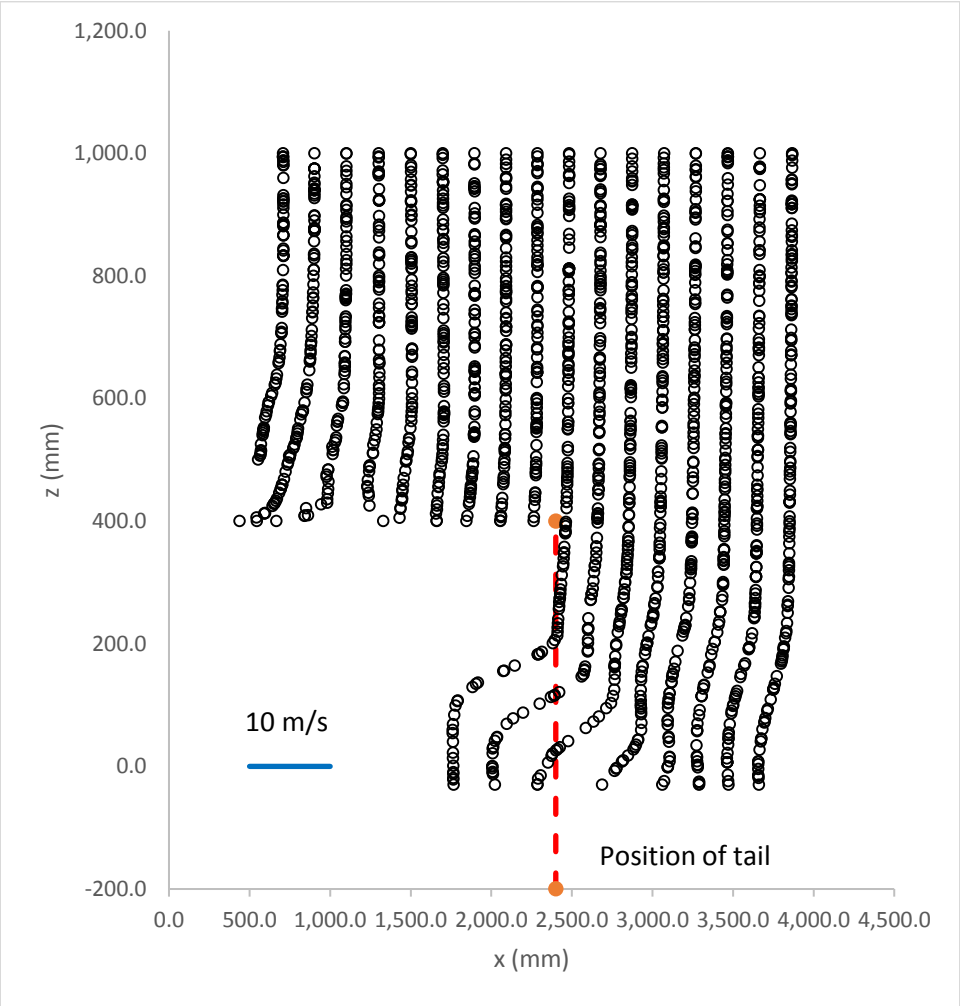

Figure 4.71- Velocity profile of sidecar with low-line motor cover at plane C (y=0.48m)

A velocity vector plot of the region directly behind the motor cover (Figure 4.72) shows a slightly larger separation region than that observed with the Kamm-inspired body region, but once again the separation region tapers away quickly, which is also observed from above in Figure 4.73.

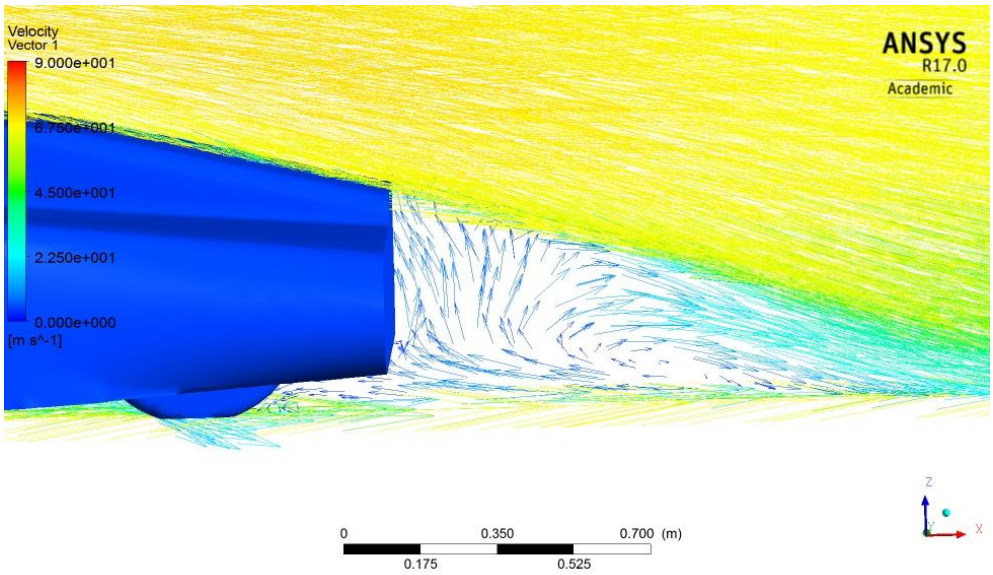

Figure 4.72- Velocity vectors in region behind motor cover plane C (y=0.48 m)

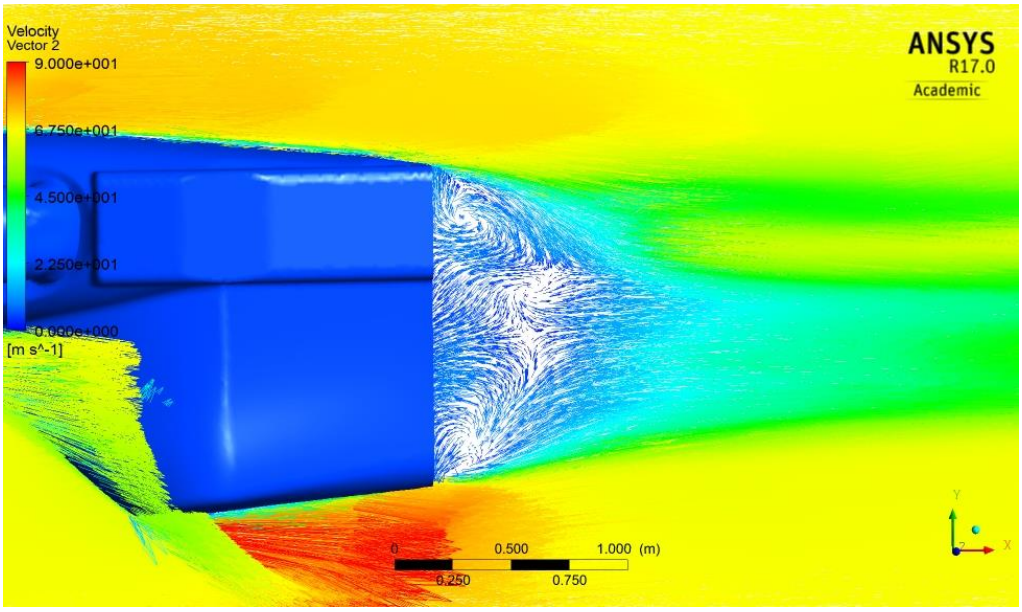

Figure 4.73- Separation region directly behind sidecar with motor cover

A plot of the velocity vortex core region in Figure 4.74 shows the vortex which had distinctly originated at the left rider's shoulder is now a part of a distinct single vortex forming from the rider, the rider's helmet and the sidecar motor cover.

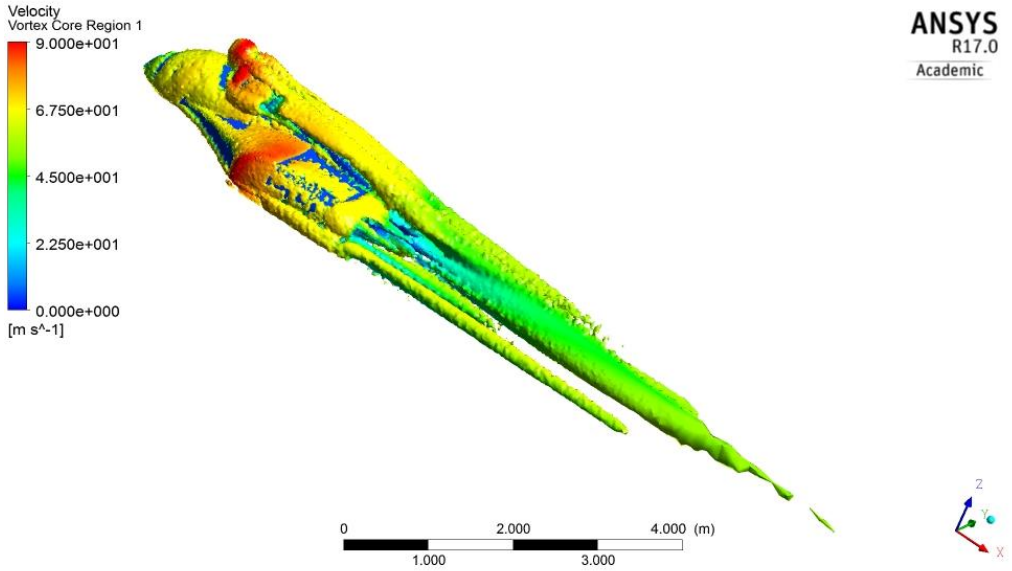

Figure 4.74- Velocity vortex core over motor cover

In Figure 4.75, the presence of the motor cover appears to have further reduced the total asymmetry of the wake region.

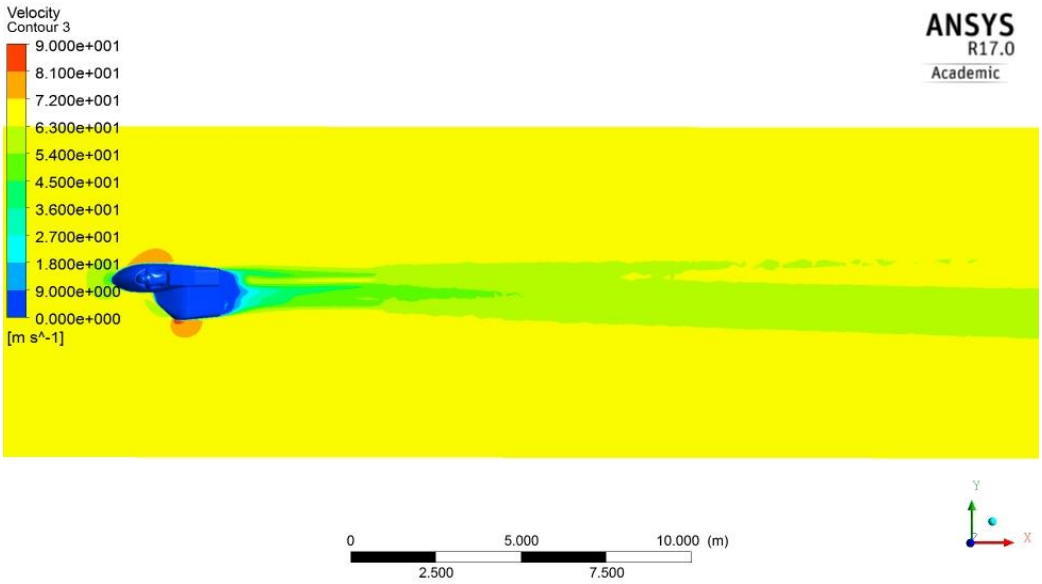

Figure 4.75- Velocity contour of wake region with motor cover

The design in Figure 4.69 looked promising, but the location of the large battery box in a longitudinal configuration could not be accommodated under the tail section. While redesigning the mounting of the battery to a transverse location was considered, modifications to the rear deck to cover the longitudinal battery mounting were explored (Figure 4.76)

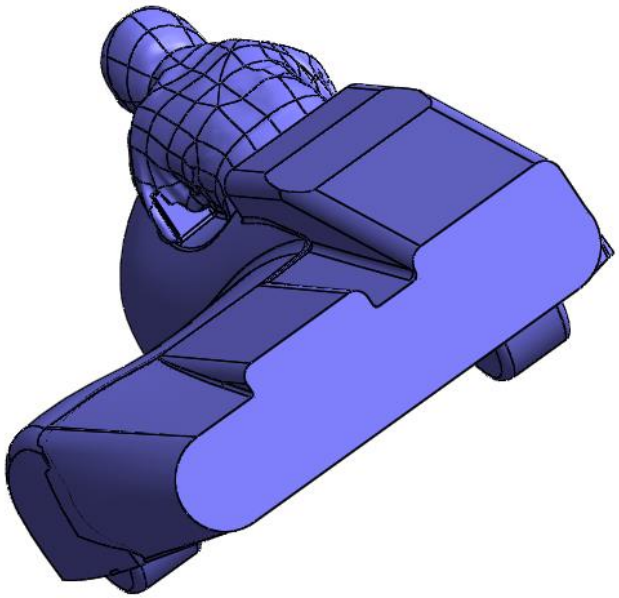

Figure 4.76- Revision of upper rear section to accommodate battery box but allow taper (Version 90-11)

C_d = 0.315

C_l = 0.011

C_y = 0.002

C_m= 0.069

The geometry in Figure 4.76 resulted in a significant increase in drag (+15.3%) relative to the geometry from Figure 4.69. Further development was done as depicted in Figure 4.77.

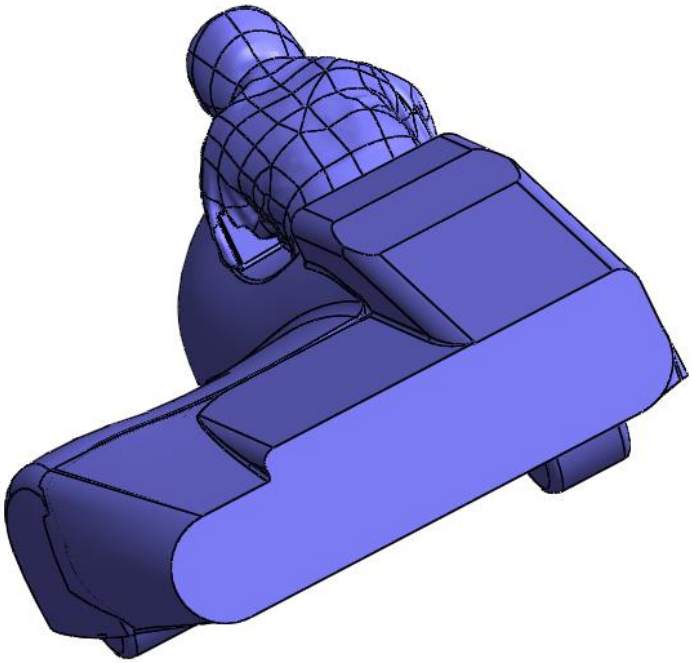

Figure 4.77- Further revision of rear upper surface (Version 90-13)

C_d = 0.273

C_l = -0.048

C_y = 0.035

C_m= 0.069

This geometry was able to accommodate the longitudinal battery placement and would be straightforward to build while still providing a C_d equal to the low drag evidenced in Figure 4.69, slight downforce and almost no lateral forces. This configuration was selected for construction, subject to the addition of some additional features, described in the remainder of this chapter.

4.5.3 **Windshield**

From a front view of the sidecar body (Figure 4.78) it was noted that an area of high pressure existed on the front of the rider's chest, shoulders and top of the helmet.

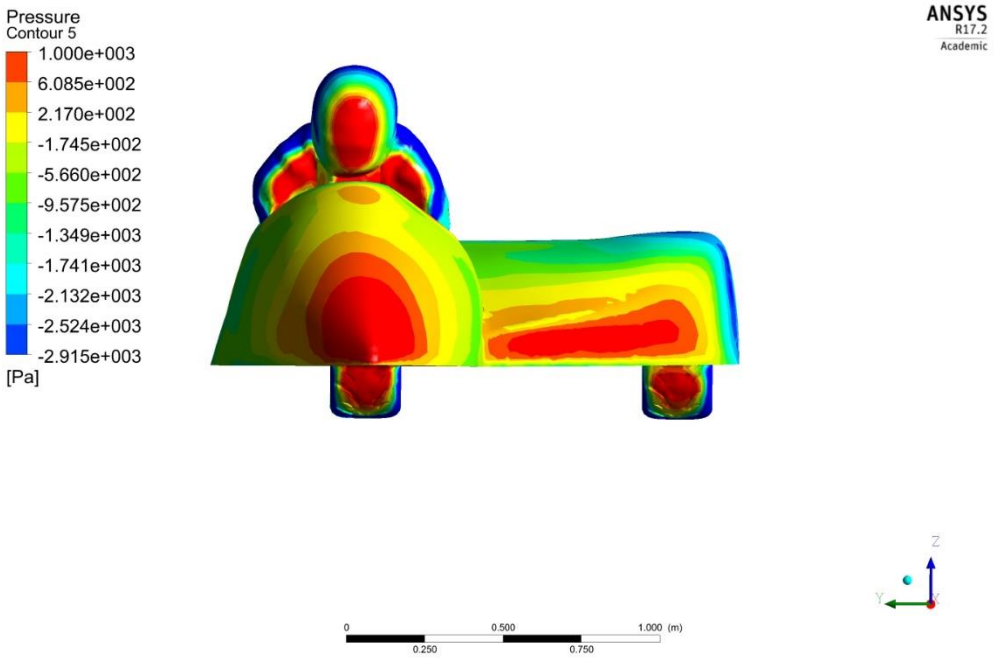

Figure 4.78- Pressure contours on rider body surface

Investigations were undertaken to determine if the presence of a windshield ahead of the rider would improve the aerodynamic drag coefficient. The initial design had a high windshield profile that was wide enough to cover the rider's upper torso. (Figure 4.79)

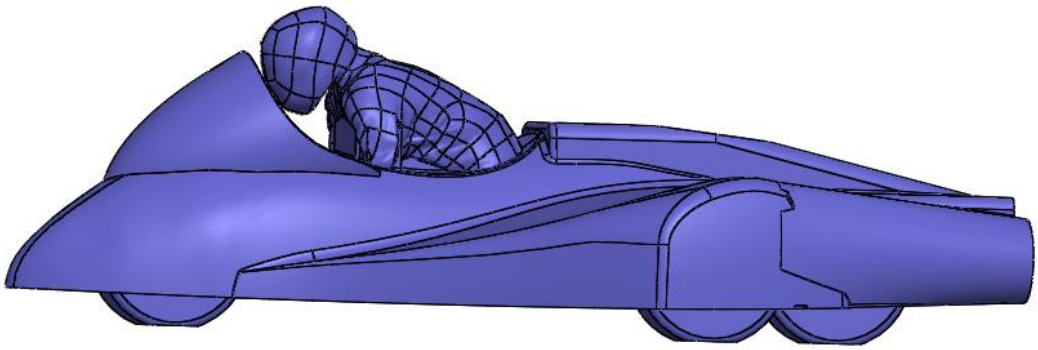

Figure 4.79- Large windshield (Version 90-16-3)

C_d = 0.267

C_l = -0.089

C_y = 0.022

C_m= 0.065

The large windshield produced a dramatic reduction in drag (11% lower than the same sidecar without a windshield). This windshield would not be legal for FIM Record completion however, as it extended too high (maximum height allowed is 800 mm). A smaller design was developed, as shown in Figure 4.80.

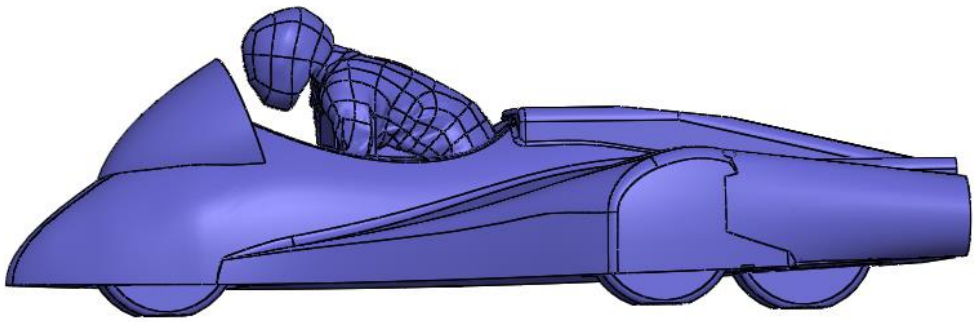

Figure 4.80- Smaller windshield to meet FIM Regulations (Version 90-16-2)

C_d = 0.276

C_l = -0.073

C_y = 0.003

C_m= 0.066

The smaller windshield increased the drag by 3.4% compared to the large windshield, but was legal for competition for FIM world records. Figure 4.81 is a pressure contour of the sidecar with the smaller windshield.

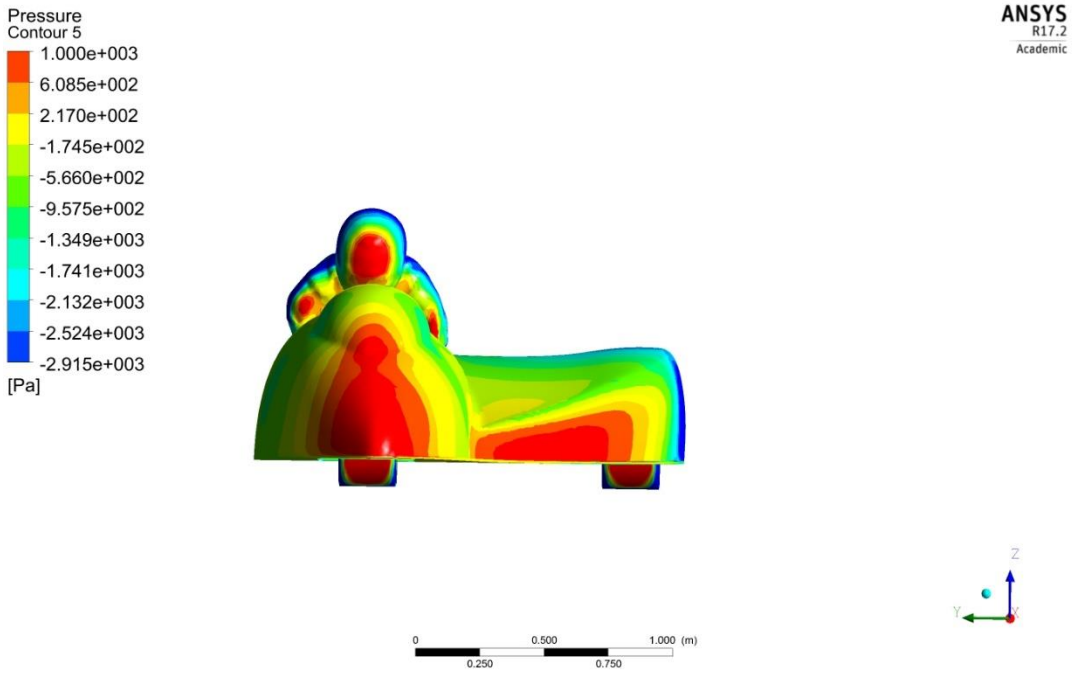

Figure 4.81- Pressure contour with small windshield

In Figure 4.81 it is evident that the pressure across the chest of the rider is less and that the region of high pressure (red) on the rider's helmet is also smaller.

4.5.4 Splitter

Modern racing cars use a "splitter" to increase front downforce with little increase in aerodynamic drag (McBeath, 2015). The splitter is a horizontal extension of the floor, forward from the leading edge of the bodywork. High pressure that forms as air impacts the front part of the bodywork is transferred onto this rigid horizontal element, putting the pressure to use by pushing down on the splitter element and producing a downward force. Figure 4.82 indicates the position and geometry of the splitter.

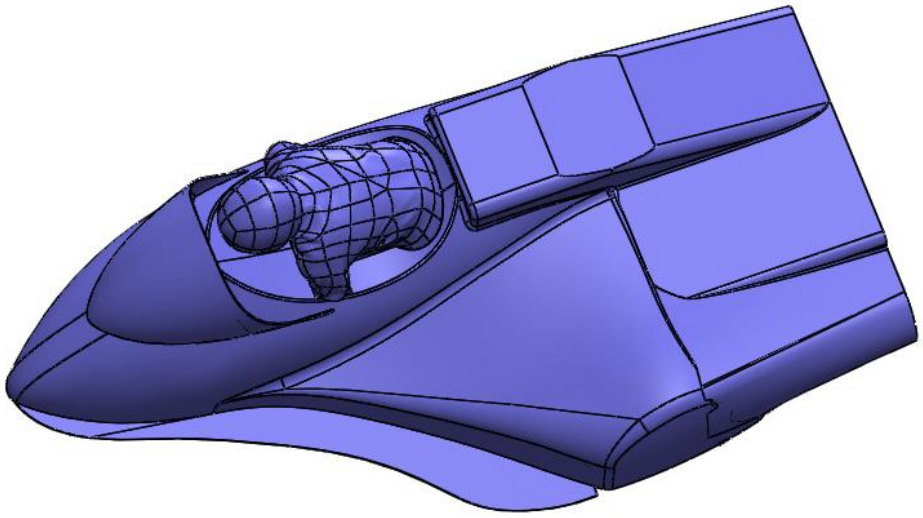

Figure 4.82- The addition of the splitter (Version 90-16-9)

C_d = 0.257

C_l = -0.120

C_y = 0.017

C_m= 0.066

The addition of the splitter had a 7% improvement in drag and significantly, increased overall downforce by more than 36%.

Figure 4.83 is a plot of surface pressure contours on the sidecar with the splitter (and low windshield) added.

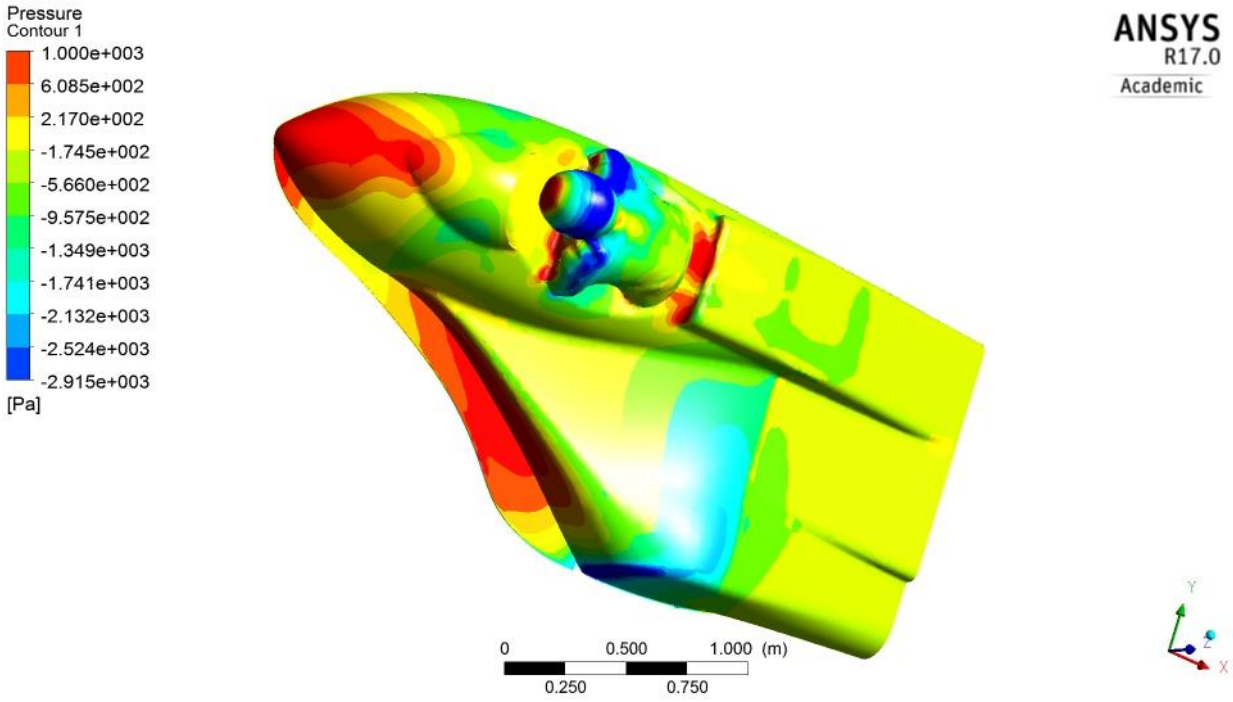

Figure 4.83- Surface pressure contours with splitter and windshield

In Figure 4.83 the high-pressure region (in red) on the top surface of the splitter generates downforce (negative lift) as is evidenced by the lift force coefficient (C_l) of -0.120.

4.6 Final Bonneville Design

The final Bonneville design of the body modifications developed for the electric land speed racing sidecar are indicated in Figure 4.84.

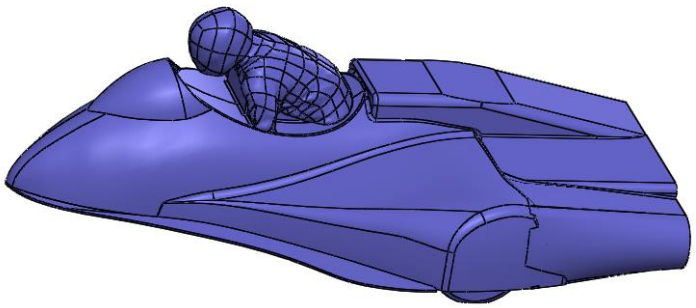

Figure 4.84- Final Bonneville design for body changes (Version 90-26)

The final Bonneville design in Figure 4.84 has a fully enclosed rear section that slants rearward at approximately 10° from horizontal, except for the area directly above the battery box, which forms the mandatory horizontal "swinger" platform. The tail has been truncated following the theory of Kamm, as previously discussed. A raised section (motor cover) behind the rider helps smooth flow from the rider. A small windshield helps to guide airflow around the rider, reducing the pressure gradient across the rider's chest and shoulders. The presence of a front splitter was found to both increase aerodynamic downforce (negative lift) and also slightly reduce aerodynamic drag.

Table 4.2 summarizes the drag, lift and lateral force coefficients for the original sidecar design (with battery box and cooling tank) and the final Bonneville design study (Figure 4.84).

Table 4.2- Drag, lift, and lateral force coefficients for sidecar study

Coefficient	Original Starting point for optimisation study	Final Bonneville Design from optimisation study
C_d	0.344	0.260 (-24.4%)
C_l	0.0026	-0.255
C_y	0.065	0.058

Using CFD, the effect of Re on the final sidecar design and a comparison to the effect of Re on the original design was undertaken and is provided in Figure 4.85.

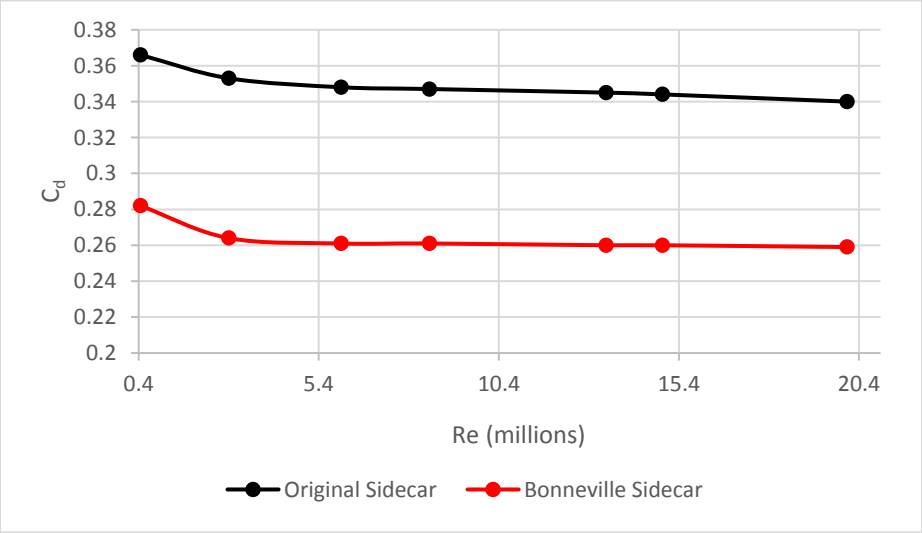

Figure 4.85- Comparison of effect of Re on original and final (Bonneville) sidecar designs

From Figure 4.85, it is shown that the effect of the design changes (addition of rear bodywork, windshield, and splitter) did not dramatically change the dependence of drag coefficient on Re when compared to the original design of the sidecar.

Flow Visualization

The effects of air flow over the surface of the sidecar body can be characterized and examined in a variety of different ways, as detailed in Chapter 3. Figure 4.85 shows shear stress lines over the surface of the sidecar.

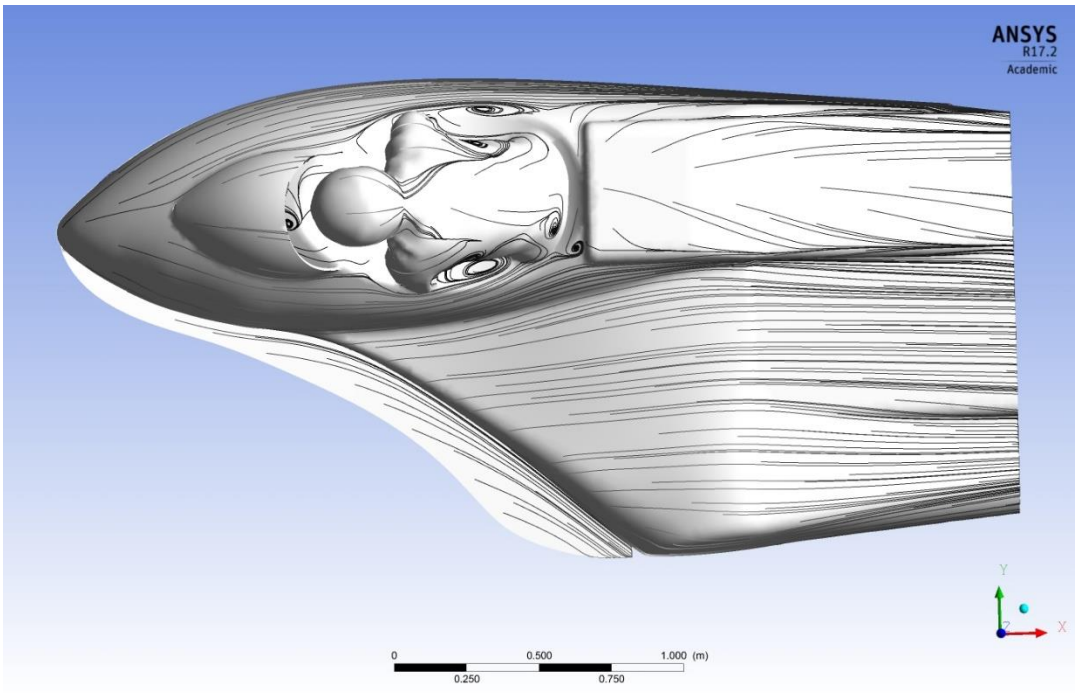

Figure 4.86- Shear stress lines over the top surface of the final design sidecar

The areas of interest in Figure 4.86 would be the left side of the rider where, as previously discussed a focus in shear stress lines occurs at the same point at which a streamwise vortex forms. In addition, flow along the top surface of the splitter ends with encountering streamwise flow at the outer point of the splitter. In Figure 4.87, the streamwise vortex associated with the focus on the left side of the rider, and the streamwise vortex caused by the lateral flow along the splitter encountering the streamwise flow at the edge of the sidecar are both evident.

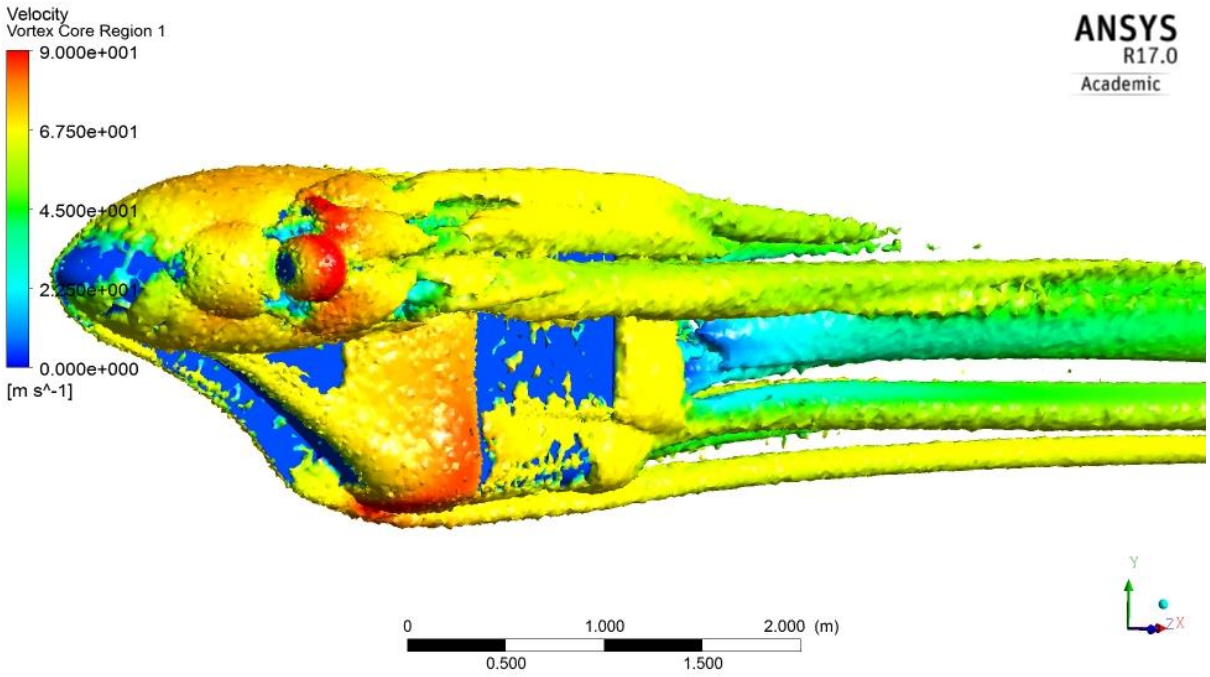

Figure 4.87- Velocity vortex core plot of splitter area from top side

On the underside of the sidecar, in Figure 4.88, shear stress lines indicate the disruption and separation of flow caused by the wheels.

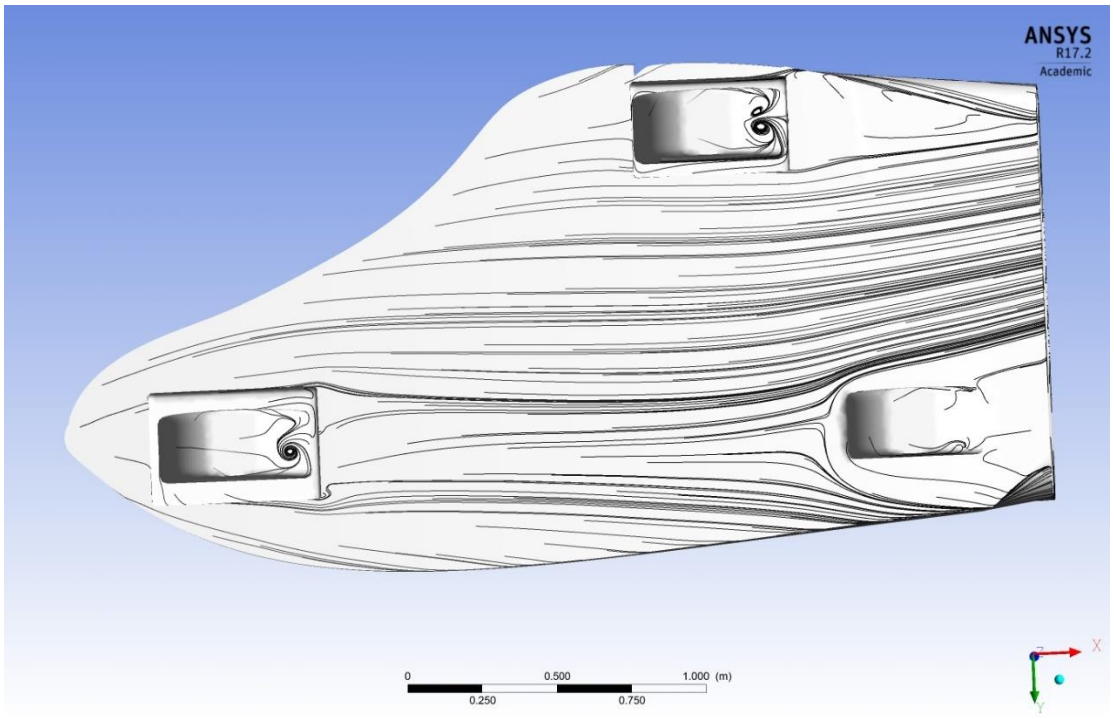

Figure 4.88- Shear stress lines on the underside of the sidecar

In Figure 4.89, the effects of the wheels in the development of streamwise vortices is clear, although their effects are minimal and the major contribution of the rear wheel and rear corner nearest the rear wheel to the vortices in the wake is evident.

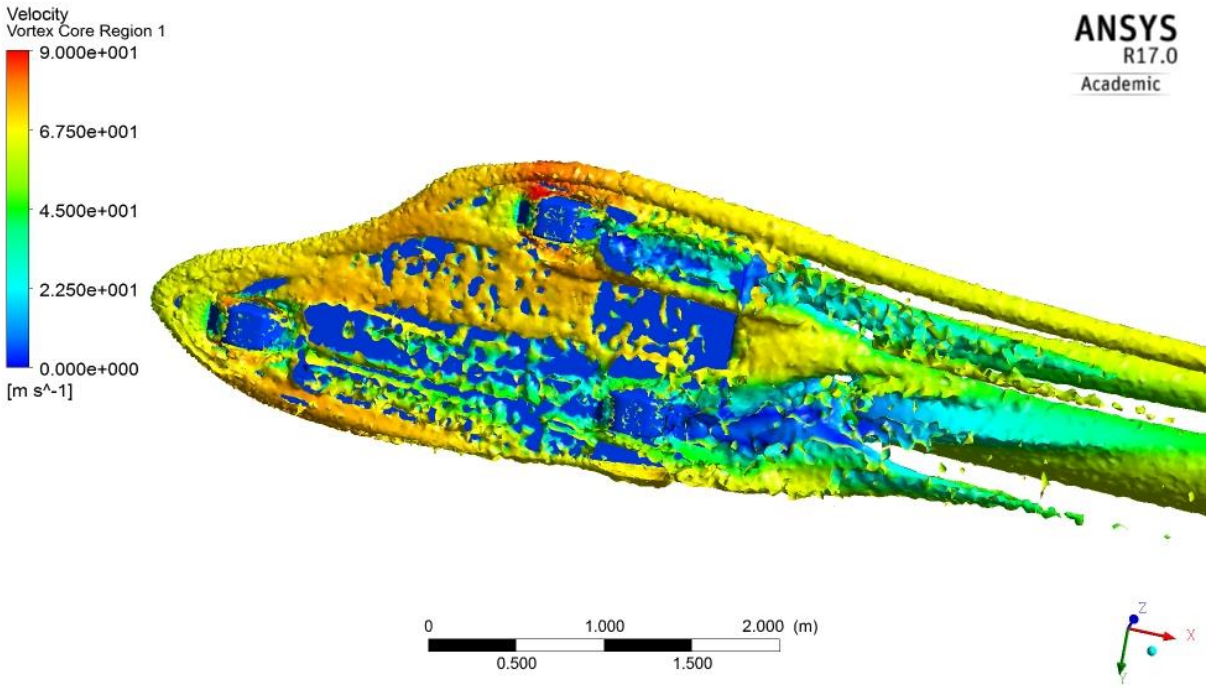

Figure 4.89- Velocity vortex core of the underside of the sidecar with splitter

The presence of the windshield in Figure 4.90 spreads the pressure more evenly over the front of the rider and reduces the high-pressure regions (in red) on the rider's shoulders and helmet.

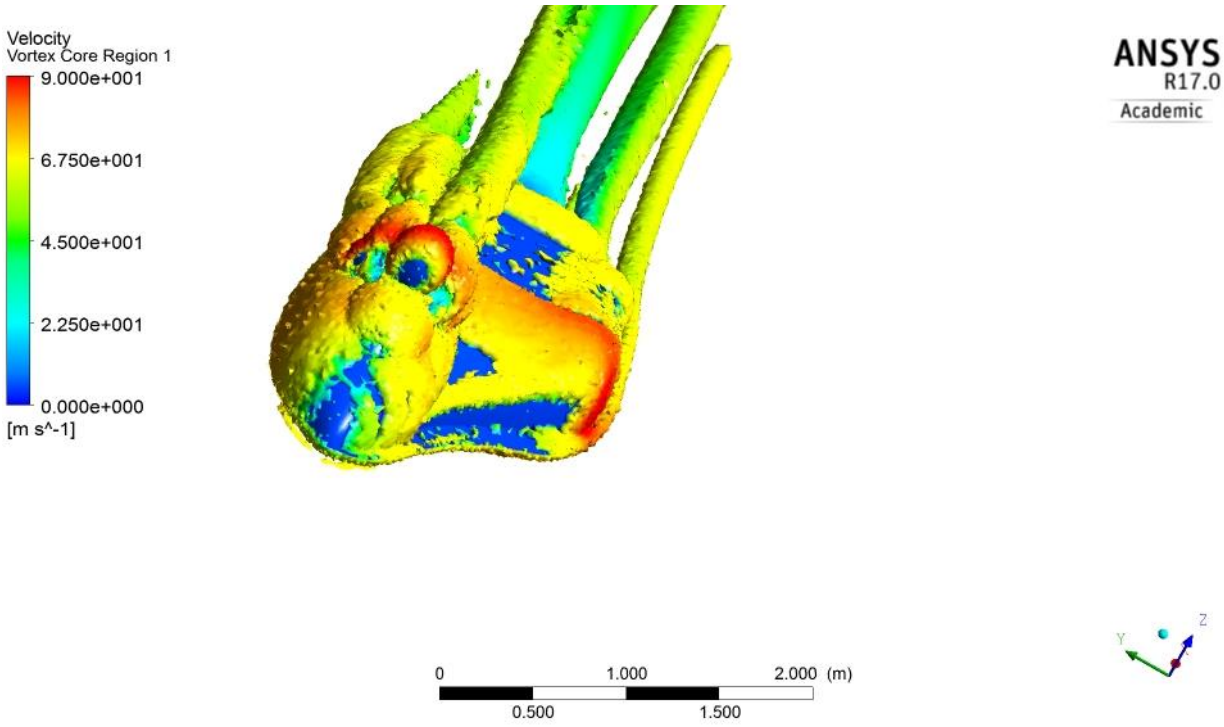

Figure 4.90- Velocity vortex core plot of sidecar with windshield and splitter from front

In Figure 4.90, the velocity of airflow that the rider's helmet is subjected to is lower than without the windshield and the vortex that forms over the riders left shoulder is less intense. Figure 4.91 shows velocity streamlines flowing over the top surface of the splitter.

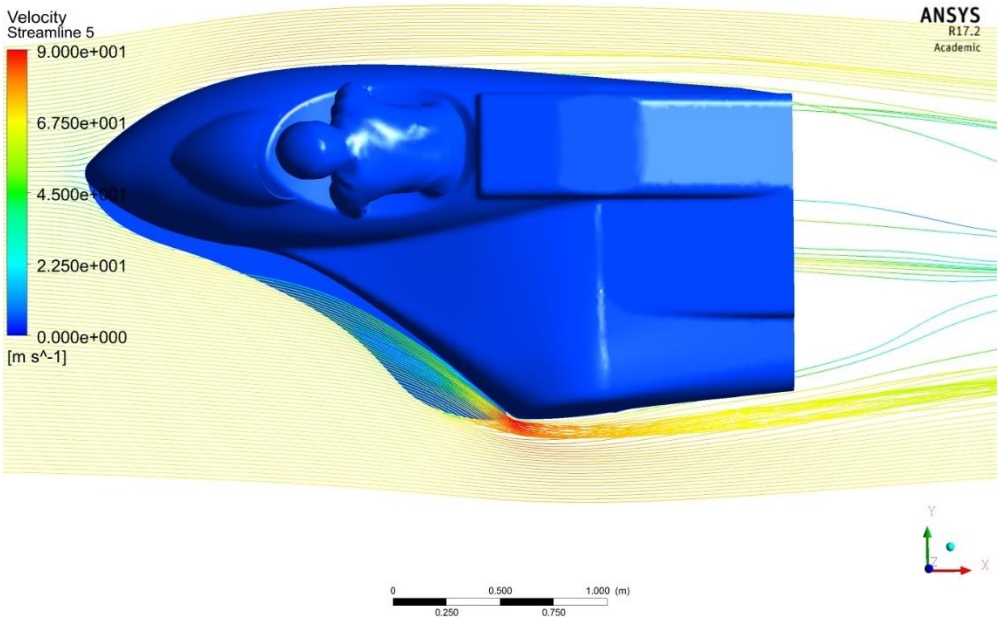

Figure 4.91- Velocity streamlines over the top surface of the splitter

In Figure 4.90 and Figure 4.91, a vortex forms at the outer edge of the splitter at the point where lateral (span-wise) flow from the splitter meets the longitudinal flow as it encounters the sidecar body. This vortex is carried past the end of the sidecar and into the wake region.

In Figure 4.92, the surface pressure contours of the underside of the sidecar are shown.

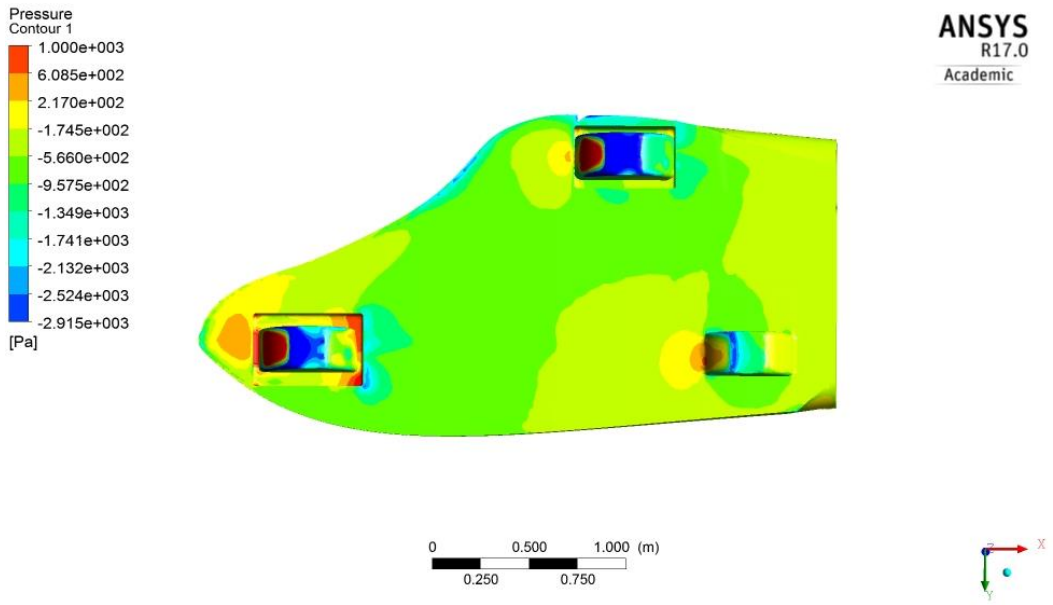

Figure 4.92- Surface pressure contours on the sidecar underside

The presence of the splitter changes both the vortices that form at the under surface of the sidecar and the surface pressure distribution on the underside. The low-pressure region that covers much of the underside results in the downforce that the splitter is evident. The presence of a spanwise vortex along the leading edge of the splitter and analogous to the formation of vortices on delta wings will be discussed in Chapter 7.

Velocity plots of the wake region without the splitter at plane A (y= -0.1) in Figure 4.93 and with a splitter (Figure 4.94) shows the differences in velocity at positions in the wake region when compared to sidecar versions without a splitter.

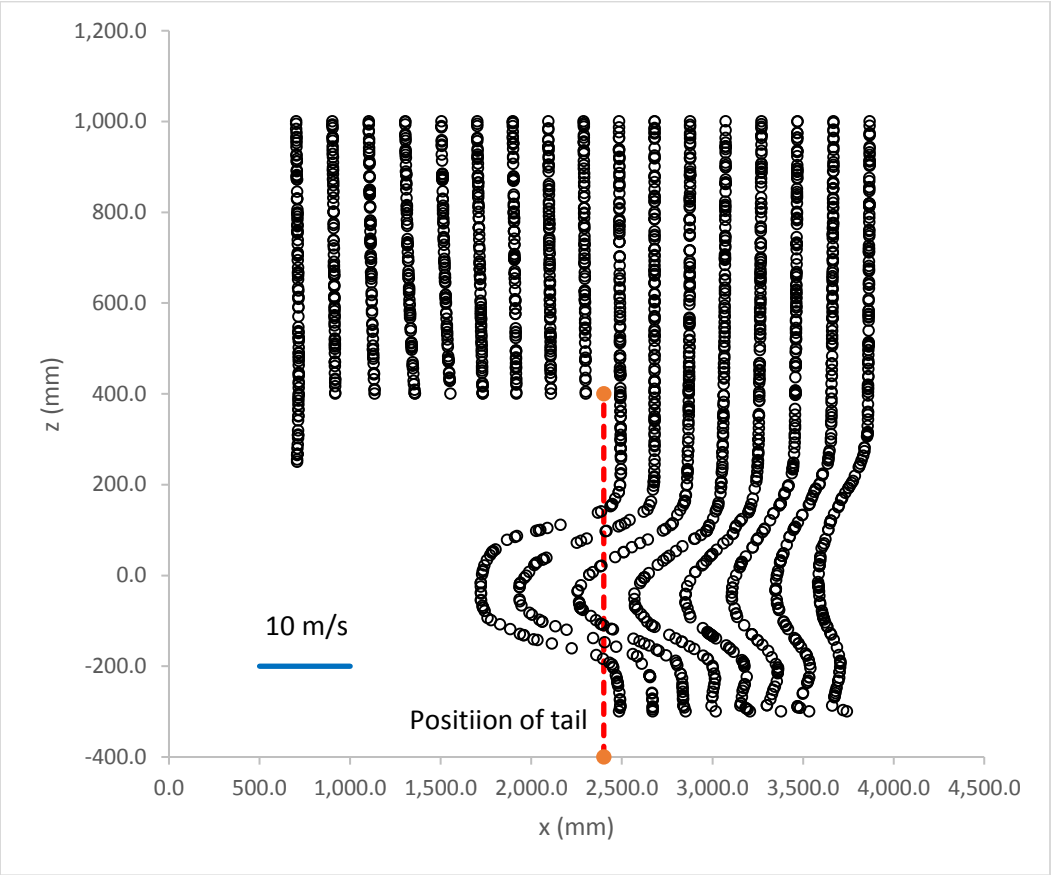

Figure 4.93- Velocity plots of the wake region without a splitter at plane A (y= -0.1 m)

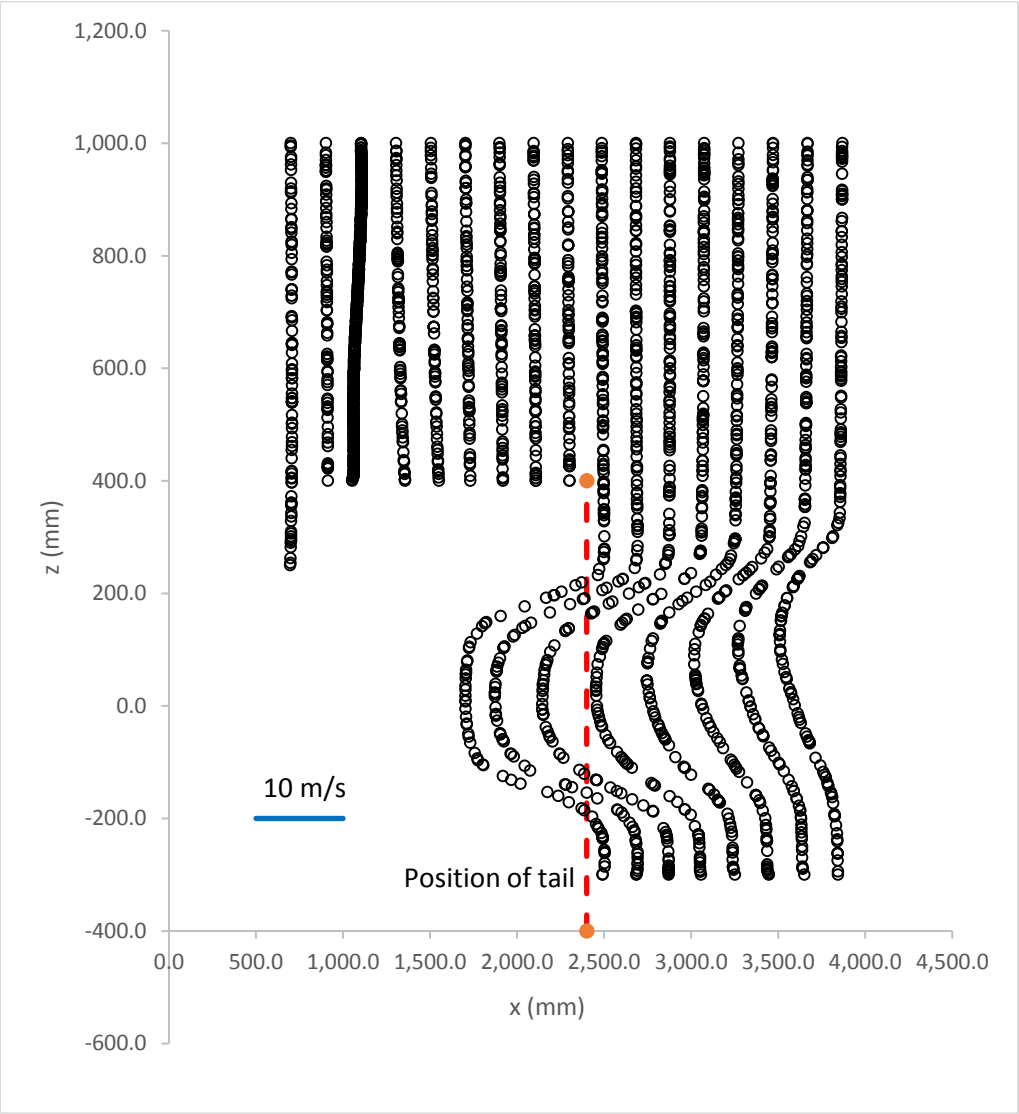

Figure 4.94- Velocity plots of the wake region with a splitter at plane B (y= 0.15 m)

In Figure 4.93, the wake region is more disturbed than when the splitter is present in Figure 4.94.

The vortices that form in the wake region (Figure 4.86) can be more closely examined from the velocity vectors on a plane at x= 2.8 m as in Figure 4.95.

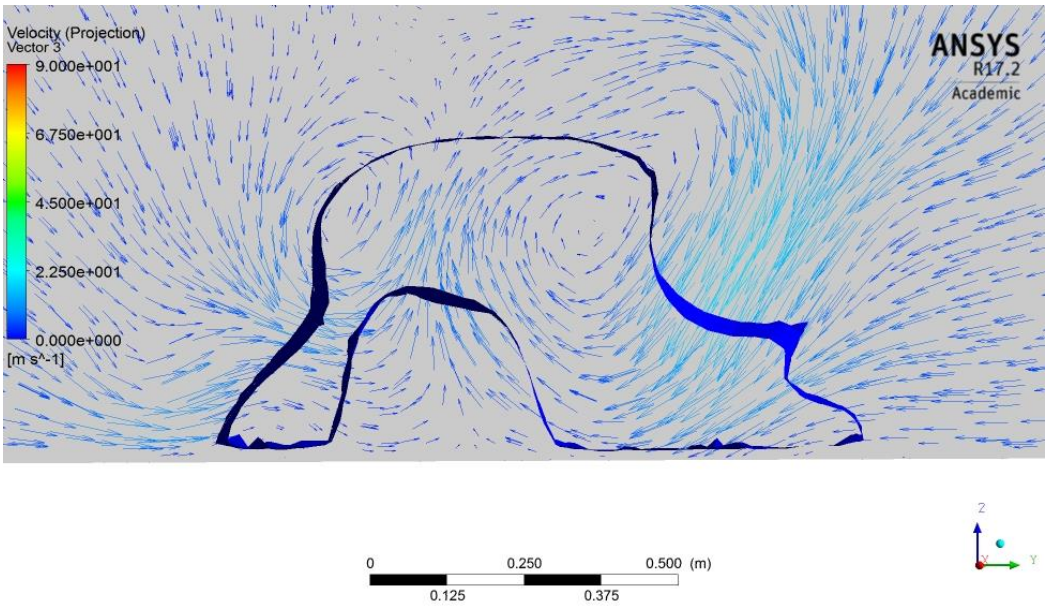

Figure 4.95- Velocity vectors on the x= 2.8 m plane with TKE iso-surface for final design

In Figure 4.95, the main streamwise vortex, generated behind the rider is turning in a clockwise direction. The second major streamwise vortex, originating from shear over the lateral vortex at the rear of the sidecar, is rotating in an anticlockwise direction. The major clockwise vortex can be visualised from streamlines at the rear of the final version of the sidecar are as indicated in Figure 4.96.

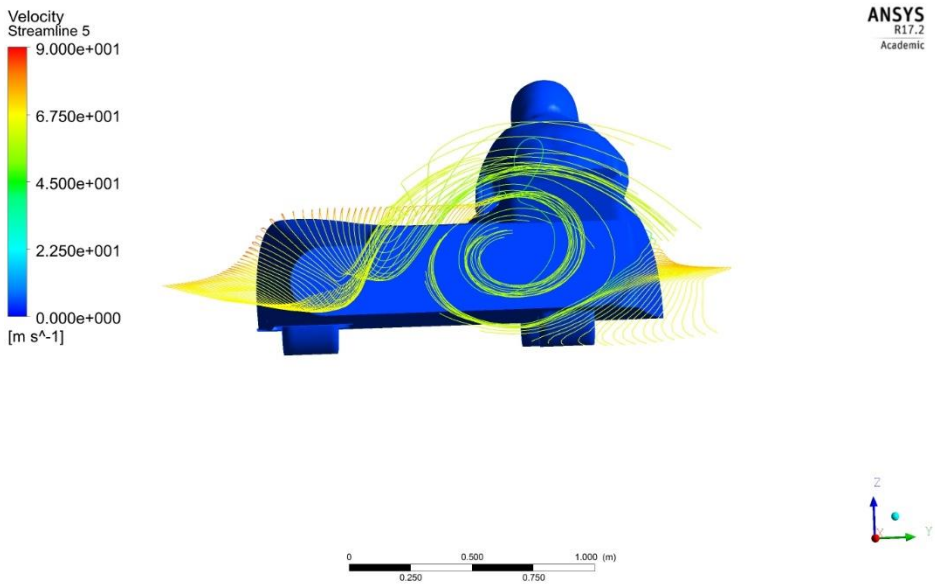

Figure 4.96- Streamlines at the rear of the sidecar Bonneville version

From Figure 4.96, the streamwise vortex coming from the rider's shoulder has joined with the streamwise vortex coming from the rear wheel and rear corner to form the major streamwise vortex in the sidecar wake. This combination of vortices is also evident in Figure 4.97.

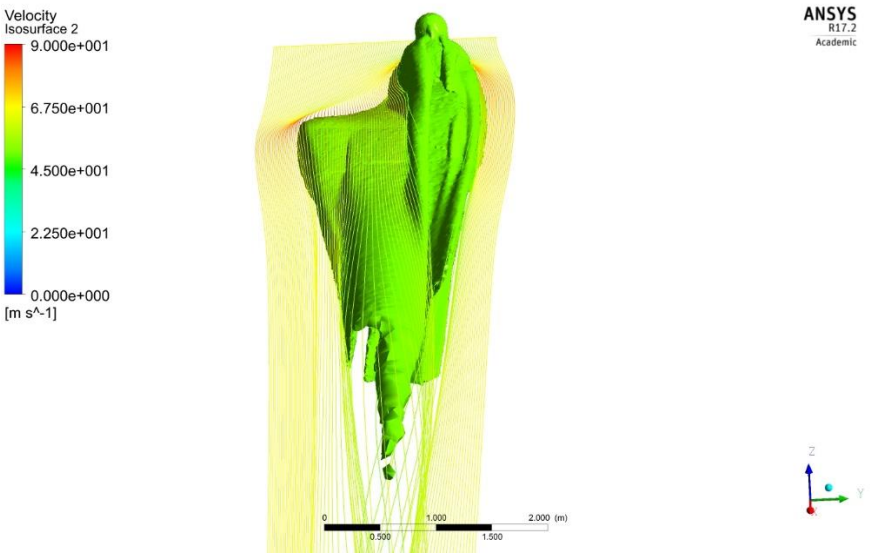

Figure 4.97- Velocity iso-surface (velocity = 46 m/s) and velocity streamlines in wake of the Bonneville sidecar design

4.7 SOME OBSERVATIONS ON THE OPTIMISATION PROCESS

Figure 4.98 is a scatter-plot of lift coefficient (C_l) versus drag coefficient (C_d) for a sampling of the sidecar designs.

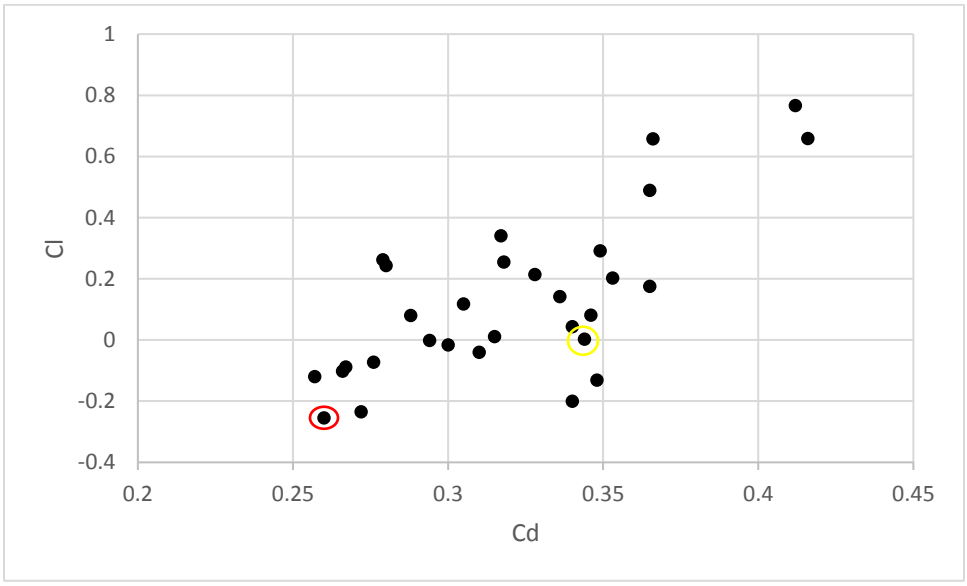

Figure 4.98- Scatter plot of lift versus drag coefficients for optimisation phase

Note in Figure 4.98 that the sidecar configurations are largely clustered indicating that the lift and drag are related to one another. If the plot had been widely more scattered it would have indicated independent control over lift and drag—something that was not achieved and might not be possible. It is important to note that the two regions not populated in Figure 4.98 are low drag and high lift and high drag low lift—both of which would be regions of no interest for the design of a land speed record vehicle. In Figure 4.98, the original sidecar is circled in yellow and the final version is circled in red.

Figure 4.99 is a scatter plot of the lateral force versus drag coefficients.

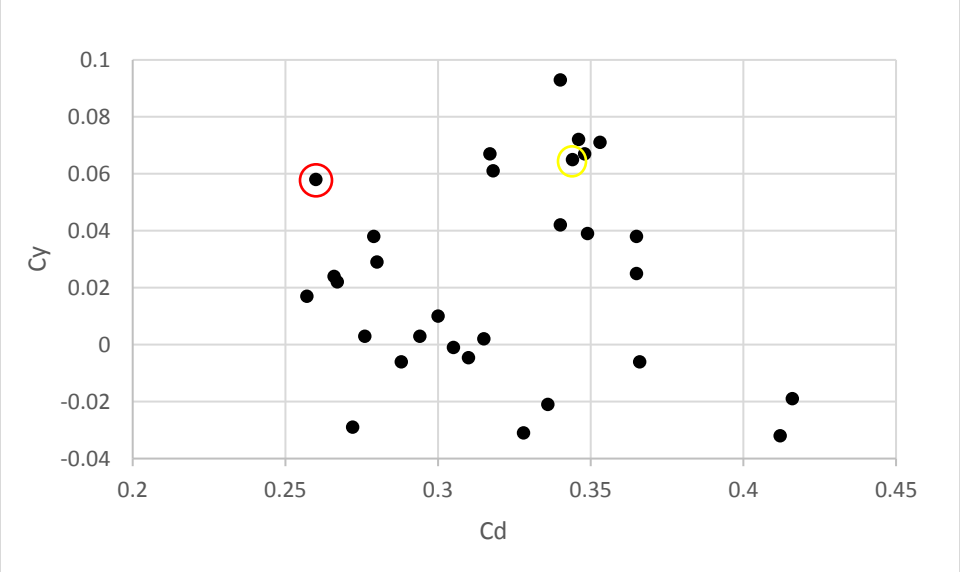

Figure 4.99- Scatter plot of lateral force versus drag coefficients for optimisation phase

In Figure 4.99, the scatter plot is much less clustered than the plot in Figure 4.98, indicating that the aerodynamic lateral force coefficient is more weakly correlated to the level of aerodynamic drag produced by the bodywork than the lift. In Figure 4.99, the original sidecar is circled in yellow and the final version is circled in red.

There had been concern in the initial stages of this design study that reducing the aerodynamic drag of the bodywork might adversely affect the level of lateral force created when the sidecar is traveling in a straight line. From Figure 4.99 it is evident that the lateral and drag forces are not interdependent—a conclusion also clear from the low lateral force coefficient observed in some of the lowest drag designs.

Figure 4.100 is a scatter plot of lateral force coefficient versus lift coefficient.

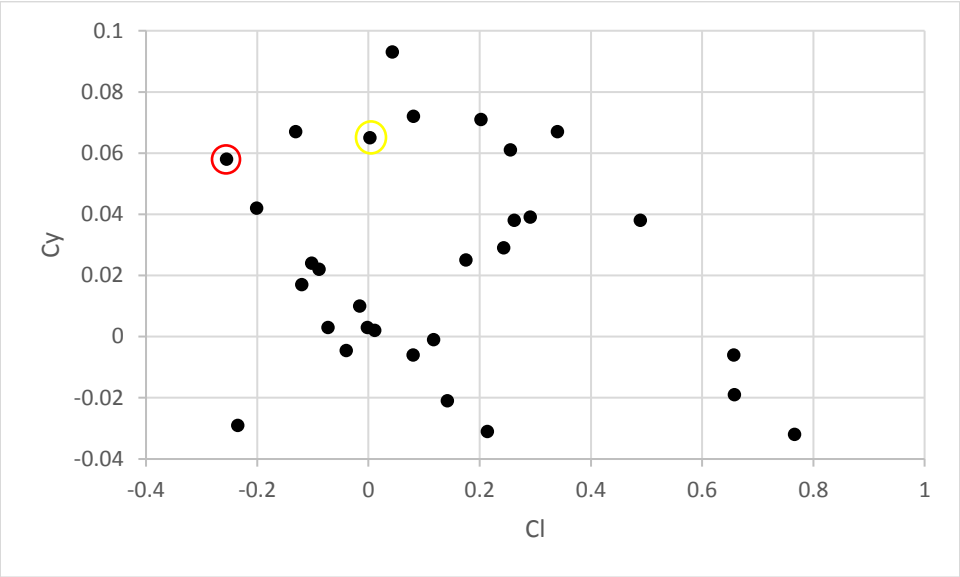

Figure 4.100- Scatter plot of lift versus lateral force coefficients for optimisation phase

In Figure 4.100, the scatter plot shows that the aerodynamic lateral force coefficient is also not simply or strongly related to the aerodynamic lift coefficient. This result shows that a body designed with little or no aerodynamic lift will not necessarily result in adverse levels of lateral force when the asymmetrical sidecar travels straight ahead—a particularly useful result from the standpoint of aerodynamic stability. In Figure 4.100, the original sidecar is circled in yellow and the final version is circled in red.

4.8 CHAPTER 4 SUMMARY

In this chapter, a comprehensive design study was undertaken using CFD to design a new add-on body section that would reduce aerodynamic drag while also controlling adverse aerodynamic lift and lateral forces. The CFD results for the final (Bonneville) design was shown to reduce aerodynamic drag while producing aerodynamic downforce (negative lift) and only a slight amount of aerodynamic lateral force resulting from the asymmetrical airflow over the sidecar bodywork.

The presence, number, location, and character of streamwise vortices in the wake region were, as expected from Hucho, et al (1993), found to depend greatly upon the rear section of the sidecar. The original sidecar, with an open rear platform containing a large battery box and water cooling tank produced a number of significant streamwise vortices into the wake region (Figure 4.101).

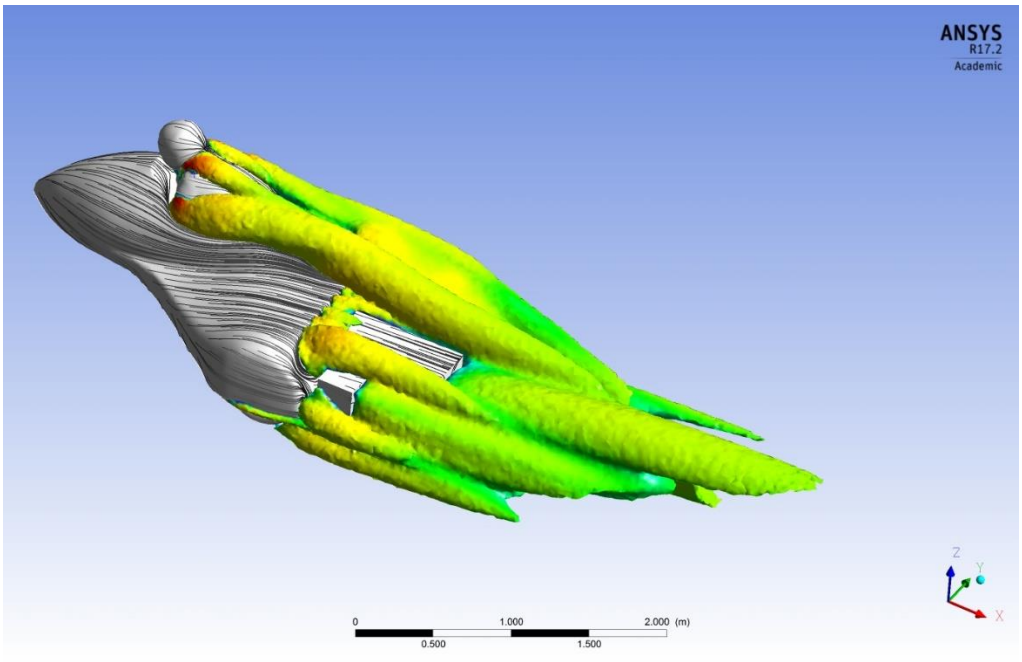

Figure 4.101- Streamwise vortices for the original sidecar

The final Bonneville design (Figure 4.102) consisted of a new rear section that could meet the FIM regulations for vehicle dimensions while reducing drag, lift, and lateral forces, asymmetry in the velocity contours of the wake region, and the overall degree of streamwise vorticity.

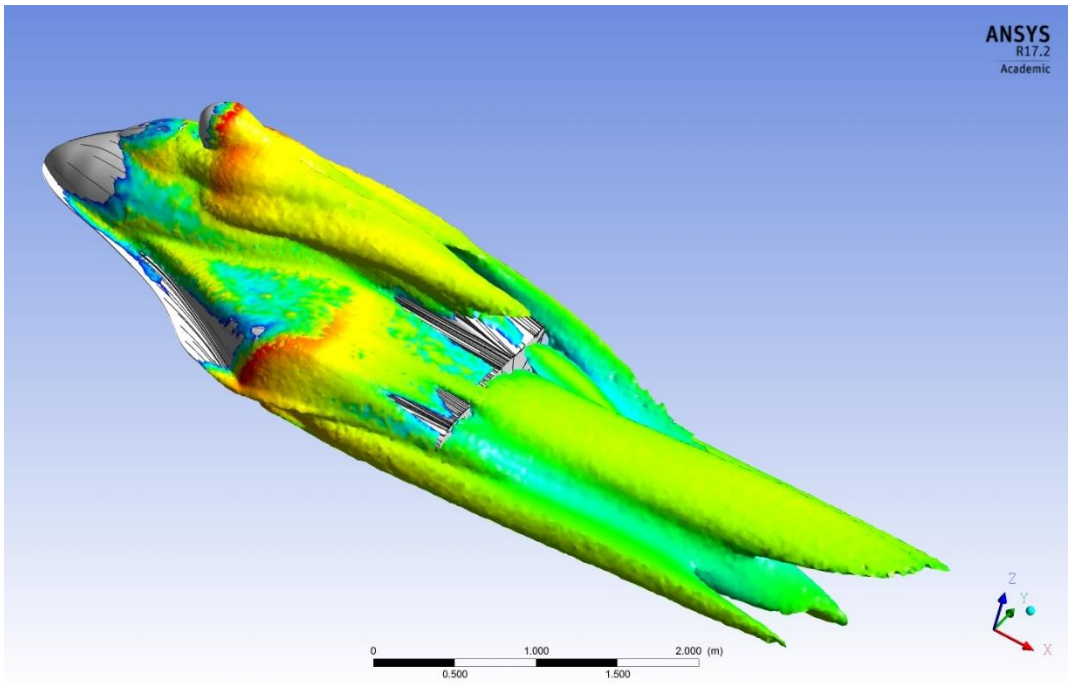

Figure 4.102- Streamwise vortices for the Bonneville sidecar

Chapter 5 will describe FIM World land speed record setting efforts at Bonneville with the newly redesigned Baker sidecar as well as testing at other venues.

CHAPTER 5 EXPERIMENTAL RESULTS

5.1 BONNEVILLE SALT FLATS, AUGUST 2014

For the first effort at Bonneville, a relatively simple electric drive system was developed, using a single liquid-cooled Motenergy ME113 brushless DC motor, with direct chain drive (no transmission). A Sevcon Gen 4 size Six controller (inverter) was used along with a lithium polymer battery pack of approximately 5 kW-hr capacity that could provide up to 100 volts and a maximum of approximately 450 amps. It was decided to run the vehicle with a passenger (swinger) on board, as is allowed for AMA National land speed record attempts (Figure 5.1).

Figure 5.1- Land Speed Record at Bonneville- August 2014 *(author)*

Conditions at the Bonneville Salt Flats in 2014 were very difficult. Heavy rains in the months prior to the August motorcycle-only event cancelled several other land speed record events and individual efforts. To reach the prepared courses required driving across at least two miles of flooded salt flats. The traction on the prepared salt surface was judged to be less than usual, largely because of the high moisture content of the salt.

The power level set through the software of the controller for the AMA record attempt was 450 amps at approximately 94 volts (accounting for voltage sag). It is reasonable to assume an 85 % efficiency for the motor and controller combination and a chain drive efficiency also equal to 97%. Therefore, the expected power output delivered by the rear drive wheel to the salt surface should have been approximately 35 kilowatts. Unfortunately, due to motor cooling issues, the Sevcon controller sensed an over-temperature condition when maximum throttle was applied and shut down the motor, typically just as the sidecar entered the beginning of the timed mile on the three-mile course. During the first pass, this motor cut-off occurred at 80.5 mph with a headwind of approximately 8 mph. Because the attempt was made running on an open record in the electric sidecar over 300Kg category, it was decided to make a return run in order to establish an AMA National Record. During the return, the controller shut down the motor at a top speed of 69.7 mph. Subsequent passes never exceeded the initial top speed.

As noted above, during these record passes at the Bonneville Salt Flats in August 2014, the drive motor cut off just as the vehicle entered the timed mile section of the course. While unfortunate for the record effort, the coast down of the sidecar from a speed greater than 70 mph (113 kph), without any brake application, allowed values for rolling resistance and aerodynamic drag coefficient to be calculated. Speed versus time data was provided during the coast down over 40 seconds from 80 mph to 24 mph through an on-board iPhone app called Track Addict. The data from the coast down was used in an on-line curve fitting program (IWillTry.org, 2007) that uses speed versus time inputs (along with vehicle weight and frontal area) to give an aerodynamic drag coefficient (C_d) and a coefficient of rolling resistance (C_{rr}) (Figure 5.2). The rolling resistance coefficient is a simplified version that depends only upon vehicle mass and has no vehicle velocity consideration, however Metz (2004) describes the C_{rr} of tyres run at Bonneville at high inflation pressures (35-50 psi) to have little velocity dependence. The C_d returned from this simple program was 0.390 with a C_{rr}=0.048. This rolling resistance coefficient is consistent with other published values for pneumatic tyres on solid sandy surfaces (Gillespie, 1992) but is higher than the C_{rr} = 0.008 value used by Metz (Metz, 2004) for his Bonneville calculations. The rolling resistance coefficient on the Salt Flats at Bonneville is expected to vary with local conditions and tyre type and construction.

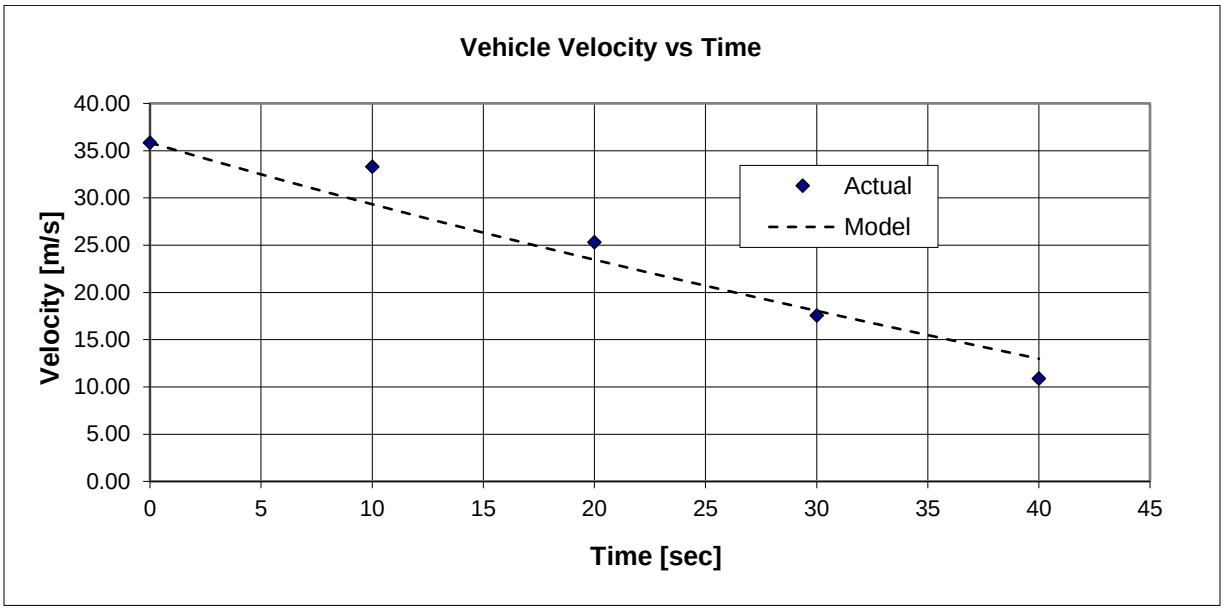

Figure 5.2- Fitting of vehicle speed versus time data to generate C_d and C_{rr} approximations

5.2 MATHEMATICAL MODELLING

Metz (2004) has pointed out that for a given course length and condition, vehicle mass and aerodynamic drag coefficient, if the acceleration (a_x) is constant, then speed (V_x) or time (t) versus position (s_x) of a vehicle with a known amount of power and gearing can be calculated from:

$$V_x(t) = \int_0^t a_x dt = a_x t + V_x(0) \quad (5\text{-}1)$$

$$s_x = \int_0^t V_x dt = \int_0^t a_x t + V_x(0) dt = \frac{1}{2} a_x t^2 + V_x(0) t \quad (5\text{-}2)$$

For $V_x(0) = 0$

$$s_x = \frac{1}{2} a_x t^2$$

$$V_x(t) = a_x t = a_x \sqrt{\frac{2s_x}{a_x}} = \sqrt{2 s_x a_x} \quad (5\text{-}3)$$

The resulting plot of speed versus distance from the starting line is particularly useful to establish the expected performance characteristics of a land speed record and to contrast the expected performance with the actual performance of the vehicle on the land speed record course.

The overall tractive force (F) required to overcome the aerodynamic drag (D) and rolling resistance at a constant speed ($F_{rolling}$) can be written as:

$$F = D + F_{rolling}$$

Professor John Sullivan, of Purdue University (Sullivan J. , 2016) has further developed this relationship, including terms for constant driving torque produced by the electric motor (T), the drive tyre radius (r), the weight of the vehicle (W), the rolling resistance ($F_{rolling}$) the air density (ρ), the frontal area (A) and the aerodynamic coefficient of drag (C_d).

$$ma_x = mV\frac{dV}{dx} = m\frac{1}{2}\frac{dV^2}{dx} = F - D - F_{rolling} = \frac{T}{r} - \frac{1}{2}\rho V^2 C_d A - W(a + bV^2) \quad (5\text{-}4)$$

$$\frac{dV^2}{\left[\frac{2T}{r\rho C_d A}\left(1-\frac{raW}{T}\right)-(1+\frac{2bW}{\rho C_d A})V^2\right]} = \frac{\rho C_d A}{m}dx \quad (5\text{-}5)$$

$$\frac{dV'^2}{[1-(1+b')V'^2]} = dx' \quad where\ V' = \frac{V}{V_{ref}} \ \ and \ \ x' = \frac{x}{x_{ref}} \quad (5\text{-}6)$$

$$V_{ref}{}^2 = \frac{2T}{r\rho C_d A}(1 - a') \ \ , x_{ref} = \frac{m}{\rho CdA} \ \ , a' = \frac{raW}{T} \ , b' = \frac{2bW}{\rho CdA} \quad (5\text{-}7)$$

$$V'^2 = \frac{1}{(1+b')}(1 - e^{-(1+b')x'}) \quad (5\text{-}8)$$

Sullivan used the above equation (5-4), but neglecting the rolling resistance term ($W(a + bV^2)$), to compare the predicted speed versus distance performance of his 150-kg electric land speed record motorcycle to the actual performance experienced with the motorcycle during a 2013 land speed record run on the Bonneville Salt Flats. The results are indicated in Figure 5.3 and show a good match between the calculated and actual performance of the motorcycle.

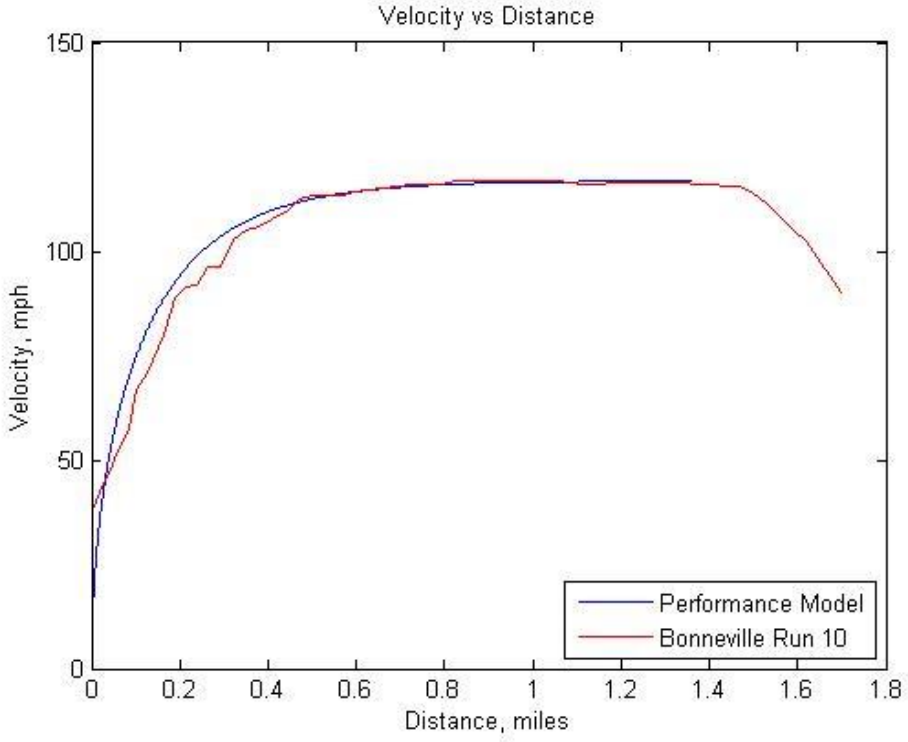

Figure 5.3- Calculated versus actual performance of an electric motorcycle during a land speed record attempt [Source: Sullivan, Purdue University]

Sullivan's model (with and without the rolling resistance contribution) was adapted for the twin-motor three-wheel electric sidecar and incorporated into an Excel spreadsheet that was used in the current research project to help predict vehicle performance from rest to top speed.

Rider with Swinger

Although an exact laser scan of the sidecar in the original 2014 configuration, single motor with rider and swinger, had not been made, a SolidWorks model of the configuration was created from existing scans (Figure 5.4) and tested using ANSYS Fluent. The CFD simulation used an unstructured mesh created by ANSYS Fluent for this test with 10.4 million primarily tetrahedral elements and the frontal area was calculated to be 1.022 square metres using the Reports → Projected Area → Min Element size (→ .0001m) function of ANSYS Fluent. The RANS k-ω SST turbulence model was used and a coupled scheme was used for pressure and velocity. For spatial discretization, a least squares gradient and second order upwind schemes for pressure, momentum, turbulence kinetic energy and dissipation rates were used. Other Fluent setup parameters were as described in Appendix A.

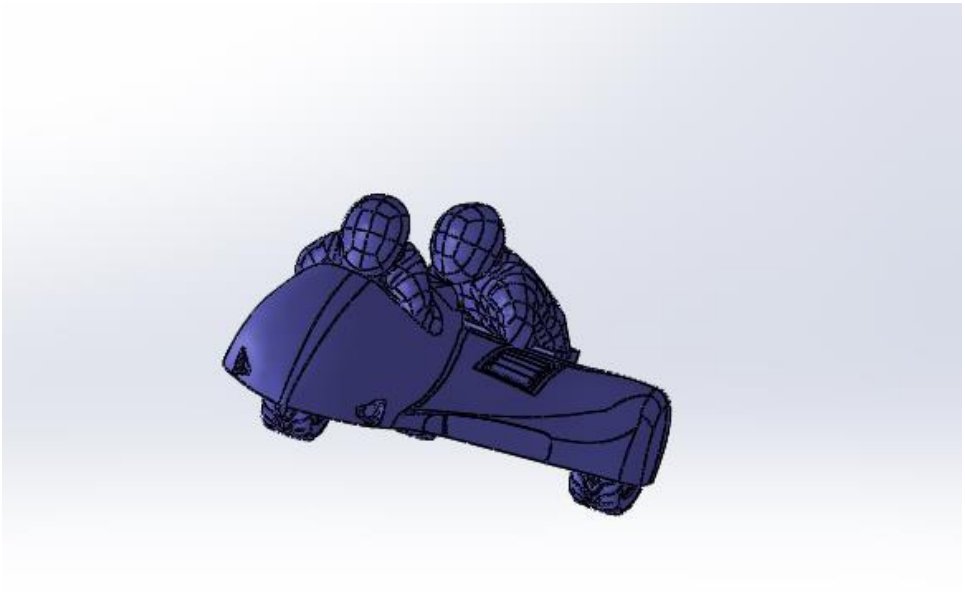

Figure 5.4- Sidecar configuration with swinger for CFD- August 2014 at Bonneville

The following coefficients were calculated from the drag, lift and lateral forces generated at 44 m/s (100 mph).

$C_d = 0.398$

$C_l = 0.245$

$C_y = 0.037$

The drag coefficient from this CFD model has good agreement (2% higher) with that estimated from the limited data obtained during the actual run (0.390) as described previously. According to the CFD result, the sidecar with swinger is demonstrating lift and a small amount of lateral force, to the right of the rider (direction away from the sidecar). The agreement between C_d obtained from the limited data on the salt flats and CFD provides a reasonable C_d for use in the mathematical model to predict what performance the sidecar with swinger should have been capable of achieving, had the motor run properly.

Using the mathematical model previously described, with the C_d (= 0.390) and rolling resistance coefficient (C_{rr} = 0.048) obtained from the actual test results and the frontal area determined from ANSYS Fluent, and an air density of $\rho = 0.996$ kg/m^3 (representative of the density at the altitude of Bonneville), Figure 5.5 shows the estimated performance of the first run of the Baker sidecar at Bonneville in August 2014.

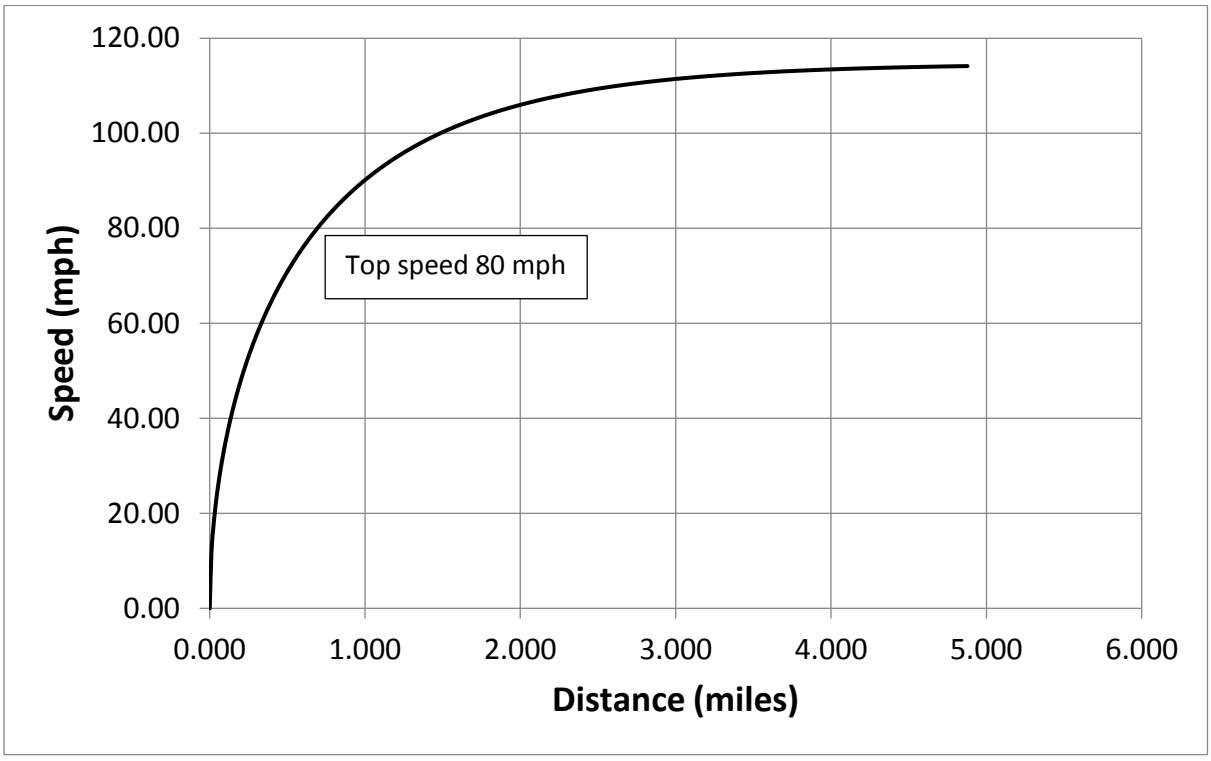

Figure 5.5- First attempt with sidecar at Bonneville- August 2014- predicted performance

The top speed observed during the run of 80 mph occurred between 0.5 and 1.0 miles into the run, consistent with the model, although the exact distance at which 80 mph was reached is not known. Had the motor operated properly throughout the entire run, a terminal speed of 114 mph could have been expected at the end of mile 3, which is consistent with the results of the Sullivan solo electric motorcycle (with 46% smaller frontal area and 65% higher estimated C_d as shown in Figure 5.3). The single electric motor used in the Baker sidecar was the same model and type motor used in Sullivan's record runs at Bonneville.

5.3 Land Speed Efforts in 2015

From the start, the intent was to run the electric sidecar with two Motenergy ME113 brushless DC motors. To do so required two Sevcon Gen 4 Size Six controllers, one for each motor. The controllers were programmed to operate in a master/slave configuration with a single throttle input to the master controller and communications via a CAN/BUS between the controllers. The initial setup, wiring and programming of the controllers, circuit contactors and motors was performed on a workbench- not on the sidecar. This allowed any problems to be solved before a new wiring harness was created for the sidecar. This effort was accomplished between April and mid-June 2015.

5.3.1 Motor Cooling

The problems with the motor shutting off before entering the measured mile at Bonneville in 2014 were determined to be a result of the large amount of current (more than 400 amps) applied over a short period to the motor windings during the acceleration of the vehicle. The cooling system in 2014 consisted of a motorcycle-sized water-air radiator and an electric pump to circulate water from the electric motor to the radiator. During subsequent discussions with other teams racing electric land speed machines with liquid-cooled motors it was found that every team consulted dispensed with a liquid-to-air radiator and instead pre-chilled the motor(s) using water pumped from a tank filled with ice. By pre-chilling the motors, it was found by other teams that they would not reach a critical motor temperature, above the Curie temperature of the rare earth magnets used in these types of brushless DC motors, during the relatively short duration of a land speed record run (Hakansson, 2015). An ice/water tank with submerged electric water pump was constructed to pre-chill both electric motors for the 2015 electric land speed record efforts.

5.3.2 Bodywork

Because the ice pre-chiller did not require the air intakes previously needed for the radiator, the intake and exhaust cooling vents were covered using fiberglass patch panels produced by epoxy vacuum-bagging on the existing two-piece body mould for the sidecar. In addition, patch panels were made to close off the NACA brake cooling ducts at the front of the sidecar, as repeated severe braking was not required for land speed record attempts. They were the first steps in an effort to reduce the aerodynamic drag produced by the sidecar's bodywork. The AMA and FIM rules permit the second rider (swinger) to be replaced by 60 kg of ballast that must be carried on the sidecar. The 60 kg of lead ballast took up a smaller volume that could be placed beneath the sidecar bodywork and thus presented lower aerodynamic drag than a human passenger. A robust bracket was made to carry 60 kg of lead to replace the swinger.

5.3.3 Battery and BMS

Prior electric solo-motorcycle land speed records by the team had been set in the 150-kg weight category and had recorded speeds up to 100 mph. With the electric sidecar, the machine would compete in the unlimited (over 300 kg) category and at speeds expected to reach 150 mph. It was felt that reaching this speed could require more distance than the three-mile course that was used for records on the 150 kg machines. Courses up to 8-10 miles in length are typically available at Bonneville during record attempts for machines capable of greater than 125 mph. In addition, for FIM World Records, a return run on the same course in the opposite direction must be made within two hours of the first run. The 5.0 kWH capacity of the sidecar's existing lithium-polymer battery pack was judged to have insufficient capacity to make passes up to 10 miles long in each direction in the time allowed, even with some recharging between runs. A new battery pack was therefore obtained. This pack was reconfigured from half of a pack from a 2012 Nissan Leaf.

The battery-electric Nissan Leaf was introduced into the U.S. market in 2010. It was equipped with a 24-kWH battery pack that contained a total of 192 $LiMn_2O_4$ cells with a rated capacity of 33.1 Ah, a nominal voltage of 3.8 volts per cell and a maximum voltage of 4.2 volts per cell. The cells were packaged into modules made up of four cells—two in-series pairs placed in parallel. The full Nissan Leaf pack consisted of 48 modules and with brackets and mounting frames weighed 294 kg (648 lbs). Nominal voltage for the entire pack was 360 volts and maximum voltage was 403.2 volts.

For the Baker electric sidecar, half of a Nissan Leaf pack was purchased. This pack came from a wrecked 2012 Leaf. In 2012, Nissan made a minor change to its battery chemistry, based upon problems with battery capacity in extremely hot climates. By purchasing a pack from a 2012 vehicle, the batteries were expected to perform better at the high temperatures often experienced at Bonneville. The 24 modules in the pack were configured to provide a maximum of 100.8 volts (with cells charged to 4.2 volts) and a total maximum capacity of 13 kW-H through parallel cells with a capacity of approximately 128 Ah. An Orion BMS system was installed and configured to balance the individual cells during charging, shut off the charger when the pack is fully charged, and sound an alarm when the pack is nearing depletion. Although the Orion BMS has a CAN/BUS that communicates with the charger, it did not operate at the same baud rate as the Sevcon controllers and full CAN/BUS integration of all of the systems on the sidecar was not accomplished.

The battery pack, with brackets weighed approximately 91 kg (200 lbs) and was 900 mm long, 300 mm wide and 200 mm high. The only space available to package this large pack on the sidecar was on the platform formerly used by the swinger. Because the FIM and AMA rules specify an exact dimension for a swinger platform that must also support the weight of a human (even if the swinger is replaced by ballast), a battery cover was fabricated from foam, carbon fibre and fiberglass that would support the required load. Brackets and plates were welded to the existing sidecar frame to support the new battery pack (Figure 5.6).

Figure 5.6- Half Nissan Leaf battery pack placed on rear platform (white container is water cooling tank) *(author)*

Previous experience with electric land speed record motorcycles suggested that at maximum throttle during a record attempt the sidecar would consume 300-500 WH per mile. With the 13-kWH pack, the sidecar would therefore be capable of running two ten mile passes at full throttle without fully depleting the pack. This was a significant amount of over-capacity, but promised to provide easier logistics on the Salt Flats.

The previous 96-volt lithium polymer pack was capable of producing bursts of current at up to sixty times its rated capacity (60C). The lithium ion pack from the Nissan did not have this capability— the Leaf uses a maximum of about 3.5-4 times rated capacity (3.5-4C). The goal on the sidecar was to eventually produce a maximum of 70 kW from the two motors, which at 96 volts requires 730 amps from the battery pack—a current approximately 5.5 times the rated value (5.5C) of the half Leaf pack as configured. This was felt to be within the capabilities of the battery pack.

Aside from the battery and ballast mounting brackets, the chassis of the Baker sidecar was largely unmodified from its road-racing configuration. The front, rear and sidecar wheels were all the same dimensions (9 in. x 13 in.) and were fitted with 245/50R13 Toyo RA1 radial tyres inflated to 40 psi. The front suspension was a leading link setup with twin coil-over Koni shock absorbers fitted with 600 pounds per inch springs. The rear swing arm was fitted with a single Koni coil-over shock absorber and 1200 pound per inch spring and was adjustable for toe and camber, both of which were set as close to zero degrees as possible. The sidecar wheel had no sprung suspension but was adjustable for toe-in and camber, both of which were set to zero degrees. Wilwood

hydraulic disc brakes were fitted on each wheel—the right handlebar lever actuated only the front disc brake, while the left handlebar brake lever actuated the rear and sidecar brake.

5.4 Testing in Colorado

In 2015, as in 2014, the weather disrupted land speed records at the Bonneville Salt Flats. The BMST motorcycle event at the end of August 2015 was cancelled due to an unsafe muddy and flooded salt surface.

To test the twin motor drive, new battery pack system, and changes in aerodynamics, an airport land speed record speed event in Colorado was entered in September 2015. The event took place on a 1.5 mile (8,000 foot) long runway at the Front Range Airport, near Denver. This airport sits at 5,512 ft. (1,680 m) elevation, similar to the 4,219 ft. (1,286 m) altitude of the Bonneville Salt Flats in Utah.

After some initial problems with improperly rated fuses, a total of nine passes were made over two days at the Colorado event. The controllers were set to provide up to 300 amps for each of the motors. On the fastest pass, a top speed of 123.8 mph was recorded. Figure 5.7 is a photograph of the sidecar at the Colorado test.

Figure 5.7- Land speed record test in Colorado- September 2015 *(author)*

The plot of speed versus distance in Figure 5.8 provides an indication of the performance of the sidecar machine. Speed data was provided by the organizers at 0.25, 0.5 and 1.0 mile locations

on the course and they are plotted on Figure 5.8 (red points). The ice-bath cooling system and new battery pack performed as expected on this short course, with no motor cut-off.

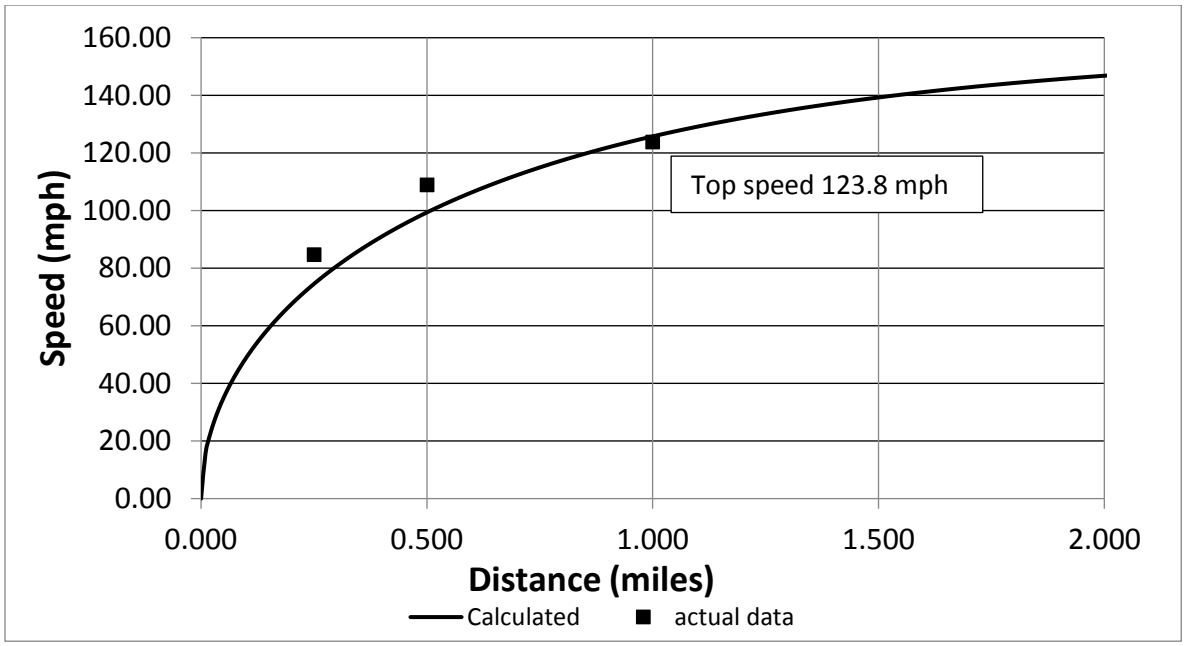

Figure 5.8- Colorado airport test- September 2015- predicted versus actual performance

To create the predicted performance curve in Figure 5.8, the parameters detailed in Table 5.1 were used in the mathematical model described above. The C_d value for use in the model came from the CFD for this configuration of sidecar as detailed in Chapter 4 (Figure 4.8). Note that rolling resistance was not included in this model and the 60-kg ballast was not carried.

Table 5.1: Parameters for Colorado test

Parameter	**Value**
Drag coefficient (C_d)	0.344
Air density (ρ)	0.996 kg/m^3
Frontal area (A)	0.99 m^2
Torque to wheel	Constant 102 Nm
Chain drive sprocket ratio	20/40
Weight	540 kg

From Figure 5.8, it is evident that the curve created by the mathematics model well matched the experimental data and the top speed at two miles was calculated to be 147 mph.

5.5 2016 CONFIGURATION

As in 2015, the 2016 version of the Baker sidecar was configured with twin Motenergy ME113 liquid-cooled electric motors running on a common chain driving the rear wheel. The motors ran

with 20 tooth sprockets while the rear wheel had a 40-tooth sprocket. Nominally, the battery pack, when fully charged had a voltage of 100.8 volts and the controllers were set up in a master/slave configuration to provide 300 amps to each of the drive motors, producing a potential total of 60 kW. Cooling of the motors was accomplished by pumping ice-chilled water through the motors. In 2016, the bodywork fully enclosed the rear section of the sidecar (as described in Chapter 4 and Appendix C) and the sidecar was fitted with a windshield and a front splitter (Chapter 4). The water cooling tank was moved forward, ahead of the ballast as it did not fit under the new rear body section.

5.6 East Coast Timing Association event in Ohio, June 2016

Prior to world land speed record attempts at Bonneville, it was decided to test the Baker sidecar with its new rear bodywork and revised cooling system at the 1.5-mile-long Wilmington, Ohio Airborne Air Park at the East Coast Timing Association's (ECTA) June 2016 land speed event. The surface of the 9,000-foot-long airport runway is grooved concrete (similar to the surface at the Colorado Front Range Airport from prior testing) and the altitude is 1,077 feet (328 metres) above sea level (air density $\rho \approx 1.18$ kg/m^3 versus $\rho \approx 0.996$ kg/m^3 at Colorado and Bonneville). The course was configured as a 1.0 mile run from a standing start, followed by a 132-foot-long timing section, and then ½ mile to slow down. The direction of travel was 217 degrees (SW). The rear body section of the sidecar had only been completed in rough form the week before the event and was run unfinished, without final body smoothing, gap filling and paint. The windshield was fitted, but not the front splitter (Figure 5.9). In order to not stress the motors before the Bonneville record attempt, the current level on the Sevcon controllers was set to provide a maximum of 250 amps per motor, resulting in an estimated 40 kW and 82 Nm torque at the drive wheel.

Figure 5.9- Baker sidecar at ECTA Ohio test- June 2016 *(author)*

Table 5.2 summarizes the results from this test.

Table 5.2: Results from Ohio Testing in June 2016

Date	**Temp °C**	**Humidity %**	**Barometric pressure mbar**	**Air Density ρ (kg/m3)**	**Wind**	**Speed (mph)**	**Comments**
June18 Pass 1 9:30 am	27.8	30	1022.6	1.180	13 mph SE Gust 23 mph	112.0239 **NEW ECTA RECORD (No prior record)**	Significant cross wind resulted-no full throttle application Front body mount broken and needed repair before further runs.
Pass 2 13:58 pm	28.9	30	1022.6	1.175	SE gusts to 23 mph	117.493 **NEW ECTA RECORD (broke record above)**	On full throttle for first part of run but needed to reduce throttle prior to reaching speed trap due to cross wind pushing sidecar to edge of course.

Pass 3 17:05 pm	28.9	30	1022.6	1.175	NE gusting to 20 mph	115.7110 mph	On full throttle early but wind had shifted from cross wind to head wind and gusting to 20 mph.
June 19 8:51 am	28.3	35	1026.5	1.177	13 mph S	113.8376 mph	Wind noted at end of course by fluttering flags to be direct headwind at approximately 10 mph.
10:13 am	28.3	35	1026.5	1.177	NE Headwind 10 mph	108.6694 mph	Tried to use part throttle for first half mile then accelerate hard in second half mile. Had strong acceleration. Headwind was still present.

The following observations were made:

Crosswind sensitivity

Cross and headwinds were present on every run. Although the sidecar was moved laterally by crosswinds (especially gusts) it was not twitchy or abrupt, but was simply pushed sideways without any change in stability, heading or directional control. Adding hysteresis to the steering systems by clicking the steering damper from its normally lowest setting by two or three clicks seemed to help resist effects of the crosswinds. It should be noted that an airport runway does not provide the width available at Bonneville and any lateral motion of the vehicle, if not checked, has the potential for disaster. Although the splitter was not available for this test, it is felt that

the additional downforce at the front of the sidecar would have been beneficial to further resist the effects of the crosswinds.

Rider position and windscreen

On some of the faster runs, air coming from the outer edges of the windscreen and hitting the rider's shoulders could be felt. This was consistent with the flow trajectories evidenced from CFD work in Chapter 4. By tucking in elbows, the air pressure on the shoulders subjectively felt less, potentially reducing drag.

Attachment of rear aerodynamic bodywork

The attachment of the rear bodywork section to the sidecar using quarter turn fasteners was successful and provided a sturdy attachment. No further attachments would be required. The port to add ice to the cooling system with the repositioned water tank needed improvement as it was awkward to use and was located in the airstream.

Table 5.3 indicates the parameters from the Ohio test. The C_d value of 0.276 was the calculated CFD result from Chapter 4, for the sidecar with new rear section but without the splitter (Figure 4.81). Using these parameters, Figure 5.10 is a plot of the predicted performance (from the mathematical model) and the speed actually attained at one mile. Rolling resistance was not included in this model and the 60-kg ballast was not carried.

Table 5.3: Parameters for Ohio test

Parameter	**Value**
Drag coefficient (C_d)	0.276
Air density (ρ)	1.18 kg/m^3
Frontal area (A)	0.99 m^2
Torque to wheel	Constant 82 Nm
Chain drive sprocket ratio	20/40
Weight	540 kg

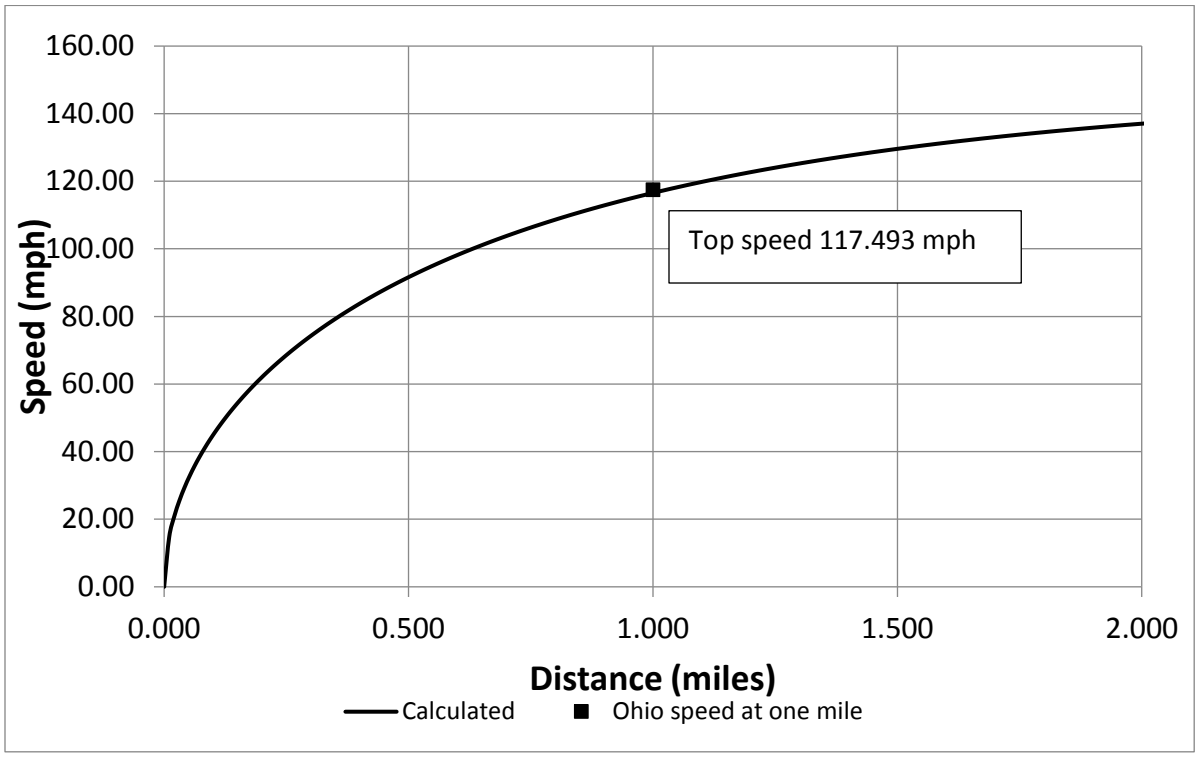

Figure 5.10- Predicted and actual performance from Ohio test

Unfortunately, at the Ohio test only the speed through the one mile trap was available from the race organizers to compare to the speed predicted from the mathematics model and the GPS data collection system did not function properly. Nevertheless, in Figure 5.10 the measured speed at one mile matches the prediction.

5.7 BONNEVILLE 2016

The 2016 Bonneville Motorcycle Speed Trials (BMST) took place from August 27th through September 1st, 2016. Although the salt was considered marginal compared to previous years, through careful preparation by the organizers the surface was reasonably smooth on the actual competition surfaces. Two courses were constructed for the event: a long or "International" course of 8 miles length and a shorter "Mountain" course of 5 miles length.

The Baker sidecar was prepared with the new rear bodywork section (now having been prepared and painted by a body shop), with the windshield and the front splitter attached (Figure 5.11 and Figure 5.12). The 60-kg ballast was carried in all Bonneville runs, per the FIM and AMA rule requirements. The Sevcon controllers were set to provide a maximum of 300 amps per motor which, with the battery pack charged to 100 volts, provided a maximum of 60 kW from the motors, or approximately 50 kW at the rear drive wheel. Prior to each run, the ice tank was filled with a mixture of ice and water and the motors pre-chilled by pumping ice water through them for approximately ten minutes.

Figure 5.11- Preparing to run with the full sidecar body *(author)*

Figure 5.12- Full bodywork including windshield and splitter *(author)*

The FIM also has a class for unstreamlined electric sidecars, so during the event, all of the bodywork (except the front splitter) was removed and the sidecar was run in this configuration

(naked) to set a world record in another electric vehicle class as competition number 7501 (Figure 5.13).

Figure 5.13- The Baker running in the unstreamlined (naked) class *(author)*

Table 5.4 summarizes the results from the world record attempts at Bonneville in 2016.

Table 5.4: Results from 2016 Bonneville Land Speed Record Attempts

Date/ configuration	Temp C	Humidity %	Barometer	Air Density ρ (kg/m3)	Wind	Speed (mph)	Comments
August 28 11:17 am	23.9	19	1022.01	1.198	3 mph NE	94 mph	Motor cut-off during pass
Full Sidecar	31.1	17	1022.01	1.169	9 mph ESE	90 mph	Motor cut-off during pass

August 29 Full Sidecar 7:20 am 8:24 am	16.1 17.2	34 29	1023.36 1023.36	1.230 1.225	3 mph WSW 3 mph WSW	105.626 mph 98.2 mph	**NEW FIM RECORDS** 1 mile: 101.825 mph 1 KM: 104.973 mph
August 29 Naked Sidecar 2pm 4:30 pm	30.0 32.2	16 14	1023.36 1023.36	1.173 1.145	0 mph 8 mph SE	89.419 mph 88.8 mph	**NEW FIM RECORDS** 1 mile: 89.113 mph 1 KM: 94.886 mph
August 30 Full Sidecar	23.9 28.9	24 14	1021.33 1019.98	1.197 1.178	8 mph ESE 8 mph E	100 mph 100 mph	Motor cut-off during passes
August 31 Full Sidecar Sprocket change to 19/40	28.9 32.8	16 14	1017.6 1015.9	1.178 1.163	8 mph ENE 6 mph ENE	107.810 mph 109.134 mph	**NEW FIM RECORDS** 1 mile: 108.499 mph 1 KM: 110.389 mph

Table 5.4 reflects the difficulties in setting land speed records at Bonneville. Despite having the sidecar meticulously prepared for competition and having previously tested at the Ohio event in June 2016, the motor cut-off problem that was experienced with a single motor drive in 2014, reoccurred with the twin motor drive in 2016.

Because FIM records were sought, only two hours were allowed between the first record pass and the return run in the opposite direction. The organizers allowed electric vehicles attempting FIM records to remain on the course and recharge their batteries under the supervision of an FIM representative, as is allowed by the international regulations. The Baker sidecar was recharged with a combination of energy obtained from a solar charging system mounted in a truck bed (Figure 5.14) and a petrol-powered generator. Approximately 30-40 percent of the vehicle charge came from the solar array. Typically, the battery pack would be charged for 60-80 minutes before the return run was made, returning it to approximately 80% of its fully charged state.

Figure 5.14- A solar charging system was capable of producing 30-40% of the energy used for record runs *(author)*

Following the successful record passes, the sidecar was placed into impound where it was inspected and the sidecar and ballast weighed to ensure it met the requirements of the over 300 kg electric sidecar class. Typically, this would take several hours, so, when taking battery charging into account (3-4 hours to fully recharge), it became difficult to make more than two passes during a day.

Although the motor cut-off issues limited the record speeds, the team was successful during the week by setting an FIM record for the flying mile and flying kilometre in the partially streamlined and unstreamlined (naked) class, and then breaking the team's own FIM record from earlier in the week in the partially streamlined class. In addition, the team broke its existing US National AMA land speed record for an over 300kg electric sidecar. The records were ratified in November 2016 by the FIM and by the AMA. The GPS tracker attached to the sidecar indicated a maximum speed with full bodywork of just over 115 mph.

5.8 DYNAMOMETER TESTING (SEPTEMBER 2016)

After returning from Bonneville, it was decided to test the sidecar on a chassis dynamometer to establish the amount of power that was being delivered by the rear driven wheel and also to further investigate the motor cut-off issue that had been experienced at Bonneville in 2014 and again in 2016. The sidecar was tested on a Dynajet 248H (high-inertia) dynamometer (Figure

5.15). The sidecar was positioned such that it powered one of the drums and the ice tank was filled with ice and water and the motors pre-chilled for approximately five minutes. After applying a slight amount of throttle to get the drum spinning, full throttle was applied until the motors cut-off after 45 seconds (Figure 5.16), with both controllers indicating an over-temperature condition for the motors.

Figure 5.15- Dynamometer testing with rear wheel on one drum *(author)*

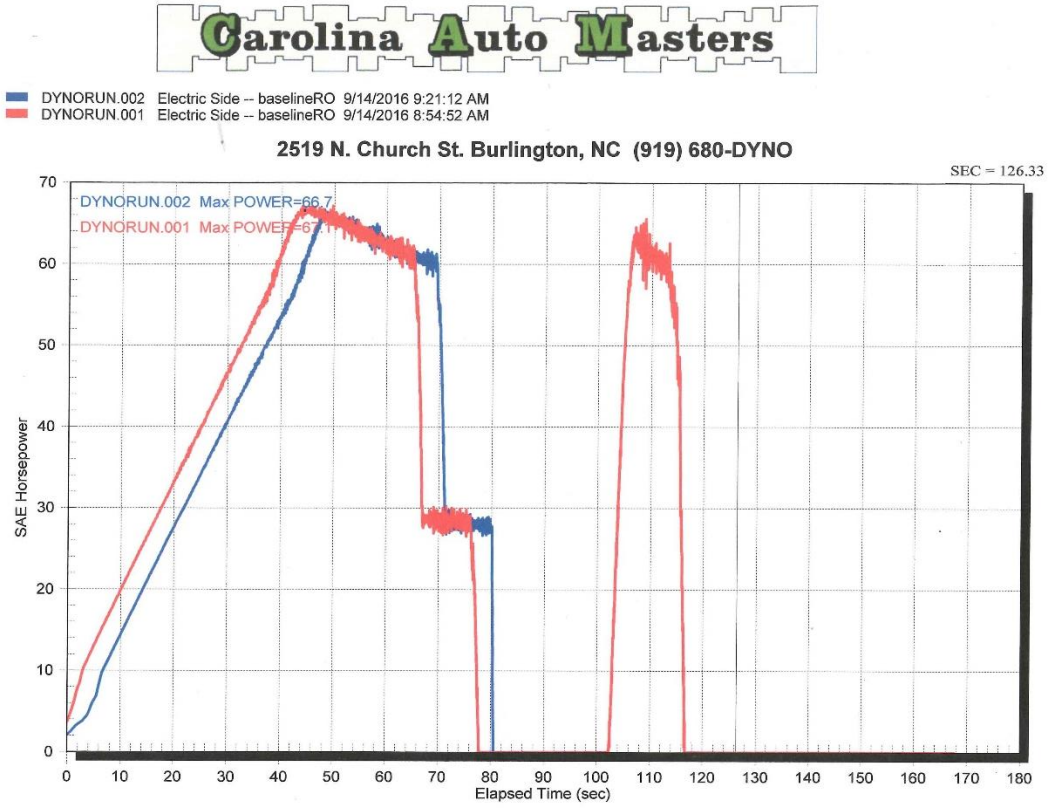

Figure 5.16- Dynamometer results for sidecar (time)

The extra peak in Figure 5.16, between 102 and 115 seconds occurred when the Sevcon controllers were reset and power was reapplied. The Sevcon controllers were set to cut-off the power to the motors when the internal thermistors in the motors reached 160 °C. This temperature was set just below the Curie temperature of the motor's rare earth magnets (165 °C). After consultation with the motor manufacturer, Motenergy, it was learned that the temperature thermistor for each motor is located on the outer surface of the coils of the stator, a region that quickly heats when high currents are applied to the motor. The transfer of this heat energy to the magnets located on the rotating commutator takes some time, so they may remain cooler than the sensor if the current is cut off at an appropriate time. Appendix B examines the heat transfer from the coils to the magnets on the rotor to determine if a higher temperature cut-off setting on the Sevcon controllers would still protect the magnets from exceeding 165 °C. A setting of up to 200°C was found to still provide protection for the magnets.

The other information available from the dynamometer test was an accurate measurement of the amount of power generated by the twin motor drive and delivered to the ground through the rear wheel. With the battery pack fully charged (100 volts) and each motor receiving 300 amps from the controllers, the electrical power applied to the motors was nominally 60 kW. From Figure 5.17, the maximum power produced is 67.1 horsepower (SAE) which converts to 50 kW. This is approximately 83% of the power delivered from the battery pack, which is consistent with

efficiency values found in the literature i.e., a motor efficiency of 90%, a controller efficiency of 95 %, and an o-ring chain drive efficiency of 97% (www.motor.doe.gov). From Figure 5.17 which is the measured tractive power versus road speed, using the rolling diameter of the rear wheel (20.2 inches) and the power output at several speeds from the figure, it is also possible to calculate the torque provided by the motors.

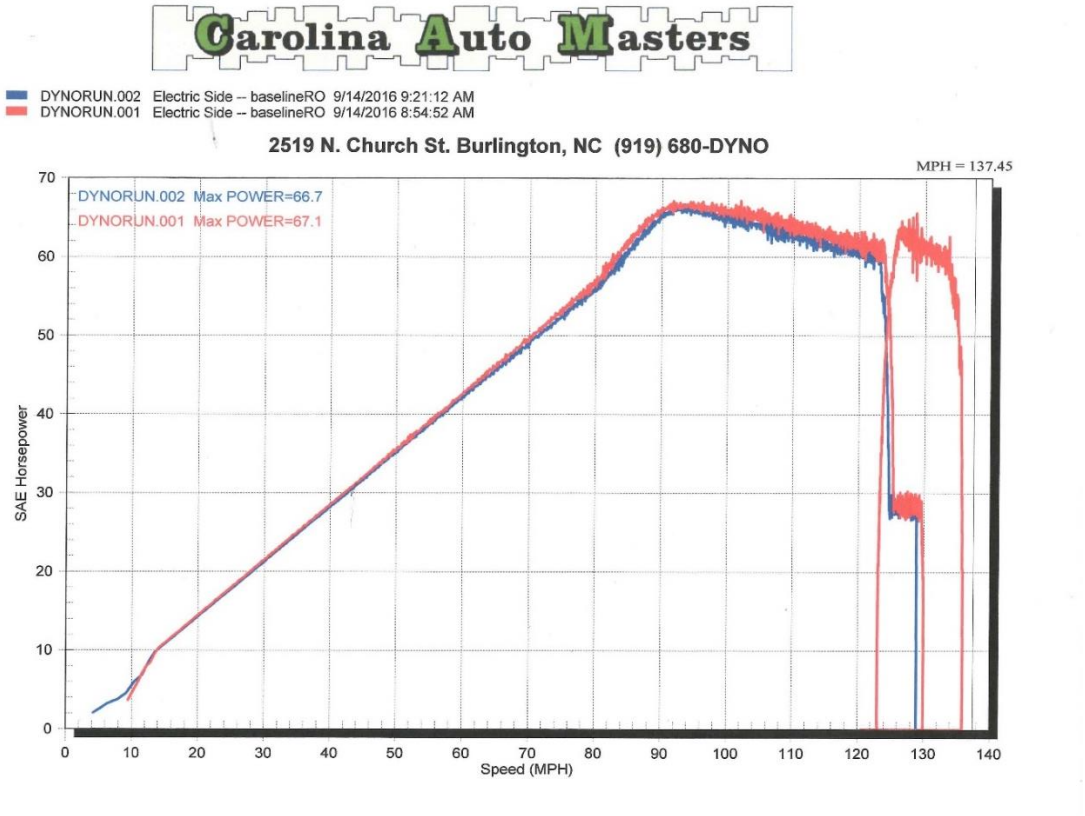

Figure 5.17- Dynamometer results for sidecar (speed)

The torque is 75 lb-ft (102 Nm) and is constant from approximately 15 mph to 90 mph in Figure 5.17.

5.9 Mathematical Modelling of Bonneville Results

To produce a curve of measured speed versus distance during the record runs at Bonneville, a Qstarz BT-Q1000ex GPS lap timer was installed on the sidecar to record position and speed data at rate of 10 Hz. However, because of the motor cut-off issue during the 2016 record runs at Bonneville, full power was delayed on some runs to try to prevent the motors from cutting off while traversing the timed mile. Thus, it was difficult to obtain a single plot that represented a full power run. Three runs from the GPS data with speed-distance curves that represented various parts of the total speed versus distance curve were chosen and a composite curve was

created by offsetting the distances run until the curves coincided to represent a total record run (Figure 5.18).

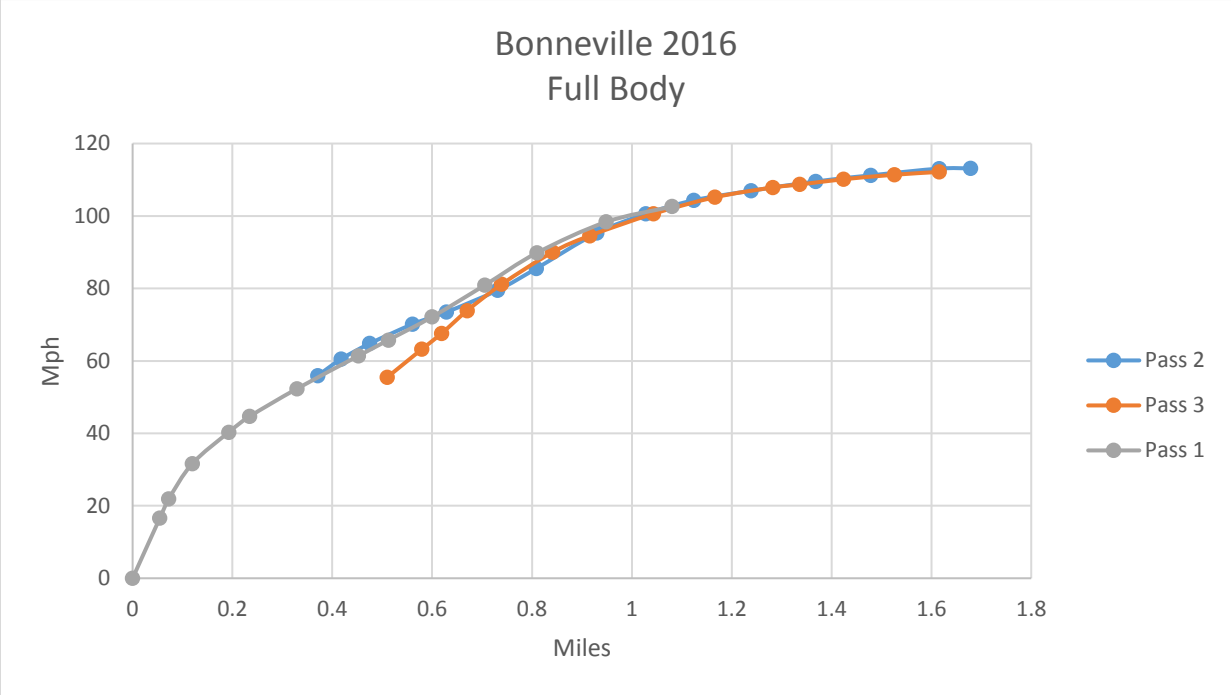

Figure 5.18- Three passes at Bonneville that were combined to create a composite performance curve

The composite curve indicated in Figure 5.18 implies the torque was not constant between approximately 0.2 and 0.8 miles, which was not the case. The data used to create the composite curve may be incompatible due to different distance offsets and torques. Because the maximum speed was the most interesting part of the curve for this work, only the upper speed curve (pass 3) was used for comparison to modelling.

Using the power and torque values delivered by the rear wheel to the road surface (from the dynamometer testing) and the value for the density of the air at Bonneville corrected for altitude, temperature and humidity, and the drag coefficient from CFD studies, it was possible to use the mathematical model (described earlier) to calculate an idealized performance curve for the sidecar and compare it to the pass 3 performance curve from Figure 5.18.

The drag coefficient from CFD was 0.341 (moving road surface at 44 m/s velocity) and the constant torque applied to the salt surface by the rear wheel from the dynamometer test was 102 Nm, the frontal area was 0.98 m^2 and the air density at the altitude of Bonneville on the day of record runs was $\rho = 0.996$ kg/m^3. In Figure 5.19 this idealized curve is compared to pass 3 of the partially streamlined sidecar at Bonneville. It is observed that the results predicted from CFD, using only aerodynamic drag, do not match the actual performance of the sidecar at Bonneville.

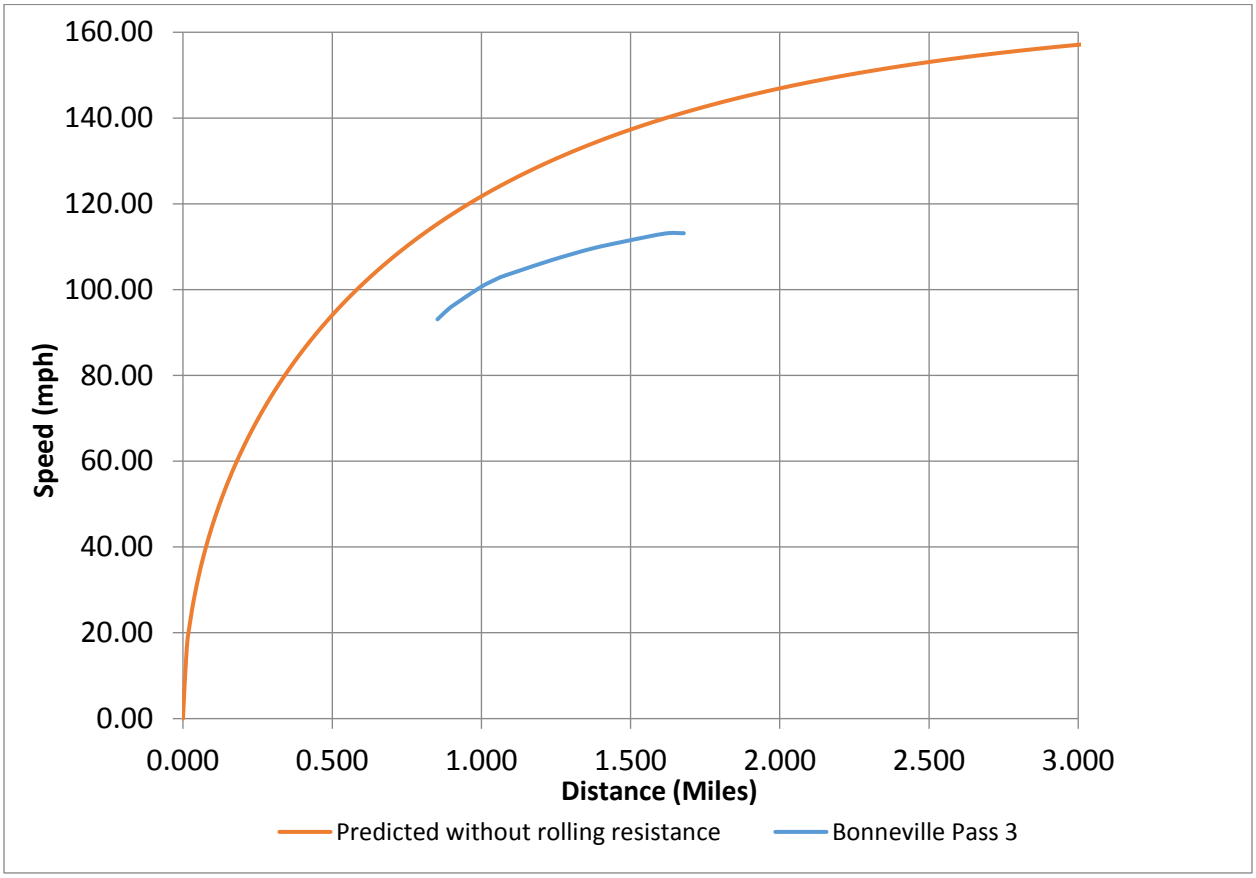

Figure 5.19- Comparison of predicted data from CFD drag coefficients to Bonneville results (without rolling resistance)

5.9.1 The contribution of rolling resistance

From Figure 5.19, it is evident that the results obtained on the salt flats at Bonneville are not well predicted by only using the aerodynamic contribution to drag from the drag coefficient (C_d) data obtained from ANSYS Fluent CFD modelling. In testing on the paved surfaces at Colorado and Ohio, the mathematical model produced a good match between predicted and actual performance without including consideration for the rolling resistance of the vehicle on the track.

Rolling resistance is defined by

$$F_{rolling} = W\ C_{rr}$$

With $F_{rolling}$ the rolling resistance force, W the weight on the wheels and C_{rr} a non-dimensional rolling resistance coefficient. The rolling resistance coefficient on a paved surface would be approximately 0.001-0.015, while on loose sand it could be as high as 0.2 – 0.4 (engineeringtoolbox.com). The salt surface used for completion is somewhat difficult to quantify (Metz, 2004). Bonneville racer Kevin Cooper used empirical methods to develop a pair of correlations for the rolling resistance coefficient, dependent upon velocity and tyre pressure (Bradley, 1996). Sullivan used Cooper's original model to create a parabolic relationship for the

rolling resistance coefficient. A comparison between Sullivan's model and Cooper's calculation is indicated in Figure 5.20.

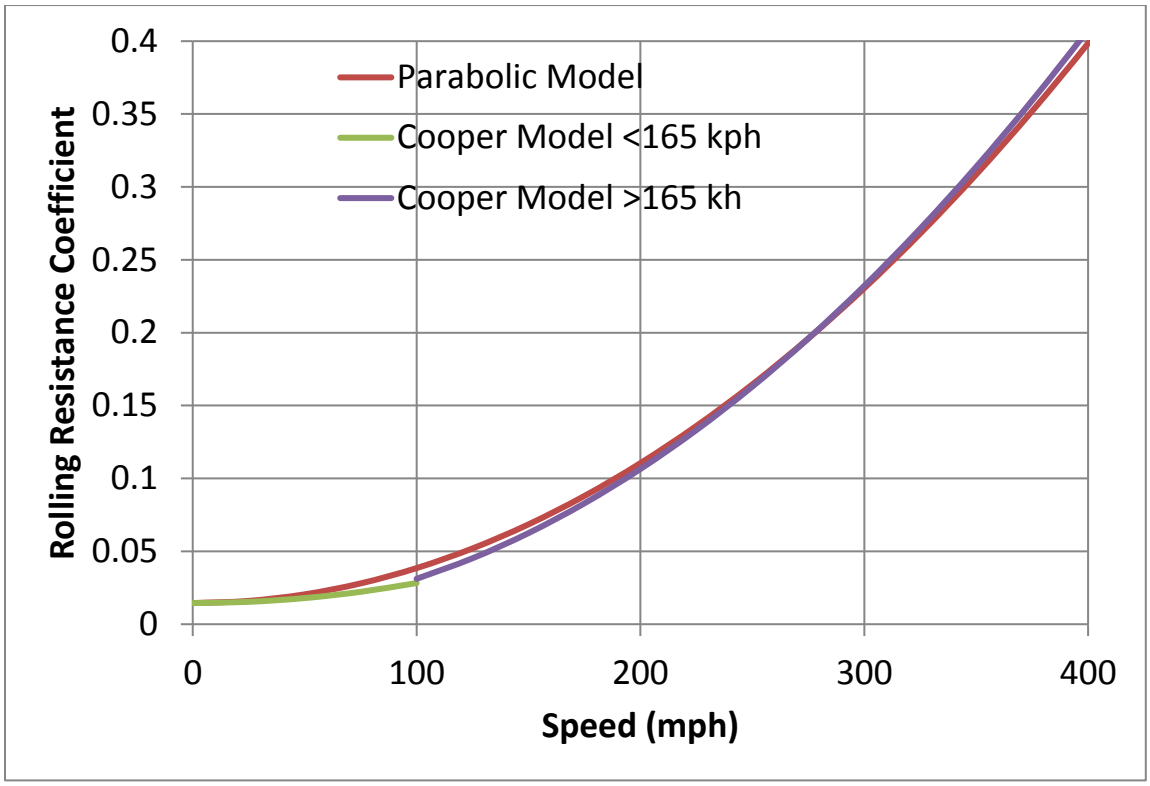

Figure 5.20- A comparison of Sullivan's parabolic rolling resistance coefficient model to Cooper's models for Bonneville [Sullivan, 2016]

From Figure 5.20, a rolling resistance coefficient of C_{rr} = 0.0385 could be expected at 100 mph (44 m/s) on the Bonneville surface, which is the same order of magnitude to the C_{rr} = 0.048 value that was found from the limited data from the 2014 record run at Bonneville. Sullivan' parabolic function is:

$$F_{rolling} = W(a + bV^2)$$

Where (a) and (b) are constants that depend upon the tyre and rolling surface characteristics. On a paved surface, a value for (a) would be 0.002 and for (b) would be 0.000002 (Sullivan J. , 2016). The small values for these coefficients indicate why the rolling resistance effects on the paved surfaces at Colorado and Ohio were negligible. It should be noted that factors beyond tyre hysteretic losses, including wheel bearing friction and brake drag are also included in the rolling resistance term.

In Sullivan's modelling of his runs at Bonneville (Figure 5.3) he did not include a rolling resistance term. However, his vehicle was a lightweight (220 kg total) solo motorcycle running narrow motorcycle tyres at high inflation pressures (50 psi). In contrast, the sidecar vehicle in the current

work has an all up mass of 600 kg and is fitted (due to geometry and speed rating considerations) with wide sports car radial tyres. The rolling resistance effects should be significant.

Determining the exact value for the rolling resistance coefficient at Bonneville would be difficult, but a value was approximated by fitting the speed-distance curve, using the CFD drag coefficient (C_d = 0.341) and the other parameters indicated in Table 5.5, to the measured pass 3 results from Bonneville.

Table 5.5: Parameters for Bonneville record

Parameter	**Value**
Drag coefficient (C_d)	0.341
Air density (ρ)	0.996 kg/m^3
Frontal area (A)	0.99 m^2
Torque to wheel	Constant 102 Nm
Chain drive sprocket ratio	20/40
Rolling resistance constants	a = 0.0385, b = 0.000005
Weight	600 kg

In Figure 5.21, the predicted curve with the rolling resistance term included is plotted along with the Bonneville measured pass 3 curve.

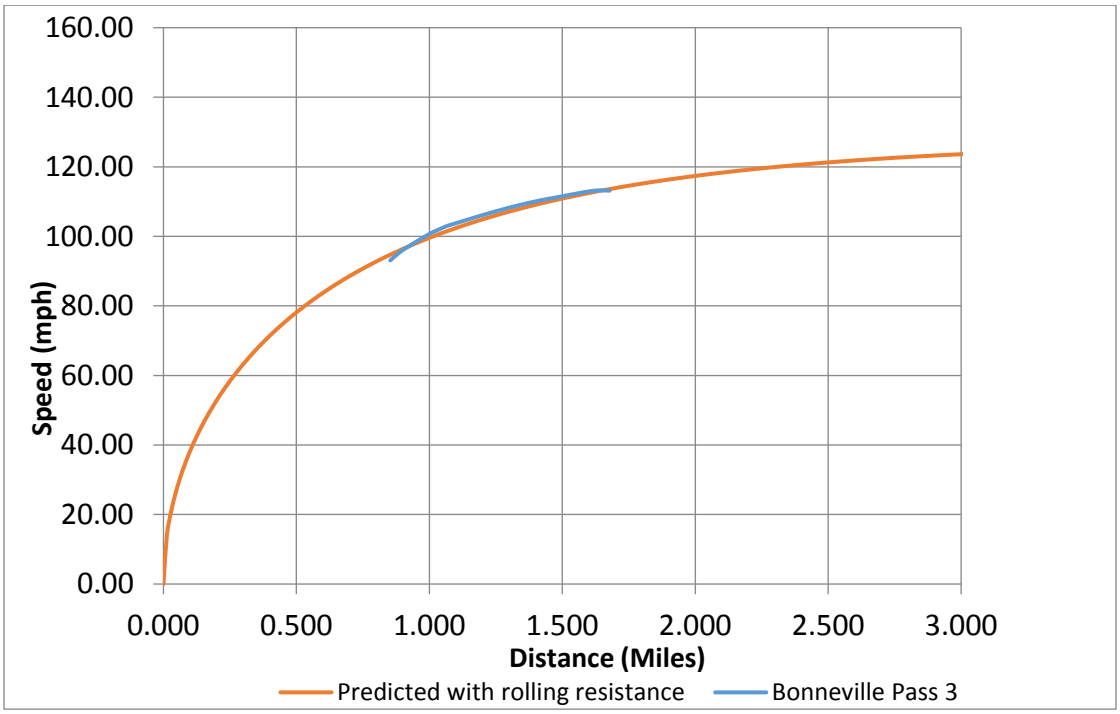

Figure 5.21- Predicted data including rolling reistance contribution

Using this constant for rolling resistance at Bonneville, along with the aerodynamic drag from the CFD study (C_d = 0.341) and the maximum power from the dynamomter test (50 kW) along with the air density at Bonneville (ρ = 0.996 kg/m^3) and the sidecar frontal area (A= 0.99 m^2), it is possible to create a plot of the power required from aerodynamic drag and rolling resistance over a range of speeds. This plot is provided in Figure 5.22.

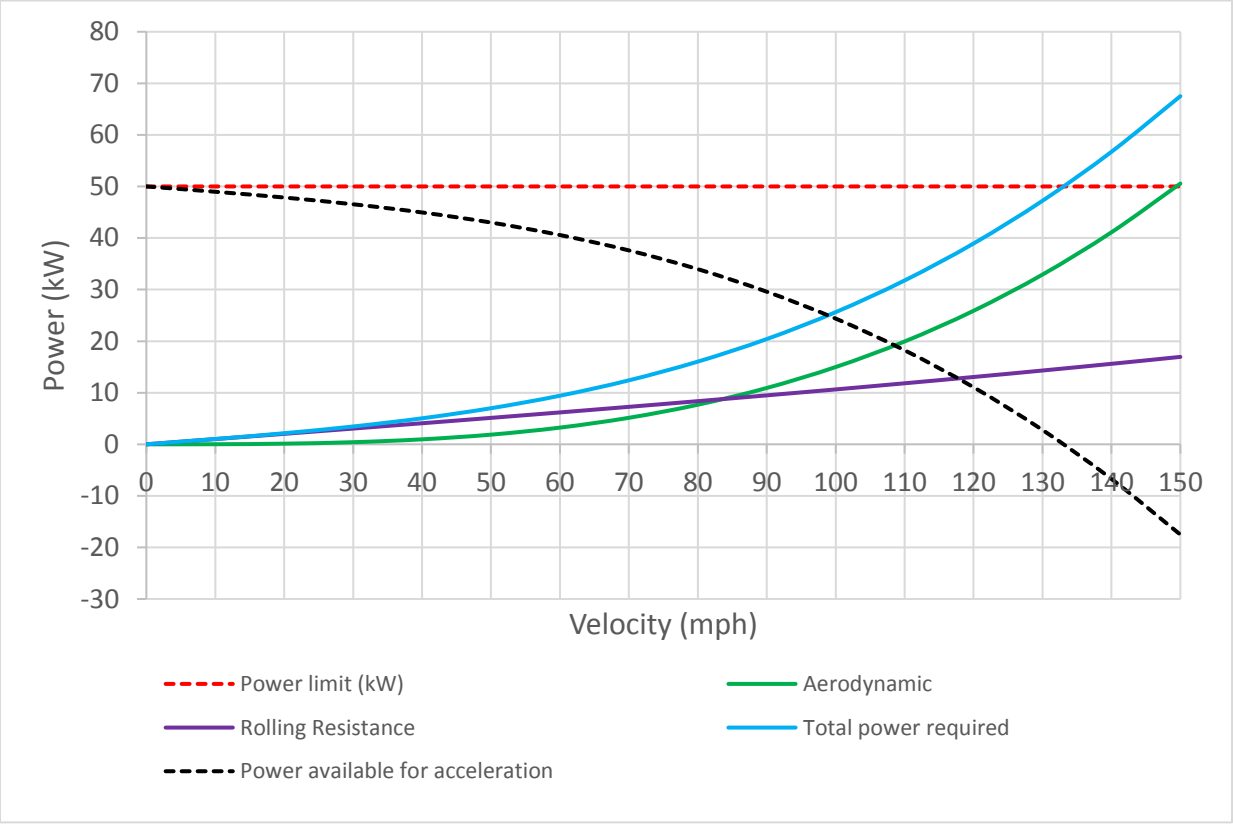

Figure 5.22- Power requirement versus velocity for sidecar at Bonneville

In Figure 5.22, the contribution of the aerodynamic drag and rolling resistance power requirements can be summed to provide a curve for the total power required to achieve a given velocity. With a limit of 50 kW (the red dashed line in Figure 5.22) the highest velocity (with rolling resistance included) would be 133 mph at Bonneville. The dashed black line in Figure 5.22 indicates the power (in kW) that is available for acceleration (to overcome d'Alembert forces). It is evident that the power available for acceleration starts out at a high level (≈50 kW) but falls away as power is consumed by rolling resistance and aerodynamic drag, until the acceleration reaches zero at the maximum speed of 133 mph.

5.10 Full-scale wind tunnel testing

Upon returning from Bonneville, it was arranged to test the full-scale sidecar in the A2 Wind Tunnel facility in Mooresville, North Carolina. A2 is used primarily by bicycle, motorcycle, and automobile racing teams to examine forces and moments and flow visualisation with wind

speeds up to 85 mph (137 kph or 38 m/s). The A2 tunnel is a closed jet tunnel that uses contoured and profiled walls that reportedly reduce blockage effects on the measured forces. The working section of the A2 tunnel is 20.9 m^2 and as the sidecar is approximately 0.99 m^2 in frontal area, the blockage was approximately 5%. The floor was stationary and the wheels were non-rotating in the tests. Although requested, a value for turbulence intensity for the A2 wind tunnel "had not been measured." The full-scale sidecar was used in the A2 wind tunnel test so the length scale would be the length of the sidecar (3.28 m). For CFD simulations of the A2 wind tunnel, a turbulence intensity of 5% and turbulence viscosity of 10 were used in a computational domain that measure 29 m long, 8 m wide and 8 m high.

The full body as run at Bonneville was tested in the A2 wind tunnel at three different Re—4.0 x 10^6, 6.0 x10^6, and 8.5 x 10^6 (length scale = 3.28 m, v= 1.81 x 10^{-05} kg m^{-1} s^{-1}). The results from the A2 data for C_d are plotted in Figure 5.23 along with CFD results for the same version of the sidecar at various Re with a stationary road surface. CFD was performed using ANSYS Fluent 17.0 with an 8.1 million element unstructured mesh using the k-ε Realizable turbulence model with a Scalable wall function as described in Chapter 4. A coupled scheme was used for pressure and velocity and spatial discretization used a least squares gradient and second order upwind pressure, momentum, turbulence kinetic energy and dissipation rates (Appendix A).

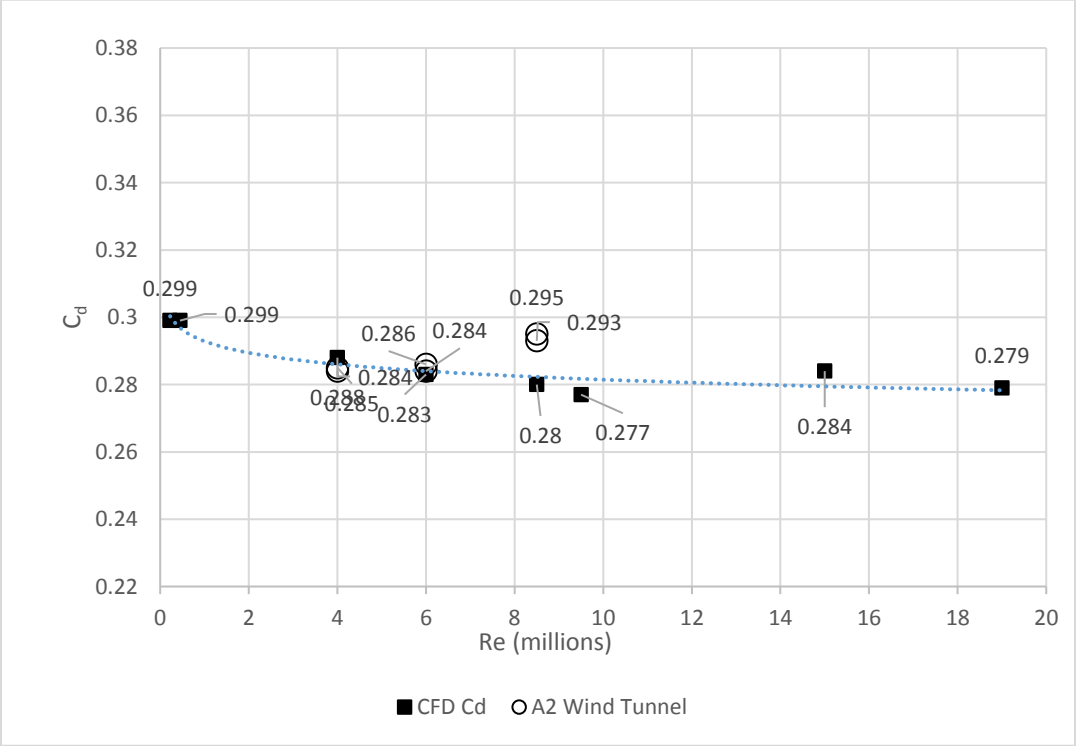

Figure 5.23- C_d for A2 full scale wind tunnel compared to CFD at different Re

In Figure 5.23, the C_d values from the wind tunnel are within 5.3% of the C_d values provided by the CFD study, which is within the accuracy expected for CFD predictions of wind tunnel data

(Chapter 3 and Lanfrit, 2005). One reason why there is not closer agreement between the CFD data and the A2 wind tunnel data could be that the actual sidecar tested in the wind tunnel has wheel openings, body panel gaps and joins between body panels that are not fully represented on the Solidworks model of the sidecar used for CFD. The actual sidecar is also sitting on a sprung suspension and this might result in a slight pitch (up or down) which could affect forces generated.

Because the A2 wind tunnel has a stationary floor, a boundary layer builds on the ground surface as air travels over it. The A2 wind tunnel has a step 6.1 metres (20 feet) in front (upwind) of the test vehicle that resets the boundary layer on the wind tunnel floor and Figure 5.24, which shows measurements of near-floor velocity by the operators of the tunnel, indicates the build-up of the boundary layer from the step onward toward the vehicle at a velocity of 38 m/s.

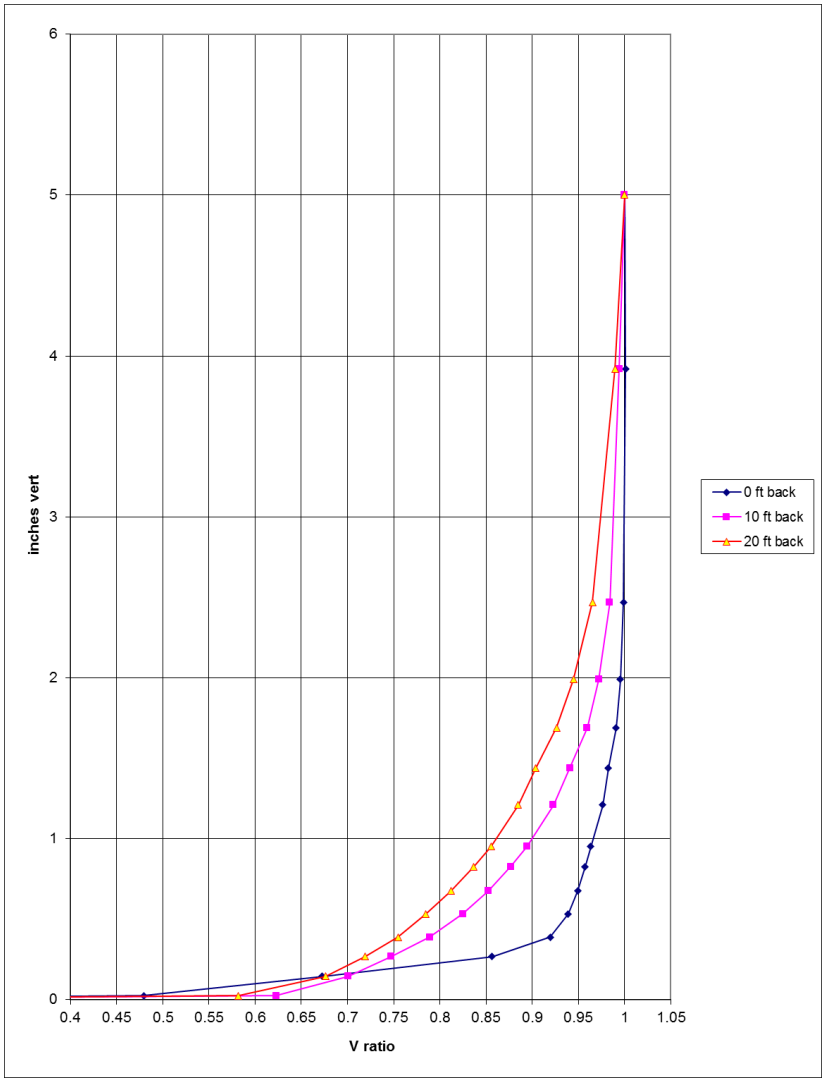

Figure 5.24- Build-up of boundary layer from the step toward the vehicle for the A2 wind tunnel [graph provided by A2]

From Figure 5.24, it is evident that at 6.1 metres (20 feet) (downwind) from the step (the position of the sidecar vehicle) the boundary layer at 0.99 freestream velocity has a thickness of approximately 89 mm (3.5 inches). Measuring the thickness of the boundary layer at 0.99 of the freestream velocity (ahead of the effects of the presence of the sidecar) in Figure 5.25 indicates a thickness of approximately 89-96 mm (3.5-3.8 inches), indicating that the CFD was adequately modelling the boundary layer thickness of the wind tunnel and may have slightly over predicted its thickness.

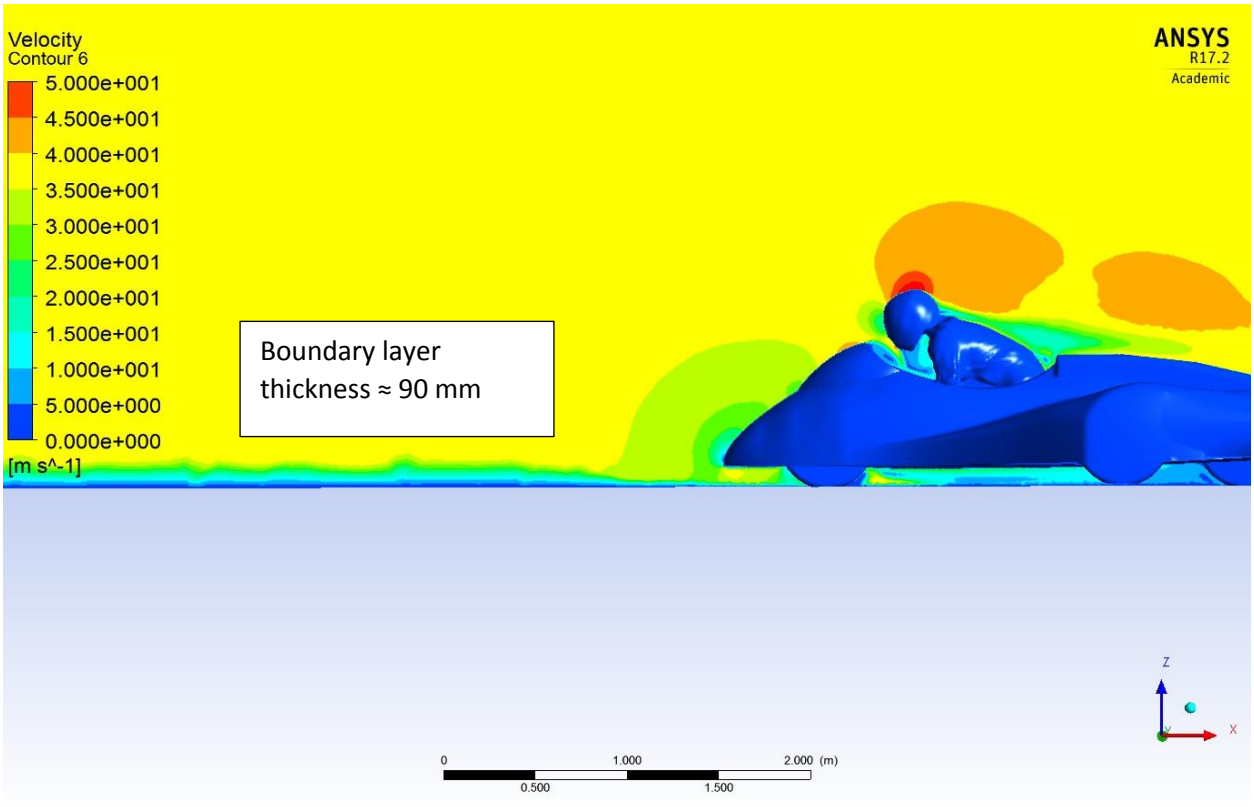

Figure 5.25- Velocity contour plot of boundary layer at 38 m/s with stationary floor

5.11 FLOW VISUALISATION

Another way to compare the results from a wind tunnel with CFD is to compare the flow patterns that form as air travels over the vehicle bodywork. Generally, flow in the wind tunnel can be visualized several ways such as with tufts of yarn, or by allowing oil to flow across a surface. A time-honoured although somewhat primitive method is to use a smoke trail produced from a point source and video or photograph the trail as it interacts with the flow stream over the vehicle. Although smoke trails are highly subjective and depend upon the position of the smoke wand and care of the operator, similarities in flow between what is observed in the wind tunnel and what is predicted using post-processing visualisation from CFD data can provide a general level of confidence that the topology of the predicted flow field is quantitatively correct, at least at the features visualised with smoke. The A2 wind tunnel uses a single point smoke source on a

wand with a wind velocity of approximately 60 mph (27 m/s). Corresponding CFD images for this comparison were produced from ANSYS Fluent 17.0 post-processing from a simulation run with a 7.2 million element tetrahedral mesh using the k-ε turbulence model with Scalable wall function with a velocity of 27 m/s (matching the Re of the wind tunnel).

Figure 5.26- Flow over the rider *(A2 wind tunnel)*

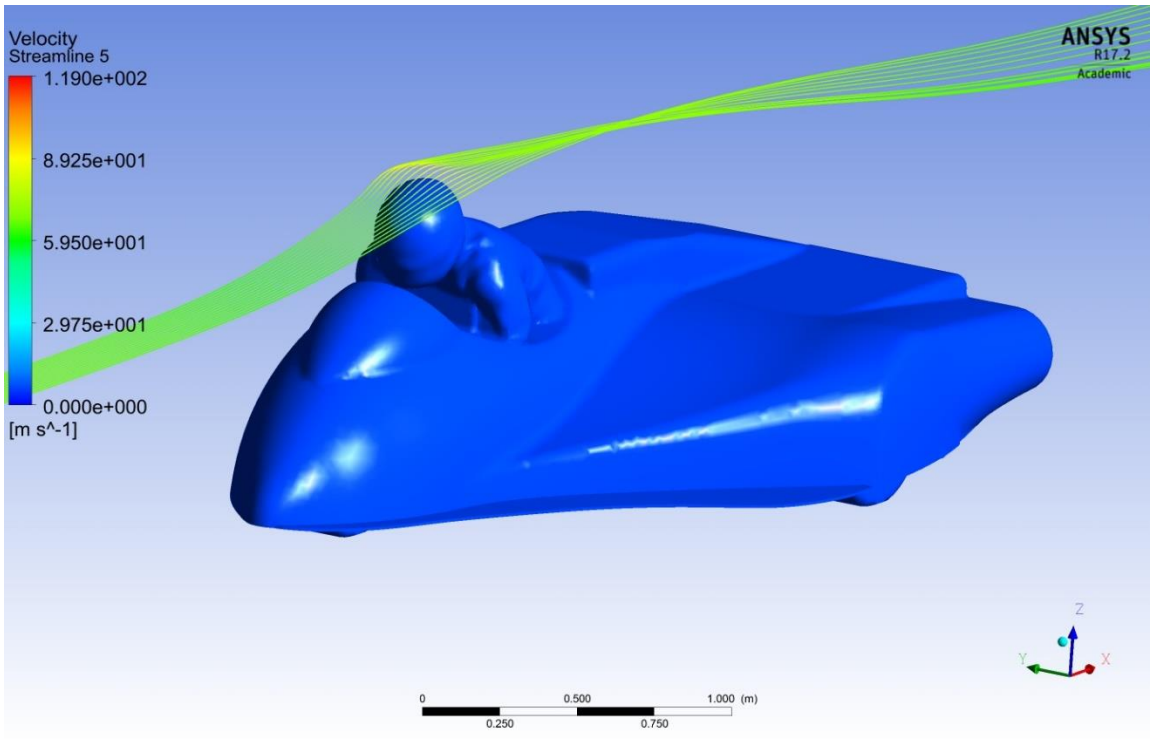

Figure 5.27- Flow over the rider CFD

In Figure 5.26 and Figure 5.27, the key point is the low vorticity flow that is seen over the rider's helmet with both the smoke and the CFD streamlines.

Figure 5.28- Flow over the windshield *(A2 wind tunnel)*

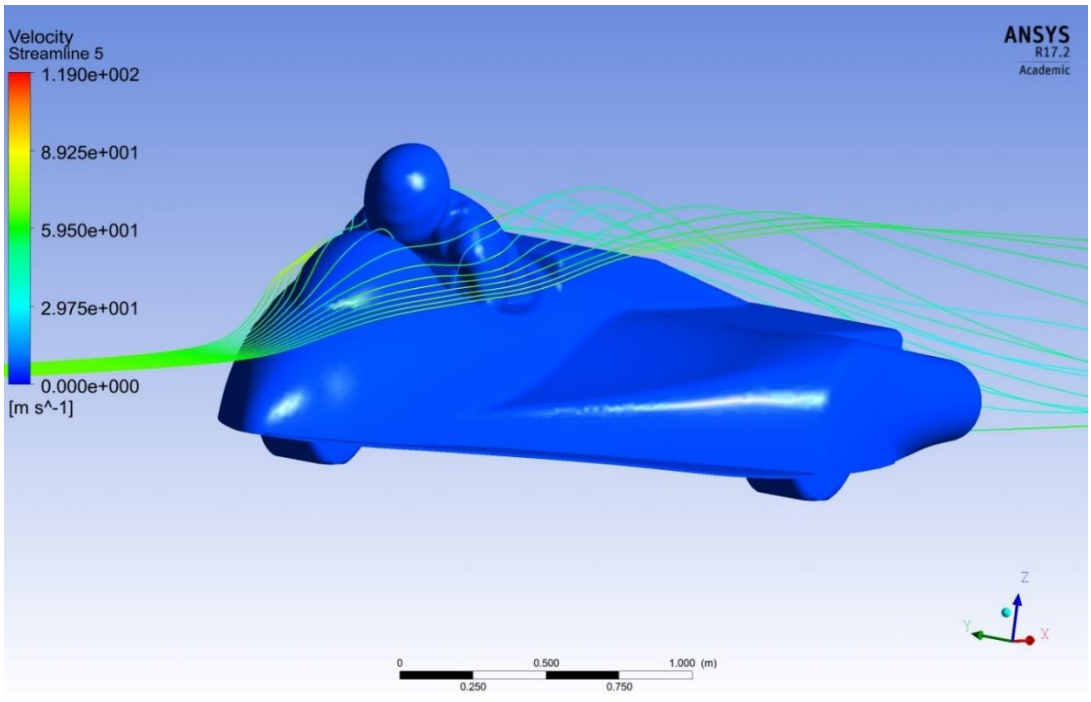

Figure 5.29- CFD Flow over the windshield

In Figure 5.28 and Figure 5.29, the flow over the windshield diverts around the rider in both cases with mixing in the gap between the rider's chest and the windshield evident only with the smoke in Figure 5.28.

Figure 5.30- Flow onto splitter *(A2 wind tunnel)*

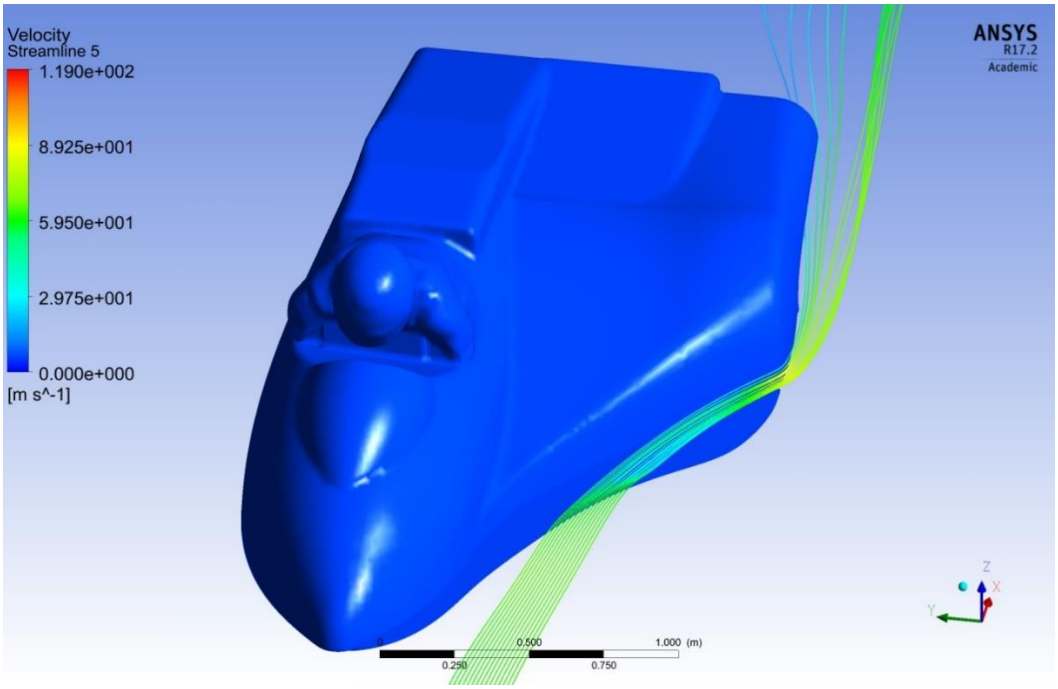

Figure 5.31- CFD Flow onto splitter

Comparing Figure 5.30 to Figure 5.31 it is evident that the splitter pulls the airflow downward and along its horizontal surface. This is more evident with the CFD in Figure 5.31 than with the smoke in Figure 5.30.

Figure 5.32- Flow over rear body section (Full body) *(A2 wind tunnel)*

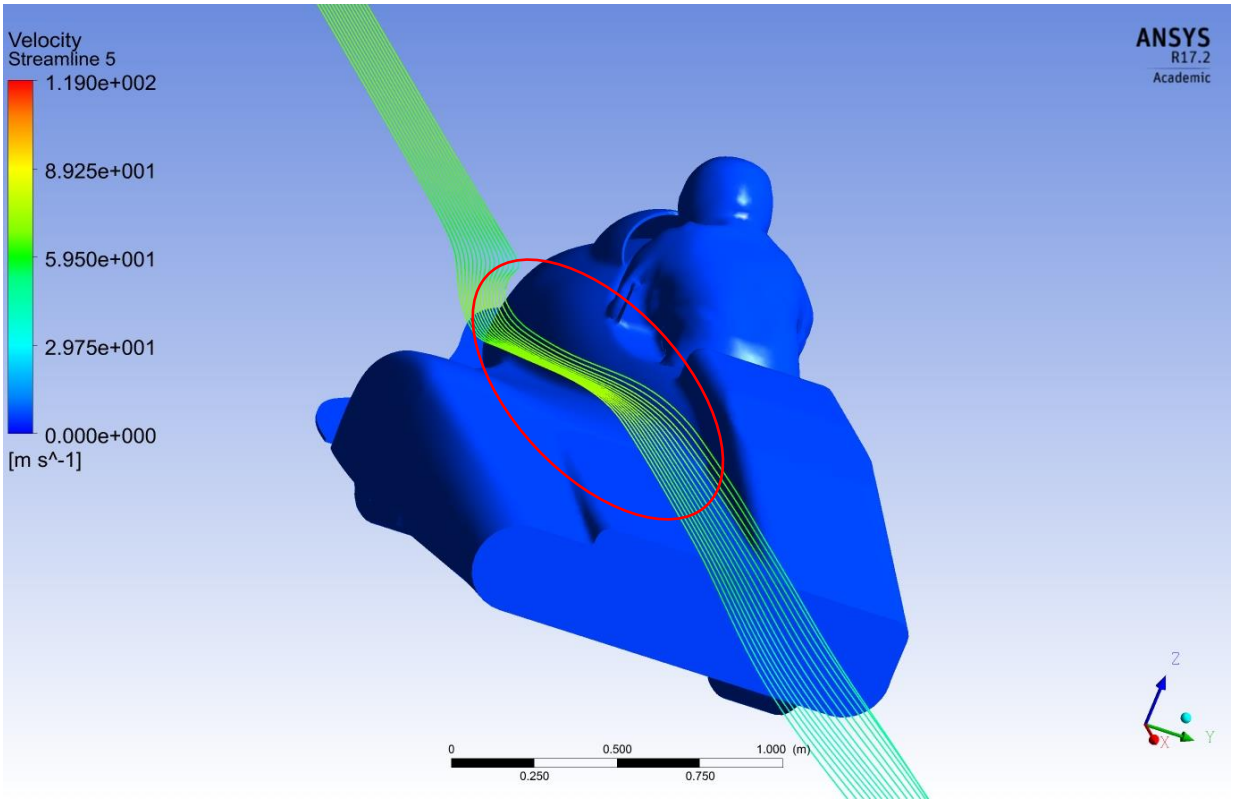

Figure 5.33- CFD Flow over rear body section (Full body)

Comparing Figure 5.32 and Figure 5.33, it is evident that flow is relatively undisturbed over the sidecar along the join between the rider portion and the sidecar portion (circled in red in figure 5.33)

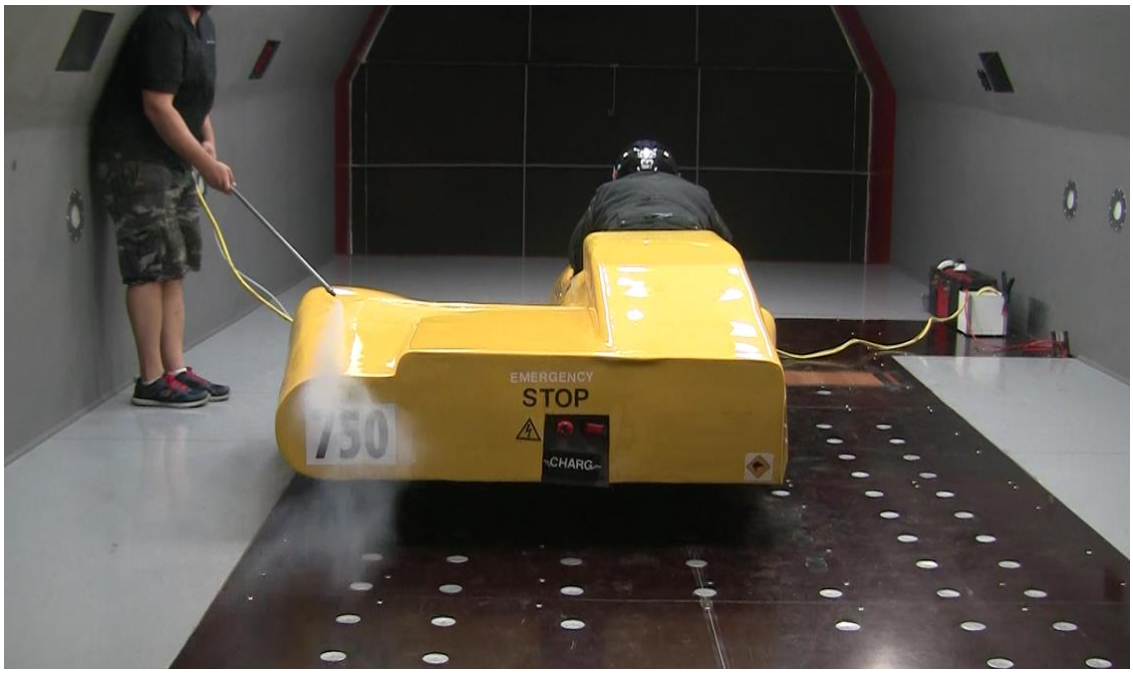

Figure 5.34- Flow over left rear body section (Full body) *(A2 wind tunnel)*

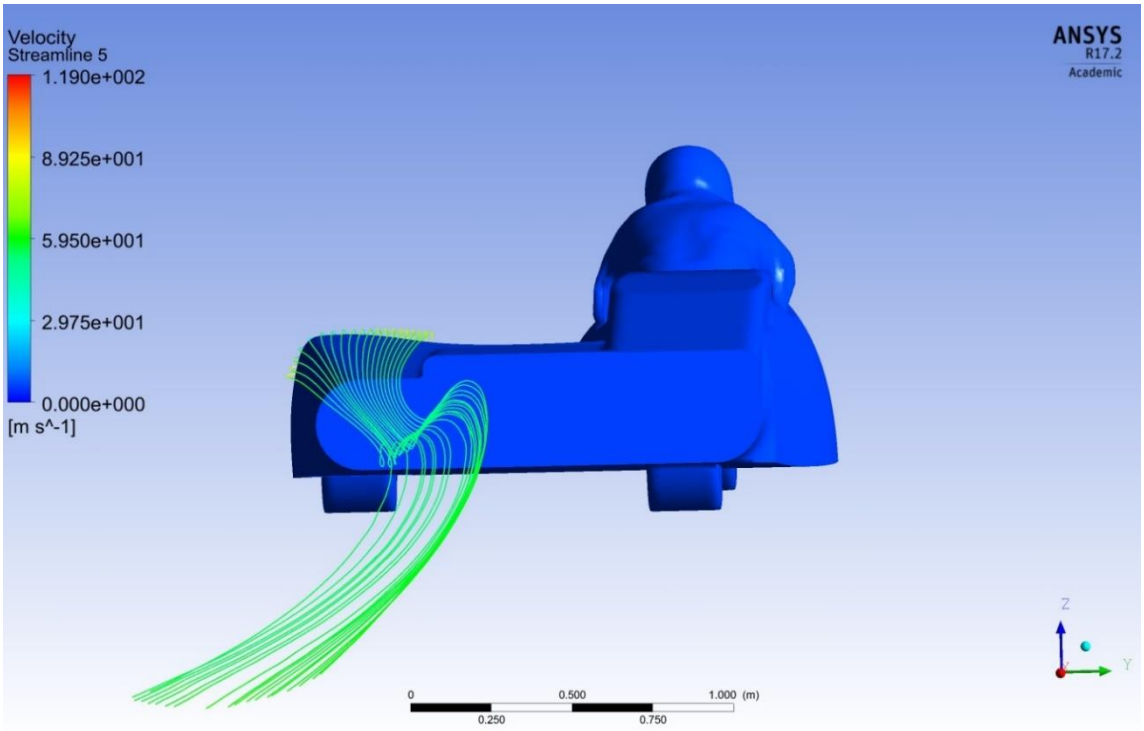

Figure 5.35- CFD Flow over left rear body section (Full body)

In Both Figure 5.34 (smoke) and Figure 5,35 (CFD) the formation of a streamwise vortex, rotating in a clockwise direction, off the left corner of the sidecar body is evident.

Figure 5.36- Flow at rear of full body *(A2 wind tunnel)*

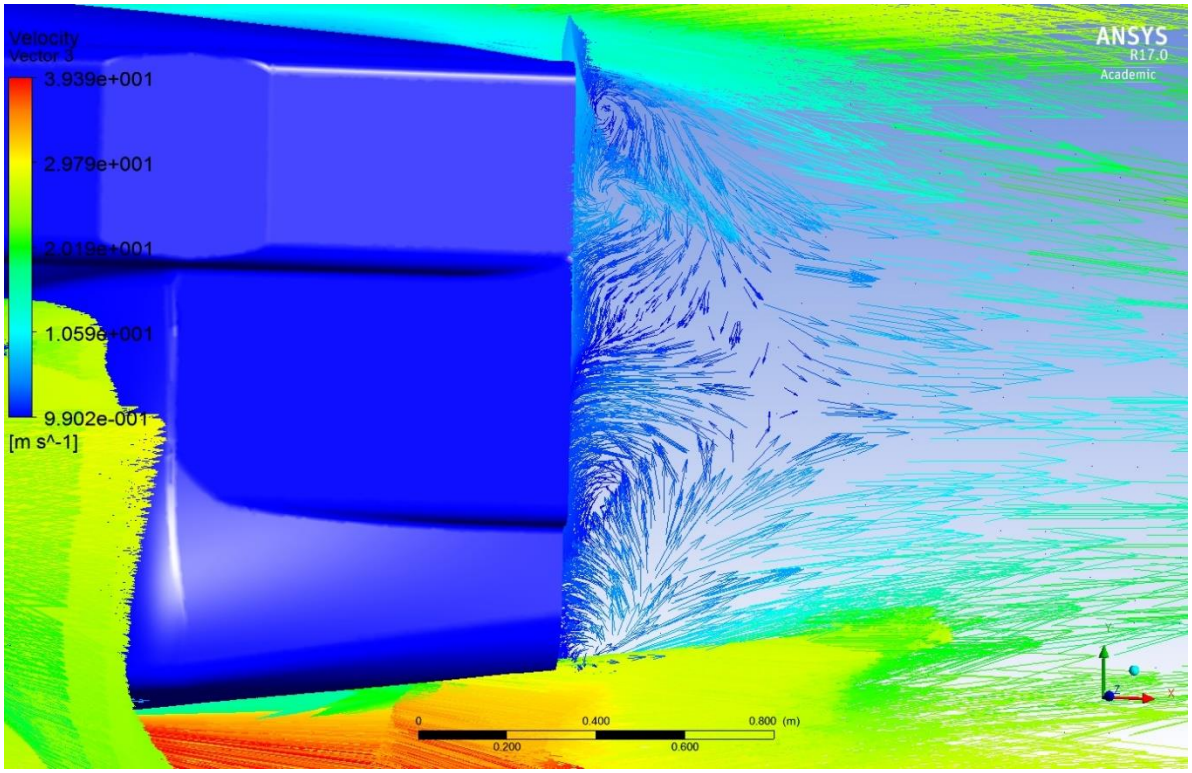

Figure 5.37- CFD vectors showing flow at rear of full body

From Figure 5.36 and Figure 5.37, the presence of the lateral vortices behind the tail of the sidecar is readily evident. The extent of this unsettled separated region in the wake is generally consistent between the smoke and CFD visualisations.

To summarize the qualitative analysis of the visualisations: the streamlines and velocity vector patterns created through CFD simulations generally recreate the patterns and indications of vorticity demonstrated by the wind tunnel smoke trails. This similarity between the location and type of flow increases confidence in the ability of the CFD studies to simulate the air flow over the asymmetrical sidecar body.

5.12 LIFT AND LATERAL FORCES

5.12.1 Lift based on A2 wind tunnel data

Although aerodynamic drag forces are a primary consideration in the development of land speed record vehicles, the generation of lift forces caused by the flow of air over the surface of the bodywork can have a destabilizing effect on the vehicle, particularly at high speeds. The generation of lift often results from interaction of the flow of air over the top surface of the vehicle versus the flow on the vehicle underside, leading to a difference in pressure distributions (McBeath, 2015). A smooth and contoured upper surface with a flat vehicle underside is more likely to produce aerodynamic lift than one that presents edges and ridges across the top surface that obstruct the disrupt flow of air and raise the pressure on the upper side.

Although excessive aerodynamic lift is something to be avoided, it is sometimes difficult to do so with body shapes that also reduce drag. The key is calculating the amount of lift generated by the vehicle at a target maximum speed and then ensure that this lift is significantly lower than the weight of the vehicle. The effects of lift on stability will be further discussed in Chapters 6 and 7. Table 5.6 indicates the measured lift (coefficient based on frontal area) generated at four speeds for the full body version of the sidecar and compares it to the static weight of the vehicle. Note that confidence intervals or estimate of error were not provided by A2 for their wind tunnel data.

Table 5.6: Lift Force of Full Body as percent of total vehicle mass

Speed (mph)	Speed (m/s)	Lift Coefficient (C_l)	Lift Force (N)	Vehicle Mass (N)	Lift as % of Vehicle mass
40 mph	18 m/s	0.099	19.6 N	5428 N	0.4 %
60 mph	27 m/s	0.106	46.8 N	5428 N	0.8 %
85 mph	38 m/s	0.114	100.2 N	5428 N	1.8 %
150 mph	67 m/s	0.150 Estimated by linear extrapolation	408.3 N	5428 N	7.5 %

It is also important to remember that the A2 wind tunnel has a stationary floor where the build-up of a boundary layer ahead of the test vehicle tends to produce positive (upward) lift that is stronger than is observed on wind tunnels with moving ground planes or vehicles moving along the road (McBeath, 2015). Thus, the value for lift in Table 5.6 at 150 mph would be a worst-case scenario.

5.12.2 Lift data from CFD results

As with aerodynamic drag coefficients (Figure 5.11), lift coefficients can also be obtained from CFD studies. ANSYS Fluent CFD simulation was undertaken with an 8.1 million element unstructured mesh using the k-ε turbulence model with a Scalable wall function. A coupled scheme was used for pressure and velocity and spatial discretization used a least squares gradient and second order upwind pressure, momentum, turbulence kinetic energy and dissipation rates. Figure 5.38 compares the lift coefficients calculated from the A2 wind tunnel data to CFD lift coefficients at the same Re for the full body version of the sidecar and with a stationary floor.

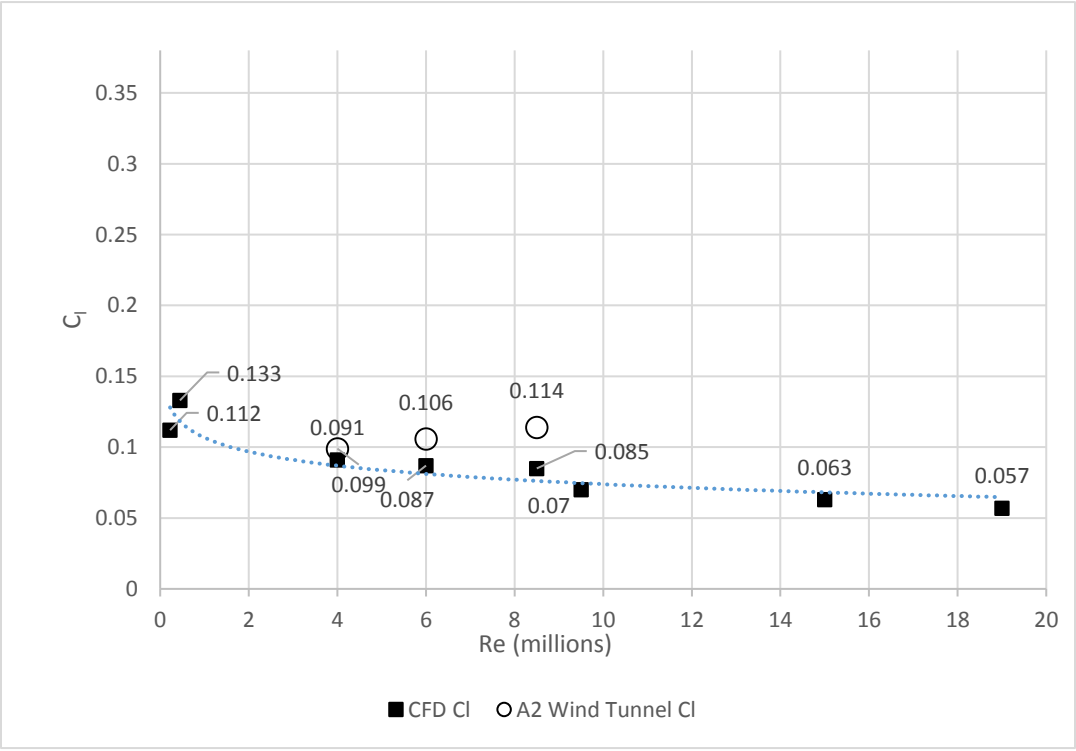

Figure 5.38- C_l from A2 wind tunnel versus CFD with Re

In Chapter 3, it was observed that the CFD results (when using the same methodology as the calculations here) over-predicted the lift force coefficients for both the 25° and 35° Ahmed bodies and over-prediction has also been observed by others in CFD studies using RANS turbulence models (Marovic, 2016), (Bordei & Popescu, 2011). As evidenced in Figure 5.38 however, the CFD

results under-predict the lift force coefficients measured in the A2 wind tunnel and predict a slight decrease with increasing Re, compared to the slight increase for the wind tunnel lift data with increasing Re.

The same geometric inconsistencies between the full scale actual sidecar and the idealized SolidWorks model of the sidecar used for CFD studies discussed for differences in drag results could potentially result in differences in lift such as those observed. In most cases, gaps and inconsistencies on the surface of the actual body would be expected to reduce lift. The higher lift coefficient shown in the A2 tests could result however from a slight upward pitch of the vehicle on its front suspension in the wind tunnel. If increasing speed caused the sidecar to pitch up (increasing the angle of attack, the lift coefficient would increase further, as observed. Induced drag would also increase (See Figure 5.23). Because the CFD model does not have a movable suspension or potential motion in the body mounting, neither of these effects would be found in CFD simulations.

Another factor might be that the splitter, which is modelled in CFD without a mounting bracket, has a significant aluminium brace running across its top surface. This brace could disrupt the flow along the leading edge of the upper surface of the splitter, reducing its effectiveness at producing downforce (negative lift), resulting in the lower than expected values when comparing CFD to the A2 wind tunnel data in Figure 5.38.

Even using the higher values of lift coefficient from A2 (C_l= 0.150 extrapolated linearly from the A2 data) to calculate the lift generated at 150 mph (67 m/s) it still only results in a total lift that is 7.5 % of the sidecar total mass (Table 5.5), a level judged to not dramatically affect the cornering forces available from the loading on the tyres (see Chapter 7).

5.12.3 Lateral forces based on A2 wind tunnel data

Perfectly symmetrical vehicles, running with zero yaw angles can be expected to produce little or no lateral force in wind tunnel testing. Sidecars are not symmetrical and can be expected to generate residual lateral forces due to the asymmetrical flow of air over their body surfaces. Figure 5.39 shows the lateral force coefficients (Cy) for CFD results and from the A2 wind tunnel with Re.

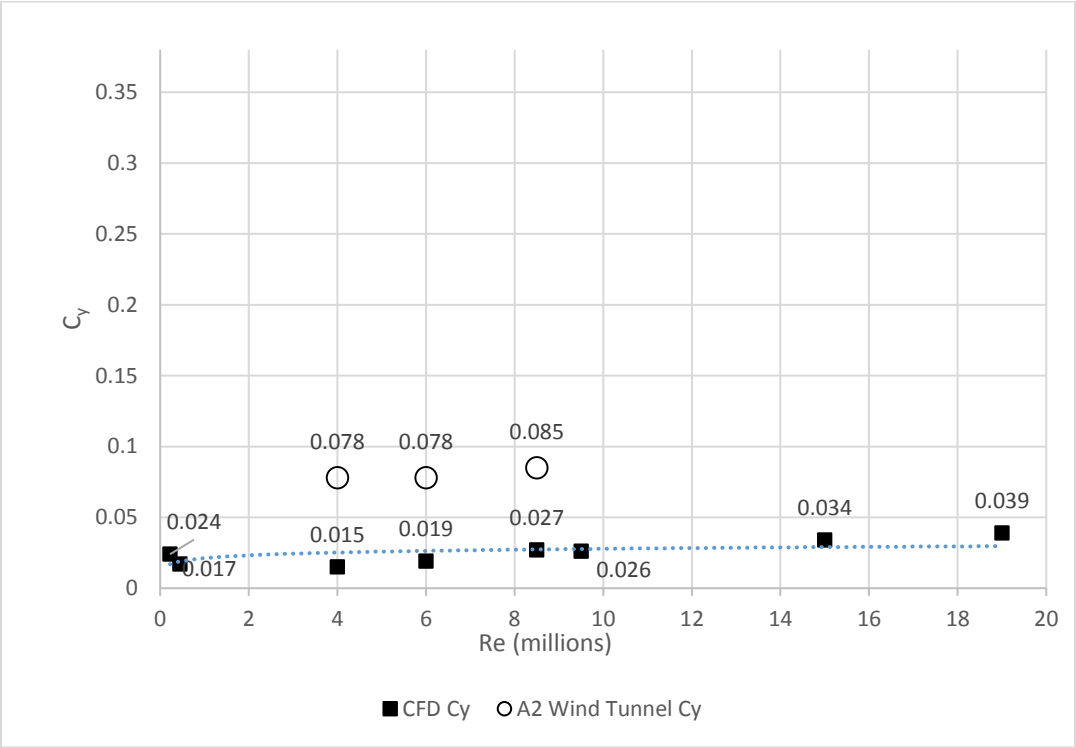

Figure 5.39- Lateral Force Coefficient (C_y) from CFD and A2 wind tunnel

As with the lift coefficients (Figure 5.38), the airflow over the full body in the wind tunnel produces a higher overall lateral force than is predicted by the CFD calculations. In this case, however the offset between wind tunnel and CFD data is consistent over the Re range of the wind tunnel tests. Note that in all cases these are small residual lateral coefficients and even at 85 mph (38 m/s) the residual force developed in the wind tunnel is only 74.4 N (7.6 kg). An imperfect zeroing of the lateral force at zero wind, or a slight misalignment of the sidecar body with the flow direction (either in the wind tunnel or alignment of the body on the chassis) would explain this offset. Still, this lateral force must be accounted for by the generation of a lateral force by the action of the tyres on the ground and thus a slight amount of yaw will be generated relative to the direction of travel in order to account for this residual asymmetrical force. This will be further discussed in Chapter 7.

5.13 Chapter Summary

Comparison of vehicle performance to a mathematical model, provides an ability to predict maximum speed performance of the Baker sidecar vehicle. The addition of a rolling resistance term to the mathematical model improves predictive capability for record attempts, specifically at Bonneville where the salt surface increases the rolling resistance coefficient compared to paved surfaces. Rolling resistance coefficients used to fit data in the current work match well to published values from other Bonneville record attempts.

The newly designed rear body section, windshield and front splitter were successfully used in a record attempt at the Bonneville Salt Flats: The result was two FIM World land speed records and one AMA National land speed record for unlimited partially streamlined electric sidecar motorcycles. Two additional FIM Word land speed records were set with the bodywork removed in the unstreamlined or naked electric sidecar class.

The measurement of drag on the full-scale A2 wind tunnel validates the general trends of drag force coefficients developed through CFD simulations using ANSYS Fluent for the modified Baker sidecar. Lift and lateral forces from the wind tunnel data are not as well matched to the CFD results, but as the forces are small the worst case still produces lift force values that are well under the vehicle mass and lateral forces within the anticipated ability of the vehicle tyres to counter these forces. Stability studies that consider dynamic effects through Equations of Motion and aerodynamic forces will be further investigated in Chapters 6 (symmetrical vehicles) and Chapter 7 (asymmetrical sidecar). The flow visualisation obtained through smoke studies in the A2 wind tunnel, although not a definitive test of fidelity, did match the flow visualisations of velocity streamlines and velocity vectors from ANSYS Fluent.

CHAPTER 6 SYMMETRICAL VEHICLE STABILITY

6.1 BACKGROUND

In this chapter, the dynamic and aerodynamic stability of four-wheel and two-wheel symmetrical vehicles will be examined to build tools that will be used for the examination of the stability of three-wheel asymmetrical vehicles in Chapter 7.

6.2 DYNAMIC STABILITY

6.2.1 Four-wheel stability

6.2.1.1 The bicycle model

A simplified way of looking at vehicle's lateral stability is to reduce the vehicle width until the front and rear tyres are both located at the centre line of the vehicle in the direction of travel (Figure 6.1). This is often called the "bicycle model." For a four-wheel vehicle, the result is a pair of front wheels and a pair of rear wheels located alongside the vehicle axis of symmetry along its centreline (Huston, Graves, & Johnston, 1982). The cornering stiffness for the two combined front tyres and for the two combined rear tyres is thus twice what it is for a single tyre.

6.2.1.2 Equations of Motion

The Equations of Motion governing the stability of a bicycle model vehicle can be derived by summing the lateral forces and the moments around the centre of mass of the vehicle. Huston et al., (1982) assumed that the lateral forces on the tyres "act perpendicular to the plane of the wheel directly below the wheel centre," that the steer angle is zero, that there are no braking, tractive, or rolling resistance forces, that the speed in the longitudinal x-direction is constant, and that all second order terms are much smaller than first order terms and can be neglected. Figure 6.1 is a free-body diagram of a four-wheel bicycle model used to examine the force and moments.

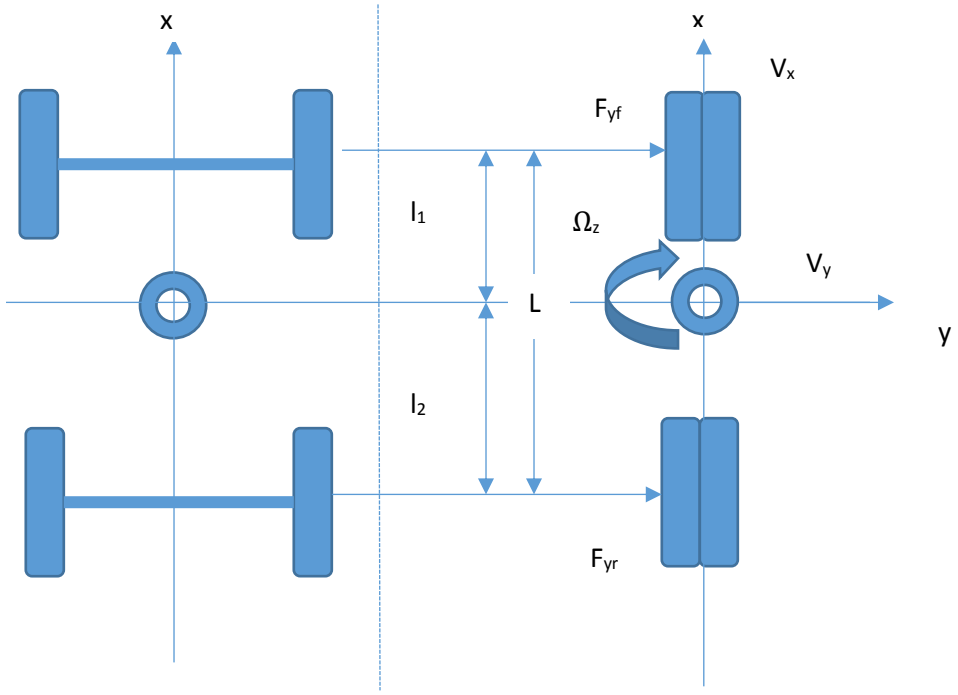

Figure 6.1- Four-wheel bicycle model

For the four-wheel bicycle, summing the lateral forces results in:

$$m\,(\dot{V}_y) + (m\mathrm{V_x} + \frac{2\,l_1\,C_{\alpha f} - 2\,l_2\,C_{\alpha r}}{Vx})\,\Omega_z + (\frac{2\,C_{\alpha f} + 2\,C_{\alpha r}}{Vx})\,V_y = 0 \qquad (6.1)$$

and, summing the moments around the z-axis (vertical) axis at the centre of mass:

$$\mathrm{I_z}\,(\dot{\Omega}_z) + (\frac{2\,{l_1}^2\,C_{\alpha f} - 2\,{l_2}^2\,C_{\alpha r}}{Vx})\,\Omega_z + (\frac{2\,l_1\,C_{\alpha f} - 2\,l_2\,C_{\alpha r}}{Vx})\,V_y = 0 \qquad (6.2)$$

where:

m = total mass of the vehicle

I_z = moment of inertia of the vehicle (with respect to vertical axis at centre of mass)

V_x = speed in x-direction

V_y = speed in y-direction

Ω_z = rotational (yaw) rate of the vehicle about the vertical axis

$\dot{V}_y$ = acceleration in the lateral direction

$\dot{\Omega}_z$ = the rate of change of the rotational (yaw) rate around the vertical axis

$C_{\alpha f}, C_{\alpha r}$ = the cornering stiffness of each individual front and rear tyre

l_1 = distance from centre of mass to front wheel

l_2 = distance from centre of mass to rear wheel

The above differential equations (6.1 and 6.2) are of the form:

$$a\lambda'' + b\lambda' + c\lambda = 0 \quad (6.3)$$

The solution to equation 6.3 can be re-written into exponential functions (Tseng, 2016). To do so, let $\lambda = e^{rt}$ be an assumed solution of the above equation, where r is a constant. With $\lambda' = re^{rt}$ and $\lambda'' = r^2e^{rt}$ this gives

$$ar^2e^{rt} + bre^{rt} + ce^{rt} = 0$$

$$e^{rt}(ar^2 + br + c) = 0$$

Because e^{rt} is never equal to zero, $\lambda = e^{rt}$ is a solution to the differential equation (6.3) if and only if the quadratic polynomial $ar^2 + br + c = 0$ equals zero (Tseng, 2016). This polynomial is called the *characteristic equation* of the differential equation (6.3) and has three possible cases of solution:

1. If $b^2 - 4ac > 0$ there will be two distinct real roots, r_1 and r_2
2. If $b^2 - 4ac < 0$ there will be two complex conjugate roots $r = \lambda \pm \mu i$
3. If $b^2 - 4ac = 0$ there is one repeat root r

Huston et al., (1982) wrote the characteristic equation for the four-wheel bicycle-model case, including lateral force and torque as:

$$\lambda^2 + \left(\frac{b1}{m} + \frac{b4}{Iz}\right)\lambda + \left(\frac{b1b4 - b2b3}{Iz\, m}\right) = 0 \quad (6.4)$$

where:

$$b_1 = \frac{2\,C_{\alpha f} + 2\,C_{\alpha r}}{Vx} \quad (6.5)$$

$$b_2 = mV_x + \frac{2\,l_1\,C_{\alpha f} - 2\,l_2\,C_{\alpha r}}{Vx} \quad (6.6)$$

$$b_3 = \frac{2\,l_1\,C_{\alpha f} - 2\,l_2\,C_{\alpha r}}{Vx} \quad (6.7)$$

$$b_4 = \frac{2\,{l_1}^2\,C_{\alpha f} - 2\,{l_2}^2\,C_{\alpha r}}{Vx} \quad (6.8)$$

Huston et al., (1982) stated that, "To ensure lateral stability for the four-wheeled vehicle, the roots of the characteristic equations of the above differential equations must be negative" (p.47).

Rather than solve for the roots, Huston et al., (1982) noted, "One requirement, which is a necessary but not a sufficient condition for stability, is that all of the coefficients of the

characteristic equation be positive" (p.47). Further, using the Routh-Hurwitz criterion, Huston et al., (1982) stated that positive coefficients are a sufficient condition for stability when the characteristic equation is quadratic (p. 47).

Because the coefficient of the second order term is greater than zero (and equal to 1), and the coefficient of the first order term is always positive, the only term that can be less than or equal to zero is the zeroth-order term.

Thus, the criteria for stability can be written as:

$$(\frac{b1b4-b2b3}{Iz\ m}) > 0 \qquad (6.9)$$

As long as this coefficient is greater than zero, the vehicle will be directionally stable. Note that this criteria for lateral stability depends only upon the cornering stiffness of the tyres, the length of the wheelbase ($l_1 + l_2$), and the position of the vehicle centre of mass.

Using the bicycle model, Huston et al., (1982) found that lateral stability placed conditions on the weight distribution on the front and rear tyres.

For a four-wheel vehicle:

$$W_f = \frac{W\ l_2}{2L} \text{ and } W_r = \frac{W\ l_1}{2L}$$

For a constant radius corner, Starr (2006) wrote the relationship for vehicle stability as:

$$L/R + \frac{Vx^2}{gR}(\frac{W_f}{C_{\propto f}} - \frac{W_r}{C_{\propto r}}) = \delta \qquad (6.10)$$

where

L	= the total distance between the front and rear axles ($l_1 + l_2$) or the wheelbase
g	= the gravitational constant
W_f, W_r	= the load on each of the front and rear tyres respectively
δ	= the steering angle of the front wheel(s)
R	=the radius of the curve

The above equation can be re-written with K_{us} as the understeer coefficient (sometimes called understeer gradient) from:

$$K_{us} = (\frac{W_f}{C_{\propto f}} - \frac{W_r}{C_{\propto r}}) \qquad (6.11)$$

and from $$a_y = \frac{{V_x}^2}{gR} \qquad (6.12)$$

to give: $$\delta = \frac{L}{R} + K_{us}\, a_y \quad (6.13)$$

From equation (6.13), if K_{us} is negative, there is a value for a_y for which $\delta = 0$. The speed at which $\delta = 0$ can be calculated from equation (6.12) and at this speed the vehicle becomes unstable—this is called the *critical speed* (Huston et al., 1982) and is calculated from:

$$V_{crit} = \sqrt{\frac{gL}{Kus}} \quad (6.14)$$

From the relationship of cornering stiffness for each tyre C_α, and tyre normal load (W_t), given by:

$$C_\alpha = (A - BW_t)\, W_t \quad (6.15)$$

Where *A* and *B* are constants that depend upon the tyre properties and are found experimentally. The definition of the understeer coefficient, K_{us}, can be re-written as (Huston et al., 1982):

$$K_{us} = \frac{W_f}{C_{\propto f}} - \frac{W_r}{C_{\propto r}} = \frac{BW(l_2 - l_1)}{2L(A - BW_f)(A - BW_r)} \quad (6.16)$$

From Equation 6.14 and 6.16, lateral stability of a four-wheel vehicle is ensured if the centre of mass of the vehicle is located in the front-half of the vehicle, or:

$$l_2 \geq l_1 \qquad \text{or} \qquad l_2 \geq \frac{L}{2}$$

6.2.2 Ahmed body as a generic vehicle

For this chapter, an Ahmed body was chosen to establish a baseline for a simulated symmetrical vehicle. Recall from Chapter 3, the Ahmed body is a simplified vehicle geometry designed primarily to study aerodynamic flow, particularly in the wake regions behind it (Ahmed, Ramm, & Faltin, 1984). Numerous investigations have been performed in both wind tunnels and using CFD and the values of forces and pressure are well established under a variety of test conditions (see Chapter 3).

The Ahmed body has a rounded front section, a slanted rear plane at the rear, and a rectangular box that connects the front and rear. In this study, the 25° Ahmed body was chosen to promote flow separation at the rear of the vehicle in the later aerodynamic stability studies. Four small round legs protrude from the bottom of the box, analogous to wheels. The standard wind tunnel Ahmed body is 0.389 metres wide, 0.288 metres high, 1.044 metres long, and has a "wheelbase" of 0.470 metres and a projected frontal area of 0.115 m^2 at zero degrees of yaw (Figure 6.2).

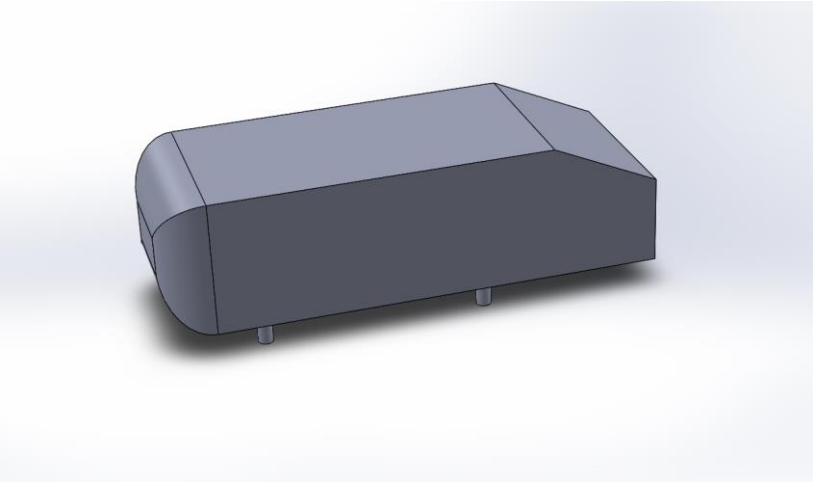

Figure 6.2- Ahmed body with 25° rear slant

Because an Ahmed body was originally designed for scale wind tunnel work, it is significantly smaller than an actual road vehicle. To be more realistic as a generic vehicle for vehicle dynamics studies, and to provide realistic Reynolds Number comparisons to the full-scale sidecar, the Ahmed body was scaled up by a factor of 4, resulting in a width of 1.556 m, a height of 1.152 m, a length of 4.176 m, a wheelbase of 1.880 m and a frontal area of 1.842 m^2. In this work, the scaled-up version will be referred to as the ““scale 4 Ahmed” body.” The Ahmed body was assumed to have uniform density and its centre of mass was defined to be at the geometric centre of the Ahmed body for this stability calculation.

6.2.2.1 Ahmed Equations of Motion

The dynamic stability of the Ahmed body can be calculated from the Equations of Motion that describe the sum of the lateral forces and moments around the centre of mass for a four-wheel vehicle as previously described (equation 6.9). The vehicle will be directionally stable when the term on the left is greater than zero.

To calculate the $b_1,\ b_2,\ b_3$, and b_4 terms, a value for the tyre cornering stiffness is required. For simplicity, the cornering stiffness of tyres similar to those used on the Baker sidecar will be used for this generic four-wheel vehicle dynamic stability study.

The tyres on the Baker sidecar are 245/50R13 Toyo RA1 radials. These ultra-performance tyres are designed for track use on small, lightweight sports cars. It is difficult to obtain accurate cornering stiffness data from tyre manufacturers (such information is considered proprietary). This is particularly true for performance tyres with the high level of inflation pressure (40 psi) used on the sidecar during land speed record attempts. Fortunately, data was found for a 13-inch radial front Formula One tyre, inflated to 38 psi, in a paper by Kasprzak, Lewis, and Milliken, (Kasprzak, Lewis, & Milliken, 2006). The Formula One tyre dimensions (width, diameter, sidewall height, rim diameter) are similar to the Toyo tyres used on the sidecar which also shares the same radial construction. The data from the Formula One tyre was used to create a second-order

polynomial relationship between tyre load and cornering stiffness at a high inflation pressure Figure 6.3, where x is the vertical tyre load (W_t) and y is the cornering stiffness (C_α).

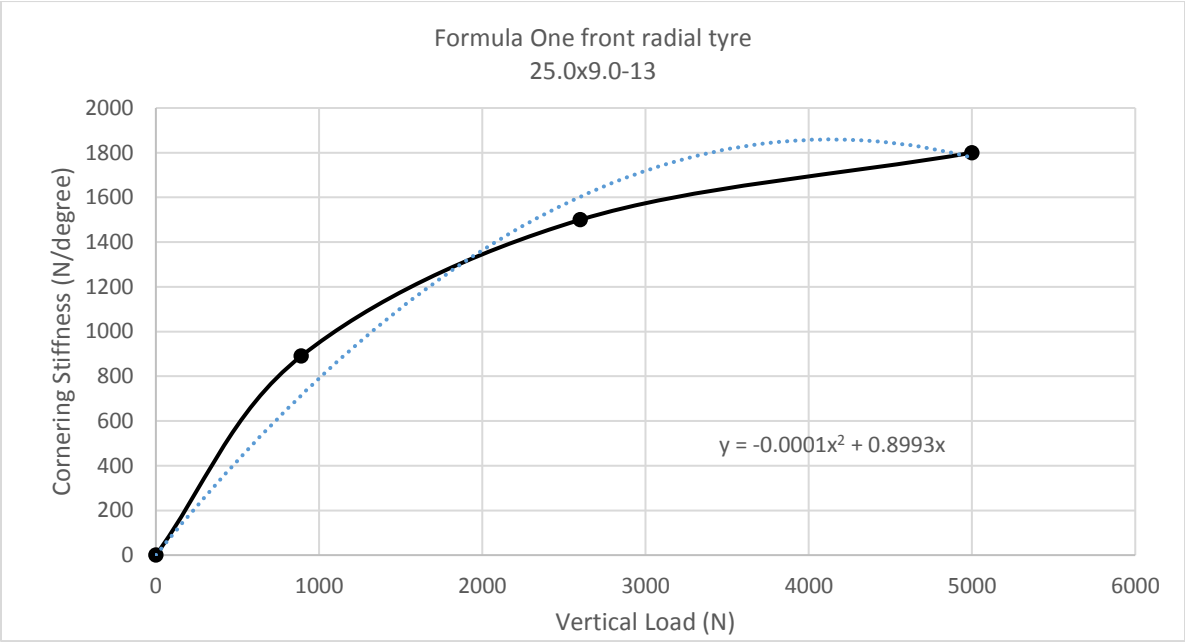

Figure 6.3- Tyre load versus cornering stiffness for high performance radial tyre

This relationship, $C_\alpha = (A_T - B_T W_t) * W * 57.3$, where $A_T = 0.899$, $B_T = .0001$ and W_t equals the tyre vertical force in N, gives the cornering stiffness in N/rad and is accurate for the range of tyre normal forces of the sidecar. This relationship was applied to generate the cornering stiffness of the tyres on the generic "scale 4 Ahmed" body vehicle.

Using the dimensions of the "scale 4 Ahmed" body, the cornering stiffness of the sidecar tyres and a total mass of 220 kg (simulating a 150-kg class vehicle with rider and ballast), it is possible to calculate the moment of inertia (I_z) around the vertical axis and apply this to the above equations to plot the stability criteria (zeroth coefficient of the characteristic equation) versus velocity in the longitudinal direction. A MATLAB program was written for the four-wheel "scale 4 Ahmed" body, based on the analysis technique described by Huston et al., (1982) and the results are plotted for the Routh-Hurwitz stability criteria (the zeroth order coefficient = $(\frac{b1b4-b2b3}{Iz\ m})$) versus vehicle velocity in Figure 6.4.

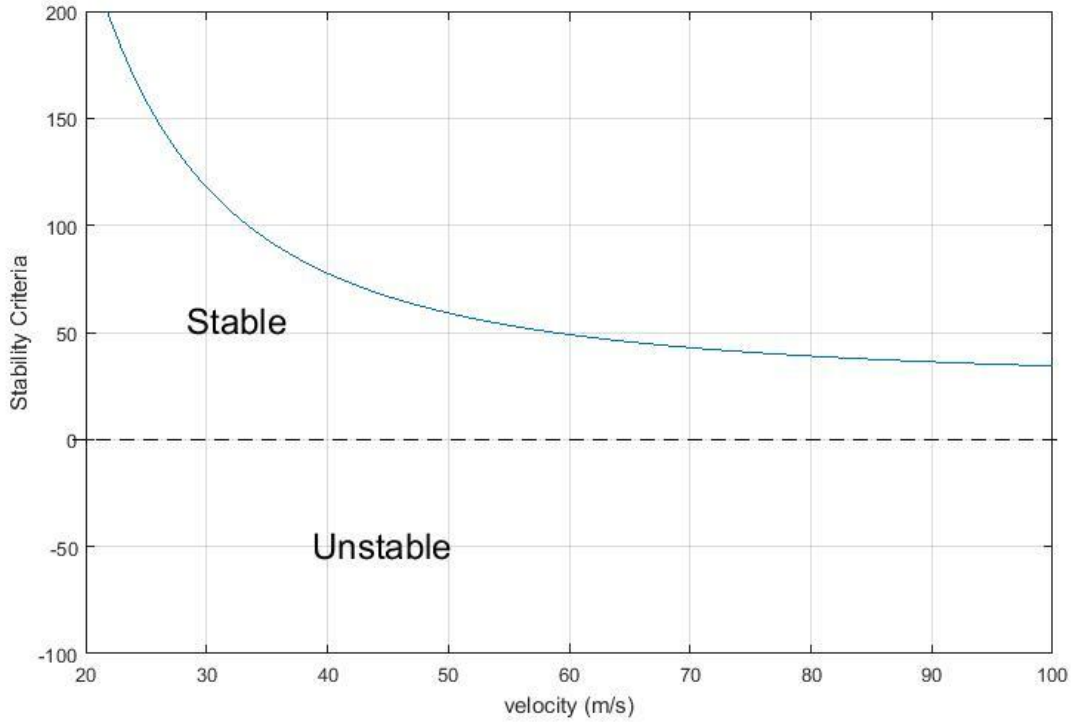

Figure 6.4- Dynamic stability of “scale 4 Ahmed” body from Equations of Motion

From Figure 6.4 the four-wheel vehicle represented by the “scale 4 Ahmed” body is dynamically stable at speeds up to and over 100 m/s.

6.3 Aerodynamic stability

The ideal case for a land speed record vehicle is to travel in a straight line, without side winds or road surface perturbations to cause yaw. Despite the best efforts to produce smooth track surfaces, and rules that prohibit the fastest vehicles from making record attempts with crosswinds higher than four miles per hour, side forces are non-zero and yaw, pitch, and roll moments must be examined when considering land speed record vehicle stability.

A vehicle exhibiting symmetry about its longitudinal axis produces no lateral force at zero yaw angle, as the forces generated by the airflow on each side of the vehicle symmetry axis are equal. When a vehicle rotates about the centre of mass through a yaw angle (Ø) however, the differences between airflow on each side creates a differential pressure resulting in the generation of a lateral force. For symmetrical vehicles, the magnitude of the lateral force is identical for corresponding positive and negative yaw angles, but, as with an asymmetrical cambered wing tilting through positive and negative angles of attack, an asymmetrically shaped vehicle geometry can be expected to generate forces that differ in magnitude if Ø is positive or negative.

6.3.1 Effect of ambient cross wind

The presence of an ambient wind aligned at an angle to the direction of travel means symmetrical vehicles often operate with a heading that is not perfectly aligned with the direction of travel (Hucho & Sovran, 1993). Hucho et al., (1993) pointed out that the angle of yaw created by a cross wind increases the aerodynamic drag in the direction opposite the direction of travel, although noted that maximum yaw angles were typically less than 10°, except during wind gusts.

During the development of the (symmetrical) JCB DIESELMAX land speed record vehicle, Lock (Lock, 2007) performed yaw and sideslip studies on the final design iteration of the streamliner vehicle. Using CFD (ANSYS Fluent V6.3), 3° of yaw and 3° and 10° of sideslip were examined. It was noted that 3° of either yaw or sideslip "exhibited near identical behaviour" with respect to an increase in drag and a reduction in downforce (negative lift). The yaw moment coefficient (=0.008) and the rolling moment coefficient (= -0.024) of this symmetrical land speed record vehicle were both judged to be low, and in the case of the yaw moment, restorative.

The effect of cross winds on an ordinary road vehicle is tested by automakers, typically by placing large fans perpendicular to the vehicle direction of travel on a test track. The most common method of simulating lateral winds with a wind tunnel or through CFD is to place the vehicle in the tunnel, or within the CFD computational domain, at a yaw angle (Ø, to the incoming air flow (William, Mohamed, & Oraby, 2013). The cross wind generated can then be easily calculated as $V_y = V_x \tan Ø$, where V_x is the longitudinal yaw velocity and V_y is the lateral cross wind velocity.

Although the goal is to investigate the effects of yaw and cross winds on a three-wheel asymmetrical sidecar, first the analysis of a four-wheel generic symmetrical vehicle was undertaken to better understand its requirements for aerodynamic stability.

6.3.2 Yaw studies

In aerodynamic studies, it is common to characterize the performance of (often asymmetrical) two-dimensional and three-dimensional wings and wing profiles by sweeping them through a range of positive and negative pitch angles and examining lift and drag forces. In an analogous way, the characteristics of airflow over three-dimensional land vehicles can be examined by sweeping the vehicle through a range of positive and negative Ø, comparing the drag, lift, lateral force and yaw moment generation (Hucho & Sovran, 1993).

6.3.3 Ahmed frontal area

Before considering the drag, lift and lateral forces generated using CFD, it is useful to examine the change in the projected frontal area of the "scale 4 Ahmed" body with changes in Ø. The projected frontal area (m^2) was determined using the Reports → Projected Area → Min Element size (→ .0001 m) function of ANSYS Fluent and is reported in Figure 6.5. It is evident that the "scale 4 Ahmed" body is geometrically symmetrical from the perspective of the projected frontal area.

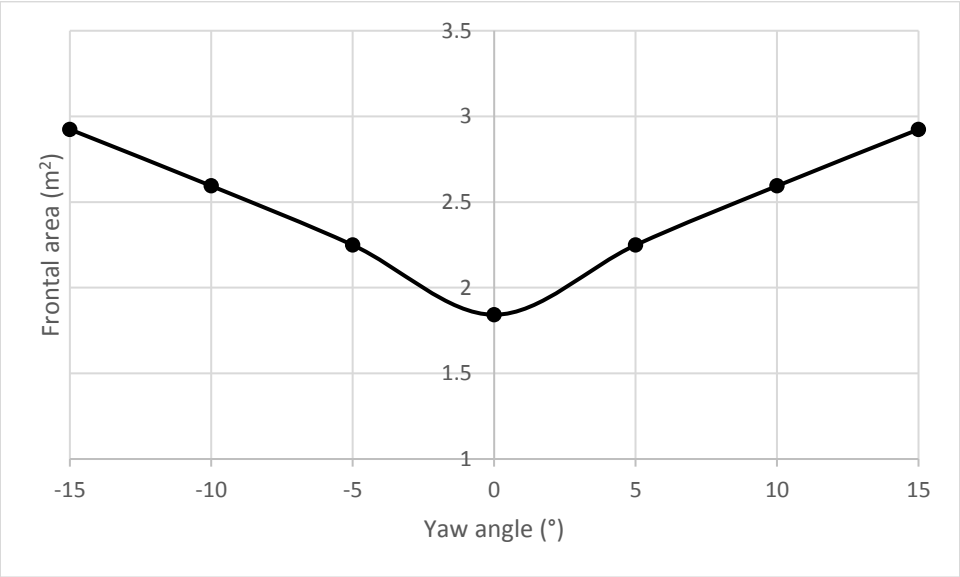

Figure 6.5- "Scale 4 Ahmed" body frontal area (A) versus yaw angle

6.3.4 Ahmed aerodynamic forces

The standard Ahmed body frame of reference has the y-axis vertical, the z-axis lateral and the x-axis longitudinal, and this convention was maintained in this study. The C_d, is calculated using Eqn. 6.17:

$$C_d = \frac{2 \cdot F_x}{V_x^2 \cdot A \cdot \rho} \tag{6.17}$$

Where F_x is the component of aerodynamic force along the x-axis, V_x is the freestream velocity, A the projected frontal area and ρ the air density. Similarly, a lift coefficient, C_l, can be calculated using the F_y forces:

$$C_l = \frac{2 \cdot F_y}{V_x^2 \cdot A \cdot \rho} \tag{6.18}$$

A computational domain enclosure consisting of a velocity inlet, a pressure outlet, three no-slip smooth walls and a smooth stationary floor was constructed surrounding the "scale 4 Ahmed" body. The walls were two body widths away, the velocity inlet was one and a half body lengths ahead of the model and outlet was five body lengths away from the vehicle to reduce any vehicle/wall interactions. The vehicle was suspended in space 0.005 meters above the road surface. Airflow was assumed to be incompressible and non-turbulent upstream.

Meshing of the "scale 4 Ahmed" body was performed using ANSYS Fluent 17.0. The initial mesh was chosen to have a moderate level of refinement (minimum cell size 0.15 m, maximum cell size 0.3 m). Two wake boxes, each the length of the Ahmed body with a refined mesh (cell size 0.05 m) consisting primarily of tetrahedral elements were positioned, one over the Ahmed body and

the other behind the tail section to accurately capture the wake topology behind and above the bluff body. Five prismatic inflation layers were meshed over the surface of the Ahmed body, with a first layer thickness of 0.001 m and an inflation growth ratio of 1.20. This resulted in a mesh of 4.3 million primarily tetrahedral elements with a y+ value of 80. This mesh and y+ is consistent with a good initial mesh size for a vehicle study using the k-ω SST turbulence model (Lanfrit, 2005). This mesh is shown in Figure 6.6.

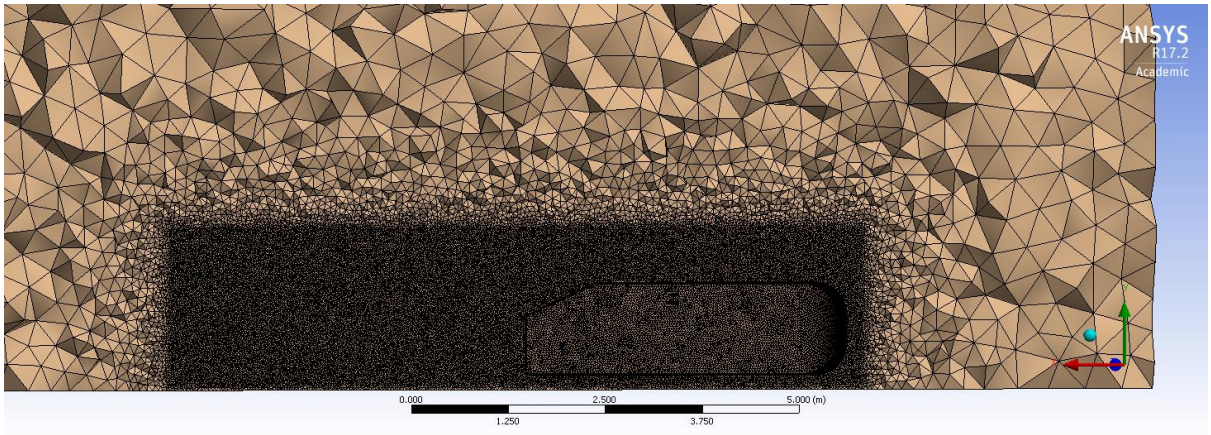

Figure 6.6- "Scale 4 Ahmed" body meshing

Flow around the "scale 4 Ahmed" body at a velocity of 67 m/s was simulated at Ø of 0°, positive and negative 5°, 10° and 15° with a moving road surface (also at 67 m/s). Simulation was performed with a *k*-ω SST turbulence model with a turbulence intensity of 5%.

C_d with Ø for the "scale 4 Ahmed" body are plotted in Figure 6.7. It is shown that the C_d generated by the "scale 4 Ahmed" body is symmetrical for -15° < Ø < 15°.

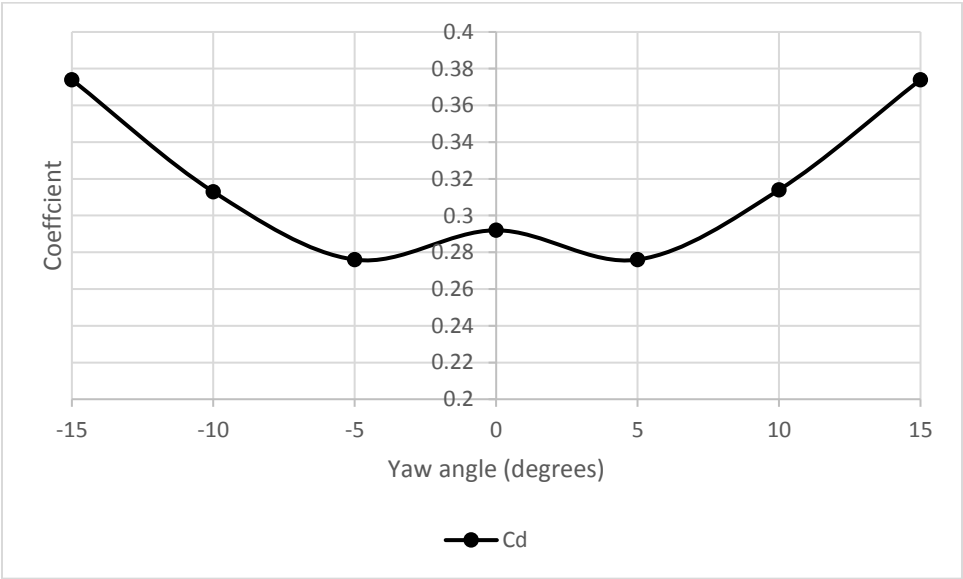

Figure 6.7- "Scale 4 Ahmed" body drag coefficient versus Ø

6.3.4.1 Ahmed drag with yaw

Figure 6.5 indicated that A also changes with changing Ø. This brings up the question whether the effect of yaw on drag should be examined using the C_d, or $C_d A$, which normalizes the drag by A. Figure 6.8 compares C_d versus $C_d A$ for the "scale 4 Ahmed" body at 67 m/s with a moving road surface for -15° < Ø < 15°.

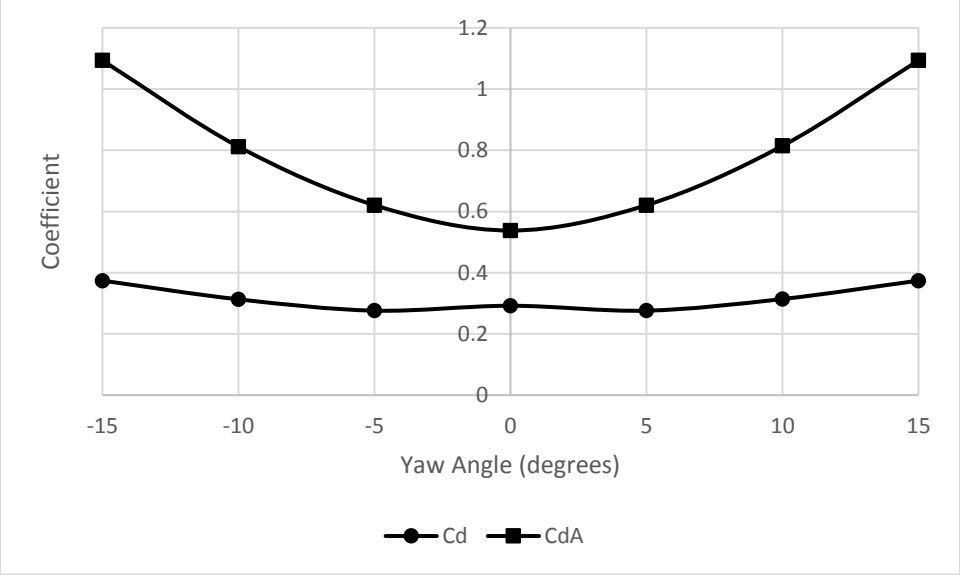

Figure 6.8- Comparison of C_d versus $C_d A$ for the "scale 4 Ahmed" body over range of Ø

It is evident that the majority of the change in C_d with change in Ø is due to the change in A presented to the airflow by the Ahmed body as it is yawed. The plot of C_d and $C_d A$ with Ø can be used to characterize the aerodynamic shape of the body of an object and how it interacts with the airflow. The behaviour of C_d with Ø is more complex than $C_d A$ (C_d has a local maximum at 0°). This complexity is negated in $C_d A$ by the shape of the A vs Ø curve (see Figure 6.5 and the change of gradient near 0°). As $C_d A$ is a smooth curve, this local maximum in C_d is of no relevance to the road forces experienced by the vehicle.

The pressure and viscous drag forces generated by the "scale 4 Ahmed" body are plotted versus Ø in Figure 6.9. As expected, pressure drag dominates (~87% of the total drag at 0^o), as the Ahmed is a bluff body. The pressure drag is dependent on frontal area, which increases with increasing Ø (Figure 6.5).

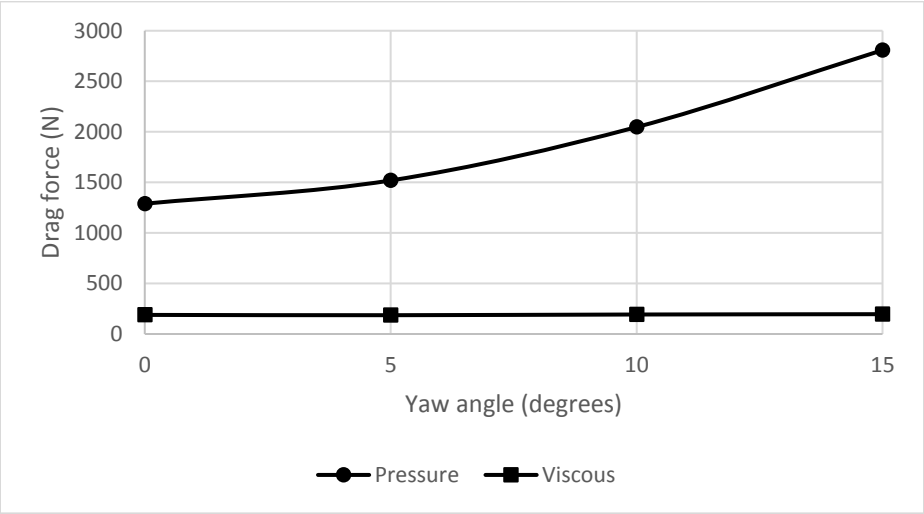

Figure 6.9- Pressure and viscous drag forces for "scale 4 Ahmed" body

The change in the flow characteristics over the yawed "scale 4 Ahmed" body were further investigated by plotting the difference in longitudinal force from that generated at Ø = 0°, versus the change in A compared to A at Ø = 0°. This is plotted in Figure 6.10. Also plotted in Figure 6.10 is the change in longitudinal force that would result if the C_d remained constant as Ø changes and equal to the pressure-only C_d at Ø = 0°.

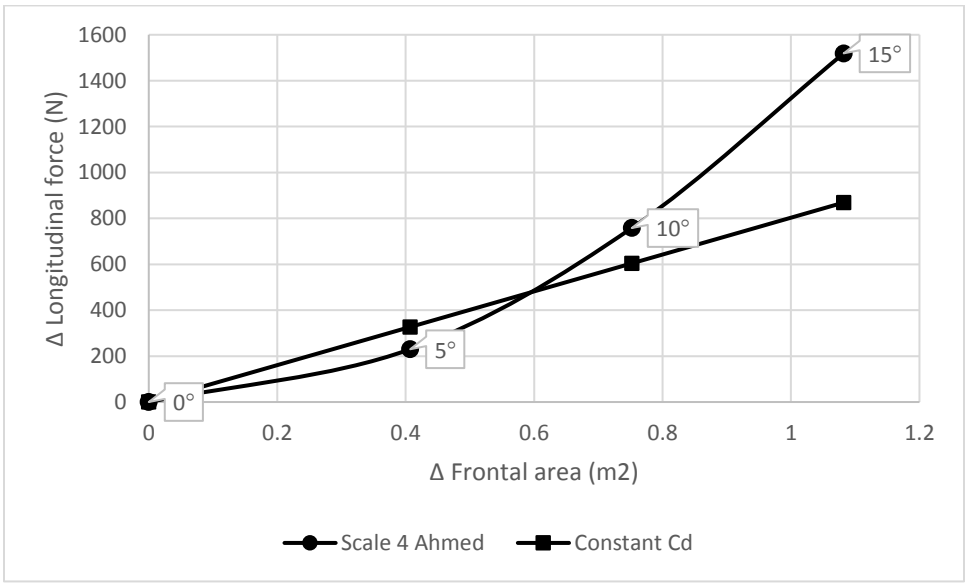

Figure 6.10- Change in drag force due to body shape change with change in Ø

The constant C_d curve indicates the linear effect of simply changing A with no change in the C_d due to changes in Ø over the 15° range. The "scale 4 Ahmed" curve in Figure 6.10 indicates how the change in body shape presented to the airflow with change in Ø increases the drag forces beyond simply changing the frontal area (A). If C_d did not rise with Ø, drag at greater than 7.5° would be less and would follow the constant C_d curve. Note that because of the need to seat

passengers and package the drivetrain and wheels, the vehicle designer has little ability to affect the change in A with changes Ø, however the body shape that the vehicle presents to the airflow has an effect as Ø increases and should be a consideration to the vehicle designer.

In Figure 6.11, contour plots of velocity, velocity vectors and turbulence kinetic energy are provided for the "scale 4 Ahmed" body at 67 m/s with a moving roadway at an Ø of 0°. The contours are plotted on a plane that is parallel to the road surface and that is located just below the junction of the rear 25° slanted deck and the vertical tail. Turbulence kinetic energy (Figure 6.10c) is the kinetic energy per unit mass that is associated with fluctuations in turbulent flow. From Figures 6.11 a, b, and c, it is evident that at least two largely symmetrical vortices form in the wake region of this bluff body (See Chapter 3). Because these vortices are symmetrical, they should have no effect on the directional stability of the vehicle when it is traveling at Ø = 0°.

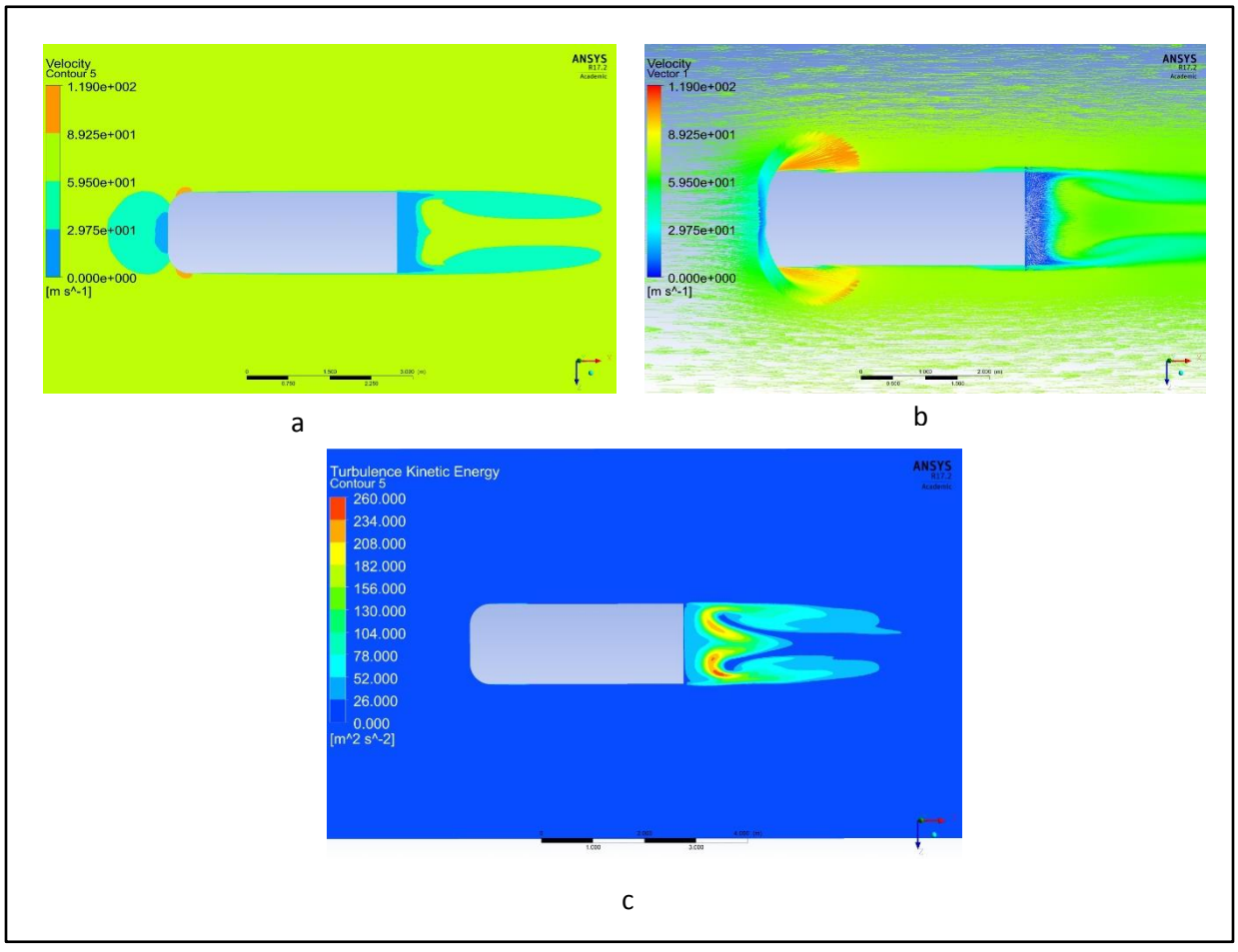

Figure 6.11- "Scale 4 Ahmed" body (67 m/s) at Ø = 0°: (a) Velocity contour, (b) Velocity vectors, (c) Turbulence kinetic energy

Figure 6.12 presents the same plots for the "scale 4 Ahmed" body at Ø = 5°. The asymmetry of flow is immediately obvious in the velocity contour (a) and velocity vector (b) and a dominant vortex forms on the upwind edge of the tail section, as evidenced from the turbulence kinetic

energy plot (c). The asymmetry of air flow over the body, caused by Ø, results in a lateral aerodynamic force that must be countered by the tyres. Their ability to do so at a low value of Ø should not be a problem.

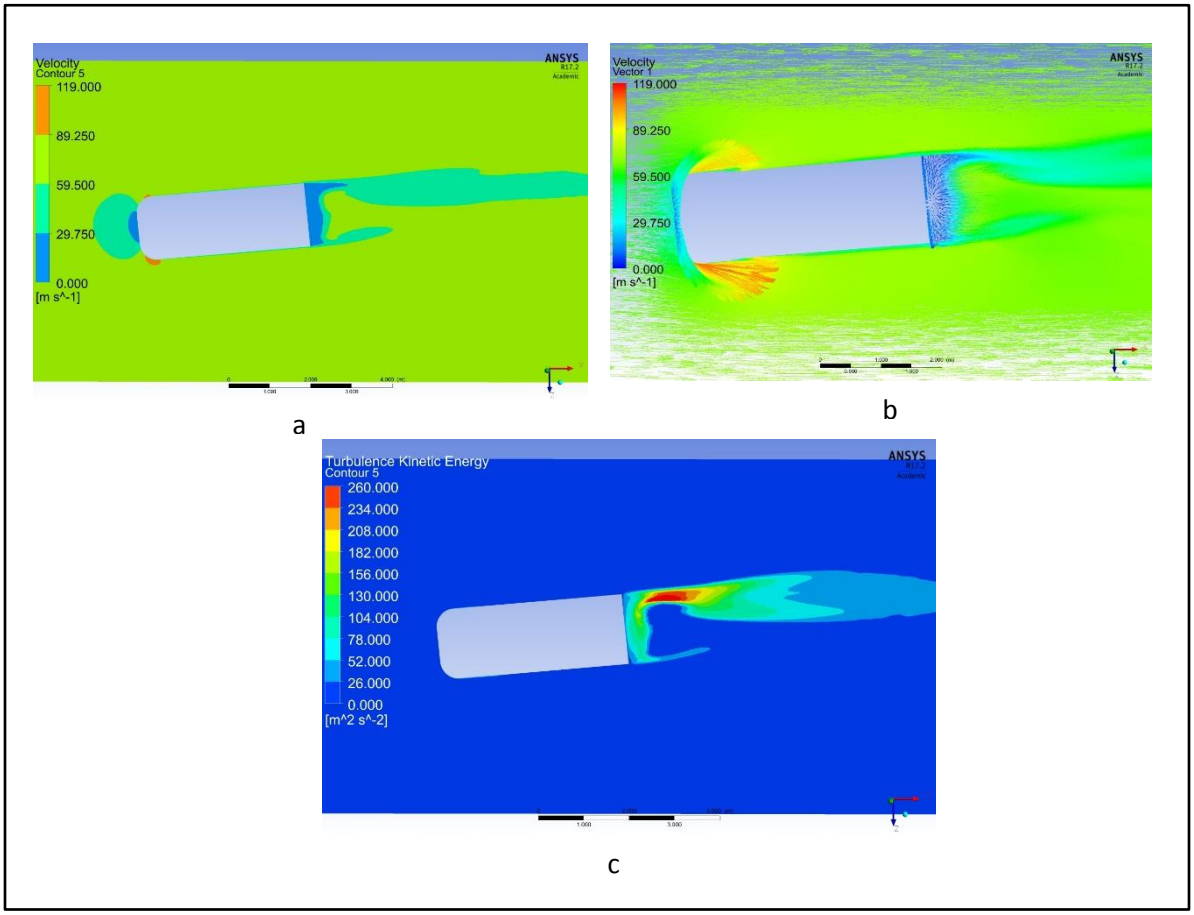

Figure 6.12- "Scale 4 Ahmed" body (67 m/s) at Ø = 5°: (a) Velocity contour, (b) Velocity vectors, (c) Turbulence kinetic energy

In Figure 6.13, where the Ø has been increased to 10°, in all three plots (a, b, c) the increased strength of the vortex in the wake from the upwind tail region is evident.

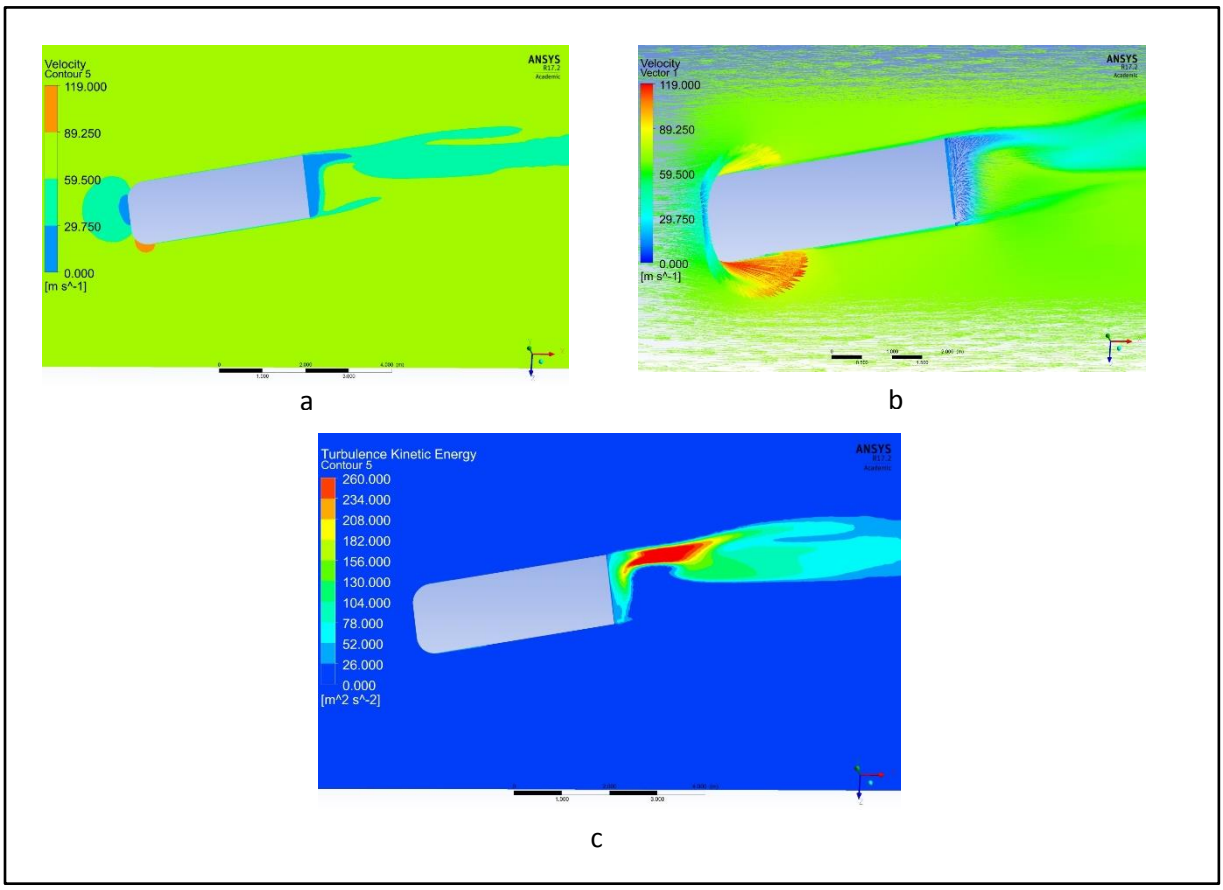

Figure 6.13- "Scale 4 Ahmed" body (67 m/s) at Ø = 10°: (a) Velocity contour (b) Velocity vectors (c) Turbulence kinetic energy

The vortices forming on the "scale 4 Ahmed" body at Ø = 10° can be further visualised from the velocity vortex core plot in Figure 6.14.

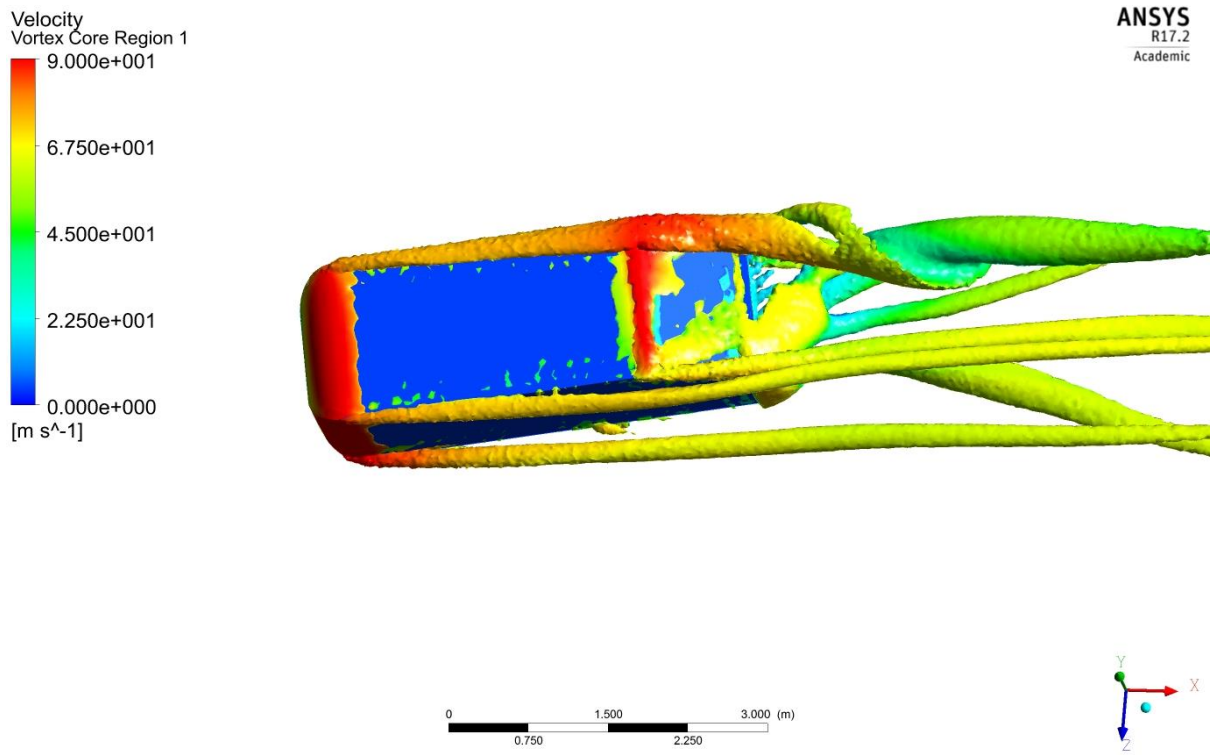

Figure 6.14- Velocity vortex core for "scale 4 Ahmed" body at Ø = 10°

From Figure 6.14, it is evident that 10° yaw results in a stronger streamwise vortex forming along the upwind side as well as the formation of streamwise vortices from the corners of the front of the Ahmed body. This is in contrast to the Ø = 0° case from Chapter 3 where the streamwise vortices were symmetrical and originated at the upper edges of the C-pillars along the edges of the backlight.

The increased strength of the upwind side vortex is further reflected in Figure 6.15, where the Ø has been increased to 15°.

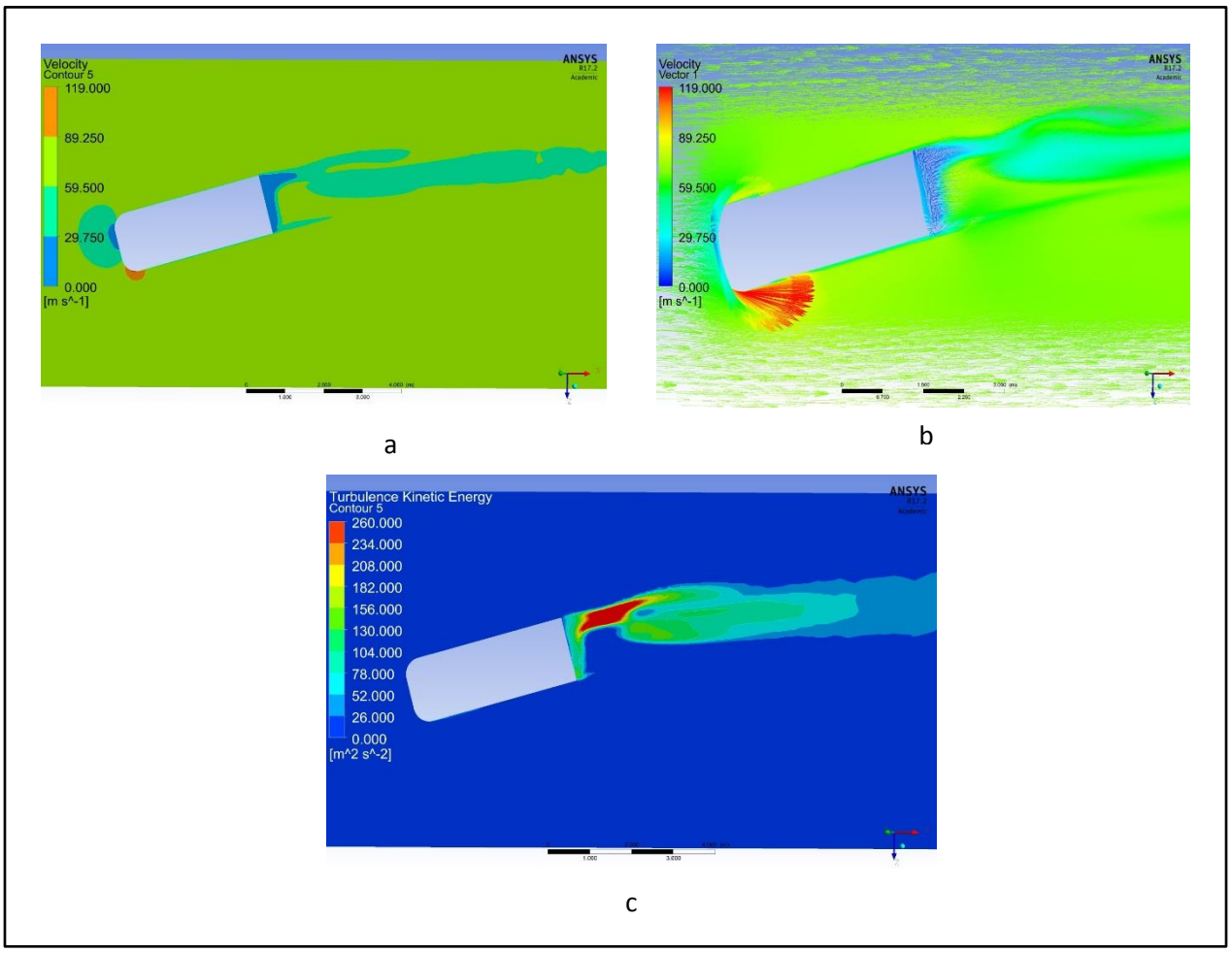

Figure 6.15- "Scale 4 Ahmed" body (67 m/s) at Ø = 15°: (a) Velocity contour, (b) Velocity vectors, (c) Turbulence kinetic energy

The increasing strength of the vortex that forms in the wake, with increasing Ø, as evidenced in Figures 6.11-6.15 matches well to the increase in longitudinal pressure drag force with change in Ø, (Figure 6.4). At this higher Ø, the lateral aerodynamic forces generated may begin to require action on the part of the vehicle operator to maintain path and heading stability. This will be further explored in Chapter 7.

6.3.4.2 Aerodynamic lift

In Figure 6.16 the viscous and pressure contributions to the lift force with change in Ø are plotted and it is shown that viscous lift is negligible.

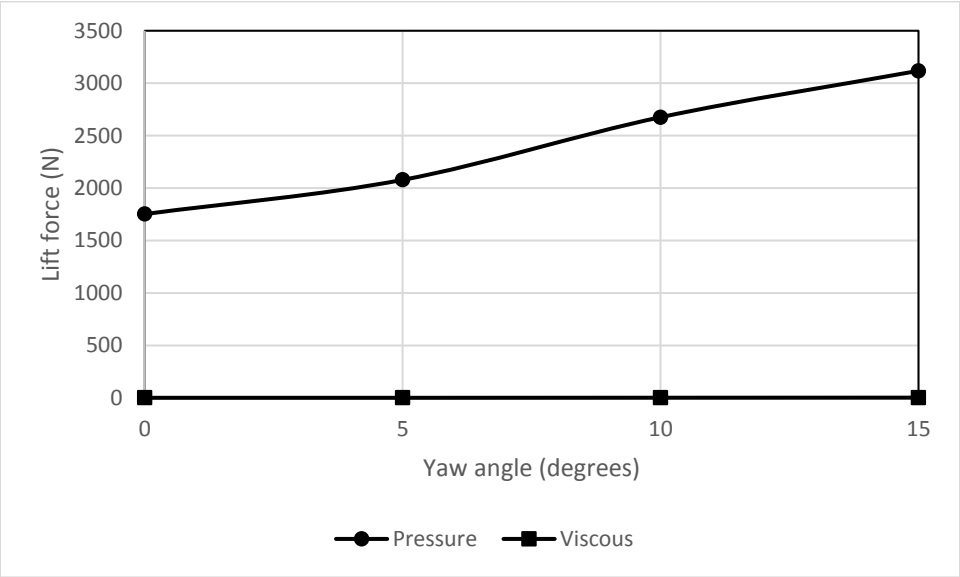

Figure 6.16- "Scale 4 Ahmed" body (67 m/s): pressure and viscous aerodynamic lift force versus Ø

The increase in pressure lift with increasing Ø indicated in Figure 6.16 can be associated with the static pressure distribution on the surface of the "scale 4 Ahmed" body. In Figure 6.17, the distribution shows an increasing amount of negative (upward) pressure on the top surface of the "scale 4 Ahmed" body with increasing Ø from 0° to 15°. The static pressure distribution on the bottom surface stays relatively constant over this Ø range and the lift observed is a result of the lower pressure on the top surface.

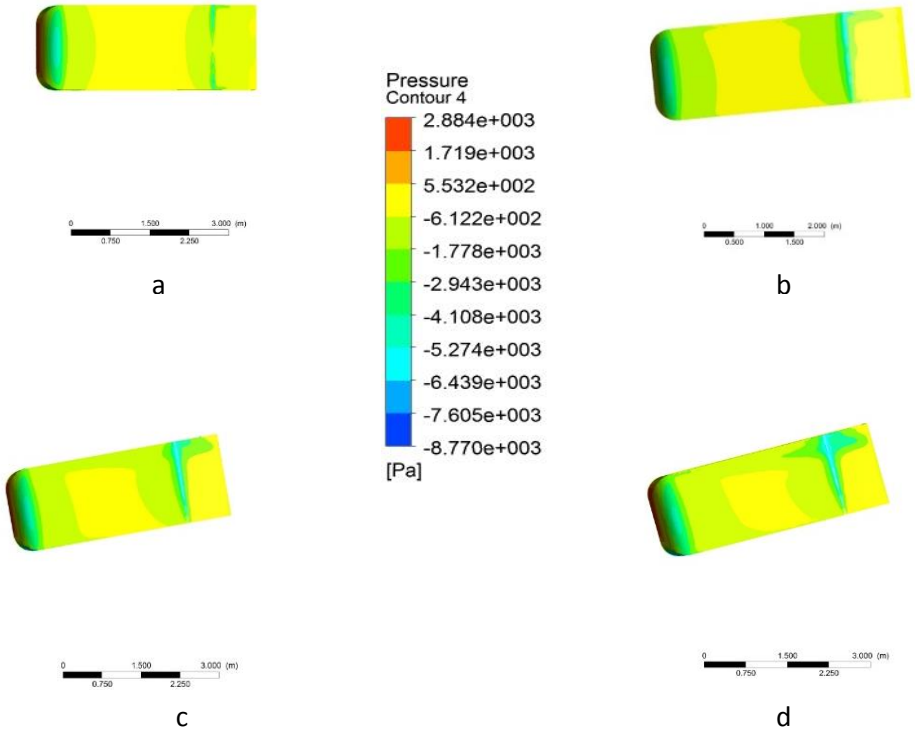

Figure 6.17 Static pressure distribution on the top surface of a "scale 4 Ahmed" body (67 m/s) with Ø of (a) 0°, (b) 5°, (c) 10°, and (d) 15°

As with aerodynamic drag forces (Figure 6.10), the body shape that the vehicle presents to the air flow can have an effect on the amount of lift force generated. Figure 6.18 shows the effect of the change in body shape, independent of change in A. The constant C_l curve indicates the linear effect of simply changing A with no change in the C_l due to changes in Ø. The "scale 4 Ahmed" curve in Figure 6.18 indicates how the change in body shape presented to the airflow with change in Ø increases the lift forces beyond simply changing the A. Because of the need to seat passengers and package the drivetrain and wheels, the vehicle designer has little ability to affect the change in A with changes in Ø, however the body shape that the vehicle presents to the airflow has an ever-increasing effect on lift forces as Ø increases and should be a stability concern to the vehicle designer. Packaging requirements may change as automated vehicles become more prevalent.

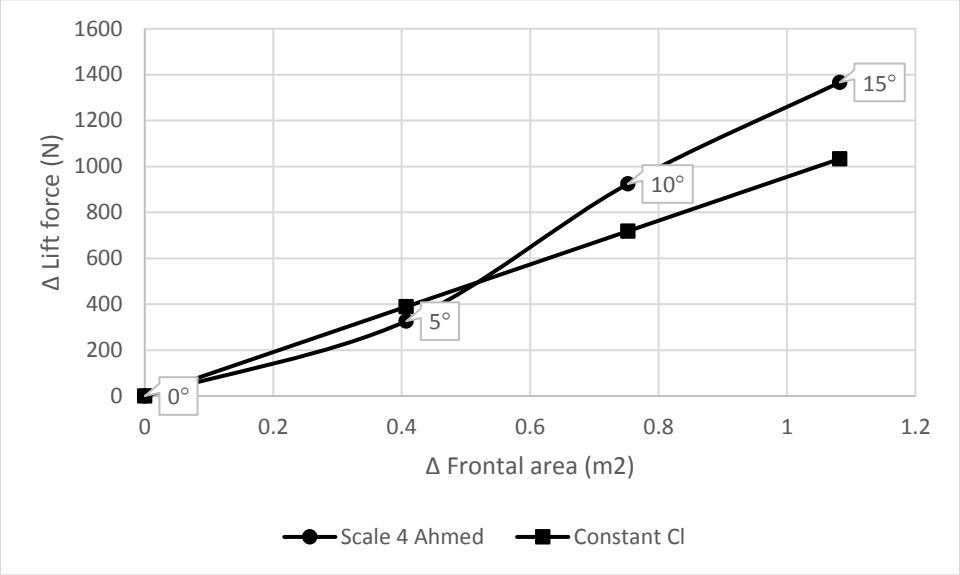

Figure 6.18- Change in lift force due to shape change with change in Ø

6.3.4.3 Large yaw angles

For a vehicle travelling at high speed (67 m/s or 150 mph), a small Ø (≤ 5°) can create a crosswind of sufficient magnitude to affect stability. Hucho, et al. (1993) notes that a Ø of greater than 10° is uncommon, except during wind gusts. Larger Ø are possible, particularly in an unintended spin caused by a loss of rear tyre traction or an accidental (often unexpected) large lateral force (such as might occur in a collision or bump in the terrain) that induces large scale vehicle rotation (Ø) about the vertical axis. This type of accident (due to loss of traction or uneven surfaces) has, historically, been common for both four-wheel and two-wheel land speed record vehicles. Figure 6.19 indicates the effect of large Ø (≥ 15°) on the C_d and C_l of a "scale 4 Ahmed" body at 67 m/s.

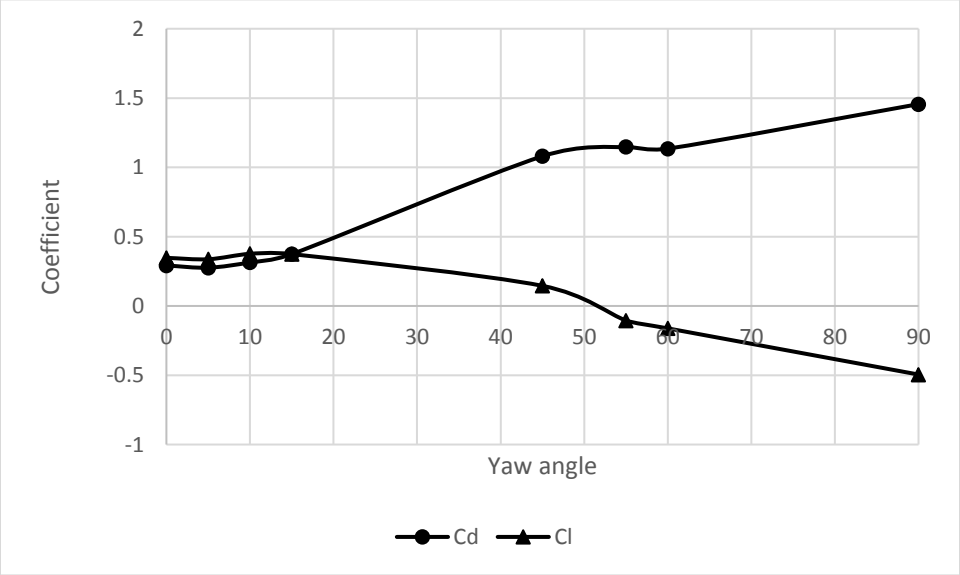

Figure 6.19- "Scale 4 Ahmed" body (67 m/s) with Ø = 0°, 15°, 30°, 45°,55°,60°, and 90°

From Figure 6.19, it is evident that the “scale 4 Ahmed” body experiences positive lift up to Ø =45°, and transitions between Ø = 45° and 55° when the aerodynamic lift becomes negative (downforce).

Figure 6.20 shows a velocity contour (a), a velocity vector contour (b), and a turbulence kinetic energy contour for the “scale 4 Ahmed” body at Ø = 45°.

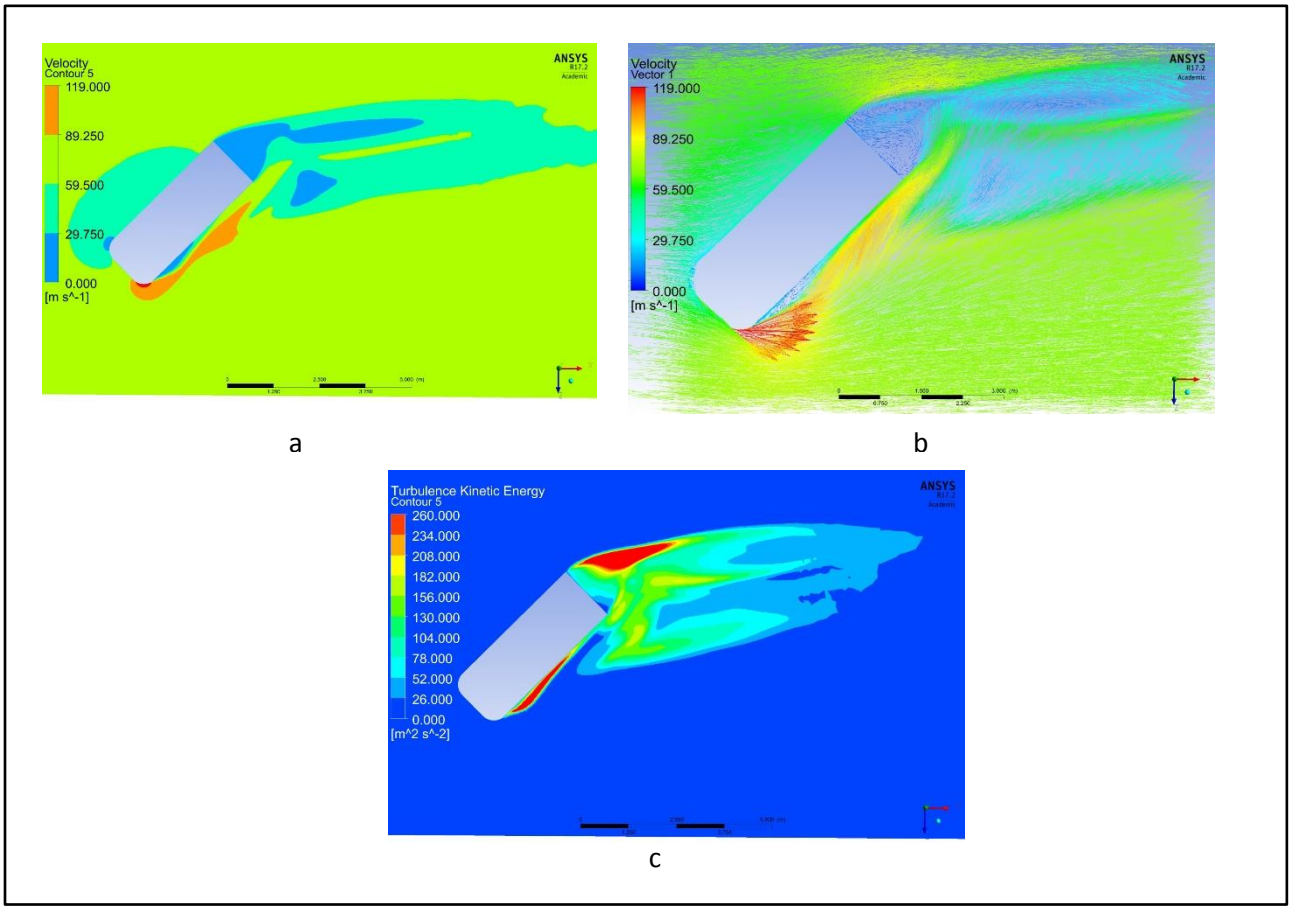

Figure 6.20- “Scale 4 Ahmed” body (67 m/s) at Ø = 45°: (a) Velocity contour (b) Velocity vectors (c) Turbulence kinetic energy

Figure 6.21 is a velocity vortex core plot for Ø = 45°.

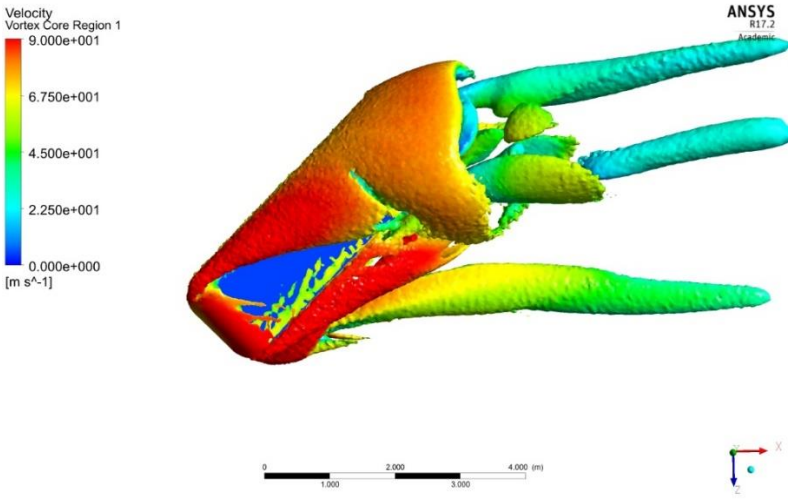

Figure 6.21- Velocity vortex core for "scale 4 Ahmed" body at Ø = 45°

Figure 6.20 and Figure 6.21 show that streamwise vortices originated at the corners of the "scale 4 Ahmed" body and that a large region of flow separation has occurred at the tail of the vehicle. Contrast this to Figure 6.22 at Ø = 60°.

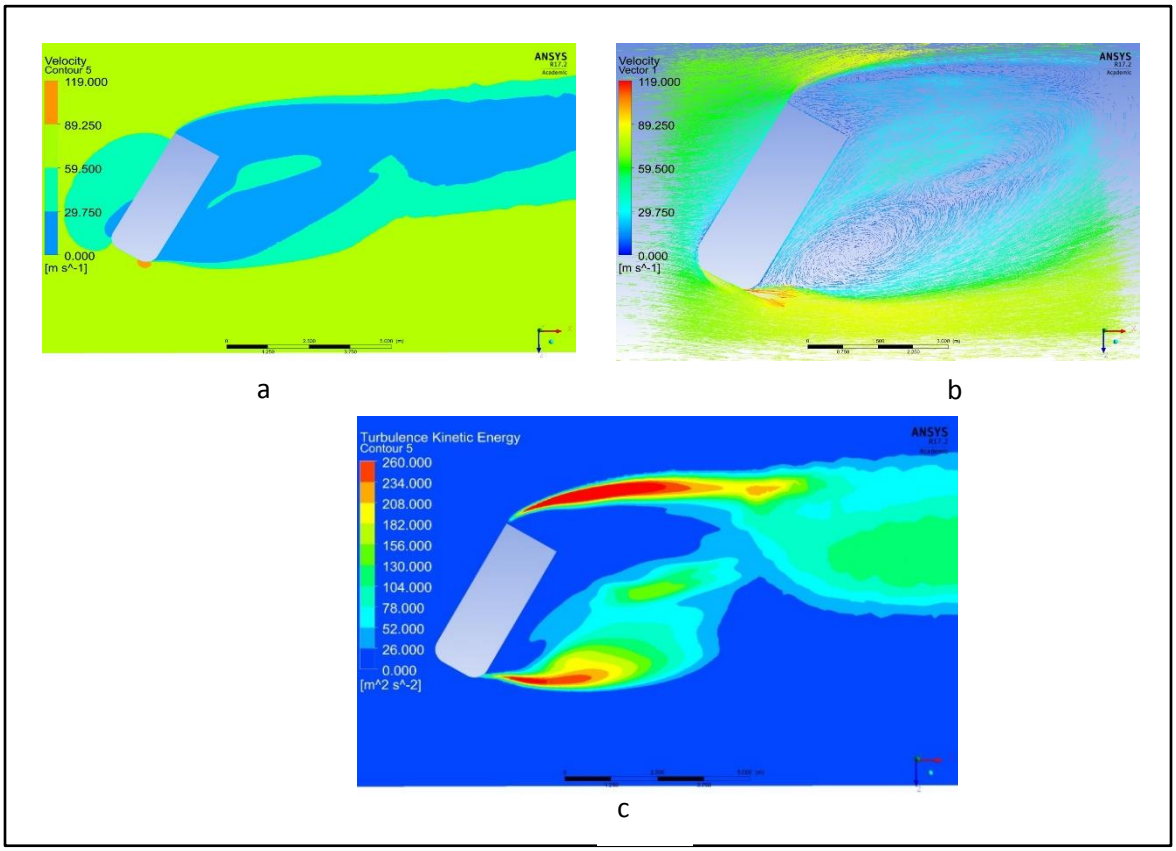

Figure 6.22- "Scale 4 Ahmed" body (67 m/s) at Ø = 60°: (a) Velocity contour (b) Velocity vectors (c) Turbulence kinetic energy

From Figure 6.22, it is evident that the flow around the ends of the “scale 4 Ahmed” body has changed relative to the Ø = 60° condition—a large region of separation on the top surface of the Ahmed body has formed, which is reflected in the change of the aerodynamic lift in Figure 6.19 from positive to negative (downforce). This change in flow topology can also be seen in Figure 6.23 when compared to 6.21.

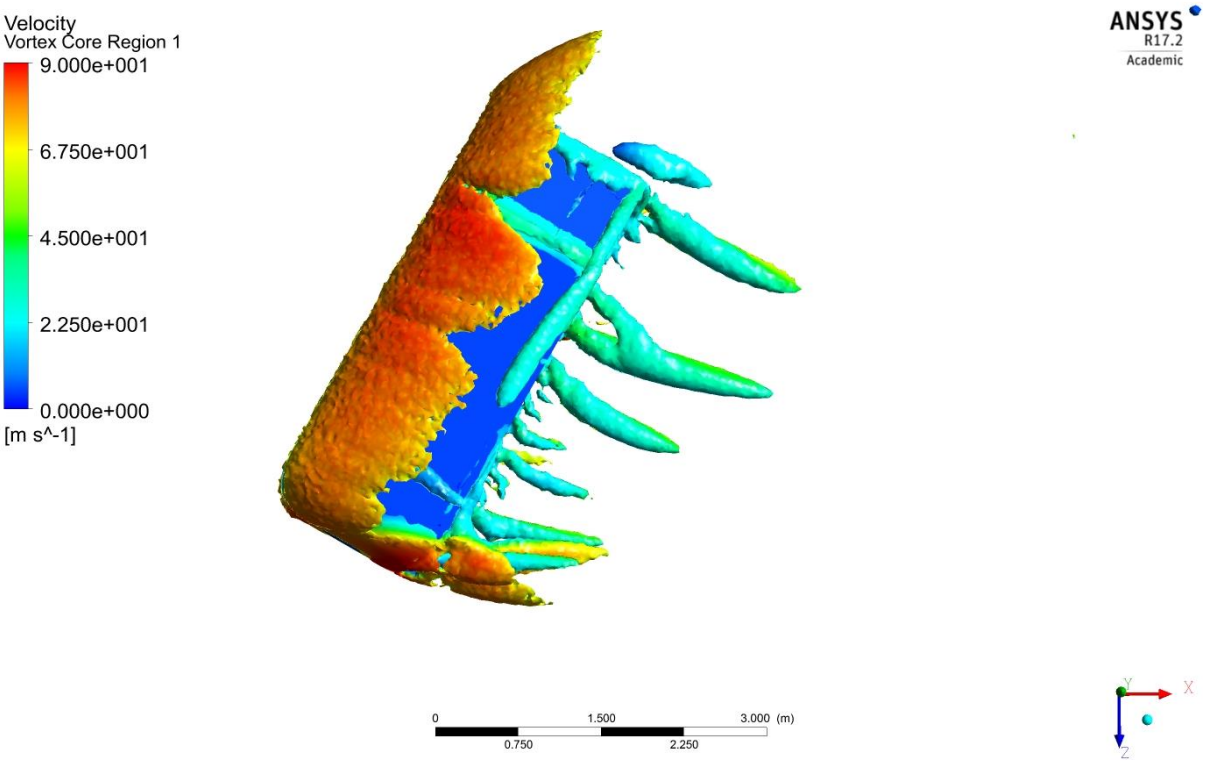

Figure 6.23- Velocity core for “scale 4 Ahmed” body at Ø = 60°

If Ø is further increased to 90° (sideways to the flow), the contours indicated in Figure 6.24 indicate a large separation zone on the leeward side, which results in the significant negative lift (downforce) evidenced in Figure 6.19.

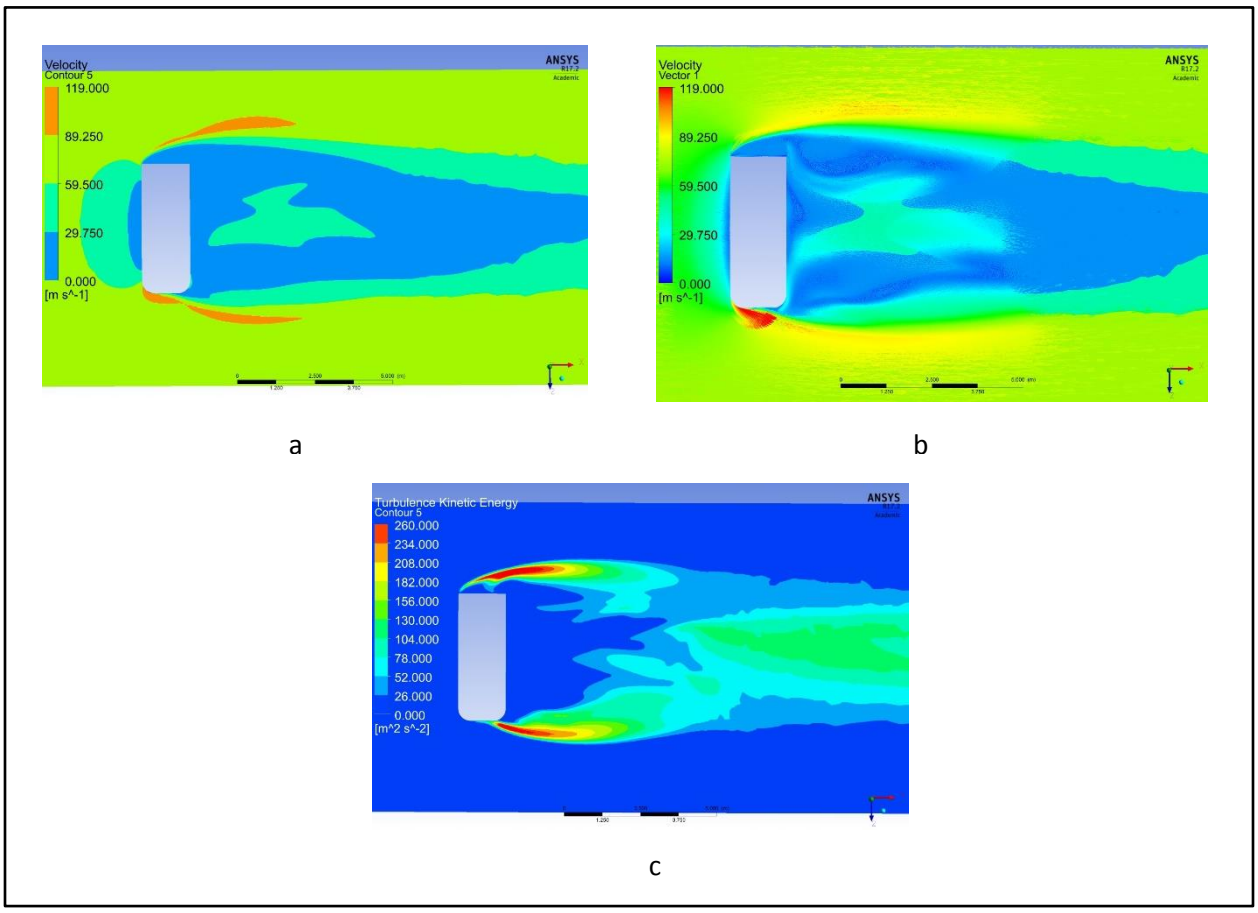

Figure 6.24- "Scale 4 Ahmed" body (67 m/s) at Ø = 90°: (a) Velocity contour (b) Velocity vectors (c) Turbulence kinetic energy

Figure 6.25 indicates the turbulence kinetic energy associated with flow over the Ø = 90° "scale 4 Ahmed" body, when viewed in the x-y plane, cut through the midpoint of the "scale 4 Ahmed" body.

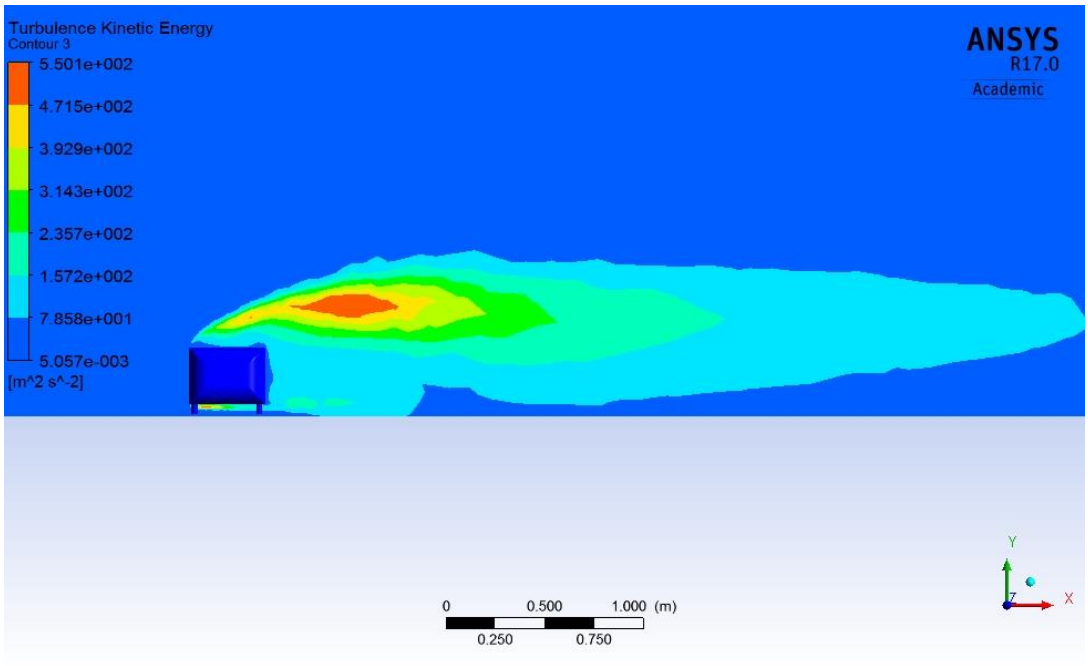

Figure 6.25- Turbulence kinetic energy in the flow over "scale 4 Ahmed" body at Ø = 90°

From Figure 6.25 it is evident that there is separation in the air flow over the top surface of the Ahmed body with Ø=90° and produces no positive lift. This is further reflected in Figure 6.26.

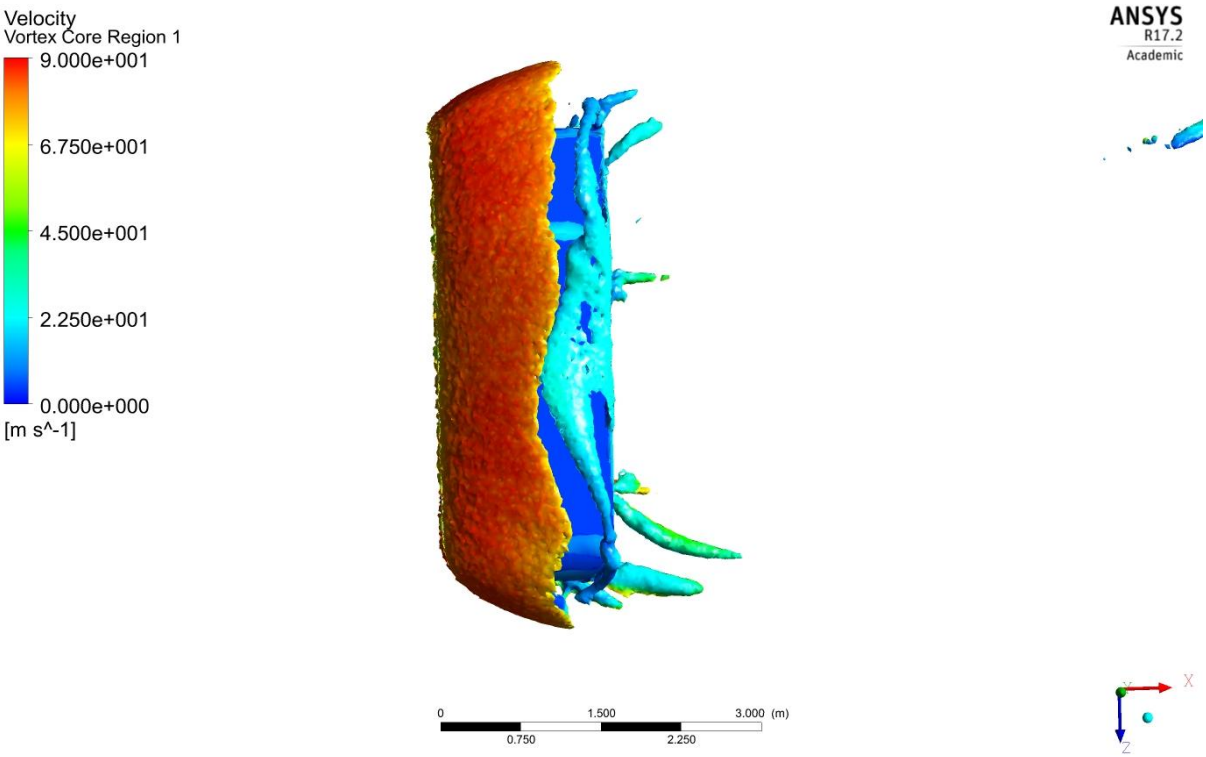

Figure 6.26- Velocity vortex core for "scale 4 Ahmed" body at Ø = 90°

6.3.4.5 Conclusions for Ahmed body yaw

Sweeping a bluff vehicle body through relatively small Ø (0-15°) and recording drag and lift forces as well as the change in frontal area is a valuable tool to examine and characterize the aerodynamics of the body shape.

With an Ahmed body, at small Ø (up to 15°) the C_d only changes slightly, while the A changes significantly. As a result, the C_dA experienced by the vehicle on the road changes a significant amount with Ø.

At high Ø, up to and including 90° to the air flow, the C_d is very large (> 1.0). Aerodynamic lift (positive or negative) at these large Ø plays a role in the aerodynamic stability of the vehicle in the event of extreme Ø, as might occur during a spin. For the "scale 4 Ahmed" body at 67 m/s, a transition from positive (lift) to negative (downforce) aerodynamic forces occurs between a Ø = 45° and Ø = 55°. This transition results from the separation over the top surface of the Ahmed body as the Ø increases. The downforce, evidenced for the "scale 4 Ahmed" body, should be beneficial for vehicle stability at large Ø, but may not be present for all vehicle geometries and shapes. It should also be noted that a vehicle (such as an Ahmed body) at a yaw angle approaching 90° (particularly at 150 mph) is probably also experiencing d'Alembert forces that will adversely affect stability beyond the issues arising from aerodynamic forces. Nevertheless, the addition of significant aerodynamic lift secondary forces could serve to make an already bad situation much worse. Note that this approach ignores inertial effects and assumes a quasi-steady behaviour, as a steady-state CFD simulation was undertaken at each discrete Ø.

6.4 SYMMETRICAL LAND SPEED RECORD STREAMLINE MOTORCYCLE

To further examine the yaw effects on a symmetrical vehicle, the design for an electric streamliner motorcycle (a project by Purdue University) was obtained. This vehicle has been extensively researched at Purdue with the goal of building the machine in order to set a world land speed record in the 150-kg electric streamliner class at Bonneville. The streamliner is depicted in Figure 6.27.

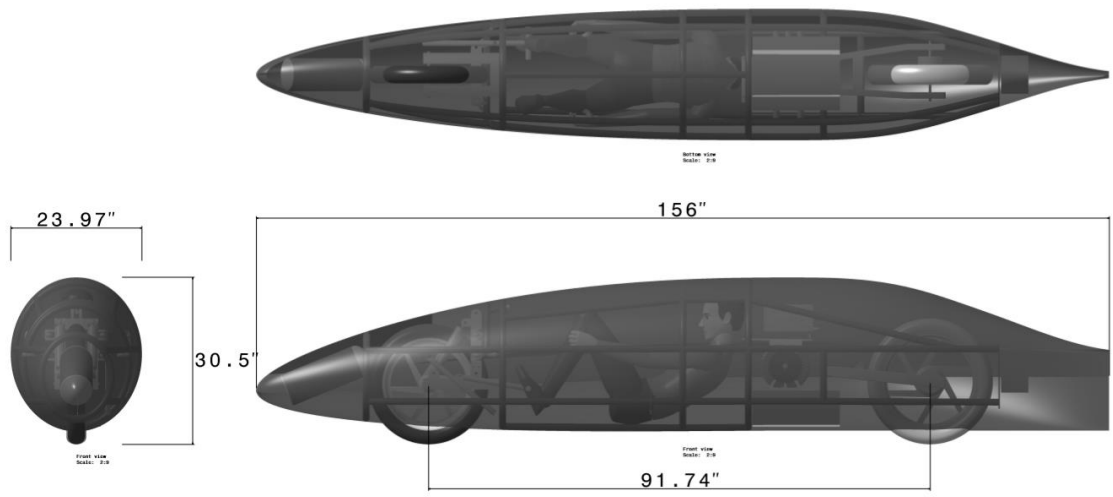

Figure 6.27- Motorcycle streamliner from Purdue University [Sullivan, 2016]

6.4.1 Streamliner Equations of Motion

Despite the use of the simplified "bicycle" model to establish dynamic stability of four-wheel vehicles, the actual stability of a two-wheel single-track vehicle is significantly more difficult to characterize (Meijaard, Papadopoulos, Ruina, & Schwab, 2007). A bicycle is described as a "non-holonomic" system—its configuration is path dependent and depends upon the history of the configuration over time (Schwab, Papadopoulos, Ruina, & Dressel, 2015). A single-track two-wheel vehicle possesses a number of dynamic modes that are used to determine the stability of the overall system.

The most common analytical model for a bicycle is the "Whipple" bicycle, developed in 1899 by Cambridge undergraduate Francis Whipple (Meijaard et al., 2007). The fundamental model is composed of four bodies: a front and a rear wheel, a rear main frame, and a front fork that pivots on a steering head and that is at an angle, λ, as indicated in Figure 6.28 (McMillan, 2015). Note that this λ is not related to the λ in Equation 6.3. In the simplified version of the model, the mass of the rider is often included as a part of the rear frame and as rigidly attached to the frame (Meijaard et al., 2007). For the Purdue streamliner, where the rider is firmly strapped into the vehicle, this is a good assumption.

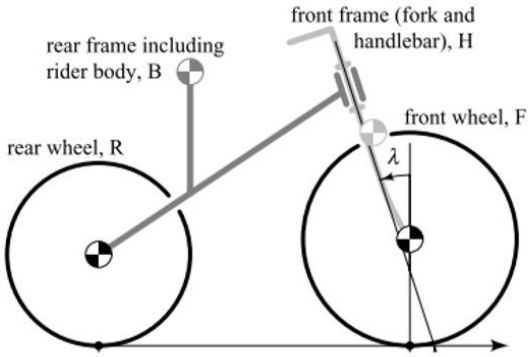

Figure 6.28- The four bodies of a single track, two-wheel vehicle [McMillan, 2015]

A set of linearized differential equations for an 11 degree of freedom bicycle model in terms of 25 bicycle parameters have been developed (Meijaard et al, 2007) and can be represented by a fourth-order linearized ordinary differential equation, or by two coupled second-order differential equations in four variables: lean angle, lean rate, steering angle and steering rate. The eigenvalues of the four variables can be calculated from the linearized differential equations to determine the vehicle dynamic modes for the two-wheel vehicle and whether it is self-stable. A bicycle is said to be self-stable if it recovers automatically from side winds or other disturbances that cause it to lean (Olsen & Papadopoulos, 1988).

The vehicle dynamic modes for a two-wheel vehicle are related to its velocity. At low speeds, oscillations in steering angle occur above the *double root speed* (so-called because at this speed there is a repeated root to the characteristic polynomial). Below this speed, the bicycle simply falls over. Above this speed the oscillations decrease to a minimum after the steering eigenvalues switch from positive to negative and will eventually die out. This is called the *weave speed*. As speed further increases, non-oscillatory lean increases and the point at which the leaning eigenvalues switch from negative to positive is called the *capsize speed*. It should be noted that a bicycle that is not self-stable is still rideable with control inputs and corrections from the rider (Olsen & Papadopoulos, 1988).

Although the Routh-Hurwitz criteria could be used to determine stability from the coefficients of the characteristic equation, several computer programs are available to calculate the eigenvalue roots of the characteristic polynomial. By solving for the real and imaginary roots, it is possible to not only determine stability (real roots), but also the frequency of any oscillations (imaginary roots). The frequency of oscillations and imaginary roots will not be considered for this work. One free computer program is JBike6, (Schwab, Papadopoulos, Ruina, & Dressel, 2015), written in MATLAB, that calculates the eigenvalues for a range of forward speeds to determine when the bicycle is self-stable. Figure 6.29 is a plot returned from JBike6 for a typical generic bicycle.

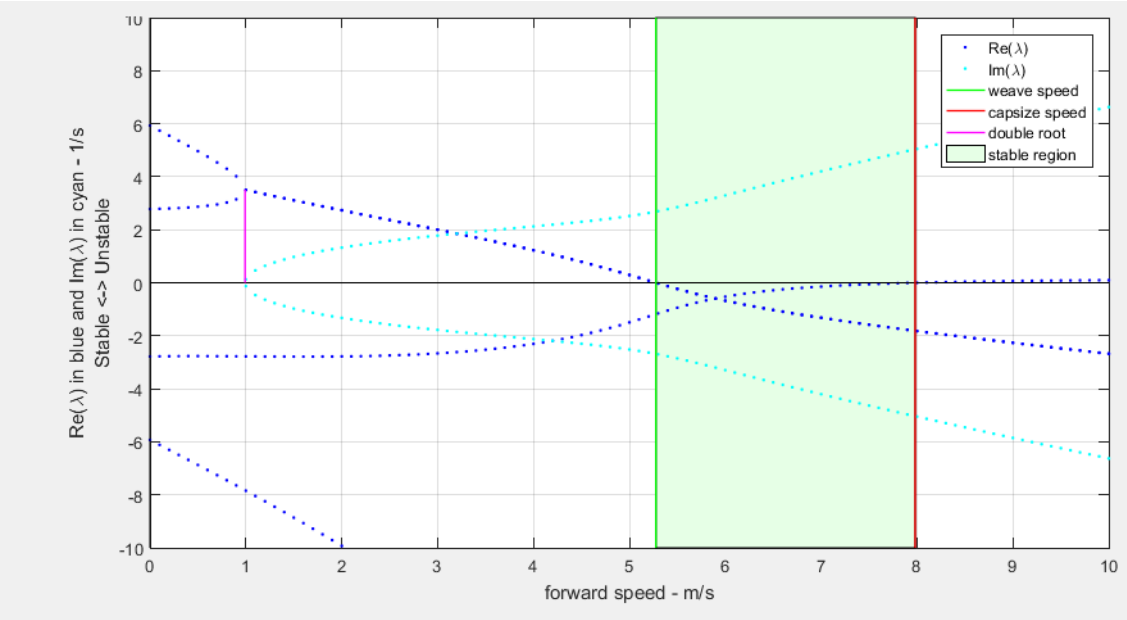

Figure 6.29- JBike6 plot of eigenvalues for a generic bicycle [Jbike6]

In Figure 6.29, the double root speed is 1 m/s (below which the bicycle falls over, above which steering oscillations occur). The weave speed is slightly higher than 5 m/s (above which steering oscillations die out) and 8 m/s is the capsize speed (above which the bicycle continues to lean until it falls over). The region between the weave speed and the capsize speed, shaded green in Figure 6.29, indicates the speed over which the bicycle will be self-stable. "When an uncontrolled bicycle is within its stable speed range, lean and steer perturbations die away in a seemingly damped fashion. However, the system has no true damping and conserves energy. The energy in the lean and steer oscillations is transferred to the forward speed rather than being dissipated" (Meijaard et al., 2007).

Although JBike6 can be applied to any two-wheel vehicle, it is limited by several of its simplifying assumptions. One of the most significant when considering the dynamic stability of a motorcycle is the lack of a tyre model. Wheels in JBike6 are modelled as non-slipping rolling point contacts with knife edges (Meijaard et al., 2007). While perhaps adequate for the high-pressure narrow tyres of a high-performance road or track bicycle, the lack of a wheel model that includes tyre response neglects one additional oscillatory mode called *wobble* in straight ahead travel (Sharp, 1971). Wobble usually occurs at high speeds (above 40 m/s) and is an oscillatory shaking of the front wheel and fork (most serious case) and rear frame (slightly less serious) (Sharp, 1971).

BikeSIM is a commercial bicycle and motorcycle dynamic stability analysis program that includes a tyre model. BikeSIM was used by Ethan McMillan of Purdue University in analyses of the potential stability of the Purdue streamliner vehicle (Sullivan J. , 2017). Figure 6.30 is the eigenvalue plot versus speed for BikeSIM for a standard motorcycle. Note the addition of the

wobble and rear wobble modes. Wobble oscillations begin when the wobble real eigenvalue becomes a positive number.

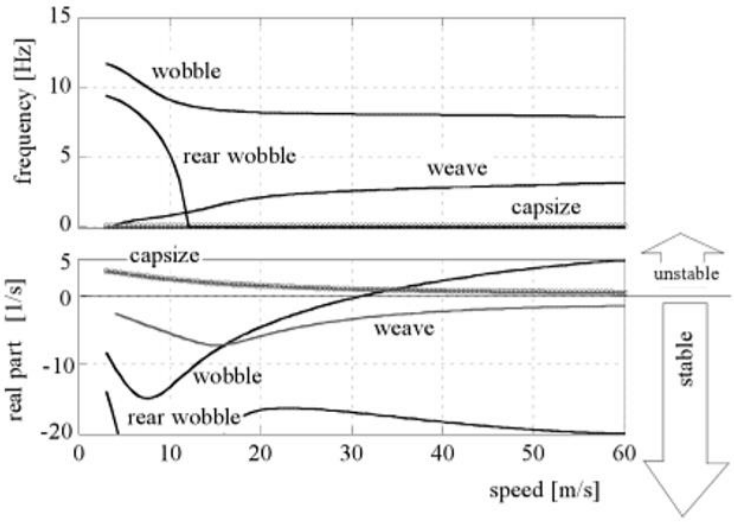

Figure 6.30- JBike6 root locus versus velocity plot [McMillan, 2015]

McMillan (McMillan, 2015) used BikeSIM to establish the stability of the Purdue streamliner in weave and wobble modes as indicated in Figure 6.31.

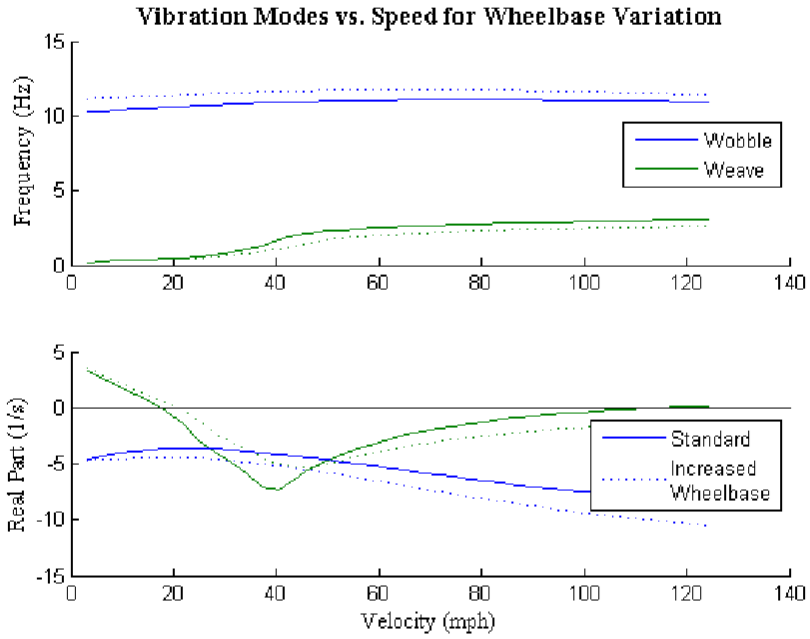

Figure 6.31- Weave and wobble modes for Purdue streamliner [McMillan, 2015]

From Figure 6.31, the Purdue streamliner exhibits dynamic stability and is free from wobble up to speeds in excess of 140 mph. Figure 6.31 also indicates that increasing the wheelbase of a motorcycle improves dynamic stability.

6.5 STREAMLINER AERODYNAMICS

It is evident that the Purdue streamliner is dynamically stable, in the absence of aerodynamic forces. Its aerodynamic stability was studied, primarily through examination of the forces, moments and wake topology obtained by simulating with CFD the vehicle at various Ø. This approach, as noted in section 6.3.1, has been occasionally used for four-wheel land speed record vehicles to predict the effects of cross-winds on stability, but little has been published using this approach to examine overall aerodynamic stability of a two-wheel single-track streamliner. It should be noted that this approach ignores inertial effects and assumes a quasi-steady behaviour, as a steady-state CFD simulation was undertaken at each discrete Ø. Using SolidWorks, a CAD model of the Purdue streamliner was created. This is depicted in Figure 6.32.

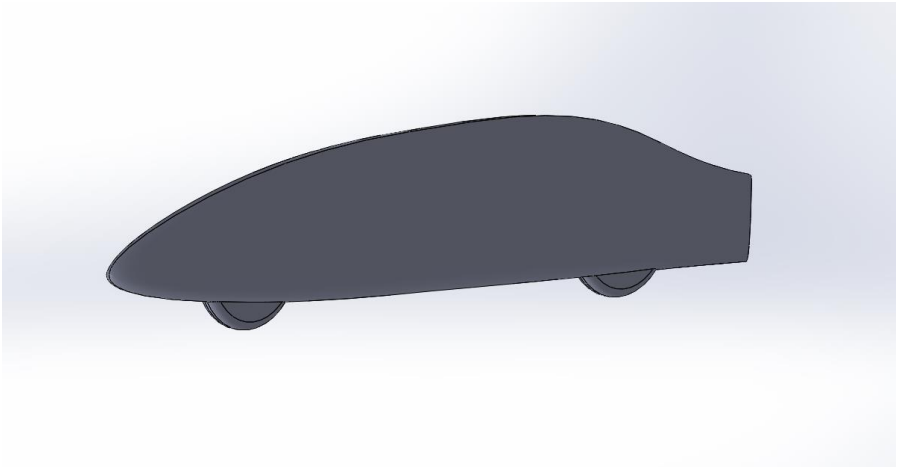

Figure 6.32- SolidWorks CAD model of the Purdue University streamliner

Air flow over the streamliner was examined using ANSYS Fluent 17.0 CFD. The mesh size was 13 million primarily tetrahedral elements. Figure 6.33 shows the details of the mesh used in the streamliner study. The boxes created over the vehicle and in the wake zone were meshed as bodies of influence with an element size of 0.02 m. The surface of the vehicle was meshed with a 0.02 m element size. There were five inflation layers, with the initial layer thickness of 0.001 m. The remainder of the computational domain was meshed, primarily in tetrahedrons with a 0.1 m minimum and 0.2 m maximum element size.

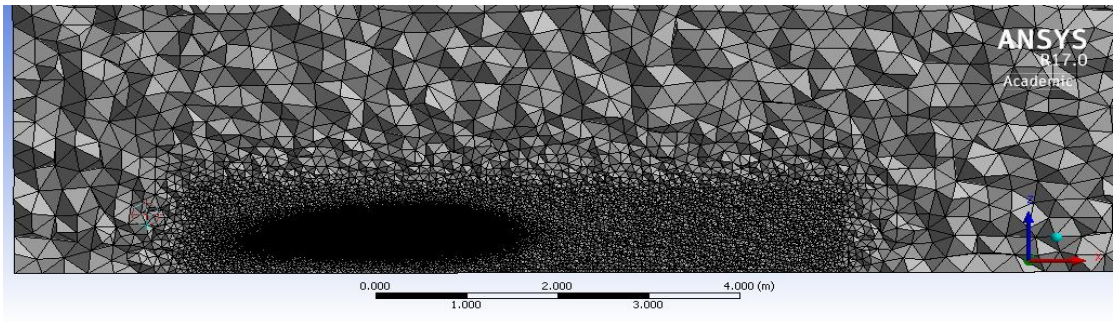

Figure 6.33- Meshing of the Purdue streamliner

The SST turbulence model was used with a moving road surface and a velocity of 67 m/s (150 mph) was used for the streamliner CFD studies. A coupled scheme was used for pressure and velocity and spatial discretization used a least squares gradient and second order upwind pressure, momentum, turbulence kinetic energy and dissipation rates. The frontal area (A), determined from ANSYS Fluent (Reports → Projected Area → Min Element size → .0001m), versus yaw angle is plotted in Figure 6.34. As before, the convention that a positive yaw is a clockwise rotation as seen from above was used. It can be seen that the streamliner is geometrically symmetrical around its longitudinal axis.

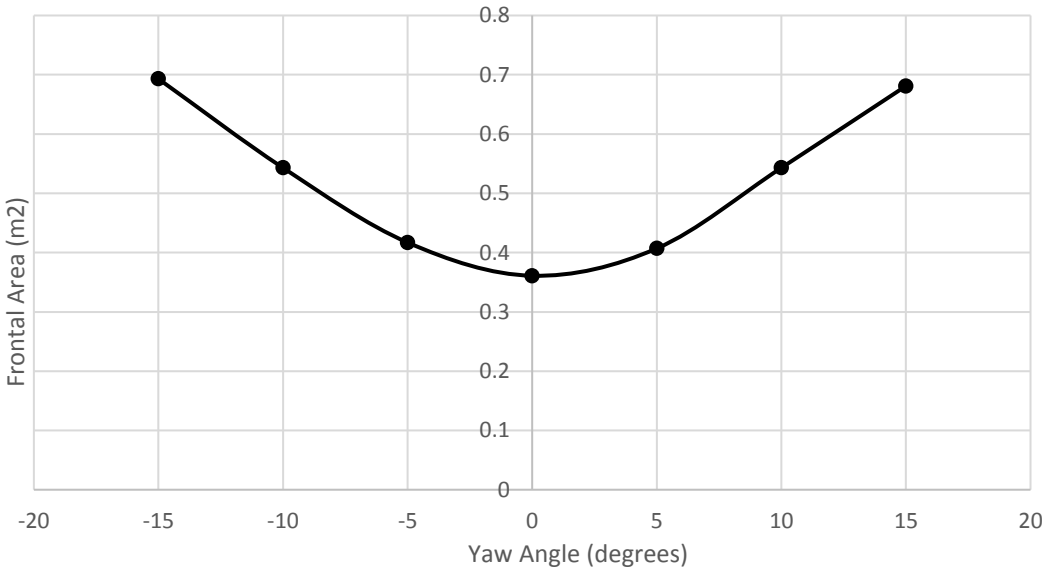

Figure 6.34- Streamliner frontal area versus yaw angle

The effect of yaw angle on drag, lift, lateral force, yaw moment and roll moment coefficients, calculated using frontal area (A) are indicated in Figure 6.35. The predicted forces and moments are symmetrical around the longitudinal axis (length scale = 3.96 m, A = 0.361 m^2)

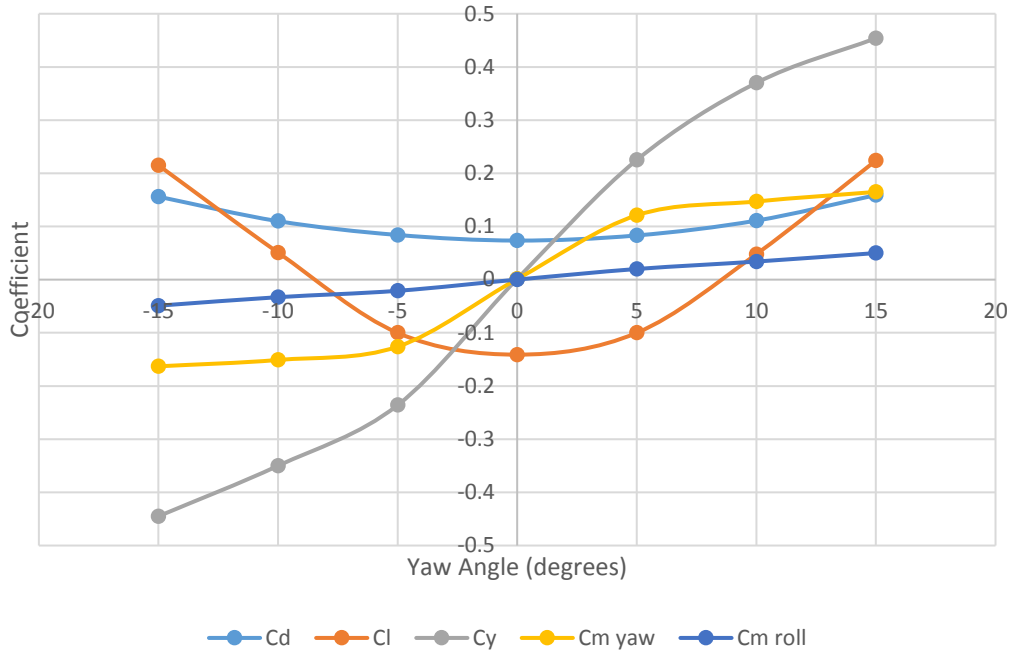

Figure 6.35- Streamliner at 67 m/s: drag, lift, lateral force and yaw and roll moment coefficients versus Ø

To compare the streamliner to the Ahmed body, it is first necessary to compare the change in frontal area with yaw angle of the two vehicles. This comparison is in Figure 6.36.

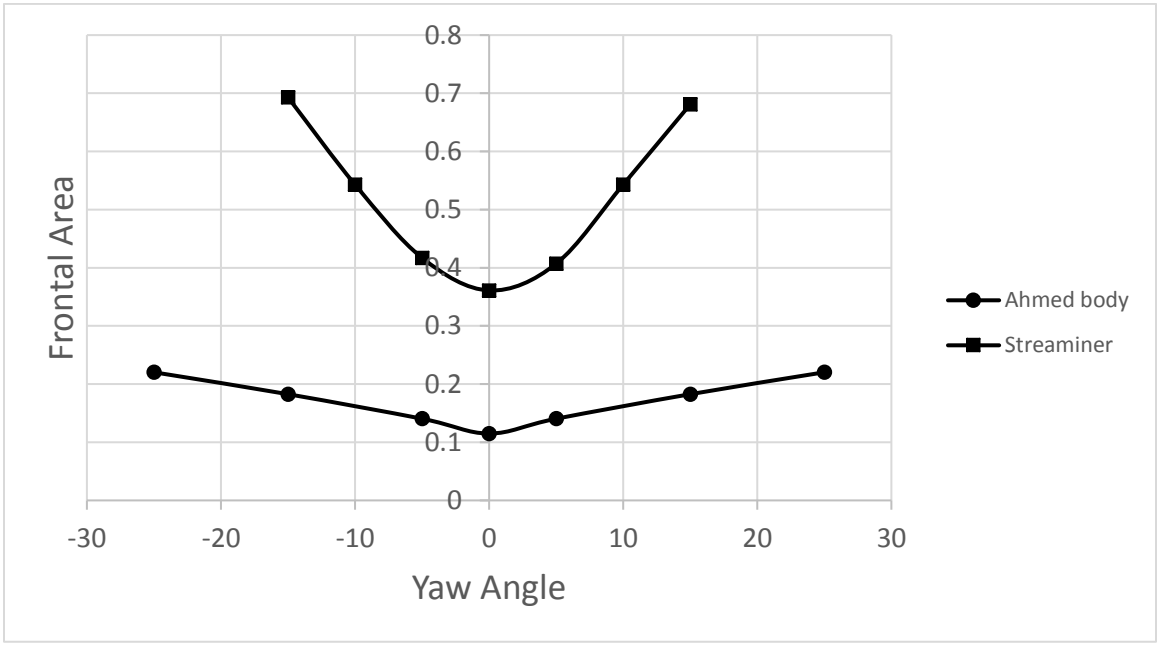

Figure 6.36- Frontal area of standard Ahmed body versus streamliner with yaw angle

From Figure 6.36, it is evident that rotating the streamliner through positive and negative Ø has a larger effect on the frontal area presented to the wind than doing the same for a standard scale Ahmed body.

As with the Ahmed body, the effect of the change in frontal area (A) with Ø on the drag coefficient (C_d) can be examined by plotting C_d and C_dA versus yaw angle, as in Figure 6.37.

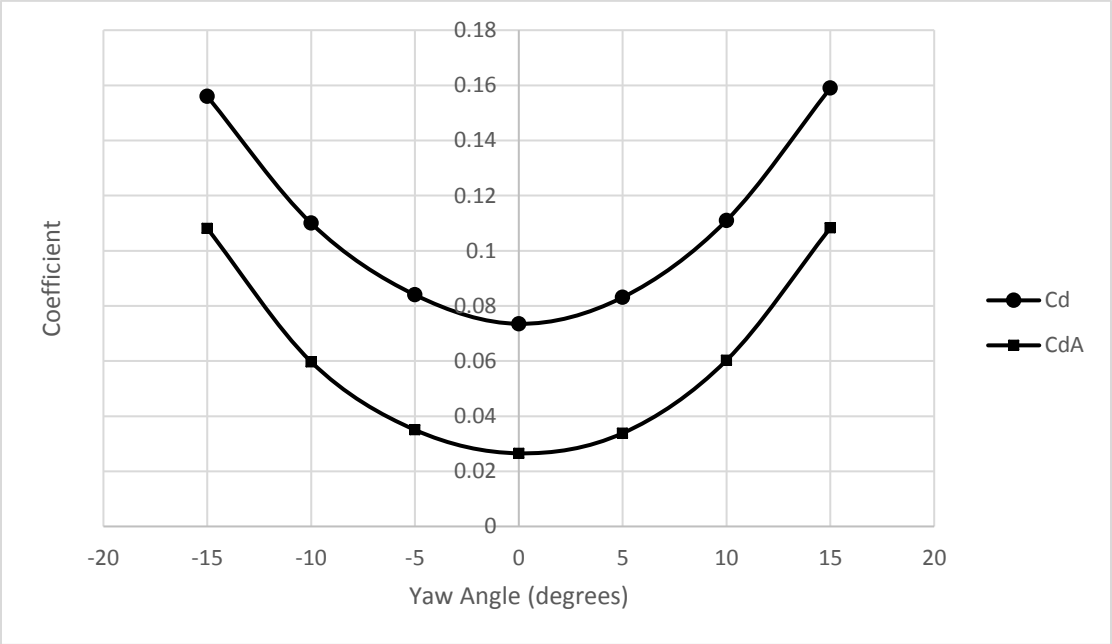

Figure 6.37- Comparison of C_d versus C_dA over range of Ø - streamliner

Examining the streamliner data in Figure 6.37, it is evident that the body shape that the streamliner presents to the air does not change dramatically with yaw angle and that the change in drag with yaw is primarily due to the increase in frontal area. This is in contrast to the Ahmed body (Figure 6.2), where the change in body shape presented to the airflow at higher yaw angles had a significant effect of the drag coefficient.

6.6 Pressure and Viscous Forces

The pressure and viscous drag forces generated by the streamliner are shown in Figure 6.38.

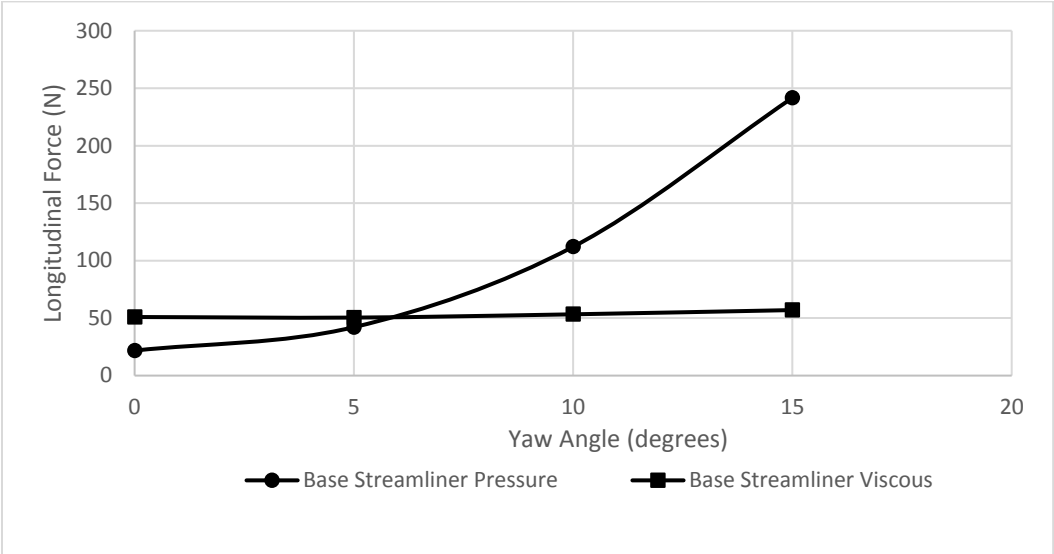

Figure 6.38- Streamliner pressure and viscous drag

It is evident in Figure 6.38 that the streamliner produces greater surface friction drag when traveling straight ahead. With increasing Ø, the pressure drag of the streamliner becomes more significant until at approximately 5° of yaw it is equal to the surface friction drag. Above 5°, although the surface friction is proportional to wetted area, which does not change with yaw angle, the pressure drag increases dramatically. The velocity field over the motorcycle streamliner is visualized at Ø = 0°in Figure 6.39.

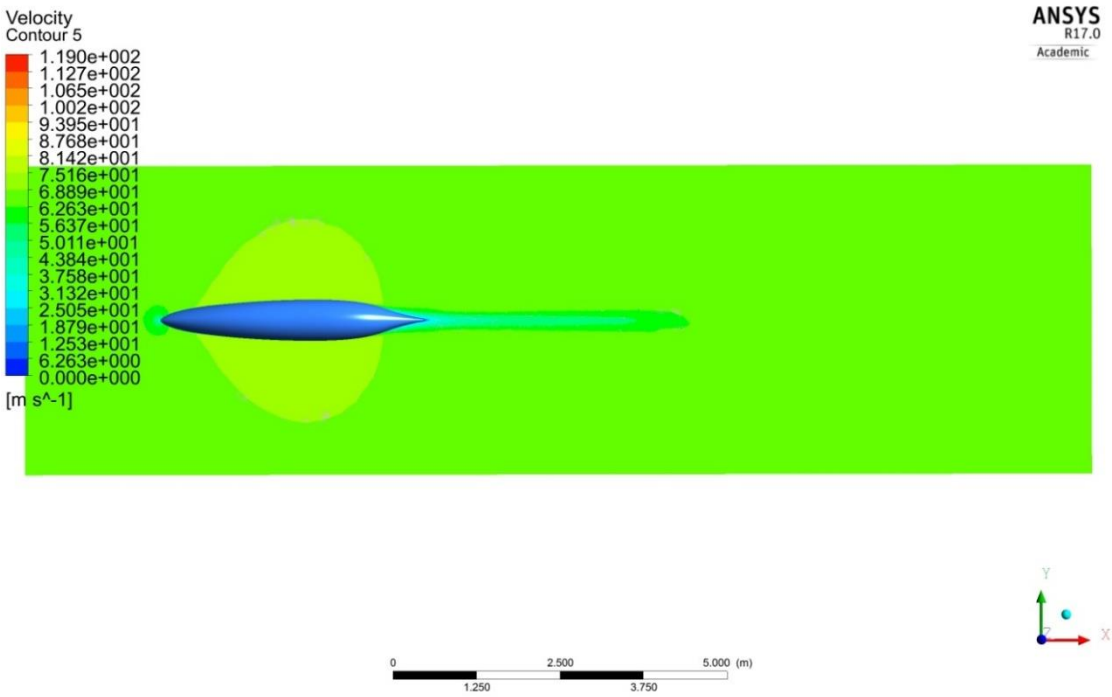

Figure 6.39- Streamliner at Ø = 0°

In Figure 6.39 it is evident that there is little flow separation caused by the flow of air over the streamliner body and hence, as found in Figure 6.19, viscous drag dominates. This is further demonstrated with the velocity vortex core plot in Figure 6.40.

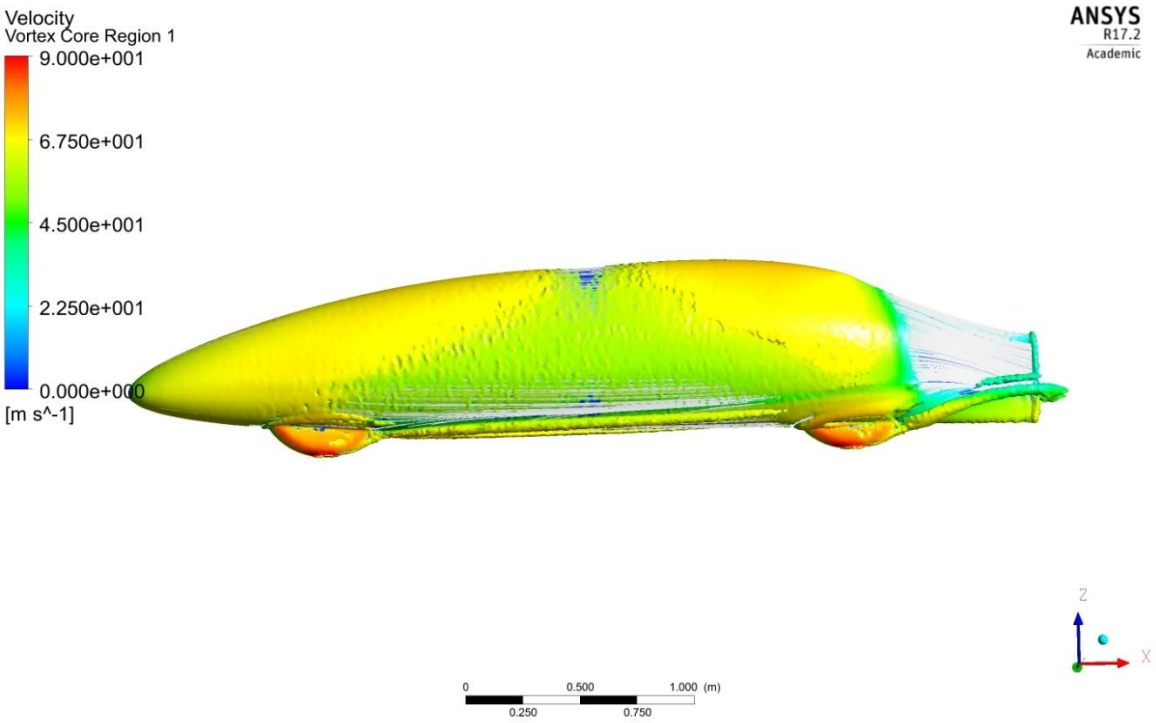

Figure 6.40- Velocity core vortex plot for streamliner with Ø = 0°

In Figure 6.40, small streamwise vortices are evident from each of the wheels and from a region at the lower part of the tail as well as a small spanwise vortex on the trailing edge of the tail. Work could be done in the regions of the streamwise vortices to potentially reduce overall drag. Figure 6.41 is a surface shear stress plot for the streamliner at Ø = 0°.

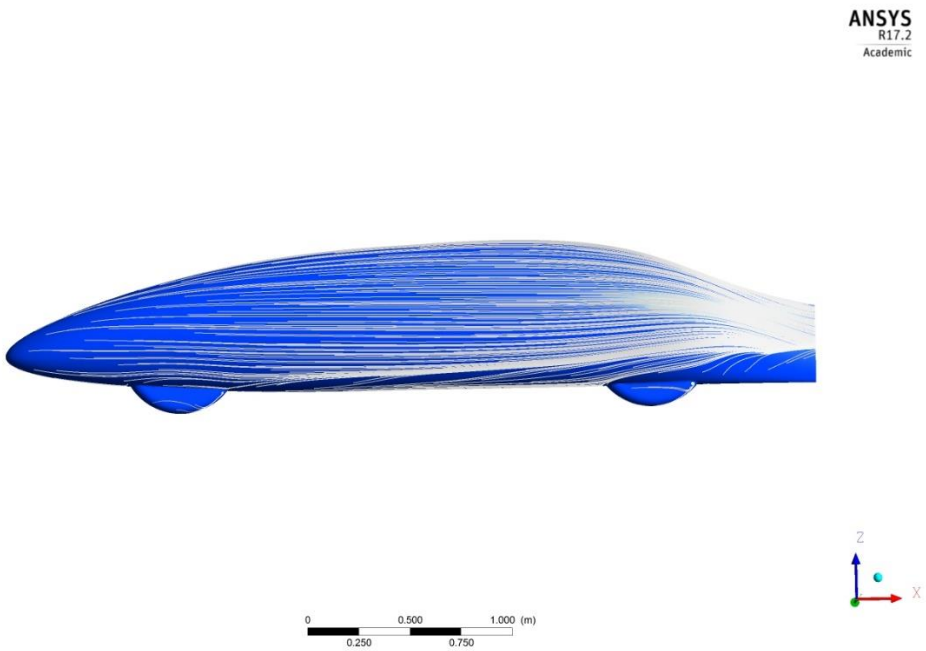

Figure 6.41- Surface shear stress lines for streamliner at Ø = 0°

In Figure 6.41, the region of curved surface shear stress lines at the bottom of the rear section of the streamliner is area where remodelling could potentially provide improvements (reductions) in aerodynamic drag.

In Figure 6.42, the streamliner wake is shown at Ø = 10°.

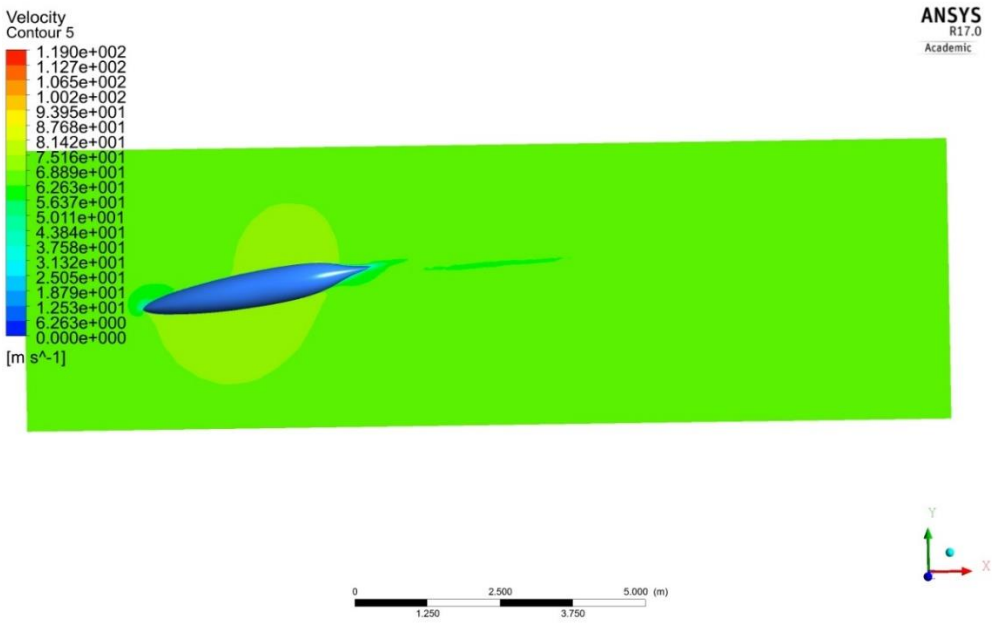

Figure 6.42- Streamliner at Ø = 10°

In Figure 6.42, with a Ø = 10°, pressure drag exceeds viscous drag as the shape now promotes a slightly larger and more prominent wake. This is also evident in Figure 6.43, where shear along the upper surface of the rear section of the streamliner results in a streamwise vortex that trails into the wake region, which is absent at Ø=0°.

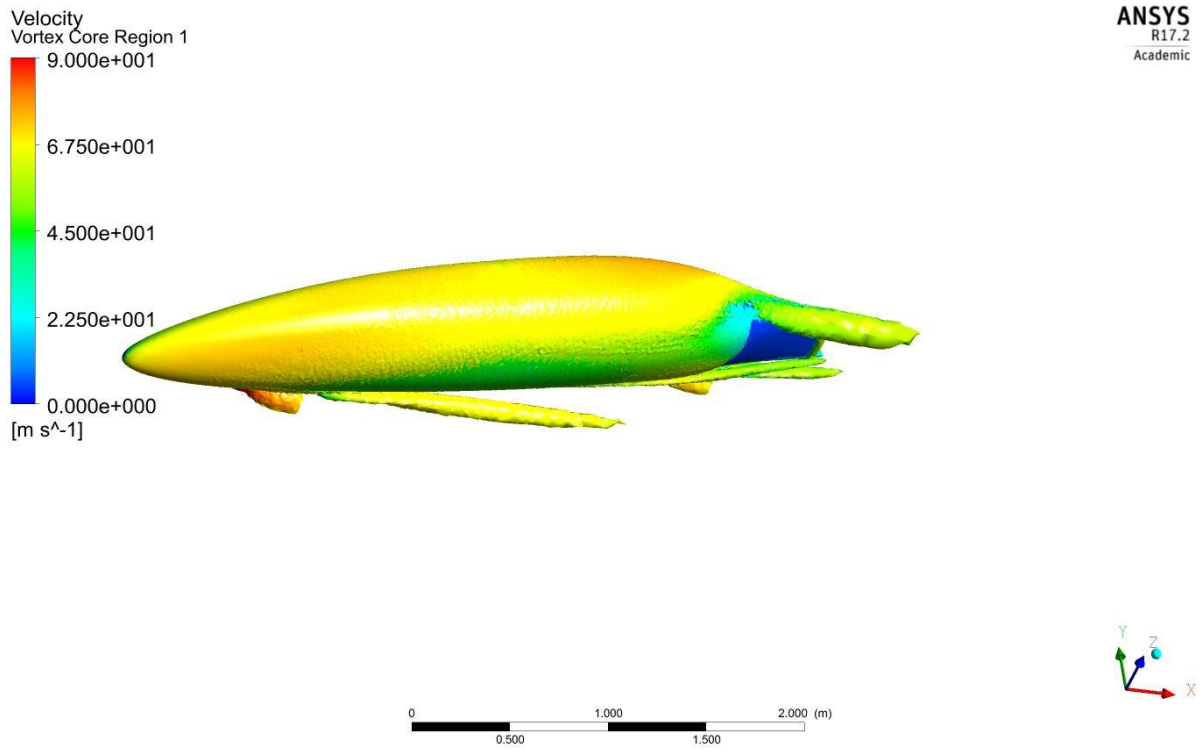

Figure 6.43- Streamwise vortex from the upper tail section of the streamliner at Ø = 10°

6.7 ADDITION OF A TAIL FIN

Recall Figure 6.35 indicates the forces and moments that are generated at Ø between positive and negative 15°. In Figure 6.35, it is evident that as the streamliner runs at an increasing Ø, the flow over its surface generates a lateral force, shown as a lateral force coefficient C_y, and an increasing yawing moment, shown as a yaw moment coefficient C_{Myaw} (length scale = 3.96 m, A = 0.361 m^2)

Note that for the frame of reference for the streamliner, a positive lateral force coefficient with a positive yaw moment coefficient indicates that the centre of pressure of the streamliner is located ahead of the centre of mass of the vehicle. Thus, a positive lateral force (pointing to the right when viewed from above and behind) would cause the streamliner to rotate in a clockwise (non-restoring) direction around the vertical (z) axis. Hucho et al. (1993) indicated that this yaw moment, that tends to turn the vehicle away from the direction of the cross-wind results in

vehicle that is aerodynamically unstable. Hucho et al. (1993) further suggest that an effective way to reduce this instability is through use of a tail fin.

Tail fins with two different heights were created for the Purdue streamliner. The profile for the tail fins was developed from a symmetrical wing profile, NACA 66-010, known for its low drag and laminar flow characteristics (Abbott & von Doenhoff, 1949). Figure 6.44 is a profile of the NACA 66-010 fin. The fin was left with a flat top and was not otherwise optimized.

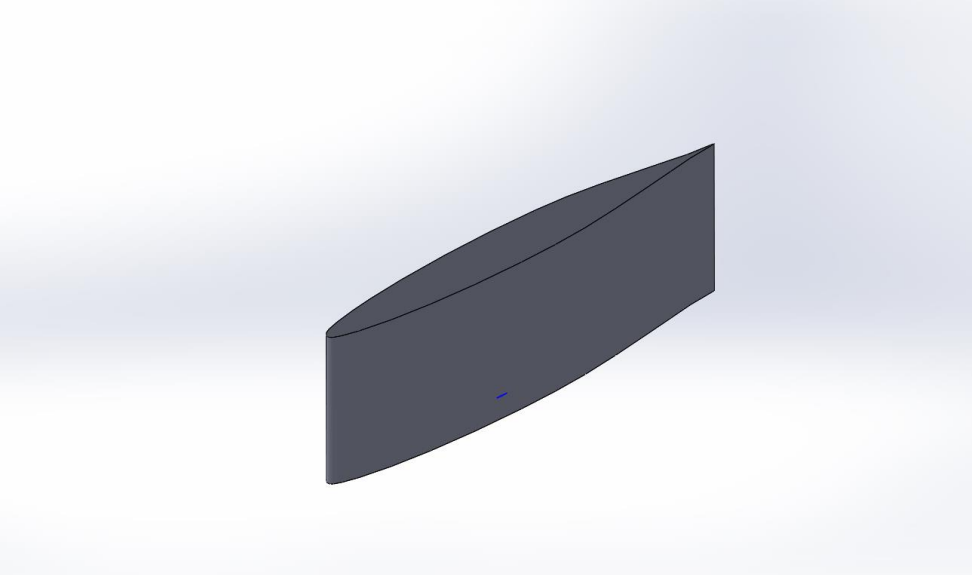

Figure 6.44- Profile of the NACA 66-010 used for CFD studies on the Purdue streamliner

The height of the low fin was set to match the overall height of the streamliner. As a result, the low fin is only impacted by the airflow when the vehicle undergoes yaw or experiences side winds (Figure 6.45).

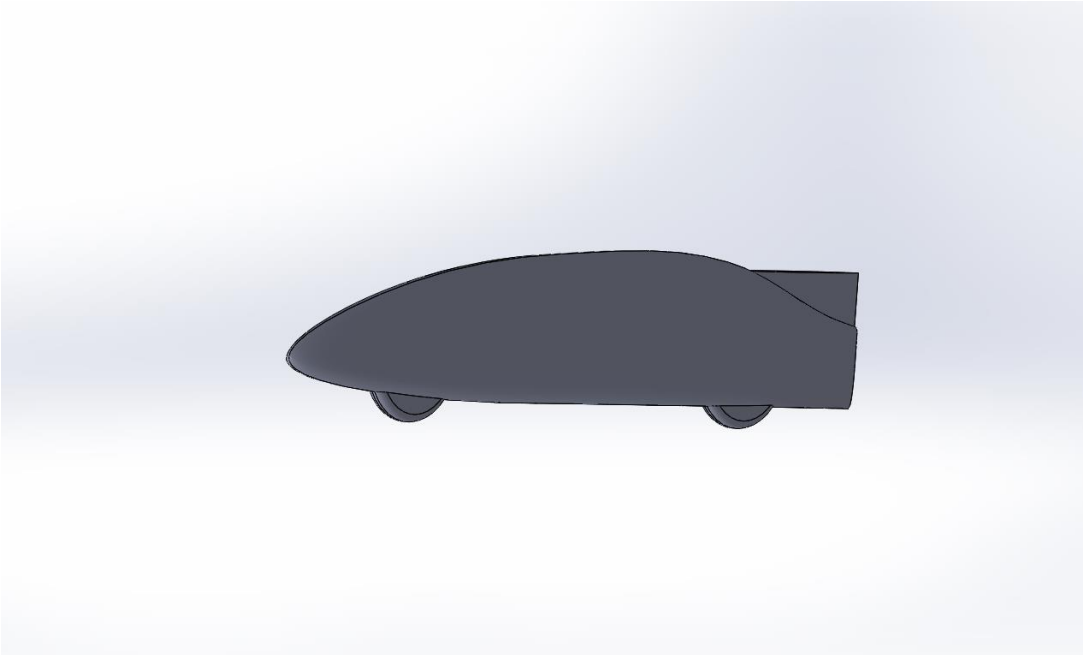

Figure 6.45- Low fin version of the Purdue motorcycle streamliner

The high fin version had a height of approximately twice the low fin, so that even at zero yaw it encountered the freestream (Figure 6.46).

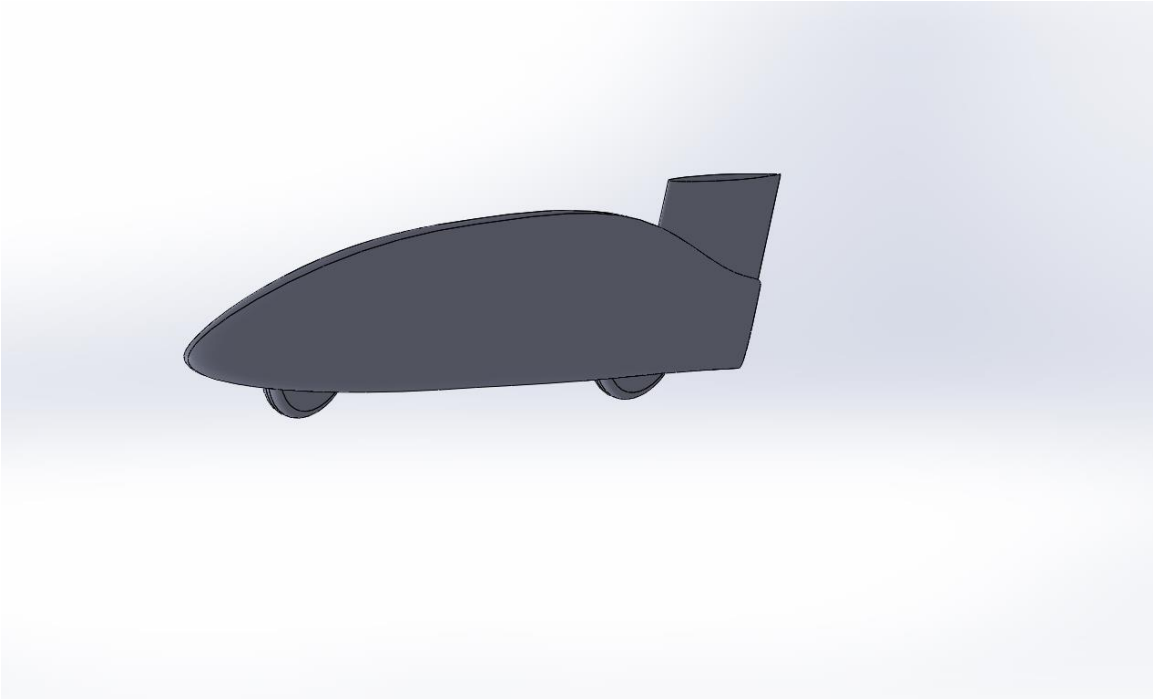

Figure 6.46- High fin version of the Purdue motorcycle streamliner

The high and low fin changed the side projected of the sidecar slightly. Table 6.1 shows the side projected area determined from ANSYS Fluent using the Reports → Projected Area → Min Element size → .0001m function, but this time specifying from a y-axis, or lateral direction.

Table 6.1: Side area of streamliner with low and high fin

Configuration	**Side area (m^2)**	**% increase from base**
Base streamliner	0.361	-----
Low fin	0.368	+ 1.9 %
High fin	0.371	+ 2.8 %

As before, CFD using ANSYS Fluent was performed at a range of yaw angles (in only one direction as the streamliner is a symmetrical vehicle) with a mesh size of 13 million unstructured elements and the SST turbulence model with a moving road surface and a velocity of 67 m/s (150 mph).

Figure 6.47 plots the drag coefficients of the base streamliner, the low fin and the high fin versions versus Ø.

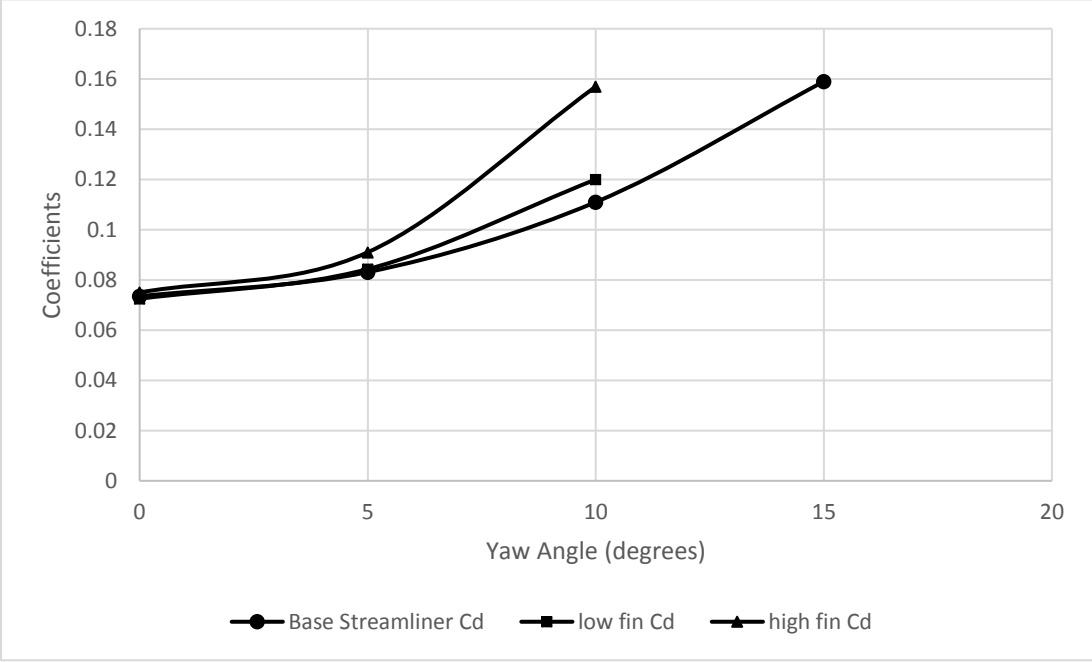

Figure 6.47- Base, low fin and high fin streamliner versus Ø

From Figure 6.47, it is evident that the fin has little or no effect on the aerodynamic drag at Ø=0°. It is only when the streamliner undergoes yaw that the fin is exposed to significant air flow and the high fin results in higher drag than either the base or low fin versions of the streamliner as the yaw angle increases.

Examining the pressure versus viscous drag of the base streamliner, and the low and high fin versions in Figure 6.48 indicates that below Ø = 5°, viscous drag predominates, but above 5°, particularly with the high fin, pressure drag takes over.

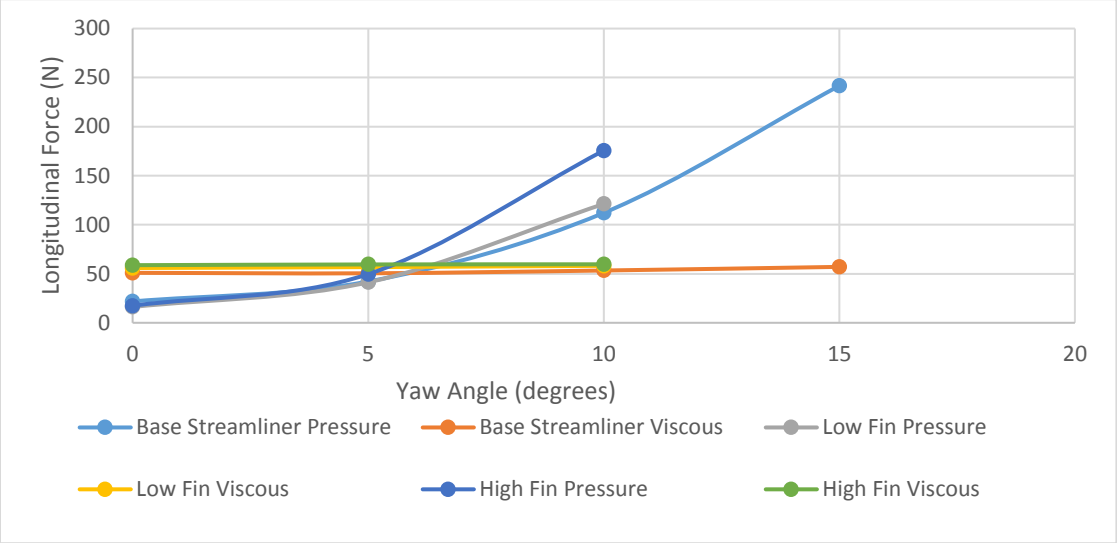

Figure 6.48- Base, low fin and high fin streamliner pressure and viscous drag versus Ø

Figure 6.49 visualizes the air flow past the streamliner without a fin, Figure 6.50 the low fin version and Figure 6.52 the high fin version of the streamliner all at Ø = 10°.

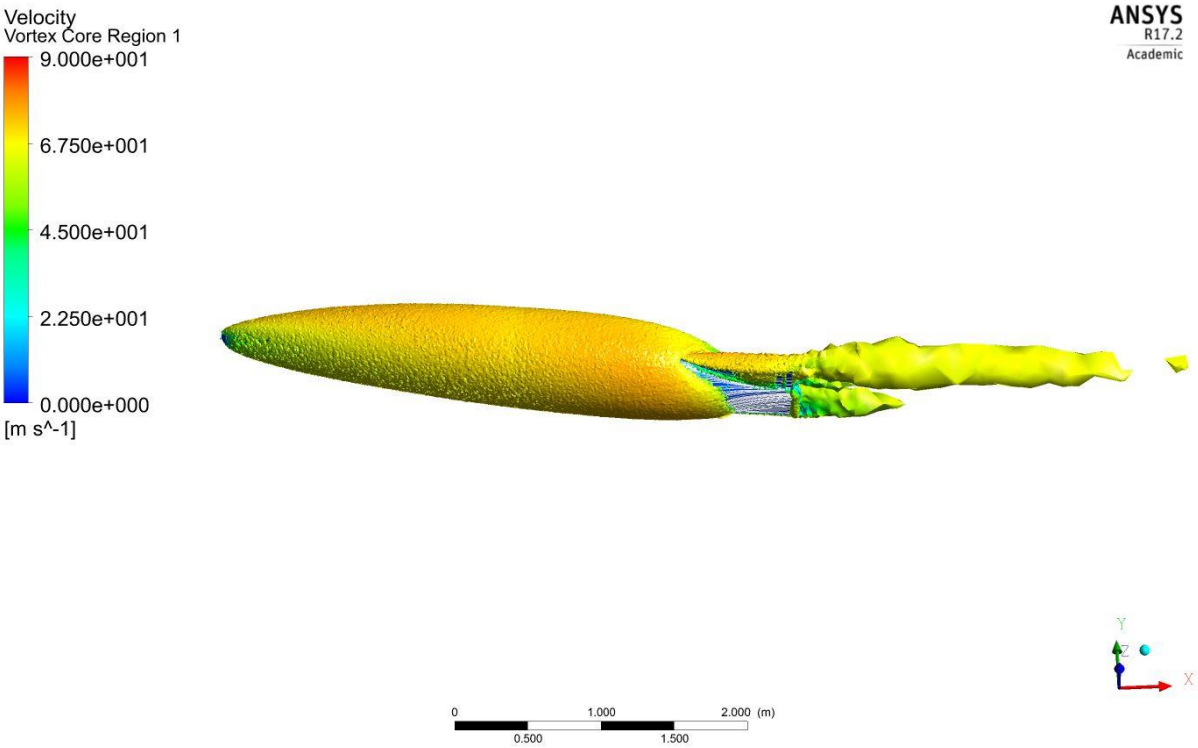

Figure 6.49- Velocity vortex core for streamliner with no fin Ø =10°

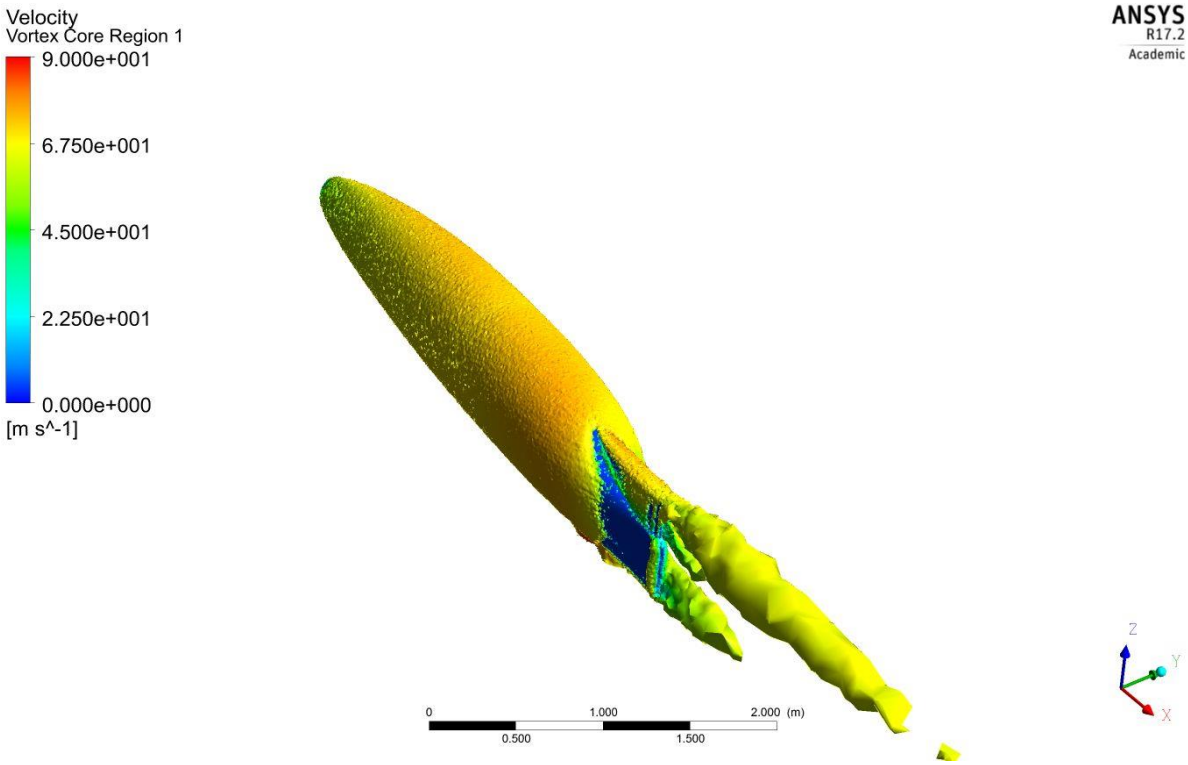

Figure 6.50- Velocity vortex core for streamliner with low fin Ø =10°

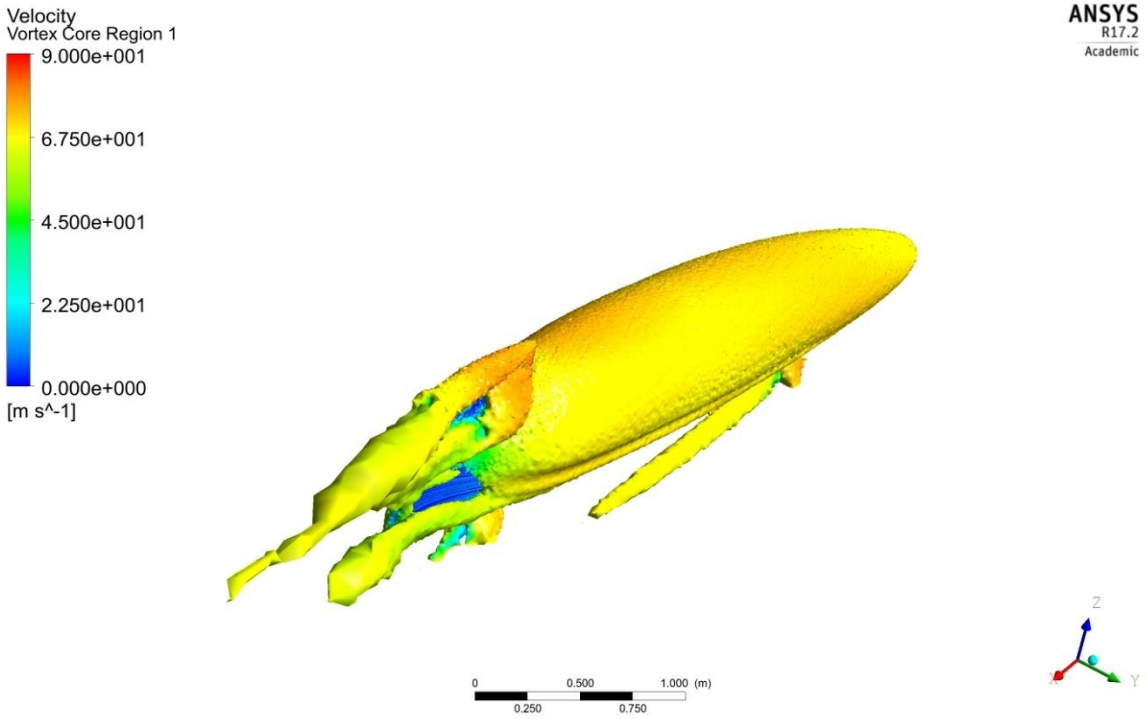

Figure 6.51- Velocity vortex core for streamliner with high fin Ø =10°

The presence of a fin clearly adds to the strength of the streamwise vortex that originates on the upper surface of the streamliner. The high fin has a stronger streamwise vortex. The primary purpose of the fin is to reduce the (adverse) yaw moment and Figure 6.52 indicates that the addition of the low and high fins both reduce the negative yaw moment compared to the base sidecar.

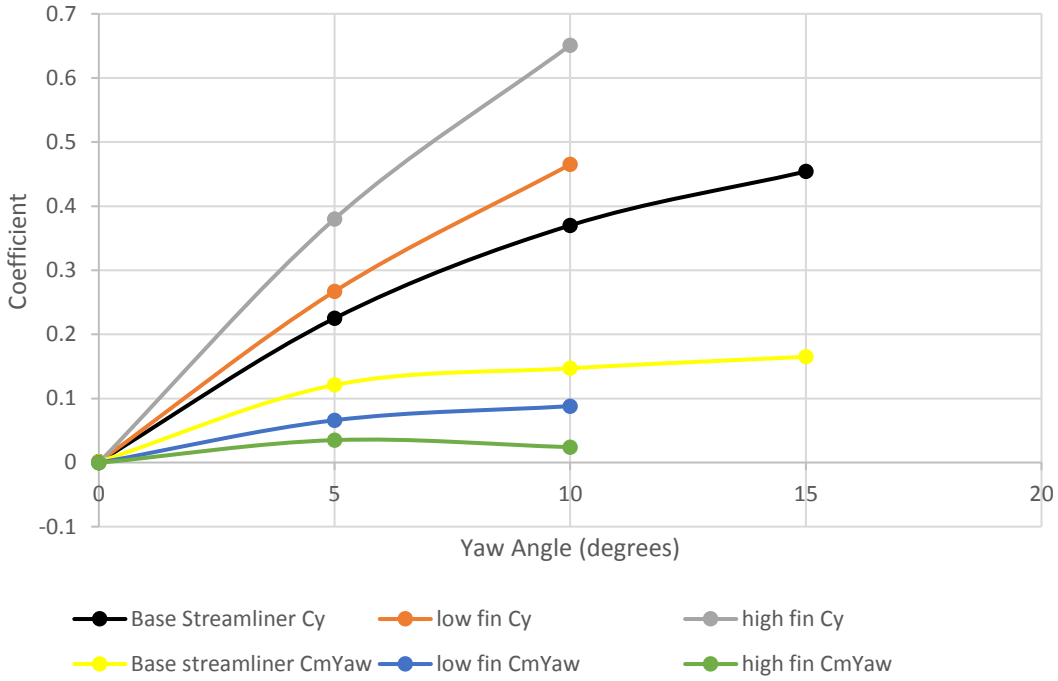

Figure 6.52- Lateral force and yaw moment coefficient for base, low fin and high fin streamliner

Also evident in Figure 6.52 is an increase in lateral force coefficient (C_y). As the high fin reduces the yaw moment coefficient C_{mYaw} to < 25% of the base streamliner value, it is evident that the addition of the fin moves the centre of aerodynamic pressure rearward, closer to the vehicle centre of mass

Although the addition of a fin adds to the aerodynamic stability by moving the centre of aerodynamic pressure rearward, the forces developed by the fin also increase the magnitude of rolling moment as indicated in Figure 6.53.

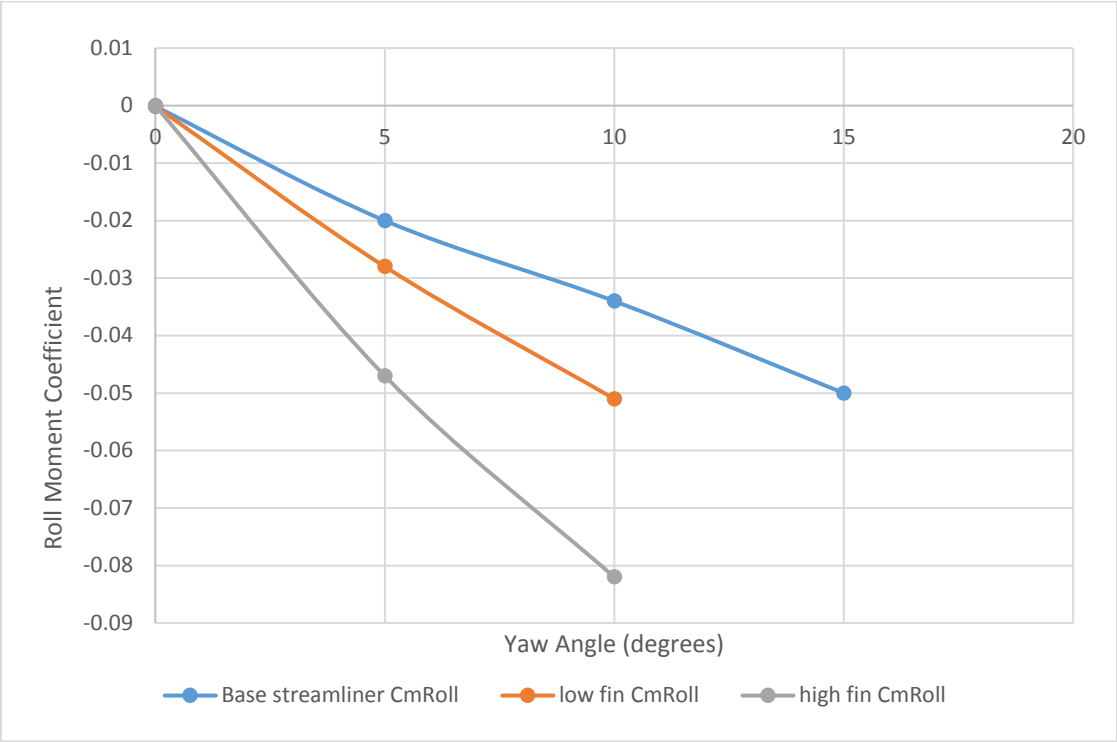

Figure 6.53- Roll Moment Coefficient versus Ø for base, low fin and high fin streamliner

A negative roll moment coefficient indicates that the streamliner will roll to the right when viewed from above and behind. From the increase in negative roll moment coefficient with an increase in the lateral force coefficient (Figure 6.53) it is evident that the addition of a fin has not only moved the centre of aerodynamic pressure rearward—it has also moved the centre of pressure upward. Physically, this is expected as there is a greater area of bodywork higher when a fin is added. The high fin rolls the vehicle more than the low fin, but both add roll to the base vehicle, which may be detrimental to stability.

Because the motorcycle streamliner is a single-track vehicle, it reacts to a roll moment differently than would a four-wheel vehicle. A four-wheel vehicle has a roll axis that is generally along the centreline of the vehicle at some height above the ground. The axis may be tilted (front roll centre higher than rear, or vice versa). The application of a roll moment is resisted by the shifting of the centre of mass as the vehicle rolls on its roll axis.

A two-wheel single-track vehicle has its roll axis aligned longitudinally between the contact patches of the front and rear wheels. Effectively, a single-track vehicle (like a bicycle or motorcycle) has zero roll stiffness and resists the roll moment created by a side wind or yaw angle by altering its centre of gravity by rotating its front wheel about the steering axis to maintain balance.

6.8 Effects of Lift and Side Forces

A plot of lift coefficient (C_l) versus yaw angle indicates that lift of the streamliner increases with increasing yaw angle and that the addition of both the low and high fin decreases the amount of lift and delays crossing into positive lift (Figure 6.54).

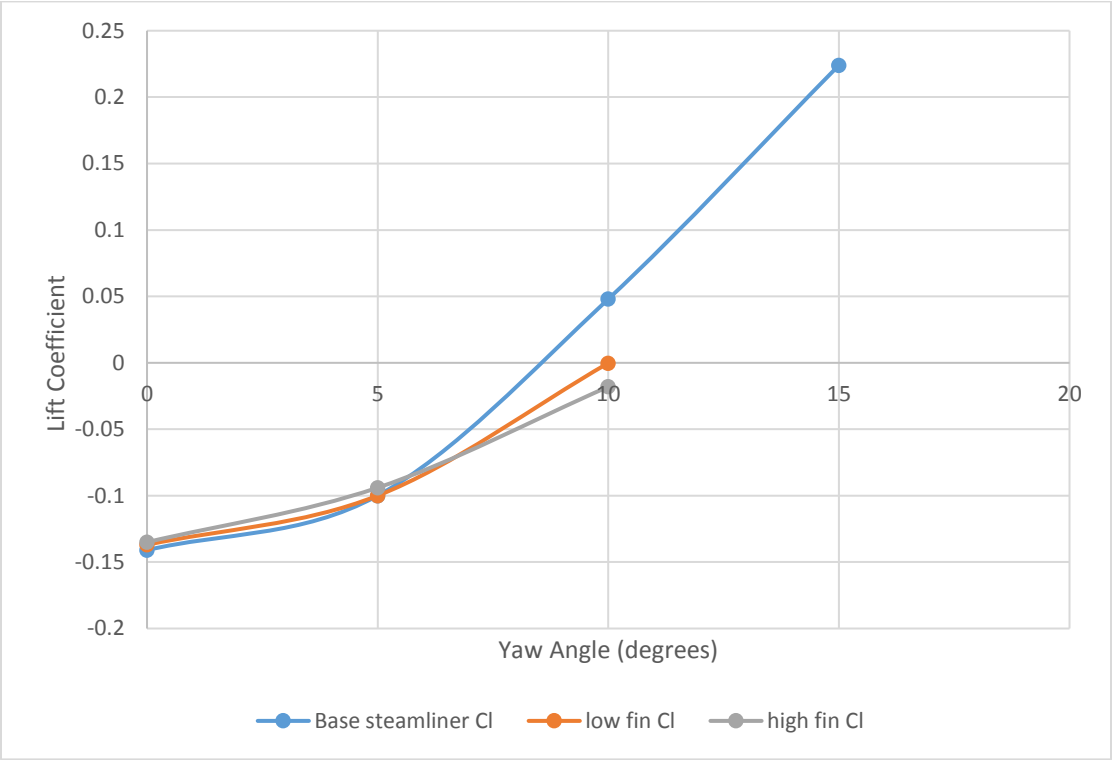

Figure 6.54- Ø versus lift coefficient (C_l) for streamliner

Plotting the roll moment coefficient versus C_l (Figure 6.55) provides an indication that the roll moment is dependent upon the lift, and that the high fin creates a higher lift and roll moment than does the base version of the streamliner.

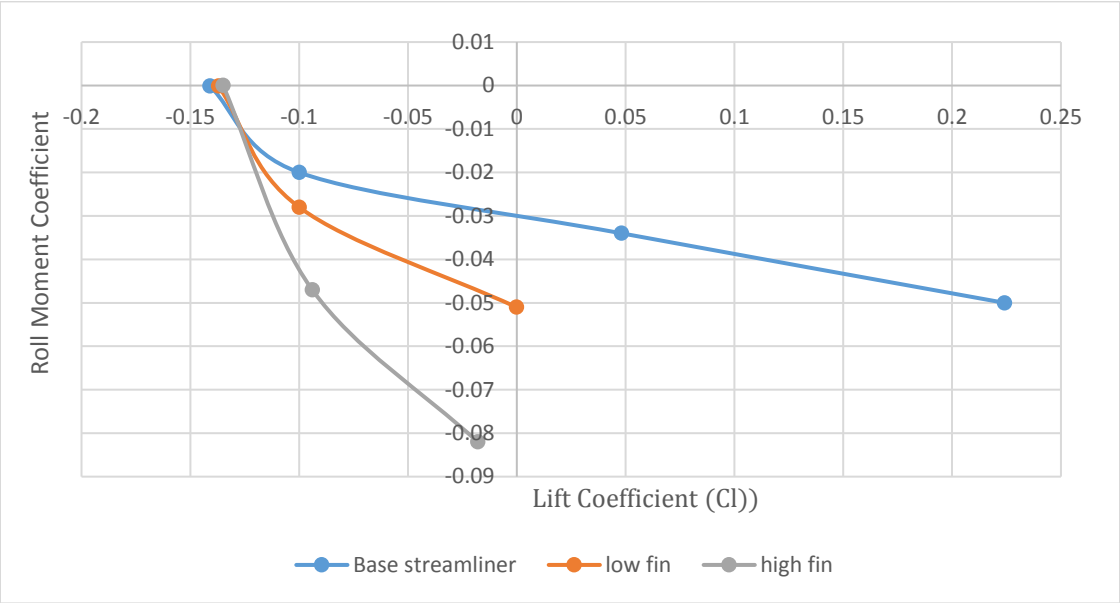

Figure 6.55- Streamliner lift coefficient versus roll moment coefficient

6.9 Streamliner Lift Stability

From Figure 6.16, the Purdue streamliner was shown to be operating within a stable speed range and thus small amounts of leaning and/or steering can be expected to die away without changing the vehicle stability. The aerodynamic lift that occurs at large yaw angles (>30°) is examined in Figure 6.56 for the base streamliner and the streamliner with low and high fins at a speed of 150 mph (67 m/s).

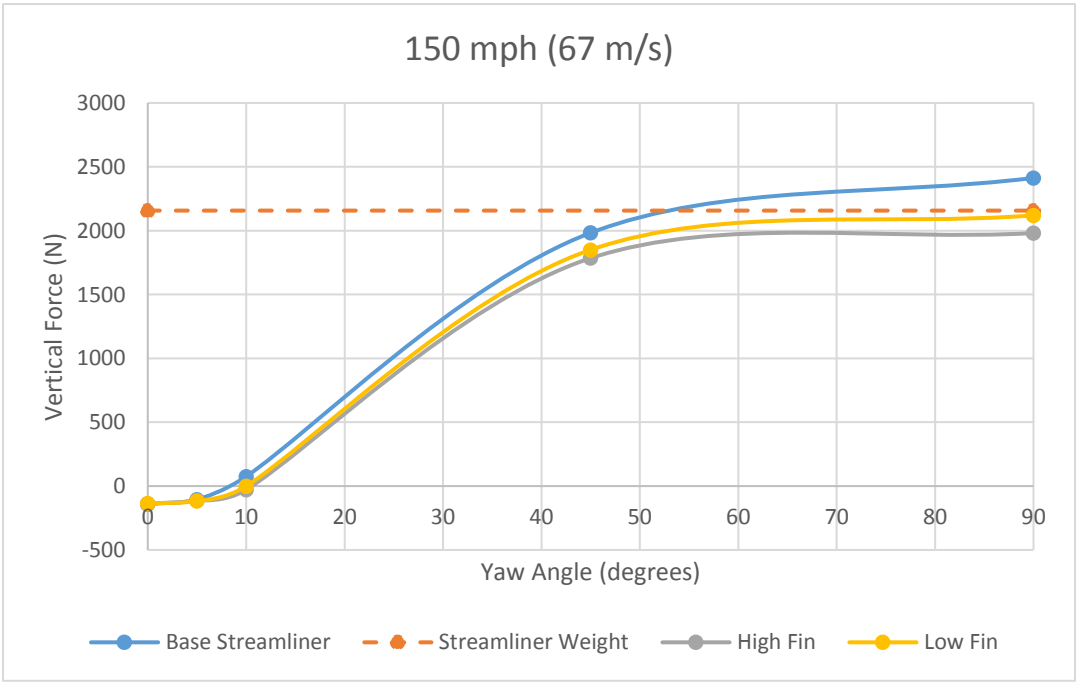

Figure 6.56- Streamliner lift force versus large yaw angle-150 mph

At 150 mph (Figure 6.56), the base streamliner almost leaves the ground at Ø = 45°—the lift force nearly exceeding the downward force of the mass of the vehicle (denoted by the dashed red line). The addition of both the low and high fins helps keep the lift force below the vehicle mass up to Ø = 90°, but without the fins the streamliner could be expected to be airborne at high yaw angles, or at lower yaw angles in presence of side wind gusts. Because of the low overall weight of the 150-kg electric streamliner (150kg vehicle + 70 kg rider), the lift forces generated by significant yaw angles are much more important than they would be for a heavier traditional streamliner.

Figure 6.57 shows the pressure distribution on the top surface of the high fin streamliner at 67 m/s and at Ø = 45°.

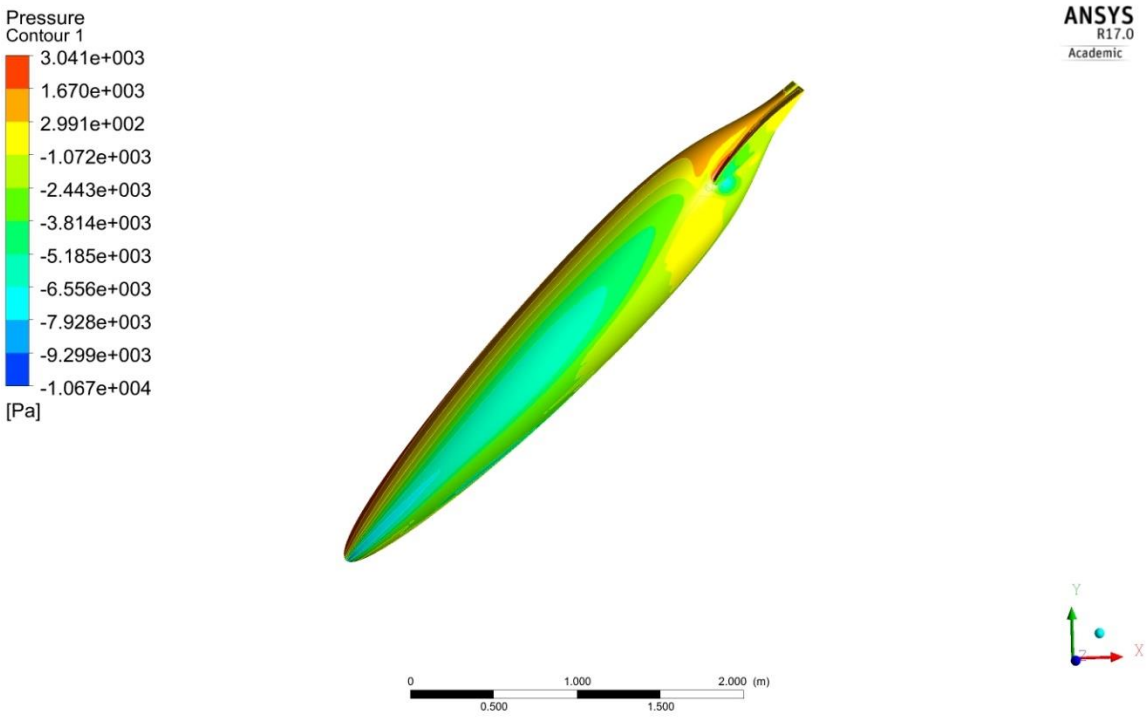

Figure 6.57- Pressure distribution on high fin streamliner at 67 m/s and Ø =45°

Note that in Figure 6.57, there is a significant low-pressure region on the top surface of the streamliner. The fast, attached flow over this area created a low-pressure region responsible for the lift.

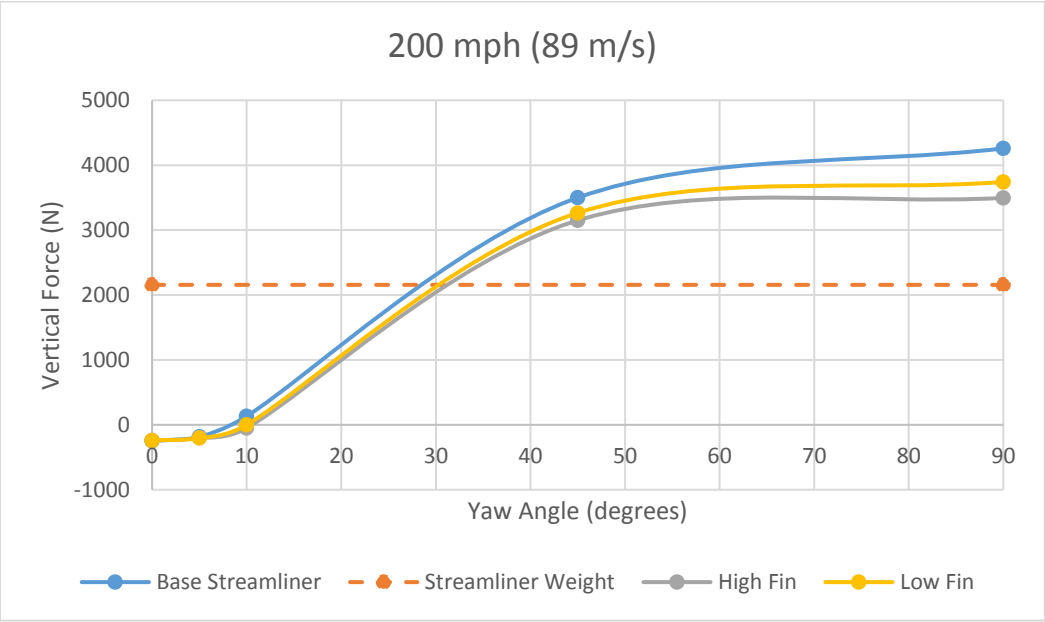

Figure 6.58- Streamliner lift force versus large yaw angle-200 mph

At 200 mph (Figure 6.58), the base streamliner and the streamliner with low and high fins all produce enough lift at Ø = 30° to become airborne, the lift exceeding the downward force of the vehicle, denoted by the dashed red line. Although 30 degrees of yaw is unlikely to be achieved in normal operation, a perturbation caused by a soft spot on the salt surface and subsequent wheel spin could cause yaw at this level.

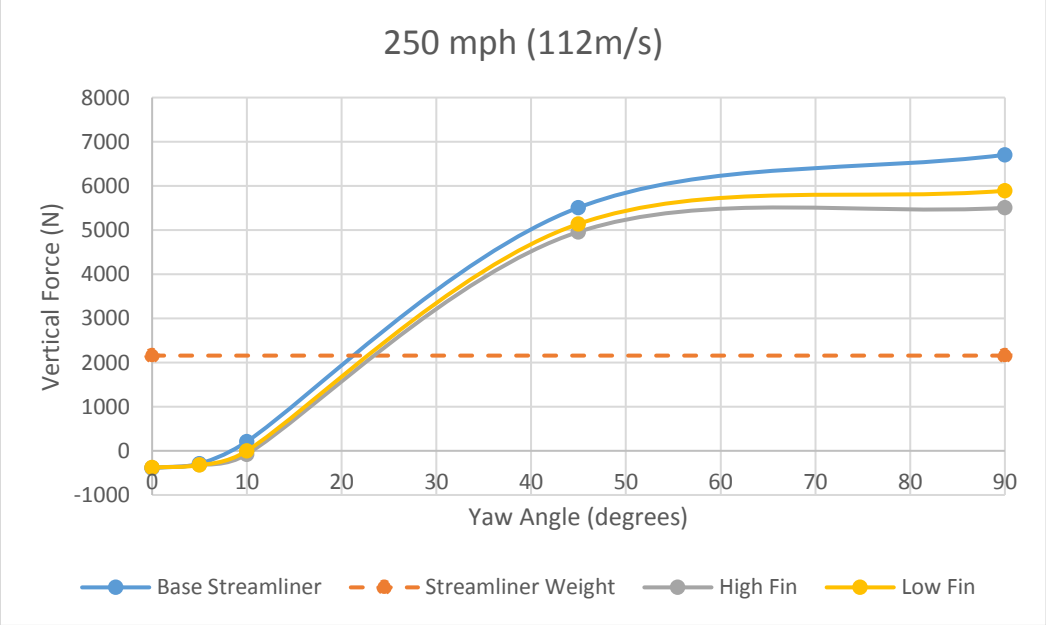

Figure 6.59- Streamliner lift force versus large yaw angle-250 mph

250 mph is the maximum design speed off the Purdue University streamliner. In Figure 6.59, it is evident that a much smaller yaw angle (>20 degrees) than at slower speeds puts the streamliner dangerously close to leaving the track surface.

6.10 Addition of a dorsal "shark" fin

The lift generated over the top surface of the Purdue streamliner (including the high fin version) could result in the vehicle becoming airborne at large yaw angles. It is possible to break up the flow somewhat by adding a vertical dorsal "shark" fin along the top of the streamliner. Figure 6.60 indicates a shark fin added to the Purdue streamliner.

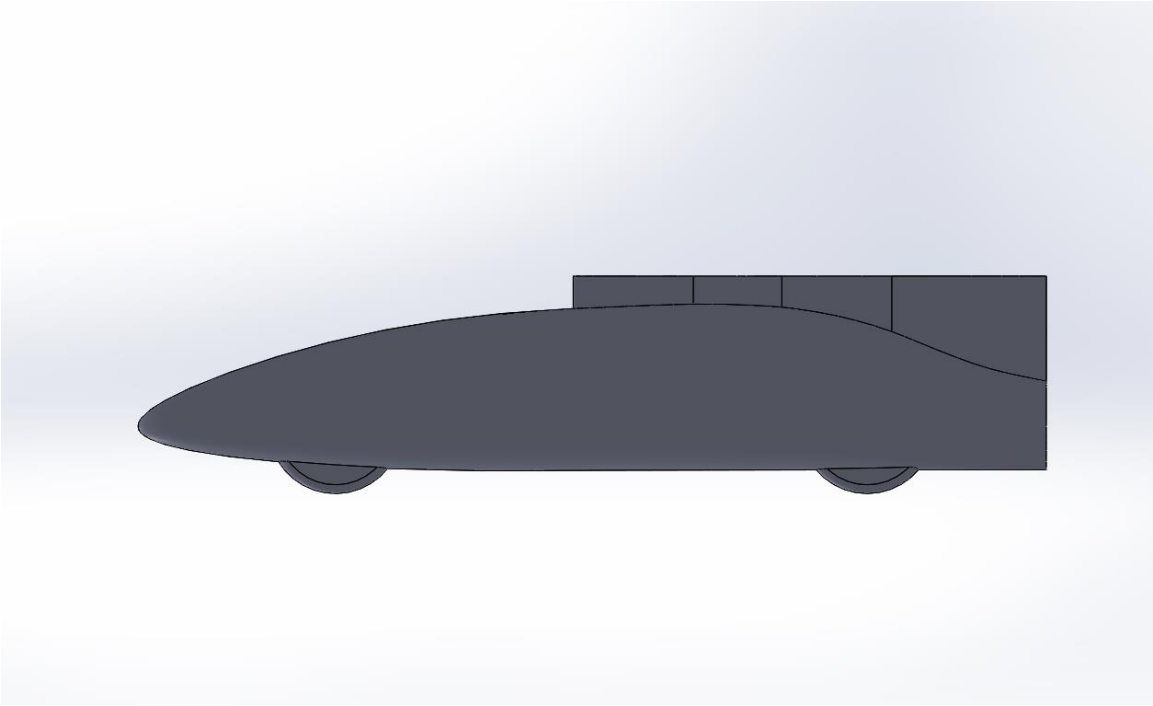

Figure 6.60- Longitudinal dorsal "shark" fin added to the Purdue streamliner

Shark fins were required on world endurance racing sports cars beginning in 2012 with the goal of reducing yaw-induced lift and vehicle rollover (f1technical.net, 2011). Flow over the Purdue streamliner with shark fin was simulated using ANSYS Fluent under the same conditions as the prior test. The results are provided at 150 mph (Figure 6.61), 200 mph (Figure 6.62) and 250 mph (Figure 6.63).

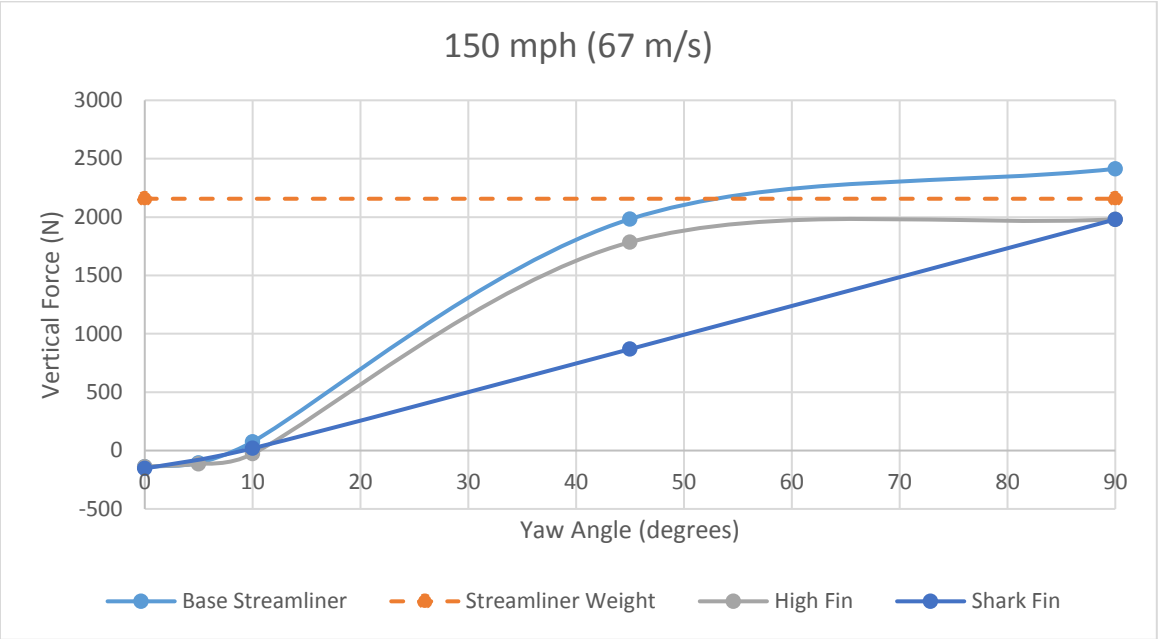

Figure 6.61- Purdue streamliner with and without shark fin at 150 mph

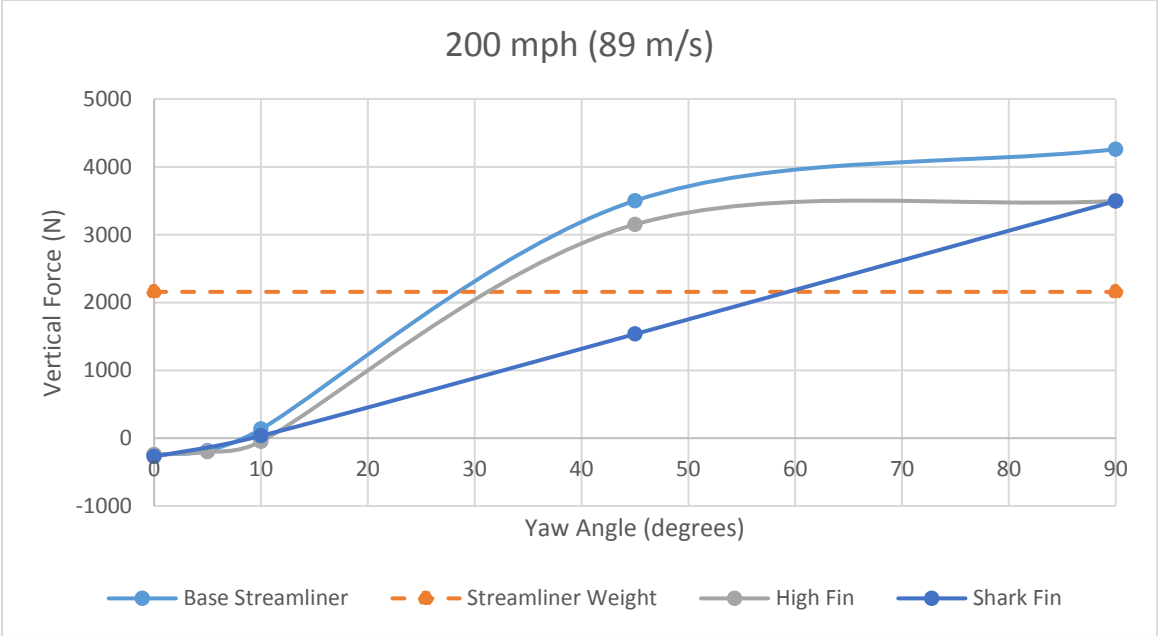

Figure 6.62- Purdue streamliner with and without shark fin at 200 mph

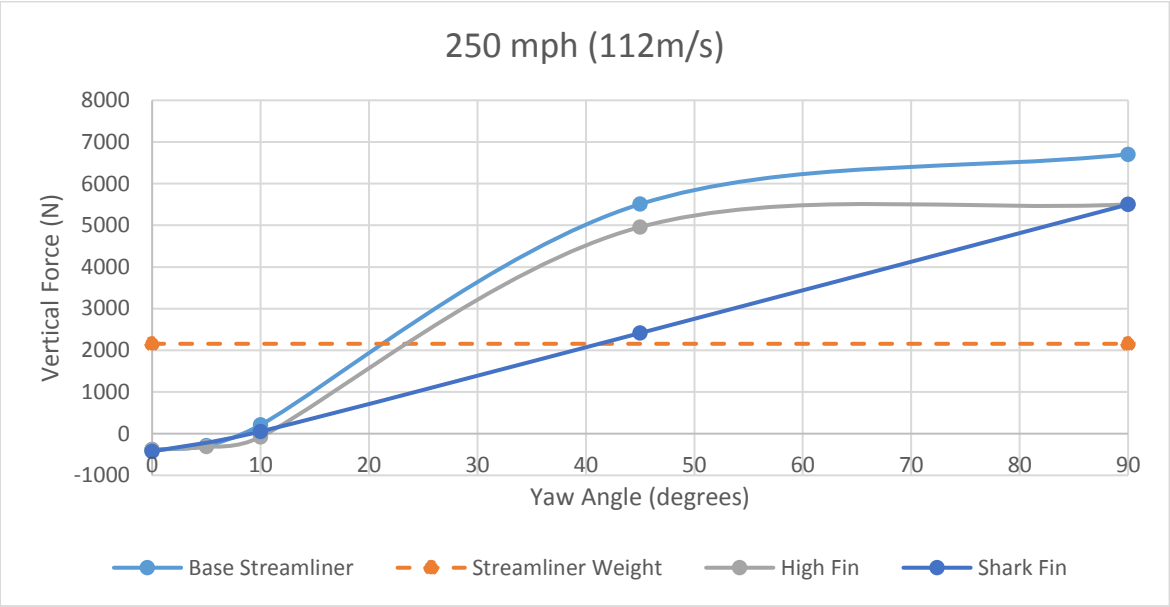

Figure 6.63- Purdue streamliner with and without shark fin at 250 mph

From the above figures, the shark fin is effective at reducing the lift created by flow over the top surface of the streamliner, allowing yaw angles of up to 40° at 250 mph without vehicle lift-off.

Figure 6.64 is a vector plot of the velocity field over the high fin version of the Purdue streamliner at Ø = 45°. In Figure 6.64, flow is coming from the left at 150 mph and remains attached over the top surface of the vehicle, allowing it to act as a wing.

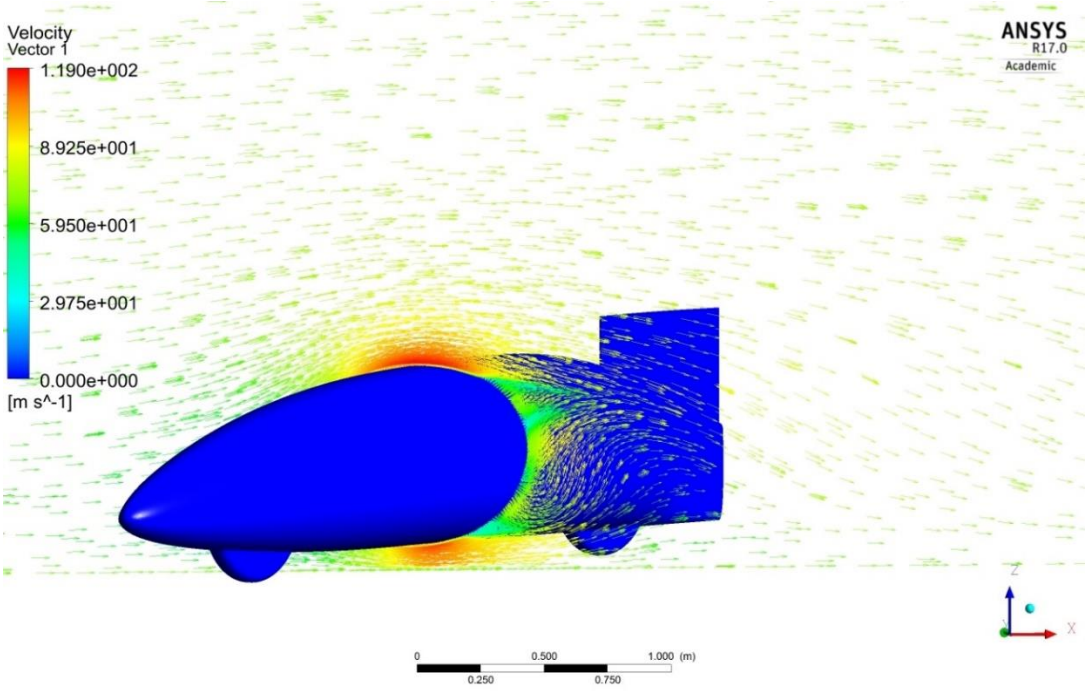

Figure 6.64- Air flow over the high fin streamliner at Ø = 45°

Figure 6.65 adds the shark fin to the streamliner at Ø = 45° and 150 mph. The shark fin breaks up the flow over the top surface, reducing the lift as observed in Figures 6.61, 6.62, and 6.63.

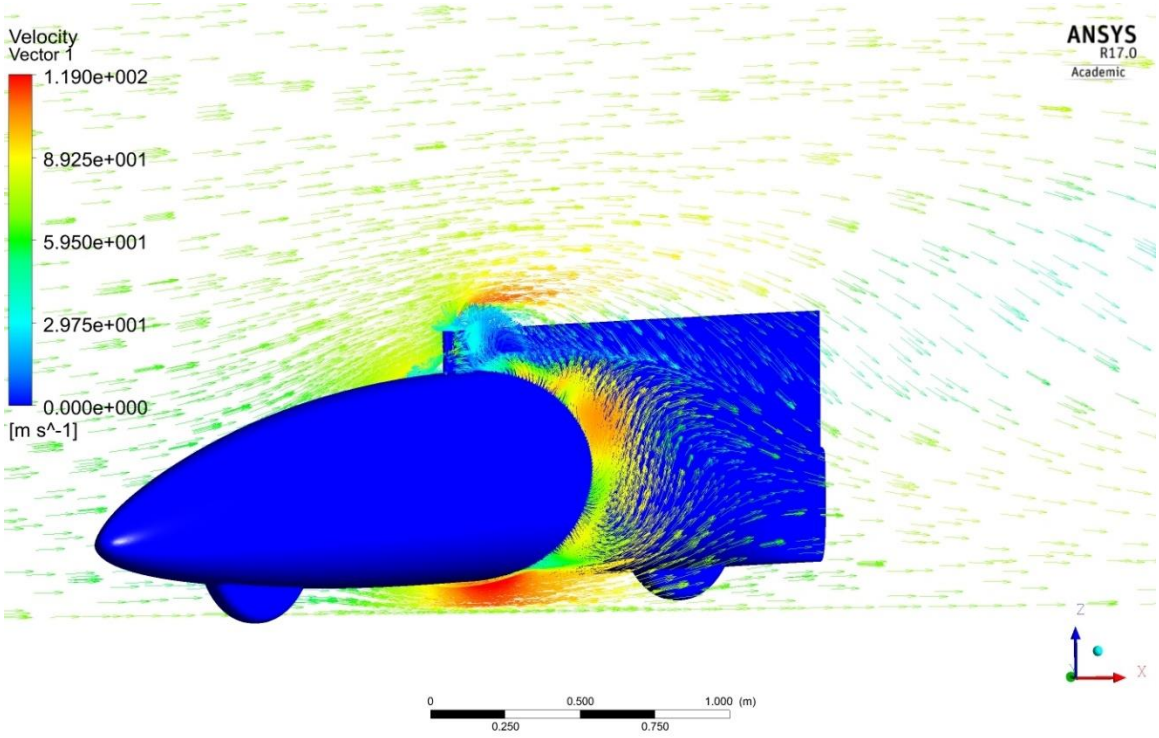

Figure 6.65- Air flow over the shark fin streamliner at Ø = 45°

Compared to the high fin streamliner in Figure 6.57, in Figure 6.66, the shark fin is seen to partially disrupt the low-pressure region on the top surface on the streamliner, reducing the amount of lift.

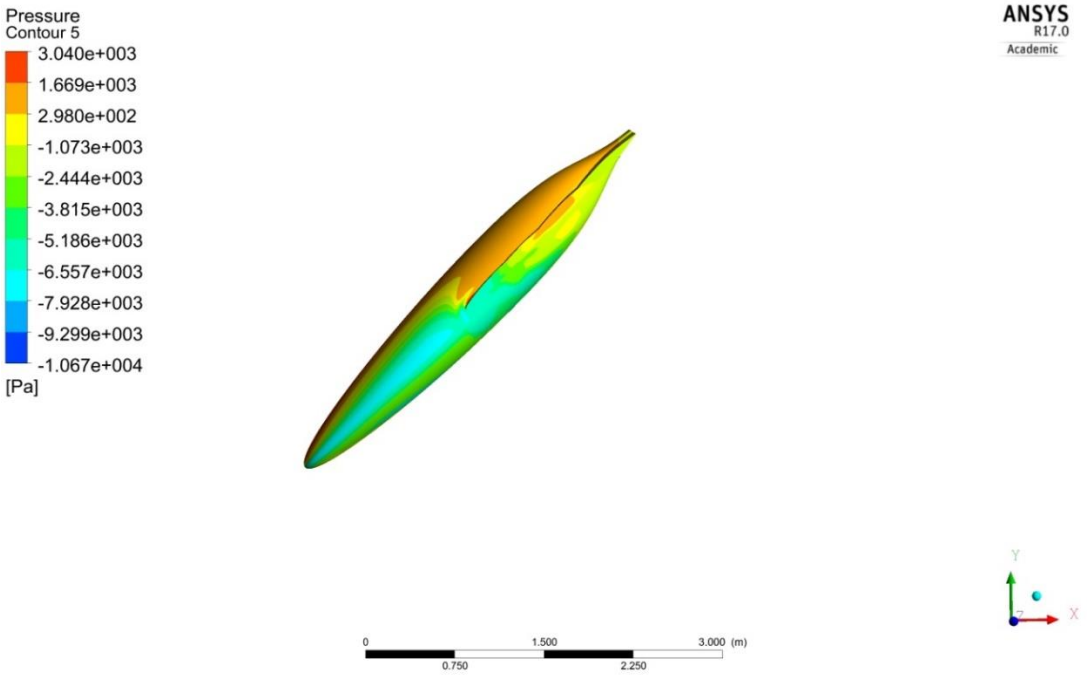

Figure 6.66- Pressure distribution on streamliner with shark fin at Ø = 45°

A plot of velocity vortex core in Figure 6.67 for the streamliner with shark fin at Ø = 45° indicates that the shark fin has disrupted the flow into the wake region which has resulted in reduced lift at this high yaw angle.

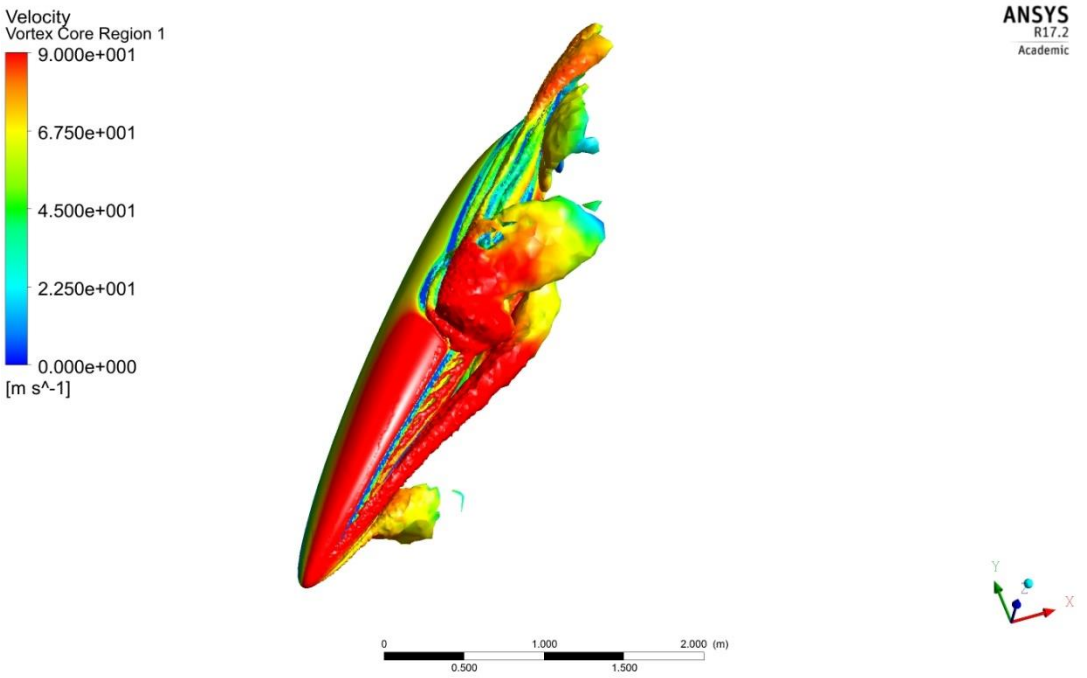

Figure 6.67- Velocity vortex core plot for streamliner with shark fin Ø = 45°

Figure 6.68, a plot of the surface shear stresses on the streamliner with shark fin at Ø = 45° also indicates regions of separation at about 80% of the vehicle height on the downwind side of the vehicle.

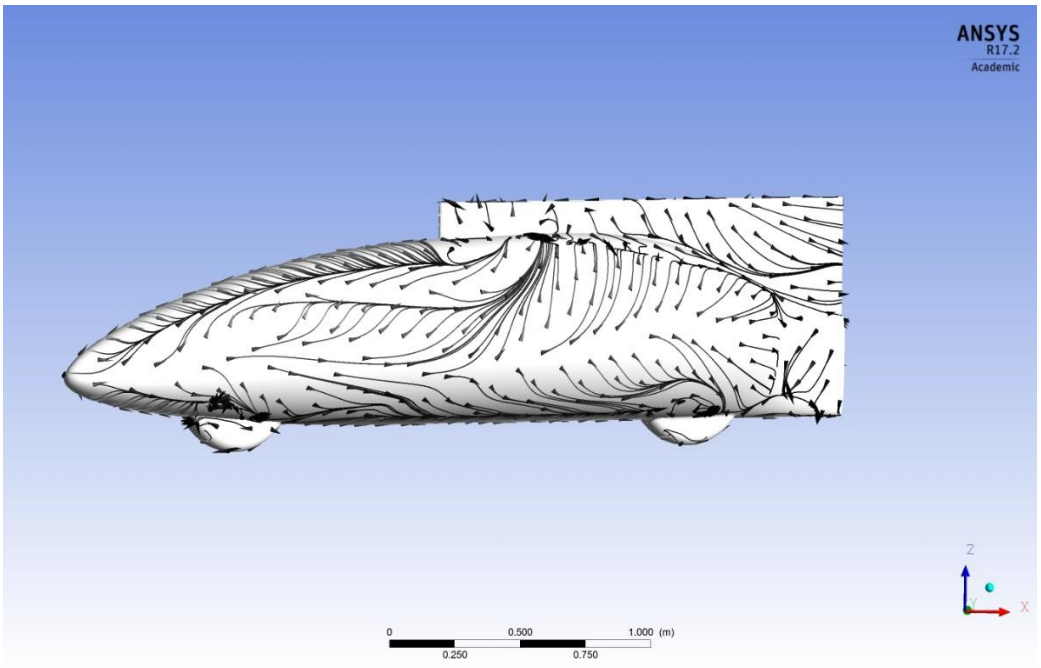

Figure 6.68- Surface shear stress plot for streamliner with shark fin at Ø = 45°

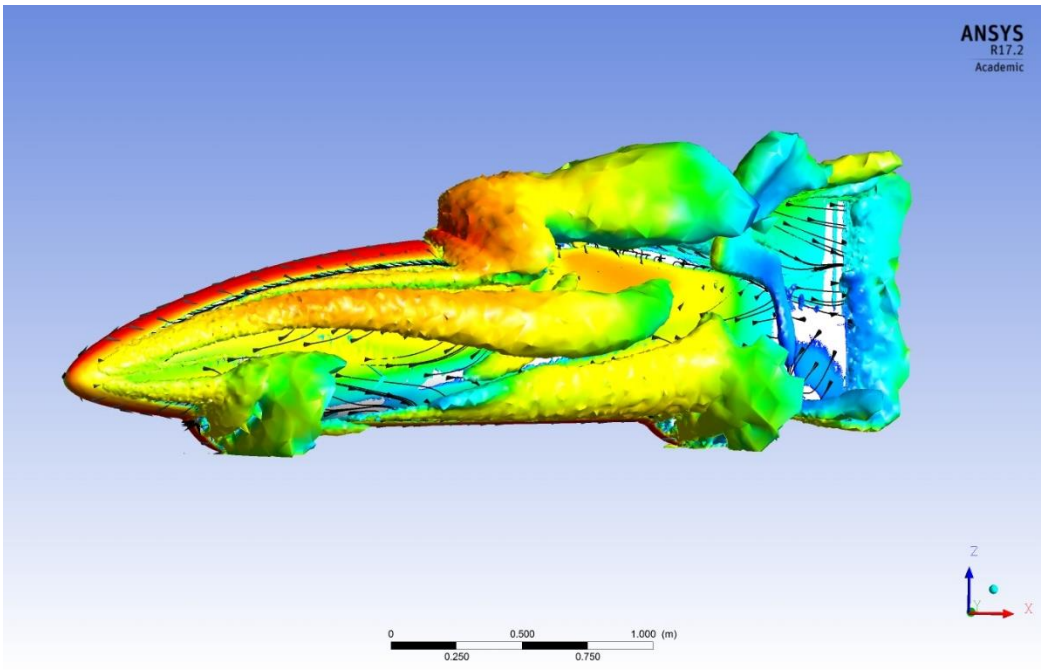

Figure 6.69- Velocity vortex core for streamliner with shark fin at Ø = 45°

In Figure 6.69, the location of the separation matches the locations of the separation lines in Figure 6.68. Figure 6.69 also shows the separation over the top of the shark fin, which helps to reduce the lift at this high angle of Ø = 45° Ø = 45°.

It must be noted that the low fin, high fin and shark fin designs used for these comparisons were simply created and have had no optimization to improve their performance. If additional design work was undertaken, their performance and effectiveness could undoubtedly be improved.

6.11 Summary of Chapter 6

In this chapter, two symmetrical vehicles were studied to determine dynamic and aerodynamic stability characteristics. Using the equations of motion, an Ahmed body simulated generic four-wheel vehicle was shown to have dynamic stability to over 100 m/s (224 mph). It was also demonstrated to have negative lift (downforce) when yawed 90° to the direction of airflow, indicating it is likely that it would roll due to aerodynamic forces caused by yawing.

A highly streamlined two-wheel symmetrical vehicle was also examined for dynamic and aerodynamic stability. Dynamically, two-wheel single-track vehicles have three important stability modes that must be considered when judging dynamic stability. Work done at Purdue University on the example streamliner used in this chapter indicated that the streamliner would be stable to a high speed.

The aerodynamics of the streamliner were also examined using CFD (ANSYS Fluent) and characterized over a range of yaw angles. The streamliner at small yaw angles (<10°) exhibited primarily surface friction viscous drag and little pressure drag. Above 10°, pressure drag dominated. A strong relationship between lift and lateral force generation and roll moment was determined. Yaw stability of the streamliner was improved by the addition of a rear fin, although the fin also increased the roll moment with increasing yaw angle.

At high yaw rates (Ø = 45° and above), significant lift was evidenced and at high speeds (>150 mph) could result in the very light streamliner (220 kg) leaving the ground. This was determined to be caused by the attached flow over the majority of the top surface of the streamliner. The addition of a dorsal vertical “shark fin” along part of the top surface was found to break up the flow, reducing the lift significantly, lift-off not occurring until approximately 45° of yaw at 250 mph. Although fins are commonly used on land speed record vehicles to enhance directional stability, the use of a shark fin on such vehicles to spoil lift at high yaw angles is not often observed. The fins and shark fin were not optimized and further improvements in aerodynamic stability of the streamliner could be expected.

The tools developed in this chapter to examine dynamic and aerodynamic stability of a two-wheel single-track vehicle and a four-wheel generic vehicle will be applied in Chapter 7 to the dynamic and aerodynamic stability of the three-wheel two-track sidecar. Table 6.2 summarizes the results from Chapter 6.

Table 6.2: Summary of results from Chapter 6

Configuration	**Dynamic stability**	**Low yaw aerodynamic stability**	**High yaw aerodynamic stability**
"scale 4 Ahmed"	Using Eq. of Motion Bicycle model stable	0-25° Stable to 150 mph	45-90° Stable to 150 mph
Base Streamliner	JBike6 and BikeSim stable	0-15° Stable to 200 mph	45-90° Lift greater than mass- airborne above 150 mph
Streamliner low fin	not tested	0-15° Stable to 200 mph-improved yaw stability	45-90° Lift greater than mass- airborne above 150 mph
Streamliner High fin	not tested	0-15° Stable to 200 mph-improved yaw stability	45-90° Lift greater than mass- airborne above 150 mph
Streamliner Shark fin	not tested	0-45° Stable to 250 mph-improved yaw stability	45-90° Lift greater than mass- airborne above 250 mph

CHAPTER 7 ASYMMETRICAL SIDECAR STABILITY

7.1 OVERVIEW

The dynamic and aerodynamic stability of two-track, three-wheel sidecar vehicles, particularly at high speeds, has been rarely studied. In this chapter, several new areas of study will be introduced including:

- Dynamic stability of an asymmetric sidecar vehicle accounting for the asymmetric generation of rolling resistance and drive forces and moments
- Dynamic stability of a sidecar vehicle accounting for the generation of asymmetric aerodynamic drag and lateral forces and moments
- Requirements for rider steering inputs to counter asymmetric dynamic and aerodynamic forces and moments
- Development of a geometric Symmetry Quotient to help characterize the geometric asymmetry of a vehicle
- The generation of asymmetric aerodynamic forces with changing yaw angle and the differences between positive and negative yaw angles
- The effects of an aerodynamic device, called a splitter, in application on an asymmetric sidecar vehicle

The chapter will begin by examining dynamic stability resulting from the configuration of the sidecar vehicle and then add in the effects of aerodynamic forces and moments.

7.1.1 Dynamic Stability

While the study of dynamic stability of two-wheel (single track) and four-wheel road vehicles has been well-established, the study of three-wheel vehicles has historically received much less attention (Huston, Graves, & Johnston, 1982). The three-wheel vehicle studies that have been undertaken have dealt with tricycle (three track) vehicles with either two wheels at the front and one at the rear ("tadpole" trike), or one wheel at the front and two at the rear ("delta" trike), both of which are designs that are symmetrical around a longitudinal axis (Huston et al., 1982). Two major power sports manufacturers (CanAm and Polaris) produce tadpole trike motorcycles and several start-up mobility companies are looking at tadpole trikes as urban vehicles. Much of the scholarly interest in three-wheel vehicle design and stability has come from university-backed solar-racing cars, where removing the fourth wheel reduces the overall rolling resistance of the vehicle (Starr, 2006).

Lurie (Lurie, 2012) briefly studied the motorcycle sidecar configuration (a vehicle leaving two tracks) with the front and rear wheels in line and the sidecar wheel offset from a line running

between the front and rear wheels. His analyses of directional stability of an asymmetrical sidecar (part of a Master's thesis) followed previous lateral stability models, using the zero-width "bicycle" model (see Chapter 6) to define lateral forces and rotation about the centre of mass of the vehicle. Lurie's work is the only dynamic study of a motorcycle sidecar in the literature.

7.2 TRIKE STABILITY

Huston et al. (1982) used the bicycle model approach described in Chapter 6 for three-wheeled tricycle vehicles by placing two front wheels side-by-side alongside the fore-aft symmetry axis and one wheel at the rear for a tadpole trike, and one wheel at the front and two wheels side-by-side at the rear for a delta trike. In this case cornering stiffness for the paired tyres is twice what it is for the single tyre (assuming all tyres are the same type).

7.2.1 Tadpole and delta trikes

Using the bicycle model, Huston et al. (1982) found that equations describing motion were the same for four-wheel vehicles and three-wheel tadpole and delta trikes. The difference in stability criteria came from the differing weight distribution for each type of vehicle and the load on the front and rear tyres.

Recall from Chapter 6, a four-wheel vehicle will be laterally stable if the vehicle centre of mass is located in the front half of the vehicle:

$$W_f = \frac{W\, l_2}{2L} \quad \text{and} \quad W_r = \frac{W\, l_1}{2L}$$

Huston et al. (1982) defined the geometry for a tadpole trike with two wheels at the front as indicated in Figure 7.1.

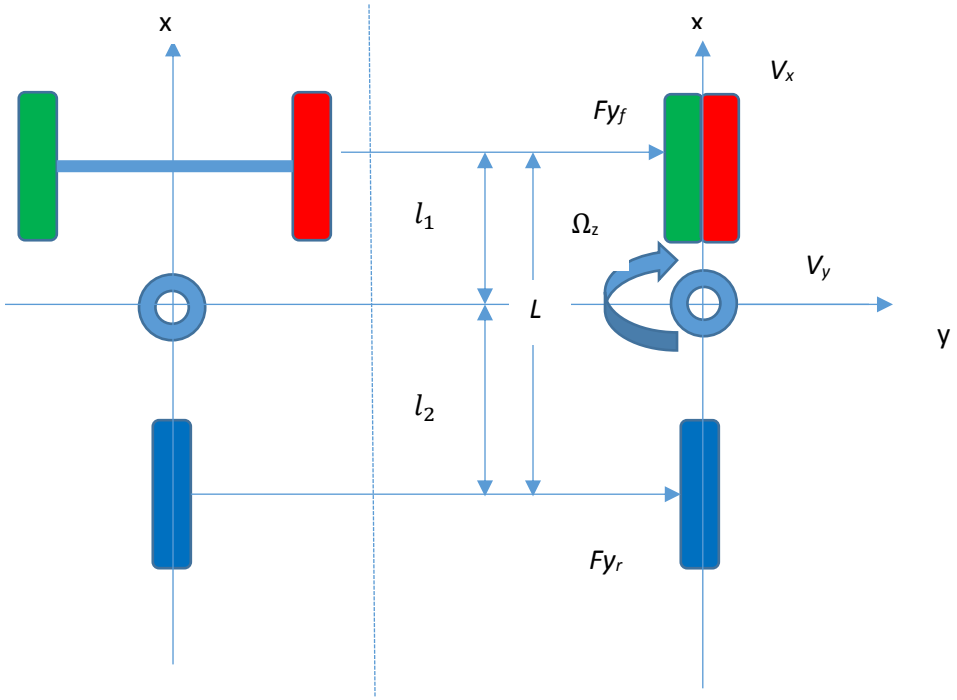

Figure 7.1- Bicycle model of tadpole trike

Working through the equations in the same way as the four-wheel case from Chapter 6, Huston et al. (1982) developed the following:

$$W_f = \frac{W\, l_2}{2L} \quad \text{and} \quad W_r = \frac{W\, l_1}{L}$$

Further, for a delta trike with two wheels at the rear (Figure 7.2):

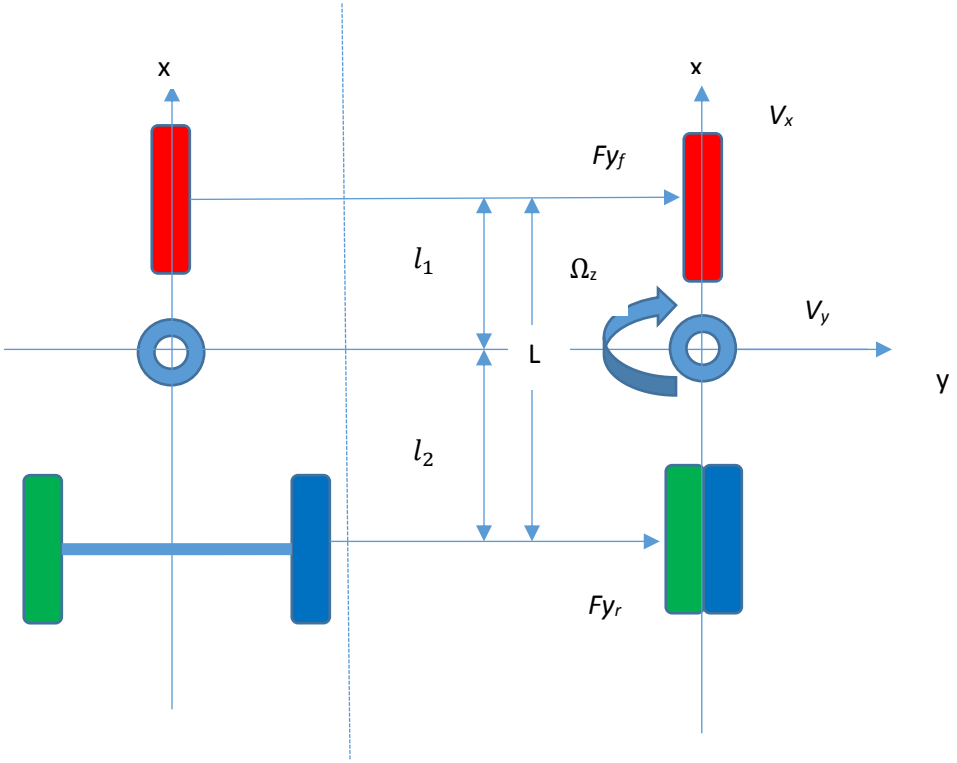

Figure 7.2- Bicycle model of delta trike

produced the result:

$$W_f = \frac{W\, l_2}{L} \quad \text{and} \quad W_r = \frac{W\, l_1}{2L}$$

Huston et al. (1982) rewrote the Chapter 6 equation 6.9 as:

$$L + \frac{Vx^2}{g}\left(\frac{Wf}{C\alpha f} - \frac{Wr}{C\alpha r}\right) > 0 \qquad (7.1)$$

where

L = the total distance between the front and rear axles $(l_1 + l_2)$

g = the gravitational constant

W_f , W_r = the weight on each of the front and rear tyres respectively

If the above equation is set to zero, the speed at which the vehicle becomes unstable, called the *critical speed*, is calculated from:

$$V_{crit} = \sqrt{((-gL)/K_{us})} \qquad (7.2)$$

where K_{us} is the understeer coefficient (sometimes called understeer gradient) from:

$$K_{us} = \left(\frac{Wf}{C\alpha f} - \frac{Wr}{C\alpha r}\right) \quad (7.3)$$

The relationship of cornering stiffness C_α and tyre normal load (W_t) is given by:

$$C_\alpha = (A - BW_t)\, W_t \quad (7.4)$$

Where A and B are positive constants that depend upon the tyre characteristics. Recall from Chapter 6, for a four-wheel vehicle, lateral stability is ensured if the centre of mass of the vehicle is located in the front-half of the vehicle.

For a three-wheel trike with two wheels at the front, from equation 7.4, the relationship for understeer coefficient, K_{us}, can be rewritten as:

$$K_{us} = \frac{W_f}{C_{\alpha f}} - \frac{W_r}{C_{\alpha r}} = \frac{BW(l_2 - 2l_1)}{2L(A - BW_f)(A - BW_r)} \geq 0 \quad (7.5)$$

Huston et al. (1982) used equation 7.5 to find:

$$l_2 \geq 2l_1 \qquad \text{or} \quad l_2 \geq \frac{2}{3}L \quad (7.6)$$

A tadpole trike with two wheels at the front will be laterally stable if the centre of mass is located in the front third of the vehicle.

For a delta trike with two wheels in the rear, the same analyses yields:

$$K_{us} = \frac{W_f}{C_{\alpha f}} - \frac{W_r}{C_{\alpha r}} = \frac{BW(2l_2 - l_1)}{2L(A - BW_f)(A - BW_r)} \geq 0 \quad (7.7)$$

$$l_2 \geq \frac{1}{2}l_1 \qquad \text{or} \qquad l_2 \geq \frac{1}{3}L \quad (7.8)$$

For a delta trike, lateral stability is ensured if the centre of mass of the vehicle is located in the front two-thirds of the vehicle.

7.2.2 Sidecar Equations of Motion

The four-wheel vehicle and three-wheel tadpole and delta trikes are all symmetrical vehicles with an axis of symmetry that coincides with the longitudinal centreline of the vehicle. Sidecars are highly asymmetrical and have no single axis of symmetry. Lurie (2012) applied the same approach as Huston et al. (1982) to write equations of motion for a “bicycle” model that placed the sidecar wheel along the same longitudinal axis as the front and rear wheels to allow lateral forces and rotational moments around the centre of gravity to be calculated (Figure 7.3).

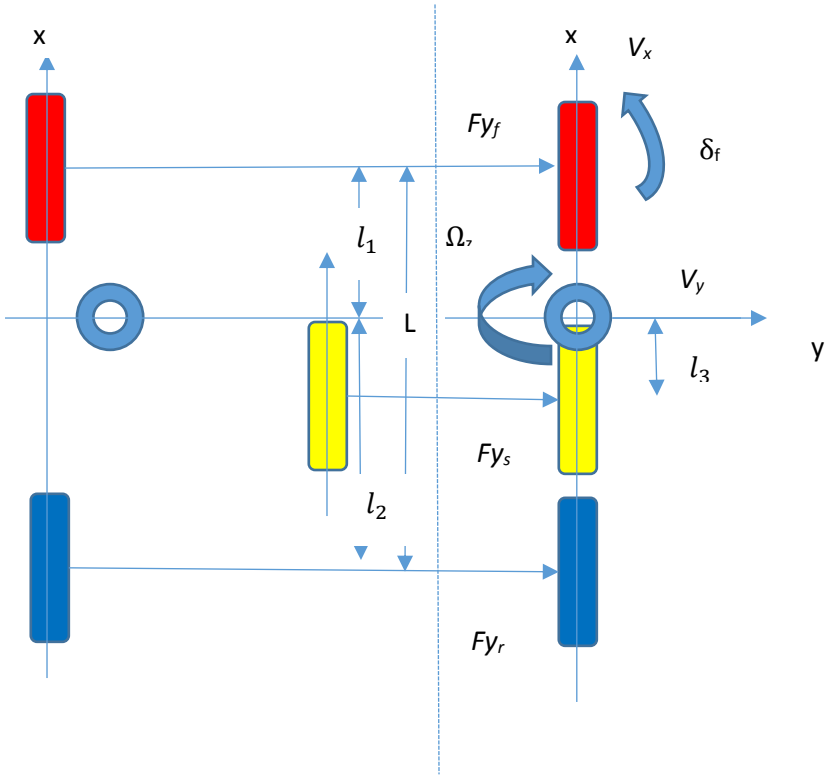

Figure 7.3- Bicycle Model for Sidecar (Left: true wheel layout; Right: layout in bicycle model)

In Figure 7.3, the circle represents the position of the centre of mass. For three-wheel sidecar, Lurie's equations written with zero steer angle (δ_f) are:

$$m\,(\dot{V}_y) + \left(\mathrm{mV_x} + \frac{l_1\,C_{\alpha f} - l_2\,C_{\alpha r} - l_3\,C_{\alpha s}}{Vx}\right)\Omega_z + \left(\frac{C_{\alpha f} + C_{\alpha r} + C_{\alpha s}}{Vx}\right)\mathrm{V_y} = 0 \quad (7.9)$$

$$I_z(\dot{\Omega}_z) + \left(\frac{{l_1}^2\,C_{\alpha f} - {l_2}^2\,C_{\alpha r} - {l_3}^2\,C_{\alpha s}}{Vx}\right)\Omega_z + \left(\frac{l_1\,C_{\alpha f} - l_2\,C_{\alpha r} - l_3\,C_{\alpha s}}{Vx}\right)V_y = 0 \quad (7.10)$$

With $C_{\alpha s}$ the cornering stiffness of the sidecar tyre and l_3 the longitudinal distance from the centre of mass to the sidecar wheel. The equations are similar to Huston et al. (1982) for three-wheel trike vehicles, but add in the sidecar cornering stiffness as a separate quantity. In this case, the subscript *f* is for the front wheel, the subscript *r*, is the rear wheel and *s* is the sidecar.

The lateral (y) forces generated by the tyres can be calculated from the cornering stiffness (*C*) and the slip angles (α).

$$F_{fy} = C_{\alpha f}\alpha_f \qquad F_{ry} = C_{\alpha r}\alpha_r \qquad F_{sy} = C_{\alpha s}\alpha_s \tag{7.11}$$

Lurie (2012) introduced an additional factor by allowing the front wheel to have a steering angle, δ_f, different from the slip angle of the rear wheel (α_r) and sidecar wheel (α_s). By countering the summed lateral forces and rotational moments generated by the sidecar with a force generated by a front steer angle (δ_f), the following equations can be written:

$$m\,(\dot{V}_y) + a_1\,(V_y) + a_2\,(\Omega_z) + C_{\alpha f}\delta_f = 0 \tag{7.12}$$

$$I_z\,(\dot{\Omega}_z) + a_3\,(V_y) + a_4\,(\Omega_z) + l_1 C_{\alpha f}\delta_f = 0 \tag{7.13}$$

where

$$a_1 = \frac{C_{\alpha f} + C_{\alpha r} + C_{\alpha s}}{Vx} \tag{7.14}$$

$$a_2 = m\,V_x + \frac{l_1\,C_{\alpha f} - l_2\,C_{\alpha r} - l_3\,C_{\alpha s}}{Vx} \tag{7.15}$$

$$a_3 = \frac{l_1\,C_{\alpha f} - l_2\,C_{\alpha r} - l_3\,C_{\alpha s}}{Vx} \tag{7.16}$$

$$a_4 = \frac{l_1^{\,2}\,C_{\alpha f} - l_2^{\,2}\,C_{\alpha r} - l_3^{\,2}\,C_{\alpha s}}{Vx} \tag{7.17}$$

By assuming that the steer angle (δ_f) and the tyre slip angles (α) were much less than 1 radian, Lurie (2012) defined the following:

$$\alpha_f = \delta_f - \tan^{-1}\frac{Vfy}{Vfx} = \delta_f - \frac{Vfy}{Vfx}$$

$$\alpha_r = \frac{Vry}{Vrx} \qquad \alpha_s = \frac{Vsy}{Vsx}$$

y-velocities	x-velocities
$V_{fy} = l_1\Omega_z + V_y$	$V_{fx} = V_x$
$V_{ry} = l_2\,\Omega_z - V_y$	$V_{rx} = V_x$
$V_{sy} = l_3\,\Omega_z - V_y$	$V_{sx} = V_x$

with the assumption that V_x is significantly larger than the contribution to the longitudinal velocity that comes from the rate of rotation from Equation (7.10) above ($I_z(\dot{\Omega}_z)$).

Lurie (2012) defined the sidecar as directionally stable as long as $a_1a_4 - a_2a_3 > 0$ and rewrote this criteria for stability as:

$$-mV_x^2\,(l_1 C_{\alpha f} - l_2 C_{\propto r} - l_3 C_{\propto s}) + C_{\alpha f} C_{\alpha r} {L_{12}}^2 + C_{\alpha f} C_{\alpha s} {L_{13}}^2 + C_{\alpha r} C_{\alpha s} {L_{23}}^2 \geq 0 \qquad (7.18)$$

where: $L_{12} = l_1 + l_2 \quad L_{13} = l_1 + l_3 \quad L_{23} = l_2 - l_3$

7.3 CALCULATING THE STABILITY OF A SIDECAR

The objective of this section is to not only characterize and quantify the Baker sidecar used for Bonneville land speed record efforts, but, because the topic has been so little researched, to explore the stability of asymmetrical sidecars in general. The stability will be examined in three ways:

- Dynamic stability based upon tyre cornering stiffness and the position of the vehicle centre of mass, neglecting aerodynamic, tractive and rolling resistance forces
- Lateral stability, based upon the generation of lateral forces by the air flow over asymmetrical vehicle bodywork
- Rotational stability, based upon the moments created by the tyre rolling resistance, aerodynamic drag and driving force of the rear tyre around the vertical axis at the vehicle centre of mass

Each of the stability conditions will be examined independently and in combination in an effort to understand the requirements for high speed straight-line stability of a sidecar.

7.3.1 Sidecar frame of reference

Lurie (2012) examined the equations of motion for a sidecar located on the right side of the motorcycle, when viewed from above and behind. This is consistent with the sidecar placement in the United States, but in other parts of the world (and particularly in countries where traffic drives on the left), the sidecar is placed on the left. Such is the case for the Baker Formula One sidecar. To remain consistent with the aerodynamic studies and the physical geometry of the Baker, for the following stability analyses the sidecar will be located on the left, and the direction of rotation with respect to the vertical z-axis will be positive when rotated clockwise when viewed from the rear and above. Consistent with the vehicle dynamics studies, the x-axis will be positive pointing forward (opposite the convention from aerodynamic studies in this work) and the y-axis positive pointing to the right, when viewed from the rear and above (Figure 7.4).

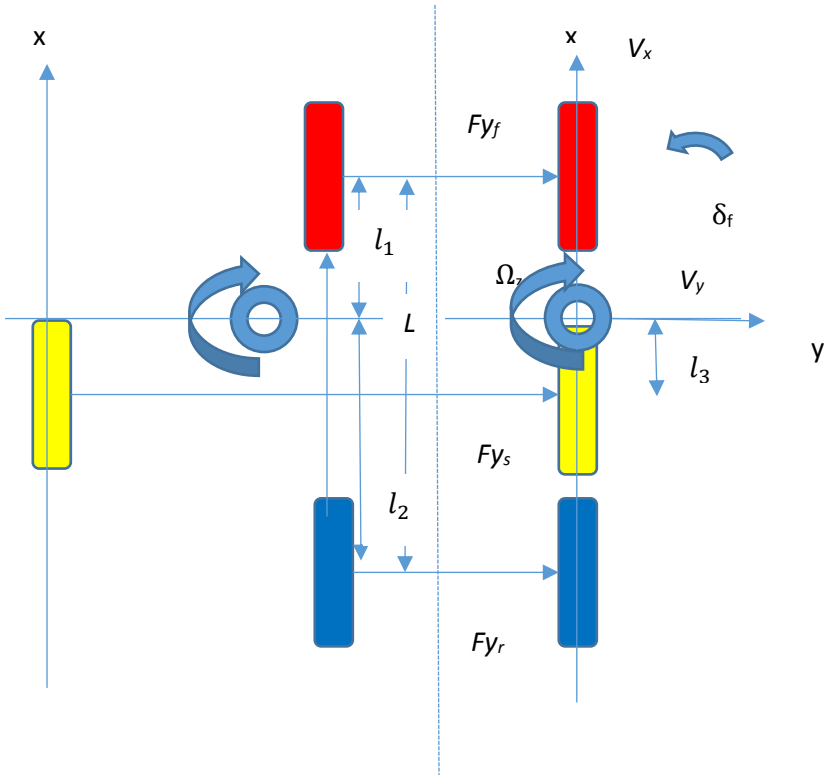

Figure 7.4- Sidecar frame of reference for longitudinal bicycle model

The sidecar is assumed to rotate around its centre of mass and the sidecar wheel is assumed to be located behind the centre of mass. As before, the Equations of Motion can be written as a sum of forces and a sum of moments.

Lateral motion

For lateral stability, the lateral forces acting on the centre of mass are summed and set equal to the term $m(\dot{V}_y + V_x\,\Omega_z)$ which is the force required to accelerate a mass in the lateral direction and a contribution in the lateral direction of the rotation Ω_z as the sidecar moves forward (V_x). The sum of forces is written as:

$$-C_{\alpha f}\,l_1\frac{\Omega_z}{V_x} + C_{\alpha r}\,l_2\frac{\Omega_z}{V_x} + C_{\alpha s}\,l_3\frac{\Omega_z}{V_x} - C_{\alpha f}\frac{V_y}{V_x} - C_{\alpha r}\frac{V_y}{V_x} - C_{\alpha s}\frac{V_y}{V_x} + L_y = m(\dot{V}_y + V_x\,\Omega_z) \quad (7.19)$$

Note that the effect of the front tyre cornering stiffness, ahead of the centre of mass, has a negative effect on the lateral force due to rotation (Ω_z), but that the rear and sidecar tyres, located behind the centre of mass have a positive contribution and counter the lateral motion

due to rotation. In the case of lateral motion (V_y) with forward velocity (V_x) which is slewing of the sidecar without rotation, all three tyres resist motion in the positive lateral direction. A positive aerodynamic lateral force (L_y), created by the asymmetrical airflow over the sidecar body produces a force in the positive lateral direction (y direction).

Moving the right-side terms to the left and multiplying by -1:

$$m(\dot{V}_y + V_x\,\Omega_z) + C_{\alpha f}\,l_1\frac{\Omega_z}{V_x} - C_{\alpha r}\,l_2\,\frac{\Omega_z}{V_x} - C_{\alpha s}\,l_3\,\frac{\Omega_z}{V_x} + C_{\alpha f}\,\frac{V_y}{V_x} + C_{\alpha r}\,\frac{V_y}{V_x} + C_{\alpha s}\,\frac{V_y}{V_x} - L_y = 0 \quad (7.20)$$

The lateral aerodynamic force caused by asymmetrical flow (L_y) is small ($L_y \approx 100$ N at 38 m/s with 0° yaw, measured in the A2 wind tunnel) relative to the size of the cornering coefficient terms and can be ignored. This allows equation 7.20 to be re-written as:

$$m\,\dot{V}_y + \left(m\,V_x + \frac{C_{\alpha f}l_1}{V_x} - \frac{C_{\alpha r}l_2}{V_x} - \frac{C_{\alpha s}l_3}{V_x}\right)\Omega_z + \left(\frac{C_{\alpha f} + C_{\alpha r} + C_{\alpha s}}{V_x}\right)V_y = 0 \quad (7.21)$$

Rotation

Rotational stability can be calculated by summing the moments that are created from longitudinal forces acting at a distance from the vertical axis at the centre of mass. Note, this is no longer the bicycle model as the rotational model considers lateral offsets of the wheels relative to the centre of mass. The sum of the moments can be set equal to $I_z\,\dot{\Omega}_z$, which is the product of the moment of inertia and the rate of change of the rotation around the vertical (z) axis (Ω_z). The sum of the moments is written as:

$$-C_{\alpha f}{l_1}^2\frac{\Omega_z}{V_x} - C_{\alpha r}{l_2}^2\frac{\Omega_z}{V_x} - C_{\alpha s}{l_3}^2\frac{\Omega_z}{V_x} - C_{\alpha f}l_1\frac{V_y}{V_x} + C_{\alpha r}l_2\frac{V_y}{V_x} + C_{\alpha s}l_3\frac{V_y}{V_x} - (F_{drive}\,w_2) - \left(D\,w_p\right) + C_{rrf}\,W_f\,w_1 + C_{rrr}\,W_r\,w_2 - C_{rrs}\,W_s\,w_3 = I_z\,\dot{\Omega}_z \quad (7.22)$$

In equation 7.22, the tyre cornering stiffness of all three tyres has a resistive effect on the rotation (Ω_z), as does the front tyre which generates a negative moment as the sidecar moves laterally (V_y). The rear and sidecar tyres, located behind the centre of mass (and hence centre of rotation) provide additive moments when the sidecar slews laterally. The drive force at the rear wheel (F_{drive}) is laterally offset from the centre of mass by a distance w_2 and creates a negative moment. The aerodynamic drag acts on the centre of aerodynamic pressure which creates a moment based upon its separation (w_p) from the centre of mass. Because of the centre of pressure is offset in the negative y direction, the contribution from the aerodynamic drag is a negative torque applied to the centre of mass. Because the front and rear wheels are offset in a positive direction from the centre of mass (w_1, w_2), their rolling resistance forces create a positive moment at the centre of mass. The rolling resistance force of the sidecar wheel acts on the

opposite side of the centre of mass at a distance w_3 and creates a negative moment around the vertical axis at the centre of mass.

Moving the right-side term to the left side and multiplying by -1:

$$I_z\,\dot{\Omega}_z + C_{\alpha f}{l_1}^2\frac{\Omega_z}{V_x} + C_{\alpha r}{l_2}^2\frac{\Omega_z}{V_x} + C_{\alpha s}{l_3}^2\frac{\Omega_z}{V_x} + C_{\alpha f}l_1\frac{V_y}{V_x} - C_{\alpha r}l_2\frac{V_y}{V_x} - C_{\alpha s}l_3\frac{V_y}{V_x} + (F_{drive}\,w_2) + \left(D\,w_p\right) - C_{rrf}\,W_f\,w_1 - C_{rrr}\,W_r\,w_2 + C_{rrs}\,W_s\,w_3 = 0 \qquad (7.23)$$

The asymmetry portion of equation 7.23,

$$(F_{drive}\,w_2) + \left(D\,w_p\right) - C_{rrf}\,W_f\,w_1 - C_{rrr}\,W_r\,w_2 + C_{rrs}\,W_s\,w_3,$$

is small (-610 N at 38 m/s) relative to the magnitude of the fifth through the seventh terms in equation 7.23 ($\sim 10^4$ N at 38 m/s) and can be ignored with respect to dynamic stability resulting from cornering stiffness and tyre loads. Equation 7.23 can be re-written as:

$$I_z\,\dot{\Omega}_z + \left(\frac{C_{\alpha f}{l_1}^2 + C_{\alpha r}{l_2}^2 + C_{\alpha s}{l_3}^2}{V_x}\right)\Omega_z + \left(\frac{C_{\alpha f}\,l_1 - C_{\alpha r}\,l_2 - C_{\alpha s}\,l_3}{V_x}\right)V_y = 0 \qquad (7.24)$$

These two second order equations (7.21 and 7.24) describe the lateral and rotational motion of the sidecar and their characteristic equation (quadratic polynomial from Chapter 6) can be written as:

$$\lambda^2 + \left(\frac{d1}{m} + \frac{d4}{Iz}\right)\lambda + \left(\frac{d1d4 - d2d3}{Iz\,m}\right) = 0 \qquad (7.25)$$

where

$$d_1 = \frac{C_{\alpha f} + C_{\alpha r} + C_{\alpha s}}{Vx} \qquad (7.26)$$

$$d_2 = m\,V_x + \left(\frac{l_1\,C_{\alpha f} - l_2\,C_{\alpha r} - l_3\,C_{\alpha s}}{Vx}\right) \qquad (7.27)$$

$$d_3 = \frac{l_1\,C_{\alpha f} - l_2\,C_{\alpha r} - l_3\,C_{\alpha s}}{Vx} \qquad (7.28)$$

$$d_4 = \frac{{l_1}^2\,C_{\alpha f} + {l_2}^2\,C_{\alpha r} + {l_3}^2\,C_{\alpha s}}{Vx} \qquad (7.29)$$

Note that some of the signs of the elements of this characteristic equation are different when compared to Huston et al. (1982) and Lurie (2012) which results from the sidecar being situated on the opposite side than in Lurie's analyses.

As with the previous four and three wheel analyses, using Routh-Hurwitz, the criteria for stability is that all of the coefficients of the characteristic quadratic equation are positive. As before the second order and first order terms are always positive, so stability depends upon the zeroth-order term being greater than zero.

$$\left(\frac{d1d4-d2d3}{Iz\ m}\right) > 0 \qquad (7.30)$$

7.3.2 Dynamic stability

The MATLAB program from Chapter 6, used to calculate dynamic stability of a four-wheel vehicle, was rewritten for the sidecar model to calculate the zero-order coefficient of the characteristic quadratic equation to examine how dynamic stability changes with forward velocity (V_x). The program also was used to determine how the asymmetrical aspects of the equations of motion affect the dynamic stability of the sidecar as speed increases. The MATLAB program code is available in Appendix D.

The first requirement for the determination of the stability of the sidecar is to locate the centre of mass. This can be calculated, knowing the distances between the front, rear and sidecar wheels and the loads on each wheel. For the Baker sidecar, this calculation is described in Appendix E.

From Chapter 6, the zeroth-coefficient of the characteristic equation (an indicator of stability) is calculated primarily from the cornering stiffness (C_α) of the tyres and the location of the centre of mass. In Chapter 6, the Toyo radial sports car tyres used on the sidecar were modelled from data obtained for a Formula One radial tyre at high pressure. The relationship for the cornering stiffness (C_α) versus normal force on the tyre (W) developed in Chapter 6 was used for the sidecar dynamic stability calculations in this chapter. It should be noted that the cornering stiffness of the type of tyre used on the sidecar (a very high performance radial racing tyre) is high, which means a small slip angle for this tyre will produce a higher cornering force than an equivalent slip angle on an ordinary passenger car tyre.

Table 7.1 defines the terms used in the equations and in the MATLAB program and provides an indication of their magnitudes.

Table 7.1: Terms used in Equations of Motion and their magnitudes for Baker Sidecar

Name	Type	Description	Magnitude
m		Total mass of sidecar	600 kg
I_z		Moment of inertia of sidecar	625.83 kg m^2
W_f	force	Normal force on front wheel	1569 N
W_r	force	Normal force on rear wheel	2609 N
W_s	force	Normal force on side wheel	1706 N
W_t	force	Total normal force	5884 N
l_1	distance	Longitudinal distance from centre of mass to front wheel	1.420 m

l_2	distance	Longitudinal distance from centre of mass to rear wheel	0.752 m
l_3	distance	Longitudinal distance from centre of mass to side wheel	0.162 m
L	distance	Wheelbase $(l_1 + l_2)$	2.172 m
l_p	distance	Longitudinal distance from centre of mass to centre of pressure	0.988 m
w_f	distance	Lateral distance from centre of mass to front wheel	0.31 m
w_r	distance	Lateral distance from centre of mass to rear wheel	0.31 m
w_s	distance	Lateral distance from centre of mass to side wheel	0.753 m
w_p	distance	Lateral distance from centre of mass to centre of pressure	0.5 m
$C_{\alpha f}$		Cornering stiffness (front)	6.1494 x 10^4 N/rad
$C_{\alpha r}$		Cornering stiffness (rear)	8.6517 x 10^4 N/rad
$C_{\alpha s}$		Cornering stiffness (side)	6.5507 x10^4 N/rad
C_d	coefficient	Aerodynamic drag coefficient	0.341
C_y	coefficient	Aerodynamic lateral force coefficient	0.110
A	area	Frontal area	1.00 m^2
D	force	Aerodynamic drag force	1100 N @67 m/s
L_y	force	Aerodynamic lateral force	412 N @67 m/s
$F_{frolling}$	force	Longitudinal rolling resistance force (front)	50.97 N @67 m/2
$F_{rrolling}$	force	Longitudinal rolling resistance force (rear)	84.76 N @67 m/s
$F_{srolling}$	force	Longitudinal rolling resistance force (side)	55.43 N @67 m/s

Using the MATLAB code from Appendix D, a plot of the zero-order coefficient (with no asymmetry terms included) from equation (7.30) versus longitudinal velocity (V_x) is provided in Figure 7.5.

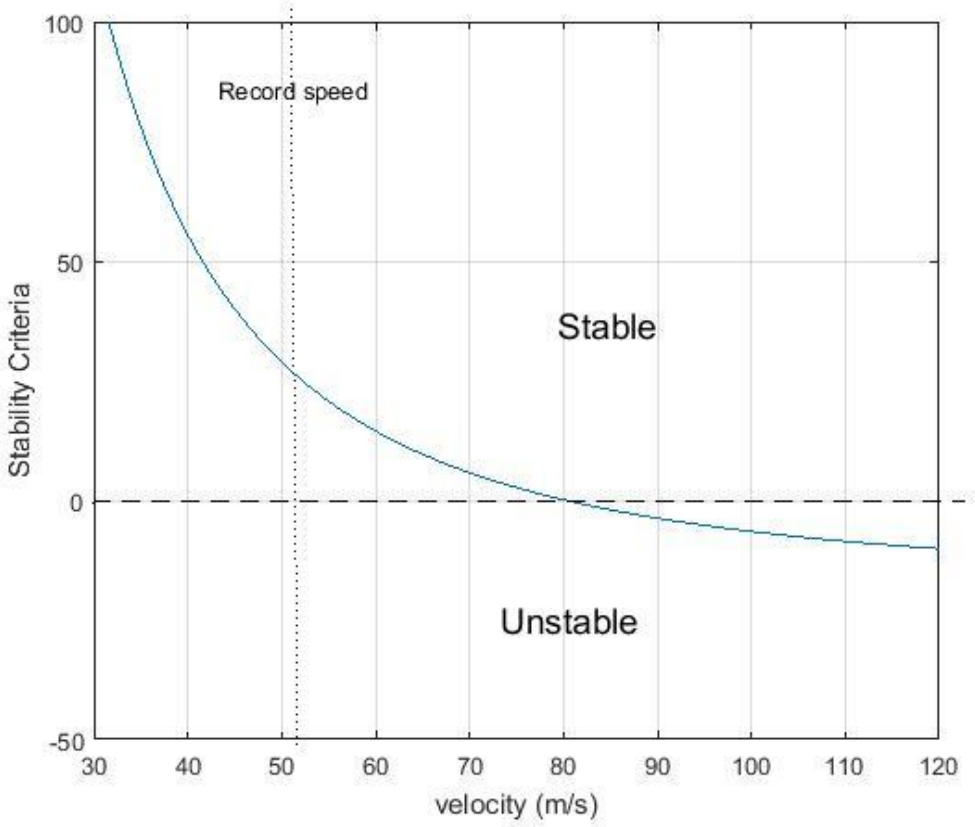

Figure 7.5 - Zero-order coefficient of sidecar characteristic equation versus velocity

It is evident from Figure 7.5, that this stability criteria remains positive to 80 m/s and that therefore the sidecar is expected to be directionally stable up to that speed (179 mph) and will be resistant to small perturbations to its path or heading. The sidecar was reported by the rider to have no stability issues up to the maximum speed of testing (~125 mph). Note that this stability criteria, as with the criteria described by Huston et al. (1982) for four and three wheel vehicles, depends only upon the position of the centre of mass and the cornering stiffness of the tyres.

7.3.2.1 Effect of tyre cornering stiffness

As noted previously, the high-performance radial tyres used on the Baker sidecar have a high level of cornering stiffness. The effect of a lower cornering stiffness tyre is evident in Figure 7.6 where the cornering stiffness (C_α) value of the three tyres (from Table 7.1) are reduced to 75% of the value from Figure 7.5. Such tyres would still be considered high performance passenger tyres.

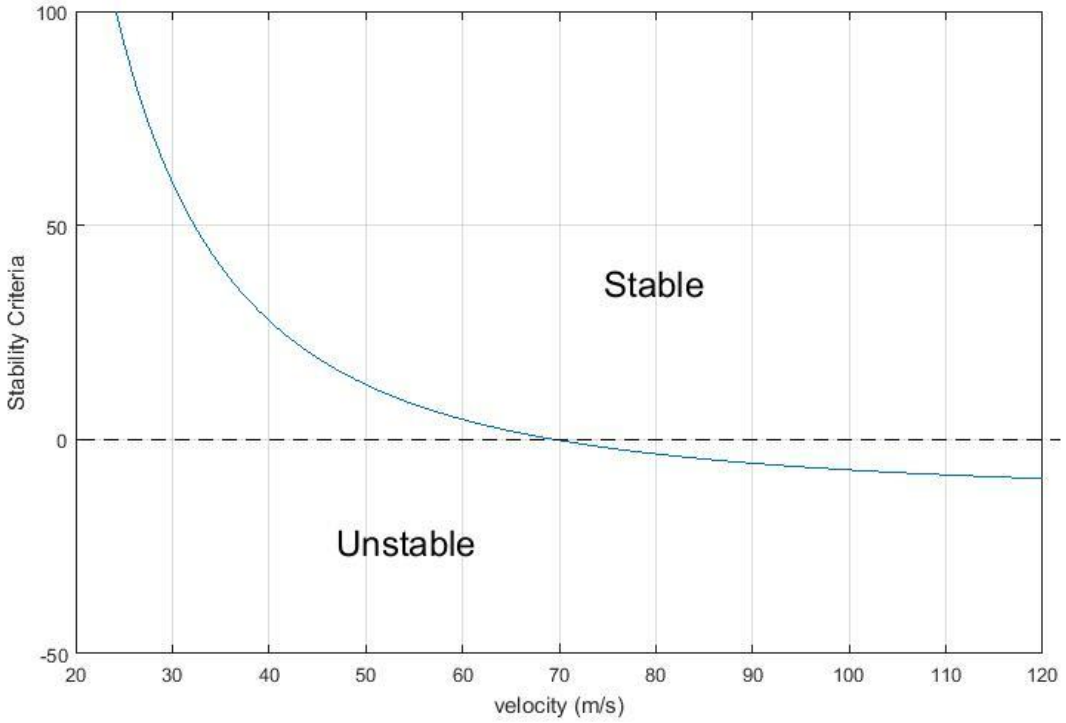

Figure 7.6- Zero-order coefficient of sidecar characteristic equation versus velocity with reduced tyre cornering stiffness

The critical speed where the sidecar becomes directionally unstable is reduced from 80 m/s to 70 m/s by the 25% reduction in tyre cornering stiffness. Thus, a tyre with a higher cornering stiffness is expected to increase the directional stability.

7.3.2.2 Position of centre of mass

Huston et al. (1982) noted that the position of the centre of mass on a three-wheel (and four-wheel) vehicle has an effect on the directional stability. The centre of mass of the Baker electric sidecar, as run at Bonneville, is located 65.4% of the length of the wheelbase from the front wheel. In Figure 7.7, the position of the centre of mass is moved so that it is 90% of the distance from the front to the rear wheel (heavily loaded at the rear).

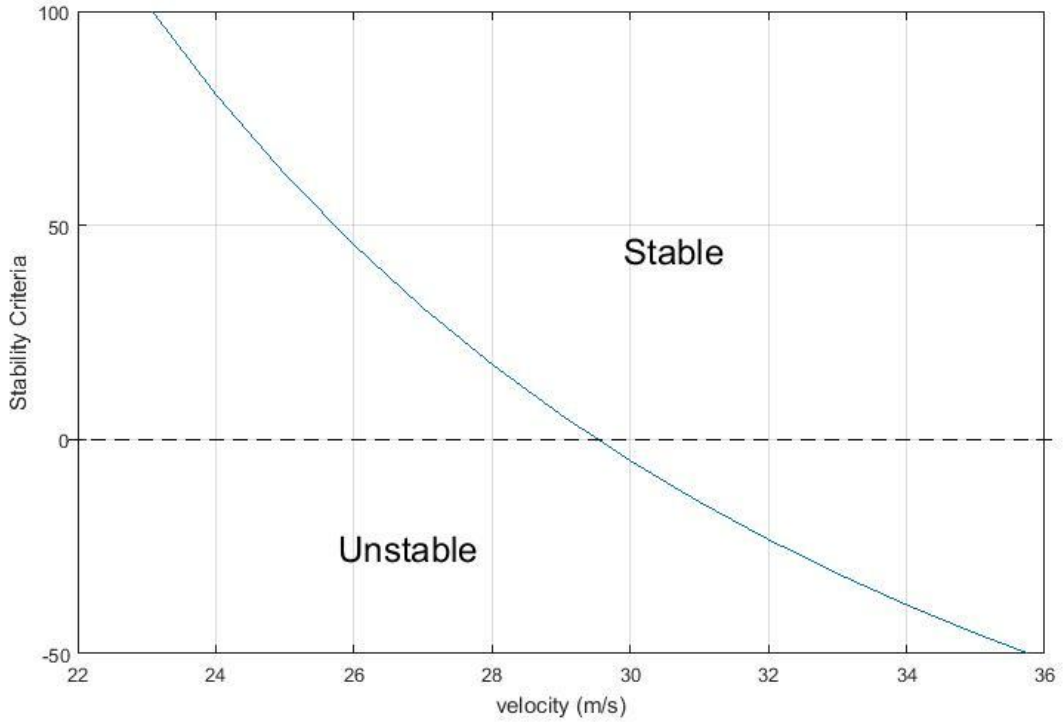

Figure 7.7- Centre of mass moved to 90% rear

In Figure 7.7, with the centre of mass moved to 90% rear, the critical velocity for stability has dropped to approximately 29.5 m/s (66 mph) from 80 m/s. Although practically it would be difficult to move the centre of mass that far back, the plot does show the negative influence on directional stability when the centre of mass is moved rearward.

In Figure 7.8, the position of the centre of mass is moved so that it is 10% of the distance from the front to the rear wheel (more heavily loaded at the front).

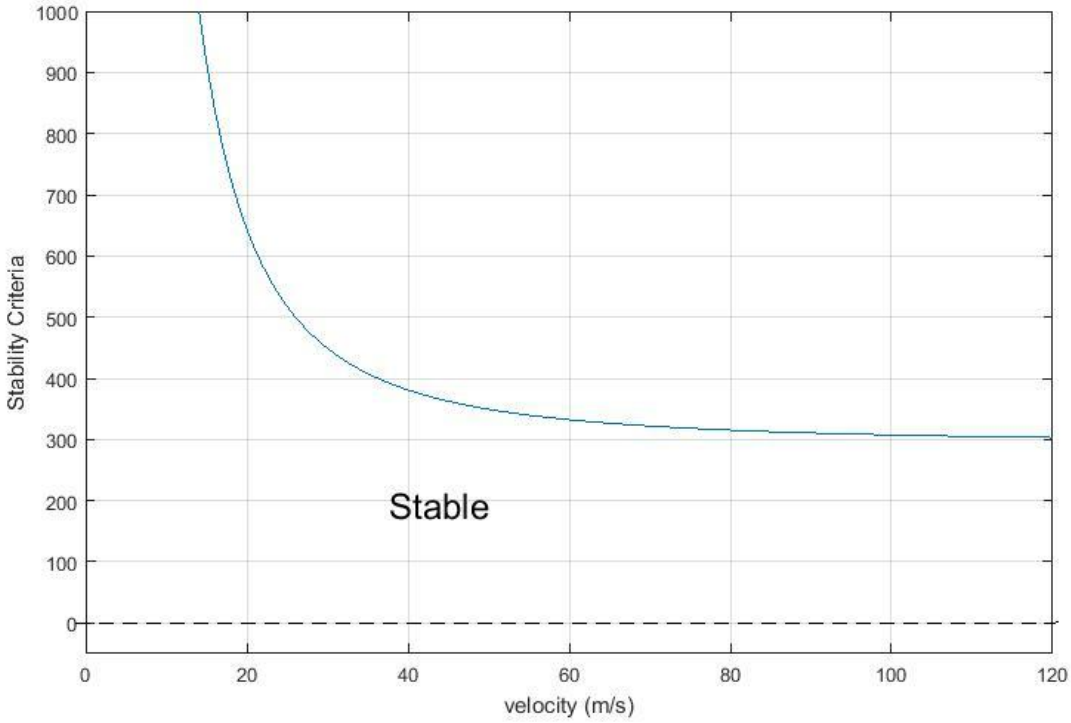

Figure 7.8- Centre of mass moved to 90% front

In Figure 7.8, the forward position of the centre of mass has resulted in dynamic stability at all speeds up to and in excess of 120 m/s (269 mph). Moving the centre of mass forward is expected to improve directional stability.

7.4 SIDECARS WITH ASYMMETRICAL FORCES

The dynamic stability model adapted for a sidecar by Lurie (2012) assumed no rolling resistance, tractive (drive) or aerodynamic forces were applied. The magnitude of the asymmetrical forces created are smaller (see Table 7.1) than the cornering stiffness forces and thus do not directly affect the lateral stability criteria detailed in Figure 7.5. If the sidecar is traveling at a speed where it is dynamically stable (the stability criteria in Figure 7.5 is positive), the remaining asymmetrical forces will have an effect on the slip angle (α) of the tyres and steering angle (δ_f) that must be applied to maintain the desired path. Lurie (2012) did not consider these forces in his sidecar analyses.

The following analyses are more complete: they take into account the asymmetrical forces that result from the sidecar configuration and aerodynamic characteristics. In this analysis, the term “path” describes the track the vehicle takes, regardless of the direction that it is pointing. When viewed from above, the path might be straight ahead, even if the vehicle has a rotational slip angle, or the vehicle might be slewing sideways as it moves forward with zero rotational angle. The term “heading” is defined as the direction that the vehicle is pointing, regardless of what

direction it is actually traveling. The heading can be thought of as the direction the rider thinks the vehicle is traveling while looking straight ahead. In general, the rider will add steering input (δ) in an effort to make the heading match the path.

Longitudinal Forces

The symmetry of a four-wheel vehicle or three-wheel tadpole or delta trike means, at zero yaw, that the longitudinal forces generated by rolling resistance or traction and aerodynamic drag on one side of the symmetry plane are equalled by the forces generated on the opposite side of the symmetry plane. Thus, they do not create a torque or add to the rotation (Ω_z) around the vertical (z) axis.

The asymmetry of the sidecar implies that the rolling resistance and tractive forces as well as the aerodynamic drag, while having no effect on the lateral force on the sidecar, will have an effect on the moment around the vertical (z) axis at the centre of mass. Just as a one-dimensional longitudinal (x-axis) bicycle model can be used to add together the lateral forces acting on the centre of mass, we can use a one-dimensional lateral (y-axis) bicycle model to add the moments created by longitudinal forces acting on the centre of mass about the vertical (z) axis. In Figure 7.9, the front and rear wheels of the sidecar are projected upward, to become a pair of wheels laying on the Q-Q' axis, while the sidecar wheel projects upward onto the Q-Q' axis at a distance w_3 from the pair of wheels.

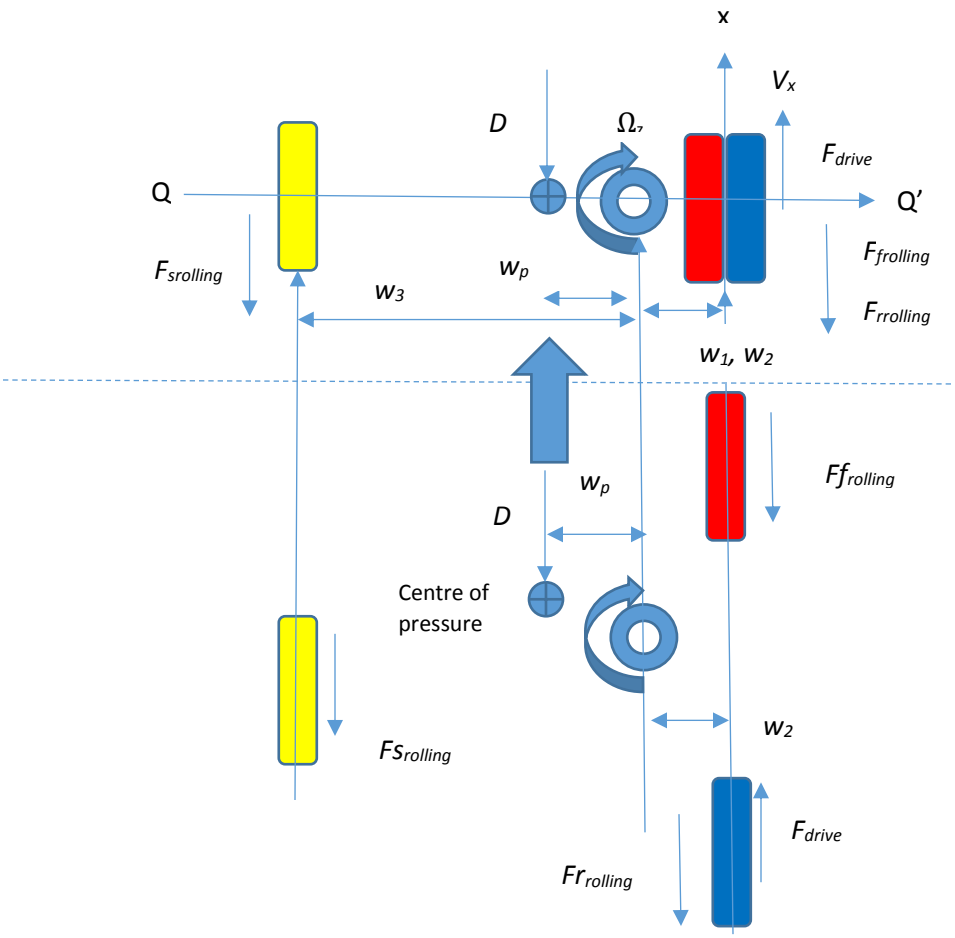

Figure 7.9- Bicycle Model for Sidecar (lateral)

The aerodynamic drag force (*D*) acts on the centre of aerodynamic pressure. From Chapter 3, the longitudinal (x) aerodynamic drag (*D*) is given by:

$$D = ½\ \rho\ V_x^2\ A\ C_d$$

with C_d the aerodynamic drag coefficient. This drag force creates an aerodynamic drag yaw moment ($D * w_p$), where w_p is the lateral displacement of the centre of aerodynamic pressure from the centre of mass.

Recall from Chapter 5 that the rolling resistance forces are calculated from:

$$F_{rolling} = W C_{rr} \qquad (7.31)$$

with $C_{rr} = (a + bV^2)$ (a and b are constants determined by the tyre characteristics and track surface)

This can be further defined for each of the vehicle wheels and the vertical force on each wheel (W_f, W_r, W_s):

$$F_{frolling} = W_f C_{rrf}$$

$$F_{rrolling} = W_r C_{rrr}$$

$$F_{srolling} = W_s C_{rrs}$$

Each of the rolling resistance forces (see Table 7.1), multiplied by the lateral distance of each wheel from the centre of mass, provides a moment on the centre of mass around the vertical axis. Because only one wheel on a sidecar vehicle is driven (the rear one), there is also a drive force, $F_{drive,}$ which adds a moment, (F_{drive} * w_2), around the centre of mass, where w_2 is the lateral distance between the rear wheel and the centre of mass.

The drive force has two elements. The first balances the rolling resistance and aerodynamic drag forces while the second accounts for the d'Alembert force required to accelerate the sidecar from a standing start to its velocity. This acceleration force decreases with speed until the maximum speed is reached (and the acceleration drops to zero). The traction force applied by the rear wheel (F_{drive}) can be calculated using the Excel spread sheet developed from the work of Dr. John Sullivan (Purdue) and described in Chapter 5. Figure 7.10 plots the driving d'Alembert force produced in the longitudinal direction at the rear wheel versus the longitudinal velocity (V_x). A polynomial curve relating the driving force to the velocity has been fitted to the data. The force at the rear wheel does not include the rolling resistance forces from the three wheels and these need to be added to the tractive force to properly account for the torque that the driving wheel applies to the centre of mass.

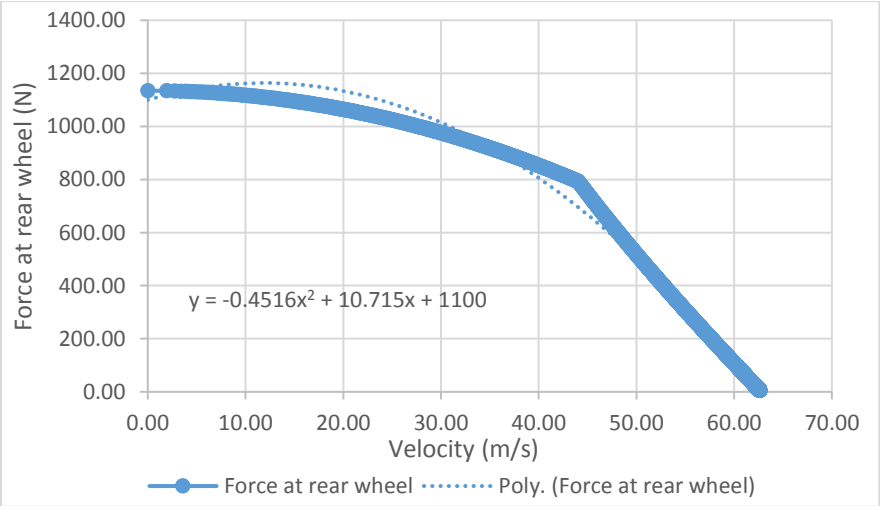

Figure 7.10- Driving force at rear wheel versus velocity

The moments produced by the asymmetrical longitudinal forces can be summed and can be balanced by force generated by a tyre slip angle (α) at each wheel operating on the distance (l_x) from the wheel to the centre of mass. In addition, a steering angle (δ_f) for the front wheel can be added to add to the force generated at the front wheel.

$$m(\dot{V}_y) + d_1(V_y) + d_2(\Omega_z) = C_{\alpha f}\delta_f \quad (7.32)$$

and as a sum of moments:

$$I_z(\dot{\Omega}_z) + d_3(V_y) + d_4(\Omega_z) = l_1 C_{\alpha f}\delta_f \quad (7.33)$$

From the equation:

$$-(F_{drive}\, w_2) - (D\, w_p) + C_{rr1}\, W_f w_1 + C_{rr2}\, W_r w_2 - C_{rr3}\, W_s w_3 =$$

$$-(\alpha + \delta_f)\, C_{\alpha f} l_1 + \alpha\, C_{\alpha r}\, l_2 + \alpha\, C_{\alpha s}\, l_3 \quad (7.34)$$

where

C_{rr1}, C_{rr2}, C_{rr3} are the rolling resistance coefficients for the front, rear and sidecar wheel (respectively).

W_f, W_r, W_s are the weights on the front, rear, and sidecar wheels (respectively).

w_1, w_2, w_3 are the distances laterally from the centre of mass to the front, rear and sidecar wheels (respectively).

Equation (7.34) can be rearranged and with zero steering angle ($\delta_f = 0$) it is possible to plot the slip angle (α) versus the velocity of the vehicle (V_x) as in Figure 7.11. It should be noted that the asymmetry of the sidecar (generating moments around the vertical axis at the centre of mass) is the reason for the slip angle α and its dependence upon velocity.

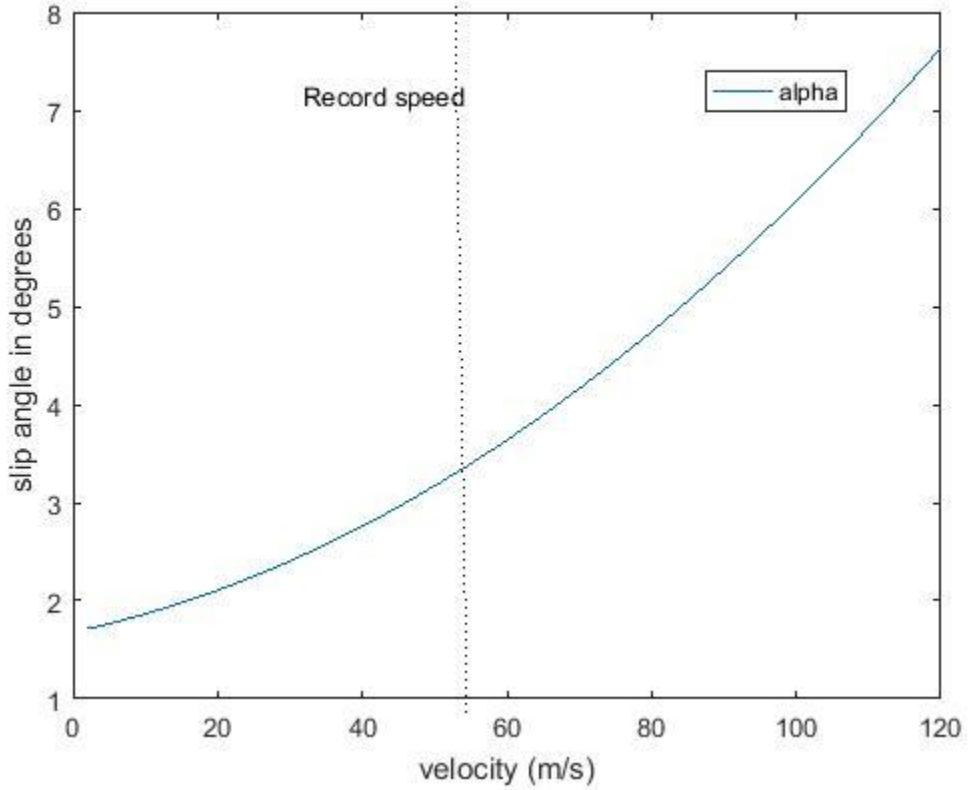

Figure 7.11- Slip angle due to asymmetry versus velocity

In Figure 7.11, if the rider adds no corrective steering input (δ), the vehicle will rotate to a heading that matches the slip angle α, but the path the vehicle will undertake will continue in the longitudinal (x-axis) direction.

7.4.1 Addition of a steering angle

To maintain a heading matching the path, the sidecar rider can be expected to add a steering angle δ_f to the front wheel. The addition of a moment from this steering angle will be equal to (δ_f) ($C_{\alpha f}$) (l_1) and will reduce the slip angle (α) of the rear and sidecar tyres. The full equation is:

$$-(F_{drive}\, w_2) - (D\, w_p) + C_{rr1}\, W_f w_1 + C_{rr2}\, W_r w_2 - C_{rr3}\, W_s w_3 =$$

$$-(\alpha + \delta_f)\, C_{\alpha f}\, l_1 + \alpha\, C_{\alpha r}\, l_2 + \alpha\, C_{\alpha s}\, l_3 \qquad (7.35)$$

The slip angle (α) at velocities (V_x) from 1-120 m/s can be calculated with steering angle settings (δ_f) iterated between 0 and 0.6 degrees (Figure 7.12).

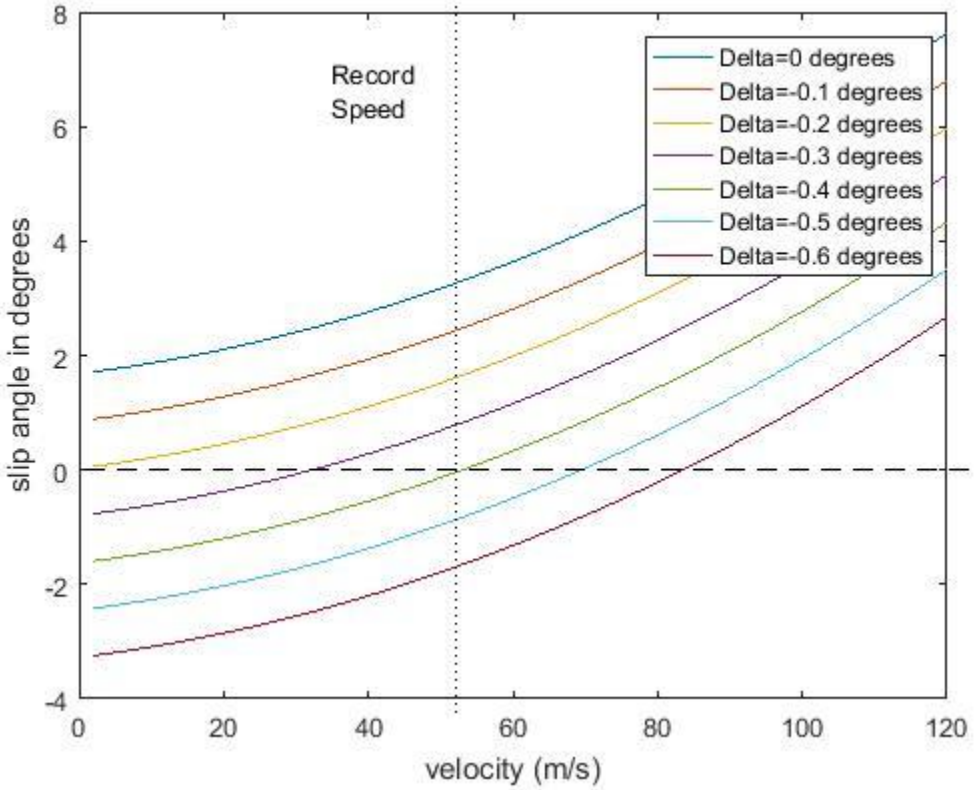

Figure 7.12- The effect of steering angle δ_f on the slip angle α

From Figure 7.12, at low speed, between 0 and 40 m/s, to maintain a straight-ahead heading (slip angle (α) equal to zero) that matches the vehicle path, the rider will need to add a steering angle, δ_f, of between 0.2 and 0.3 degrees. As the velocity increases above 40 m/s (89 mph) the steering angle, δ_f, will gradually increase from 0.3 to 0.6 degrees up to a speed of over 80 m/s (179 mph). This small amount of steering angle introduced by the rider to counteract the asymmetry of forces and moments will probably be added unconsciously and be unnoticed by the rider. Figure 7.13 indicates the amount of steer angle, δ_f, in degrees that must be added by the rider to maintain zero slip angle (α) as the speed increases.

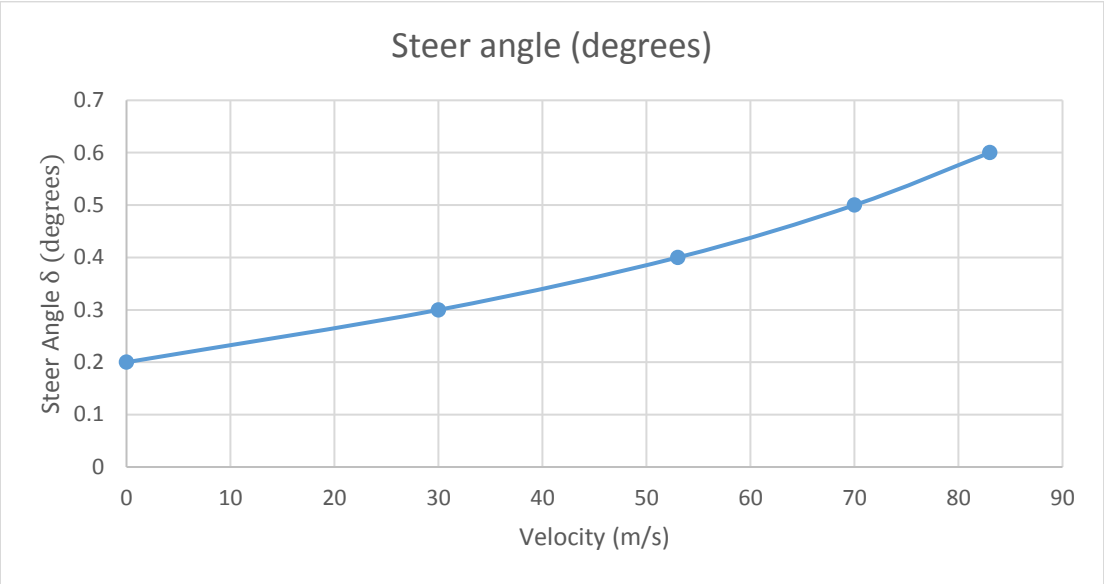

Figure 7.13- Steer angle δ_f required to maintain zero slip angle

A steering angle, even a small one, creates additional rolling resistance drag compared to a tyre rolling straight-ahead. Although data on the effect of small steering angles on rolling resistance is scarce, it has been reported (Yurko, 1978) that a 1° slip angle will increase the rolling resistance by 25%. From Figure 7.13, at a velocity of 53 m/s (120 mph) the steering addition to the front wheel is 0.4 degrees. This should result in an increase in rolling resistance of 10%. From the previous relationship between velocity, normal load, and the rolling resistance coefficient for the front wheel, a zero-slip rolling resistance force of 48.34 N results from the front tyre. A steering angle of 0.4 degrees will increase the rolling resistance force by 4.83 N. The power required is the product of the velocity and the force. The extra power required at 53 m/s will be 256 watts, which, when compared to the 50-kW delivered to the rear wheel, will have a negligible effect on top speed.

7.5 ASYMMETRICAL FORCES AND STABILITY OF THE SIDECAR MOTORCYCLE

7.5.1 Geometric effects of asymmetry

In Figure 7.14, the projected frontal area, A (m_2), determined from the Reports → Projected Area → Min Element size (→ .0001m) function of ANSYS Fluent is plotted versus the yaw angle.

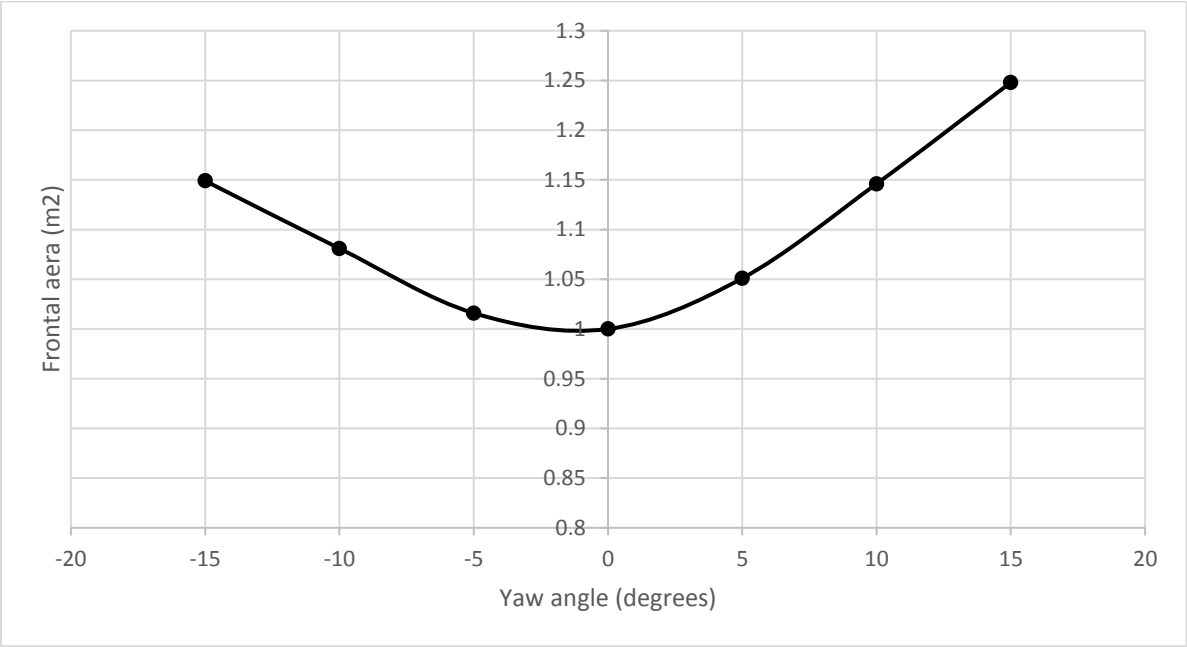

Figure 7.14- Sidecar Frontal Area with Yaw Angle

Unlike Figure 6.5 with the Ahmed body and Figure 6.17 for the streamliner, Figure 7.14 indicates that the Baker sidecar is geometrically asymmetrical—it presents a significantly different frontal area (A) when it is yawed at angles of positive and negative 5, 10 and 15 degrees. This difference is further explored in Figure 7.15.

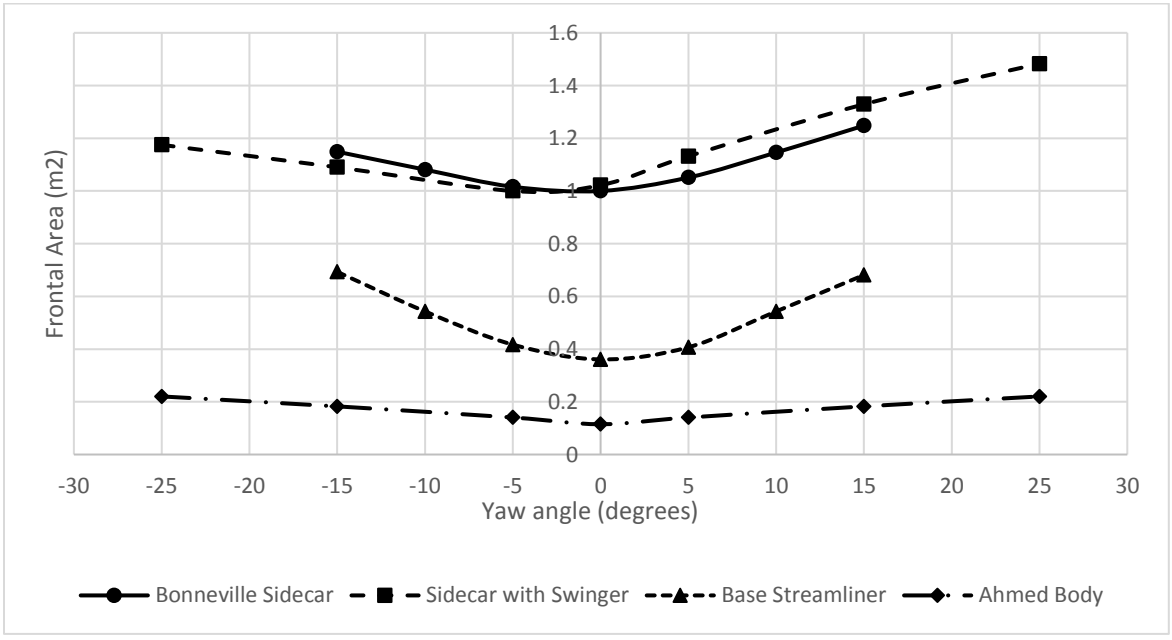

Figure 7.15- Frontal area versus yaw angle for sidecar, streamliner and Ahmed body

From an examination of Figure 7.15, a comparison of the Ahmed body and base streamliner curves to the original sidecar with swinger and the Bonneville sidecar results, there are two features where the asymmetry of the sidecars is evident. As the test bodies are swept through a yaw angle (around the vertical z-axis), their frontal areas increase around a minimum. For the symmetrical Ahmed body and the Base Streamliner, the minimum is approximately centred on zero yaw and the increase in frontal area is approximately the same with equal positive (right) or negative (left) yaw angle changes. This is in contrast to the two sidecars where the change in frontal area sweeping in one direction is different from the sweep in the other and the minimum frontal area is offset slightly from the zero-yaw point. The difference in frontal area with positive and negative yaw angle and the minimum frontal area offset from zero are two geometric ways to characterize the asymmetry of a vehicle.

7.5.2 Introduction of the Symmetry Quotient

A numerical characterization, introduced here as the **Symmetry Quotient,** can be used to compare the degree of asymmetry of one vehicle shape to another. Figure 7.16 compares the front view of the Baker sidecar at -15°, 0°, and +15° of yaw.

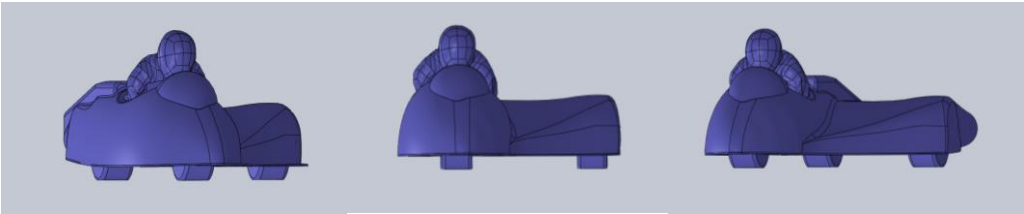

Figure 7.16- Front view of the Baker sidecar at -15°, 0°, and +15° of yaw

The dimensionless Symmetry Quotient, Σ, is calculated by dividing the smaller of the slopes of the Frontal Area (A) versus Yaw Angle (Ø) curves by the slope of the curve with the opposite yaw angle. The slope = (frontal area at 15° - frontal area at 5°)/10°). Table 7.2 summarizes the calculation of the Symmetry Quotient for the vehicles represented in Figure 7.15

Table 7.2: Symmetry Quotient calculation for Ahmed, streamliner and sidecar

Vehicle	Slope from -5 to -15 degrees (m^2 / degree)	Slope from +5 to +15 degrees (m^2/degree)	Symmetry Quotient (Σ)
Ahmed body	0.00422	0.00422	1.0
Base streamliner	0.0276	0.0274	0.993
Sidecar with swinger	0.009	0.0197	0.457
Bonneville sidecar	0.0132	0.0198	0.667

From Table 7.2, the symmetrical Ahmed Body and streamliner both have Symmetry Quotients approximately equal to 1, which is expected for a symmetrical vehicle shape (the streamliner is slightly less than one, perhaps as a result of slightly different meshing on the two sides of the vehicle). The sidecar with swinger has a Symmetry Quotient of Σ=0.457, exhibiting a high degree of asymmetry, while the Bonneville version of the sidecar has Σ=0.667, indicating less asymmetry than the sidecar with swinger, but still with significant asymmetry.

Although the Symmetry Quotient is a practical way to characterize the degree of asymmetry of a vehicle or shape, it is noted that some shapes (for example a sphere) may have no change in frontal area with yaw, resulting in a division by zero and would thus be undefined.

7.5.3 Asymmetrical forces and moments

To study the effect of yaw angles on aerodynamic forces and moments, an unstructured tetrahedral mesh between 6 and 11 million elements (depending upon the yaw angle) was created using ANSYS Fluent 17.0 for each yaw angle. Refinement boxes created in the computational domain over the vehicle and in the wake zone were meshed as bodies of influence with an element size of 0.02 m. The surface of the vehicle is meshed with a 0.02 m element size. There are five inflation layers, with the initial layer thickness of 0.001 m. The remainder of the computational domain is meshed, primarily in tetrahedrons with a 0.1 minimum and 0.2 maximum element size.

The SST turbulence model was used with a moving road surface and a velocity of 67 m/s (150 mph) as had been used in Chapter 6 CFD studies. A coupled scheme was used for pressure and velocity and spatial discretization used a least squares gradient and second order upwind pressure, momentum, turbulence kinetic energy and dissipation rates. The coefficients of drag, lift, lateral force, yaw moment, and roll moment for the Bonneville version of the sidecar were examined at yaw angles of zero and positive and negative 5, 10 and 15 degrees (Figure 7.17).

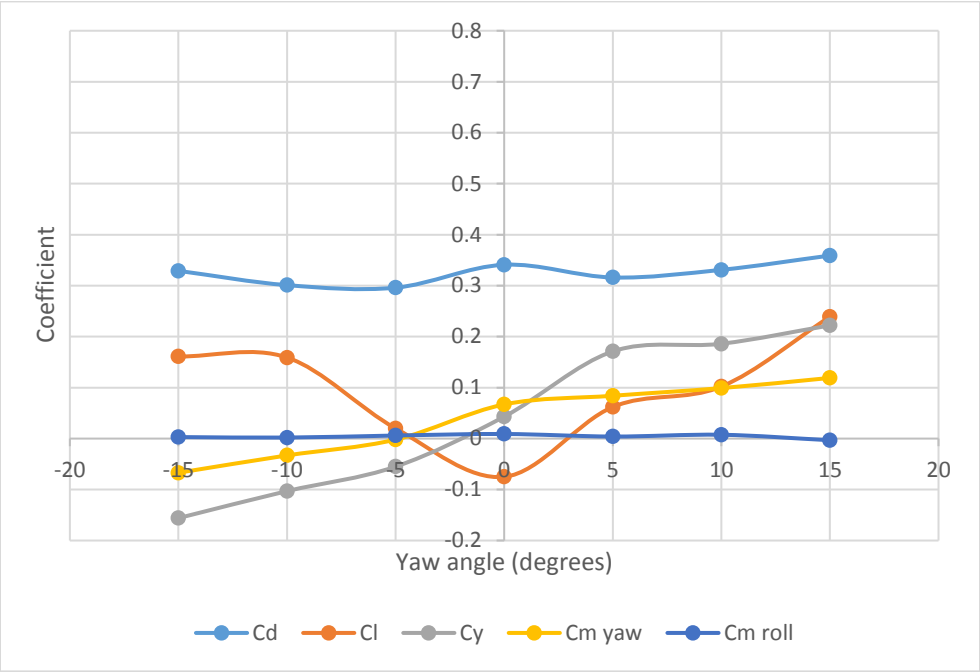

Figure 7.17- Bonneville sidecar drag, lift, lateral force, and roll and yaw moment coefficients versus yaw angle (Ø)

Note from Figure 7.17 that the forces and moment generated with a positive yaw are different than those generated when the sidecar is yawed in a negative direction. Because the centre of aerodynamic pressure is ahead of the centre of mass, the aerodynamic yaw torque generated around the vertical axis does not act to restore the yaw. The yaw moment is quite small (~ 0.100) and thus adverse yaw will not have a large effect. At zero degrees of yaw, there is a small amount of lift and also a lateral force and a small yaw moment present, caused by the asymmetrical airflow along one side of the sidecar body compared to that along the different geometry of the other side.

As in Chapter 6 (Figures 6.7 and 6.20), the effect of the frontal area on the drag can be examined by plotting C_d and C_dA for the Bonneville sidecar versus yaw angle, as in Figure 7.18.

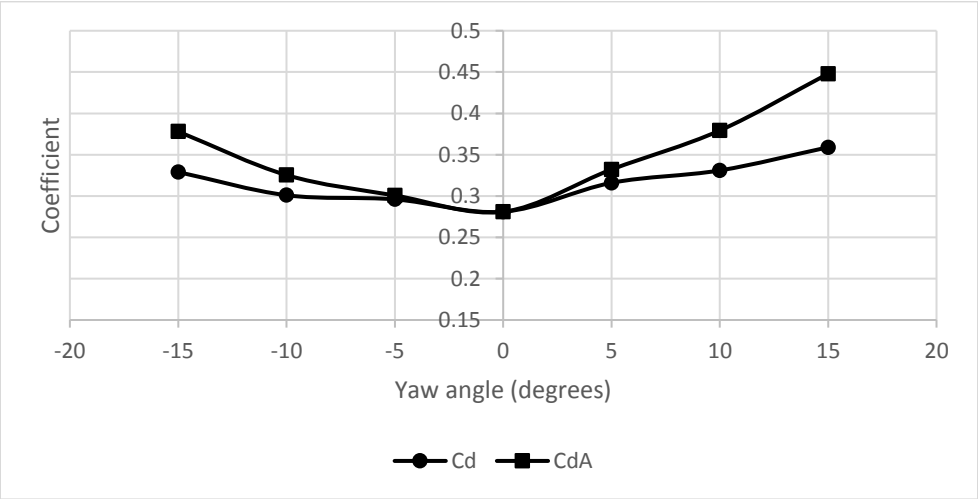

Figure 7.18- Comparison of C_d versus C_dA over range of yaw angles- Bonneville sidecar

From Figure 7.18, it is evident that the change in drag coefficient is coming from both a change in frontal projected area and also a change in the body shape that is presented to the airflow as the sidecar rotates through positive and negative yaw. Rotating to the right (positive yaw) produces a greater effect, which is to be expected as it exposes more of the sidecar part of the vehicle— and hence more asymmetry— to the airflow.

7.5.4 Pressure and Viscous **Forces**

Recall from Chapter 3, Chapter 4, and Chapter 6 that aerodynamic drag forces result largely from flow separation as air travels over bluff bodies (drag force proportional to frontal area) and skin frictional forces that occur when a viscous attached layer flows along the vehicle surface. Pressure drag is generated by the separation while viscous drag results from the surface friction forces. The pressure and viscous drag forces generated by the Bonneville sidecar are plotted versus yaw angle in Figure 7.19.

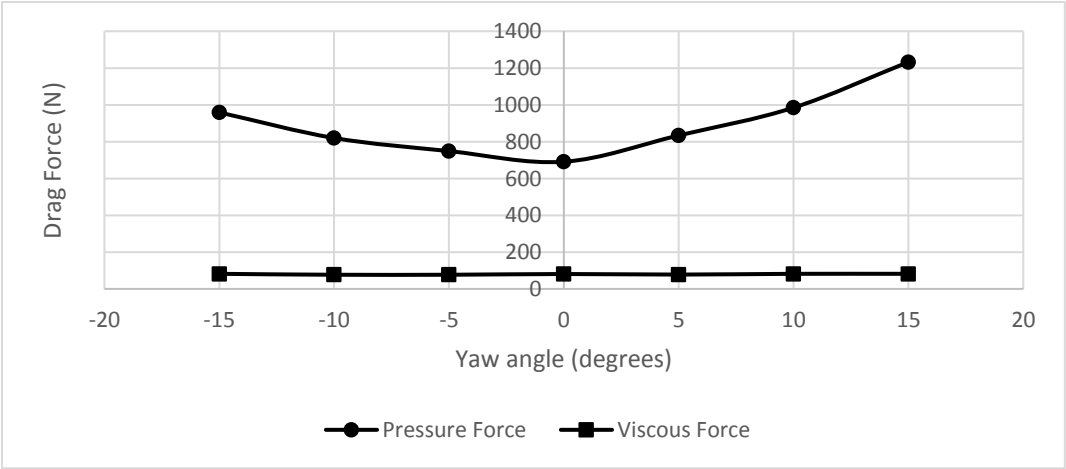

Figure 7.19- Bonneville sidecar pressure and viscous drag forces

It is evident in Figure 7.19 that the Bonneville streamliner, as with the Ahmed body in Chapter 6 (Figure 6.21), produces almost entirely pressure drag and the contribution from surface fraction is minimal. This is in contrast to the Purdue streamliner (Figure 6.22) which produces almost entirely surface friction drag when traveling straight ahead. The Bonneville sidecar is a bluff body. This implies that separation and the effect of the wake on drag has a greater significance than surface friction.

It is useful to compare the degree of asymmetry of the wake from the original swinger sidecar that ran at Bonneville in 2014 (Figure 7.20) with the wake of the 2016 Bonneville sidecar (Figure 7.21).

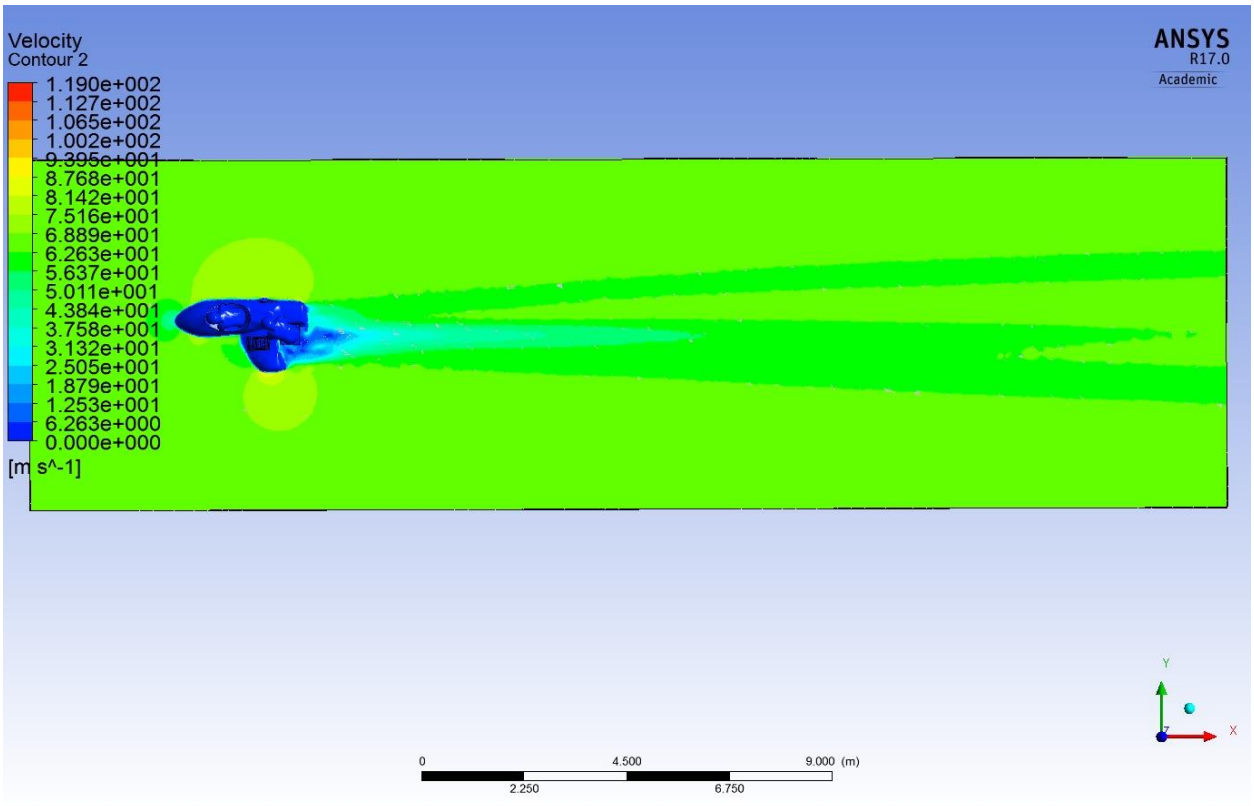

Figure 7.20- Wake of the original swinger sidecar at 67 m/s

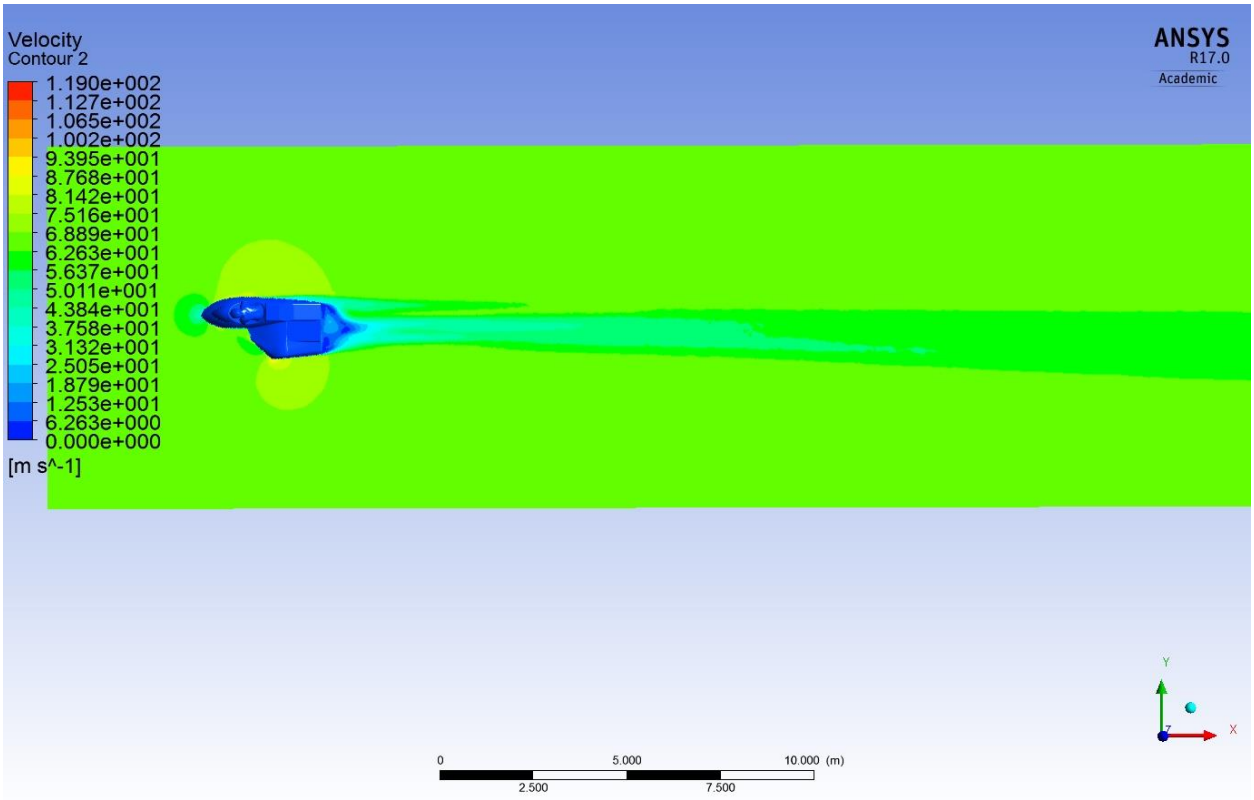

Figure 7.21- Wake of the Bonneville sidecar at 67 m/s

In Figure 7.20, the wake of the swinger sidecar is wide and asymmetrical with a high degree of disturbed flow on the left side of the sidecar body. In Figure 7.21, the Bonneville version of the sidecar displays a much smaller wake that is more symmetrical and is centred on the approximate centreline of the sidecar body. The swinger version of the sidecar also has a higher amount of pressure drag as a percentage of total drag as indicated in Table 7.3.

Table 7.3: Pressure and viscous drag of swinger and Bonneville sidecar

CFD Results at 67 m/s with moving road	**Swinger sidecar (2014)**	**Bonneville sidecar (2016)**
Drag Coefficient (C_d)	0.394	0.281
Pressure drag (N)	1108 (94.2%)	772 (90.5 %)
Viscous drag (N)	68 (5.8%)	81 (9.5%)

7.5.5 Lateral Forces

From Chapter 4, it is evident that a small aerodynamic lateral force can exist, caused by the asymmetrical flow of air over the sidecar body.

Slewing

The magnitude of the aerodynamic lateral force acting on the centre of aerodynamic pressure can be calculated from the sidecar frontal area (A), the lateral force coefficient C_y, the sidecar longitudinal velocity (V_x) and the density of the air (ρ) with the following equation:

$$L_y = ½\ \rho\ V_x^2\ A\ C_y \qquad (7.36)$$

This lateral (y) force (see also Table 7.1), acting on the centre of mass will be balanced by a tyre slip angle (α) at each wheel. In addition, a steering angle (δ_f) for the front wheel can be added to counter the lateral force Ly.

$$L_y = (\alpha + \delta_f) * C_{\alpha f} + \alpha * (C_{\alpha r} + C_{\alpha s}) \qquad (7.37)$$

This slip angle is a lateral displacement as the vehicle moves with a constant zero-degree heading (no rotation about the vertical axis), while the path deviates from straight-ahead by an amount equal to the slip angle. This can be called slewing of the sidecar. This slip angle is plotted in Figure 7.22.

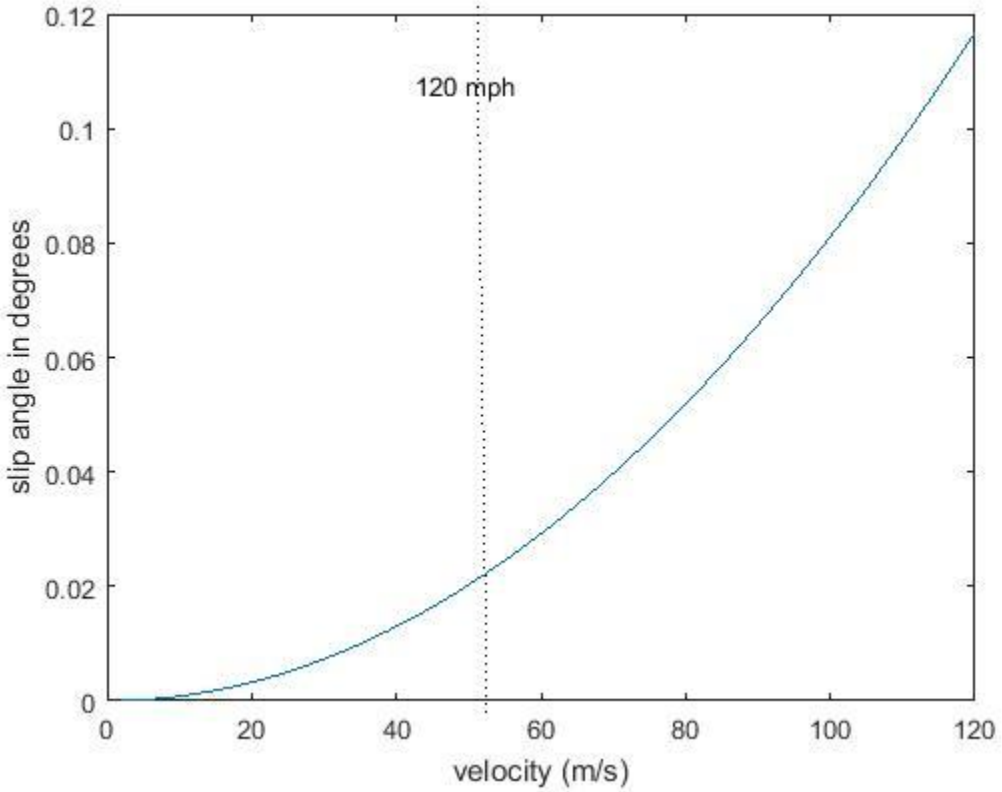

Figure 7.22- Slip angle with zero cross wind

Note from Figure 7.22 that the slip angle that counters the small lateral aerodynamic force resulting from asymmetry, with no cross winds is small enough to be unnoticeable by the rider.

If a cross wind is present it can be resolved to be a lateral cross wind force acting on the centre of aerodynamic pressure, slewing the path of the sidecar. In Figure 7.23, the slip angle (in degrees) is calculated for various cross wind velocities (in mph) using the lateral force coefficients (C_y) found in Figure 7.17. The cross-wind velocity is calculated from V_X tan(α) for several small angles and the C_y values at these angles are used to calculate the slip angles based upon $C_{\alpha f}$, $C_{\alpha r}$, $C_{\alpha s}$, and W_f, W_r, and W_s from Table 7.1. A single speed of V_x =53 m/s (120 mph) was chosen for this plot.

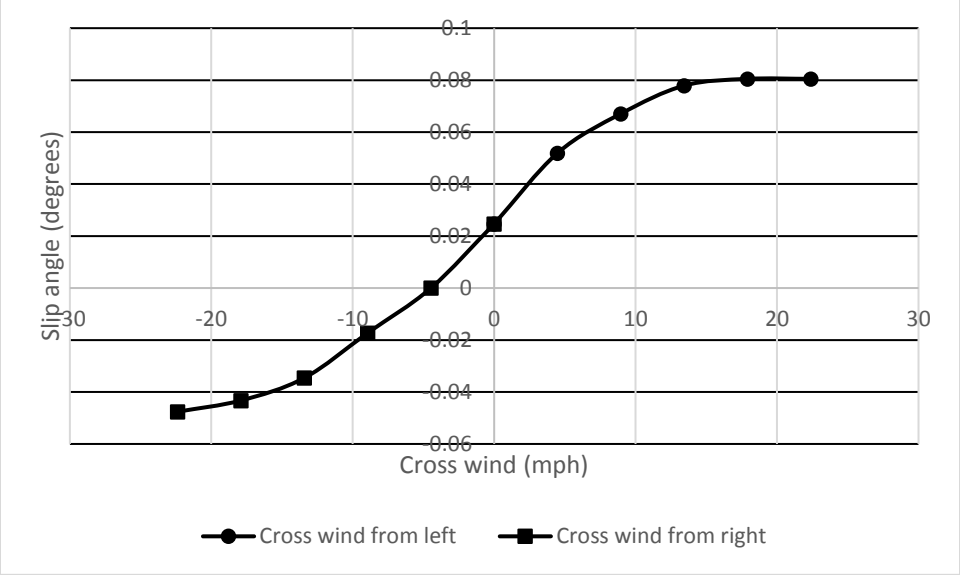

Figure 7.23- Slip angle (α) at V_x=120 mph resulting from cross winds

Note that a cross wind from the left produces a lateral slewing from the original path to the right, while a cross wind from the right produces a slewing to the left. The difference between the right and the left curves is a result of the asymmetrical bodywork when the cross-wind hits one side of the sidecar versus the other. Note also that the lateral force at zero cross wind, as observed in Figure 7.22 is not equal to zero, due to the asymmetrical flow over the sidecar body. The effect of cross winds on the slewing angle is negligible and would be unnoticeable by the rider. This is only the slewing effect and it is overwhelmed by the rotational slip angle described by Figure 7.12.

Rotation

A cross wind also adds to the rotational moment of the sidecar, based upon the magnitude of the force and the longitudinal offset of the centre of aerodynamic pressure from the centre of mass. In this case, only rotation (no slewing) is considered.

If the same conditions are used, at 120 mph (53 m/s) a cross wind will create a force (L_y) which creates a rotation around the vertical axis. As in Figure 7.13, the slip angle generated can be countered by a steering angle (δ). Figure 7.24 is a plot of the required steering angle to achieve a straight-ahead heading with cross winds from the left and from the right.

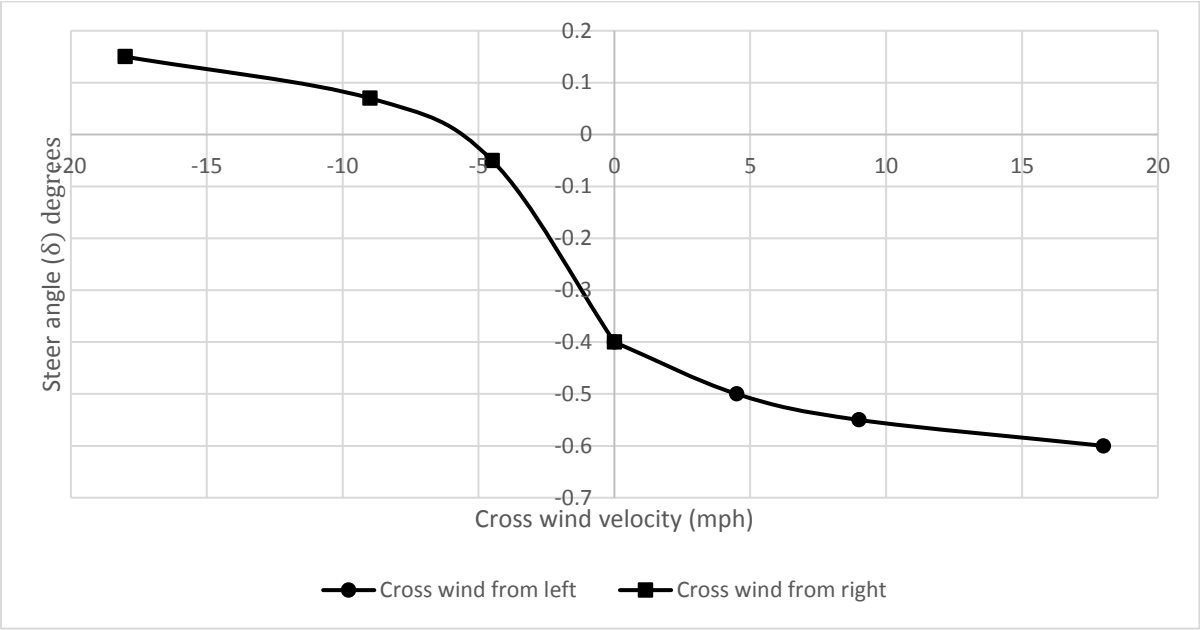

Figure 7.24- Steering angle (δ) required to counter cross winds

Note in Figure 7.24, with zero cross wind, a slight (0.4°) steering input is required to maintain zero slip, due to the asymmetrical forces that are present (see Figure 7.12 and 7.13). Because the centre of aerodynamic pressure is located ahead of the centre of mass, a cross wind from the right will rotate the vehicle to the left (requiring a right or positive steering angle addition) and a cross wind from the left will rotate the vehicle to the right, eventually requiring a positive steering angle correction. The asymmetrical effects of right and left cross winds are clearly evident in Figure 7.24.

7.5.6 Stability at large yaw angles

The effect on aerodynamic forces and moments of rotating the Bonneville sidecar through higher positive and negative yaw angles, up to 90° (perpendicular to the air flow) in both directions is plotted in Figure 7.25. Note that, as with the Ahmed body and the streamliner analyses, this approach ignores inertial effects and assumes a quasi-steady behaviour, as a steady-state CFD simulation was undertaken at each discrete Ø.

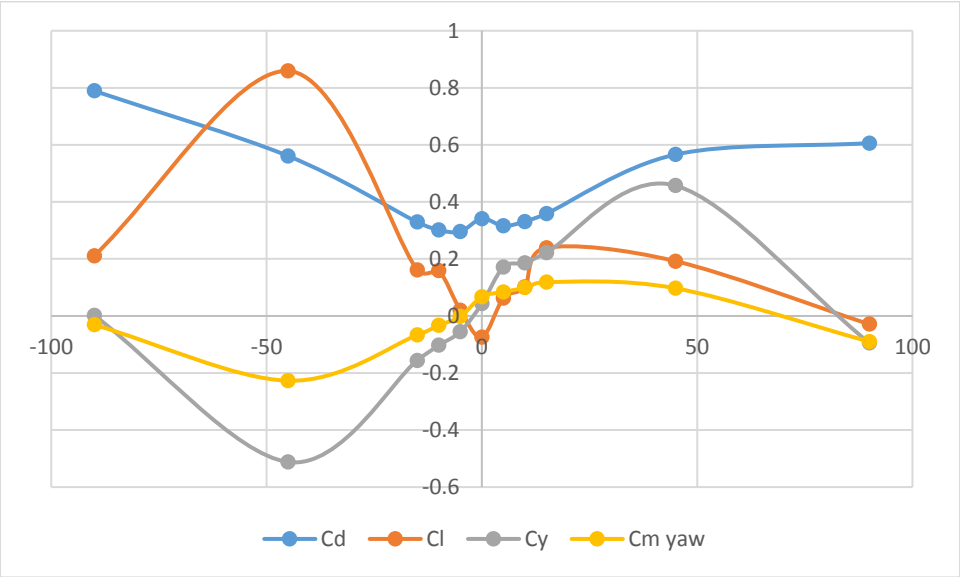

Figure 7.25- Bonneville sidecar at high yaw angles

7.5.6.1 Lift

From Figure 7.25, it is evident that the amount of aerodynamic asymmetry becomes even more significant at a yaw angle of 45°. The large difference in lift (C_l) between negative (left) and positive (right) high yaw angles can be explained from the profile that is presented to the airflow, as observed in Chapter 6. Recall the Purdue streamliner has a smoothly rounded surface that, when presented to the airflow at 45°, acted like a wing profile, producing lift. Likewise, the Bonneville sidecar, when yawed 45° to the left (negative yaw) presents at least a portion of the bodywork as a smooth and rounded profile which allows attached flow over the surface reducing the pressure on the surface (Figure 7.26). This reduced pressure results in the lift observed in Figure 7.25.

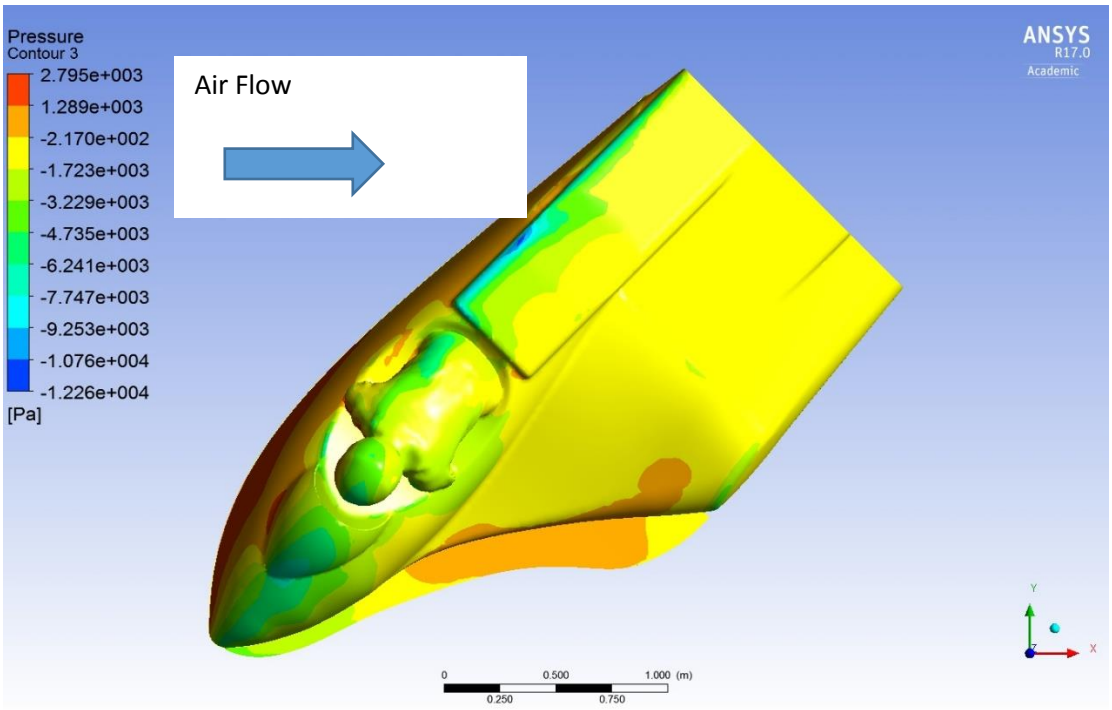

Figure 7.26- Sidecar surface pressure at Ø =- 45°

In Figure 7.27, a large number of strong streamwise vortices are evident when the air flow comes from the right side of the sidecar. These streamwise vortices also contribute to the lift shown in Figure 7.25.

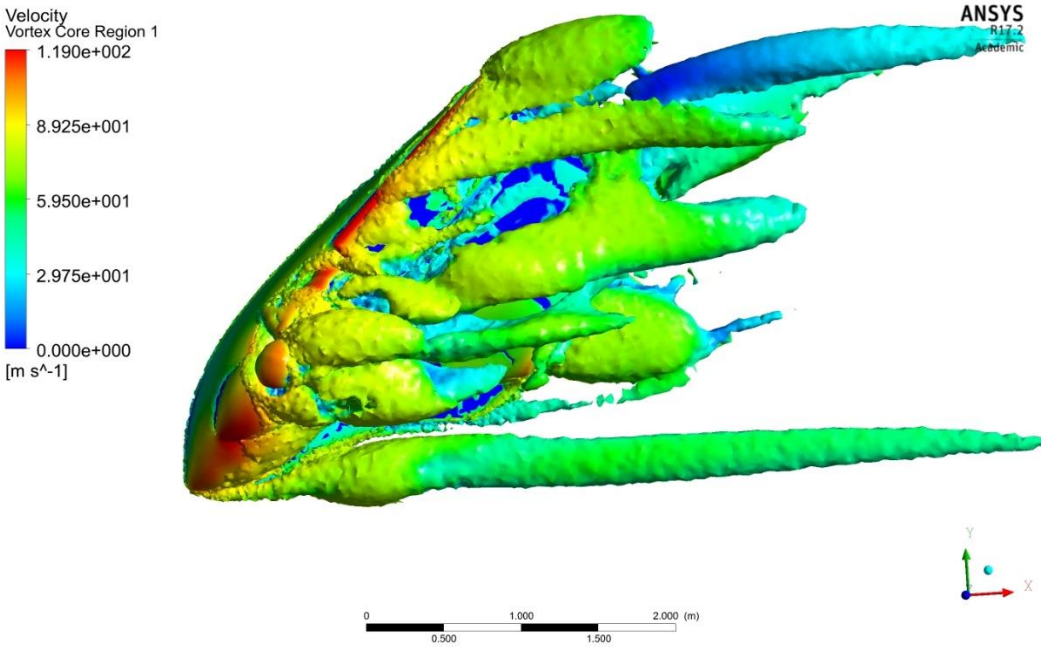

Figure 7.27- Velocity vortex core of sidecar at Ø = -45°

When the Bonneville sidecar is rotated into 45° of positive yaw (to the right), the profile presented to the air flow is much less rounded and results in airflow that separates from the surface, preventing the formation of a low-pressure region on the top of the body and therefore not producing as much lift as was observed when the sidecar yawed to the left (negative). This lower surface pressure is evident in Figure 7.28.

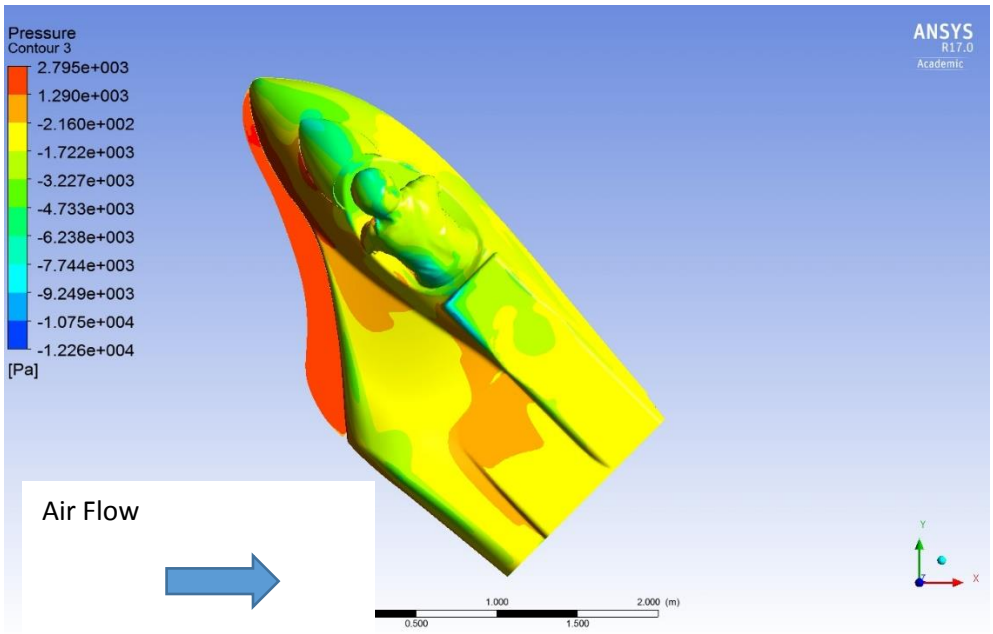

Figure 7.28- Sidecar surface pressure at Ø = + 45° yaw

In Figure 7.29, the streamwise vortices are not as strong when the airflow is from the left side of the vehicle and the lift generated by the sidecar is lower.

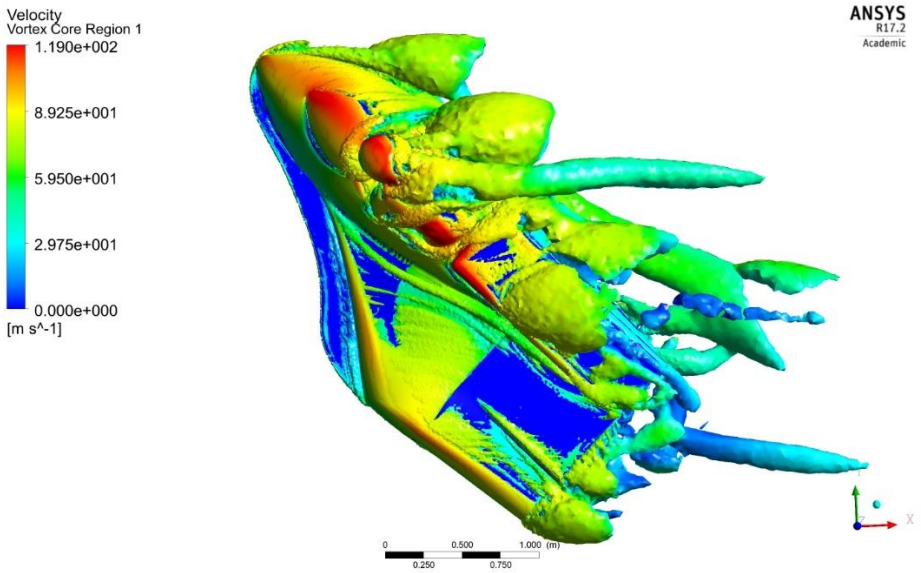

Figure 7.29- Velocity vortex core of sidecar with Ø = +45°

7.5.5.2 Effect of the splitter

In the initial design study detailed in Chapter 4, the addition of a "splitter" at the front edge of the sidecar portion of the vehicle was found to reduce lift with little detrimental effect on drag. To examine the effect of the splitter, CFD studies with ANSYS Fluent were undertaken for yaw angles between positive and negative 45°. The CFD for each condition used an unstructured mesh of 6.3 million elements with a velocity of 67 m/s and a moving roadway with the RANS SST turbulence model. Figure 7.30 compares drag coefficient (C_d) with and without the presence of a splitter.

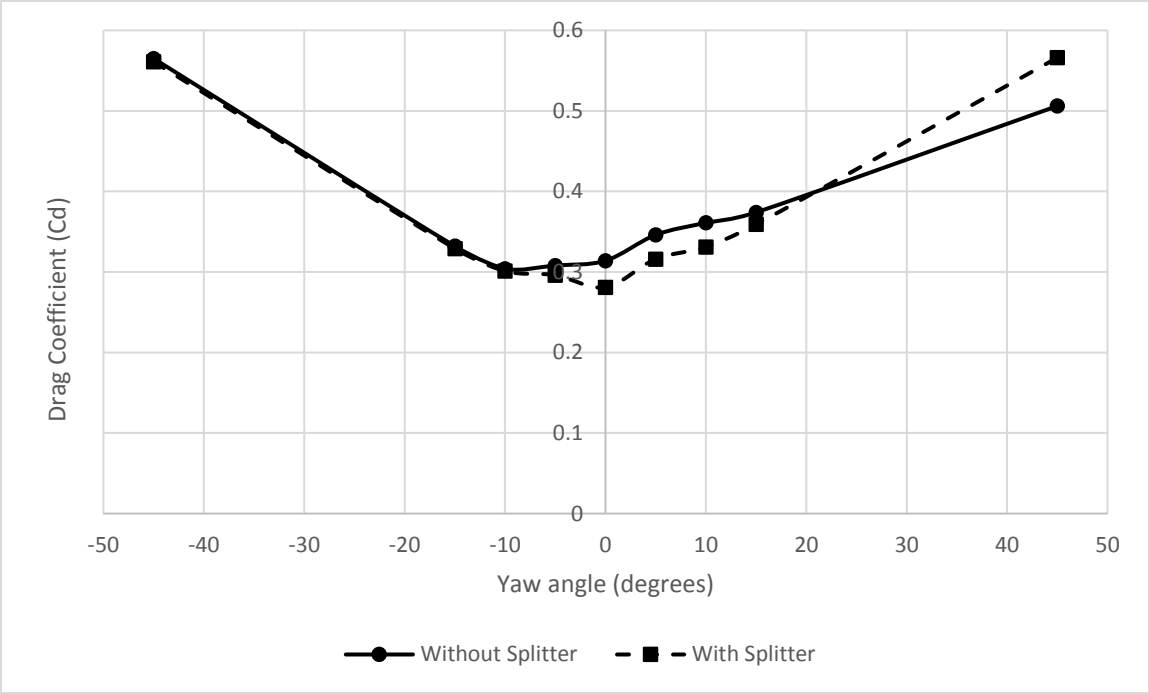

Figure 7.30- Drag coefficient of Bonneville sidecar with and without splitter

From Figure 7.30, the splitter only has a small effect of drag coefficient (C_d) and only when yaw is in the positive direction. This makes physical sense as the splitter is blocked by the sidecar bodywork when the vehicle rotates into negative yaw angles. At low positive yaw angles (less than +15°) the splitter improves drag (by 8.7%) whereas at high yaw angles (+45°) the drag coefficient with the splitter is 11.8% higher.

Figure 7.31 shows the flow at the front edge of the sidecar portion of the vehicle at positive 5° yaw without the splitter, while Figure 7.32 indicates the flow at positive 5° yaw with the splitter in place.

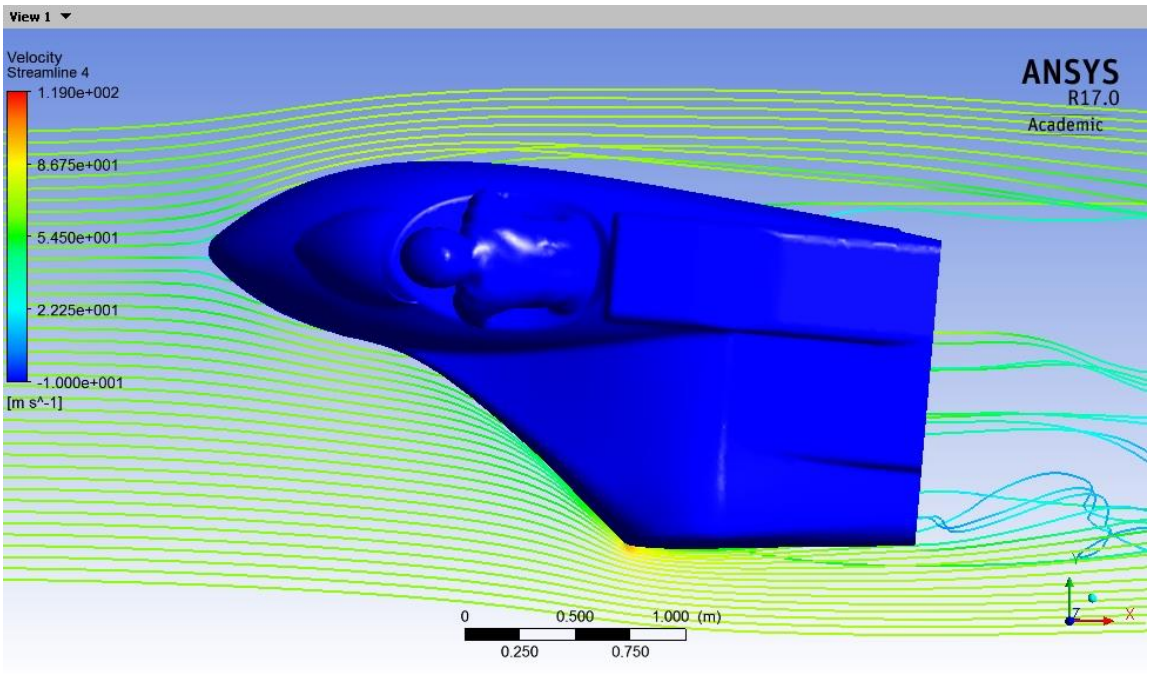

Figure 7.31- Airflow over sidecar at Ø = +5° without splitter

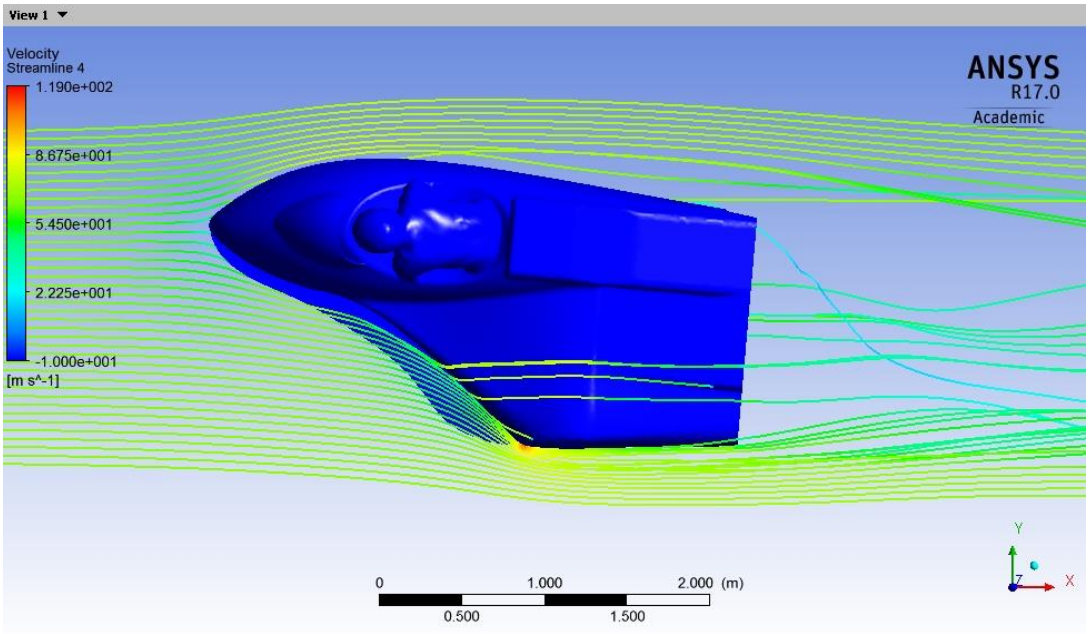

Figure 7.32- Airflow over sidecar at Ø = +5° with splitter

The streamlines in Figures 7.31 and 7.32 originate from the same height (0.2 m below the reference origin, or approximately 0.01m above the height of the leading edge of the splitter). It is evident from Figures 7.31 and 7.32 that the flow with the splitter present is diverted around and over the sidecar body and has reduced the disturbance in the wake, helping to reduce the drag, as observed in Figure 7.30.

Airflow over delta shaped wings is characterized by a vortex that starts at the apex of the delta and extends along the leading edge (Cummings & Schutte, 2008). The shear layer over the leading edge rolls up to form a primary vortex and the shear layer continues to feed the vortex down the length of the wing (Figure 7.33).

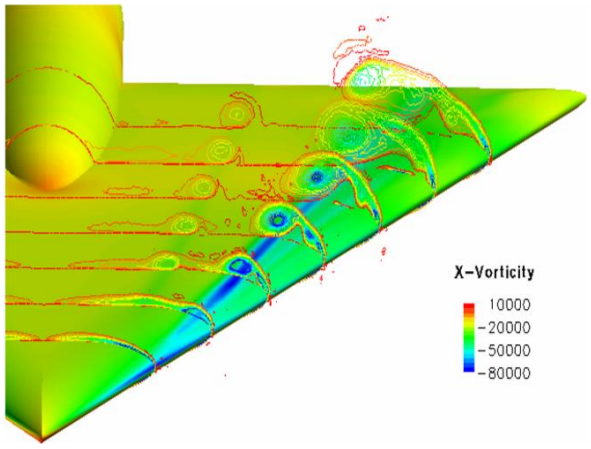

Figure 7.33- Surface pressure distribution and x-vorticity on a VFE-2 delta wing [Cummings & Schütte, 2008]

Figure 7.34 and Figure 7.35 compare velocity vortex core plots at zero yaw (67 m/s) from the top with and without the splitter. Along the top surface of the splitter, there is no indication that the shear layer is rolling up at the leading edge of the upper surface to form a primary vortex, as with a delta wing. It is possible that the presence of the sidecar body where the splitter joins with the body prevents this from occurring.

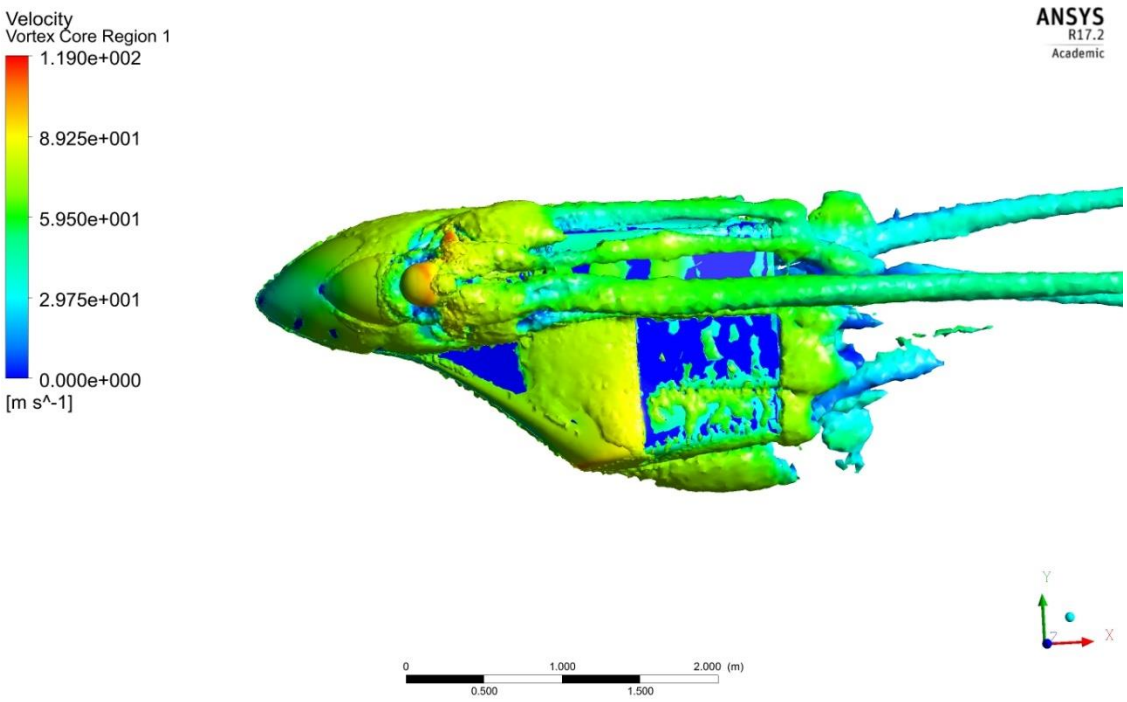

Figure 7.34- Sidecar at 67 m/s without splitter (top view, Ø =0°)

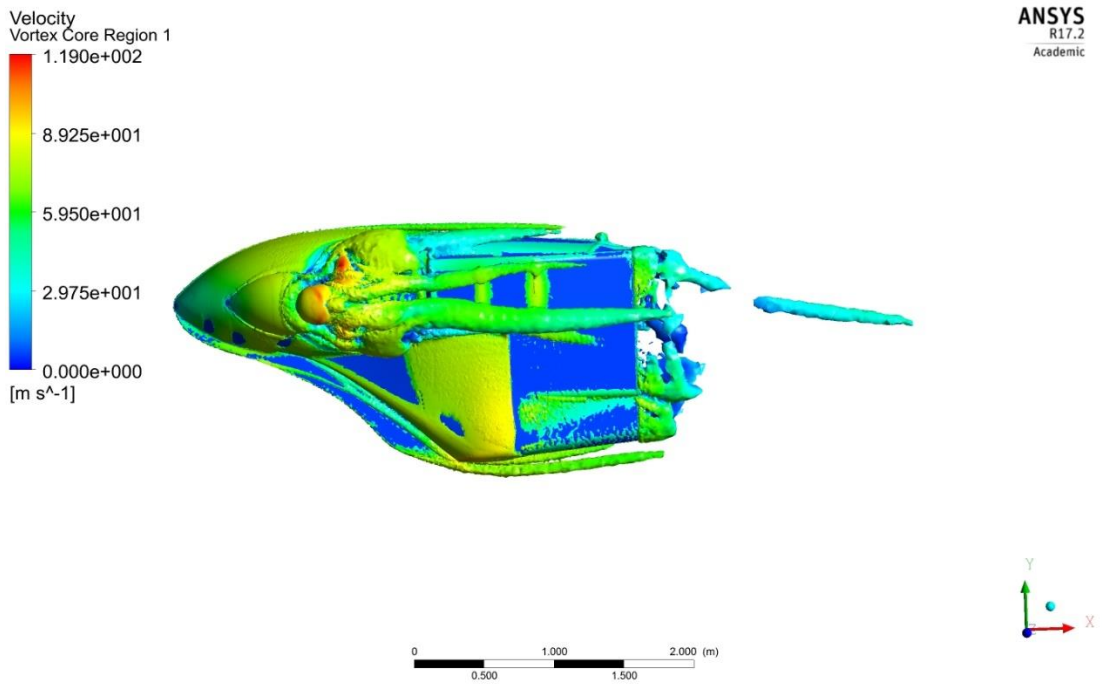

Figure 7.35- Sidecar at 67 m/s with splitter (top view, Ø =0°)

On the underside of the sidecar, Figure 7.36 and Figure 7.37, there is an indication both with and without the splitter that the flow along the leading edge of the underside results in a vortex along the length of the bodywork created by the shear of the flow at the leading edge outer edge. When the splitter is present this primary vortex is much better defined and when it reaches the outer edge of the splitter and encounters the freestream flow it creates a distinctive streamwise vortex. This streamwise vortex is not as well defined when the splitter is not present. The leading-edge vortex on the underside of the splitter acts similar to the ones observed on a delta wing and is expected to contribute to the downforce the splitter generates.

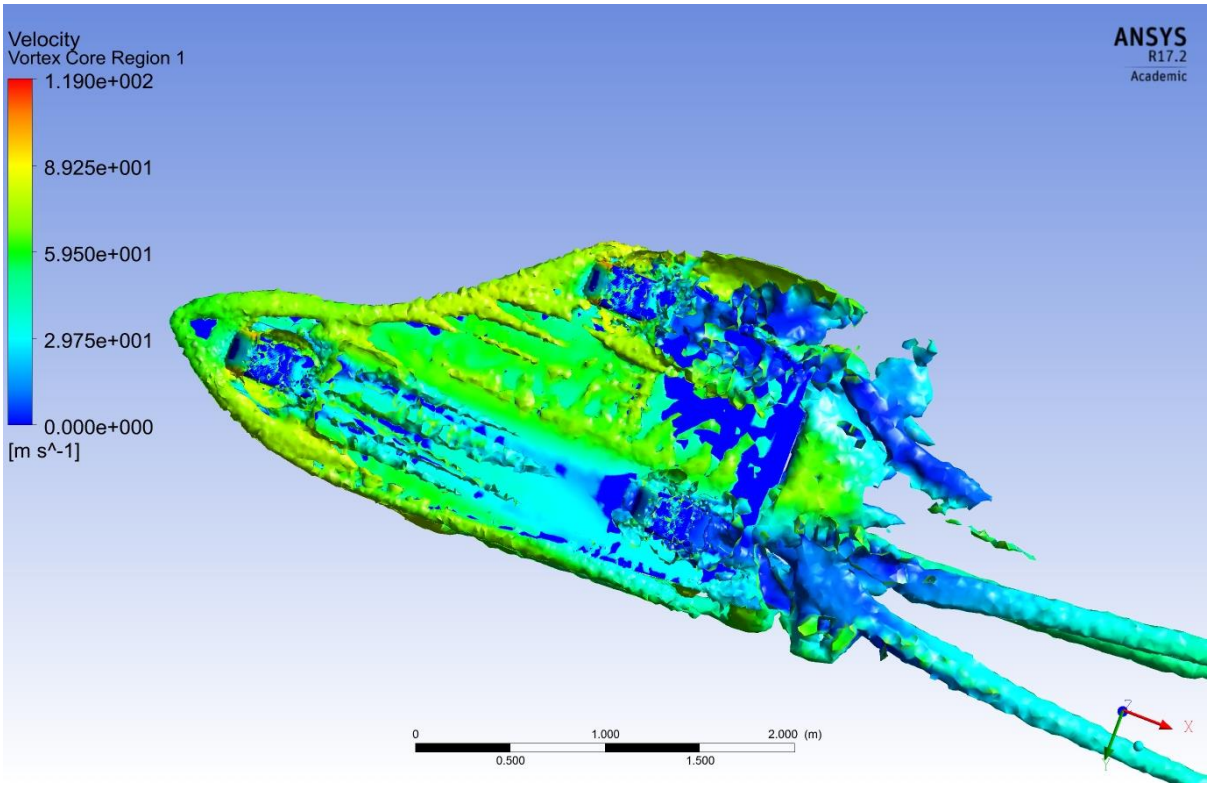

Figure 7.36- Sidecar at 67 m/s without splitter (bottom view, Ø= 0°)

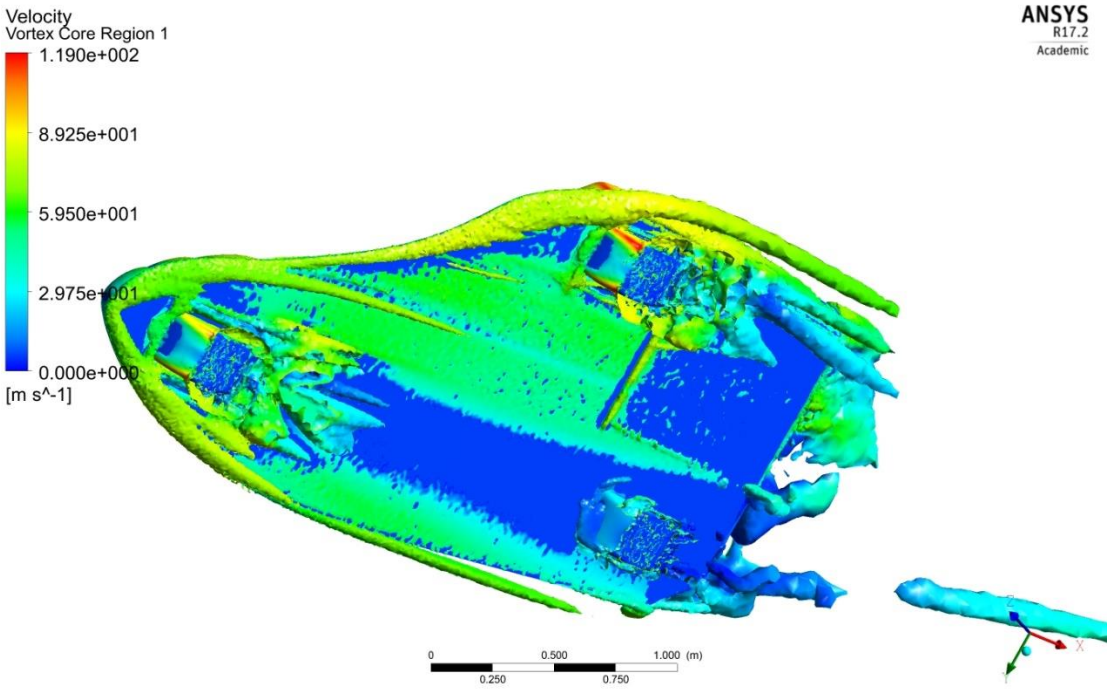

Figure 7.37- Sidecar at 67 m/s with splitter (bottom view, Ø =0°)

The purpose of the splitter was to reduce lift (McBeath, 2015) and Figure 7.38 indicates the lift force in Newtons with and without the splitter when rotated between positive and negative 45° yaw angles.

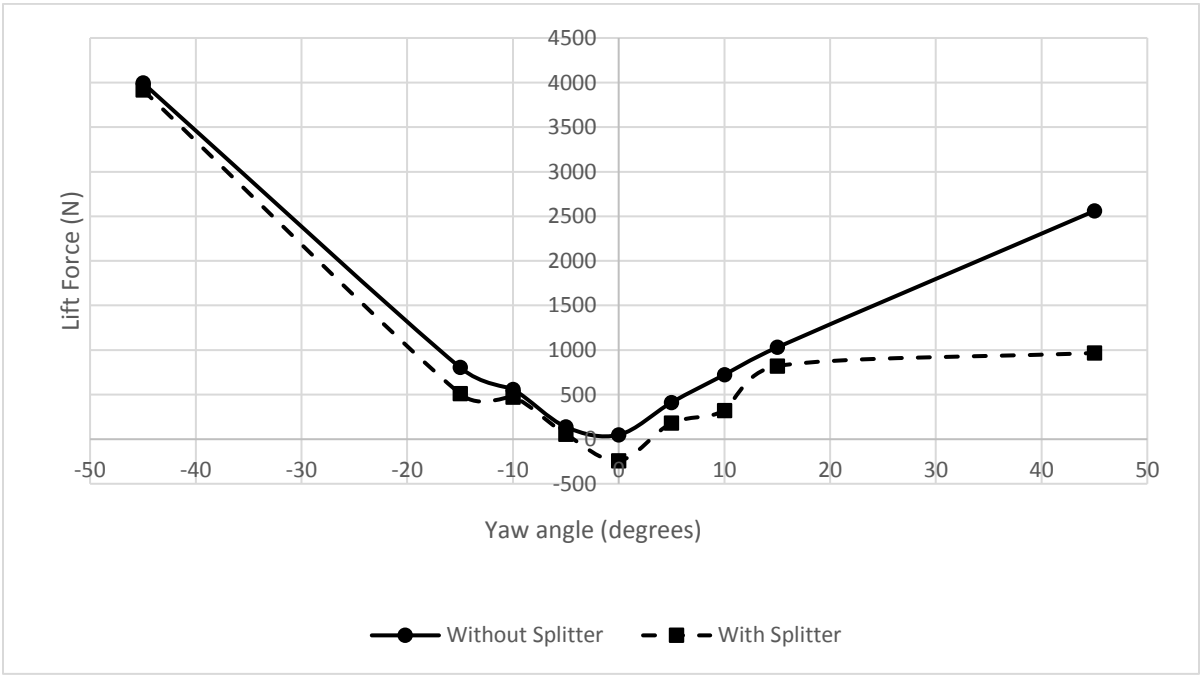

Figure 7.38- Lift force (N) of Bonneville sidecar with and without splitter

As observed with drag (Figure 7.30) the lift force generated with the splitter in place is lower than without the splitter. At zero degrees yaw, there is a negative lift (downforce) present when the splitter is in place (as observed in the Chapter 4 design study). With negative yaw angles, the splitter has only a small effect (explained above the blocking of the splitter by the sidecar body) while at positive yaw angles the splitter is effective at reducing lift, dramatically so at positive 45° yaw (Figures 7.39 and 7.40). The reduction in lift is expected to improve vehicle aerodynamic stability, and the addition of a splitter does so without increasing drag, at least at the moderate yaw angles experienced in normal operation.

The downforce can be observed from pressure contours on the sidecar surface in Figure 7.39 and Figure 7.40.

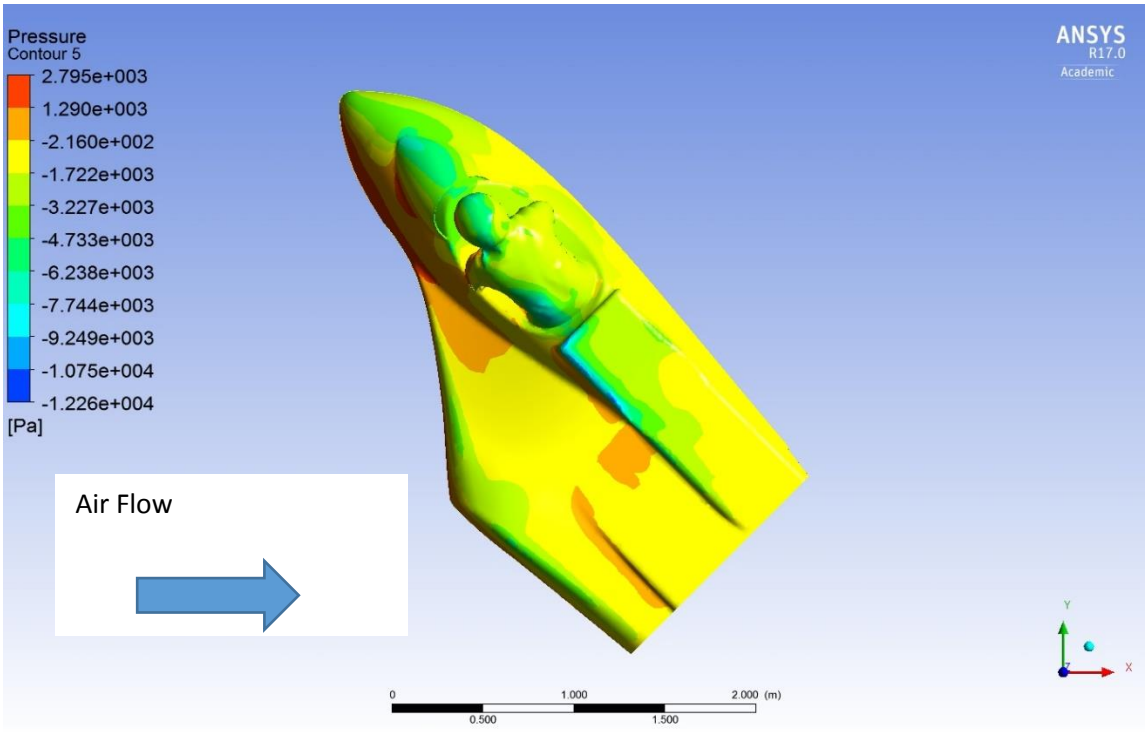

Figure 7.39- Sidecar surface pressure at positive Ø = +45° without splitter

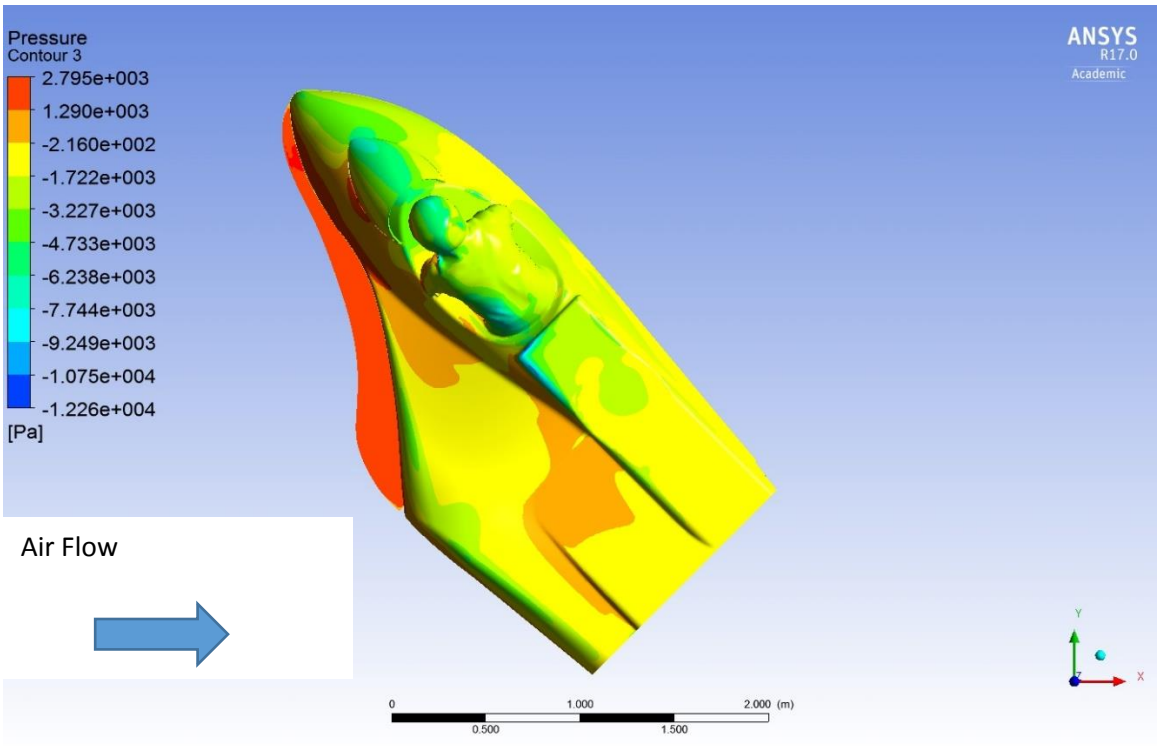

Figure 7.40- Sidecar surface pressure at positive Ø = +45° with splitter

When comparing Figure 7.40 with the splitter to Figure 7.39 without the splitter is clear that the high positive pressure pressing downward on the surface of the splitter (red in Figure 7.39) is producing negative lift (downforce).

Flow under the sidecar was also examined. Figure 7.41 is a pressure distribution of the underside of the sidecar without the splitter, while Figure 7.42 shows the pressure distribution with the splitter present.

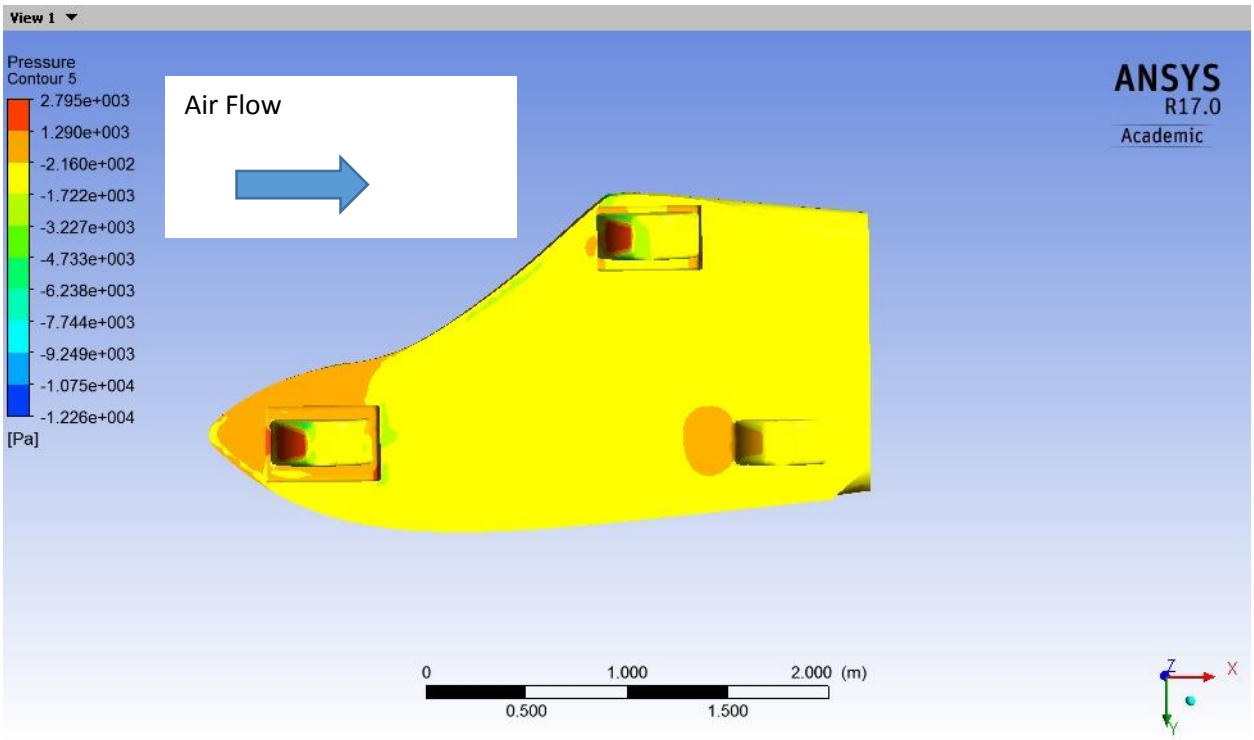

Figure 7.41- Pressure on the underside of the sidecar at Ø = 0° without splitter

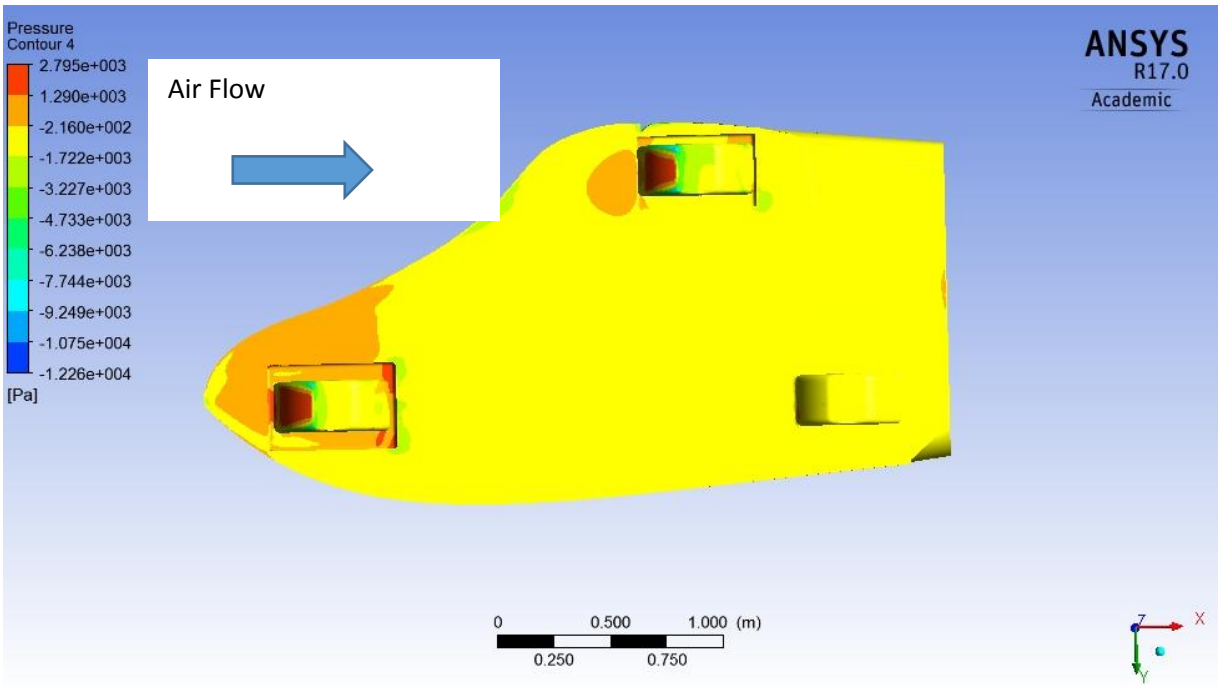

Figure 7.42- Pressure on the underside of the sidecar at Ø = 0° with splitter

Figure 7.41 and Figure 7.42 indicate that at 0° yaw the splitter has little or no effect on the pressure distribution on the underside of the sidecar.

7.5.5.3 Yaw Moment

Another factor that has the potential to improve aerodynamic stability is a restorative yaw moment. Figure 7.43 compares the yaw moment coefficient (C_{myaw}) with and without the presence of a splitter.

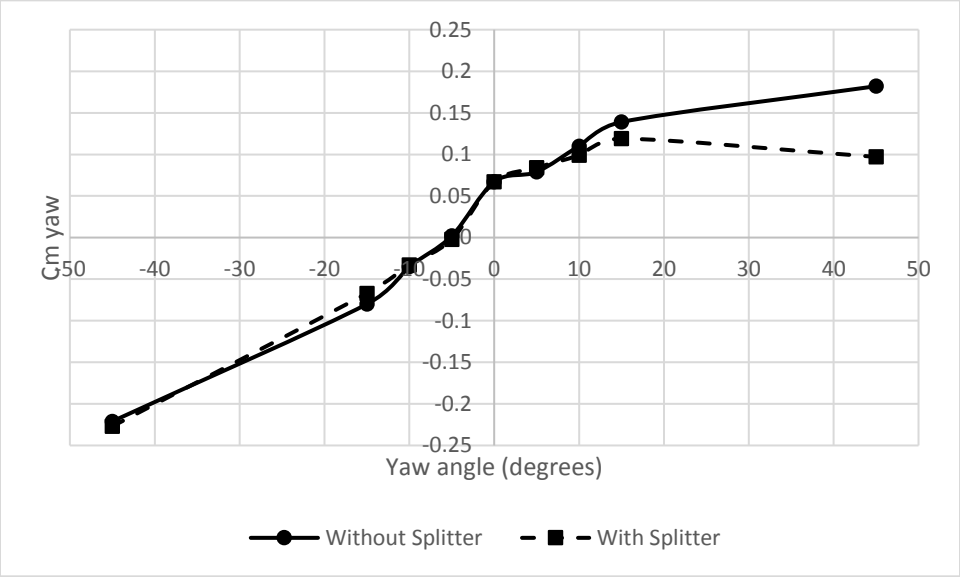

Figure 7.43- Yaw moment coefficient of Bonneville sidecar with and without splitter

In Figure 7.43, when the sidecar is yawed in the negative direction, the splitter has little or no effect on the yaw moment coefficient. At positive yaw angles, the splitter has a beneficial effect, reducing the adverse yaw moment coefficient as the yaw angle increases.

From Figure 7.43, it is noted that the yaw moment coefficient is adverse when the vehicle is yawed in both the negative and positive direction. This results from a centre of aerodynamic pressure that is located forward of the vehicle centre of mass and traditionally is an indication of potential vehicle instabilities at high speeds (Hucho & Sovran, 1993).

The x-axis (longitudinal) location of the centre of aerodynamic pressure can be calculated by dividing the yaw moment coefficient (C_{myaw}) by the lateral force coefficient (C_y) to obtain a distance x in metres from the origin reference which is located at the vehicle centre of mass. Recall that the convention chosen was for a positive yaw moment to be a clockwise (right) rotation, when viewed from above and behind. This is the opposite than is used by ANSYS Fluent and thus the distance obtained is in the opposite sign. In Table 7.4 the standard ANSYS Fluent sign convention has been corrected to represent the yaw moment convention used throughout this work. A negative x-axis distance points forward in the direction of longitudinal motion.

Table 7.4- Position of centre of aerodynamic pressure with and without splitter

Without Splitter				
Yaw angle (degrees)	**C_y**	**$C_{m\ yaw}$**	**Distance (m)**	**Distance (m) Corrected from ANSYS yaw direction convention**
-15	-0.176	-0.08	0.454	-0.454
-10	-.095	-0.035	0.368	-0.368
-5	-0.36	0.002	-0.056	0.056
0	0.064	0.049	0.754	-0.754
5	0.146	0.079	0.541	-0.541
10	0.203	0.110	0.548	-0.548
15	0.244	0.139	0.570	-0.570
With Splitter				
-15	-0.156	-0.067	0.430	-0.430
-10	-0.103	-0.033	0.320	-0.320
-5	-0.055	-0.002	0.036	-0.036
0	0.043	0.067	1.58	-1.58
5	0.171	0.004	0.491	-0.491
10	0.186	0.099	0.532	-0.532
15	0.222	0.119	0.536	-0.536

The results from Table 7.4 are plotted in Figure 7.44.

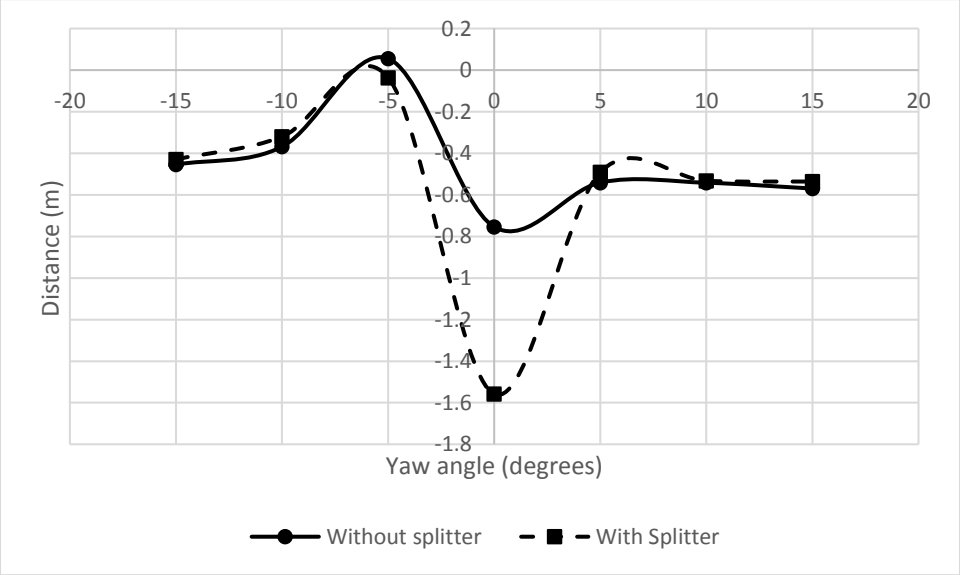

Figure 7.44- Longitudinal position of sidecar centre of aerodynamic pressure relative to centre of mass

Figure 7.45 is a velocity vortex core plot at Ø = -5°, Figure 7.46 at Ø = 0° and Figure 7.47 at Ø = +5°.

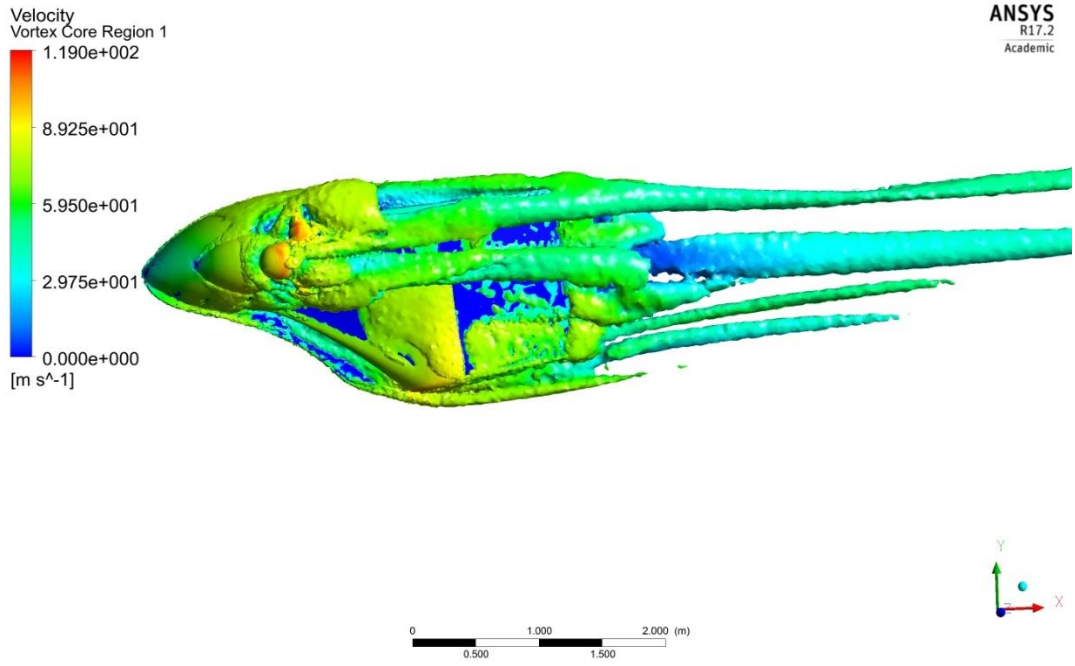

Figure 7.45- Velocity vortex core at Ø = -5°

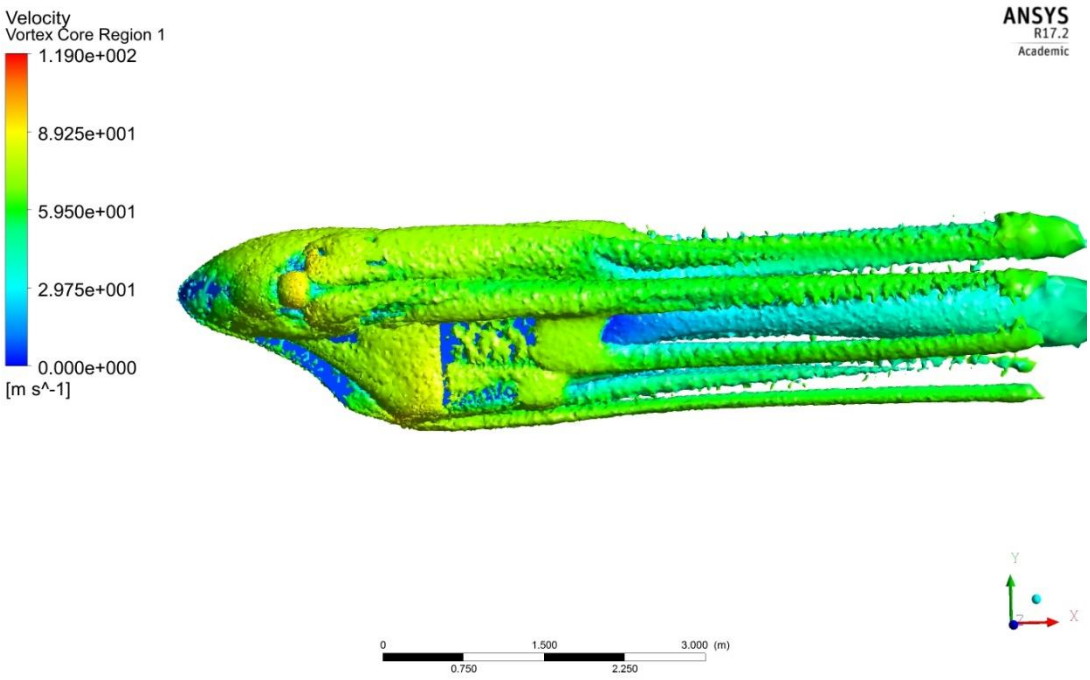

Figure 7.46- Velocity vortex core at Ø = 0°

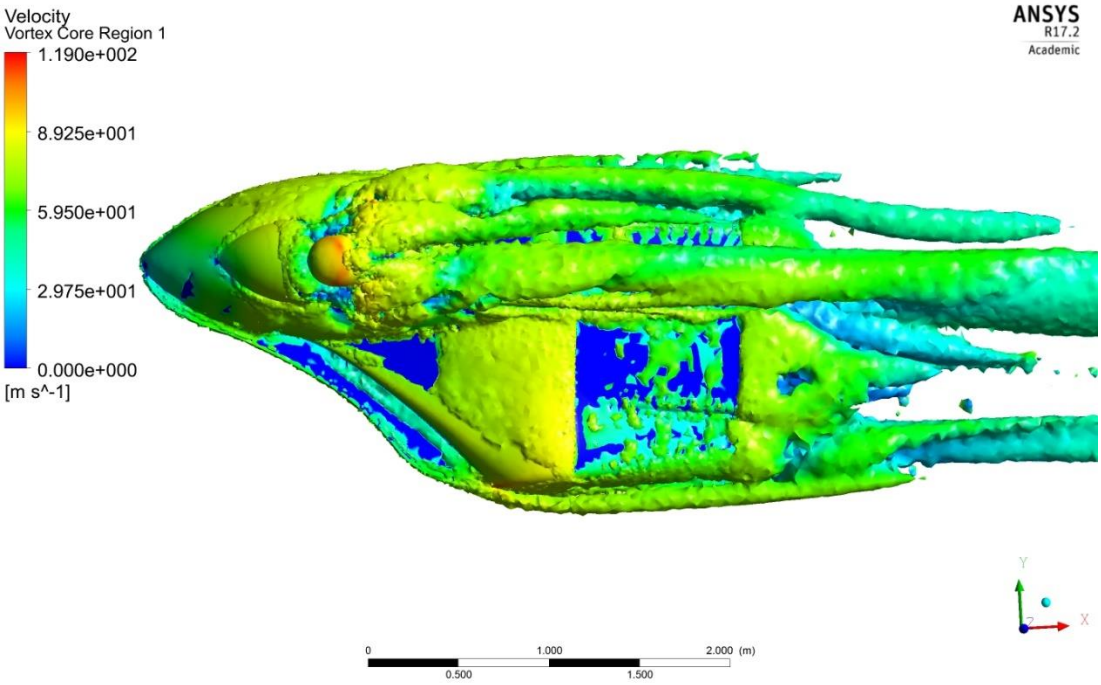

Figure 7.47- Velocity vortex core at Ø = 0°

In Figure 7.46 (at Ø = 0° with a splitter) the streamwise vortices originating at the rider are more significant than in either the -5° or +5° cases, particularly on the rider's right shoulder. Because the rider is significantly further forward than the centre of mass of the vehicle, it is reasonable to assume that the rider is at least part of the cause of the farther forward position of the centre of aerodynamic pressure at 0° yaw noted in Figure 7.44. As the vehicle yaws, the strength of the streamwise vortices coming from the rider lessens and the effect of the rest of the sidecar body on the location of the centre of aerodynamic pressure increases. In Figure 7.48, at Ø = 0° without a splitter, the flow topology along the side of the sidecar is different as the distinct streamwise vortex that forms at the edge of the splitter is no longer present and a larger more widespread separation zone is apparent. This may explain the difference in Figure 7.44 between a splitter and no splitter at Ø = 0°.

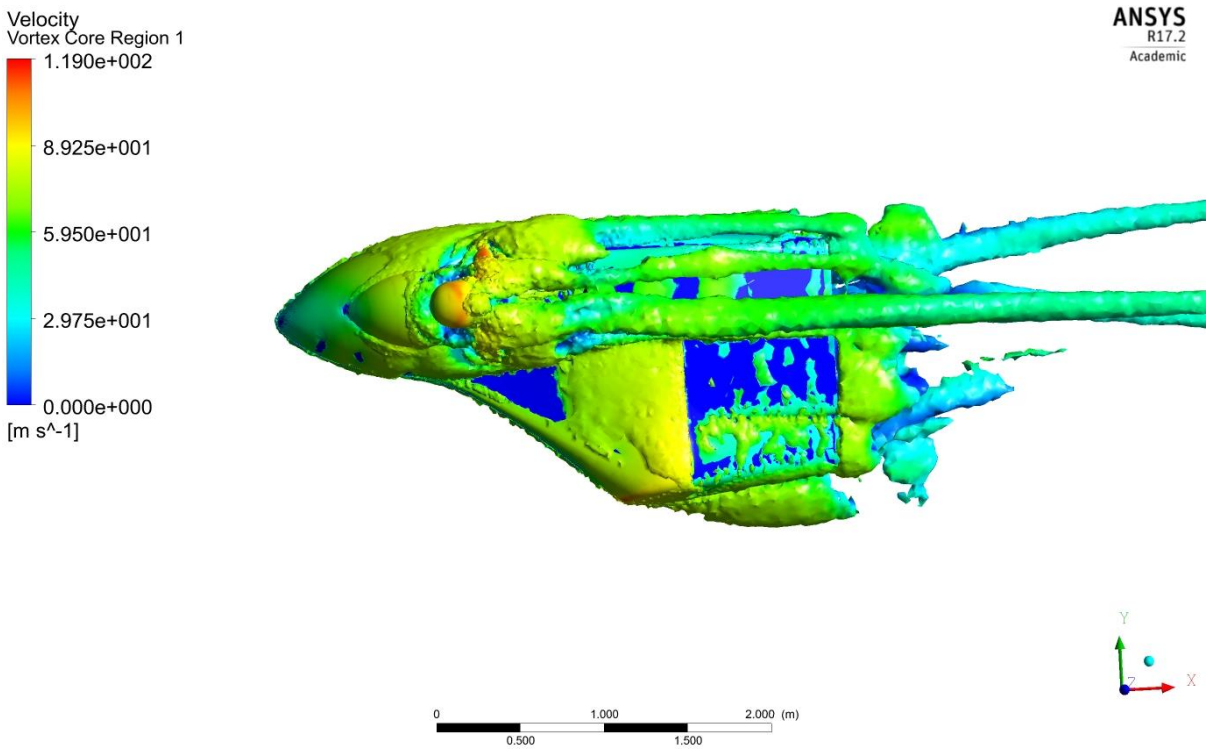

Figure 7.48- Velocity vortex core at Ø = 0° with no splitter

It should be noted that the significant distance between the centre of mass and centre of pressure at zero yaw (with the splitter) was not noted to produce any instabilities when the vehicle was driven in record attempts at any of the land speed record venues. The value obtained for this distance (x) in Table 7.4 seems high relative to the distances obtained at other yaw angles and may result from errors in dividing small numbers into each other. In all probability, the corrective forces from the tyres dominate the destabilizing aerodynamic forces, so that the vehicle is stable.

The forward position and large side profile of the rider undoubtedly results in the forward position of the centre of aerodynamic pressure. As in Chapter 6, the effect of the rider could possibly be countered by positioning a fin at the rear of the sidecar, however the FIM international rules limit the overall height of the sidecar (without rider) so that a fin is not possible for world record attempts. Likewise, the position of the rider above the bodywork is regulated, so that moving the centre of aerodynamic pressure rearward on this class of vehicle is difficult. When the human “swinger” is used in place of ballast, it is possible that the greater side profile of the human, positioned on the rear platform, may help move the centre of aerodynamic pressure rearward, assisting in stability.

7.5.5.3 Roll

Roll stability, while extremely important in the case of the single-track streamliner vehicle, is less important with the extra support provided on the three-wheel sidecar. Figure 7.49 is a plot of roll moment coefficient versus yaw angle.

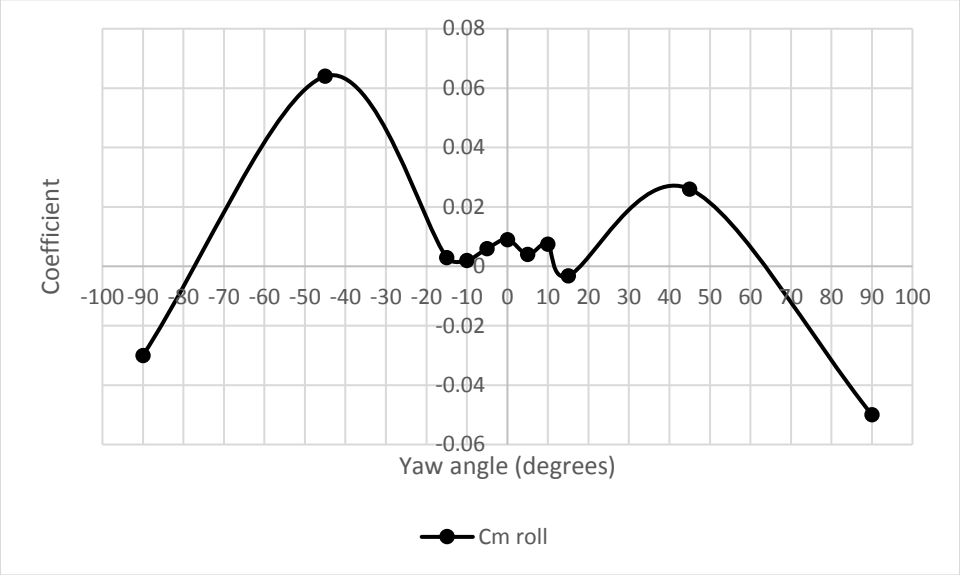

Figure 7.49- Bonneville sidecar roll moment coefficient versus yaw angle

From Figure 7.49 it is evident that the roll moment increases away from zero to 45° degrees of positive or negative yaw but then decreases as yaw approaches positive or negative 90°. Note there is asymmetry of the roll coefficient in positive and negative yaw. It should also be noted that numerically, the values of the roll moment coefficient are small, indicating only a small amount of roll will be imparted to the vehicle, particularly over the relatively flat region between -10° to +10°, the normal riding range.

7.5.5.4 Pitch

The change in pitch moment coefficient (C_{mpitch}) is plotted versus yaw angle for the Bonneville sidecar in Figure 7.50.

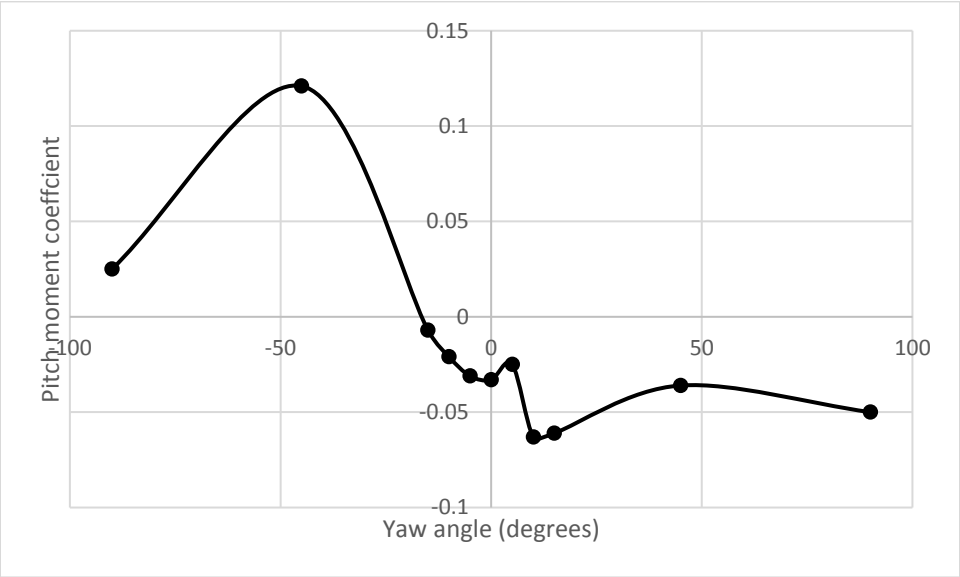

Figure 7.50- Bonneville sidecar pitch moment coefficient versus yaw

From Figure 7.50, the tendency of the sidecar to pitch with yaw is negligible with positive yaw, but increases with negative yaw. The pitch moment results from the action of the vertical (lift) forces located at the centre of aerodynamic pressure and acting on the centre of mass through the longitudinal distance between the two. In this convention, a negative pitch moment coefficient indicates the nose will pitch upward. At a first approximation, this pitch moment must be greater than the moment created from the weight of the front wheel (W_f) acting over the distance from the front wheel to the centre of mass (l_1) for pitch to become a problem. From Figure 7.50, the pitch moment is at a maximum at negative 45° of yaw. Using $C_{m\ pitch}$ = 0.121, l_1= 1.42 m, V_x = 67 m/s, A=1.658 m^2 and W_f = 1569 N, from

$$M_{pitch} = ½\ \rho\ V_x^2\ A\ C_{m\ pitch}$$

the pitch moment M_{pitch} = 551 Nm. The moment created by the weight of the front wheel is equal to (W_f * l_1)= 2228 Nm. Even at its maximum, the aerodynamic pitch moment is at a low enough level to have an unnoticeable effect on vehicle stability. Problems could arise, however, if the aerodynamic pitch causes the nose to rise on its suspension, increasing the angle of attack and hence the lift.

7.5.5.5 Reversed direction

During an accident, the potential exists for the sidecar vehicle to spin completely around and travel backward. In this worst case, it would be useful to understand the lift characteristics of the rearward traveling vehicle. Using ANSYS Fluent 17.0, the Bonneville version of the sidecar was simulated at 67 m/s traveling backward. The high drag (C_d =0.452) experienced would be expected to quickly slow the vehicle. The lift generated (C_l = 0.433) at 67 m/s (150 mph) was 1190 N, which is a significant lift force but less than the 2609 N that the rear wheel static load and the rear of the vehicle will not become airborne, at zero pitch. Figure 7.51 shows the formation of a

region of separation over the rear of the rearward traveling sidecar and streamwise vortices into the wake region.

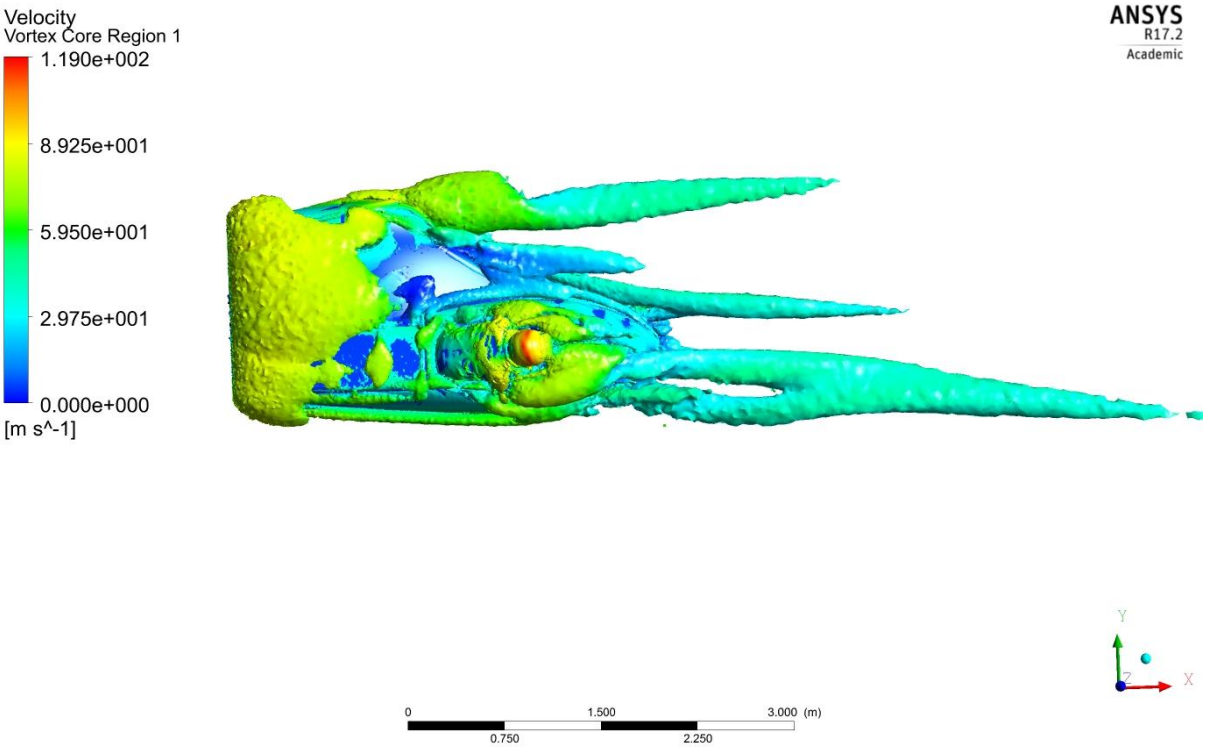

Figure 7.51- Rearward traveling sidecar at 67 m/s (view from above)

7.6 SURFACE FRICTION VISUALISATION

Recall from Chapter 3, Tobak et al. (1982) described the flow features associated with characteristic skin friction surface patterns. Of particular relevance here are:

- Where skin friction lines converge toward a single line, separation occurs as flow lifts from the surface.
- Where skin friction lines diverge from a separator line, flow attachment is expected.
- Where the skin friction lines form a spiral, called a focus, the flow forms a vortex that is centred on the spiral.

Although a complete survey of skin friction topology on the entire surface of the sidecar was not undertaken, the examination of some key areas provides an understanding of interesting flow regions. The shear stress surface lines which can be visualized in ANSYS Fluent are analogous to skin friction lines.

Figure 7.52 shows formation of several foci on and around the rider. The focus near the rider's shoulder is particularly important as plots of velocity vortex core (Figure 7.45) show that the

streamwise vortex that originates at this point extends into the wake region, becoming one of the wake region's most significant flow topologies.

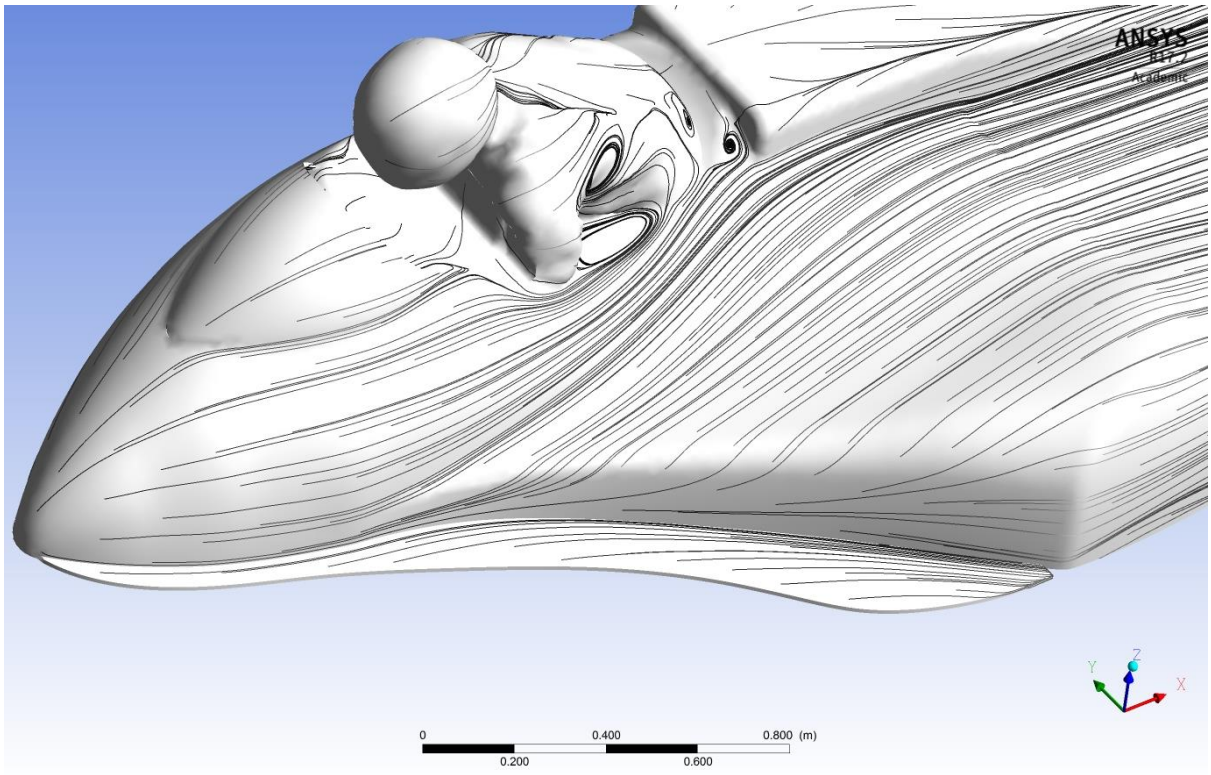

Figure 7.52- Several foci form on and around the rider, serving as an origin for vorticity

Because rules require the torso of the rider to be visible from the side and above, there is little that can be done to reduce the significant flow disruption of flow caused by the presence of the rider. The raised region behind the rider, called the motor cover in the design study, is shown in Figure 7.53. In this figure directional arrows have been added to show whether the shear stress lines are converging or diverging from separator lines.

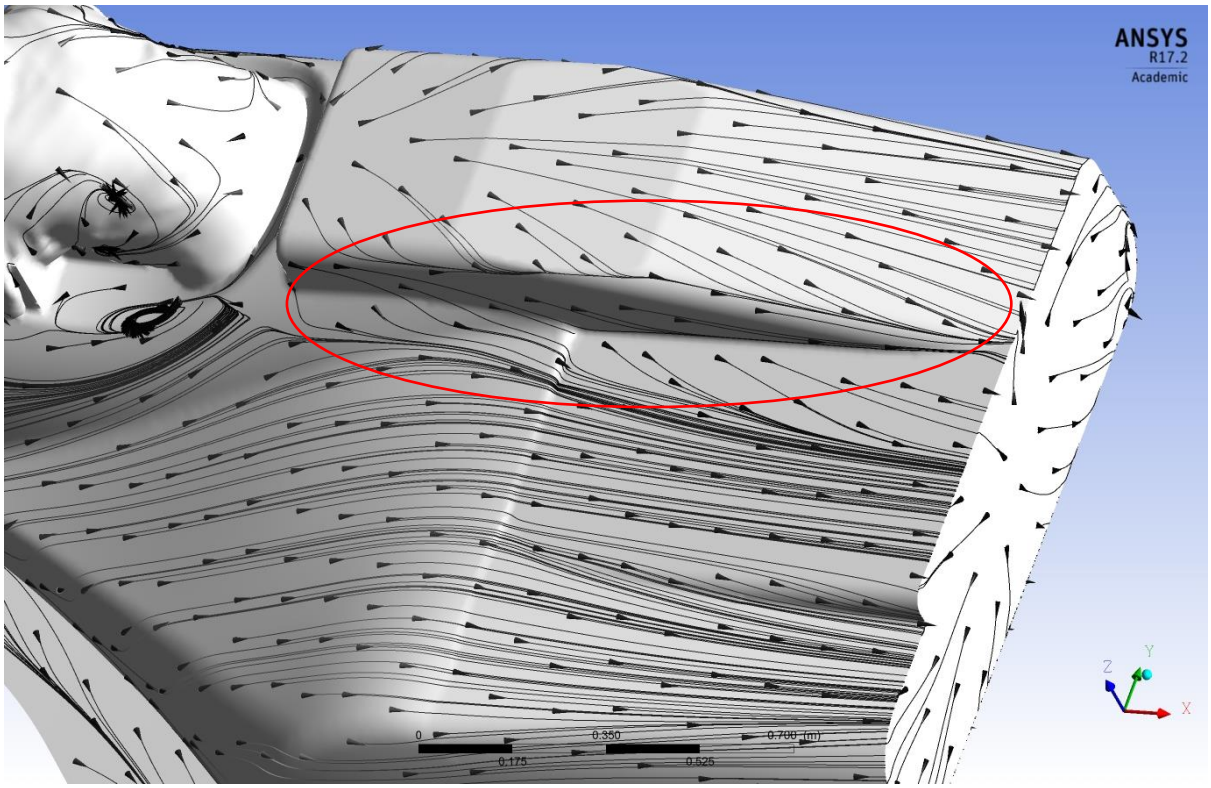

Figure 7.53- Flow separation on the rear motor cover

In Figure 7.53, flow is attached over the central part of the motor cover but the shear lines are observed to converge to a separator line at the edge where it rolls over to meet the sidecar surface (indicated in the figure). From Tobak et al. (1982) this convergence indicates flow separation occurs in this region.

The rear vertical surface of the tail of the sidecar shows a region of convergent shear stress lines in Figure 7.54.

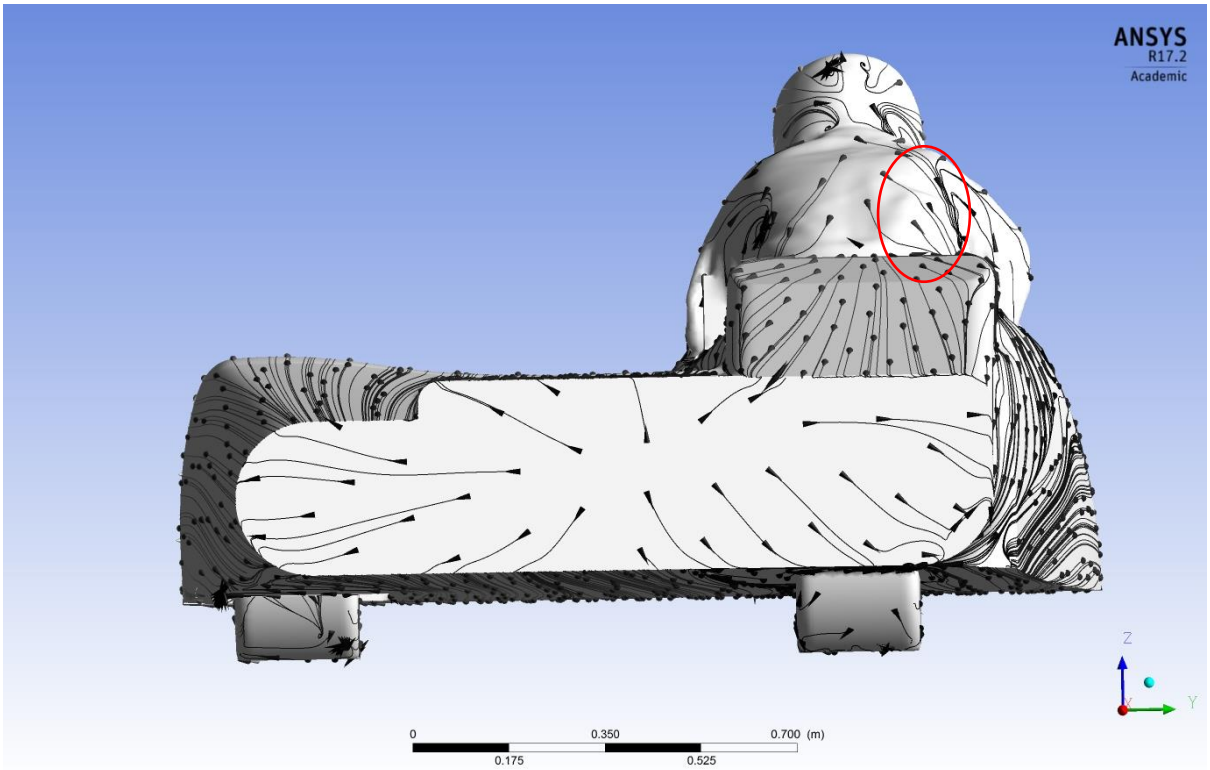

Figure 7.54- Convergent shear stress lines at the tail of the sidecar

Note that in Figure 7.54, the shear stress lines are uniform in their distribution and divergence, indicating that the region of flow across the vertical surface and to the edges is uniform.

Also evident in Figure 7.54 are the divergent flow lines across the back of the rider that indicates a region of attached flow until the flow converges onto a separator line (indicated in red) where the flow then separates.

It was shown (in Figure 7.45) that streamwise vortices form from shear with the lateral flow from the tail section meeting the longitudinal flow along the sides of the sidecar body. The location of the meeting of these two flows on the right side of the sidecar is indicated in Figure 7.55 in red. The shear due to flow from both the upper and lower surfaces over the flow on the tail region forms a broad lateral vortex behind the sidecar tail and nearly as wide as the vehicle.

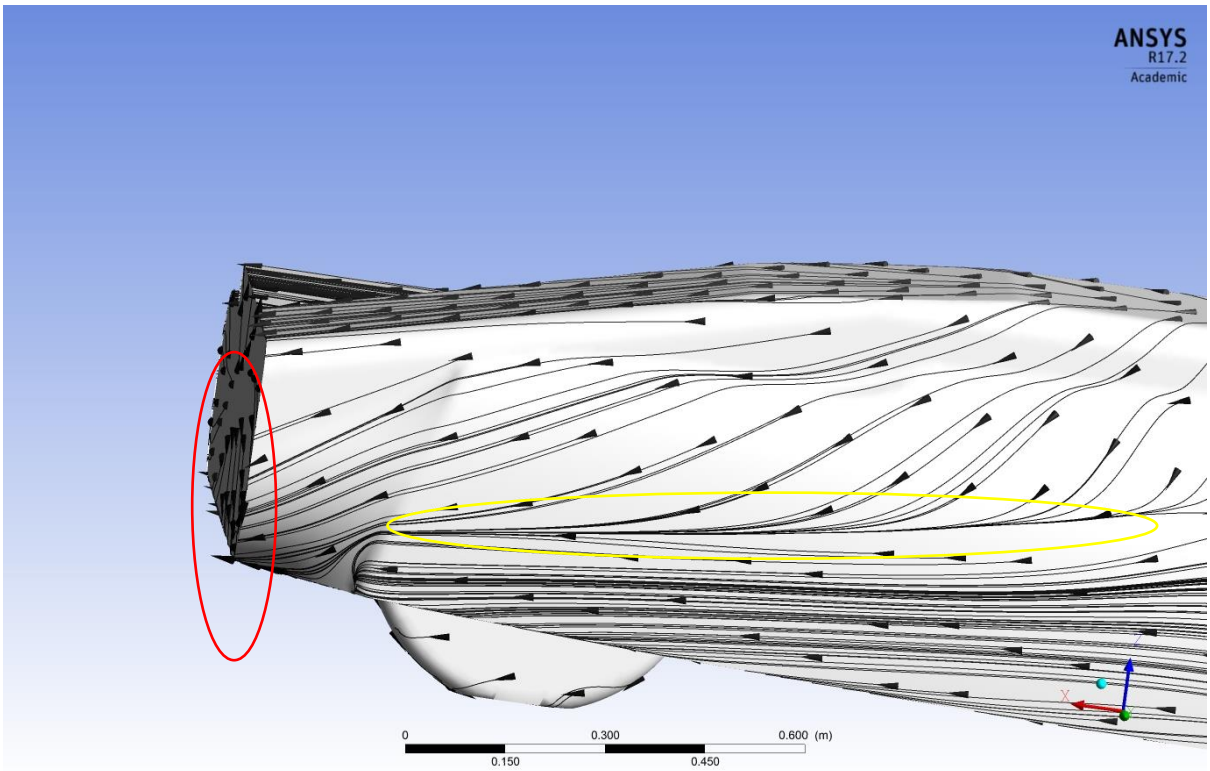

Figure 7.55- Shear stress lines on the right side of the sidecar body

In Figure 7.55, in addition to the streamwise vortex that forms from the shear of lateral and longitudinal flow at the tail of the sidecar (indicated in red), there is also a separation region where the shear stress lines converge to a separation line, as indicated in yellow. This additional separation may contribute to the streamwise vortex formed at the rear of this side of the sidecar body.

On the opposite side of the sidecar body (Figure 7.56), in addition to a similar region of shear between the lateral and longitudinal flow (in red), there is similar area in which the shear stress lines converge to a separator line (in yellow), indicating flow separation.

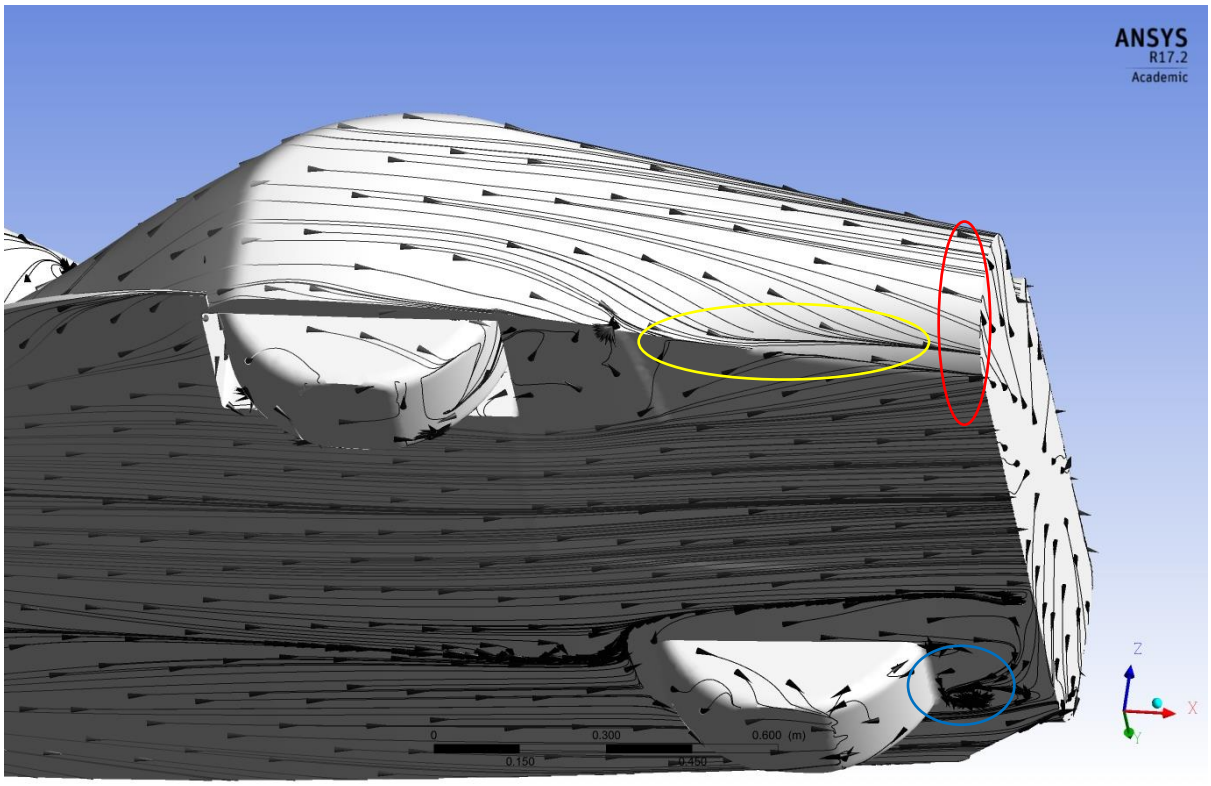

Figure 7.56- Shear stress lines on the underside of the sidecar body

Also evident in Figure 7.56, is a focus behiond the rear wheel (in blue) indicating the origin of a streamwise vortex which continues into the wake.

Figure 7.57 shows shear stress lines on the underside of the sidecar.

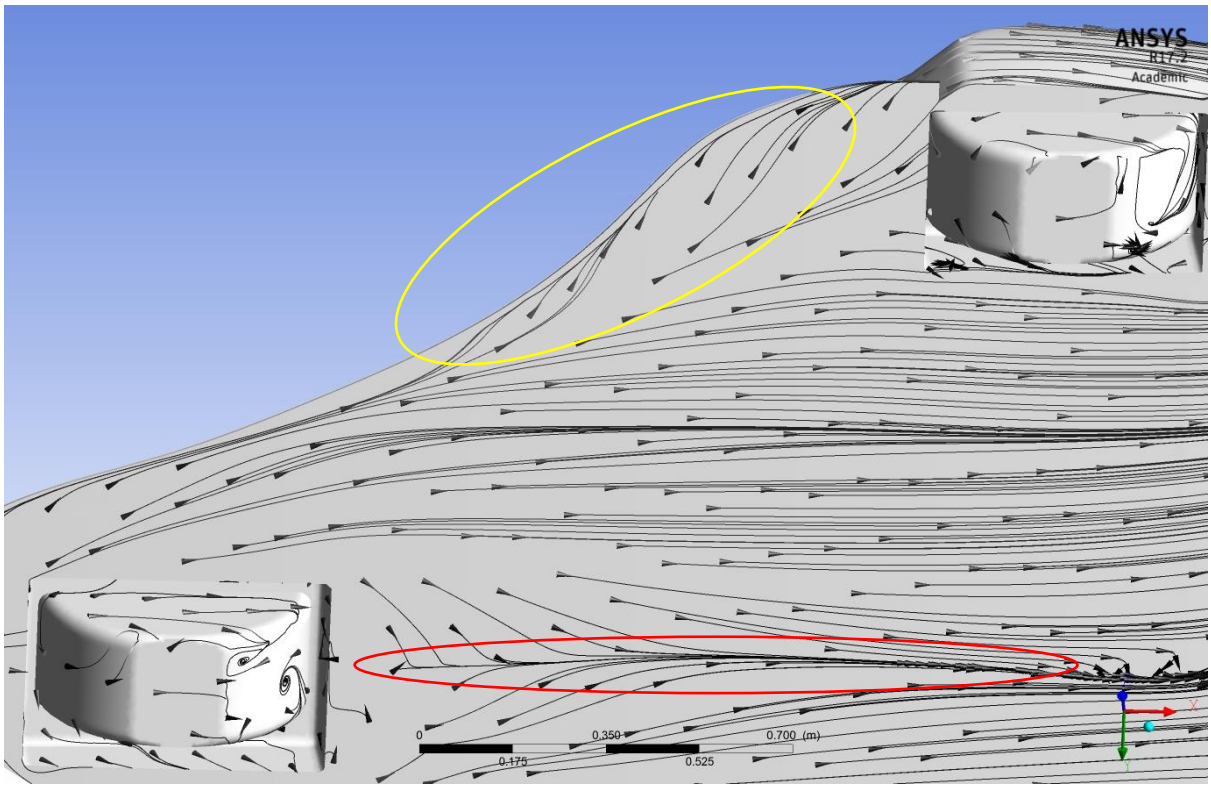

Figure 7.57- Shear stress lines on the underside of the sidecar

In Figure 7.57, the shear stress lines converge to a separator line directly behind the front wheel (in red), indicating a region of separation behind the front wheel. Also evident if Figure 7.57 is a convergence of shear stress lines to a separator line on the underside of the splitter (in yellow). This separation was discussed earlier and is similar to the development of a vortex along the leading edge of a delta wing.

In Figure 7.58, on the top surface of the splitter, this same convergence of shear stress lines to a separator line also indicates separation on the top surface of the splitter, creating a separation where the splitter meets the sidecar body.

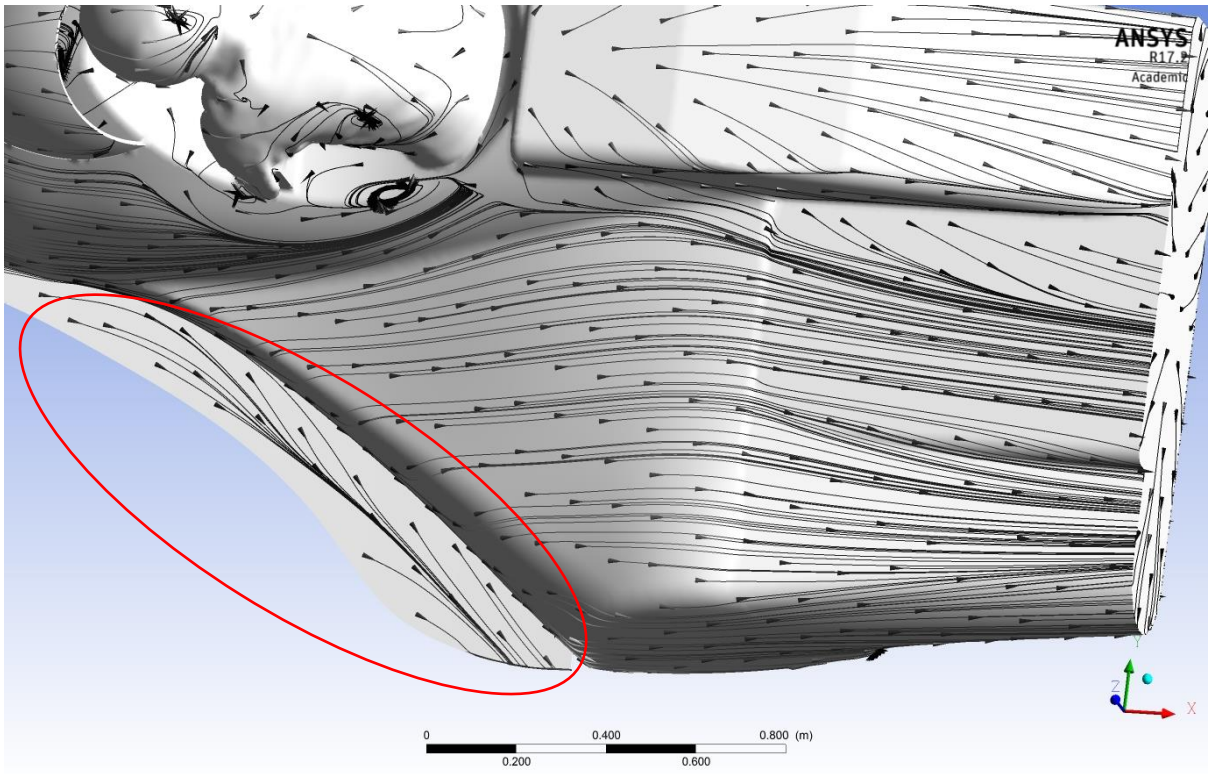

Figure 7.58- Shear stress lines converging on the top surface of the splitter

Note also in Figure 7.58 that the flow over the top surface of sidecar side of the bodywork remains attached until it reaches the trailing edge of the bodywork.

7.7 Summary of Chapter 7

In this chapter, the dynamic and aerodynamic stability of the asymmetrical three-wheel sidecar vehicle was examined. Using the Routh-Hurwitz criteria, the zeroth-order coefficient of the characteristic quadratic polynomial derived from the Equations of Motion was found to be positive (indicating stability) to a velocity of 80 m/s.

The geometric asymmetry of the sidecar produces asymmetric dynamic forces due to rolling resistance and drive forces and an aerodynamic lateral force (even at 0° yaw) that have an effect on the vehicle heading and slew. These forces and moments had not been examined in previous published works. The forces and moments are countered by the addition of a small steering angle input at a level that is often small enough to be unnoticeable by the rider.

Aerodynamic stability of the sidecar was examined primarily by sweeping the vehicle through positive and negative yaw angles up to 90°. A new Symmetry Quotient (Σ) was introduced to characterize the geometric asymmetry, based upon change in frontal area with change in positive and negative yaw angles.

The sidecar was found to have asymmetrical force and moment generation when comparing the negative and positive yaw angles. A negative yaw angle was found to produce greater lift than when the vehicle is yawed in the positive (right) direction. This is explained by the smoother flow over the surface of the sidecar main body compared to over the sidecar itself and the pressure distribution on the top surfaces of the vehicle helped to confirm this. The generation of asymmetric aerodynamic forces on a sidecar vehicle had not been previously examined in the published literature.

The presence of a cross wind will cause the vehicle to slew slightly (negligible) and to rotate (direction depending upon the position of the centre of pressure) enough to require a minor steering correction from the rider.

The addition of the splitter, as described in Chapter 4, was found to slightly decrease drag coefficient and reduce lift, particularly at positive yaw angles when the splitter was most exposed to airflow. The splitter was not observed to change the surface pressure distribution on the underside of the vehicle. Splitters had not been previously studied on an asymmetrical land speed record vehicle.

The yaw moment of the sidecar was found to be adverse, due to the position of the centre of aerodynamic pressure ahead of the centre of mass. Although this is not considered ideal for aerodynamic stability, the vehicle itself did not display instabilities during land speed record attempts. The addition of the splitter was found to improve the adverse yaw moment when the vehicle is in positive yaw.

The roll and pitch moments generated by aerodynamic forces were found to be negligible.

Table 7.5 summarizes some of the findings from Chapter 7.

Table 7.5: Summary of Chapter 7 findings

Considered	Effect on	Size of effect	Result
Vehicle asymmetrical geometry	Dynamic stability	large	Vehicle stable to at least 80 m/s
Steer angle	Dynamic and aerodynamic stability	large	Small steer angles easily counter dynamic and aerodynamic asymmetrical forces
Yaw	Aerodynamic stability	large	Vehicle expected to remain stable even at high yaw angles
Position of Centre of Aerodynamic Pressure	Aerodynamic stability	moderate	Positioned ahead of Centre of Mass resulting in adverse yaw moment- no stability issues noted in testing- difficult to change based upon position of rider

Cross winds	Aerodynamic stability	moderate	A cross wind will cause the vehicle to slew slightly (negligible) and to rotate (direction depending upon the position of the centre of pressure) enough to require a minor steering correction from the rider
Splitter	Lift, drag, yaw moment	moderate	Splitter resulted in: Slight drag reduction Decrease in lift Decrease in Yaw Moment
Roll	Aerodynamic stability	negligible	Too small to have an effect
Pitch	Aerodynamic stability	negligible	Too small to have an effect

The results and observations from Chapter 7 can be further summarized into a set of design guidelines for land speed record sidecar motorcycles:

1. Research appropriate rules (national or FIM) to determine class requirements and dimensional limitations and determine a target speed
2. Lay out position of front, rear and sidecar wheels to determine wheelbase and sidecar wheel offset
3. Decide upon power train components and position them within the wheelbase defined above
4. Estimate load on front, rear and sidecar wheels at contact patch
5. Calculate position of centre of mass (see Appendix E)
6. Using information from tyre manufacturer or from information about similar tyres, estimate cornering stiffness for front, rear and side tyres
7. Using the Routh-Hurwitz method, plot the zeroth-order term from the Equations of Motion versus velocity to ensure dynamic stability to a speed greater than the target speed
8. If stability is not achieved up the target speed consider moving the centre of mass (by rearranging component layout), lengthening the wheelbase, or finding tyres with a higher cornering stiffness (or run the existing tyres at higher pressure)
9. Having achieved dynamic stability, use a CAD program like Solidworks to design an appropriate bodywork to cover the vehicle
10. Using a CFD program (ANSYS Fluent) with appropriate meshing and the proper turbulence model, examine the lift, drag, lateral force and yaw moment coefficients over a range of velocities up to and including the target speed

11. Use CFD as a tool to iterate the design to minimize drag and lateral forces while limiting the amount of aerodynamic lift
12. If possible, 3D print a scale model of the vehicle for use in wind tunnel validation studies
13. Once a useful body shape has been created, use CFD to study the effect of yaw angles, both small angles (5°-15°) and large angles (45°-90°) to examine lateral force, lift forces, and yaw, pitch and roll moments. Consider the addition of a fin or shark fin if the rules will allow it
14. Once a design has been established, examine the Equations of Motion to determine the slip angle (α) and steer angle (δ) that will be required to maintain heading as velocity increases
15. Use the information obtained from these steps to calculate the expected performance of the vehicle to ensure it will set the desired records

Following these design guidelines will not guarantee that the vehicle will be stable at high speed, but should result in a vehicle that produces few unexpected stability issues while meeting the performance goals.

In Chapter 8, the results from this and previous chapters will be further discussed, resulting in conclusions and directions for further work.

CHAPTER 8 CONCLUSIONS

The aim of this thesis was to understand the relationship between design and performance of a land speed record electric sidecar, through physical vehicle testing and CFD studies and to discover the features of streamlined sidecar vehicles which limit aerodynamic performance. It was also an aim to discover ways to reduce lift and drag without radical alterations to the mechanical layout to set a world land speed record at Bonneville for unlimited electric sidecar motorcycles. An additional goal was to develop a method to establish performance and vehicle stability predictions, particularly for asymmetrical vehicles, based upon modelling results.

8.1 SUMMARY OF RESEARCH

This chapter provides a summary of the work, it's conclusions, and relevance to vehicle studies and land speed record vehicles. The original aims and objectives described in Chapter 1 will be re-examined. and the specific research questions raised in Chapter 2 will be addressed. The end of this chapter will also discuss areas for future study and research.

8.1.1 Objective 1: Validation of CFD technique to provide a tool to study the aerodynamics of an asymmetrical sidecar design

In order to provide useful data for design and modelling of a vehicle, the process and procedures used for Computational Fluid Dynamics (CFD) must be validated. In this work, CFD studies of a standard Ahmed body using ANSYS Fluent 17.0 were undertaken. The results were compared to published works to ensure that the aerodynamic forces, surface shear stress lines, wake velocity profiles and topology of structures in the wake were well matched to ERCOFTAC and other published data. Comparisons were made using both a 25° backlight and a 35° backlight on the Ahmed body to better examine and ensure capture of flow separation effects. The comparison between published wind tunnel drag and lift data and flow topology and ANSYS Fluent CFD results provided an assurance that the CFD data provided a valid basis for comparison of bodywork changes, including a new tail section, addition of a splitter, and a windshield during the design portion of the current work (Chapter 4), within the accuracy reported in published work (Chapter 3).

8.1.2 Objective 2: An aerodynamic design study to examine modifications to the sidecar body to develop a lower drag configuration

A series of body modifications, primarily to the rear tail section of the sidecar, were modelled in SolidWorks and drag, lift and lateral force generation was evaluated using CFD. The goal was to

achieve a new rear body section that would reduce aerodynamic drag while not inducing excess lift and also while remaining within the international rules set by the FIM for land speed record sidecar motorcycles. The best results to reduce drag in this study were found for a sidecar with an elongated long tail section, however international rules limit the overall length of a sidecar vehicle and instead a truncated Kamm style tail was investigated and ultimately adopted for the final design. In addition, a front aerodynamic "splitter" was modelled, as well as a design for a windshield ahead of the rider. The final design predicted a reduction of 24.4 % in aerodynamic drag, a change in C_l from +0.0026 (lift) to -0.255 (downforce) and a lateral force coefficient (C_y) that was reduced 11% compared to the original sidecar.

8.1.3 Objective 3: Fabrication of new body panels in composite materials based upon the design study

Using a computer generated STL profile, a male mould of the new rear body section was cut from urethane foam blocks and a new rear body section was constructed from fibreglass and carbon fibre composites. A splitter was constructed by vacuum bagging composite materials and a windshield was sourced from an outside supplier per the design provided to them.

8.1.4 Objective 4: Set the FIM world land speed record for unlimited electric sidecar motorcycles

During the last week of August, 2016, the following FIM world and AMA US National land speed records were set:

FIM: Category I/Group B1/Division B Partially Streamlined/ Electric (over 300kg)
Flying Mile: 108.499 mph (174.612 kph)
Flying Kilometre: 110.389 mph (177.654 kph)

FIM: Category I/Group B1/Division A Non-streamlined/Electric (over 300kg)
Flying Mile: 101.825 mph (163.872 kph)
Flying Kilometre: 104.973 mph (168.939 kph)

AMA US National: Sidecar/electric/over 300kg
Flying Mile: 108.499 mph (174.612 kph)

8.1.5 Objective 5: Establish a physical model to help predict electric sidecar land speed record performance

A model predicting the top speed versus distance performance of an electric land speed record vehicle was developed from Newton's Second Law and included terms for aerodynamic drag, tyre rolling resistance, d'Alembert forces and tractive forces. This constant torque model used power and torque curves produced by Purdue University for the electric motor(s) used in this study, air density appropriate for the test venue, aerodynamic drag, frontal area, tyre diameter, and rolling resistance criteria estimated or calculated for the Baker sidecar to establish a predicted

performance curve fitting speed versus distance travelled. The performance predicted for the electric sidecar at tests in Colorado and Ohio, and record efforts with and without body streamlining at Bonneville, matched well (generally within 1 mph) to the data for speeds at various distances recorded for the sidecar by the event organizers and the GPS tracker data from the vehicle. This physical model is helpful to also predict the effects of design changes and changes in local weather conditions (temp, pressure, humidity) and altitude that change the air density and thus the aerodynamic drag.

8.1.6 Objective 6: Testing of the full-scale modified vehicle on a chassis dynamometer, wind tunnel, and test track venue and compare results to predictions

Although the objective of setting US National and FIM world land speed records was achieved, the top speed of the electric sidecar was less than expected from modelling. To obtain performance data from the full-scale sidecar, it was tested on a chassis dynamometer to determine the level of power transmitted through the driven (rear) tyre, and at the A2 Wind Tunnel facility in Mooresville, North Carolina (U.S.A.) to measure drag, lift and lateral forces.

The dynamometer testing showed the power output was approximately what was expected, given the voltage and current levels and efficiencies of the electric motors and chain drive system. The testing also showed that the electric drive motors were shut down by the Sevcon controllers due to an over-temperature reading on the thermistors inside the motors. The thermistors are located on the stator copper windings and heat up quickly when current is applied. The magnets, located on the rotor, are not in direct contact with this heat source (separated by a 1.5 mm air gap) and a heat-transfer study (described in Appendix 3) suggests that the settings in the controllers could be set much higher (200°C or more) without the magnets reaching their Curie temperature of 160°C.

The full-scale sidecar was tested at the A2 Wind Tunnel facility with the rider on-board and in the configuration as run at Bonneville, and without the rear body section. The actual sidecar has gaps and seams and places where the airflow can interact with the mechanical components under the bodywork. It is possible that the sidecar tested in the wind tunnel was slightly “nose up” relative to the CFD simulation, which would explain higher drag figures. Overall, it is not surprising that the wind tunnel would have a higher drag coefficient (Cd) than the Solidworks CAD model. This was the case—however the wind tunnel data was within 5-8% of the drag calculated through the CFD studies, a result that was considered acceptable and representative.

Smoke studies in the wind tunnel matched well from a subjective view to the flow visualisation from ANSYS Fluent CFD. Both wind tunnels and CFD are valuable predictive tools for design and analyses, but neither alone should be accepted as providing an accurate representation of the flow over an actual vehicle on a racetrack.

8.1.7 Objective 7: Establish methods to examine dynamic and aerodynamic stability of a symmetrical bluff body four-wheel vehicle and a two-wheel single-track aerodynamic streamliner

A generic four-wheel symmetrical model vehicle was used to develop Equations of Motion to describe its dynamic stability, based upon cornering stiffness of the tyres and the position of the vehicle centre of mass. A study, using JBike6 open source software, was also undertaken to establish the dynamic stability of a two-wheel single-track symmetrical land speed record streamliner using a free-body modelling approach.

To establish aerodynamic stability criteria for symmetrical two and four-wheel vehicles, CFD studies were undertaken with the two vehicles swept through varying yaw angles. Yaw was determined to have a significant effect on potentially destabilizing forces, particularly lift over the smooth surface of the streamlined body, and the development of an adverse yaw moment, particularly when the centre of aerodynamic pressure was located ahead of the vehicle centre of mass.

8.1.8 Objective 8: Use dynamic and aerodynamic stability methods to examine three-wheel symmetrical trike and three-wheel asymmetrical sidecar motorcycle vehicles

Using the free-body modelling approach, dynamic stability criteria were established for two three-wheel symmetrical trike vehicles and for an asymmetrical three-wheel sidecar vehicle. The sidecar vehicle was found to have a high degree of dynamic stability, even at high speeds ($>$80 m/s).

The effect of asymmetry on path stability and the need for the rider to introduce steering corrections was also examined. As the sidecar has no longitudinal axis of symmetry, forces from tyre rolling resistance, aerodynamic drag, asymmetrical aerodynamic lateral force, and traction forces all act either directly upon the centre of mass (in the case of lateral forces) or over a distance that creates moments around the vertical axis at the centre of mass. The forces and moments can be summed and set equal to the cornering force initiated by the rider through the introduction of a steering angle. Although in the particular case of the modified Baker sidecar the resulting forces and moments are small and require a steering correction of less than a degree (even at high speed), the analysis is a valid way to determine if other future sidecar vehicles will attain path stability. The small steering angle required to maintain vehicle path and heading does increase the front tyre rolling resistance. The total power consumed for the small ($\sim$0.4°) steering input was calculated to be approximately 250 watts at 120 mph.

Aerodynamic studies of asymmetrical airflow over the sidecar body was undertaken using CFD. A Symmetry Quotient (Σ) was derived to establish the amount of asymmetry a vehicle demonstrates, based upon the differences in the frontal area the vehicle projects as it is yawed in positive and negative directions.

Aerodynamic forces and moments for the asymmetrical sidecar vehicle were found to depend on whether the rotation was through negative or positive yaw angles. The distribution of forces on the surface of the sidecar body and the topology of wake structures help to explain differences in lift between positive and negative yaw angles and the changes in yaw angle were also used to examine the effectiveness of the front splitter to reduce drag and lift. Vortices originating on the rider's shoulders and helmet result in the greatest disruption of the air flow and creates in the most significant streamwise vortex in the wake region. A vortex originating at the rear wheel along with one from the shear along the right side of the sidecar also produce significant streamwise vortices in the wake region (Figure 8.1).

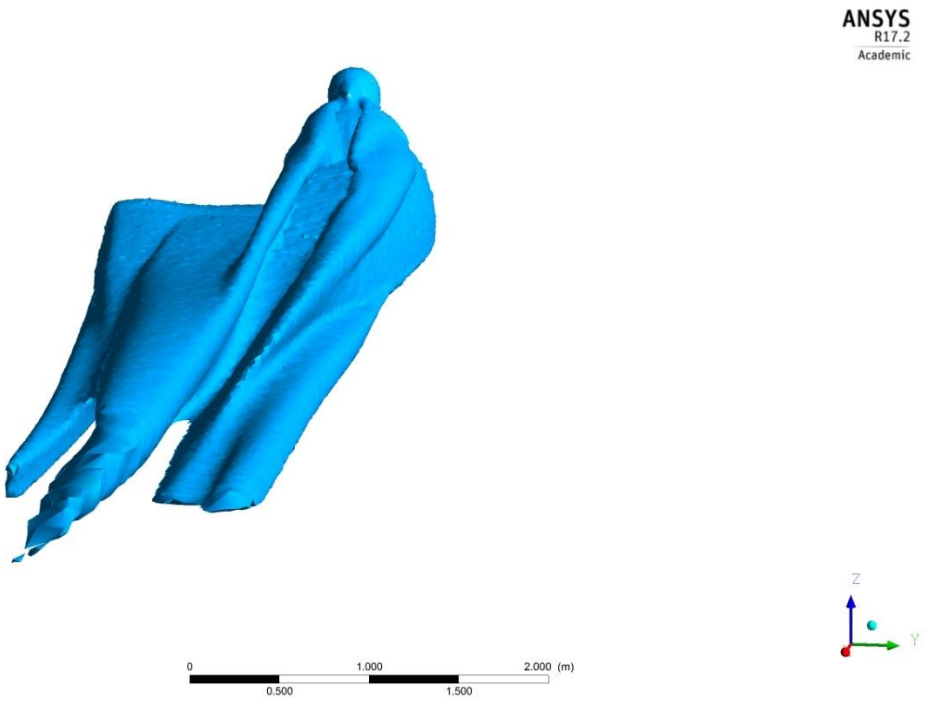

Figure 8.1- Visualisation of streamwise vortices in the sidecar wake region

The splitter produces downforce (negative lift), largely due to a region of high pressure on its top surface. The splitter also demonstrates on its underside some of the same vortex structures that are seen on delta wings as a shear layer across the slanted leading edge rolls up into a primary vortex that runs the length of the splitter. Upon reaching the freestream airflow at the end of the splitter, the primary vortex forms a streamwise vortex that extends into the wake. This primary vortex along the leading edge of the splitter does not occur on the upper surface.

The relatively small roll and pitch moment coefficients generated by the sidecar at high speed were demonstrated to have little or no effect on the predicted stability of the sidecar, and indeed were not noted to be a problem by the rider.

8.2 QUESTIONS ANSWERED IN THE CURRENT WORK

In Chapter 2, a series of questions, based upon the review of the literature and the specific requirements to meet the goal of safely setting a world land speed record, were posed. The answers to the questions follow:

- How can the drag of an asymmetric vehicle (compliant with a specific set of international rules) be reduced without adversely affecting vehicle aerodynamic stability by increasing lateral or lift forces?

The most significant drag reduction (from CFD study) came with the lengthening of the tail of the sidecar. However, the rules limit the vehicle length, so truncating the tail, and tapering it using the techniques developed in the 1930's by Kamm resulted in drag coefficients 5% higher those from the long tail. Rounding the edges on the tail reduced the formation of streamwise vortices. The rider is the largest source of streamwise vortices in the wake region, but the international (FIM) rules prevent the rider from being more effectively shielded from the air flow. The addition of a splitter on the leading edge of the sidecar resulted in an increase of 36% in downforce (negative lift). Lateral forces were shown to be relatively independent of drag and lift forces and were minimized by maintaining a low side profile for the vehicle.

- What CFD methodology reliably predicts force coefficients for a land speed record sidecar motorcycle at Reynolds numbers representative of racing speeds?

The meshing of the sidecar vehicle was undertaken using an unstructured mesh of 5-10 million elements and included a refinement region around the sidecar and in the wake region. 5-11 inflation layers were used to capture the flow characteristics near the sidecar surface. The size of the mesh was validated through a mesh dependency study and meshes chosen were of sufficient size to predict valid C_d values. Several RANS turbulence models were shown to provide adequate modelling results. RANS modelling with Realizable k-ε with a Scalable wall function, k-ω SST, and Transition SST were all used, typically with y+ values between 1 and 80. A coupled scheme was used for pressure and velocity and spatial discretization used a least squares gradient and second order upwind pressure, momentum, turbulence kinetic energy and dissipation rates. The typical speeds tested resulted in a Re between 5 and 15 million.

LES modelling was also examined and, although the topology of the wake region for an Ahmed body was better matched than by RANS modelling, values for C_d and C_l were less well matched to those published from wind tunnel data. Because of the need to understand drag and lift characteristics of the sidecar to improve its performance and ensure rider safety, RANS simulations that provided reasonable accuracy for drag and lift values were primarily used in the current work.

- How does the wake topology affect the drag, lift, and lateral forces of an asymmetrical land speed record sidecar motorcycle and how does it change with changes to the geometric design of the sidecar bodywork?

The geometrical characteristics of the sidecar body determine the pattern of separation and vortices which can extend into the wake region. The distribution of pressure creates shear stresses within the boundary layer that result in flow disruptions, separation and the formation of vortices which can extend into the wake region. From a practical view, it is observed in the current work that reducing the number and strength of the streamwise vortices in the wake region reduces the overall drag levels. In addition, if the wake can be made more symmetric (by adjusting the shape of the rear bodywork for example) the generation of lateral forces is less. Although the presence of the abrupt vertical rear panel at the rear of the Kamm tail produces a significant lateral vortex at the rear of the sidecar, flow over the top of this lateral vortex is not greatly disrupted and appears similar to the flow over bodywork with a longer tail. The strongest single source of drag, as evidenced by the strongest streamwise vortices in the wake region, appears to come from the shoulders and helmet of the rider. A minor improvement was evidenced by the addition of a windshield ahead of the rider. Additional vortical structures originate at the trailing edges of the sides of the sidecar where flow shears against the flow developed by the lateral vortex at the tail of the sidecar. The splitter demonstrates a primary vortex along both its lower surface, analogous to the flow observed on delta wings. This primary vortex is caused by the roll up of a shear layer along the leading edge of the splitter.

- Does the addition of aerodynamic lateral forces developed by an asymmetrical sidecar motorcycle adversely affect the dynamic stability of the vehicle at speeds up to or in excess of 150 mph?

Because of a premature cut-off of the motor drive system, the predicted top speed of 150 mph was not attained. Nevertheless, CFD modelling provides aerodynamic forces which were applied to the force and moment summations from the free-body study in Chapter 7 to determine the effects of aerodynamic lateral forces. In the current study, the aerodynamic lateral forces are small (and relatively independent of Re) and create a small change in both heading and path of the sidecar. The changes produced from the lateral force generation are small enough (requiring a steering input from the rider of less than 1° at the handlebars) to be automatic and unnoticed by the rider.

- Does the asymmetry of aerodynamic forces created by vehicle yaw adversely affect the stability of symmetric highly streamlined vehicles at high speed?

From the examination of a streamliner single-track two-wheel vehicle in Chapter 6, vehicle yaw can result in lift forces that could create instability, particularly at speeds in excess of 150 mph (67 m/s). The lift from flow across the upper surface of the streamliner body can be enough to exceed the mass of the vehicle, allowing it to become airborne at moderate yaw angles $\emptyset > 25°$). Note that this particular streamliner is extremely lightweight (~220kg) and most land speed streamliners weigh more than 1000kg. The addition of a dorsal “shark fin” longitudinally along

the upper surface was found to reduce the lift tendency, even with significant yaw angles (Ø >45°), and at high speeds (up to 250 mph).

8.3 CONCLUSIONS

- Dynamic and path stability are affected by asymmetrical force and moment generation, although in this work the forces and moments were small enough to require only small steering corrections from the rider
- A series of models to predict dynamic and aerodynamic stability have been created to help in the design of future land speed record vehicles
- CFD is a valuable comparative tool to sort between competing designs, particularly if the designs and flow conditions are relatively similar
- A three-wheel sidecar vehicle can be designed and built with low levels of lateral force at zero degrees of yaw, despite significant difference in how the air flows over each side of the vehicle bodywork
- The addition of a splitter at the leading edge of the sidecar slightly reduces drag, reduces lift, and reduces the sensitivity of the sidecar to yaw instabilities. The flow along the length of the splitter is analogous to the flow on a delta wing.
- The wake generated at the rear of the vehicle was much more symmetrical than that of the original design and showed a significant reduction in vorticity
- The streamwise vortices created from the presence of the rider are the most significant vortical structures in the wake region
- CFD can be used to visualize air flow over vehicle surfaces and as a predictive tool, but care must be taken when the CFD model does not accurately represent all of the possible surface features and geometric inconsistencies
- CFD can be used to predict the pressure distribution on the various surfaces of the vehicle to help predict lift (or downforce) characteristics within 8-10%
- The large frontal area of the current Baker sidecar will limit its overall top speed and if the goal is to reach speeds approaching 200 mph, a new design with smaller frontal area would be required

8.4 FUTURE WORK

This study has shown that asymmetrical vehicles, particularly those employed in land speed record efforts, can be designed to have high levels of dynamic and aerodynamic stability. Because of limited prior research on land vehicle asymmetry, and sidecars in particular, there exists a broad range of future work that can be undertaken.

The dynamic stability of a sidecar, established through a free-body approach, used a simplistic “bicycle” model to calculate the zeroth order coefficient stability criteria using the characteristic polynomial. This approach could be replaced by a more sophisticated eigenvalue calculation similar to that which is used to calculate dynamic stability and vibration modes and frequencies

of two-wheel vehicles. The inclusion of a tyre model would make such a dynamic stability model a much more useful tool to those who wish to design dynamically stable sidecar vehicles.

A **Symmetry Quotient** was introduced and could be used in future investigations to help characterize the degree of asymmetry a vehicle exhibits. Study could be undertaken to determine if the Symmetry Quotient can be used to predict the amount of correction an operator must apply to maintain the desired path when faced with yaw or crosswinds.

The aerodynamic flow of the new rear body design reduced the generation of lateral forces when compared to the original body design. The FIM rules limited the overall length of the sidecar vehicles, but the AMA US national land speed record rules do not have a length limitation for sidecars and initial studies in this work indicate a longer tail would further reduce drag and degree of lateral force generation. Further work to design a new longer tail, or one that attaches to and lengthens the existing tail structure may provide higher top speeds.

Although CFD has been shown in this work to provide a valuable tool for design and optimization, wind tunnel studies of asymmetric sidecar vehicles could explore flow topology in greater detail.

Because the rolling resistance characteristics of the Bonneville salt surface had such a significant influence on the mathematical modelling of vehicle performance, actual measurements of the rolling resistance of various tyre designs and configurations might provide a benefit to engineers who wish to design future land speed record vehicles, or better understand and optimize current designs.

The approach used in this work ignored inertial effects and assumed a quasi-steady behaviour, as a steady-state CFD simulation was undertaken at each discrete Ø. Inertial forces, particularly at high yaw angles and yaw rates might be significant and could further compromise vehicle stability. A worthwhile project for future study would be to develop a model that incorporates yaw rate and inertial effects.

Future concepts for land speed record vehicles should take full advantage of the suite of technologies available to designers and racers in order to assure vehicle dynamic and lateral stability are maintained. It is the author's hope that this work will have contributed an approach that others might follow, considering not just top speed, but also dynamic and aerodynamic stability in the design of future land speed record vehicles.

BIBLIOGRAPHY

Abbott, I., & von Doenhoff, A. (1949). *Theory of Wing Sections.* New York: Dover Publications.

Ahmed, S., Ramm, G., & Faltin, G. (1984). Some Salient Features of the Time-Averaged Ground Vehicle Wake. *SAE International*, 34.

AIAA. (1998). *Guide for the Verification and Validation of Computational Fluid Dynamics Simulations .* Reston, VA: American Institute of Aeronautics and Astronautics.

Ashton, N., West, N., Lardeau, S., & Revell, A. (2016). Assessment of RANS and DES methods for realistic automotive models. *Computers and Fluids*, 1-15.

Bacon, B., & Gregory, I. M. (2007). *General Equations of Motion for a Damaged Asymmetric Aircraft.* Reston, VA: AIAA.

Bacon, R. (1982). *BMW Motorcycles: The Postwar Range.* Oxford: Osprey/Niton.

Bayraktar, I., Landman, D., & Baysal, O. (2001). Experimental and Computational Investigation of Ahmed Body for Ground Vehicle Aerodynamics. *SAE International*, 321-331.

Baysal, O., & Bayraktar, I. (2001). Unsteady wake behcind a bluff body in ground effect. *Proceedings of AME FEDSM'01* (pp. 717-725). New Orleans: ASME.

Bordei, S., & Popescu, F. (2011). Aerodynamic Results for a Notchback Car. *Technologies in Machine Building*, 159-178.

Bradley, J. (1996). *The Racing Motorcycle: A Technical Guide for Constructor, Vol. I.* Broadland Leisure Publishers.

Brown, D. (2016). (Clemens, Interviewer)

Brzustowicz, J. P., Lounsberry, T. H., & & Esclafer de La Rode, J. (2002). Experimental & Computational Simulations Utilized During the Aerodynamic Development of the Dodge Intrepid R/T Race Car. *Motorsports Engineering Conference and Exhibition* (p. p.382). Indianapolis, IN: SAE International.

Campbell, G., & Meech, M. (1988). *Bluebirds: The Story of the Campbell Dynasty.* London: Sidgwick & Jackson, Ltd.

Caridi, D., Cokljat, D., Schuetze, J., & Lechner, R. (2012). Embedded Large Eddy Simulation of flow around the Ahmed body. *SAE Intl. J. Commer. Veh*, 208-214.

Carroll, D. (2003). *The Winning Solar Car.* Warrington, PA: SAE International.

Castro, N., Lopez, O., & Munoz, L. (2013). Computational Prediction of a Vehicle Aerodynamics Using Detached Eddy Simulation. *SAE International*, 414-423.

Bibliography

Caughey, D., & Hafez, M. (2005). *Frontiers of Computational Fluid Dynamics.* World Scientific.

Cummings, R., & Schutte, A. (2008). Detached Eddy simulation of the vortical flowfield about the VFE-2 Delta Wing. *46th AIAA Aerospace Sciences Meeting* (pp. 1-24). Reno, Nevada: AIAA.

Dacy, G. (1930, March 1). 400 Miles an Hour? *Scientific American*.

Delassaux, F., Herbert, V., Mortazavi, I., & and Ribes, C. (2016). Comparison of the flow around rounded and sharp edges Ahmed bodies using hybrid RANS/LES turbulence models. *Sixth HRLM Symposium* (pp. 1-2). Strassbourg: HRLM.

Délery, J., Legende, R., & Werlé, H. (2001). Toward the elucidation od three dimensional separation. *Annual Review of Fluid Mechanics 33 (1)*, 129-154.

Fisher, H. (2012, September 10). *Motorcycle Land Speed Record*. Retrieved from Road and Track: http://roadtrackcaranddriver.blogspot.co.nz/2012/09/motorcycle-land-speed-record.html

Fiumara, F. (2008). Analyis of an Overtaking Manoeuvre. *ATZ Autotechnology*, 64-68.

Gallagher, K., Ahmed, S., Nelson, P., & Dees, D. (2015, June 9). PHEV and EV Battery Performance and Cost Assessment. Argonne Naional Laboratory.

Gerasimov, A. (2016, May). *Quick Guide to Setting up LES-type Simulations, Version 1.4.* Retrieved from www.tfd.chalmers.se/...files/Quick_Guide_to_Setting_Up_LES_version_1.4_for_Lars...

Gillespie, T. (1992). *Fundamentals of Vehicle Dynamics.* Warrandale: SAE.

Green, W. (1979). *Warplanes of the Third Reich.* London: Macdonalds and Jane's Publishers.

Hakansson, E. (2015). (Clemens, Interviewer)

Harmand, S., Pelle, J., Poncet, S., & Shevchuk, I. (2013). Review of fluid flow and convective heat transfer within roating disk cavities with impinging jet. *International Journal of Thermal Sciences*, 1-30.

Hornung, H., & Perry, A. (1984). Some aspects of three dimensional separation. Part I. Streansurface bifurcations. *Z. Flugwiss Weltraumforsch*, 77-87.

Hucho, W., & Sovran, G. (1993). Aerodynamics of Road Vehicles. In *Annual Review of Fluid Mechanics Vol 25* (pp. 485-537). Annual Review of Fluid Mechanics.

Huston, J., Graves, B., & Johnston, D. (1982). Dynamics of Recreational Vehicles. *SAE International*, 45-58.

Kasprzak, E., Lewis, K., & Milliken, D. (2006). Inflation Pressure Effects in the Nondimensional Tire Model. *SAE International*, 1-12.

Katz, J. (1995). *Race Car Aerodynamics: Designing for Speed.* Cambridfge, MA: Robert Bentley, Inc.

Keogh, J., Barber, T., Diasinos, S., & Doig, G. (2016). The aerodynamic effects on a cornering Ahmed body. *J. Wind Eng. Ind. Aerodyn. 154*, 34-46.

Lanfrit, M. (2005). *Best practice guidelines for handling Automotive External Aerodynamics with Fluent.* Darmstadt: Fluent Deutschland.

Bibliography

LEAP CFD. (2013, April 12). *Turbulence Part3- Selection of wall functions and Y+ to best capture the Turbulent Boundary Layer*. Retrieved from Computational Fluid Dynamics: https://www.computationlfluiddynamics.com.au/turbulence-part-3-selection-of-wall-functions-and-y-to-best-capture-the-turbulent-boundary-layer/

Lienhart, H., Becker, S., & Stoots, C. (2017, 05 11). *Flow around a simplified car body (Ahmed body)*. Retrieved from ERCOFTAC Classic Database: http://cfd.mace.manchester.ac.uk/cgi-bin/cfddb/prpage.cgi?82&EXP&databas/cases/

Lienhart, H., Stoots, C., & Becker, S. (2003). Flow and turbulent structures in the wake of a simplified car model (Ahmed model). *SAE Technical Paper 2003-1-0656*, 1-8.

Lock, A. (2007). Computational Fluid Dynamics Development of the JCB DIESELMAX Land Speed Record Vehicle. *AeroTech Congress and Exhibition* (pp. 1-7). Los Angeles: SAE International.

Lurie, D. (2012). *The Stability of Three-Wheeled Vehicles& Two Wheel Bicycles.* Worcester, MA: Worcester Polytechnic Instituite.

Malik, M. R., & Bushnell, D. M. (2012). *Role of Computational Fluid Dynamics and Wind Tunnels in Aeronautics R&D.* Hampton, VA: NASA.

Marovic, B. (2016). *JSAE Benchmark of Automotive Aerodynamic Test Measurements.* Mentor Graphics.

McBeath, S. (2015). *Competition Car Aerodynamics.* Dorchester: Veloce.

McMillan, E. (2015, August). THE DESIGN OF THE COMET STREAMLINER: AN ELECTRIC LAND SPEED RECORD MOTORCYCLE. West Lafayette, IN: Purdue University.

Meijaard, J., Papadopoulos, J., Ruina, A., & Schwab, A. (2007). Linearized dynamic equations for the balance and steer of a bicycle:benchmark and review. *Proc. R. Soc.*, 1-63.

Meile, W., Brenn, G., Reppenhagen, A., Lechner, B., & Fuchs, A. (2011). Experiments and numerical simulations on the aerodynamics of the Ahmed body. *CFD Letters (Vol 3-1)*, 32-39.

Metz, L. (2004). Engineering of a Bonneville Land Speed Record Streamliner. *Proceedings of the 2004 SAE Motorsports Engineerng Conference and Exhibition*, 1-11.

Milliken, W., & Milliken, D. (1995). *Race Car Vehicle Dynamics.* Warrendale, PA: SAE International.

Murman, S., Aftosmis, M., & Rogers, S. (2005). Characterization of Space Shuttle Ascent Debris Aerodynamics Using CFD Methods. *43rd AIAA Aerospace Sciences Meeting* (pp. 1-20). Reno: AIAA.

NASA. (2012). *NPARC Alliance CFD Verification and Validation.* NASA.

NASA Langley Research Center. (2017, June 2). *The Langtry-Menter 4-equation Transition SST model*. Retrieved from Turbulence Modelling Resource: https://turbmodels.larc.nasa.gov/langtrymenter_4eqn.html

Noble, R. (1998). *Thrust: The Remarkable Story of One Man's Quest for Speed.* London: Transworld Publishers, Ltd.

Olsen, J., & Papadopoulos, J. (1988, December). Bicycle Dynamics. *Bike Tech*, pp. 13-15.

Reisenthel, P., & Childs, R. (2007). Surrogate-based Design Optimization of a Large Asymmetric Launch Vehicle Payload Fairing. *45th AIAA Aerospeace Sciences Meeting* (pp. 1-11). Reno: AIAA.

Rose, S., & Abrams, A. (2016, December 10). *Land Speed Record Vehicles, Part One: The Pioneers*. Retrieved from Dark Roasted Blend: darkroastedblend.com

Rutan, B. (2005). *Moldless Composite Sandwich Aircraft Construction.* Tabermas, CO: Aircraft Technical Book Company.

Salim, S. M., & Cheah, S. (2009). Wall y+ Strategy for Dealing with Wall-bounded Turbulent Flows. *International Multiconference of Engineers and Computer Scientists* (pp. 1-6). Hong Kong: IMECS.

Schwab, Papadopoulos, Ruina, & Dressel. (2015, February 08). JBike6. *JBike6*. Ithica , NY, USA: Cornell University.

Serre, E., Minguez, ,. M., Pasquetti, R., Guilmineau, E., Deng, G., & Kornhaas, M. (2013). On simulating the turbulent flowaround the Ahmed body: A French and German collaborative evaluation of LES and DES. *Computers & Fluids*, 78-123.

SHARCNET: Vortex Core Region. (2017, May 30). Retrieved from SHARCNET: http://www.sharcnet.ca/Software/Ansys/16.2.3/en-us/help/cfd_post/vort-core_details_v.html

Sharp, R. (1971). The Stability and Control of Motorcycles. *Journal of Mechanical Engineering Science*, 316-329.

Starr, P. (2006). *Designing Stable Three Wheeled Vehicles, With Application to Solar Racing cars.* Minneapolis, MN: University of Minnesota.

Sullivan, J. (2016). Private communication.

Sullivan, J. (2017). (Clemens, Interviewer)

Swanson, K., & Spinks, A. (2007). *Flying Kiwis: a quest for speed.* Dunedin, NZ: Flying Kiwi Productions.

Tamai, G. (1999). *The Leading Edge: Aerodynamic Design of Ultra-streamlined Land Vehicles.* Cambridge, MA: Robert Bentley, Inc.

Thawley, J. (1980). *How to go Racing at Bonneville.* Los Angeles: Steve Smith Autosports.

Tobak, M., & Peake, D. (1982). Topology of three dimesional separated flows. *Ann Rev Fluif Mech*, 61-85.

Tseng, Z. S. (2016, January 20). *The Characteristic Polynomial*. Retrieved from Math PSU: www.math.psu.edu/tseng/class/Math251/Notes-2nd%20order%20ode%pt1.pdf

Versteeg, H., & Malalasekera, W. (1995). *An introduction to computational fluid dynamics The finite volume method.* London: Longman Group, Ltd.

Vino, G., Watkins, S., Mousley, P., Watmuff, J., & Prasad, S. (2005). Flow structures in the near-wake of the Ahmed model. *Journal of Fluids and Structures*, 673-695.

Bibliography

Wang, X., Zhou, Y., Pin, Y., & Chan, T. (2013). Turbulent near wake of an Ahmed vehicle model. *Exp. Fluids 54:1490*, 1-19.

White, G. (2006). *Ab & Marvin Jenkins.* Hudson, WI: Iconografix.

William, Y., Mohamed, M., & Oraby, W. (2013). Investigation of Crosswind Aerodynamics for Road Vehicles Using CFD Technique. *Eleventh International Conference of Fluid Dynamics* (pp. 1-11). Alexandria, Egypt: ICFD11.

Yankolonis, A., & Simeone, F. (2015). Function or Form? A Design Comparison of the Ferrari GTO and the Shelby Daytona Coupe. *Automotive History Review*, 4-13.

Yurko, J. (1978). *The Effcet of Wheel Alignment on Rolling Resistance- A Literature Search and Review.* Ann Arbor, MI: U.S. Environmental Protection Agency (EPA).

APPENDIX A COMPUTATIONAL FLUID DYNAMICS ANSYS FLUENT SETUP

Overview

Over the course of this research, the settings for geometric, meshing and the CFD choices changed and evolved. The settings indicated below are for the simulations run at the end of the project and represent what was considered optimal for simulations of this vehicle. All simulations reported in this work were run on ANSYS Fluent 17.0 and geometric modelling, meshing and setup were all run through ANSYS Workbench 17.0.

Geometry

Computational Domain Enclosure: +x = 25 m, +y = 4 m, +z = 4 m, -x = 4 m, - y = 4 m, -z = 0.005 m

Body box: x = -.25 m, y = -.1.2 m, z = -0.3 m, Diagonal x = 4 m, Diagonal y = 2 m, Diagonal z = 2 m

Wake box: x= 1.5 m, Wake box 2= 5.5 m

Mesh

Size function: Proximity and Curvature

Smoothing: medium

Transition: slow

Curvature normal: 13°

Number of cells across gap: 3

Minimum size: 0.150 m

Maximum face size: 0.2 m

Maximum tetrahedral size: 0.2 m

Inflation: On chosen named selection: sidecar

First layer thickness

First layer height: 0.001 m

Max layers: 5

Growth rate: 1.2

Face Sizing: 0.01 m

Body box (body of influence): 0.05 m

Wake Box 1 (body of influence): 0.05 m

Wake box 2 (body of influence): 0.1 m

Number of elements: 8.6 million

Solver

10 parallel cores, 64 GB ram memory

Pressure based

Velocity formulation: absolute

Time: steady

Viscous Model: k-ω SST

Boundary conditions

Road: Moving wall, 67 m/s,

Pressure Outlet: Absolute Gauge: 0 pascal

Sidecar: Stationary wall, no slip

Velocity Inlet: Absolute frame of reference: 67 m/s, 5% turbulence,

Total viscosity ratio=10

Reference Values

Area-= 1 m^2

Density= 1.225 (kg/m^3)

Length= 3.3 m

Temperature = 285.16 K

Velocity= 67 m/s

Viscosity= 1.789 E-05 (kg/m-s)

Solution:

Scheme: Coupled

Gradient: Least Squares cell based

Momentum: Second order upwind

Turbulence kinetic energy: Second order upwind

Specific dissipation rate: Second order upwind

Intermittency: Second order upwind

Momentum thickness Re: Second order upwind

Flow Courant Number: 100

Explicit relation factors:

Momentum= 0.25

Pressure= 0.25

Under relation factors

Density= 1

Body force= 1

Turbulence kinetic energy= 0.8

Specific dissipation rate= 0.8

Intermittency= 0.8

Momentum Thickness RE= 0.8

Turbulence viscosity= 1

Run Conditions:

Standard Initialization using Velocity Inlet

Typical: 200-400 iterations

Convergence criteria: The solution was judged to have converged when the aerodynamic drag coefficient (C_d) began to vary only in the third decimal place. In cases where aerodynamic lift (C_l) was examined, convergence was judged by variation in the third decimal place of that coefficient.

APPENDIX B MOTOR HEATING STUDIES

Overview

During competition at Bonneville in 2014, the Motenergy ME1301 motor used in the single-motor drive system repeatedly shut down in the middle of the timed mile during record runs. Although data was not available, experience by the Purdue University land speed record team (who used the same motor on their solo motorcycle) led to the assumption that the motor was overheating (Sullivan J. , 2016).

The redesign of the drive system for the Baker sidecar included development of a twin-motor drive system (twice the thermal mass) and the replacement of the water/air radiator with a recirculating ice-bath and water system to pre-chill the motors. Despite the changes, in 2016 at Bonneville the same motor shut down was experienced, again during the middle of the measured mile of the five-mile course. It was noted that this motor shut-down had not been experienced in prior testing on one mile airport runway courses in Colorado and Ohio. Despite the motor shut down at Bonneville in 2016, four FIM world records and one AMA national record were set, but the sidecar did not achieve its expected top speed.

Upon returning from Bonneville in 2016, the sidecar was tested on a rolling-road chassis dynamometer, as described in Chapter 5. The results of this testing indicated that the Sevcon controllers were sensing a temperature higher than 160°C and shutting off the motors to protect the rare-earth magnets. If the magnets go above approximately 165°C (their Curie temperature) they will demagnetize.

After several discussions with the designer at Motenergy, and an examination of the drawings provided by Motenergy, a question arose about how close to 160°C the magnets (located in the spinning rotor) were getting. The temperature measurement thermistor in the motor was found to be located on the surface of the stator coils, a point which would experience rapid heating, particularly when 500+ amps are applied to the motors.

The key question is: at what temperature measured by the thermistors in the motors could the cutoff be set in the controllers so that the rare earth magnets would remain below 160°C over the time period of a five-mile land speed record attempt at Bonneville?

Motor configuration

A SolidWorks drawing of the ME113 motor was obtained from Motenergy as indicated in Figure B.1.

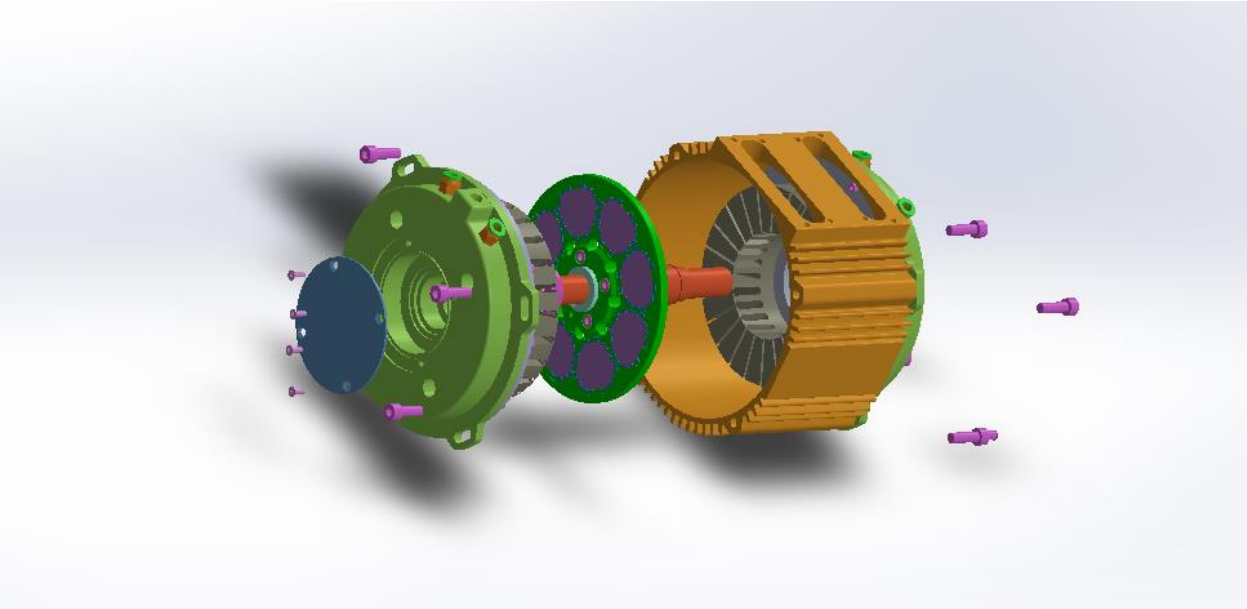

Figure B.1- Motenergy ME113 motor- exploded view

In Figure B.1, the rotor with the magnets (in green and purple in Figure B.1) is located between the two armature coils. A water cooling chamber is located at each end of the motor, acting to cool the coils from their outer ends. The thermistor is located on the surface of the armature coil (in grey inside the orange housing). Table B.1 summarizes the physical dimensions and properties of the motor.

Table B.1: Physical dimensions and properties of the motor

Part, component, material	**Dimension, property**
Rotor diameter	0.17 m
Rotor thickness	0.006 m
Rotor % aluminum	40% by area
Rotor % rare earth magnets (Nd based)	60% by area
Air gap between rotor and stator	0.0015 m
Stator coil diameter	0.15 m
Stator coil inside diameter	0.08 m
Coil % steel	50% by volume
Coil % copper	50% by volume
Coil thickness	0.0385 m
Water passage diameter	0.15 m
Water passage inside diameter	0.08 m
Water passage thickness	0.01 m
Water passage material	100% aluminum

Geometry

A simplified geometry for one-dimensional heat transfer was created and is indicated in Figure B.2.

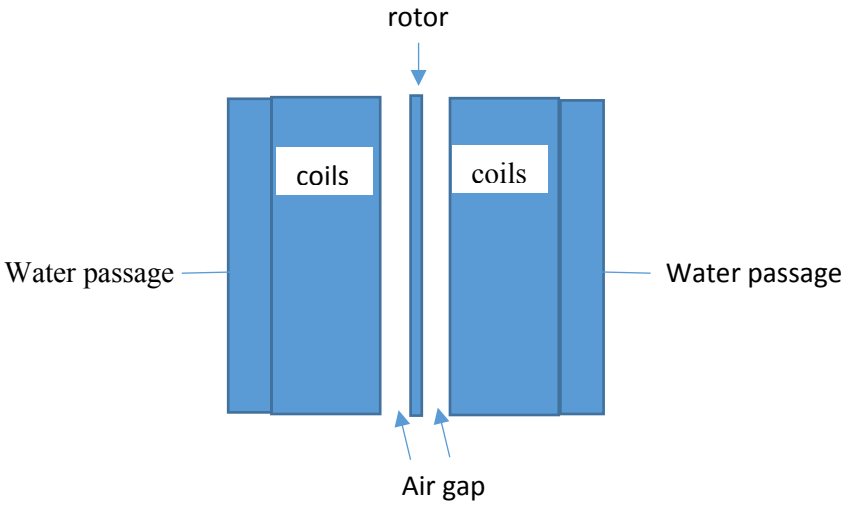

Figure B.2- Simplified geometry for one-dimensional heat transfer

Coil heating rate

Information on the initial heating of the coils, upon the application of current from the controllers is available from two sources. At Bonneville, during record runs, the temperature measured by the thermistor went from approximately 5°C (motor cooled by ice bath) to the cutoff temperature of 160°C in 62 seconds, indicating a rise of 2.5 °C/ second (assuming a linear increase). In dynamometer testing, the temperature went from approximately 10°C (ice bath) to 160 °C in 45 seconds (3.3 °C/sec) and 10°C to 165°C in 48 seconds (3.23°C/sec). For this study, the worst-case heating rate of the coils of 3.3°C/sec will be used and will be assumed to be linear.

Reynolds Number

The Reynolds Number for flow over a spinning disk can be used to characterize the flow as either laminar or turbulent. From Harmand, S., Pellé,J., Poncet, S., and Sheuchuk, I.V., (Harmand, Pelle, Poncet, & Shevchuk, 2013), the rotational Reynolds Number for a rotating disc and stationary stator is calculated from:

$$RE_{\Omega} = {\Omega R^2}/{\nu}$$

Where, Ω = rotational speed in rad/sec (209 at 4,000 rpm)

R = radius of the rotor (m)

ν = kinematic viscosity of air (m^2/s)

In the case where flow occurs in a cavity between a rotor and stator (Figure E.2), the aspect ratio of the cavity changes the Reynolds Number. The aspect ratio is defined (p.41) as:

$G = e/R$

With e = air gap distance (m)

R = Radius of the rotor (m)

So that the Reynolds Number based on flow within the gap is:

$Re_e = G^2 RE_\Omega$

Using the dimensional values for the motor and a rotational speed of 4,000 rpm (209 rad/sec) with a kinematic viscosity of air at 100°C equal to 2.3 E-05, the Reynolds Number based upon flow Re_e = 20.3. According to the table provided on p.42 of Harmand et al., (Harmand, Pelle, Poncet, & Shevchuk, 2013), this value of Reynold's Number indicates that flow within the gap is laminar. There is only a small (≈1.0 mm) gap between the outer edge of the rotor and the housing and it is assumed that this airspace can be neglected in this study.

Convective heat transfer coefficient (h_c)

The convective transfer of heat energy across a fluid depends upon the difference in temp from one side of the fluid to the other (dT), the surface area (A) involved in the transfer and the connective heat transfer coefficient (h_c) in (W/ (m^2 K).

The heat transferred per unit time (q) in Watts (W) is given by:

$q = h_c A dT$

The convective heat transfer coefficient depends upon the characteristics of the fluid and the character of the flow and, for air, can vary between 10-1000 W/m^2K. To find an approximate value for h_c the Nusselt Number (N_u) can be used from the relationship:

$$N_{uL} = \frac{h_c L}{k}$$

With L the characteristic length, assumed in this case to be the radius of the rotor and k the thermal conductivity of air. For laminar flow, the Nusselt number is typically close to one, while turbulent flow has Nusselt Numbers in the 100-1000 range.

Assuming a Nusselt number of 75 for this study (indicating predominately laminar flow), and k=0.024 W/(mK) for air, with an L= 0.085 m, the value of h_c can be calculated from:

$$h_c = \frac{Nu_L k}{L}$$

which gives an h_c = 21.2 W/m^2/°K

One dimensional heat transfer

In this model of motor heating and cooling, the following steps occur:

1. The motor is pre-chilled to 5°C
2. The coils are heated at 3.3 °C/sec for 100 seconds
3. The coils transfer heat to the rotor during the heating phase
4. The rotor continues to heat after the coil heating phase as the coils continue to transfer heat to the rotor

The heating time of 100 seconds is the time calculated from the Sullivan model described in Chapter 5 to cover three miles from a standing start (2 miles run up and one mile timed for record.

- Other assumptions:
- There was no loss to the motor casing
- After the current was cut off, the windings only lost heat to the rotor and not to the cooling water (worst case)
- No conduction through shaft

The convective transfer of heat from the coils to the rotor through the air gap is given by:

$$\text{Rotor Temperature (convective)} = \frac{h_c A}{(rotor\ specific\ heat\ capacity)(\frac{rotor\ mass}{2})}(winding\ temperature - rotor\ temperature)$$

There is also an amount of radiation heating of the rotor, which is given by:

$$\text{Rotor Temperature (radiation)} = \frac{(Bolzman\ Constant)(A)}{(rotor\ specific\ heat\ capacity)(\frac{rotor\ mass}{2})}(winding\ temperature - rotor\ temperature)$$

The rotor temperature is the sum of the convection and radiation heating.

Although the coils transfer some of their heat to the water passages, they only do so at the ends of the coils opposite the rotor. In the worst case, the temperature of the coil surface near the rotor does not change greatly during the time frame investigated. For this reason, the cooling of the coils by the water passages was ignored.

Results

A MATLAB code was written with the help of Dr. Mark Jermy to calculate the winding and rotor temperature over the course of 200 seconds. A first order explicit Euler solver was used and the time step was reduced until results converged.

This result is provides in Figure B.3.

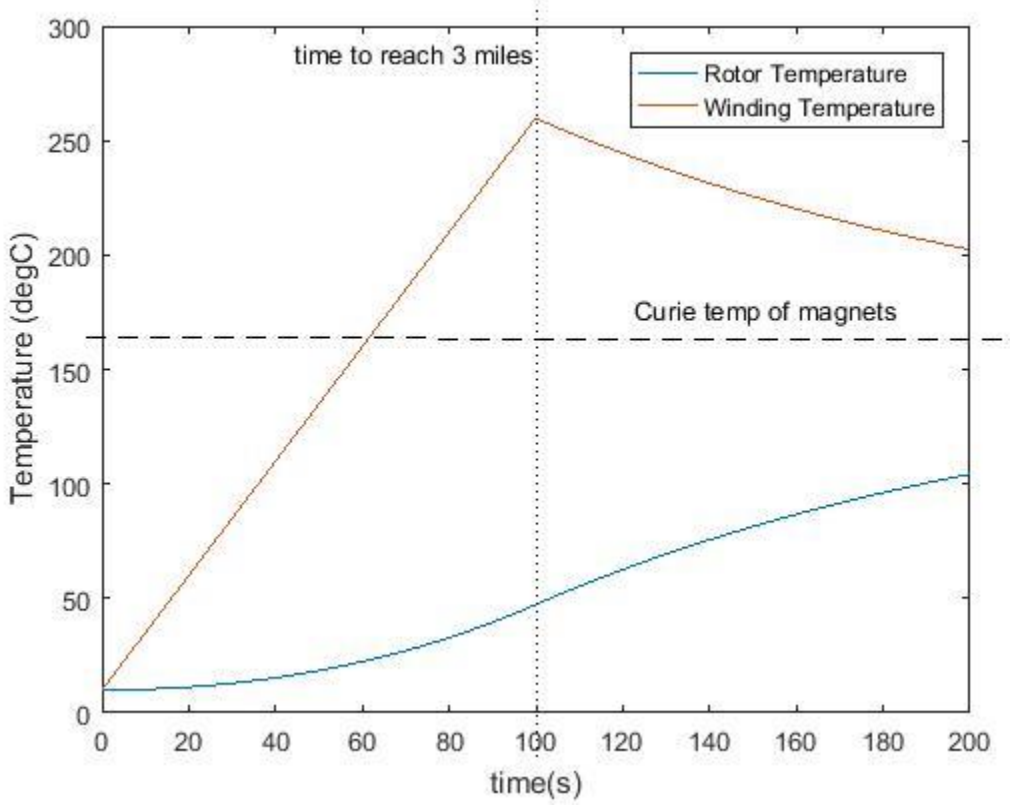

Figure B.3- Winding and rotor temperature plot

Recall the 100 seconds is the time required to accelerate from a standing start and cover three miles (two miles run up and one mile timed for the record). From Figure B.3 it is evident that setting the Sevcon controllers to a temperature cutoff of 250°C will provide an acceptable safety margin for the rare-earth magnets on the rotor. It is important to remember that this temperature setting would only be safe for a short run over the time frame required for a three-mile full-power record at Bonneville.

In Figure B.4, the temperature of the rotor and windings is plotted out to the point at which they converge. Note that this point is approximately 100°C, still well below the 160°C Curie temperature of the magnets in the rotor.

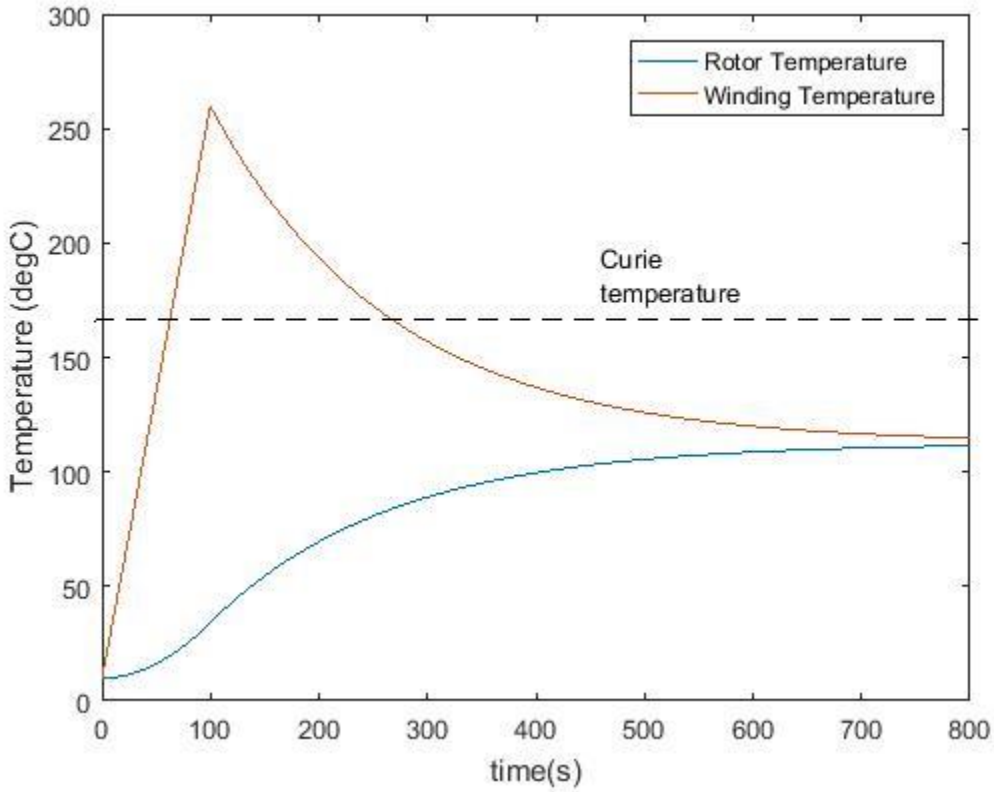

Figure B.4- Temperature at which the windings and rotor temperatures converge

Although the water cooling of the ends of the coils was ignored, and this cooling should help reduce the temperature of the entire motor quickly, care should be taken not to stop the motor suddenly if the coils have been heated to 250°C. If the rotor is stopped too quickly the temperature of the rotor would have a potential to rise above the Curie temperature.

MATLAB Code

```
% Rotor Heat Transfer
%Approach: calculate heat flux across air gap from windings to rotor and
%increment rotor temperature
%Assumptions:
%Convective heat transfer through the air gap on both sides of the rotor
% Radiation heat transfer from windings to rotor
%No conductive heat transfer
%Heat transfer from windings
%No heat transfer to casing or water passage
%First order time integration
%Windings at temp linear rise

%Housekeeping
clear all;
close all;
```

```
% properties of components
rotorDiameter=0.17; % meters
rotorThickness=0.006; % meters
rotorDensity=5520; % kg/m3 40% aluminium (2700 kg/m3) 60% rare earth
%magnets (Nd based 7400kg/m3)
rotorSpecificHeatCapacity=615; % J/(kg.K) 40% aluminium (900 J/(kg.K) 60%
%rare earth magnets (350-500 J/(kg.K)
rotorToWindingGap=0.0015; % meters 1.5 +/- 0.5 mm, worst case selected
rotorInitialTemp=283; % deg K
rotorArea=3.141*0.25*rotorDiameter^2;
rotorMass=rotorArea*rotorThickness*rotorDensity;
windingDiameter=0.15; % meters
windingInsideDiameter=0.08; % meters
windingThickness=0.0385; % meters
windingDensity=8315; % kg/m3 50% steel (7830 kg/m3) 50% Copper (8800 kg/m3)
windingSpecificHeat=440; % J/(kg.K) 50% Steel (490 J/kg.K)
%50% Copper (390 j/kg.k)
windingArea=3.141*0.25*(windingDiameter^2)-...
    (3.141*0.25*(windingInsideDiameter^2));
windingMass=windingArea*windingThickness*windingDensity;
windingK=385; %thermal conductivity of copper
aluminumDensity=2800; % kg/m3 for water passage
aluminumK=205;% thermal conductivity of Aluminum (J/sec/m.K)
waterpassageDiameter=0.15; %meters
waterpassageInsideDiameter=0.08; %meters
waterpassageThickness=0.01;  %meters
waterpassageDensity=2700;  % kg/m3 Aluminum
waterpassageSpecificHeat=900; %J/(kg.K) Aluminum
waterpassageArea=3.141*0.25*(waterpassageDiameter^2)-...
    (3.141*0.25*(waterpassageInsideDiameter^2));
waterpassageMass=waterpassageArea*waterpassageThickness*...
    waterpassageDensity;
waterpassageTemperature=283; %degrees K
Bolz=5.67E-08; %Bolzman Constant for Thermal Radiation in W/m^2K^4
%Coil diameter 15 cm
%Coil inside diameter 8 cm
%Coil depth 3.85 cm
%Coil steel 50%
%Coil copper 50%

RPM=4000; % rpm
airViscosity=0.000023; % Air kinematic viscosity at 100 deg C
tangentialSpeedEdge=RPM*3.141*rotorDiameter/60; %tangential speed of
%edge of rotor
ReEdge1=tangentialSpeedEdge*rotorToWindingGap/airViscosity; %Reynolds
%number at edge speed
ReEdge2=(rotorDiameter/2)*sqrt((RPM*3.141/(30*airViscosity)));
%Different definition Re

windingInitialTemp=283; % deg K
windingTempRiseRate=2.5; % degrees K per second
heatingTime=100.0; %Current is applied for this time then windings cool
%at same rate as heated
%At Bonneville, the temperature went from approximately 5 degrees C to 160
%degrees C in 62 seconds.
%On the dynamometer, 10 deg C to 160 deg C in 45 s or 10 to 165 in 48 s:
```

```
%worst case 3.3 deg/s

k=0.024; %thermal conductivity of air W/(m.K)

%solver settings
deltat=0.1; % timestep duration [seconds]
nsteps=2000; % number of timesteps
windingHeating=2; % =1 if constant windingTemp, =2 if linear rise in
%windingTemp

%rate of change of temperature of rotor=flux of heat from winding * area of
%rotor face / heat capacity of rotor

time=zeros(nsteps,1);
rotorTemp=zeros(nsteps,1);
rotorTemp(1)=rotorInitialTemp;
if windingHeating==1
    windingTemp=windingInitialTemp*ones(nsteps,1);
end
windingTemp(1)=windingInitialTemp;

h=21.2; %chosen based upon Nusselt number of 75 for laminar flow

for i=2:nsteps
    time(i)=(i-1)*deltat;
    if windingHeating==2
        if time(i)<heatingTime
            windingTemp(i)=windingInitialTemp+windingTempRiseRate*time(i);
        else

            WindingFactor(i)=(deltat*((h*windingArea)/...
                (windingSpecificHeat*windingMass))*(windingTemp(i-1)-...
                (rotorTemp(i-1)))/windingThickness);

            windingTemp(i)=windingTemp(i-1)-WindingFactor(i);
            windingTempC=windingTemp-273;  % Convert to degree C

    end
    end
    rotorTempConv(i)=deltat*(h*rotorArea/(rotorSpecificHeatCapacity*...
        (rotorMass/2)))*((windingTemp(i-1)-rotorTemp(i-1)));
    rotorTempRad(i)=deltat*(rotorArea*Bolz/((rotorMass/2)*...
        rotorSpecificHeatCapacity))*(((windingTemp(i-1))^4)-...
        (rotorTemp(i-1))^4);
    rotorTemp(i)=rotorTemp(i-1)+rotorTempConv(i-1)+rotorTempRad(i-1);
    rotorTempC=rotorTemp-273; % Convert to degrees C

end

figure(2);
plot(time,rotorTempC,time,windingTempC);
xlabel('time(s)');
ylabel('Temperature (degC)');
legend('Rotor Temperature','Winding Temperature');
```

```
%EOF
```

APPENDIX C FABRICATION OF THE NEW BODY SECTION

Overview

The design of the new, more aerodynamic rear body section for the sidecar provides for a shell-like covering that fits onto the rear of the existing bodywork. After considering several different alternative methods of fabrication for this body section, it was decided to employ a "mouldless" technique that was described by Rutan (Rutan, 2005) as a relatively simple and cost-effective way to build one-off composite structures.

Rutan's mouldless technique uses a foam plug whose surface is cut to the desired shape. This foam plug is then layered with reinforcing cloth (typically fiberglass). Layers are built up to produce a rigid structure. After curing, the foam can be selectively or completely removed, leaving behind the rigid composite shell. The technique does not produce an extremely smooth surface and the application of conventional automotive bodywork techniques with fillers and sanding is necessary prior to painting to get a smooth finish.

The first step, using the SolidWorks drawing of the modified sidecar, was to create a drawing of just the rear section part that needed to be fabricated (Figure C.1). As the mouldless technique results in the outer surface of the foam plug as the inner surface of the final part, care must be taken to determine how the thickness of the composite layers will affect the final external dimensions of the part. For this project, the combined thickness of the composite layers was estimated to be 5 mm, and the desire was for the part to be slightly larger than the designed part.

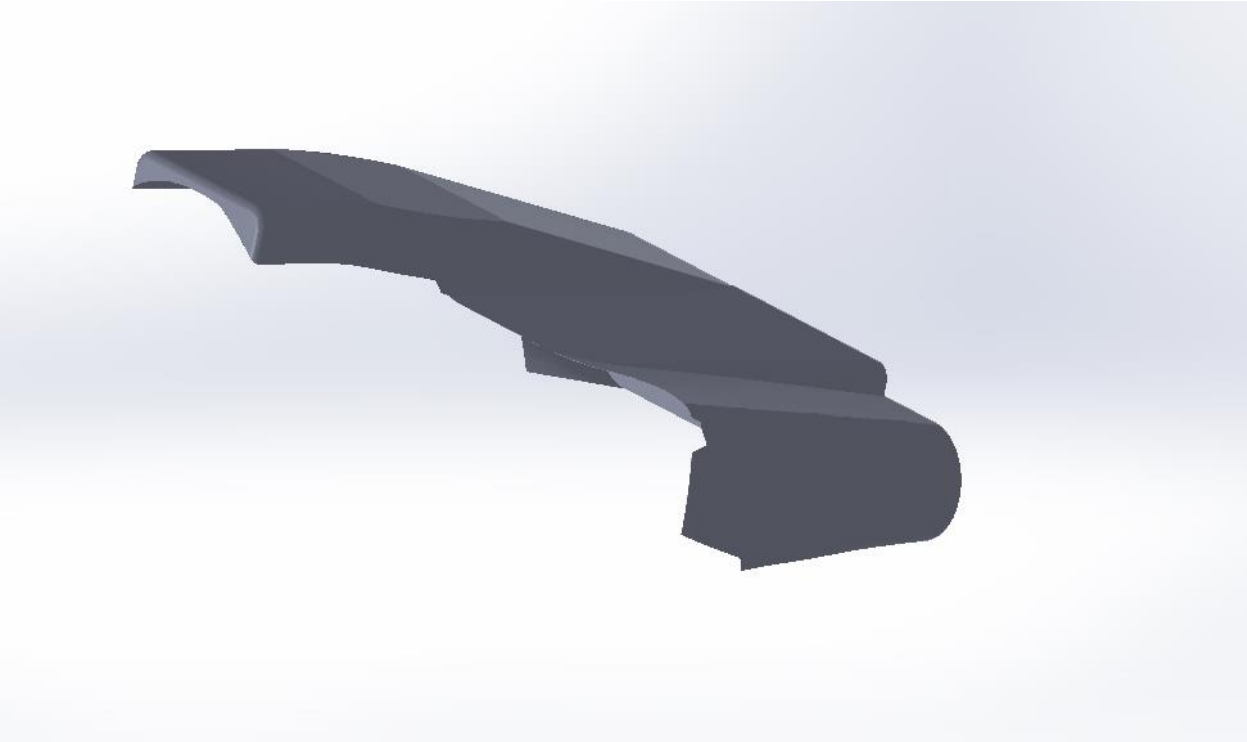

Figure C.1- Rear body section in SolidWorks

The Solidworks drawing of the new rear bodywork section was provided to a commercial vendor who used a ShopBot® CNC router to machine 2-inch-thick layers of polystyrene construction foam in a profile that copied the Solidworks part. The layers were glued and pinned together to produce a foam plug whose surface, after light filling and sanding, accurately duplicated the desired shape (Figures C.2-4).

Figure C.2- Foam stack used to form plug (*author*)

Figure C.3- ShopBot® CNC Router was used to shape the foam (*author*)

Figure C.4- Layers of shaped foam are stacked together and glued (*author*)

Preparation of the foam plug included painting the surface with latex paint to help seal any porosity and small gaps. Following this, several coats of polyvinyl alcohol were applied to assist in mould release (Figures C.5).

Figure C.5- Foam plug is painted with white latex paint and then coated with polyvinyl alcohol mould release (*author*)

The first layer of composite was 2 oz. fiberglass veil cloth with West System® epoxy. West System two-part epoxy resin was used for each layer. The veil coat was followed by a layer of 6 oz. fiberglass fabric. Next, the body was covered by a layer of 3K twill weave carbon fibre fabric, except for the section where the "swinger" would sit, which was covered with thicker 12K twill weave carbon fibre fabric to produce a platform with greater stiffness in this area. Finally, the body was covered with another layer of 6 oz. fiberglass and a layer of 2 oz. fiberglass veil coat (Figure C.6-8).

Figure C.6- First veil coat covering the plug (*author*)

Figure C.7- Carbon fibre layers added (*author*)

Figure C.8- Carbon fibre adds stiffness with very little weight and thickness (*author*)

The foam plug was removed from the composite part, except in areas that required some additional support and in the portion on top of the battery box to provide support for the required weight carrying capability on the swinger platform (Figure C.9).

Figure C.9- Removing foam of the plug from the composite part (*author*)

After trimming the new body part to fit onto the existing body (Figure C.10-11), and mounting several quarter-turn fasteners to hold the body-part in place, the body section was taken to an automotive body shop to smooth out ripples and paint the part (Figure C.12).

Figure C.10- Fitting the rough new part to the existing body (*author*)

Figure C.11- Rear body section has the proper profile but needs finishing bodywork (*author*)

Figure C.12- After bodywork and paint the new part accurately represents the desired body shape (*author*)

Front Splitter

A front aerodynamic splitter was made from carbon fibre and Kevlar® fabrics, sandwiching a piece of 1/8" (3.2 mm) plywood. The combination of Kevlar®, carbon fibre and a veil coat of 2 oz. fiberglass cloth was coated with West System® two-part epoxy and then vacuum-bagged overnight (Figure C.13). After curing, the splitter part was removed (Figure C.14), trimmed, painted and mounted on the front edge of the sidecar.

Figure C.13- Vacuum-bagging the splitter (*author*)

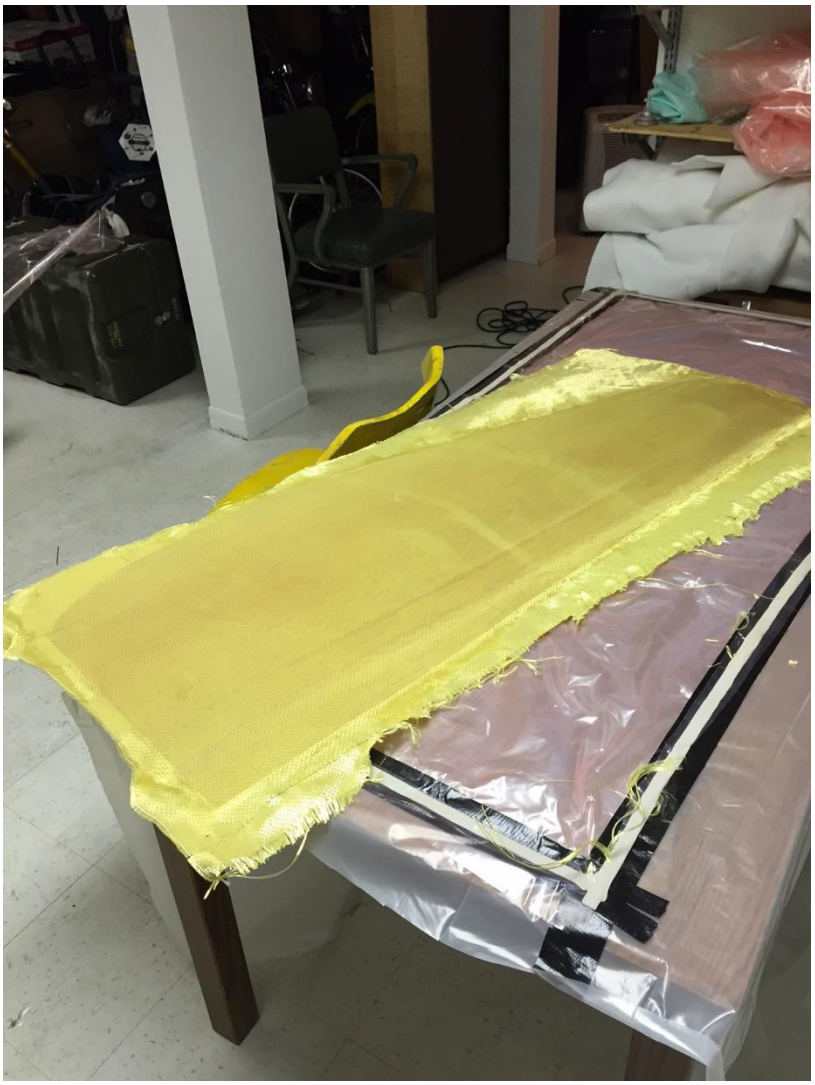

Figure C.14- Splitter removed from bagging and ready to be trimmed (*author*)

Windshield

The windshield was fabricated by a specialist manufacturer after a cardboard template, based upon the SolidWorks design was provided to them.

APPENDIX D MATLAB CODE FOR SIDECAR DYNAMIC STABILITY

Overview

From Chapter 7, the sidecar Equations of Motion for lateral force and moments applied to the centre of mass can be used to create a characteristic quadratic polynomial. Using the Routh-Hurwitz criteria, dynamic stability is assured if the zeroth-order term of the quadratic polynomial is greater than zero. The coding below, calculates the zeroth-order coefficient over a range of velocities (vx) from 1-100 m/s and plots them on a semi-logarithmic scale.

The program also calculates the amount of slip angle present from the lateral (y) aerodynamic force generated by the sidecar body asymmetry (alpha2) and the slip angle (alpha) present due to moments created around the vertical axis at the centre of mass due to asymmetrical aerodynamic drag, drive, and rolling resistance forces and plots these angles versus velocity (vx) from 1-100 m/s.

The program also calculates the slip angle at velocities (vx) between 1-100 m/s with small steering angles (delta) from 0 to -0.6 degrees in order to determine the amount of steering correction the rider must apply to maintain a straight-ahead path.

Code

```
% === sidecar dynamics ===
%This program calculates the dynamic stability of a sidecar vehicle and
%also calculates the slip angle (alpha) and required steer angle
%(delta)required to overcome the asymmetry.

clc; close all;clear all;

%Variables defined
global m I vx Nf Ns Nr lr ls lf wr ws wf lp a b d1 d2 d3 d4 rho Cd A Cy
global Calpha1 Calpha2 Calpha3 Fdrive Crit1
global Crrf Crrr Crrs wp L D Fr Fs Ff W AT BT  Asemconst
global Ly alpha alpha2 delta Frear
global alphaA alphaB alphaC alphaD alphaE alphaF alphaG alphaH alphaI
global alphaJ

% === parameters ===
m = 600; %kg total mass
I = 625.83; % Moment of Inertia


Nf=1569; % measured normal force at front tire in N
```

```
Ns=1706; % measured normal force at side tire in N
Nr=2609; % measured normal force at rear tire in N

W=Nf+Ns+Nr; %Total weight in N

lr=0.752; % longitudinal distance from CG to rear tire in m
ls=0.162; % longitudinal distance from CG to side tire in m
lf=1.42;  % longitudinal distance from CG to front tire in m

L=lf+lr; %Length of the wheelbase
wr=0.31; % lateral distance from CG to rear tire in m
ws=0.753; % lateral distance from CG to side tire in m
wf=0.31; % lateral distance from CG to front tire in m

lp=0.988; % longitudinal distance from CG to CP in m
wp=0.5; % lateral distance from CG to CP in m

%stepping part
deltavx=1.0;
nsteps=100;
vx(1)=1;

% aerodynamic quantities
rho=1.225;
Cd=0.341;
A=1.01;
Cy=0.115;

% lateral coefficient

AT=0.8993; % Formula One radial tire cornering stiffness (from literature)
BT=.0001; % Formula One radial tire cornering stiffness (from literature)
Calpha1=((AT-BT*Nf)*Nf)*57.3; % N/rad; cornering coeff front tire (rad)
Calpha2=((AT-BT*Nr)*Nr)*57.3; % N/rad; cornering coeff rear tire (rad)
Calpha3=((AT-BT*Ns)*Ns)*57.3; % N/rad; cornering coeff sidecar tire (rad)



% input angles
delta=.10; % steer angle in radians starting point

for i=2:nsteps
    vx(i)=vx(i-1)+deltavx;%step the velocity from 0 to 100 m/s

    % calculate aerodynamic forces

Ly(i)=Cy*A/2*rho*vx(i)^2;
D(i)=Cd*A/2*rho*vx(i)^2;

Frear(i)=-0.4516*(vx(i)^2)+10.715*vx(i)+1100; %Force  at rear wheel

% rolling resistance coefficient constants (depend upon surface)
a=0.01; %for pavement
b=0.00001; %for pavement
```

```
%Rolling resistance coefficients
Crrf(i)=(a+b*vx(i));
Crrr(i)=(a+b*vx(i));
Crrs(i)=(a+b*vx(i));

% rolling resistance forces
Fr(i)=Crrr(i)*Nr;
Fs(i)=Crrs(i)*Ns;
Ff(i)=Crrf(i)*Nf;

Fdrive(i)=Frear(i)+Fr(i)+Fs(i)+Ff(i)+D(i); % summary of drive forces at
%rear wheel

%coefficients for Eq of Motion
d1(i)=(Calpha1+Calpha2+Calpha3)/vx(i);
d2(i)=((lf*Calpha1-lr*Calpha2-ls*Calpha3)/vx(i))+(m*vx(i));
d3(i)=(lf*Calpha1-lr*Calpha2-ls*Calpha3)/vx(i);
d4(i)=((lf^2)*Calpha1+(lr^2)*Calpha2+(ls^2)*Calpha3)/vx(i);

Crit1(i)=((d1(i)*d4(i))-(d2(i)*d3(i)))/(I*m); %Criteria for stability must
%be greater than zero

%Now for the asymmetrical part
Asemconst(i)=[-(Fdrive(i)*wr)-(D(i)*wp)+Crrf(i)*Nf*wf+Crrr(i)*Nr*wr-...
    Crrs(i)*Ns*ws];

alpha(i)=(Asemconst(i)/(-lf*Calpha1+lr*Calpha2+ls*Calpha3))*53.7;
%Slip angle caused by longitudinal asymmetrical
%forces causing a moment around the CG

alpha2(i)=((Ly(i))/(Calpha1+Calpha2+Calpha3))*53.7;
%Slip angle caused by asymmetrical lateral force (aero)

%adding in small negative steer angles to counter asymmetrical slip angle
alphaA(i)=[(((Asemconst(i)+((.1/53.7)*lf*Calpha1)))/...
    (-lf*Calpha1+lr*Calpha2+ls*Calpha3))*53.7];
alphaB(i)=[(((Asemconst(i)+((.2/53.7)*lf*Calpha1)))/...
    (-lf*Calpha1+lr*Calpha2+ls*Calpha3))*53.7];
alphaC(i)=[(((Asemconst(i)+((.3/53.7)*lf*Calpha1)))/...
    (-lf*Calpha1+lr*Calpha2+ls*Calpha3))*53.7];
alphaD(i)=[(((Asemconst(i)+((.4/53.7)*lf*Calpha1)))/...
    (-lf*Calpha1+lr*Calpha2+ls*Calpha3))*53.7];
alphaE(i)=[(((Asemconst(i)+((.5/53.7)*lf*Calpha1)))/...
    (-lf*Calpha1+lr*Calpha2+ls*Calpha3))*53.7];
alphaF(i)=[(((Asemconst(i)+((.6/53.7)*lf*Calpha1)))/...
    (-lf*Calpha1+lr*Calpha2+ls*Calpha3))*53.7];
alphaG(i)=[(((Asemconst(i)+((.7/53.7)*lf*Calpha1)))/...
    (-lf*Calpha1+lr*Calpha2+ls*Calpha3))*53.7];
alphaH(i)=[(((Asemconst(i)+((.8/53.7)*lf*Calpha1)))/...
    (-lf*Calpha1+lr*Calpha2+ls*Calpha3))*53.7];
alphaI(i)=[(((Asemconst(i)+((.9/53.7)*lf*Calpha1)))/...
    (-lf*Calpha1+lr*Calpha2+ls*Calpha3))*53.7];
alphaJ(i)=[(((Asemconst(i)+((1.0/53.7)*lf*Calpha1)))/...
    (-lf*Calpha1+lr*Calpha2+ls*Calpha3))*53.7];
```

```
%end of the iterations
end

figure(1)
%plot y axis in log scale
semilogy(vx(2:nsteps),(Crit1(2:nsteps)));
xlabel('velocity (m/s)');
ylabel('Stability Criteria (log)')
legend('Criteria1');

figure(2)
plot(vx(2:nsteps),alpha(2:nsteps),vx(2:nsteps),alpha2(2:nsteps));
xlabel('velocity (m/s)');
ylabel('slip angle in degrees');
legend('alpha','alpha2');

figure(3)
plot(vx(2:nsteps),alpha(2:nsteps),vx(2:nsteps),alphaA(2:nsteps),...
    vx(2:nsteps),alphaB(2:nsteps),vx(2:nsteps),alphaC(2:nsteps),...
    vx(2:nsteps),alphaD(2:nsteps),vx(2:nsteps),alphaE(2:nsteps),...
    vx(2:nsteps),alphaF(2:nsteps));
xlabel('velocity (m/s)');
ylabel('slip angle in degrees');
legend('Delta=0 degrees','Delta=0.1 degrees','Delta=0.2 degrees',...
    'Delta=0.3 degrees','Delta=0.4 degrees','Delta=0.5 degrees',...
    'Delta=0.6 degrees');



%End of the program
%EOF
```

APPENDIX ECENTRE OF MASS

Overview

Knowing the position of centre of mass of a vehicle is useful. It can be used to calculate vehicle dynamic stability and, when compared to the longitudinal position of the centre of aerodynamic pressure can be an indicator of aerodynamic yaw stability.

For a three-wheel asymmetrical vehicle, calculating the longitudinal and lateral horizontal position of the centre of mass requires information on the distances between the wheels and the weight on each wheel.

Longitudinal calculation

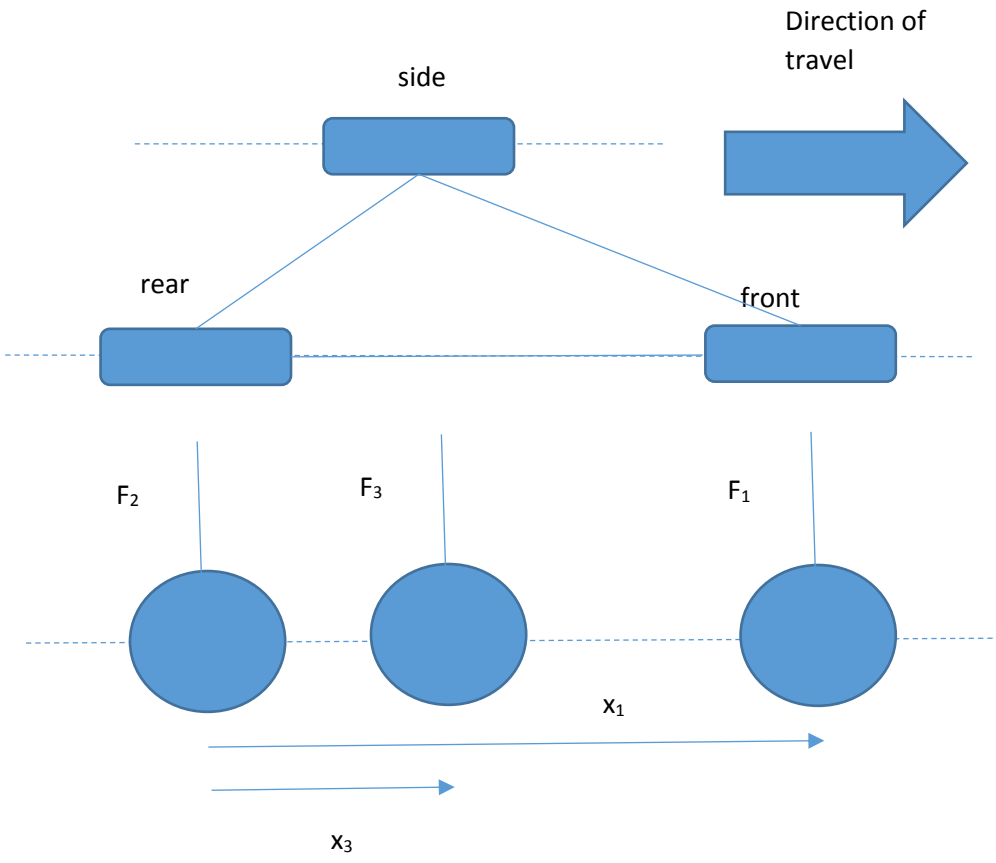

Figure E.1- Layout of sidecar for longitudinal centre of mass calculation

x_1 = 2.180 m

x_3 = 0.590 m

F_1 = 1569 N

F_2 = 2609 N

F_3 = 1706 N

$$x_G = \frac{F_1\, x_1 + F_2\, x_2 + F_3\, x_3}{\Sigma F_i}$$

$$x_G = \frac{(1569)(2.18) + (2609)(0) + (1706)(0.590)}{1569 + 2609 + 1706}$$

x_G = 0.752 m

Recall from Chapter 7, l_1 is the distance from the centre of mass to the axis of the front wheel, l_2 is the distance from the centre of mass to the axis of the rear wheel and l_3 is the distance from the centre of mass to the axis of the sidecar wheel. Using x_G, the distance from the centre of mass to the rear wheel axis, l_1, l_2 and l_3 can be calculated as:

$l_1 = x_1 - x_g = 2.18 - 0.752 = 1.428$ m

$l_2 = x_g = 0.752$ m

$l_3 = x_3 - x_g = 0.590 - 0.752 = 0.162$ m

Lateral Calculation

In a similar manner, as above for the longitudinal position of the centre of mass, the lateral (y-axis) position can be located with the help of Figure E.2.

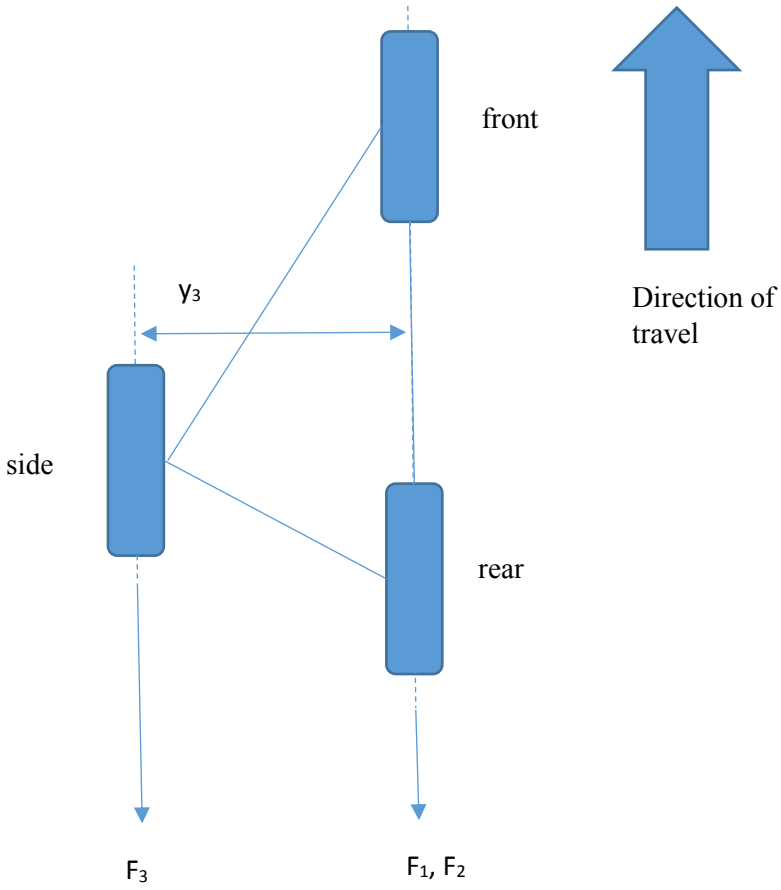

Figure E.1- Layout of sidecar for lateral centre of mass calculation

The distance y_3 from the axis between the front and rear wheels and the centre of the sidecar wheel is equal to 1.06 m. The lateral location of the centre of mass, relative to the axis between the front and rear wheels is given by:

$$y_g = \frac{(F_1 + F_2)(0) + (y_3)(F_3)}{\Sigma F_i}$$

$$y_g = \frac{(1569+2609)(0) + (1.06)1706}{1706+2609+1569}$$

$$y_g = 0.307 \text{ m}$$

From Chapter 7, w1 and w2 are the distance from the front and rear wheels to the centre of mass (in a negative y direction) and w3 is the distance from the centre of mass to the sidecar wheel (in a negative y direction).

In the case depicted in Figure E.2,

$w_1 = w_2 = 0.307$ m

$w_3 = y_3 – y_g = 1.06 – 0.307 = 0.753$ m

Vertical calculation

Calculating the vertical location of the centre of mass is much more complicated than locating the longitudinal and lateral locations. Typical methods involve tipping the vehicle through a known angle and measuring the load at each wheel. Through the application of trigonometry, the vertical position of the centre of mass is calculated. Because the exact vertical position of the centre of mass is not important for any of the calculations in this work, its position is estimated to be approximately equal to one half the height of the sidecar, or $z_g = 0.31$ m above the ground surface. This is reasonable as most of the sidecar mass is centred around a horizontal plane located at that height.